Research Topics

Natural and nature-based features for flood risk management

Edited by
Jane McKee Smith, Tori Tomiczek, Brian C. McFall and Jens Figlus

Published in
Frontiers in Built Environment

ISSN 1664-8714
ISBN 978-2-83252-181-6
DOI 10.3389/978-2-83252-181-6

About Frontiers

Frontiers is more than just an open access publisher of scholarly articles: it is a pioneering approach to the world of academia, radically improving the way scholarly research is managed. The grand vision of Frontiers is a world where all people have an equal opportunity to seek, share and generate knowledge. Frontiers provides immediate and permanent online open access to all its publications, but this alone is not enough to realize our grand goals.

Frontiers journal series

The Frontiers journal series is a multi-tier and interdisciplinary set of open-access, online journals, promising a paradigm shift from the current review, selection and dissemination processes in academic publishing. All Frontiers journals are driven by researchers for researchers; therefore, they constitute a service to the scholarly community. At the same time, the *Frontiers journal series* operates on a revolutionary invention, the tiered publishing system, initially addressing specific communities of scholars, and gradually climbing up to broader public understanding, thus serving the interests of the lay society, too.

Dedication to quality

Each Frontiers article is a landmark of the highest quality, thanks to genuinely collaborative interactions between authors and review editors, who include some of the world's best academicians. Research must be certified by peers before entering a stream of knowledge that may eventually reach the public - and shape society; therefore, Frontiers only applies the most rigorous and unbiased reviews. Frontiers revolutionizes research publishing by freely delivering the most outstanding research, evaluated with no bias from both the academic and social point of view. By applying the most advanced information technologies, Frontiers is catapulting scholarly publishing into a new generation.

What are Frontiers Research Topics?

Frontiers Research Topics are very popular trademarks of the *Frontiers journals series*: they are collections of at least ten articles, all centered on a particular subject. With their unique mix of varied contributions from Original Research to Review Articles, Frontiers Research Topics unify the most influential researchers, the latest key findings and historical advances in a hot research area.

Find out more on how to host your own Frontiers Research Topic or contribute to one as an author by contacting the Frontiers editorial office: frontiersin.org/about/contact

Natural and nature-based features for flood risk management

Topic editors
Jane McKee Smith — Engineer Research and Development Center (ERDC), United States
Tori Tomiczek — United States Naval Academy, United States
Brian C. McFall — Coastal and Hydraulics Laboratory, U.S. Army Engineer Research and Development Center, United States
Jens Figlus — Texas A&M University, United States

Citation
Smith, J. M., Tomiczek, T., McFall, B. C., Figlus, J., eds. (2023). *Natural and nature-based features for flood risk management*. Lausanne: Frontiers Media SA. doi: 10.3389/978-2-83252-181-6

Table of contents

Frontiers in Built Environment

TYPE Editorial
PUBLISHED 10 January 2023
DOI 10.3389/fbuil.2022.1128508

OPEN ACCESS

EDITED AND REVIEWED BY
Barbara Zanuttigh,
University of Bologna, Italy

*CORRESPONDENCE
J. Figlus,
figlusj@tamu.edu

SPECIALTY SECTION
This article was submitted to Coastal and Offshore Engineering,
a section of the journal
Frontiers in Built Environment

RECEIVED 20 December 2022
ACCEPTED 28 December 2022
PUBLISHED 10 January 2023

CITATION
Figlus J, Smith JM, Tomiczek T and McFall BC (2023), Editorial: Natural and nature-based features for flood risk management.
Front. Built Environ. 8:1128508.
doi: 10.3389/fbuil.2022.1128508

Editorial: Natural and nature-based features for flood risk management

J. Figlus[1]*, J. M. Smith[2,3], T. Tomiczek[4] and B. C. McFall[5]

[1]Department of Ocean Engineering, Texas A&M University, College Station, TX, United States, [2]Engineer Research and Development Center (ERDC), Vicksburg, MS, United States, [3]Department of Civil and Coastal Engineering, University of Florida, Gainesville, FL, United States, [4]United States Naval Academy, Annapolis, MD, United States, [5]Coastal and Hydraulics Laboratory, Engineer Research and Development Center (ERDC), Vicksburg, MS, United States

KEYWORDS

coastal flooding, risk reduction, engineering, nature-based interventions, infrastructure

Editorial on the Research Topic
Natural and nature-based features for flood risk management

Introduction

Flood risk mitigation and management are among the great societal challenges of our time. Around the world humans, communities, infrastructure, and ecosystems in coastal areas are facing the reality of rising sea levels, intensifying storm impacts, accelerated erosion, and the resulting flood-related problems such as loss of life, loss of property, and loss of economic, social and environmental sustainability. At the same time the ever-present push for economic development of coastal regions through enhanced maritime trade, increased number of industrial and residential assets, and population growth in many coastal counties leads to heightened risk from the impact of flooding. Natural and nature-based features (NNBF) offer a strategy for mitigating and managing coastal flood risk by harnessing the inherent ability of nature and natural processes to adapt and evolve under changing conditions. The idea is to utilize NNBF either exclusively, alongside traditional ("gray") flood risk mitigation measures (such as seawalls, levees, etc.), or, ideally, in symbiosis with traditional flood risk mitigation strategies to create resilient, adaptive, and ecosystem-enhancing solutions that can improve the viability, beauty, and success of our coastal systems in a changing climate. While the topic addressed here is approached primarily from an engineering and scientific perspective, meaningful NNBF solutions for flood risk reduction require multidisciplinary collaborations beyond creative science and engineering innovations that include socio-economic and policy aspects. However, before NNBF can become one of the go-to tools for flood risk management, a detailed understanding of their mechanics under forcing conditions, evolution over time, and acceptance by designers, planners, and society is required. Therefore, fundamental and applied research on NNBF topics is now more relevant and important than ever.

The collection of 16 articles featured as part of this Research Topic addresses a variety of advances related to flood risk reduction *via* NNBF that will be critical as we move forward in making nature and natural processes an essential component in the design of systems intended to limit the impact of flooding to society. The original research articles as well as case-study reviews and engineering design framework creation provide a well-balanced mix of relevant fundamental knowledge dissemination and actionable science and engineering advances applicable to real-life

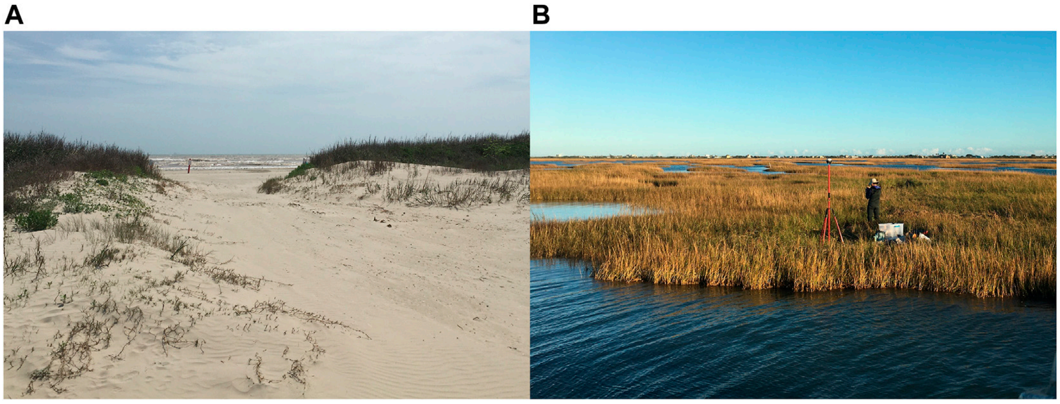

FIGURE 1
Engineered vegetated dune with cut for beach access **(A)** and researcher surveying a wetland system **(B)** as part of a scientific study on NNBF. The location of both photos is Galveston, Texas.

problem solving and coastal management. The specific NNBF addressed in this collection of articles include oyster castle breakwaters, coir logs, beach wrack material, sand trapping fences, sand spits and tidal lagoons, floating vegetated canopies, salt marshes, vegetated dune systems, mangroves, wetland vegetation, and emergent vegetation in general. An engineered vegetated dune and a wetland system, respectively, are depicted in Figure 1. Forcing mechanisms impacting the NNBF range from coastal storm waves and water level fluctuations to wind and ship wake dynamics, and several articles incorporate climate change-induced sea level rise scenarios. In this Research Topic, methodologies to advance NNBF knowledge include detailed field case study analyses, medium to large-scale physical model experiments in wave flumes and basins, as well as numerical model simulations compared to field or laboratory data to better understand NNBF utilization for erosion and flood risk mitigation. The key concepts addressed by the various authors are synthesized in the following, and contributions are placed into broader context.

Field case studies

Detailed field studies on NNBF are essential to better understand how these systems behave under real-life, full-scale conditions and varying forcing mechanisms, as well as their impacts on the environment. The field scale also encourages engagement with a variety of stakeholders and allows for assessment of the multiple benefits that projects using NNBF produce. Palinkas et al. particularly focus on the implementation, remaining challenges, and multiple benefit aspects of three coastal restoration case studies using NNBF features across geographical locations that cover the East, Gulf, and West Coasts of the United States. This case study summary sends the clear message that successful projects require a well-designed monitoring approach and an emphasis on stakeholder engagement. Creative sediment management is a major component in many NNBF systems with the aim to preserve habitat, protect against storm impacts and sea level rise, as well as to maintain navigability of coastal waterways. An example of how sand spit and tidal lagoon multifunctionality is enhanced through NNBF is presented by Dabees et al. for a case in Florida where enhanced resiliency of the overall system is a key element. Bredes et al. looked at oyster castle breakwater systems in an extensive field study along the New Jersey coastline and found that under certain conditions when these breakwaters are submerged during high water events they actually produce significant amplification of wave heights in their lee compared to attenuation when their crests are emergent. Salatin et al. investigated these data numerically. Findings like this are important to consider in the design of future living breakwater systems to avoid detrimental effects to adjacent shorelines. Impacts of extreme events on systems containing NNBF and subsequent recovery are important pieces of the puzzle when trying to understand overall system performance. The work presented by Cadigan et al. highlights differences between shoreline responses to multiple hurricanes along the southwest Louisiana coastline with and without breakwater protection. Provost et al. conducted a field study investigating the effect of wrack material washed up on the beach to help build up engineered dunes which has implications for how this naturally occurring material should be managed. NNBF are not only used to increase resilience of coastal systems from natural hazards, but have also been successfully employed to protect against vessel-induced wave energy near high marine traffic areas as investigated by Everett et al. for coir logs placed on an estuarine shoreline along the Delaware River.

Physical model experiments

While field case studies play an essential role in our understanding of NNBF performance, oftentimes it is necessary to investigate certain features in a controlled laboratory setting to isolate forcing conditions and create repeatable scenarios. Such studies allow for the identification of effects of individual parameters, investigation of trends in hydraulic response, and validation of numerical models which can then be extrapolated to a broader range of conditions. Eichmanns and Schüttrumpf quantified the aeolian sediment trapping efficiency of sand fences under various configurations in a detailed wind tunnel study. Vegetated nearshore systems fronting urban areas or coastal protection structures have been investigated for their wave energy attenuating properties. Different floating vegetated mat configurations were analyzed by Hopkins et al. in a large scale wave basin facility whereas Baker et al. conducted scaled basin tests on the effectiveness of marsh vegetation in reducing wave energy in front of a dike. The effect of various above- and below-ground dune vegetation characteristics on dune erosion were quantified in a wave flume study by Figlus et al. where real sediment and live plants at different stages of growth in a dune were subjected to storm wave forcing.

Numerical modeling

It is crucial to continue to enhance our numerical modeling capabilities to better simulate NNBF behavior under various environmental loading conditions. This is often done by calibrating or modifying existing numerical models based on field and laboratory data to advance understanding of NNBF and their use in flood and erosion risk mitigation. Mori et al. parameterized the structure of mangrove roots for optimized use in numerical modeling efforts whereas Abdolali et al. implemented wave-vegetation interaction capabilities into a spectral wave model to compute wave attenuation by spatially variable wetland vegetation fields. The work by Salatin et al. using Boussinesq-type wave modeling highlighted that complex nearshore wave transformations and wave interactions with oyster breakwaters need to be simulated carefully to avoid design situations where leeward wave energy is amplified by the NNBF (see also Bredes et al.) or other unintended consequences occur. The performance of NNBF under catastrophic events such as tsunamis is a topic that has also received increasing attention recently. To that end, von Häfen et al. improved a numerical multi-phase computational fluid dynamics model dealing with dam-break waves to simulate tsunami propagation over composite bathymetry. Huff et al. explored the utility of the Delft3D model suite to aid coastal managers assess various living shoreline and NNBF design alternatives for construction in a Texas bay system.

Engineering framework for use of NNBF

NNBF are poised to take a prominent place in designing flood risk reduction measures with a growing body of research and project experience supporting their development. For the case of emergent vegetation systems, Ostrow et al. synthesized the current state of practice and the still existing barriers to implementation. They also suggested that the knowledge on NNBF incorporating emergent vegetation is already sufficient for adequate design solutions and proposed a framework to assess such designs based on wave attenuation performance.

As we continue the work on NNBF for flood risk reduction and encourage the reader to browse the mentioned articles, we would like to take this opportunity to thank all contributing authors, research funding agencies, reviewers, and editors for their help in making this collection of knowledge advances on natural and nature-based features for flood risk management a success. The featured works will certainly spur further advances in this field and contribute to a future where we strive to be conscious stewards of the coastal systems that mean so much to all of us.

Author contributions

JF, JS, TT, and BM wrote and edited this editorial.

Conflict of interest

The authors declare that the research was conducted in the absence of any commercial or financial relationships that could be construed as a potential conflict of interest.

Publisher's note

frontiers
in Built Environment

ORIGINAL RESEARCH
published: 04 January 2022
doi: 10.3389/fbuil.2021.782219

Parameterization of Mangrove Root Structure of *Rhizophora stylosa* in Coastal Hydrodynamic Model

Nobuhito Mori[1,2]*, Che-Wei Chang[1], Tomomi Inoue[3], Yasuaki Akaji[3], Ko Hinokidani[4], Shigeyuki Baba[5], Masashi Takagi[6], Sotaro Mori[6], Hironoshin Koike[6], Miho Miyauchi[6], Ryosuke Suganuma[6], Audrius Sabunas[6], Takuya Miyashita[1] and Tomoya Shimura[1]

[1]Disaster Prevention Research Institute, Kyoto University, Kyoto, Japan, [2]Graduate School of Engineering, Swansea University, Swansea, United Kingdom, [3]National Institute for Environmental Studies, Tsukuba, Japan, [4]Graduate School of Agriculture, Tokyo University of Agriculture, Tokyo, Japan, [5]International Society for Mangrove Ecosystems, Okinawa, Japan, [6]Graduate School of Engineering, Kyoto University, Kyoto, Japan

OPEN ACCESS

Edited by:
Tori Tomiczek,
United States Naval Academy,
United States

Reviewed by:
Reza Marsooli,
Stevens Institute of Technology,
United States
Edgar Mendoza,
National Autonomous University of
Mexico, Mexico

***Correspondence:**
Nobuhito Mori
mori@oceanwave.jp

Specialty section:
This article was submitted to
Coastal and Offshore Engineering,
a section of the journal
Frontiers in Built Environment

Received: *24 September 2021*
Accepted: *06 December 2021*
Published: *04 January 2022*

Citation:
Mori N, Chang C-W, Inoue T, Akaji Y, Hinokidani K, Baba S, Takagi M, Mori S, Koike H, Miyauchi M, Suganuma R, Sabunas A, Miyashita T and Shimura T (2022) Parameterization of Mangrove Root Structure of Rhizophora stylosa *in Coastal Hydrodynamic Model.*
Front. Built Environ. 7:782219.
doi: 10.3389/fbuil.2021.782219

Mangroves are able to attenuate tsunamis, storm surges, and waves. Their protective function against wave disasters is gaining increasing attention as a typical example of the green infrastructure/Eco-DRR (Ecosystem-based Disaster Risk Reduction) in coastal regions. Hydrodynamic models commonly employed additional friction or a drag forcing term to represent mangrove-induced energy dissipation for simplicity. The well-known Morison-type formula (Morison et al. 1950) has been considered appropriate to model vegetation-induced resistance in which the information of the geometric properties of mangroves, including the root system, is needed. However, idealized vegetation configurations mainly were applied in the existing numerical models, and only a few field observations provided the empirical parameterization of the complex mangrove root structures. In this study, we conducted field surveys on the Iriomote Island of Okinawa, Japan, and Tarawa, Kiribati. We measured the representative parameters for the geometric properties of mangroves, *Rhizophora stylosa,* and their root system. By analyzing the data, significant correlations for hydrodynamic modeling were found among the key parameters such as the trunk diameter at breast height (*DBH*), the tree height *H*, the height of prop roots, and the projected areas of the root system. We also discussed the correlation of these representative factors with the tree age. These empirical relationships are summarized for numerical modeling at the end.

Keywords: mangrove, prop roots, *Rhizophora stylosa*, root structure, parameterization

INTRODUCTION

Green infrastructure, known as ecosystem-based disaster risk reduction (Eco-DRR), has become popular in the context of coastal flooding reduction following the *Intergovernmental Panel on Climate Change Fifth Assessment Report*, AR5 (Intergovernmental Panel on Climate Change (IPCC) Fifth Assessment Report—Working Group II, 2014) and the *Sendai Framework for Disaster Risk Reduction* 2015–2030 (UNISDR,2015). Its cost-efficiency, capability, and sustainability of adapting to changing climate have been drawing attention worldwide (e.g., Sutton-Grier et al., 2015; Guannel et al., 2016; Reguero et al., 2018).

As natural barriers against coastal hazards, green infrastructures primarily regard coastal dunes, sandy beaches, coastal forests, mangroves, coral reefs, and wetlands. Coastal trees and mangroves are recognized for their protective function in terms of the reduction of wave/hydrodynamic energy during extreme events (e.g., storm waves, surges, and tsunamis). Based on several reports of the 2011 Tohoku Earthquake Tsunami (e.g., Tanaka 2012), coastal pines can be critical in attenuating wave energy under small-to medium-sized tsunamis. Another major type of coastal vegetation, mangroves were identified as useful buffers in the tropics and subtropics during the 2004 Indian Ocean Earthquake Tsunami (e.g., Danielsen et al., 2005) and other major natural disasters (e.g., Goda et al., 2019). In addition to their protective function against coastal disasters, afforestation and reforestation of mangroves have been adopted in Southeast Asia and the Pacific islands to improve the capacity for carbon storage and environmental recovery as a measure of climate change mitigation. Despite the findings in simplified analytical and numerical modeling of wave attenuation based on the other vegetation study, the current scientific knowledge and modeling tools to assess the effectiveness of mangroves are relatively limited considering the realistic shape of mangroves (e.g., Chang and Mori 2021). Generally, a forcing term in the Euler equation or shallow-water equation is used to account for the energy dissipation by vegetation in various studies (e.g., Dalrymple et al., 1984; Mendez and Losada 2004; Mazda et al., 2005). The vegetation effects were integrated as enhanced bottom friction in some studies (e.g., Augustin et al., 2009; Yang et al., 2015), while the Morison-type formula (Morison et al., 1950) has recently been considered more straightforward to parameterize vegetation-induced resistance (e.g., Huang et al., 2011; Chakrabarti et al., 2017; Alagan Chella et al., 2020).

Despite the development of numerical models, idealized vegetation conditions (e.g., cylinders) or bottom friction was mostly applied in the models mentioned above, indicating an over-simplification of the structural complexity of mangrove root systems. The complex root system of mangroves reduces flow velocity and dissipate wave energy (e.g., Tanaka et al., 2007; Zhang et al., 2015) and is necessary to be well addressed in numerical modeling. Based on the Morison-type formula, the general expression of vegetation-induced force $\boldsymbol{R}_{vg}$ can be written as a summation of the drag force and the inertia force:

$$\boldsymbol{R}_{vg} = \frac{1}{2(\eta + h)} C_{\mathrm{D}} \int_{-h}^{\eta} \boldsymbol{u}|\boldsymbol{u}| d\boldsymbol{A}(z) + \frac{1}{(\eta + h)} C_{\mathrm{M}} \int_{-h}^{\eta} \frac{\partial \boldsymbol{u}}{\partial t} d\boldsymbol{V}(z) \quad (1)$$

where η represents the free surface elevation, h the water depth, $\boldsymbol{u}(z)$ the fluid velocity, and C_{D} and C_{M} the drag and inertia coefficients, respectively. The vertical variation of the frontal area and the submerged volume of mangroves are included in $\boldsymbol{A}(z)$ and $\boldsymbol{V}(z)$ of **Eq. 1**. The effects of mangroves can be modeled in terms of C_{D}, C_{M}, $\boldsymbol{A}(z)$, and $\boldsymbol{V}(z)$, which are all related to mangrove structure (morphology). A recent experimental study (Chang et al., 2019) reproduced the root structures of a specific mangrove by using 3D scanned and 3D-printed tree models in laboratory tests. With direct measurements of wave forces exerted on tree models, the empirical formulas to estimate the force coefficients (C_{D} and C_{M}) were proposed. As indicated in Zhang et al. (2015) and Chang et al. (2019), proper parameterization, including the complex structure of mangrove roots based on field conditions, is needed to quantify better mangrove effects on wave attenuation in the development of numerical models. However, there are very limited mangrove structure data that are related to hydrodynamic models, such as **Eq. 1** and the others.

The *Genus Rhizophora* consists of seven species (Tomlinson 2016) and are widely distributed along tropical and subtropical coastlines (Duke 2006). They are also common species used for mangrove afforestation and reforestation. As *Rhizophora* species have complex bifurcated and looping structures (so-called prop root system), several researchers conducted field surveys on *Rhizophora* species for root structure (e.g., Ohira et al., 2013; Mendez-Alonzo et al., 2015). They examined the parameterization of mangrove root structures (e.g., the relationship between tree height and the trunk diameter at breast height) to understand their shape characteristics. Besides biological interests, parametrization of trunk shape is quite essential for wave attenuation. Ohira et al. (2013) measured the trunk shapes and estimated the hydraulic resistance in tsunami inundation simulations. Based on their proposed relations, the projected area and submerged volume of mangrove roots can be calculated and used in numerical computations. However, their target was large and older trees, and the variation of shape parameters associated with the tree age was not discussed in their study, which is not enough for the model application targeting early to middle term of afforestation and reforestation. The biological and physical characteristics (e.g., Komiyama et al., 2008) in addition to the structural properties, should be well addressed in the future development of numerical models when considering the impact of changing climate under a longer time scale.

In this study, we conducted field surveys to collect the fundamental characteristics of mangrove tree shape by focusing on the *Rhizophora* species. Based on the field data analysis, the relationships among different geometric diameters and the tree age are examined, although the available field data is limited. The parameterization of the shape of *Rhizophora* species is proposed for the future development of coastal wave models. In the following, the outline of the field surveys and the data processing procedures are provided in *Outline of Field Survey and Measurements*. The parameterization of mangrove root structure is presented in *Results and Discussions*. Finally, the results of the current study are summarized in *Summary*.

OUTLINE OF FIELD SURVEY AND MEASUREMENTS

Survey Areas

Two sets of field surveys were conducted in 2019 and 2020 to investigate mangrove root structure. The field sites included natural mangrove forests in the Iriomote Island of Okinawa, Japan, and a planted mangrove area in Tarawa, Kiribati.

Iriomote Island, one of the Yaeyama Islands in Okinawa Prefecture, Japan, is a subtropical island located in the Northwest Pacific Ocean, as shown in the upper panel in **Supplementary Figure S1**. As a part of the Ryukyu Islands Archipelago, Iriomote Island is mountainous (highest altitude: 470 m) with 29 rivers culminating in the coast. The island is 290 km^2 in area, and the majority of its landmass is covered by natural forests, in which 85% is national forests. Mangrove forests are mainly located in the low-lying areas along the rivers with several species such as *Rhizophora stylosa* Griff. and *Bruguiera gymnorhiza* L. (Lam.) targeting one of the dominant species distributed in estuaries and tidal areas, *R. stylosa,* we conducted surveys on natural mangroves along the Urauchi River (the longest river in Iriomote), as shown in the **Supplementary Figure S1**. Natural mangroves in an estuary were selected for the measurements. The effect of waves is very limited in this area. Several isolated mangroves were picked for field measurements due to the difficulty of imaging measurements.

The other field site was Tarawa, Kiribati, a tropical island located in the Central Pacific Ocean (1°27′ N, 172°58′ E), as shown in the **Supplementary Figure S1**. Tarawa is an atoll comprising a long flat reef partially enclosing a shallow lagoon with a wide range of astronomical tides. It is 500 km^2 in area, and the highest altitude is 3 m. *R. stylosa* has been planted by the International Society for Mangrove Ecosystems (ISME) since 2005 for multiple purposes, such as environmental recovery, coastal protection, and environmental education. Each year around 7,000–11,000 propagules were planted uniformly with 50 cm as the tree spacing by the close group planting method (Baba, 2011) in the designated afforested patches. The afforestation areas are mainly located west of Bonriki in Tarawa with calm coastal environmental conditions to avoid exposure to severe wind waves and swells. The effect of waves is very limited due to geophysical effects in this area. Therefore, the afforested mangroves inside of the atoll were selected for the measurements. Thus, clear records can be obtained, including the date of afforestation, density, and others in this area. Comparing with natural forests, the afforested mangroves in Tarawa provided an ideal condition to investigate the relationship between mangrove root structure and the associated tree age (**Supplementary Figure S2**).

In both surveys, the fieldwork included the manual measurements of the representative parameters of mangrove root structure and the use of a 3D laser scanner for detailed root structures. In addition, the 2D projected visualization of mangrove root shapes was obtained by using a digital camera in Iriomote Island. As the 2D and 3D visualization measurements required space, we selected front trees of groups, but the basic tree characteristics (e.g., tree heights, DBH, or age) were measured both front and inside of trees in Tarawa. In this paper, we analyzed the field measurements and the 2D image visualization of mangrove root system structure. At the same time, the 3D scanned data will be presented in the forthcoming analysis along with further field surveys in future work.

Methodology

Firstly, we measured the characteristic geometry of mangrove structure, *R. stylosa*, in fields. As shown in **Figure 1**, the measured parameters included the tree height H and the trunk diameter at breast height (DBH), which refers to the measured diameter at 1.30 m above the ground. We also measured the trunk diameter at the top of the root system D_1 (equivalent to DBH for a shorter tree), the height of the root system H_{root}, and the spanning radius of the root system W (i.e., the distance from the tree trunk to the outermost root). Note that the spanning radius was measured in six major orientations whose average was used as characteristic W. The six orientations of spanning radius were combined major two axes plus four major roots. Furthermore, avoiding the difficulty of measurement, the diameter of individual roots was measured at 20 cm above the ground, and the number of prop roots N was recorded. Forty-two trees were picked for field measurements in Iriomote Island and four trees in Tarawa, Kiribati.

In addition to the measurements of the representative parameters of mangrove root structure, we collected the 2D

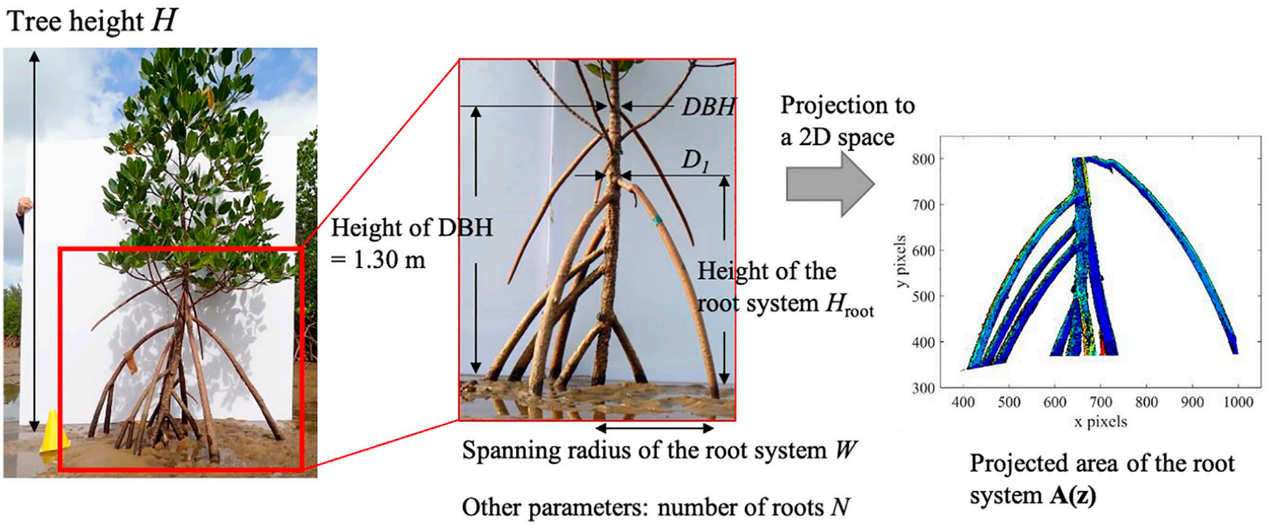

FIGURE 1 | Characteristic mangrove root morphology and the measured parameters in fields (red boxed area in the photo corresponds to the root system).

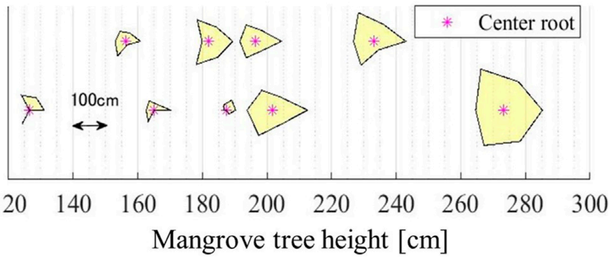

FIGURE 2 | Example of the relationship between tree height and the spanning width of the root system of *Rhizophora stylosa*.

images of mangrove roots using a digital camera (Olympus TG-6, 4,000 × 3,000 pixels) along with a whiteboard as the background (**Figure 1**). The 2D images were taken in two different directions in two major axes of the root system, and no image correction was applied due to the difficulty of the detail of calibration in the field. Following the previous studies (salt marsh by Lemein et al., 2015, mangrove by Maza et al., 2017), the projected area of the root system A_{root} can then be estimated by image processing as shown in **Supplementary Figure S2**. We summarize the procedures for image processing as follows.

1. Binarize the image using the threshold values of the RGB image.
2. Extract the outline of the root system from the binary image (left panel in **Supplementary Figure S3**).
3. Extract the root system from the RGB image in step 2 (right panel in **Supplementary Figure S3**).
4. Counting the number of pixels of the root system in step 3.
5. Convert pixel to length scale.

Note that step 2 focuses on the image analysis, excluding the outside area of the root system. Image preprocessing in steps 1 and 2 can reduce the misperception of the analysis. In some cases, sunlight may disturb the color intensity of the image; therefore, the effect was corrected in steps 2 and 3 manually. The counted

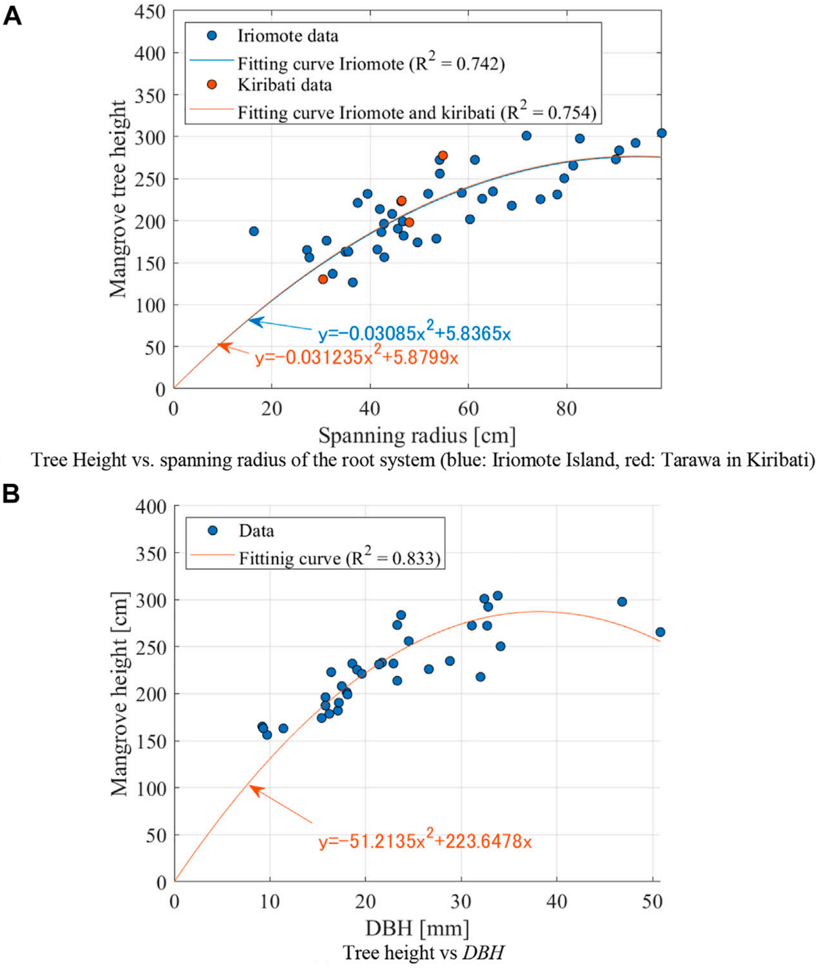

FIGURE 3 | Relationship of the tree height *H* with the spanning radius of the root system *W* and *DBH* (circles: measured data, solid lines: regression curve) (*Rhizophora stylosa*). **(A)** A^*_{root} vs *DBH*. **(B)** A^*_{root} vs H^*_{root}.

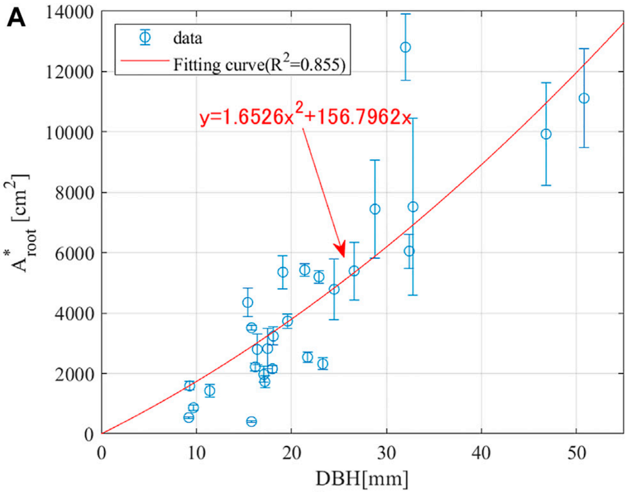

(a) A^*_{root} vs DBH

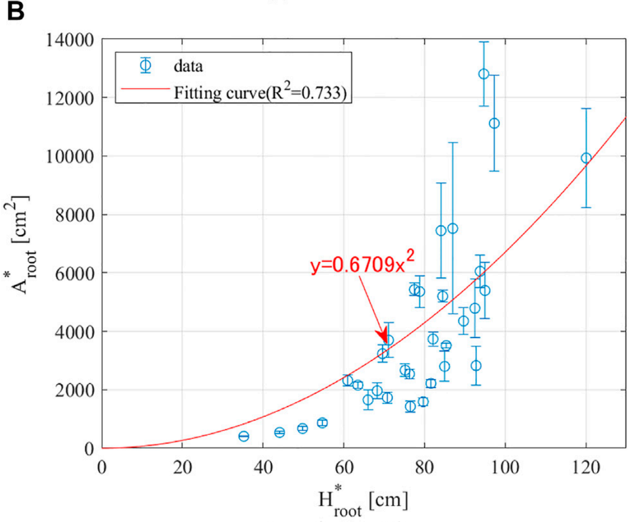

(b) A^*_{root} vs H^*_{root}

FIGURE 4 | Relationships of the projected areas of the root system A^*_{root} with DBH and the height of the root system H^*_{root} (circle: measured data, solid line: regression curve) (*Rhizophora stylosa*). Note that the error bars indicate the variation of frontal areas taken from different orientations (See *Methodology*).

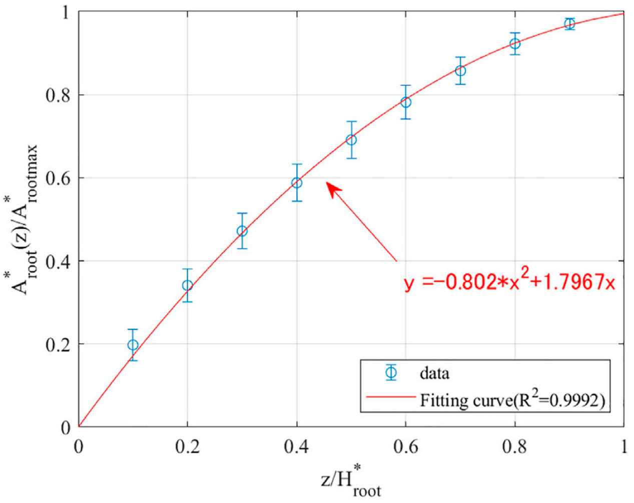

FIGURE 5 | Relationship between the normalized projected area of the root system A_{root} and the normalized distance z from the ground (circle: measured data, solid line: regression curve) (*Rhizophora stylosa*).

number of pixels was in the range 10,000–242,000, which is equivalent to approximately 300–3,700 cm^2. As the number of pixels was sufficient to capture the area of the root system, the accuracy of the estimated projected area was reliable for further discussions with other parameters.

RESULTS AND DISCUSSIONS

Relationships Among the Main Parameters of Mangrove Root Structure

We first examined the measured tree height and the main geometric parameters of the root system. Major three axes were analyzed by the 2D imaging following *Methodology*. In **Figure 2**, a proportional relationship can be seen between the tree height H and the spanning radius of the root system W. Asymmetric root system can also be observed for shorter trees (approximately <180 cm). These morphological characteristics of mangrove trees and root systems are discussed in this section. As the spanning radius of the root system varied in different orientations, the averaged value was applied hereafter.

Figure 3A shows the relationship between the tree height H and the spanning radius W by Iriomote Island and Tarawa with two empirical fitting formulas presented by blue and red solid lines, respectively. Note that zero intercepts were assumed when defining the empirical fitting formula. Obviously, these two parameters are highly correlated, as presented in **Figure 2**. Although the data in Tarawa is fewer than Iriomote Island, two different data in different locations show the quite similar relation for H and W. Next, the relationship between the tree height H and the trunk diameter at breast height DBH for Iriomote Island data with the empirical fitting formula is shown in **Figure 3B**. According to the measurements, the tree height increases linearly with smaller DBH (<25 mm) and tends to be convergent around 300 cm for larger DBH (>30 mm) within the measured DBH range (<50 mm). Note that the comparison with the results in Ohira et al., 2013 for *Rhizophora apiculata* Blume and *Rhizophora mucronata* Lam. with this dataset is quite similar but slightly higher tree height by the current parameterization for *R. stylosa*.

Secondly, we discussed some of the representative parameters of the root system. **Supplementary Figure S4** shows the proportional relationship between the height of the root system H_{root} and the number of prop roots N, which can be expected as a part of the natural growing process. Note that the height of the root system was estimated by analyzing the 2D images taken from different orientations (*Methodology*), and an averaged value (with an asterisk) is presented here. The results

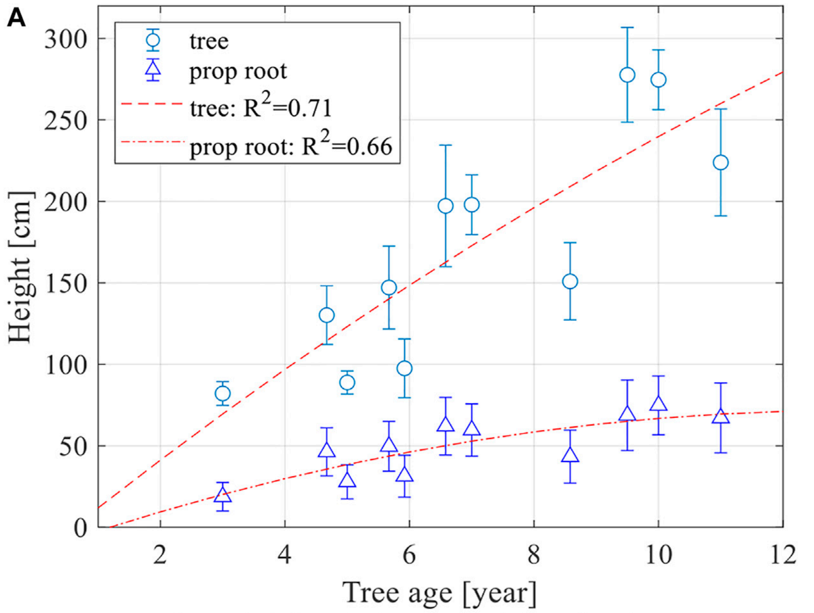

Tree and root height (circles: tree height, triangles: root height)

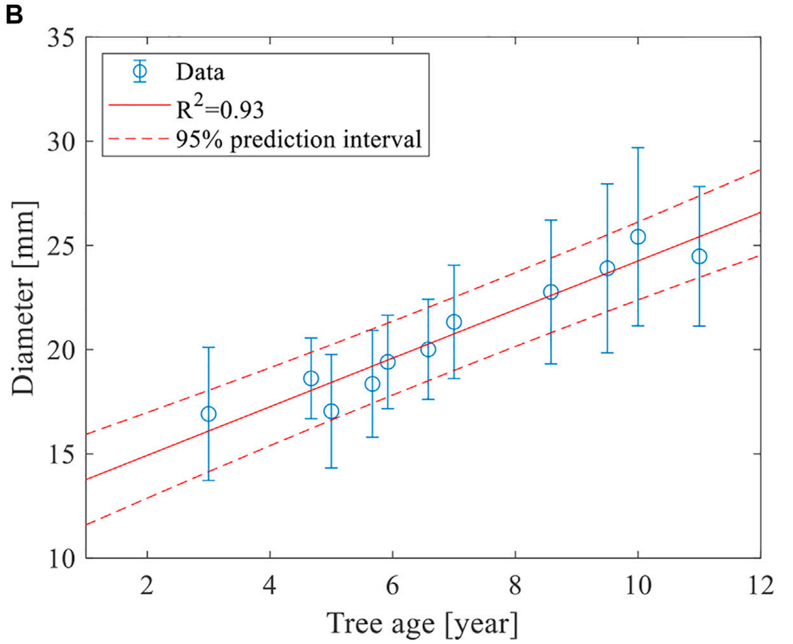

D_1 (solid lines: regression lines, dashed lines: confidential intervals)

FIGURE 6 | Growth curves of diameter D_1 and tree height H vs. tree age by Kiribati data (*Rhizophora stylosa*).

reported in Ohira et al., 2013 were also included in the same figure for comparison, although their target mangrove species are *R. apiculata* and *R. mucronata*.

In addition to the relationships among distinguishing factors of mangrove root structure, another objective of this study was to understand the intertwined connections between the aforementioned geometric parameters and the projected area of the root system, which is critical to establish the proper parameterization of mangrove effects as shown in **Eq. 1**. Therefore, we here present the projected area of the root system A^*_{root} and its relationships with two representative parameters of mangrove root structure—*DBH*, and H^*_{root}. In **Figure 4A**, the projected area A^*_{root} increases with *DBH*, in which *DBH* approximately ranges from 8 to 52 mm, monotonically. The projected area A^*_{root} against the height of the root system H^*_{root} can be found in **Figure 4B**, showing a quadratic proportional relationship. Both the relation of *DBH* and H^*_{root} to A^*_{root} shows quadric increases as their increase. It indicates the nonlinear increase

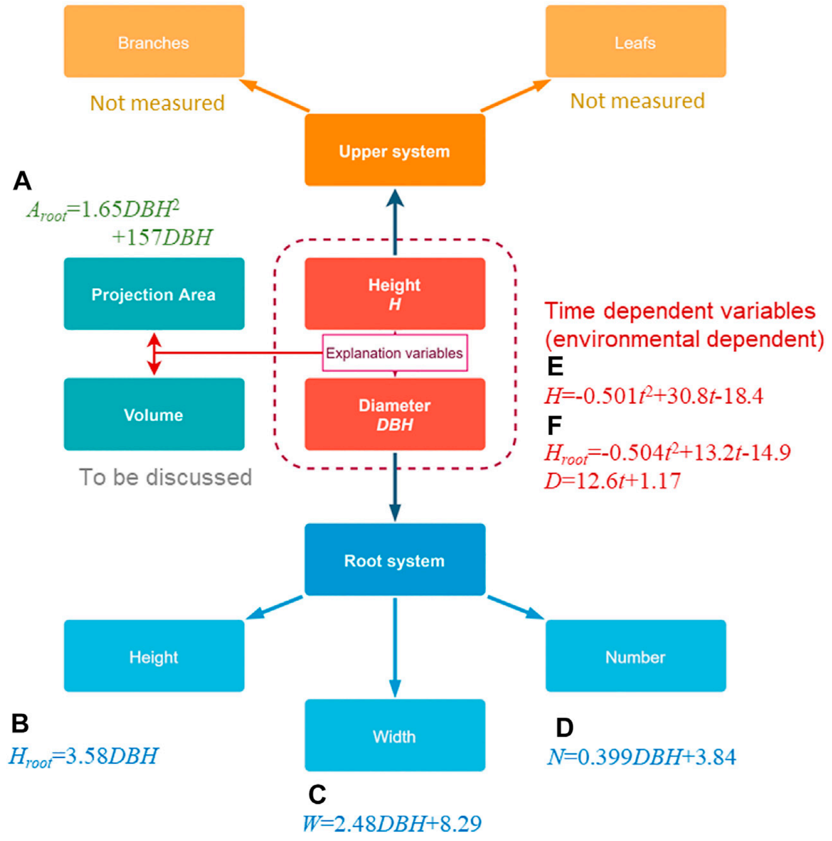

FIGURE 7 | Summary of the geometric characteristics of mangroves (*Rhizophora stylosa*).

of wave damping by the root system as the mangrove becomes larger. Furthermore, **Figure 5** shows the normalized A^*_{root} in terms of the normalized vertical distance z from the bottom by H^*_{root}. Both the ensemble average and its standard deviation are presented. The normalized frontal area quadratically increases from the bottom, and it gradually approaches the maximum near the top of the root system. As observed in fields, the projected area of mangrove roots shows nonlinear profiles (unlike other coastal trees with relatively simple geometry), which need to be properly parameterized, especially under low water-level conditions.

The current analysis obtained the empirical relationships among the representative parameters of mangrove root structure and the root system. Although solely using the relationship based on *DBH* in numerical modeling may yield uncertainties by ignoring the contributions from other factors, the above results relate other characteristics of mangrove root structure (e.g., height of the root system, the number of prop roots and the frontal area of the root system) which shall compensate the parameterization in numerical modeling.

Relationships Between Tree Age and Geometric Characteristics

As presented in the previous section, the bulk geometric characteristics of mangroves and the root system can be parameterized as a function of tree height H, DBH, and height of prop roots H_{root}. On the other hand, the information on these parameters and their variation in time is critical to assess mangrove effects on wave damping, especially when conducting afforestation or reforestation. The potential impact of growth rate on mangrove root structure should also be included in the development of numerical models for longer time-scale estimation (e.g., in 10 years or later).

In **Figure 6A**, we first present the relationships of tree age with the tree height (circles) and the height of the prop roots (triangles) by Kiribati data. The regression curves (dashed lines) obtained by the least-square fitting method are included in the same plot. A higher growth rate of the tree height was observed in comparison with that of the root system. Recalling the quasi-linear relationship between H and W in **Figure 3A**, the increasing rate of the spanning radius of the root system (as well as the number of prop roots) can be expected to be greater compared to the growth rate of the height of mangrove roots. It should also be noted that the growth or height of the root system is not only determined by age but also the other environmental conditions. Therefore, the shown relation in **Figure 6** is neither directly related to Iriomote Island data or general. The field variation and the different site-to-site environmental conditions should be considered when discussing the proper parameterization quantitatively. However, the summary of the combined field data can give us the first approximation of mangrove shape parameterization for hydrodynamic modeling.

In **Figure 6B**, the diameter D_1 is plotted versus the tree age. Note again that D_1 denotes the trunk diameter right above the root system. A clear linear relationship can be observed in **Figure 6B**, and the regression curve is also provided. The diameter D_1 approximately ranges from 15 mm (3-year-old tree) to 25 mm (11-year-old tree). The empirical relationships in **Figures 6A,B** provide a valuable reference to estimate the variation of the representative parameters of mangrove root structure in time.

SUMMARY

In this study, we conducted two field surveys in the Iriomote Island of Okinawa, Japan, and Tarawa, Kiribati. Targeting at the parameterization of mangrove root structure, we collected the representative characteristics of mangrove geometry in fields, such as the tree height, the height of the root system, the spanning width of mangrove roots, the trunk diameter, and the frontal projected area. By analyzing the field data, we aimed to find out empirical formulas among the characteristic parameters of mangrove root geometry which are critical for the implementation of mangrove effects in numerical models for wave propagation.

Distinct relationships were found among the tree height, the spanning radius, the trunk diameter at breast height (*DBH*), and the projected area $\boldsymbol{A}(z)$ of the root system. Here, we summarize the estimated relationships of mangrove bulk characteristics in **Figure 7** (see additional data in **Supplementary Figures**). Based on **Figure 7**, we can estimate the root height, root width, and the number of the root system as well as the frontal projected area A(z) as a function of tree age *t*. Although the upper system of the mangrove (i.e., leaves and branches) was not measured, we succeeded in obtaining several empirical relationships in terms of the representative factors of mangrove geometry as an example. As presented in **Eq. 1**, one of the key factors to determine mangrove effects in wave modeling is the frontal projected area $\boldsymbol{A}(z)$ of the root system. Applying the empirical relationships along with the Morison-type formula in **Eq. 1**, mangrove-induced dissipation can be parameterized in numerical models with inputs of field measurements of the characteristic geometric diameters and heights. To account for the potential impacts of the growth rate of mangroves, we also analyzed the relationship of the tree age with the tree height and the trunk diameter D_1 (or DBH). Both the tree heights and trunk diameter showed monotonically increasing relationships with the tree age. This information is useful in future long-term assessment of mangrove effects, especially in the afforested or reforested areas.

It is necessary to continue field surveys in different environments and accumulate the dataset to cover other parameters, parameter spaces and reduce the uncertainty for parameterizing mangrove effects in numerical modeling. The detailed 3D structures and shapes of mangrove roots will be discussed using the 3D scanned data. More measurements such as the upper system (e.g., leaves and branches), other physical properties of mangroves (e.g., stiffness) and density of trees will be included in the next phase of the field survey.

DATA AVAILABILITY STATEMENT

The raw data supporting the conclusion of this article will be made available by the authors, without undue reservation.

AUTHOR CONTRIBUTIONS

NM, C-WC led the research and wrote the main part of the manuscript. TI, YA, KH, SB, AS, TM, and TS conducted a field survey and analyzed data in Kiribati. MT, SM, HK, MM, and RS conducted a field survey and analyzed data in Iriomote.

FUNDING

This research was supported by the Environment Research and Technology Development Fund JPMEERF20172012 and the Climate Adaptation Program in NIES and JSPS Grant-in-Aid for Scientific Research (Kakenhi) 20KK0095, and JST/JICA SATREPS Indonesia.

SUPPLEMENTARY MATERIAL

The Supplementary Material for this article can be found online at: https://www.frontiersin.org/articles/10.3389/fbuil.2021.782219/full#supplementary-material

REFERENCES

Alagan Chella, M., Kennedy, A. B., and Westerink, J. J. (2020). Wave Runup Loading Behind a Semipermeable Obstacle. *J. Waterway, Port, Coastal, Ocean Eng.* 146, 04020014. doi:10.1061/(asce)ww.1943-5460.0000569

Augustin, L. N., Irish, J. L., and Lynett, P. (2009). Laboratory and Numerical Studies of Wave Damping by Emergent and Near-Emergent Wetland Vegetation. *Coastal Eng.* 56, 332–340. doi:10.1016/j.coastaleng.2008.09.004

Baba, S. (2011). Close Group Planting of Mangroves on Atolls and Coral Islands of the Pacific. *ISME/GLOMIS Electron. J.* 9 (4), 11–12.

Chakrabarti, A., Brandt, S. R., Chen, Q., and Shi, F. (2017). Boussinesq Modeling of Wave-induced Hydrodynamics in Coastal Wetlands. *J. Geophys. Res. Oceans* 122, 3861–3883. doi:10.1002/2016jc012093

Chang, C. W., and Mori, N. (2021). Green Infrastructure for the Reduction of Coastal Disasters: a Review of the Protective Role of Coastal Forests against Tsunami, Storm Surge, and Wind wavesCoastal Engineering Journal. *Taylor Francis* 63 (3)), 370–385. doi:10.1080/21664250.2021.1929742

Chang, C.-W., Mori, N., Tsuruta, N., and Suzuki, K. (2019). Estimation of Wave Force Coefficients on Mangrove Models. *J. Jpn. Soc. Civil Eng. Ser. B2 (Coastal Eng.)* 75, I_1105–I_1110. doi:10.2208/kaigan.75.i_1105

Dalrymple, R. A., Kirby, J. T., and Hwang, P. A. (1984). Wave Diffraction Due to Areas of Energy Dissipation. *J. Waterway, Port, Coastal, Ocean Eng.* 110, 67–79. doi:10.1061/(asce)0733-950x(1984)110:1(67)

Danielsen, F., Sørensen, M. K., Olwig, M. F., Selvam, V., Parish, F., Burgess, N. D., et al. (2005). The Asian Tsunami: A Protective Role for Coastal Vegetation. *Science* 310, 643. doi:10.1126/science.1118387

Duke, N. C. (2006). *Australia's Mangroves. The Authoritative Guide to Australia's Mangrove Plants*. Brisbane, Australia: University of Queensland, 200p.

Goda, K., Mori, N., Yasuda, T., Prasetyo, A., Muhammad, A., and Tsujio, D. (2019). Cascading Geological Hazards and Risks of the 2018 Sulawesi Indonesia Earthquake and Sensitivity Analysis of Tsunami Inundation Simulations. *Front. Earth Sci.* 7, 261. doi:10.3389/feart.2019.00261

Guannel, G., Arkema, K., Ruggiero, P., and Verutes, G. (2016). The Power of Three: Coral Reefs, Seagrasses and Mangroves Protect Coastal Regions and Increase Their Resilience. *Plos One* 11, e0158094–22. doi:10.1371/journal.pone.0158094

Huang, Z., Yao, Y., Sim, S. Y., and Yao, Y. (2011). Interaction of Solitary Waves with Emergent, Rigid Vegetation. *Ocean Eng.* 38, 1080–1088. doi:10.1016/j.oceaneng.2011.03.003

Intergovernmental Panel on Climate Change (IPCC) Fifth Assessment Report – Working Group II (2014). *Climate Change 2014: Impacts, Adaptation, and Vulnerability*. New York, NY: Cambridge University Press.

Komiyama, A., Ong, J. E., and Poungparn, S. (2008). Allometry, Biomass, and Productivity of Mangrove Forests: A Review. *Aquat. Bot.* 89, 128–137. doi:10.1016/j.aquabot.2007.12.006

Lemein, T., Cox, D., Albert, D., and Mori, N. (2015). Accuracy of Optical Image Analysis Compared to Conventional Vegetation Measurements for Estimating Morphological Features of Emergent Vegetation. *Estuarine, Coastal Shelf Sci.* 155, 66–74. doi:10.1016/j.ecss.2014.12.051

Maza, M., Adler, K., Ramos, D., Garcia, A. M., and Nepf, H. (2017). Velocity and Drag Evolution from the Leading Edge of a Model Mangrove forest. *J. Geophys. Res. Oceans* 122 (11), 9144–9159. doi:10.1002/2017jc012945

Mazda, Y., Kobashi, D., and Okada, S. (2005). Tidal-scale Hydrodynamics within Mangrove Swamps. *Wetlands Ecol. Manage.* 13, 647–655. doi:10.1007/s11273-005-0613-4

Méndez-Alonzo, R., Moctezuma, C., Ordoñez, V. R., Angeles, G., Martínez, A. J., and López-Portillo, J. (2015). Root Biomechanics in Rhizophora Mangle: Anatomy, Morphology and Ecology of Mangrove's Flying Buttresses. *Ann. Bot.* 115 (5), 833–840. doi:10.1093/aob/mcv002

Mendez, F. J., and Losada, I. J. (2004). An Empirical Model to Estimate the Propagation of Random Breaking and Nonbreaking Waves over Vegetation fields. *Coastal Eng.* 51, 103–118. doi:10.1016/j.coastaleng.2003.11.003

Morison, J. R., Johnson, J. W., Schaaf, S. A., and Schaaf, S. A. (1950). The Force Exerted by Surface Waves on Piles. *J. Pet. Tech.* 2, 149–154. doi:10.2118/950149-g

Ohira, W., Honda, K., Nagai, M., and Ratanasuwan, A. (2013). Mangrove Stilt Root Morphology Modeling for Estimating Hydraulic Drag in Tsunami Inundation Simulation. *Trees* 27, 141–148. doi:10.1007/s00468-012-0782-8

Reguero, B. G., Beck, M. W., Bresch, D. N., Calil, J., and Meliane, I. (2018). Comparing the Cost Effectiveness of Nature-Based and Coastal Adaptation: A Case Study from the Gulf Coast of the United States. *PLOS One* 13, e0192132–24. doi:10.1371/journal.pone.0192132

Sutton-Grier, A. E., Wowk, K., and Bamford, H. (2015). Future of Our Coasts: The Potential for Natural and Hybrid Infrastructure to Enhance the Resilience of Our Coastal Communities, Economies and Ecosystems. *Environ. Sci. Pol.* 51, 137–148. doi:10.1016/j.envsci.2015.04.006

Tanaka, N., Sasaki, Y., Mowjood, M. I. M., Jinadasa, K. B. S. N., and Homchuen, S. (2007). Coastal Vegetation Structures and Their Functions in Tsunami protection: Experience of the Recent Indian Ocean Tsunami. *Landscape Ecol. Eng.* 3, 33–45. doi:10.1007/s11355-006-0013-9

Tanaka, N. (2012). Effectiveness and Limitations of Coastal forest in Large Tsunami: Conditions of Japanese pine Trees on Coastal Sand Dunes in Tsunami Caused by Great East Japan Earthquake. *J. Jpn. Soc. Civil Eng. Ser. B1* 68, II_7–II_15. doi:10.2208/jscejhe.68.ii_7

Tomlinson, P. B. (2016). *The Botany of Mangroves* (2nd ed.). New York, USA: Cambridge University Press, 418p.

UNISDR (United Nations International Strategy for Disaster Reduction) (2015). *Sendai Framework for Disaster Risk Reduction 2015-2030*. Sendai, Japan: United Nations Office for Disaster Risk Reduction (UNISDR).

Yang, Y., Irish, J. L., and Socolofsky, S. A. (2015). Numerical Investigation of Wave-Induced Flow in mound-channel Wetland Systems. *Coastal Eng.* 102, 1–12. doi:10.1016/j.coastaleng.2015.05.002

Zhang, X., Chua, V. P., and Cheong, H.-F. (2015). Hydrodynamics in Mangrove Prop Roots and Their Physical Properties. *J. Hydro-Environ. Res.* 9 (2), 281–294. doi:10.1016/j.jher.2014.07.010

Conflict of Interest: The authors declare that the research was conducted in the absence of any commercial or financial relationships that could be construed as a potential conflict of interest.

frontiers | Frontiers in Built Environment

ORIGINAL RESEARCH
published: 14 April 2022
doi: 10.3389/fbuil.2022.878197

A Nature-Based Solution for Coastal Protection: Wind Tunnel Investigations on the Influence of Sand-Trapping Fences on Sediment Accretion

Christiane Eichmanns* and Holger Schüttrumpf

Institute of Hydraulic Engineering and Water Resources Management, RWTH Aachen University, Aachen, Germany

Sand-trapping fences are a frequently used nature-based solution in coastal protection for initiating and facilitating coastal dune toe growth. However, only a few researchers have evaluated the trap efficiency of sand-trapping fences based on their porosity and height. Subsequently, the design of their properties has only been based on empirical knowledge, to date. However, for restoring and maintaining coastal beach–dune systems, exact knowledge of sand-trapping fence's optimal properties is essential. Thus, we conducted physical model tests focusing on the most crucial parameters: fence height (h = 40, 80, 120 mm) and fence porosity (ε = 22.6, 41.6, and 56.5%). These tests were conducted in an indoor subsonic, blowing-sand wind tunnel equipped with a moveable sediment bed (d_{50} ~ 212 µm). The experimental mean wind velocities were u_1 = 6.1 m/s, u_2 = 7.4 m/s, and u_3 = 9.3 m/s. We used a hot-wire anemometer to measure the flow fields, a vertical mesh sand trap to determine the sediment fluxes, and a 2D laser scanner to record the sediment accretion around the sand-trapping fences over time. The study results provide substantial theoretical and practical support for the installation and configuration of trapping fences and improving their design. The fence porosity, for example, should be chosen depending on the installation purpose. While denser fence porosities (ε_1 = 22.6% and ε_2 = 41.6%) can be used for initiating and facilitating the dune toe growth, fences with higher porosity (ε_3 = 56.5%) are more suitable to favor the sediment accretion between foredunes and white dunes as they allow further dune growth downwind.

Keywords: wind tunnel experiments, nature-based solutions, sand-trapping fences, porous fences, sediment transport, coastal protection

Edited by:
Jens Figlus,
Texas A&M University, United States

Reviewed by:
Alec Torres-Freyermuth,
Universidad Nacional Autónoma de México, Mexico
Edgar Mendoza,
National Autonomous University of Mexico, Mexico

****Correspondence:***
Christiane Eichmanns
eichmanns@iww.rwth-aachen.de

Specialty section:
This article was submitted to Coastal and Offshore Engineering, a section of the journal Frontiers in Built Environment

Received: *17 February 2022*
Accepted: *16 March 2022*
Published: *14 April 2022*

Citation:
Eichmanns C and Schüttrumpf H (2022) A Nature-Based Solution for Coastal Protection: Wind Tunnel Investigations on the Influence of Sand-Trapping Fences on Sediment Accretion. Front. Built Environ. 8:878197. doi: 10.3389/fbuil.2022.878197

INTRODUCTION

Coastal dunes are present along sandy coastlines worldwide and have various functions, such as contributing to biodiversity, socioeconomic services including nature conservation, recreation, and tourism, and natural flood protection for the low-lying hinterland against storm surges (van Thiel de Vries, 2009; Hesp, 2011; de Vries, 2013; Keijsers et al., 2015). Coastal dunes also act as sediment resources in case of erosive storm events; the sediments can naturally shift and move to the beach or nearshore areas and dissipate wave energy and, thus, mitigate erosion (van Thiel de Vries, 2009). Aeolian sediment transport processes from the beach toward the coastal dunes increase coastal dune volumes, while marine processes, which predominately occur during storm surges, lead to dune erosion (Hesp, 2011). However, along with aeolian sediment transport marine processes can also contribute to foredune growth along dissipative coastlines. The highest dune growth rates are often observed during winter months, when the beach is eroding, at the highest wind velocities, and high water levels (Cohn et al., 2018; 2019). Due to the rise in the sea level caused by climate change, it is currently assumed that erosion processes will accelerate and land loss will increase as well (Harff et al., 2011; Hesp, 2011; Keijsers et al., 2015). In addition, socioeconomic pressure in coastal areas is increasing (NASA, 2020). In order to address the challenges in coastal protection and at the same time respond to people's growing environmental awareness, there is a great need for nature-based solutions that aim to use natural processes and resources. Since sand-trapping fences are part of nature-based solutions, they are commonly installed along sandy coastlines along with barrier island systems to strengthen coastal dunes and increase the flood protection level (Li and Sherman, 2015; Itzkin et al., 2020a; Eichmanns et al., 2021). They cause a local reduction in wind velocity, leading to downwind sediment accumulation around the fences (Hotta and Horikawa, 1990; Li and Sherman, 2015; Lawlor and Jackson, 2021). The functions of sand-trapping fences in coastal areas vary and thus, range from rehabilitating eroded areas such as blowouts in coastal dunes, strengthening coastal dune toe establishment, preventing sand drifting from protectable infrastructures, limiting human access to nature, or initiating the formation of coastal dunes through selective sand deposition (O'Connel,; Adriani and Terwindt, 1974; Gerhardt, 1990; Li and Sherman, 2015; Eichmanns and Schüttrumpf, 2021). For detailed information about sand-trapping fences, refer to Eichmanns et al. (2021).

Generally, it is found that using sand-trapping fences at the seaward side of the dune leads to an increased foredune growth rate compared to no fenced areas (Jackson and Nordstrom, 2011; Eichmanns and Schüttrumpf, 2021). This additional sediment buffer can protect coastal dunes by attenuating wave energy (Ruz and Anthony, 2008; Itzkin et al., 2020b). However, the application of such sand-trapping fences can impair the sediment supply for the beaches and landward coastal dunes and create a physical boundary for the natural movement of fauna. Subsequently, a less dynamic beach–dune system affects the beach width and, therefore, the coastal protection against coastal erosion (Itzkin et al., 2020a). Wider beaches generally offer greater coastal protection against erosion than smaller beaches (Itzkin et al., 2020b). Thus, sand-trapping fences influence the natural topography of coastal dunes and present vegetation (Gallego-Fernández, 2013). For example, Itzkin et al. (2020a) found that coastal dunes are typically shorter, wider, and smaller in volume than natural foredunes in non-fenced and undeveloped areas. However, this may also be explained because fences tend to be installed close to more vulnerable coastal dunes, which are usually smaller.

Numerous studies consider the wind and turbulence field behind porous fences with variable geometry (height and length) (Mulhearn and Bradley, 1977; Ning et al., 2020), porosity (Perera, 1981; Hotta and Horikawa, 1990; Lee and Kim, 1999; Dong et al., 2007), opening size (Manohar and Bruun, 1970; Lee and Kim, 1999), incoming wind velocity, or wind turbulence (Dong et al., 2007; Yu et al., 2020). It is found that fence porosity and fence height are the predominant influencing factors on the wind field and, thus, the sand-trapping efficiency (Li and Sherman, 2015). However, recommendations on the fence height and porosity of sand-trapping fences in coastal areas are commonly based on empirical practice (Li and Sherman, 2015; Eichmanns et al., 2021). Thus, the correlation of sand-trapping efficiency as a function of, for example, fence porosity and fence height is needed.

In this study, indoor wind tunnel experiments were carried out to study the wind regime and sand-trapping efficiency of sand-trapping fences with different fence porosities and fence heights. The objective is to evaluate different fence porosities and fence heights influencing trap efficiency. Therefore, the following research goals were set:

1) Investigation of the influence of fence height and fence porosity on the wind regime.
2) Investigation of reproducibility of the sediment accretion around a single sand-trapping fence.
3) Considering the model effetcs on the sediment accretion around a single sand-trapping fence.
4) Evaluation of trap efficiency of a single sand-trapping fence over time.
5) Investigation of the influence of fence porosity on trapping sediment.
6) Giving general recommendations on fence properties.

MATERIALS AND METHODS

Experimental Design

Physical model tests were conducted on sand-trapping fences with different heights and porosities in an indoor subsonic, blowing-sand wind tunnel at the Institute of Hydraulic Engineering and Water Resources Management (IWW), Rheinisch Westfälische Hochschule (RWTH) Aachen University, Germany. Fence porosity and grain size distribution of the sediment is based on *in situ* measurements conducted in Langeoog and Norderney, where the influence of sand-trapping fences on the dune toe growth and its relation with potential aeolian sediment transport was already investigated by the authors (see Eichmanns and Schüttrumpf, 2020, 2021).

For this work, a wind tunnel was built by the IWW itself and was constructed mainly from wooden panels, except the test section was built from polymethylmethacrylate to allow visual observation of the experiments. The wind tunnel had a total length of $L = 25.8$ m, see **Figure 1**. The cross-sectional area was $H = 1.0$ m (height) and $B = 0.58$ m (width). The wind tunnel consisted of the following four parts: the power section with the wind machine, rectifier section followed by contraction section, channel with test section, and diffusion section. A sediment bed with a length of $l = 4$ m, a width of $b = 0.4$ m, and a depth of $t = 0.15$ m was installed in the test section. The sand-trapping fence as the focus of the investigation was installed within the sediment bed, $d = 2$ m from the edge of the sediment bed in the windward direction. In addition, a sediment source with a layer

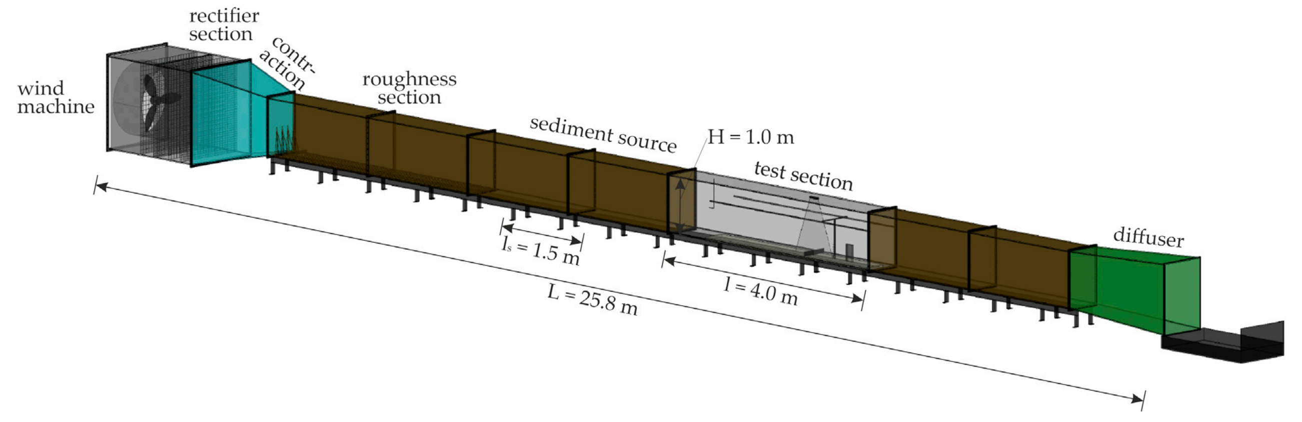

FIGURE 1 | Subsonic, blowing-sand wind tunnel built at IWW, RWTH Aachen University, Germany.

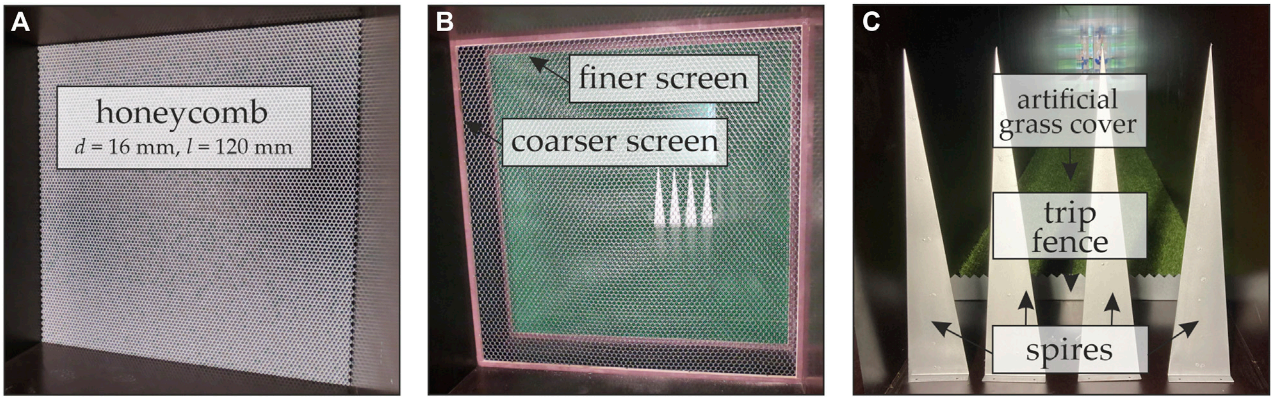

FIGURE 2 | (A) Honeycomb and **(B)** coarser and finer screens to straighten the airflow in the main wind direction, and **(C)** spires, trip fence, and an artificial grass cover to increase the surface roughness.

with a volume of $V = 0.0435\ \text{m}^3$ was placed about 1 m behind the roughness section in the main wind direction.

The Trotec TTW (Trotec) wind machine generates a continuous airflow of $Q = 45.600\ \text{m}^3/\text{h}$. The wind machine is equipped with an inverter that allowed mean wind velocities to be adjusted between $u_{mean} \sim 1\text{–}10$ m/s. The wind first passes through a honeycomb, see **Figure 2A**, and second, through a coarser and a finer screen, see **Figure 2B**, to straighten the airflow. The honeycomb is designed following the findings of Barlow et al. (1999) and Mehta (1979) and was built out of ~7.500 bounded polyvinylchloride tubes with an outer diameter of $d = 16$ mm and a length of $l = 120$ mm. In addition, the surface roughness is increased by four spires, a trip fence, and a 6-m-long artificial grass cover, see **Figure 2C**.

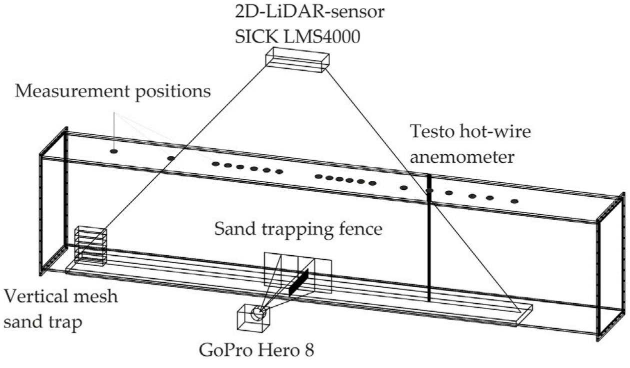

FIGURE 3 | Instrumentation setup for the test section, including 2D LiDAR sensor SICK LMS4000, Testo hot-wire anemometer for the different measurement positions, vertical mesh sand trap, and GoPro Hero 8.

Experimental Setup

The flow field and sediment flux measurements were conducted separately. First, a fixed sediment surface was installed to measure the wind velocities *via* a hot-wire anemometer. Since the hot-wire anemometer is susceptible to damages from the windblown sediment, a thin layer of sediment glued to a wooden panel was installed while measuring the wind profiles in the test section. Only wind directions perpendicular to the fences were investigated in

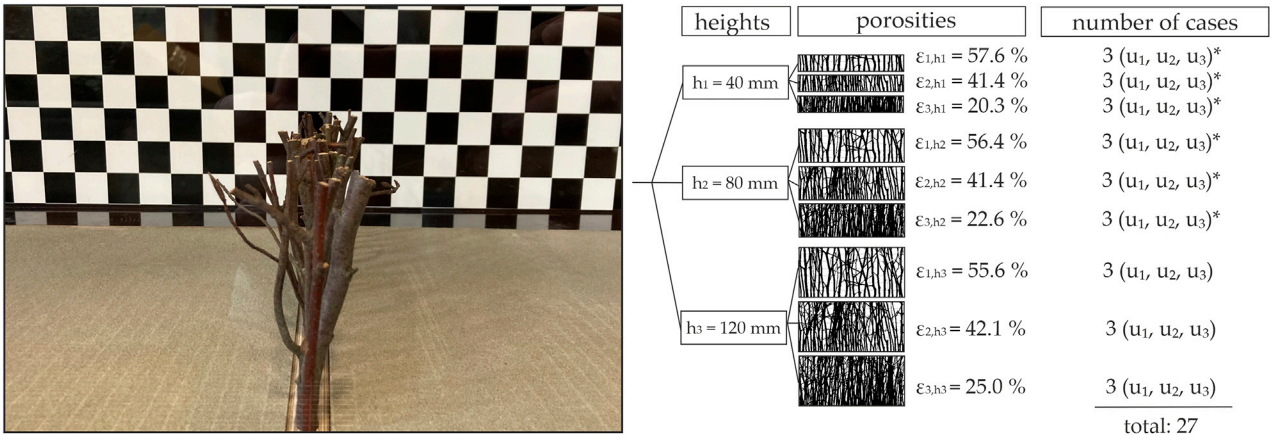

FIGURE 4 | Modeling nine different sand-trapping fences with changing fence heights and fence porosities and showing the number of cases investigated (*only wind profiles were measured).

the wind tunnel. The experimental mean wind velocities were u_1 = 6.1 m/s, u_2 = 7.4 m/s, and u_3 = 9.3 m/s. Then a moveable sediment bed combined with a sediment source was established, where a vertical sediment trap determined the sediment flux and a 2D LiDAR sensor SICK LMS4000, the sediment accretion around the sand-trapping fence. This fixed and moveable sediment bed procedure was already carried out in comparable wind tunnel experiments such as Hotta and Horikawa (1990). A GoPro Hero 8 recorded each experiment for visual observation. In **Figure 3**, the instrumentation setup for the test section is shown.

The sediment source is added, such as in experiments by Creyssels et al. (2009) or Ho et al. (2011, 2012), to favor the development of a steady state of saltation. Experiment's duration is set to t = 10 min to ensure almost stationary sediment fluxes. This is in agreement with other investigations such as Chen et al. (2019, 2020), Wang et al. (2018), or Miri et al. (2019), where short measuring intervals, up to several minutes, are common. Some of these experiments were even shorter. Exceeding this experiment duration would empty the sediment source and the sediment bed. Furthermore, vertical mesh sand traps are limited to a constant sand-trapping capacity that will exceed if testing times are excessive. Moreover, we wanted to avoid the effects of supply limitations on the dune development (Swann et al., 2015) or increase the model effects at the physical boundaries (transition from wooden panels to the sediment bed).

Sediment from the study site Norderney was used for the experiments. To ensure the defined moisture content of M < 0.1%, for all investigations, the sediment was dried in a dry oven at a temperature of around T = 105°C. According to the specifications in DIN EN ISO 14688-1 (2018), a sedimentological analysis was conducted. The median grain size of the sediment was d_{50} ~ 212 μm.

The investigated sand-trapping fences were modeled using locally available brushwood branches with a diameter of d ~ 2–10 mm. In total, nine different fence configurations were investigated in the wind tunnel, varying in both fence height (h = 40, 80, 120 mm) and fence porosity (ε ~ 20–58%). The two-dimensional porosity was determined as the open to total surface ratio. The exact porosities are shown in **Figure 4** and were determined by evaluating photographs of the sand-trapping fences. Therefore, the photographs were processed with the MATLAB, 2018's (R2018b, version 9.510.944444) Color Thresholder Application. The areas overlaid by the brushwood branches were identified and colored in black with a chosen threshold value. The contrast toward the background was increased and colored in white to indicate that there is no brushwood. For more information about the segmentation of the photographs, refer Eichmanns and Schüttrumpf (2021).

The porosity of the different sand-trapping fence configurations varies slightly over height due to the uneven nature of the branches. Thus, the modeled fences tend to become a little more porous in their upper parts. In the following, the mean porosity is determined for the three different fence heights and used for low (ε_1 = 22.6%), medium (ε_2 = 41.6%), and high (ε_3 = 56.5%) porosity. The mean porosities generally correspond to the porosities of Langeoog and Norderney's sand-trapping fences (Eichmanns and Schüttrumpf, 2021). However, the brushwood bundles differ in their stem characteristics, such as the stem diameter (d ~ 2–10 mm). At present, the authors are not aware that the stem diameter significantly influences the sediment accretion around the sand-trapping fence, especially since, in a scientific research, the fence's porosity was identified as a significant influence on trapping sediments (e.g., Arens et al., 2001; Zhang et al., 2010; Li and Sherman, 2015; Miri et al., 2019; Yu et al., 2020).

To measure the wind fields, all fence heights and porosities were investigated (27 cases); to measure the sediment accretion around the sand-trapping fence, only the highest fence height was installed (nine cases), see also **Figure 4**. Researching this fence height ensures that the saltation layer height does not significantly exceed the fence height, allowing the fence to capture most of the windblown sediment, see also *Sediment Transport Fluxes*. The influence would be more remarkable for other fence heights since the fence heights are considerably lower than the saltation layer height, and thus, the aeolian sediment would also blow over the fence.

Similarity to Nature and Compliance with Physical Model Laws

The type of aerodynamic flow in the wind tunnel can be characterized by the Mach number M (-), as follows

$$\mathrm{M} = \frac{\mathrm{u}}{c}, \tag{1}$$

where $c \sim 343$ m/s (temperature $T = 20^{\circ}\mathrm{C}$) is the speed of sound of the medium. At any point in the wind tunnel, the velocity is less than the speed of sound of the air ($M < 1$), and thus it is a subsonic flow (Barlow et al., 1999; Anderson, 2017). The thickness of the boundary layer in the test section was determined to be approximately δ ~ 650 mm. Incompressible airflows are primarily characterized by their Reynolds number and are decisive for their dynamic similarity. The following conditions must be met: Reynolds number of the flow must be greater than $Re_{flow} > 10^5$ and the roughness Reynolds number must be greater than $\mathrm{Re}_R > 2.5$ (Barlow et al., 1999; Cattafesta et al., 2010). The Reynolds number of the flow is defined as follows:

$$Re_{flow} = \frac{u_{\infty} \cdot \delta}{\nu}, \tag{2}$$

where u_{∞} (m/s) is the free flow velocity in front of the test section and $\nu \sim 1.516 \cdot 10^{-5}$ m^2/s ($T = 20^{\circ}\mathrm{C}$) is the kinematic viscosity of air (White, 1996; Barlow et al., 1999; Cattafesta et al., 2010). The roughness Reynolds number Re_R (-) is defined as follows:

$$Re_R = \frac{z_0 \cdot u_*}{\nu}, \tag{3}$$

where u_* (m/s) is the shear velocity and z_0 (mm) is the aerodynamic roughness length (Nikuradse, 1933; Vithana, 2013), see also *Measurement of Wind Velocity Characteristics*. The first criterion was achieved with $Re_{flow} \sim 3 \times 10^5$, whereas the roughness Reynolds number was not achieved. The roughness Reynolds number could only be determined for experiments with the immobile sand bed, as the sensitive hot-wire probe could otherwise be destroyed by saltating sediment grains. However, we assumed that the roughness Reynolds number independence was achieved during experiments with the moveable sediment bed because the saltation process generally increases the roughness Reynolds number (Cermak, 1987; White, 1996; Barlow et al., 1999).

The minimal entrance length $L_{in,min} \sim 10\text{–}25 \cdot \delta$ (m) for describing the logarithmic wind profile is considered sufficiently long with $L_{in} = 15$ m under the assumption that saltation is present and the Froude criterion Fr (-) is fulfilled, as follows:

$$Fr = \frac{u_{\infty}}{\sqrt{g \cdot H}}, \tag{4}$$

where $g = 9.81$ m/s^2 is the gravitational acceleration and H (m) is the wind tunnel height. The smaller the Froude number, the faster a constant shear stress velocity, and thus, a constant velocity profile is achieved during saltation (White, 1996). The Froude criterion is fulfilled for the investigated flow velocities $u_{1-3} = 6.1\text{–}9.3$ m/s with $Fr << 20$ (Owen and Gillette, 1985). Sidewall effects are not expected with the investigated low wind velocities and corresponding shear stress velocities in the wind tunnel. For the blockage ratio two criteria exist. The maximum blockage ratio BR_1 (-) defined as

$$BR_1 = \frac{A_{fence}}{A} \overset{!}{<} 0.1\,, \tag{5}$$

which is fulfilled for fence models with heights $h_1 = 40$ mm and $h_2 = 80$ mm, whereas the blockage ratio BR_2 (-) can only be met for the lowest fence height $h_1 = 40$ mm. It is defined as the ratio of the fence height h (mm) to the height of the boundary layer δ (mm):

$$BR_2 = \frac{h}{\delta} \overset{!}{<} 0.15. \tag{6}$$

These criteria were not always met in past studies either, such as Dong et al. (2007), Wang et al. (2018), and Yu et al. (2020), but assumed to have a minor influence as long as the fence height was at least smaller than the height of the boundary layer. Since the selected fence heights are considerably smaller than the boundary layer height, it can be assumed that no significant influence is expected by exceeding this limit value.

Measurement of Wind Velocity Characteristics

The Testo hot-wire anemometer (testo, 2021), equipped with an external data logger Testo 440 dp, was placed in the center of the wind tunnel at predefined heights ($z = 3, 6, 12, 24, 40, 80, 120, 200$, and 250 mm) above the surface to measure wind velocities. For this purpose, the hot-wire anemometer was inserted *via* a hole in the wind tunnel cover, and after measurement of the wind profile, the anemometer was moved to the next position downwind. The respective holes in the lid were sealed tightly with plugs, see **Figure 3**. For the flow field test, the wind velocity profiles near the sand-trapping fence were measured on the leeward side at a distance of 2, 5, 8, 10, 12, 15, and 20 h from the fence, on the windward side at distances of $-2h$, $-5h$, and $-10h$, and at a reference position over the wooden panel at $x = -2{,}200$ mm from the fence, where h is the height of the sand-trapping fence. We recorded a steady and uniform airflow field in the test section without a sand-trapping fence, see also **Figure 7**. The hot-wire anemometer has an accuracy of ±0.03 m/s and 3% of the mean wind velocity. In order to obtain reliable measurement results, the measurement duration is decisive. A measurement duration that is too short can lead to incorrect measurement results. The longer the measurement duration, the more representative the measurement results. The wind velocity was measured for 10 min at two locations and then analyzed. The 10-min measurement period is divided into ten intervals of equal time (t = 1 min), and the difference between the mean flow velocity over each 1-min interval over the whole 10-min interval is determined. The maximum difference was ±1.2%. Therefore, a measurement interval of 1 min is defined as sufficiently accurate

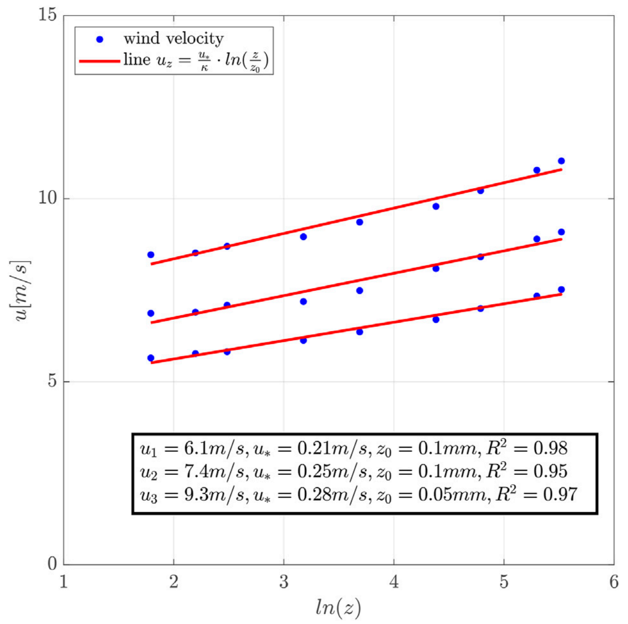

FIGURE 5 | Examples of the velocity profile for u_1 = 6.1 m/s, u_2 = 7.4 m/s, and u_3 = 9.3 m/s. The blue dots represent the measured wind velocity and the red lines indicate the regression lines, see **Eq. 7**.

for this investigation. Moreover, the reproducibility of the measured data for the wind profiles was ensured by repeating several measurements randomly with a maximum deviation of ±4% at one measuring point.

An appropriate analytical approach to describe the wind velocity distribution over the viscous sub boundary layer for aerodynamically rough surfaces is the law of the wall, which is valid for neutral atmospheric stability conditions, as follows (Bagnold, 1954):

$$u_z = \frac{u_*}{\kappa} \cdot ln \frac{z}{z_0}, \tag{7}$$

where u_z (m/s) is the wind velocity at height z (m) and κ (−) is the Kármán constant (here 0.41) (Nikuradse, 1933; Vithana, 2013). **Figure 5** exemplifies the velocity profiles for u_1 = 6.1 m/s, u_2 = 7.4 m/s, and u_3 = 9.3 m/s at the reference position with corresponding shear velocities u_{1*} = 0.21 m/s, u_{2*} = 0.25 m/s, and u_{3*} = 0.28 m/s, and coefficient of determination R^2 = 0.95–0.98 is shown. It describes the approaching airflow entering the test section.

For all measurement heights at the reference position, the corresponding standard deviations were less with $\sigma_{\min}$ = 0.19 m/s, $\sigma_{\max}$ = 0.61 m/s, and σ_{mean} = 0.39 m/s, respectively.

When a particular critical value of drag and lift force on the sediment grain is exceeded, sediment transport is initiated. This is the so-called critical shear stress u_{*t} (18):

$$u_{*t} = A \cdot \sqrt{\left(\frac{\rho_s}{\rho_a} - 1\right) \cdot g \cdot d_{50}}\,. \tag{8}$$

The empirical constant is given with A (-) (here 0.11), the density of air is given with ρ_a (kg/m^3) (here 1.2 kg/m^3), and the density of sediment grains with ρ_s (kg/m^3) (here 2,650 kg/m^3). The empirical constant considers the effect of cohesion; however, the influence of the protective layer of shells or moisture contents is not taken into account (Shao and Lu, 2000; Han et al., 2011; van Rijn and Strypsteen, 2019). The critical shear velocity was calculated for the wind tunnel investigations as u_{*t} = 0.24 m/s. However, it was noted that sediment transport occurred with critical shear velocities above u_{*t} = 0.20 m/s.

To describe the influence of different fence porosities and fence heights on the wind profile at a certain height z (mm) and distance x (mm) from the fence, the wind reduction coefficient R_c (-) is used (Cornelis and Gabriels, 2005; Wang et al., 2018; Yu et al., 2020):

$$R_c = 1 - \frac{u_{x,z}}{u_{0_{x,z}}}. \tag{9}$$

The horizontal wind velocity is given with $u_{x,z}$ (m/s) and the horizontal wind velocity at that exact position without any fence with $u_{0x,z}$ (m/s). A high value indicates a high wind reduction.

Measurement of Sediment Flux

For each experimental mean wind velocity, mean sediment transport rates were measured to determine the incoming sediment flux from the sediment source. Thus, vertical mesh sand traps constructed according to Sherman et al. (2014) and already used in field experiments of Eichmanns and Schüttrumpf (2020), covering a height of z = 0.3 m above the surface, see **Figure 3**, were used. The vertical mesh sand trap consists of six rectangular aluminum tubes arranged one above the other. One rectangular aluminum tube has the dimensions of 0.1 m (width) × 0.05 m (height) × 0.25 m (length) and 2 mm (edges). One rectangular aluminum tube is equipped with a nylon monofilament with opening sizes of *size* = 50 µm. The vertical mesh sand traps were exposed to sediment flow during the defined time interval of t = 10 min, and, afterward, the collected sand was weighed per height. The empirical exponential decay function is used to describe the vertical distribution of sediment transport as follows (Ellis et al., 2009; Poortinga et al., 2014):

$$q_z = q_0 \cdot \exp(-\beta \cdot z), \tag{10}$$

where q_z (kg/m^2/s) is the sediment transport rate at a predefined height z (m), q_0 (kg/m^2/s) is the extrapolated saltating sediment mass transport at the surface, and the decay rate β (1/m) is a constant to describe the vertical concentration gradient. A regression analysis of the experimental data gives the parameters β and q_0 (Bauer and Davidson-Arnott, 2014). According to the scientific literature, the range of values for the fitting coefficient can vary significantly due to the weak correlation to physical aeolian parameters such as grain size or shear velocity (Bauer and Davidson-Arnott, 2014). Integrating **Eq. 10** gives the total mass transport, as follows:

$$Q_s = \int_0^\infty q_z \cdot dz = \frac{q_0}{\beta}. \tag{11}$$

The total mass transport by saltation is given as Qs (kg/m/s) (Bauer and Davidson-Arnott, 2014). Since aeolian sediment

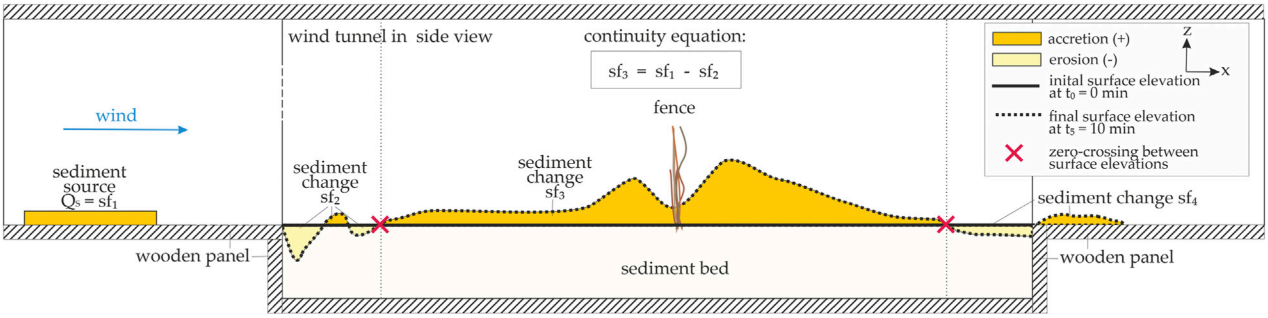

FIGURE 6 | Two-dimensional side view of the wind tunnel test section showing the different sediment fluxes schematically: sf_1–sf_4 for determining the trapped sediment, see **Eq. 13**.

transport is highly variable spatially and temporally, the experiments were repeated three times and the average value was used for further analysis (Baas and Sherman, 2006; Bauer and Davidson-Arnott, 2014; Strypsteen, 2019; van Rijn, 2019).

Measurement of Sand Accretion Around Sand-Trapping Fence Configurations

We deployed a 2D LiDAR scanner at the centerline of the wind tunnel, where the wind velocity profiles were also measured. We found that the centerline represents the sediment accretion around the sand-trapping fence well based on the camera recordings. The laser scanner detected the sediment surface elevations every $\Delta t = 2$ min with a systematic error of ±1.5 mm and a statistical error of ±2.5 mm (distances between 1.97–2.40 m). The measuring frequency was set to 10 Hz, and the angular resolution was 0.0833°.

In the following, the trap efficiency is used to evaluate the different sediment accretions around the configurations of the sand-trapping fence. In order to eliminate model effects on the sediment accretion caused by the fence, the sediment fluxes were distinguished based on the continuity equation. Thus, **Figure 6** presents a schematic side view of the wind tunnel test section with the sediment accretion around the fence at timestep $t_0 = 0$ min and $t_5 = 10$ min. The yellow areas show the typical erosion areas, whereas the colored areas in orange give the accretion areas. The zero-crossing between two sediment surface elevations at different timesteps is defined as boundary condition distinguishing between the different sediment changes (sf_2, sf_3, and sf_4), see red crosses in **Figure 6**.

During the experiments, local scouring always occurred at the transition between the wooden panel and sediment bed and vice versa, see *Sediment Accretion Around the Sand-Trapping Fence Configurations*. These sediment changes sf_2 and sf_4 were caused by increasing shear stress associated with increasing surface roughness, which lead to fluctuations and turbulences, thus, initiating erosion processes (Swann et al., 2015). Since in a steady-state equilibrium, foredunes generally oscillate about a geomorphic equilibrium, accreting (recovery) and eroding (response), it is assumed that the scour sf_4 at the end of the sediment bed would extend over a longer distance followed by a sediment accretion (Swann et al., 2015). Thus, this sediment change sf_4 is excluded from further analysis. Excluding the sediment flux sf_4 ($sf_4 << sf_3$) still provides valid results.

It is assumed that during the experimental time frame of $t = 10$ min, the scours have a minor effect on the accretion of sediment around the sand-trapping fence. According to experiments of Hotta and Horikawa (1990) and Ning et al. (2020), the zero-crossing between two surface elevations at different timesteps shifts insignificantly toward the fence (maximum $x/h \sim 2$) such as in our experiments. Thus, it is assumed that the morphodynamics around the sand-trapping fence is modeled correctly in our experiments, see also *Sediment Accretion Around the Sand-Trapping Fence Configurations*. However, this can only be determined adequately with a sufficiently long wind tunnel and extensive test durations.

For evaluating the sand-trapping of different fence configurations, the trap efficiency E (-), see for example, Ning et al. (2020) or Chen et al. (2019), is defined as follows:

$$E = \frac{Q_t}{Q_s}. \tag{12}$$

The trapped sediment transport Q_t (kg/m/s) is estimated as the product of the bulk density of the sediment γ (kg/m³) and the cross-sectional dune area ΔA (m²) (sediment change sf_3) in the time interval Δt (s), as follows:

$$Q_t = \frac{\gamma \cdot \Delta A}{\Delta t}. \tag{13}$$

The sediment transport for initiating the sediment accretion around the sand-trapping fence is calculated based on total mass transport Q_s, see **Eq. 11**, from which the sediment change sf_2 is subtracted. The bulk density was $\gamma = 1{,}550$ kg/m³ (average out of three measurements).

Since windblown sediment transport is highly variable both spatially and temporally, the experiments were repeated three to four times (Baas and Sherman, 2006; Bauer and Davidson-Arnott, 2014; van Rijn, 2019).

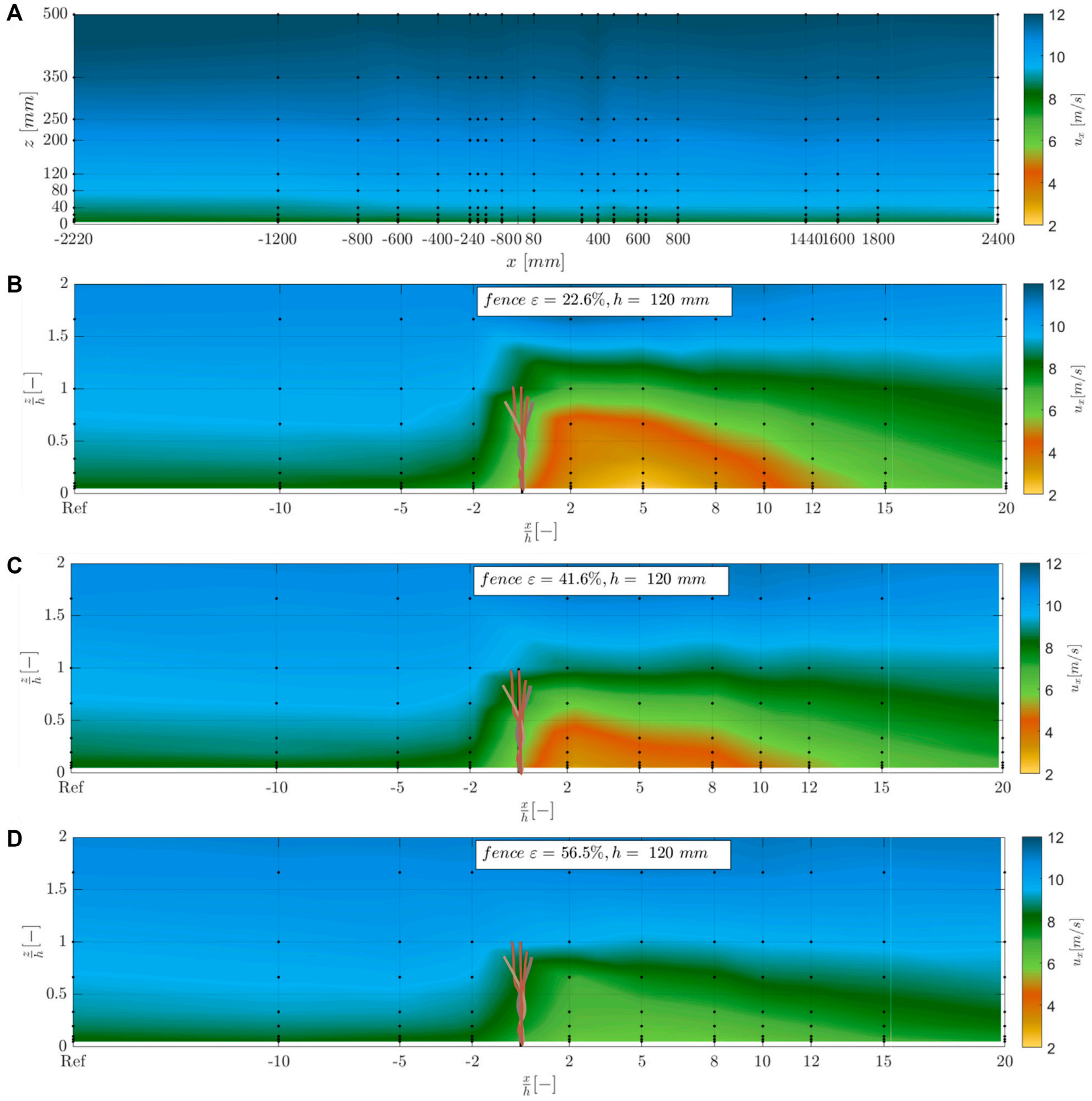

FIGURE 7 | Flow fields **(A)** without a sand-trapping fence **(B)** in the vicinity of a sand-trapping fence at $x/h = 0$ with $h_3 = 120$ mm and **(B)** a porosity of $\varepsilon_1 = 22.6\%$, **(C)** $\varepsilon_2 = 41.6\%$, and **(D)** $\varepsilon_3 = 56.6\%$. The free mean wind velocity was $u_3 = 9.3$ m/s. The black dots show the measuring locations of the hot-wire anemometer, and the brown lines indicate the sand-trapping fence.

RESULTS

Wind Velocity Characteristics

Figure 7A presents the flow field in the x-direction (mm) over the height z (mm) without a sand-trapping fence; **Figures 7B–D** depicts the flow fields in the vicinity of a sand trapping. The free mean velocity was $u_3 = 9.3$ m/s, and the x-axis and the y-axis were normalized by the fence height. The black dots represent the measurement positions of a hot-wire anemometer with the mean wind velocity values over the 1-min measuring interval, and the brown lines indicate the fence. Generally, the airflow slows down on the upwind side of the fence. Above the fence, the airflow accelerates, and on the leeward side, the vertical eddy zone occurs, resulting from the difference of the wind velocity above and through the fence.

The complexity of the airflow fields decreased while the fence porosity increased. For the low porosity fence, the wind velocity profiles show a higher range of measured wind velocities between $u = 2.3–11.3$ m/s than the high porosity fence profiles showing

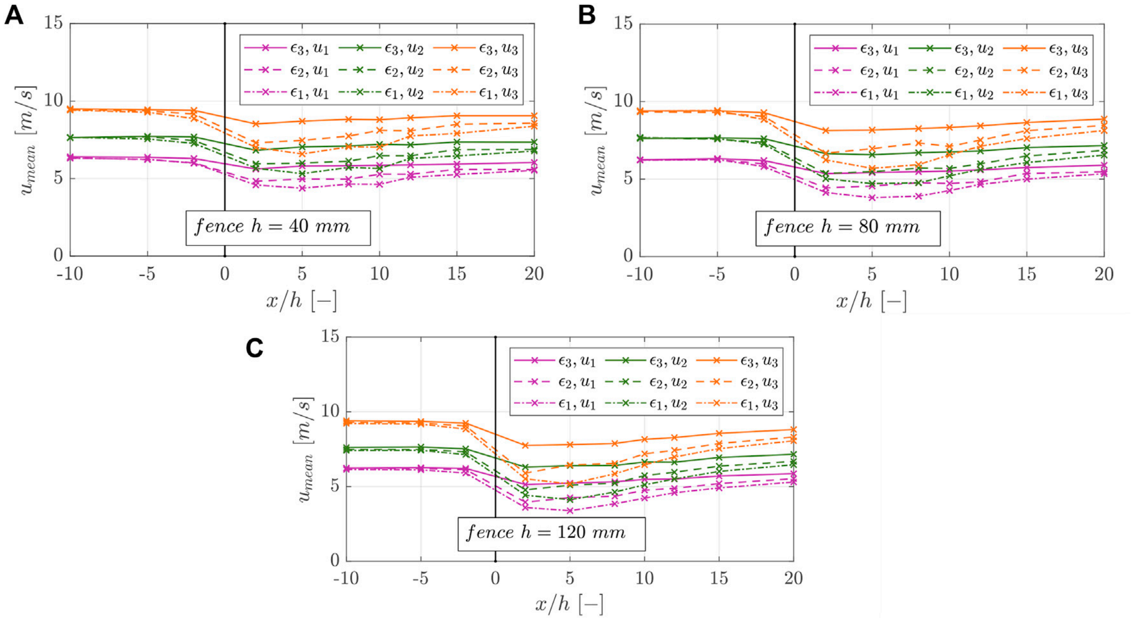

FIGURE 8 | Mean wind velocity u_1–u_3 in the x-direction of fences with different characteristics ε_1–ε_3, divided into **(A)** the fence heights h_1 = 40 mm **(B)** h_2 = 80 mm, and **(C)** h_3 = 120 mm.

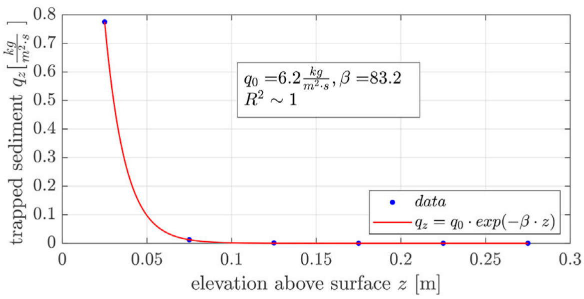

FIGURE 9 | Vertical distribution of sediment transport flux obtained from the vertical mesh sand trap for wind velocity u_3 = 9.3 m/s and the best fit exponential decay function for experiment No. 3.3.

wind velocities between u = 6.3–11.1 m/s. In addition, the wind velocities in front of and behind the fence are reduced to a greater extent. For better illustration, **Figure 8** represents the mean wind velocities in the x-direction for the different fence configurations, divided into the following fence heights: (A) h_1 = 40 mm (B) h_2 = 80 mm, and (C) h_3 = 120 mm. The mean wind velocity in the x-direction was averaged by values of wind velocities at heights of z = 3, 6, 12, 24, 40, 80, 120, 200, and 250 mm. The mean wind velocities were averaged up to a height of z = 250 mm within the boundary layer rather than the entire wind tunnel height of H = 1,000 mm.

Comparing the wind fields for the different fence heights (h_1 = 40 mm, h_2 = 80 mm, and h_3 = 120 mm), we detected no significant differences in the mean wind velocities under constant porosity and constant free wind velocity.

For the lowest fence porosity (ε_1 = 22.6%) and the highest fence height (h_3 = 120 mm), the wind reduction is most significant at position x/h = 5. For the mean free wind velocity u_1 = 6.1 m/s, the lowest mean wind velocity in the x-direction was u_{mean} = 3.4 m/s, whereas for the lowest fence height (h_1 = 40 mm) and the lowest fence porosity (ε_1 = 22.6%), the lowest mean wind velocity was u_{mean} = 4.4 m/s at position x/h = 5. In the downwind direction, the wind velocity increased, reached their minimum at position x/h = 5, and then increased again to the initial wind velocity. For all fences with the characteristics of ε_2 = 41.6%, the minimum value was already reached at position x/h = 2. The higher the porosity of the fence was, the earlier the initial wind velocity of the fence was reached in the free stream.

Sediment Transport Fluxes

Figure 9 exemplifies the vertical distribution of sediment transport fluxes obtained from the vertical mesh sand traps for the wind velocity u_3 = 9.3 m/s. We found that sediment was mainly caught in heights of less than $z \leq 0.05$ m for all wind velocities studied. This finding is in agreement that most sediment transport in coastal areas occurs for $z < 0.05$ m above the surface (Strypsteen, 2019). No sediment was caught in heights over $z > 0.15$ m, so the saltation layer height does not significantly exceed the fence height (h_3 = 120 mm), see *Experimental Setup*.

Table 1 presents the results of the trapped sediment from the vertical mesh sand traps with the total mass flux Qs (kg/m/s), the decay rate ß (1/m), the extrapolated saltating sediment mass transport at the surface q_0 (kg/m^2/s), and the correlation coefficients R^2 (-) of the regression analysis. The measuring duration was t = 10 min. The transport fluxes varied between Qs = 0.005–0.078 kg/m/s for wind velocities ranging between

TABLE 1 | Total mass flux results over the measuring duration, decay rate, extrapolated saltating sediment mass transport at the surface, and correlation coefficients of the vertical sediment profile regression analysis.

Wind velocity	No.	t (min)	q_0 (kg/m^2/s)	$ß$ (1/m)	Q_s (kg/m/s)	R^2 (-)
u_1 = 6.1 m/s	1.1	10	0.72	92	0.008	~1.0
	1.2		0.83	90	0.009	
	1.3		0.44	91	0.005	
u_2 = 7.4 m/s	2.1		4.01	105	0.038	
	2.2		3.31	102	0.033	
	2.3		3.70	104	0.036	
u_3 = 9.3 m/s	3.1		6.79	87	0.078	
	3.2		6.40	85	0.075	
	3.3		6.20	83	0.075	

u_1 = 6.1 m/s and u_3 = 9.3 m/s. For the lowest wind velocity u_1 = 6.1 m/s, the total mass fluxes show larger fluctuations than those at higher wind velocity u_2 = 7.4 m/s and u_3 = 9.3 m/s.

The regression parameters varied between $ß$ = 83–105/m and q_0 = 0.44–6.79 kg/m^2/s, indicating that the higher the wind velocity, the higher the extrapolated saltating sediment mass transport at the surface and the amount of the total sediment transport rate. However, the decay rate and the sediment transport height did not vary significantly during the experiments for different wind velocities.

Sediment Accretion Around the Sand-Trapping Fence Configurations

Figure 10 shows sediment accretion around the investigated sand-trapping fences h_3 = 120 mm over time, starting at t_0 = 0 min and ending at t_5 = 10 min. Both the x-axis (-) and the y-axis (-) are normalized over the fence height. The results for the investigated wind velocity u_1 = 6.1 m/s are shown in **Figures 10A,D,G**, u_2 = 7.4 m/s in **Figures 10B,E,H**, and u_3 = 9.3 m/s in **Figures 10C,F,I**, respectively. The first row shows the results for ε_1 = 22.6%, the second row for ε_2 = 41.6%, and the third row for ε_3 = 56.5%. The different colors of the lines indicate the different timesteps Δt = 2 min. The sediment changes are Δsf_2 and Δsf_3 is given in the legend.

The sediment accretion occurred predominantly horizontally and vertically, which corresponds to the first phase of dune growth, see for example Ning et al. (2020). Longer experiment durations would probably lead to the sediment accretion according to the second dune growth phase with almost exclusive horizontal dune growth if a sufficient sediment supply is provided. It is well seen that the higher the investigated wind velocity, the higher the total amount of deposited sediment at the sand-trapping fence at a given time, caused by a higher aeolian sediment transport rate. Furthermore, the denser the fence porosity, the higher the deposited sediment on the windward side of the sand-trapping fence at any given time. For example, for the lowest fence porosity of ε_1 = 22.6%, the deposited sand reached a height of maximum z/h ~ 0.4, whereas for the highest fence porosity of ε_3 = 56.5%, the maximum height of z/h = 0.28 was reached. Generally, it can be recognized that for fences with ε_2 = 41.6% and ε_3 = 56.5%, scouring occurred in the main wind direction directly behind the fence at position x/h ~ 1, whereas for ε_1 = 22.6%, only little scouring was recorded at this position.

The sediment accretion on the leeward side developed simultaneously but faster than the sediment accretion on the windward side of the fence. For the lower and middle wind velocities (u_1, u_2), the height of the sediment accretion of the windward side is approximately the same as the height of the leeward side of the fence. For the fence with the lowest porosity, the sediment accretion on the leeward side of the fence occurred until x/h ~ six to eight, whereas fence with the medium porosity until x/h ~ seven to nine and for the most porous fence until x/h ~ 8–12.

DISCUSSION

Regarding the similarity of the physical model tests to nature, it must be taken into account that some influencing factors such as non-stationary wind conditions, attacking wind direction, moisture, salt content of the sediment, shell fragments, the presence of vegetation, or the topography cannot be modeled in the wind tunnel experiments adequately. For example, the main wind direction was modeled solely orthogonal and onshore to the fence that does not correspond to nature. In nature, the wind forces attack the fence from all wind directions. However, wind directions play a significant role in controlling the apparent fetch length, which refers to the continuous increase in sediment transport rates with increasing fetch length downwind until an equilibrium condition is reached (critical fetch length) (Jackson and Cooper, 1999; Bauer and Davidson-Arnott, 2003). When estimations of aeolian sediment transport rates from the beach toward the coastal dunes are made, they are often divided into longshore and cross-shore sediment fluxes, see for example Nickling and Davidson Arnott, (1990). Furthermore, in nature, the presence of vegetation generally increases the surface roughness, favoring sediment deposition and dune formation (Adriani and Terwindt, 1974; Hacker et al., 2012; Keijsers et al., 2015; Cohn et al., 2019; Miri et al., 2019). The presence of vegetation and the natural formation of coastal dunes also influence the sand-trapping efficiency of sand-trapping fences and may superimpose or

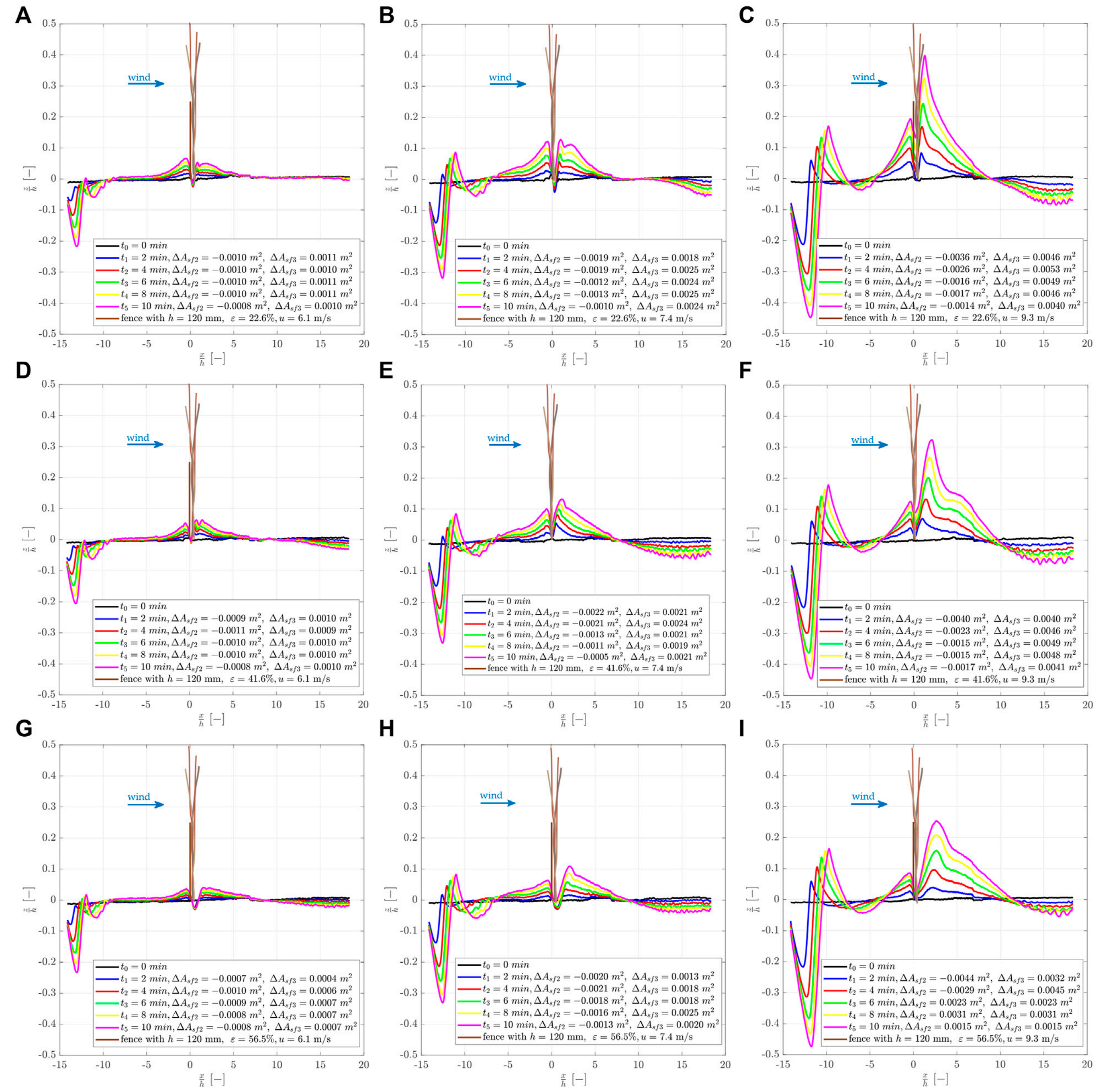

FIGURE 10 | Sediment accretion around a porous fence $h = 120$ mm varying in fence porosity and investigated wind velocity. The first row **(A-C)** shows the results for $\varepsilon_1 = 22.6\%$, the second row **(D-F)** for $\varepsilon_2 = 41.6\%$, and the third row **(G-I)** for $\varepsilon_3 = 56.5\%$. The first columns show $u_1 = 6.1$ m/s, the second column $u_2 = 7.4$ m/s, and the third column $u_3 = 9.3$ m/s.

interact with them (Houser et al., 2015). Generally, moisture content of sediment strongly affects aeolian sediment transport. With increasing moisture content the cohesion is increasing leading to lower sediment transport rates. In our investigations the sediment was dried before testing, leading to higher sediment transport rates compared to nature (Davidson-Arnott et al., 2005; van Rijn and Strypsteen, 2019). However, these influencing factors, which are usually subject to strong spatial and temporal fluctuations, have a decisive influence on the sediment accretion around sand-trapping fences in nature. The standardized wind tunnel investigations, on the other hand, offer the great possibility to observe the influence of certain fence properties under constant boundary conditions. The influence of other factors, such as the natural dune formation, can thus be eliminated, allowing us to evaluate the effeciency of sand-trapping fences in a standardized manner.

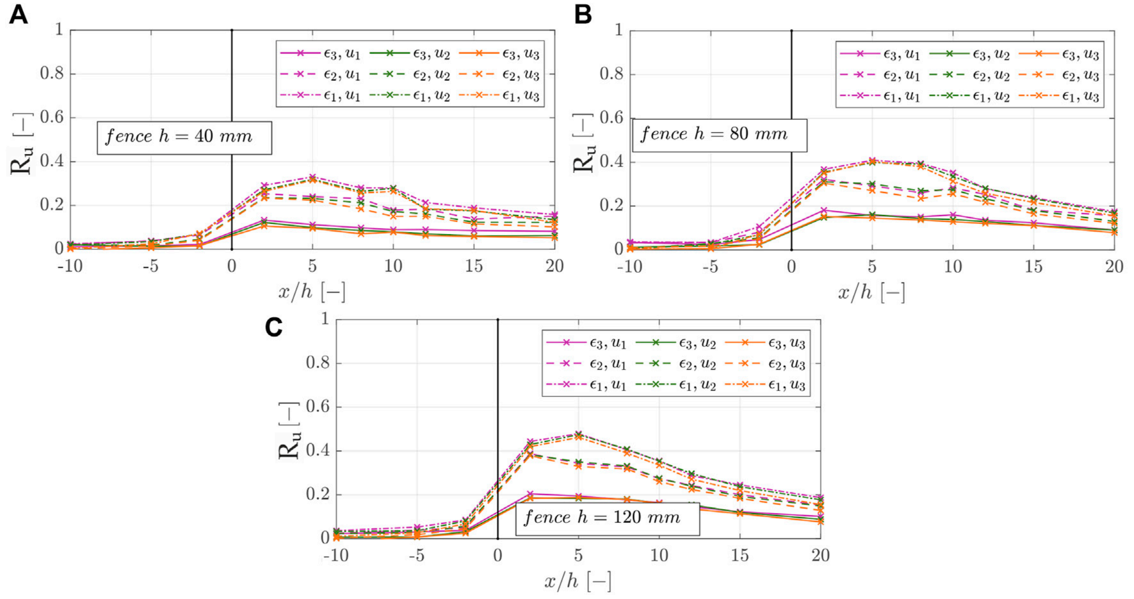

FIGURE 11 | Wind reduction coefficients accordingly to **Eq. 9** in the *x*-direction of fences with different characteristics, which are divided into **(A)** the fence heights h_1 = 40 mm **(B)** h_2 = 80 mm, and **(C)** h_3 = 120 mm.

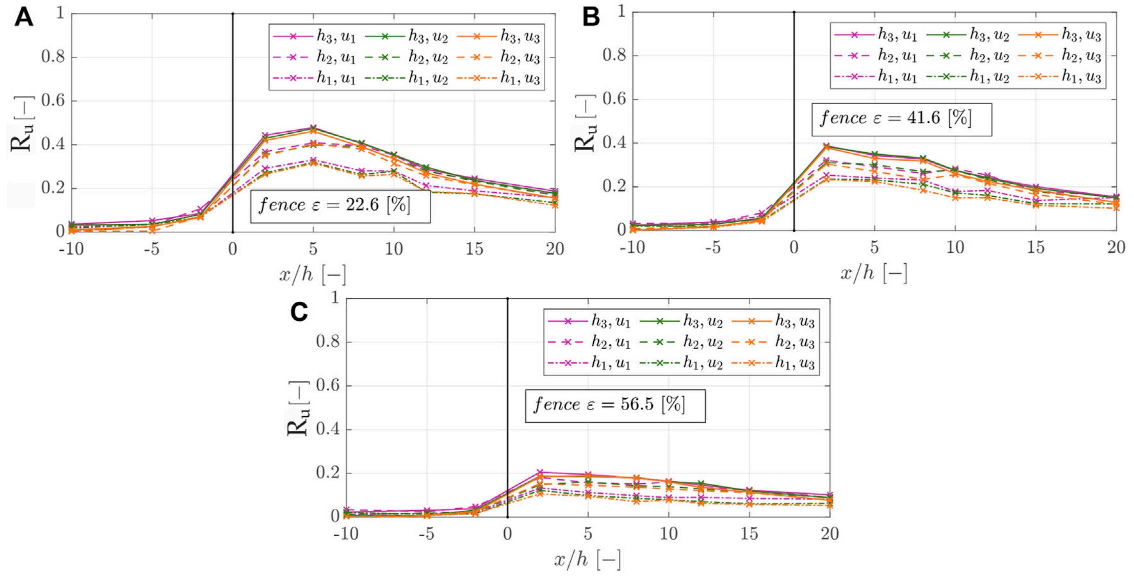

FIGURE 12 | Wind reduction coefficients accordingly to **Eq. 9** in the *x*-direction of fences with different characteristics, which are divided into **(A)** the fence porosities ε_1 = 22.6%, **(B)** ε_2 = 41.6%, and **(C)** ε_3 = 56.5%.

Wind Velocity Characteristics

The wind profile could be measured well and provide reproducible data in repeated experiments with the applied methodology. In **Figure 11**, the wind reduction factors R_u (-), according to **Eq. 9**, for the fence heights h = 40, 80, 120 mm are shown along the *x*-axis, normalized over the fence heights.

In **Figure 12**, the wind reduction factors R_u (-) for the fence porosities of ε = 22.6, 41.6, 56.5% are shown respectively.

Note that a higher wind reduction factor indicates a more substantial reduction in wind velocity and thus favors sediment deposition around the sand-trapping fence. We recognized that the wind reduction coefficients were almost the same for varying free wind velocities but varied significantly for different fence porosities and fence heights. The results show that, with increasing distance from the fence, the wind reduction coefficient increased to the maximum value and then decreased or stabilized again. The position at which R_u

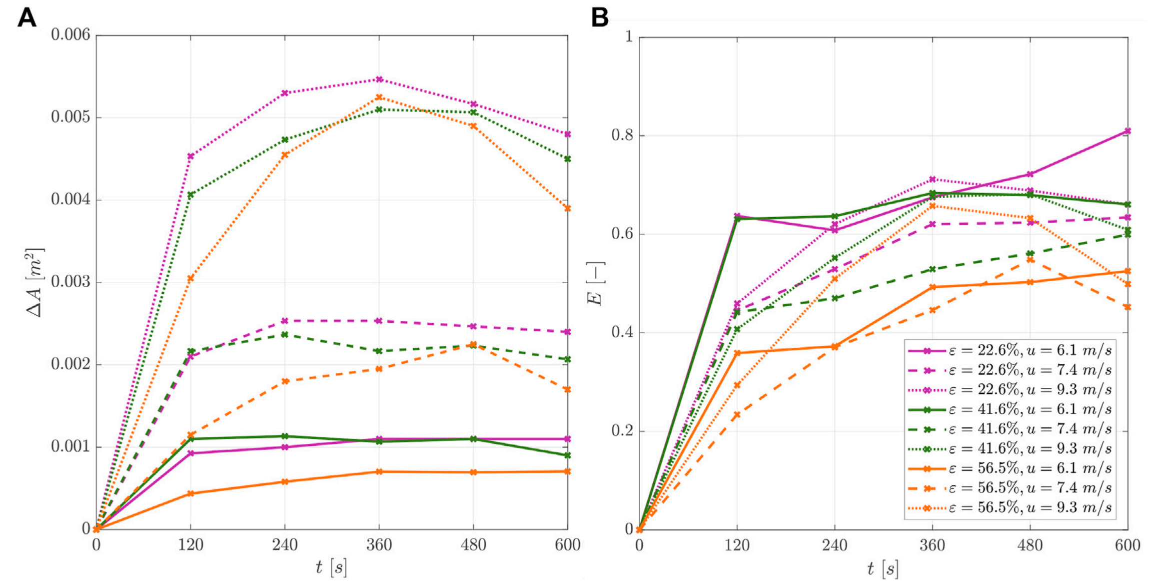

FIGURE 13 | Change of **(A)** cross-sectional area *ΔA* (-) and **(B)** trap efficiency *E* (-) for different investigated fence configurations varying in fence porosities ε_1 = 22.6%, ε_2 = 41.6%, and ε_3 = 56.5% for investigated wind velocities u_1 = 6.1 m/s, u_2 = 7.4 m/s, and u_2 = 9.3 m/s expressed over the experiment duration *t* (s).

begins to decrease or stabilize, the protection range, generally lies between *x/h* = 2–5. The wind reduction coefficient was substantially greater for higher fences ($R_{u,max}$ = 0.48) than lower fences ($R_{u,max}$ = 0.21) and also higher for less porous fences ($R_{u,max}$ = 0.48) than for more porous fences. Furthermore, it becomes clear that for the medium and high fences, the influence of the porosity is greater than for the low fences since the variety of R_u is also smaller. However, the fence height plays a minor role in the case of the most porous fence. This is in agreement with findings of Perera (1981), who found in wind tunnel experiments with vertical and horizontal slats (porosity >30–50%) or Lee and Kim (1999) who found with perforated fences (circular openings with porosity >40%), no recirculating zone occurred due to the strong bleed flow. For ε_1 = 22.6% and ε_2 = 41.6%, the typical airflow conditions around a single porous fence can be identified (Plate, 1971). However, for the fence of porosity ε_3 = 56.5%, a strong bleed flow leads to smaller wind velocity reduction, the recirculating zone disappears, and the airflow zones become less complex (Dong et al., 2007).

Sediment Transport Fluxes and Sediment Accretion Around the Sand-Trapping Fence Configurations

We found that the two-dimensional development of the sediment accretion around the sand-trapping fences could be measured well with the 2D LiDAR scanner and is quantitatively reproducible in repeated experiments (maximum standard deviation of the sediment accretion σ ~ 0.15). However, for low wind speeds, the ratio of the measurement error to the deposition heights is so small that the measurement error has a significant influence on the results. In addition, the aeolian sediment fluxes showed large temporal fluctuations, which were noticed especially during experiments with the wind velocity u_1 = 6.1 m/s, see **Table 1**. As far as the authors know, the reproducibility of the sediment accretion around a sand-trapping fence is investigated for the first time with the results presented herein.

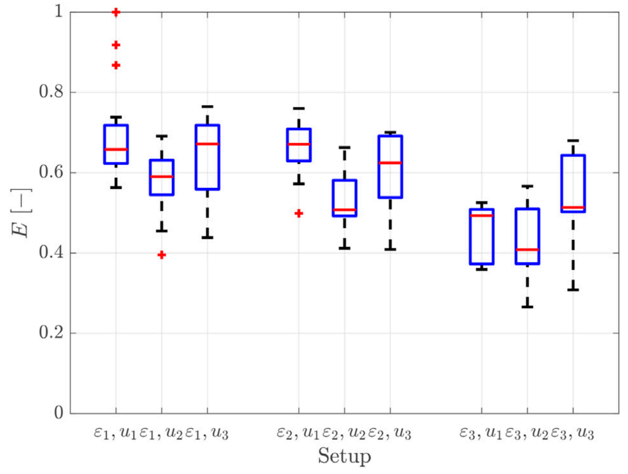

FIGURE 14 | Trap efficiency *E* (-) calculated by **Eq. 12** for different investigated fence configurations varying in fence porosity ε_1 = 22.6%, ε_2 = 41.6%, and ε_3 = 56.5% for investigated wind velocities u_1 = 6.1 m/s, u_2 = 7.4 m/s, and u_3 = 9.3 m/s over the whole measuring time *t* = 600 s.

Figure 13A gives the changes of cross-sectional area and **Figure 13B** the trap efficiency for all configurations over time. The changes of cross-sectional areas *ΔA* (m^2) and the trap efficiencies *E* (-) are shown as the average value of three up to four repeated measurements. Generally, as the sediment transport rates increase, the cross-sectional areas around the sand-trapping fence also increase; with the densest fence tending to accumulate the most sediment, then the medium-density fence, and then the porous fence. At the beginning of the experiments, the trap efficiency increases, and as time passes, the efficiency decreases or stabilizes.

For the medium (u_2 = 7.4 m/s) and high wind velocity (u_3 = 9.3 m/s), the maximum trap efficiency is reached between t = 360–600 s, whereas, for the lowest wind velocity (u_1 = 6.1 m/s), the maximum is reached at t = 360 s. After the trap efficiency increases to its maximum, it decreases slightly or stagnates to equilibrium during the time investigated in our experiments. This is in accordance with findings of Ning et al. (2020), where the sand-trapping is highest at the beginning of the first phase, drops significantly until the end of the first phase, and continues to drop slowly until the end of the second phase.

For the different investigated sand-trapping fence's porosities (ε_1 = 22.6%, ε_2 = 41.6%, ε_3 = 56.5%) and wind velocities (u_1 = 6.1 m/s, u_2 = 7.4 m/s, u_3 = 9.3 m/s), the calculated trap efficiencies, see **Eq. 12**, are shown as boxplots (**Figure 14**). Since the efficiencies vary over time, all timesteps of the experiments are included showing the variations. The mean trap efficiencies for the dense fence (ε_1 = 22.6%) $E_{h120,e22.6}$ are 0.69 (u_1 = 6.1 m/s), 0.57 (u_2 = 7.4 m/s), 0.63 (u_3 = 9.3 m/s) and for the medium fence $E_{h120,e41.6}$ are 0.66 (u_1 = 6.1 m/s), 0.52 (u_2 = 7.4 m/s), 0.58 (u_3 = 9.3 m/s). For the highest fence porosity (ε_3 = 56.5%), the efficiencies $E_{h120,e56.6}$ are 0.45 (u_1 = 6.1 m/s), 0.41 (u_2 = 7.4 m/s), 0.52 (u_3 = 9.3 m/s).

Generally, the trap efficiency for the dense and medium fence are higher than for the lowest porosity fence. However, the shape of the resulting sediment accretion differs for the fences. Sand-trapping fences with lower porosities (ε_1 = 22.6% and ε_2 = 41.6%) favor localized sediment accretion directly at their brushwood lines. Fences with higher porosity (ε_3 = 56.5%), allow for more sediment accretion further downwind, see also **Figure 10**. Thus, denser fence porosities are more suitable for constructing sand-trapping fences to initiate and facilitate the coastal dune toe growth. Fences with higher porosity could be used where the sediment accretion would occur over a longer downwind distance, for example, to allow a smoother transition between the foredunes and the white dunes.

Moreover, for the same porosity, the low wind velocity (u_1 = 6.1 m/s) always gives the highest trap efficiency, followed by efficiency for the highest wind velocity (u_3 = 9.3 m/s) and the medium wind velocity (u_2 = 7.4 m/s). This can be explained by the fact that the critical shear stress velocity is minimally exceeded at the lowest wind velocity.

We strongly recommend extending the wind tunnel experiments over longer test sections to gain more quantitative data. This would require much larger wind tunnel dimensions with a larger sediment bed as well as a continuous sediment supply. With these proposed boundaries, it could be measured over more extended periods. Furthermore, installing numerous rows of fences in a larger wind tunnel would allow us to evaluate the optimal distance between numerous rows of fences to favor sediment accretion.

CONCLUSION

Physical model tests were conducted on sand-trapping fences with different fence heights (h = 40, 80, and 120 mm) and fence porosities (ε = 22.6, 41.6, and 56.5%). These tests occurred in an indoor subsonic, blowing-sand wind tunnel equipped with a moveable sediment bed (d_{50} ~ 212 µm). The experimental mean wind velocities were u_1 = 6.1 m/s, u_2 = 7.4 m/s, and u_3 = 9.3 m/s. We used a hot-wire anemometer to measure the flow fields, a vertical mesh sand trap to determine the sediment fluxes, and a 2D laser scanner to record the sediment accretion around the sand-trapping fences over time. The results of these experiments gave the following conclusions:

1) The wind profiles could be measured well with the hot-wire anemometer and provide reproducible data in repeated experiments. We recognized that the wind reduction coefficients varied significantly for different fence porosities and fence heights. It becomes clear that for the medium and high fence, the influence of the porosity is more significant than for the low fence height. However, the fence height plays a minor role for the high fence porosity. For the lower fence porosities, ε_1 = 22.6% and ε_2 = 41.6%, the typical airflow conditions around a single porous fence could be identified. The airflow zones around the fence of porosity ε_3 = 56.5% are less complex.
2) The two-dimensional development of the sediment accretion around the sand-trapping fences could be measured well with the 2D LiDAR scanner and is quantitatively reproducible in repeated experiments. However, for the quantitative evaluation, low wind velocities and high fence porosities associated with low sediment accretion significantly influence the trapping efficiency, where the ratio of the measurement error to the deposition heights is small.
3) For the first time, the influence of model effects in wind tunnel experiments on the sediment accretion around a fence is considered. For this purpose, the different sediment fluxes are differentiated so that the sand-trapping efficiency is specified to the close range of the fence.
4) At the beginning of the experiments, the trap efficiency increases until its maximum, and as time passes, the efficiency decreases slightly or stagnates over an equilibrium during the time investigated in our experiments.
5) The porosity of the fence significantly controls the efficiency to trap sediment. More sediment deposits for fences with porosities of ε_1 = 22.6% and ε_2 = 41.6%, where localized sediment accretion directly at the sand-trapping fence takes place. Fences with higher porosity (ε_3 = 56.5%) and an associated stronger bleed flow, allow for sediment accretion further downwind.
6) We recommend coastal managers to choose the fence porosity depending on the installation purpose. Lower fence porosities can be used to initiate and facilitate the dune toe growth, whereas fences with higher porosity would be more suitable to favor the sediment accretion between the transition of foredunes and white dunes as they have a wider range in which sediment accretes downwind.

The study results are of considerable significance for guidelines on installing sand-trapping fences and can provide theoretical support for their design.

Since experimental time, wind velocity, fence height, and the number of fence rows in wind tunnel investigations are often limited by the dimensions of the wind tunnel, long-term *in situ* measurements of sediment accretion around sand-trapping fences are needed containing data of changes in topography, beach slope, wet and dry beach width, tidal range, wind direction, and wind velocity.

DATA AVAILABILITY STATEMENT

The raw data supporting the conclusion of this article will be made available by the authors, without undue reservation.

AUTHOR CONTRIBUTIONS

Conceptualization: CE; methodology: CE; formal analysis: CE; investigation: CE; data processing: CE; resources: HS; original draft preparation: CE; review and editing: HS; visualization: CE; supervision: HS; project administration: HS; and funding acquisition: CE, HS and others. All authors have read and agreed to the published version of the manuscript.

FUNDING

This research was funded by the German Federal Ministry of Education and Research (BMBF) within the project ProDune (Grant Number 03KIS125) that was initiated in the framework of the German Coastal Engineering Research Council (KFKI).

ACKNOWLEDGMENTS

The authors thank the project partner Lower Saxony Water Management, Coastal Protection and Nature Conservation Agency for sharing their expertise in the project support group. The authors also thank Holger Blum for organizing sediments from the East Frisian Island of Norderney. We, furthermore, thank the technical staff and student assistants Sonja Möller, Mariana Vélez Perez, Marie Künzel, Michael Nelles, and Andrea Limberg of the IWW for their help in constructing and conducting the wind tunnel experiments.

REFERENCES

Adriani, M. J., and Terwindt, J. (1974). *Sand Stabilization and Dune Building. Gov. Publ. off; Government Publ. Office, GBV Gemeinsamer Bibliotheksverbund, the Hague*, 68. The Hague: Rijkswaterstaat Communications.

Anderson, J. D. (2017). *Fundamentals of Aerodynamics*. McGraw-Hill series in aeronautical and aerospace engineering, 1130.

Arens, S. M., Baas, A. C. W., Van Boxel, J. H., and Kalkman, C. (2001). Influence of Reed Stem Density on Foredune Development. *Earth Surf. Process. Landforms* 26, 1161–1176. doi:10.1002/esp.257

Baas, A. C. W., and Sherman, D. J. (2006). Spatiotemporal Variability of Aeolian Sand Transport in a Coastal Dune Environment. *J. Coastal Res.* 225, 1198–1205. doi:10.2112/06-0002.1

Bagnold, R. A. (1971). *The Physics of Blown Sand and Desert Dunes*. 2nd Edition. doi:10.1007/978-94-009-5682-7

Barlow, J., William, H., and Pope, A. (1999). *Low-Speed Wind Tunnel Testing.*

Bauer, B. O., and Davidson-Arnott, R. G. D. (2003). A General Framework for Modeling Sediment Supply to Coastal Dunes Including Wind Angle, beach Geometry, and Fetch Effects. *Geomorphology* 49, 89–108. doi:10.1016/S0169-555X(02)00165-4

Bauer, B. O., and Davidson-Arnott, R. G. D. (2014). Aeolian Particle Flux Profiles and Transport Unsteadiness. *J. Geophys. Res. Earth Surf.* 119, 1542–1563. doi:10.1002/2014JF003128

Cattafesta, L., Bahr, C., and Mathew, J. (2010). Fundamentals of Wind-Tunnel Design. *Encyclopedia Aerospace Eng.* 58, 467. doi:10.1002/9780470686652.eae532

Cermak, J. E. (1987). Advances in Physical Modeling for Wind Engineering. *J. Eng. Mech.* 113113, 7375–7756. doi:10.1061/(ASCE)0733-939910.1061/(asce)0733-9399(1987)113:5(737)

Chen, B., Cheng, J., Xin, L., and Wang, R. (2019). Effectiveness of Hole Plate-type Sand Barriers in Reducing Aeolian Sediment Flux: Evaluation of Effect of Hole Size. *Aeolian Res.* 38, 1–12. doi:10.1016/j.aeolia.2019.03.001

Cohn, N., Hoonhout, B., Goldstein, E., de Vries, S., Moore, L., Durán Vinent, O., et al. (2019). Exploring Marine and Aeolian Controls on Coastal Foredune Growth Using a Coupled Numerical Model. *JMSE* 7, 13. doi:10.3390/jmse7010013

Cohn, N., Ruggiero, P., Vries, S., and Kaminsky, G. M. (2018). New Insights on Coastal Foredune Growth: The Relative Contributions of Marine and Aeolian Processes. *Geophys. Res. Lett.* 45, 4965–4973. doi:10.1029/2018GL077836

Cornelis, W. M., and Gabriels, D. (2005). Optimal Windbreak Design for Wind-Erosion Control. *J. Arid Environments* 61, 315–332. doi:10.1016/j.jaridenv.2004.10.005

Creyssels, M., Dupont, P., El Moctar, A. O., Valance, A., Cantat, I., Jenkins, J. T., et al. (2009). Saltating Particles in a Turbulent Boundary Layer: experiment and Theory. *J. Fluid Mech.* 625, 47–74. doi:10.1017/S0022112008005491

Davidson-Arnott, R. G. D., MacQuarrie, K., and Aagaard, T. (2005). The Effect of Wind Gusts, Moisture Content and Fetch Length on Sand Transport on a beach. *Geomorphology* 68, 115–129. doi:10.1016/j.geomorph.2004.04.008

de Vries, S. (2013). Physics Of Blown Sand and Coastal Dunes. *Dissertation*. Delft,Netherlands: Delft University of Technology.

DIN EN ISO 14688-1 (2018). *Geotechnische Erkundung und Untersuchung – Benennung, Beschreibung und Klassifizierung von Boden: Teil 1*. Benennung und Beschreibung. doi:10.31030/2748424

Dong, Z., Luo, W., Qian, G., and Wang, H. (2007). A Wind Tunnel Simulation of the Mean Velocity fields behind Upright Porous Fences. *Agric. For. Meteorology* 146, 82–93. doi:10.1016/j.agrformet.2007.05.009

Eichmanns, C., Lechthaler, S., Zander, W., Pérez, M. V., Blum, H., Thorenz, F., et al. (2021). Sand Trapping Fences as a Nature-Based Solution for Coastal Protection: An International Review with a Focus on Installations in Germany. *Environments* 8, 135. doi:10.3390/environments8120135

Eichmanns, C., and Schüttrumpf, H. (2021). Influence of Sand Trapping Fences on Dune Toe Growth and its Relation with Potential Aeolian Sediment Transport. *JMSE* 9, 850. doi:10.3390/jmse9080850

Eichmanns, C., and Schüttrumpf, H. (2020). Investigating Changes in Aeolian Sediment Transport at Coastal Dunes and Sand Trapping Fences: A Field Study on the German Coast. *JMSE* 8, 1012. doi:10.3390/jmse8121012

Ellis, J. T., Li, B., Farrell, E. J., and Sherman, D. J. (2009). Protocols for Characterizing Aeolian Mass-Flux Profiles. *Aeolian Res.* 1, 19–26. doi:10.1016/j.aeolia.2009.02.001

Gallego-Fernández, J. B. (2013). *Restoration of Coastal Dunes*. Berlin, Heidelberg: Springer Berlin/Heidelberg.

Gerhardt, P. (1990). *Handbuch des deutschen Dünenbaus*. Berlin.

Hacker, S. D., Zarnetske, P., Seabloom, E., Ruggiero, P., Mull, J., Gerrity, S., et al. (2012). Subtle Differences in Two Non-native Congeneric beach Grasses

Significantly Affect Their Colonization, Spread, and Impact. *Oikos* 121, 138–148. doi:10.1111/j.1600-0706.2011.18887.x

Han, Q., Qu, J., Liao, K., Zhu, S., Zhang, K., Zu, R., et al. (2011). A Wind Tunnel Study of Aeolian Sand Transport on a Wetted Sand Surface Using Sands from Tropical Humid Coastal Southern China. *Environ. Earth Sci.* 64, 1375–1385. doi:10.1007/s12665-011-0962-7

Harff, J., Björck, S., and Hoth, P. (2011). *The Baltic Sea basin*. Berlin: Springer.

Hesp, P. (2011). Dune Coasts. *Earth Syst. Environ. Esciences*, 193–221. doi:10.1016/B978-0-12-374711-2.00310-7

Ho, T. D., Dupont, P., Ould El Moctar, A., and Valance, A. (2012). Particle Velocity Distribution in Saltation Transport. *Phys. Rev. E* 85, 52301. doi:10.1103/PhysRevE.85.052301

Ho, T. D., Valance, A., Dupont, P., and Ould El Moctar, A. (2011). Scaling Laws in Aeolian Sand Transport. *Phys. Rev. Lett.* 106, 94501. doi:10.1103/PhysRevLett.106.094501

Hotta, S., and Horikawa, K. (1991). Function of Sand Fence Placed in Front of Embankment. *Proc. 22nd Conf. Coastal Eng.*, 2754–2767. doi:10.1061/9780872627765.211

Houser, C., Wernette, P., Rentschlar, E., Jones, H., Hammond, B., and Trimble, S. (2015). Post-storm beach and Dune Recovery: Implications for Barrier Island Resilience. *Geomorphology* 234, 54–63. doi:10.1016/j.geomorph.2014.12.044

Itzkin, M., Moore, L. J., Ruggiero, P., Hacker, S. D., and Biel, R. G. (2020b). *The Influence of Dune Aspect Ratio, Beach Width and Storm Characteristics on Dune Erosion for Managed and Unmanaged Beaches*.

Itzkin, M., Moore, L. J., Ruggiero, P., and Hacker, S. D. (2020a). The Effect of Sand Fencing on the Morphology of Natural Dune Systems. *Geomorphology* 352, 106995. doi:10.1016/j.geomorph.2019.106995

Jackson, D. W. T., and Cooper, J. A. C. (1999). Beach Fetch Distance and Aeolian Sediment Transport. *Sedimentology* 46, 517–522. doi:10.1046/j.1365-3091.1999.00228.x

Jackson, N. L., and Nordstrom, K. F. (2011). Aeolian Sediment Transport and Landforms in Managed Coastal Systems: A Review. *Aeolian Res.* 3, 181–196. doi:10.1016/j.aeolia.2011.03.011

Keijsers, J. G. S., De Groot, A. V., and Riksen, M. J. P. M. (2015). Vegetation and Sedimentation on Coastal Foredunes. *Geomorphology* 228, 723–734. doi:10.1016/j.geomorph.2014.10.027

Lawlor, P., and Jackson, D. (2021). "A Nature-Based Solution for Coastal Foredune Restoration: The Case Study of Maghery, County Donegal, Ireland," in *Book: Exploring the Multiple Values of Nature: Connecting Ecosystems and People across Landscapes*. 1st Edition (Springer Nature).

Lee, S.-J., and Kim, H.-B. (1999). Laboratory Measurements of Velocity and Turbulence Field behind Porous Fences. *J. Wind Eng. Ind. Aerodynamics* 80, 311–326. doi:10.1016/S0167-6105(98)00193-7

Li, B., and Sherman, D. J. (2015). Aerodynamics and Morphodynamics of Sand Fences: A Review. *Aeolian Res.* 17, 33–48. doi:10.1016/j.aeolia.2014.11.005

Manohar, M., and Bruun, P. (1970). Mechanics of Dune Growth by Sand Fences. *Dock and harbour authority*, 243–252.

MATLAB (2018). Natick, Massachusetts: The MathWorks Inc. Version 9.510.944444 (R2018b)Available at: https://de.mathworks.com/products/new_products/release2018b.html (Accessed March 31, 2021).

Mehta, R. D. (1979). The Aerodynamic Design of Blower Tunnels with Wide-Angle Diffusers. *Prog. Aerospace Sci.* 18, 59–120. doi:10.1016/0376-0421(77)90003-3

Miri, A., Dragovich, D., and Dong, Z. (2019). Wind-borne Sand Mass Flux in Vegetated Surfaces - Wind Tunnel Experiments with Live Plants. *CATENA* 172, 421–434. doi:10.1016/j.catena.2018.09.006

Mulhearn, P. J., and Bradley, E. F. (1977). *Secondary Flows in the lee of Porous Shelterbelts*.

NASA (2020). *Living Ocean*.

Nickling, W. G., and Davidson-Arnott, R. G. D. (1990). Aeolian Sediment Transport on Beaches and Coastal Sand Dunes. Proceedings Canadian Symposium on Costal Sand Dunes 1990. *Proc. Symp. Coastal Sand Dunes*, 1–36.

Nikuradse, J. (1933). *Strömungsgesetze in Rauhen Rohren. English: Flow laws in rough pipes*.

Ning, Q., Li, B., and Ellis, J. T. (2020). Fence Height Control on Sand Trapping. *Aeolian Res.* 46, 100617. doi:10.1016/j.aeolia.2020.100617

O'Connel, J. (2008). Coastal Dune Protection & Restoration: Using 'Cape' American Beach Grass And Fencing.

Owen, P. R., and Gillette, D. (1985). "Wind Tunnel Constraint on Saltati," in *Proceedings of the International Workshop on the Physics of Blown Sand*, 253–269.

Perera, M. D. A. E. S. (1981). Shelter behind Two-Dimensional Solid and Porous Fences. *J. Wind Eng. Ind. Aerodynamics* 8, 93–104. doi:10.1016/0167-6105(81)90010-6

Plate, E. J. (1971). The Aerodynamics of Shelter Belts. *Agric. Meteorology* 8, 203–222. doi:10.1016/0002-1571(71)90109-9

Poortinga, A., Keijsers, J. G. S., Maroulis, J., and Visser, S. M. (2014). Measurement Uncertainties in Quantifying Aeolian Mass Flux: Evidence from Wind Tunnel and Field Site Data. *PeerJ* 2, e454. doi:10.7717/peerj.454

Ruz, M.-H., and Anthony, E. J. (2008). Sand Trapping by Brushwood Fences on a beach-foredune Contact: the Primacy of the Local Sediment Budget. *zfg_suppl* 52, 179–194. doi:10.1127/0372-8854/2008/0052S3-0179

Shao, Y., and Lu, H. (2000). A Simple Expression for Wind Erosion Threshold Friction Velocity. *J. Geophys. Res.* 105, 22437–22443. doi:10.1029/2000JD900304

Sherman, D. J., Swann, C., and Barron, J. D. (2014). A High-Efficiency, Low-Cost Aeolian Sand Trap. *Aeolian Res.* 13, 31–34. doi:10.1016/j.aeolia.2014.02.006

Strypsteen, G. (2019). *Monitoring and Modelling Aeolian Sand Transport at the Belgian Coast*. Leuven, Belgium: Dissertation. KU Leuven, Faculty of Engineering Technology, 1–226. doi:10.13140/RG.2.2.19781.88806

Swann, C., Brodie, K., and Spore, N. (2015). *Coastal Foredunes: Identifying Coastal, Aeolian, and Management Interactions Driving Morphologic State Change: ERDC/CHL TR-15-17*. Washington, DC 20314: U.S. Army Corps of Engineers–1000.

testo (2021). *Hot-wire Anemometer and External Data Logger: Product Specifications*. Testo SE & Co. KGaA.

van Rijn, L. C. (2019). *Aeolian Transport over a Flat Sediment Surface*.

van Rijn, L. C., and Strypsteen, G. (2020). A Fully Predictive Model for Aeolian Sand Transport. *Coastal Eng.* 156, 103600. doi:10.1016/j.coastaleng.2019.103600

van Thiel de Vries, J. S. M. (2009). Dune Erosion during Storm Surges. *Dissertation*. Netherlands. Amsterdam: Delft University of Technology, Civil Engineering and Geosciences, Hydraulic EngineeringTechnische Universität Delft.

Vithana (2013). *The Effect of Stone Protrusion on the Incipient Motion of Rock armour under the Action of Regular Waves*. London: Department of Civil, Environmental & Geomatic Engineering, University College London.

Wang, T., Qu, J., Ling, Y., Liu, B., and Xiao, J. (2018). Shelter Effect Efficacy of Sand Fences: A Comparison of Systems in a Wind Tunnel. *Aeolian Res.* 30, 32–40. doi:10.1016/j.aeolia.2017.11.004

White, R. R. (1996). *Laboratory Simulation of Aeolian Sand Transport and Physical Modeling of Flow Around Dunes*. Annals of Arid Zone, 187–213.

Yu, Y.-p., Zhang, K.-c., An, Z.-s., Wang, T., and Hu, F. (2020). The Blocking Effect of the Sand Fences Quantified Using Wind Tunnel Simulations. *J. Mt. Sci.* 17, 2485–2496. doi:10.1007/s11629-020-6095-2

Zhang, N., Kang, J.-H., and Lee, S.-J. (2010). Wind Tunnel Observation on the Effect of a Porous Wind Fence on Shelter of Saltating Sand Particles. *Geomorphology* 120, 224–232. doi:10.1016/j.geomorph.2010.03.032

Conflict of Interest: The authors declare that the research was conducted in the absence of any commercial or financial relationships that could be construed as a potential conflict of interest.

frontiers | Frontiers in Built Environment

ORIGINAL RESEARCH
published: 27 April 2022
doi: 10.3389/fbuil.2022.885215

Impacts of Coastal Infrastructure on Shoreline Response to Major Hurricanes in Southwest Louisiana

Jack A. Cadigan[1], Jasmine H. Bekkaye[2,3], Navid H. Jafari[2,3], Ling Zhu[4], Ashley R. Booth[5], Qin Chen[4,6], Britt Raubenheimer[7], Brian D. Harris[1], Chris O'Connor[8], Robert Lane[9], G. Paul Kemp[10], Jason N. Day[9], John W. Day[10] and Hanssel Omar Ulloa[2]*

[1]Coastal Hydraulics Laboratory, U.S. Army Corps of Engineers Research and Development Center, Vicksburg, MS, United States, [2]Department of Civil and Environmental Engineering, Louisiana State University, Baton Rouge, LA, United States, [3]Coastal Studies Institute, Louisiana State University, Baton Rouge, LA, United States, [4]Department of Civil and Environmental Engineering, Northeastern University, Boston, MA, United States, [5]School of Renewable Natural Resources, Louisiana State University, Baton Rouge, LA, United States, [6]Department of Marine and Environmental Sciences, Northeastern University, Boston, MA, United States, [7]Department of Applied Ocean Physics and Engineering, Woods Hole Oceanographic Institution, Falmouth, MA, United States, [8]Department of Marine Sciences, University of North Carolina at Wilmington, Wilmington, NC, United States, [9]Comite Resources, Inc., Baton Rouge, LA, United States, [10]Department of Oceanography and Coastal Sciences, Louisiana State University, Baton Rouge, LA, United States

OPEN ACCESS

Edited by:
Jens Figlus,
Texas A&M University, United States

Reviewed by:
Stephanie M. Smallegan,
University of South Alabama, United States
Takayuki Suzuki,
Yokohama National University, Japan
Jon Miller,
Stevens Institute of Technology, United States

***Correspondence:**
Jack A. Cadigan
Jack.A.Cadigan@usace.army.mil

Specialty section:
This article was submitted to Coastal and Offshore Engineering, a section of the journal Frontiers in Built Environment

Received: 27 February 2022
Accepted: 08 April 2022
Published: 27 April 2022

Citation:
Cadigan JA, Bekkaye JH, Jafari NH, Zhu L, Booth AR, Chen Q, Raubenheimer B, Harris BD, O'Connor C, Lane R, Kemp GP, Day JN, Day JW and Ulloa HO (2022) Impacts of Coastal Infrastructure on Shoreline Response to Major Hurricanes in Southwest Louisiana. Front. Built Environ. 8:885215. doi: 10.3389/fbuil.2022.885215

The Rockefeller Wildlife Refuge, located along the Chenier Plain in Southwest Louisiana, was the location of the sequential landfall of two major hurricanes in the 2020 hurricane season. To protect the rapidly retreating coastline along the Refuge, a system of breakwaters was constructed, which was partially completed by the 2020 hurricane season. Multi-institutional, multi-disciplinary rapid response deployments of wave gauges, piezometers, geotechnical measurements, vegetation sampling, and drone surveys were conducted before and after Hurricanes Laura and Delta along two transects in the Refuge; one protected by a breakwater system and one which was the natural, unprotected shoreline. Geomorphological changes were similar on both transects after Hurricane Laura, while after Delta there was higher inland sediment deposition on the natural shoreline. Floodwaters drained from the transect with breakwater protection more slowly than the natural shoreline, though topography profiles are similar, indicating a potential dampening or complex hydrodynamic interactions between the sediment—wetland—breakwater system. In addition, observations of a fluidized mud deposit in Rollover Bayou in the Refuge are presented and discussed in context of the maintenance of wetland elevation and stability in the sediment starved Chenier Plain.

Keywords: hurricane impact, wave attenuation and erosion control, storm surge, chenier plain, breakwater, field measured data, natural infrastructure, shoreline retreat

INTRODUCTION

During the hurricane season of 2020, the sequential landfalls of Hurricane Laura (27 August 2020) and Hurricane Delta (09 October 2020) in southwest Louisiana caused widespread damage and led to estimated economic losses in excess of $7 billion USD (Xi and Lin, 2021). These storms led to devastating impacts in a region that is already subject to environmental stressors such as altered hydrology, shoreline erosion, wetland loss, and saltwater intrusion (Gary, 1979; Shiner Mosley and Associates, 2002; Penland et al., 2005; Morton and Barras, 2011; (LACPRA, 2017). Prior to the 2020 hurricane season, to conserve ecosystem and infrastructure integrity, breakwaters were installed along portions of the southwest Louisiana shoreline (Campbell et al., 2005; Jafari et al., 2020; Reid, 2021). The landfalls of Hurricane Laura and Hurricane Delta led to a unique opportunity to examine the effects of two major hurricanes impacting the same location, half of which was protected by a system of breakwaters by the time of the 2020 hurricane season.

Both Hurricanes Laura and Delta underwent a process known as rapid intensification, i.e., an increase in the maximum sustained winds of at least 56.3 km/h over a 24-h period, prior to landfall (Eley et al., 2021; Zhou et al., 2021; Zhu et al., 2021). Rapid intensification is a highly dangerous process that is difficult to forecast, but which seems to be increasing in frequency for Atlantic storms and worldwide (Balaguru et al., 2018). Hurricane Laura rapidly intensified from being a Category 1 hurricane the day prior to landfall, to a Category 4 hurricane at landfall and the strongest hurricane to strike Louisiana since Hurricane Camille in 1969 (Pasch et al., 2021). Hurricane Delta rapidly intensified from a tropical depression to a Category 4 hurricane over a 30-h period. However, it weakened while passing over the tip of the Yucatan Peninsula before then re-strengthening and making landfall as a Category 2 near Creole, Louisiana, six weeks after and only 19 kms east of the landfall location of Hurricane Laura (Cangialosi and Berg, 2021; Pasch et al., 2021).

Southwest Louisiana is home to significant oil and gas infrastructure (Martin Associates, 2021) and supports a large portion of the state's agriculture and fisheries industries (LACPRA, 2017). The part of southwest Louisiana in which these storms made direct landfall notably features the Cameron Liquified Natural Gas facility and a variety of other industrial shipping terminals on the Calcasieu Ship Channel, estimated to have provided $39 billion USD in economic value in 2020 to the United States and supported 53,722 jobs (Martin Associates, 2021). Impacts from the 2020 hurricane season on the fishing-related businesses in Louisiana including commercial fishers, marinas, charters, etc., are estimated on the lower bound to be $117 million, on the upper bound to be $205 million, and estimated on average to be on the order of $161 million (Caffey et al., 2022). The region is also home to several state and federal wildlife refuges, including the Rockefeller Wildlife Refuge (RWR or Rockefeller). Located proximal to the Calcasieu Ship Channel in southwest Louisiana, and having experienced direct landfall impacts from Hurricanes Laura and Delta, RWR and adjacent areas provided a unique case study to monitor the response of coastal wetlands using field observations to sequential major hurricane passage. In addition, at the time of the 2020 hurricane season, approximately half of Rockefeller's Gulf of Mexico shoreline was protected by an artificial breakwater system with the remainder slated for construction, providing the opportunity to evaluate differences in wetland system response to the storms and help provide guidance to stakeholders and practitioners in the coastal engineering community.

STUDY SITE: ROCKEFELLER WILDLIFE REFUGE

The Rockefeller Wildlife Refuge (**Figure 1**) is a state-managed wildlife refuge in Cameron and Vermillion Parishes, Louisiana, located in the Chenier Plain, a geographic feature that spans much of coastal southwest Louisiana and southeast Texas (Oscar et al., 2001). The Chenier Plain is one of two distinct geomorphological zones in Louisiana; the Mississippi River Delta Plain is located in the southeastern portion of Louisiana while the Chenier Plain resides in the southwestern portion of Louisiana (Roberts, 1997; McBride et al., 2007; McBride et al., 2013) Considered one of the most biologically diverse refuges in the nation, RWR has 43 km of shoreline and covers 287 km^2 of *chenier* ridges and a range of fresh, brackish, and salt marshes (LDWF, 2021). Due to its location at the southern terminus of the Mississippi and Central Flyways, RWR hosts hundreds of thousands of birds annually, serving as a critical seasonal stop-over for tropical passerines, a wintering ground for migratory waterbirds, and a year-round habitat for resident species - including species of concern like western Gulf Coast Mottled Ducks (*Anas fulvigula)*(Selman et al., 2011; LDWF, 2021).

When the land was donated to the state of Louisiana by the Rockefeller Foundation in 1919, Rockefeller Wildlife Refuge encompassed an area of approximately 348 km^2; due to rapid coastal erosion this area was reduced to 309 km^2 by 2004, 294 km^2 by 2011, and by more recent estimates, approximately 287 km^2 (Wise et al., 2004; Selman et al., 2011; LDWF, 2021). The average rate of erosion-driven shoreline retreat derived by remote sensing has been measured at approximately 14.5 m/yr between 1998–2017, with extreme rates of 19 m/yr and 25.5 m/yr during the years Hurricanes Rita (2005) and Ike (2008) struck (Yao et al., 2018). In fact, Yao et al. (2018) estimated a total erosion of approximately 300 m of shoreline between 1998 and 2017. Aerial imagery between 1998 and 2002 indicate an approximate erosion rate of 17 m/yr (Wise et al., 2004). Comparisons between shoreline positions from U.S. Department of Agriculture (USDA) National Agricultural Imagery Program (NAIP, +/− 1 m resolution) images from 2009 to 2019 (**Figures 2A,B**) show an approximate shoreline retreat of 170 m over the ten-year period, yielding similar results to the aforementioned Wise et al. (2004) erosion rate of 17 m/yr.

To protect the shoreline in this region from these high rates of retreat, extensive systems of breakwaters have been placed along the shoreline of southwest Louisiana (Reid, 2021). The breakwaters are part of a shoreline stabilization effort that has been discussed since at least 2001 (Hill and Belhadjali, 2005). The system was a collaboration between the National Oceanographic and Atmospheric Association (NOAA), the Louisiana Coastal Protection and Restoration Authority (CPRA), Louisiana Department of Wildlife and Fisheries (LDWF), and the National Marine Fisheries Service, with $34 million of funding secured from the Coastal Wetlands Planning, Protection and Restoration Act (CWPPRA) to construct a 6.4 km transect of emergent breakwaters along the RWR shoreline designed for Category 1 conditions (Jafari et al., 2020; Cohen et al., 2021; Reid, 2021). Funded as "ME-18," the multi-million-dollar project incorporated a Light Weight Aggregate Concrete (LWAC) breakwater system. The extremely soft subsurface sediments that extend for nearly 12 m below the ground surface make employing traditional shoreline stabilization structures difficult (Shiner Mosley and Associates, 2002), and thus the breakwaters

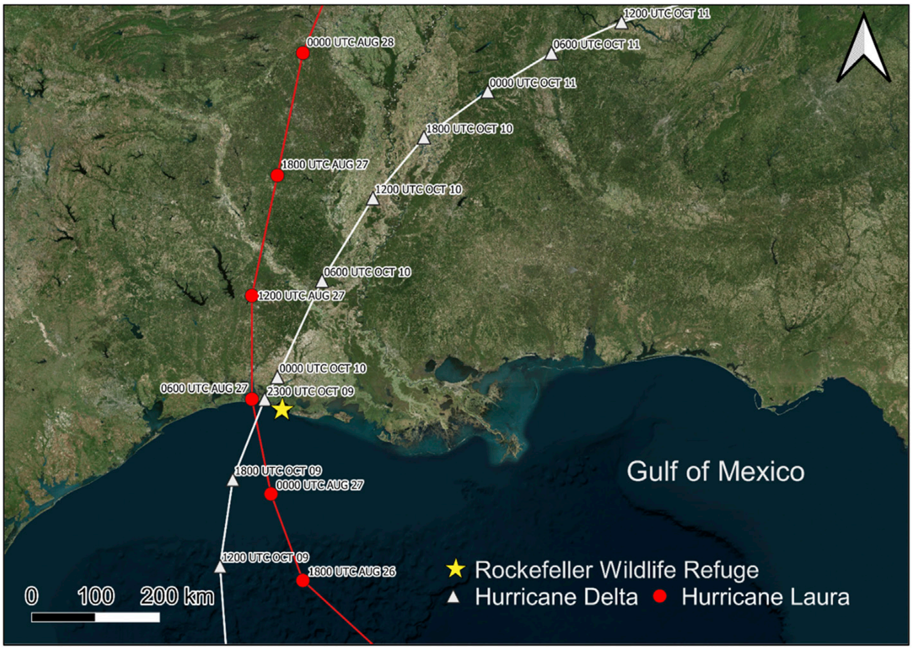

FIGURE 1 | Location of the study site, Rockefeller Wildlife Refuge (yellow star), on the Louisiana coastline and the time-stamped (UTC) paths of Hurricane Delta (white triangles) and Hurricane Laura (red circles) (Basemap: Satellite imagery courtesy of the U.S. Geological Survey, Google Earth Engine).

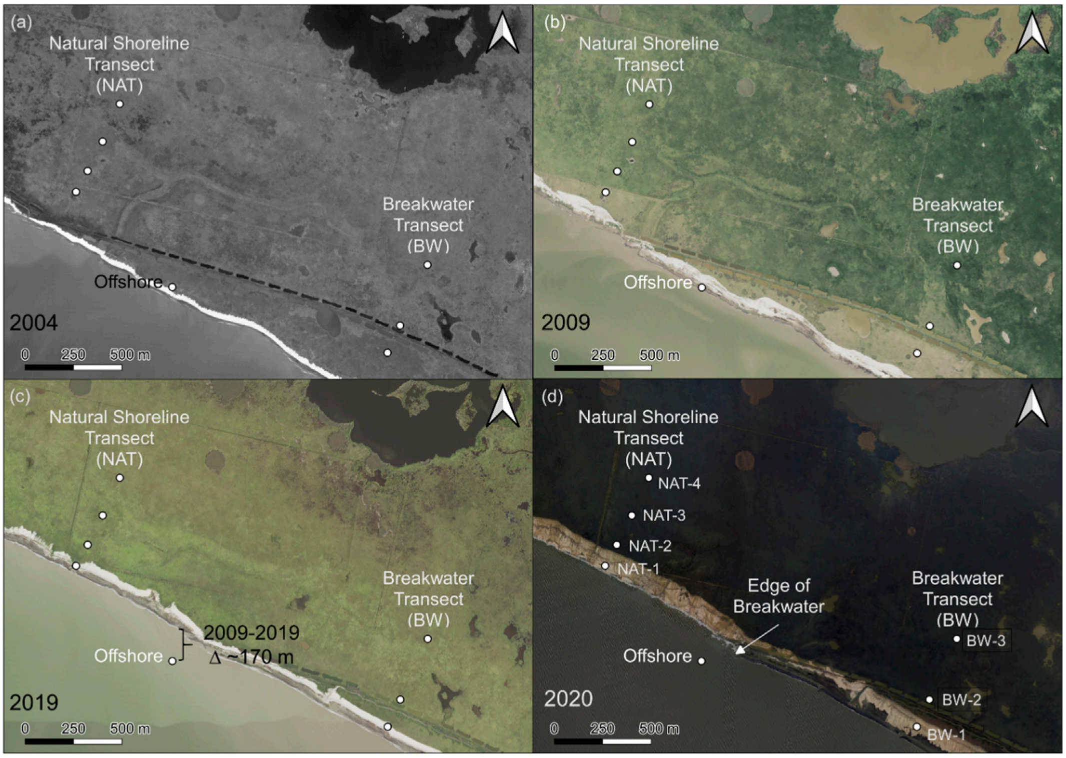

FIGURE 2 | USDA NAIP imagery of the study site in 2004 **(A)**, in 2009 **(B)**, in 2019 showing ~170 m of shoreline retreat **(C)**, and NOAA post-Delta aerial imagery in 2020 **(D)** showing the location of the two transects in relation to the breakwater structure.

were designed specifically to function atop the ultra-soft sediments offshore of the RWR shoreline through the use of lightweight aggregates enclosed in a geotextile fabric, which local engineers refer to as "pillows." During an experimental period in which various breakwater systems were placed along the RWR shoreline, the LWAC pillow system performed very well, and the protected shoreline lost approximately one meter of land while the unprotected shoreline eroded by nearly fourteen meters (Wise et al., 2004; Hill and Belhadjali, 2005; Geesey et al., 2011; Shows, 2019). The construction of the original 6.4 km reach of breakwaters was completed by June 2020, just prior to the period of major storm activity in Southwest Louisiana.

INSTRUMENTATION AND DATA COLLECTION PLAN

Prior to the landfall of Hurricane Laura, a collaborative team of members from Louisiana State University (LSU), Northeastern University (NEU), Woods Hole Oceanographic Institution (WHOI), and the University of North Carolina at Wilmington planned and rapidly mobilized to deploy instrumentation as part of a National Science Foundation Nearshore Extreme Events Reconnaissance (NEER) effort. The team repeatedly deployed along coastal Louisiana to monitor the effects of the devastating 2020 hurricane season on the fragile and rapidly eroding Louisiana shoreline. Due to the inherent time-restraints imposed by extreme event reconnaissance, namely the uncertainty in exact landfall location, site access, instrumentation, and crew availability, as well as the logistical and health concerns due to the timing of field work and the COVID-19 pandemic, data reconnaissance methods were restricted to instruments and equipment that could be rapidly deployed by a small crew. Post-Laura reconnaissance was performed at RWR on 04 September 2020. Due to the short time period between arrival of major storms in the Gulf of Mexico, the post-Laura reconnaissance also acted as pre-storm reconnaissance for Hurricane Delta. Prior to the landfall of Hurricane Delta (07 October 2020), a pre-storm reconnaissance was performed in the wetlands of Terrebonne Bay, near Houma, Louisiana, where the storm track was originally projected to make landfall. Post-Delta reconnaissance was performed at RWR on 26 October 2020. Two transects within RWR were the primary interest for this study: one termed the natural shoreline (not fully protected by the breakwater) and one in an area with a protected shoreline (protected by the breakwater). The two transects were visited for instrumentation staging and data reconnaissance on 25 August 2020 before the landfall of Hurricane Laura, on 4 September 2020 after the landfall of Hurricane Laura, and on 26 October 2020 after the landfall of Hurricane Delta.

USDA National Agricultural Imagery Program (NAIP) aerial imagery of the study site in 2004 (**Figure 2A**), 2009 (**Figure 2B**), and 2019 (**Figure 2C**), and NOAA Hurricane Delta (2020) post-storm aerial imagery (**Figure 2D**) are shown in **Figure 2**. Each of the four aerial images are geo-referenced and cropped to display the same region, and each show the locations of the two study transects and the eight monitoring stations which were implemented in the pre-storm deployment. All eight monitoring stations were located on land in 2004 (**Figure 2A**) and 2009 (**Figure 2B**). The shoreline monitoring stations, NAT-1 and BW-1 were both located in vegetated saltmarsh wetlands well inland of the shoreline in 2004 and 2009. Between 2009 and 2019, the shoreline experienced approximately 170 m of retreat (**Figure 2C**) as evidenced by the transition of the offshore monitoring station from wetland to open-water. No significant pond expansion is visible inland, suggesting that wetland elevation and vegetation health in the saltmarsh in this system are relatively stable until directly affected by processes such as shoreline retreat (Cadigan et al., 2020). The location of the edge of the breakwater noted in **Figure 2D** corresponds to the progress made towards construction of the breakwater system between 2019–2020 prior to the 2020 hurricane season.

During each of these field explorations, the breakwater and natural transects were surveyed with a GPS-RTK system to monitor elevation profiles from the shoreline inland to infer geomorphological changes and sediment deposition on the marsh platform. To avoid issues with identifying the shoreline location in the dynamic environment of RWR, each transect featured a consistent location across all three site visits from which distance inland was measured. In the natural shoreline transect, wave gauges were placed at four (4) locations at equal spacing from the shoreline inland. In the breakwater transect, gauges were placed at three (3) locations from the shoreline inland. In addition, a wave gauge was placed offshore in water depth of 3.3 m. At each wave gauge location apart from the offshore gauge, above-ground biomass samples were collected by randomly placing a 0.25 m × 0.25 m PVC square on the ground, cutting, removing and bagging all vegetation within the square. To help preserve the quality of the above-ground biomass during transport back to the laboratory, all samples were kept cool in an ice-chest from collection until transfer to a cold-storage room at Louisiana State University. Site instrumentation is depicted in **Figure 3**.

At each wave gauge site, TruBlue piezometer arrays were placed with one piezometer located just beneath the root mat (~30 cm below surface) and another approximately 1 m below surface. The wave gauges and piezometers recorded pressure hourly. Unfortunately, due to faulty equipment only two of the total twenty TruBlue sensors placed along the two main transects (as well as those further inland near buildings which house RWR's research facilities) retained recorded data. To rapidly capture high-resolution aerial products of the sites, two different UAVs were deployed; the DJI Mavic Pro 2 and the DJI Matrice 210. While the DJI Mavic Pro 2 was used to capture aerial imagery to be processed into high-resolution orthorectified images (orthomosaic), the DJI Matrice 210 was flown with a MicaSense Altum multispectral sensor attached to collect multispectral imagery that could be utilized to calculate Normalized Difference Vegetation Index (NDVI) (Broussard et al., 2018; Klemas 2013). All UAV surveys were planned using Pix4Dcapture, a commercial software application developed for creating and executing autonomous UAV flight plans (Pix4D). The DJI Mavic Pro 2 was flown in a grid pattern of parallel flight lines with 80% frontal overlap and 70% side overlap

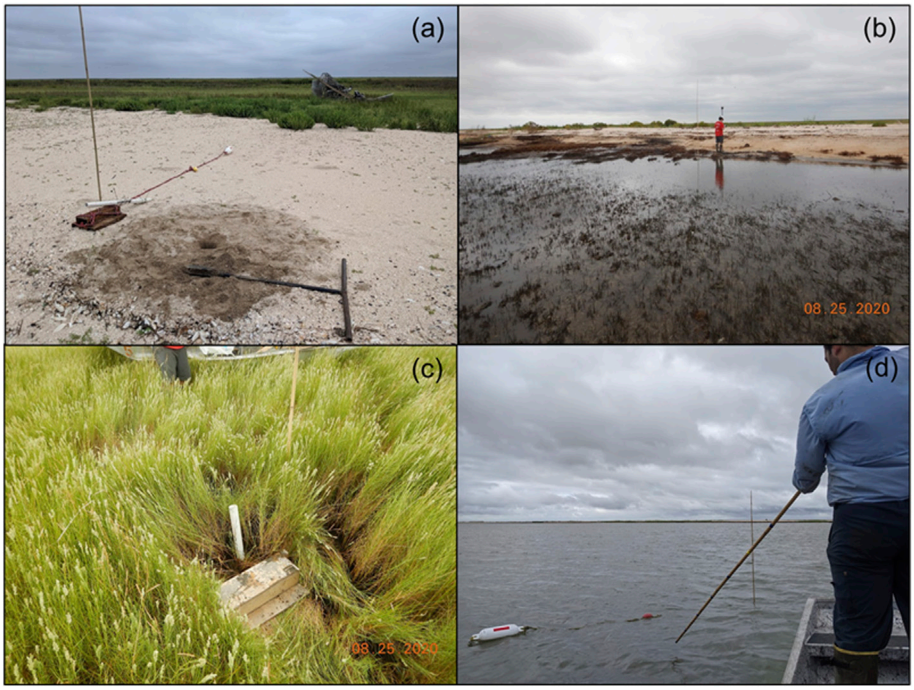

FIGURE 3 | Placing wave gauge and burying piezometers along beach shoreline **(A)**, conducting GPS-RTK measurements from the shoreline-inland **(B)**, typical study site layout with wave gauge, cane-pole marker, and PVC pipe attached to buried piezometers **(C)**, and deploying wave gauge offshore **(D)**.

from an approximate altitude of 40 m and a camera angle set at 70°. The DJI Matrice 210 was flown with all of the same flight settings as the DJI Mavic Pro except for the camera angle, which was set at 90°. Images were geotagged during capture through the UAVs' on-board GPS. Image processing was executed using Pix4Dmapper, a commercial software designed to be compatible with Pix4Dcapture and built for processing UAV imagery and data (Pix4D). Multispectral imagery was radiometrically calibrated in the program using images captured of a calibrated reflectance panel prior to the DJI Matrice 210 surveys. The resulting NDVI maps were compared to NDVI values calculated from Sentinel-2 satellite imagery retrieved and processed using Google Earth Engine (Gorelick et al., 2017). Cone penetrometer tests (CPT) were performed using a modified sleeve designed to better capture the effects of vegetation in the soil column after Hurricane Delta on 26 October 2020 along both transects to measure sediment shear strength and to identify any stratigraphic changes (Jafari et al., 2019a; Harris B. D. et al., 2020; Cadigan et al., 2020; Harris et al., 2021). Multispectral imagery at both transects was collected through DJI Matrice 210 surveys on 4 September 2020 and 26 October 2020 and true-color aerial imagery at both transects was captured *via* DJI Mavic Pro 2 surveys after Hurricane Delta on 26 October 2020. In addition to instrumentation placed along the natural and breakwater-protected transects, observations were made of a large, fluidized mud deposit at Rollover Bayou. Sediment density observations and deposition thickness measurements were made on-the-ground by researchers from Comite Resources, Inc. Drone surveys using similar methodology to the aforementioned transects were also conducted on the fluidized mud deposit.

WAVE CHARACTERISTICS

The wave gauges were sampled at 10 Hz to take continuous absolute pressure data. The recorded pressure (P) consists of hydrostatic pressure, hydrodynamic pressure, and atmospheric pressure (P_{atm}). The raw P was firstly converted to gauge pressure $P_{gage} = P - P_{atm}$ in which P_{atm} was measured at a nearby NOAA station (8768094) in Calcasieu Pass, LA, about 51 km northwest of the offshore wave gauge. The continuous time series of gauge pressure data was divided into bursts with each burst containing 30-min data. For each burst, the gauge pressure data were corrected and transformed from the time domain to the frequency domain by using the Ocean Wave Analyzing Toolbox, OCEANLYZ V2.0 (Karimpour and Chen, 2017). Specifically, OCEANLYZ detrends the pressure signal, computes and applies the pressure response factor, and conducts Fast Fourier Transform (FFT) to generate a wave energy spectrum ($S_{\eta\eta}$) from each 30-min pressure record. Characteristic wave parameters, such as the zero-moment wave height (H_{m0}) and peak wave period (T_p), can be obtained from $S_{\eta\eta}$ as below:

$$H_{m0} = 4\sqrt{m_0} = 4\sqrt{\int_{f_{min}}^{f_{max}} S_{\eta\eta}(f)df}, T_p = \frac{1}{f_p} \qquad (1)$$

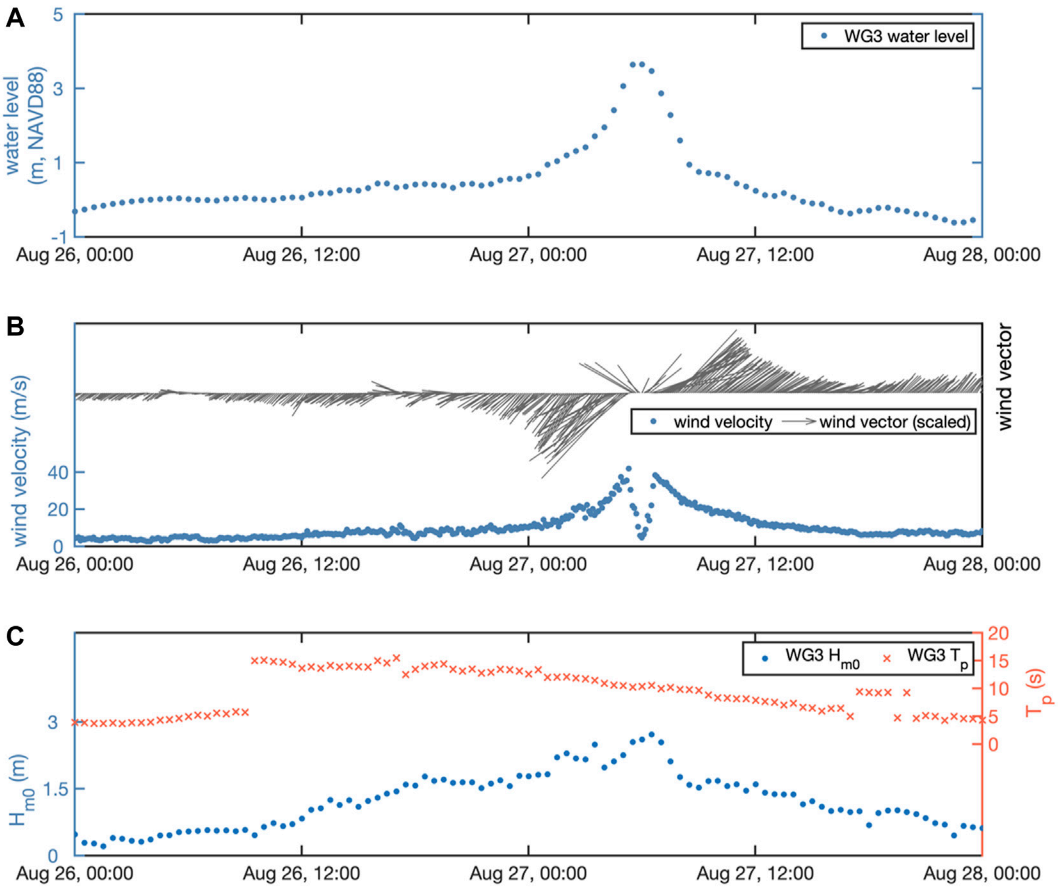

FIGURE 4 | Time series of water level at the offshore wave gauge **(A)**, wind speed and direction at NOAA station 8768094 **(B)**, and zero-moment wave height H_{m0} and peak wave period T_p at the offshore wave gauge **(C)**.

where m_0 is the zeroth moment, f is the frequency, and f_p is the peak frequency associated with the maximum value of $S_{\eta\eta}$. In this study, the maximum frequency to cut off the upper part of the spectrum is $f_{max} = 1$ Hz, whereas the minimum frequency to cut off the lower part of the spectrum is $f_{min} = 0.04$ Hz. During the data processing, the P_{atm} is measured 51 km away from the study site. A sensitivity analysis using P_{atm} taken from another NOAA station 8770822 in Texas Point, Sabine Pass, TX (about 97 km west of the study site) show the dramatic pressure gradients associated with the hurricane introduce small differences to water depth and wave height. The peak P_{atm} from Station 8770822 was 4 kPa larger than the P_{atm} used in this study, and the peak mean water depth and H_{m0} associated with P_{atm} from Station 8770822 are 0.4 and 0.1 m smaller, respectively.

The temporal variations of water level, H_{m0} and T_p at the offshore wave gauge, together with the measured wind velocity and direction at NOAA 8768094 are shown in **Figure 4**. The offshore wave gauge is placed on the seabed with an elevation of −3.39 m (NAVD88). At the offshore wave gauge, T_p ranges from 3.5 to 16.5 s during the event. The change of T_p at 9 a.m. UTC on August 26 indicates that the dominant wave energy switched from wind sea energy to swell energy. The swell energy became stronger than the wind sea energy at 9 a.m. UTC on August 26 and caused the abrupt change of T_p. The maximum H_{m0} is 2.7 m and the maximum water level reaches 3.6 m (NAVD88) around 06:00 UTC on 27 August 2020, about the same time as Hurricane Laura made landfall near Cameron, LA.

The wave height reductions along the two transects are quantified and demonstrated in **Figure 5**. The wave height reduction rate is calculated as $\gamma = (H_{m0,1} - H_{m0,2})/H_{m0,1}$ in which the subscripts "1" and "2" indicate the locations along the transect in the wave propagation direction. The threshold of $H_{m0} > 5$ cm is applied to filter out small waves from measurements. Along the natural transect, the averaged γ from the offshore wave gauge (OF) to NAT-1 is around 56%, whereas along the protected transect, the averaged γ from OF to BW-1 is around 42%. The larger γ from OF to NAT-1 is related to the smaller wave heights recorded at NAT-1. **Figure 6** illustrates the time series of H_{m0} at OF and the first onshore wave gauge, i.e., NAT-1 and BW-1. Although protected by the low-crested light-weighted breakwaters, BW-1 recorded slightly larger waves than did NAT-1. The larger wave heights at the BW-1 are likely caused by the combined three-dimensional effects of wave-structure-bathymetry interaction when the breakwaters were submerged. Similar wave amplifications behind submerged breakwaters were observed in the field (Zhu et al., 2020) and

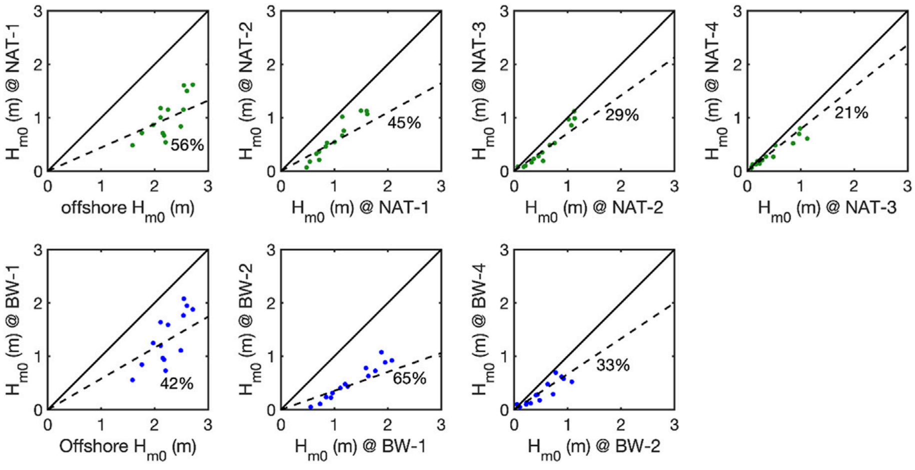

FIGURE 5 | Comparison of measured zero-moment wave heights at neighboring wave gauges along the two transects.

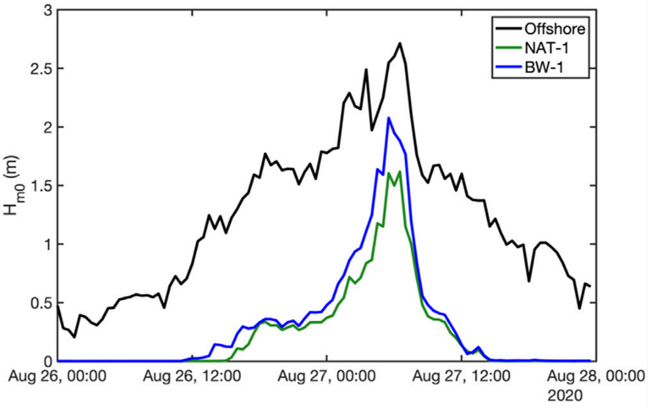

FIGURE 6 | Comparisons of zero-moment wave heights at the offshore wave gauge, NAT-1 and BW-1.

in the laboratory (Seabrook and Hall, 1998) with transmission coefficient greater than 1. A phase-resolving numerical model with fine spatial resolution for the study site is needed to understand the observed nearshore wave processes of hybrid infrastructure under hurricane conditions.

Compared with γ from NAT-1 to NAT-2 (= 45% from **Figure 5**), the γ from BW-1 to BW-2 is greater (= 65% from **Figure 5**). **Figure 7** shows the temporal variations of H_{m0}/h ratios at NAT-1, NAT-2, BW-1 and BW-2. The high H_{m0}/h ratios at NAT-1 and BW-1 (**Figure 7A**) suggest that the depth-limited wave breaking contributes to the wave attenuation near the marsh edge. The H_{m0}/h ratio is greater at BW-1 than NAT-1. This means there was greater depth-limited wave breaking at BW-1, and thus, there was greater wave height reduction at BW-1. Starting from NAT-2 and BW-2 landward, the H_{m0}/h ratios were always less than 0.3 (**Figure 7B**), suggesting that the depth-limited wave breaking became negligible and vegetation plays a more important role in wave attenuation.

The wave height reduction rate per meter, denoted as δ, is estimated as $\delta = \gamma/\Delta x$, where γ is the average wave height reduction rate and Δx is the distance between a pair of wave gauges, respectively. The greatest reduction in wave height occurs along the shorelines for both transects. Using the offshore wave gauge (OF) which was located approximately halfway between the two transects (**Figure 2**), the δ afforded by the breakwater system was 1.78% during Hurricane Laura. For the natural shoreline transect, the δ was slightly greater at 4.67%.

On both transects, once the waves reach the interior wetlands, the wave height reduction rate per meter is essentially identical. Between sites BW-1 and BW-2, δ = 0.42%, and between sites NAT-1 and NAT-2, δ = 0.46%. Between BW-2 and BW-4, separated by a distance of 342 m, δ = 0.10%, similar to the δ between NAT-2 and NAT -3 as well as NAT-3 and NAT-4 at 0.17 and 0.10%, respectively. The similarity in wave height reduction rate per meter between the sites is likely attributable to the similar topography (**Figure 8**) and vegetation (**Figures 12**, **13**). Of interest is the difference between the offshore sites and the sites closest to the shoreline on both natural and breakwater-protected transects. While a greater reduction in wave energy would be expected for a breakwater protected system, and while this reduction has been observed for typical (non-major storm) waves at the site, a more complex hydrodynamic interaction between the breakwater system and storm-driven waves may be occurring. As previously mentioned, a phase-resolving numerical model with high spatial resolution is needed to better understand the unexpectedly lower wave height reduction afforded by the breakwater system during hurricane-scale events such as observed here at RWR during Hurricane Laura.

SHORELINE GEOMORPHOLOGICAL IMPACTS

The coupled effects of erosive removal of overlying sediments by storm-driven overwash, inland deposition of suspended

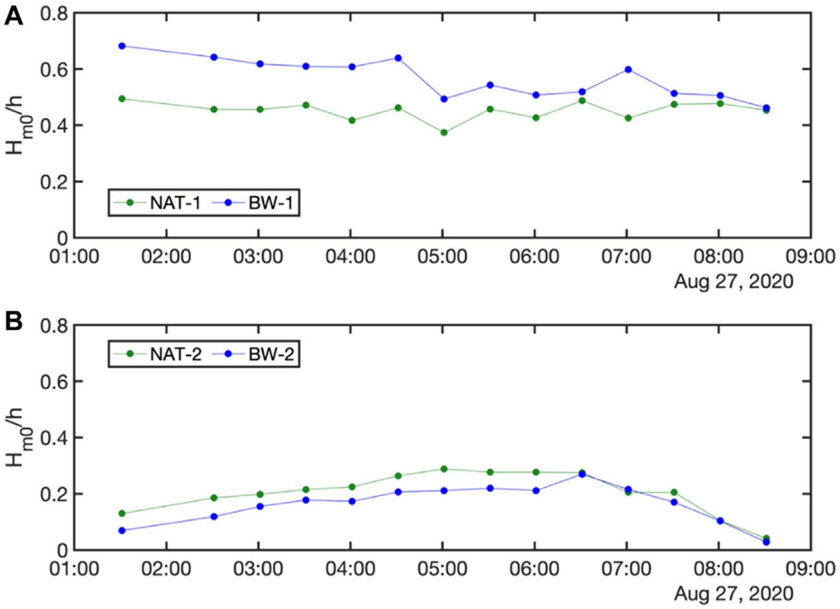

FIGURE 7 | Time series of wave height to water depth ratio at wave gauges near the shoreline, i.e., NAT-1 and BW-1 **(A)**, and at inland wave gauges NAT-2 and BW-2 **(B)**.

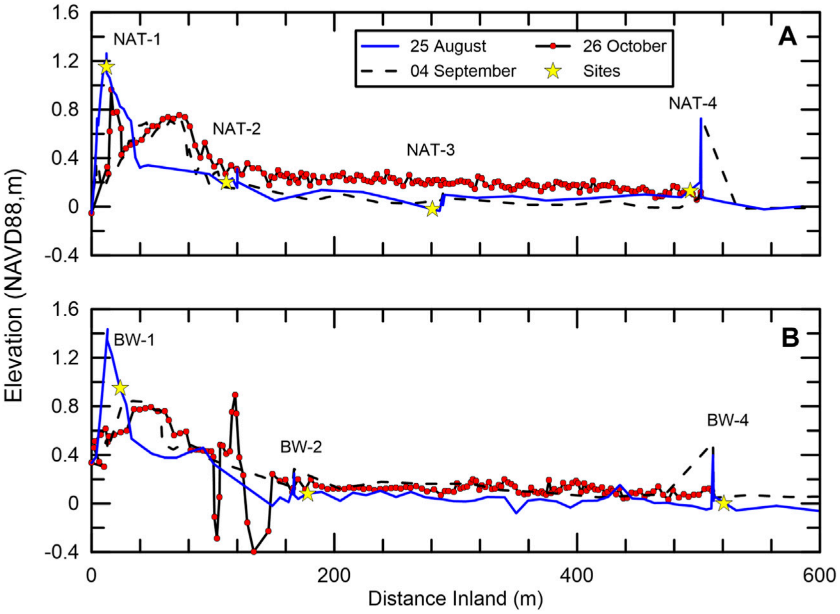

FIGURE 8 | RTK-GPS elevation transects from the shoreline inland for the natural shoreline **(A)** and the **(B)** breakwater protected shoreline showing the locations of study sites on 25 August 2020, 4 September 2020, and 26 October 2020.

sediments, and consolidation of the soft wetland sediments characteristic of RWR can create significant differences in the forecasted surface elevation over long time periods. These differences become critically important to predicting the viability of shoreline protection projects in coastal Louisiana, where an estimated $50 billion worth of restoration projects are underway or planned (LACPRA, 2017; Harris B. D. et al., 2020). Therefore, there is an important economic and engineering rationale for understanding if and how the geomorphological effects of major storms differ between shorelines protected by engineered systems such as breakwaters and natural unprotected shorelines. The elevation profiles for the breakwater protected

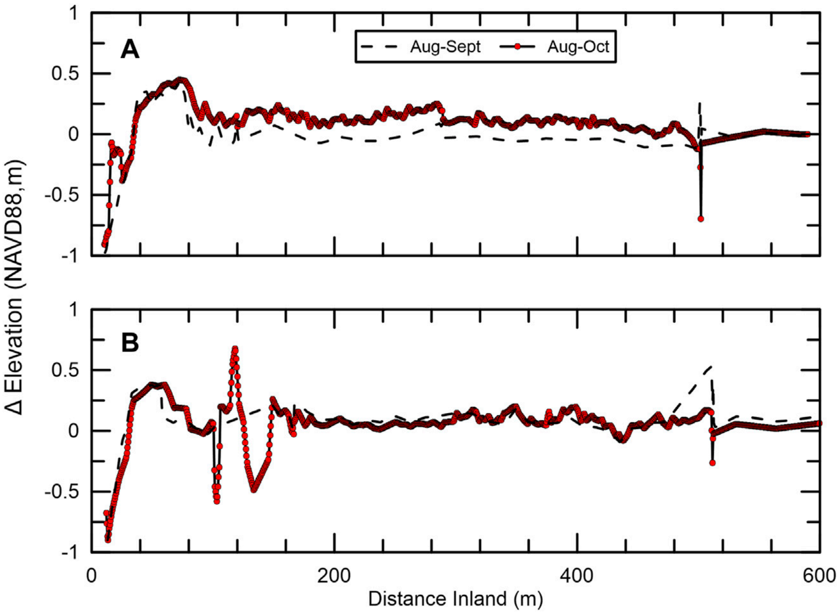

FIGURE 9 | Change in elevation from pre-storm baseline after Hurricanes Laura (Aug-Sept) and Delta (Aug-Oct) for the natural transect **(A)** and the breakwater transect **(B)**.

shoreline and natural shoreline on 25 August 2020, 4 September 2020, and 26 October 2020, are presented in **Figure 8**. The August 25th profile represents a pre-storm baseline with which the post-storm effects of Laura and Delta can be compared. Following Hurricane Laura, there is a significant loss of elevation at the shoreline in both the natural **Figure 8A** and breakwater-protected **Figure 8B** transects.

The material which composed this elevation appears to have been pushed inland, rather than eroded and transported offshore. After the storms, both transects show a more shallow, rounded ridge at the shoreline than in the pre-storm condition when the ridges were very steep on the side facing the Gulf of Mexico, and slightly less steep on the landside. The high elevation peak present near the shoreline prior to storm landfall is characteristic of elevation profiles at RWR. The natural transect appears to feature more severe overwash and rounding of the beach ridge, as well as more in-land deposition. The half-width of the ridge on the natural transect prior to the passage of Hurricane Laura is approximately 20 m. Following the passage of Hurricane Laura, the half-width of the ridge on the natural transect broadened to 50 m. For the breakwater-protected transect, the half-width of the ridge broadened to 40 m. The location of the high elevation point on the shoreline is located 80 m inland from the shoreline following Hurricane Laura on the natural transect, indicating that the high point was pushed 60 m inland. The location of the high elevation point on the shoreline for the breakwater transect was located 40 m inland, indicating that the high point was pushed 20 m inland after Hurricane Laura.

To better compare the elevation changes after both storms, the RTK-GPS elevation data were processed by linearly interpolating the transects at regularly spaced intervals using MATLAB. The elevation data at the regularly spaced intervals can be directly subtracted from the pre-storm baseline elevations to determine the total elevation changes after Hurricane Laura in September and the total elevation changes after the combined effects of Hurricanes Laura and Delta in October. Using the elevation profiles measured after Hurricane Laura (Aug-Sept) and Delta (Aug-Oct), the differences between the breakwater-protected and natural shoreline transects are shown in **Figure 9**. The majority of elevation change on both transects at the shoreline occurred following the landfall of Hurricane Laura. For the natural, unmodified shoreline shown in **Figure 9A**, the elevation loss as the beach is overwashed inland is approximately 1 m between 24 August 2020, and 4 September 2020. In both transects, the elevation loss shown at the shoreline transitions to elevation gain 40 m inland from the shoreline as the low-lying wetlands undergo storm-driven deposition. Following Hurricane Delta, the elevation profile at this site seems to suggest that some material from offshore was deposited along the shoreline. The breakwater transect profile shown in **Figure 9B** exhibited a similar, but lesser decrease in elevation of about 80 cm at the shoreline ridge.

The overwashed sediment forms a mound which extends approximately 20 m further inland on the natural transect (**Figure 9A**) when compared to the breakwater-protected transect (**Figure 9B**). Interestingly, while the inland deposition following Hurricane Laura appears to be similar on both the breakwater-protected and natural shorelines, the breakwater-protected transect exhibits less inland deposition following Hurricane Delta than the natural shoreline transect. Following Delta, approximately 25 cm of sediment was deposited broadly across the interior wetlands behind the beach ridge over a distance of 400 m. The breakwater protected transect exhibits no significant elevation change between the post-Delta and post-Laura surveys apart from the interior ridge located between 80–120 m inland. As the interior ridge is bordered to the landside by a depression, the ridge is inferred to be composed of sediments which were deposited as floodwaters retreated from the interior back to the Gulf of Mexico, though the mechanisms behind this potential erosion and deposition event and the reasons why this process is observed in the breakwater transect but not the natural shoreline transect are not well-understood.

SURGE AND INUNDATION

The water depths measured across an array of field sensors and the nearby NOAA station located in Calcasieu Pass are displayed in **Figure 10**. The piezometer measurements for the three piezometers which retained data are shown in **Figure 10A**. All piezometers which retained data were embedded approximately 30 cm below the marsh surface and are assumed to transmit the full hydrological load from the inundation on the marsh surface. The piezometers which retained data were located at sites NAT-3 and NAT-4, as well as the furthest inland site on the breakwater-protected transect BW-4. The rise in inundation recorded at all three sites is nearly identical as Hurricane Laura began to make landfall at RWR, reaching a peak of just under 4 m. As the eye of the storm passes over the measurement stations, there is a visible drop in ponded depth above the wetland surface (**Figure 10A**-inset) commiserate with the lowered pressure within the center of the storm (Willoughby, 1998). The drop in measured water levels which corresponds to a decrease in pressure, is approximately 20 cm at each of the three sites. Following passage of the eye, water levels immediately recover to the peak achieved prior to the eye passage before rapidly decreasing as the storm moves inland. The offshore site and water levels measured at station NOAA 8768094 are compared in **Figure 10B**. The levels measured by the offshore site achieve a much higher peak than the NOAA site located within Calcsieu Pass. The difference of approximately 1.5 m is inferred to be caused by the lcoation of the NOAA station on the weaker western side of the storm, while the offshore site was located in the path of the stronger wind and waves associated with the eastern section of the hurricane. Following the passage of the storm, the water levels begin to again converge, however the NOAA site water levels are slightly lower likely as the station is located further to the north and protected within the shipping channel whereas the offshore site is directly exposed to the Gulf of Mexico. The water levels above the ground surface measured at each of the three sites on the breakwater transect are presented in **Figure 10C**. Accounting for ground surface elevation, the site at BW-1 measured a greater surge (**Figure 10**), however the measurements above ground surface for the interior sites provide insight into the period of time which the interior wetlands remain inundated following the passage of the storm. At both interior breakwater sites, BW-2 and BW-4, even while the surge caused by the passage of the hurricane subsides quickly, the sites remain inundated for days after the event. The long inundation period may induce stress on the wetland vegetation within the interior of the wetland, weakening the wetland at the same time that the shoreline is eroded towards those locations. The exposure of site BW-1 directly to the Gulf of Mexico following the drastic elevation change and inland migration of the beach ridge (**Figures 8**, **9**) can be readily observed by comparing the observations recorded at the offshore site and NOAA station in **Figure 10B**. Similar observations were made along the natural shoreline transect (**Figure 10D**), though the response to tidal variations in the Gulf of Mexico is more muted and is observed to be delayed by approximately a 12 h period. Again, a numerical model is likely required to determine the observed time delay, though one inference is that the delay may be due to floodwaters draining more rapidly from the interior wetlands out to the Gulf of Mexico on the natural transect, dampening the ability of the shallow tidal variations to be measured by the wave gauge NAT-1.

A comparison showing the water levels above the ground surface at four sites which occur across both transects is shown in **Figure 11**. This comparison allows for better insight into the time that the interior wetlands remained inundated after the storm passed, as well as the rate at which the inundated wetlands drained as sites NAT-2 and BW-2 and sites NAT-4 and BW-4 are located at similar distances from the shoreline, respectively. As the storm passes, the sites all record nearly identical increases in water depth to approximately 4.1 m. As the storm passes and flood waters retreat, clear differences begin to emerge. Comparing sites NAT-2 and NAT-4, a total time difference of four hours is required for the inundation depth at NAT-4 to drain to a similar depth as NAT-2 (12:00 p.m. 08/27/20, cross-mark in **Figure 11**). The inundation difference of 30 cm over a period of four hours gives an initial drainage rate of 1.8m/day from the interior wetlands to the shoreline on the natural shoreline, and a hydraulic slope of 0.078% from the interior of the wetlands to the shoreline. The breakwater transect drains at nearly the same rate at both locations of the transect, however for BW-2 to reach the same inundation depth as NAT-2 took eight hours. Taking the difference between the two transects as approximately 1750 m, a hydraulic slope from east-to-west in the interior wetlands of 0.029%. For both transects, the long term drainage rate is 0.20 m/day, however the breakwater transect drained more slowly and thus remains inundated for a longer period of time. The longer inundation period may place more stress on the interior vegetation, leading to long-term differences in vegetative health along the two transects. Given the similar elevation profiles (**Figure 8**) between the two transects, the observed difference between the time for the floodwaters to retreat seem to indicate that the presence of engineered systems within the wetlands (**Figure 2**) and the breakwater structure acted to dampen the floodwater retreat in some way.

VEGETATION

The results of above-ground biomass (AGB) measurements, processed according to the procedure in Snedden et al. (2015), at each location along both transects are displayed in **Figure 12**. The AGB values are initially lowest at site BW-1, and highest at site NAT-2, with the remaining sites falling within a range of

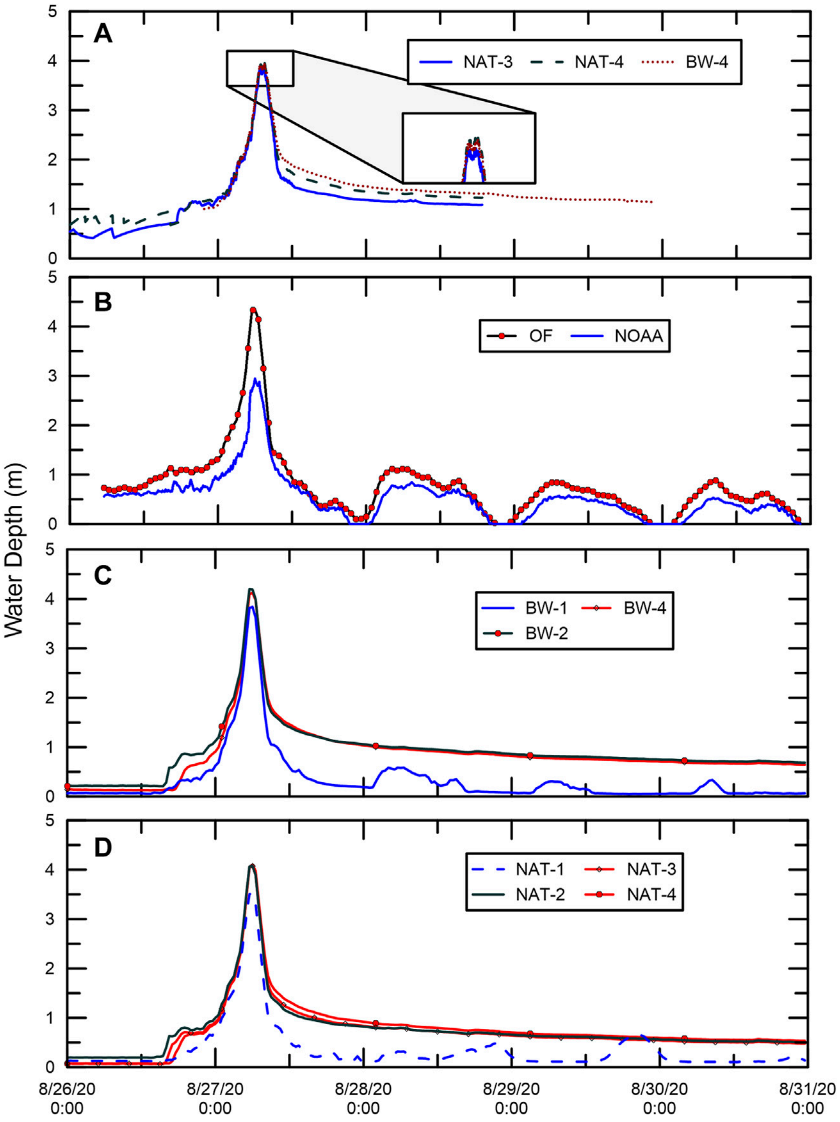

FIGURE 10 | Piezometer water levels above surface from Hurricane Laura on **(A)**, Offshore (OF) and NOAA Calcasieu Pass water levels **(B)**, water levels above surface from wave gauges on the breakwater transect **(C)** and on the natural transect **(D)**.

1,500–2000 g/cm^2. Following Hurricane Laura, there is a sharp decrease in AGB for site NAT-2, and moderate decreases in all other sites except for BW-1. The increase in AGB at site BW-1 is likely due to experimental error and is not reflective of field observed conditions. Between Hurricanes Laura and Delta, the vegetation appears to have recovered somewhat, as the post-Delta measurements are marginally higher at each study site apart from NAT-2, which endured the most severe degradation following Hurricane Laura. The most in-land sites exhibit the strongest recovery and highest AGB following delta, while there is no clear or discernable trends between the remaining sites or transects apart from site NAT-2 which endured the most severe damage following Hurricane Laura.

NDVI measurements taken from drones (UAV) during field reconnaissance and claculated from satellite measurements along the two transects before Hurricane Laura (August 23), after Laura (September 4) and after Hurricane Delta (October 26) are presented in **Figure 13**. The NDVI values for the natural shoreline transect (**Figure 13A**) increase from a value near zero at the shoreline to 0.25 at a distance of 20 m inland. At a distance of 40 m inland, the NDVI values level off and indicate similar vegetative health in the interior wetlands. A similar trend is shown for the breakwater-protected transect (**Figure 13B**). In both transects, the NDVI values dropped significantly following Hurricane Laura, indicating severe damage to the vegetation in the interior wetlands. The drop in NDVI corresponds to a drop in ABG in **Figure 12**. The inferred damage to the vegetation in the interior wetlands decreases with distance inland from the shoreline, leading to a trend of increasing NDVI with increasing distance inland. Neither transect displays a significant difference in NDVI after Laura across the entire time period of study.

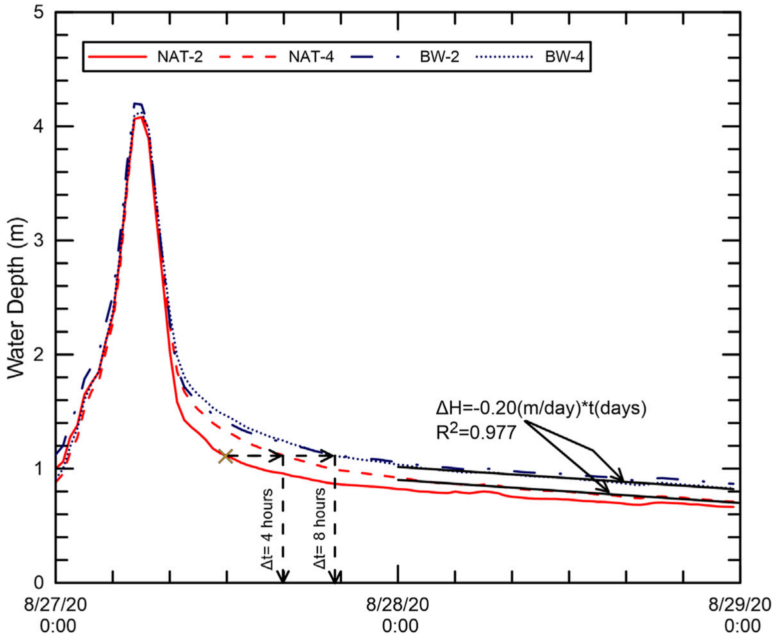

FIGURE 11 | Water depth with time at BW-2 and BW-4, and NAT-2 and NAT-4.

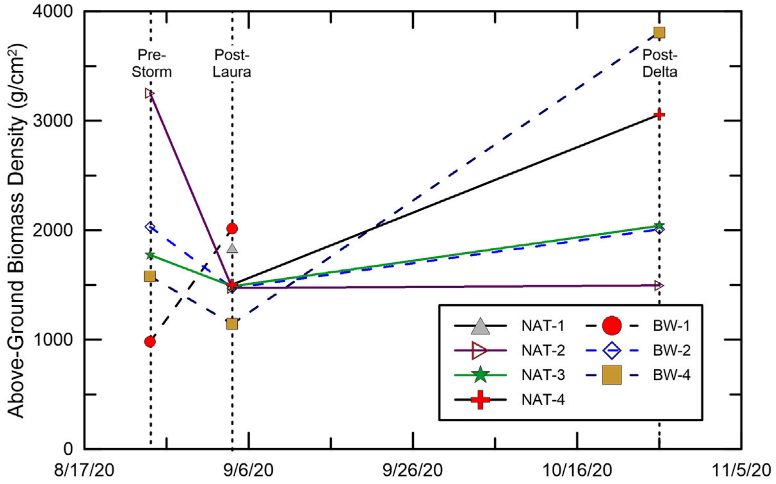

FIGURE 12 | Above-ground biomass measurements pre-Laura, Post-Laura, and Post-Delta.

WETLAND STRENGTH

The results from the modified cone penetrometer sleeve testing taken following Hurricane Laura using a modified cone designed to more effectively characterize the shear strength of the vegetated upper-most layer of the wetlands are shown in **Figure 14**. The sites closest to the shoreline, **Figure 14A**, show very little shearing resistance in the upper 30 cm of the soil column. A slight peak, indicative of a layer of vegetated soil, can be seen at a depth of approximately 40 cm in both the breakwater-protected and natural transects. Moving further inland, the vegetated peak can be seen at a shallower depth in the soil column (**Figure 14B**). A double-peak shape can be seen in the curve, with the first, weaker peak present in the upper 10–20 cm of the column. This first peak is likely due to sediments deposited on top of the original wetland surface. At this location, coarse grained deposits were not as prevalent as they were close to the shoreline, and the double peak may be due to re-worked and re-deposited vegetative material. The breakwater-protected transect shows a higher resistance value at the deeper peak in the soil column, indicative of the original soil profile prior to storm deposition atop of the soil surface. The higher resistance value at this site for

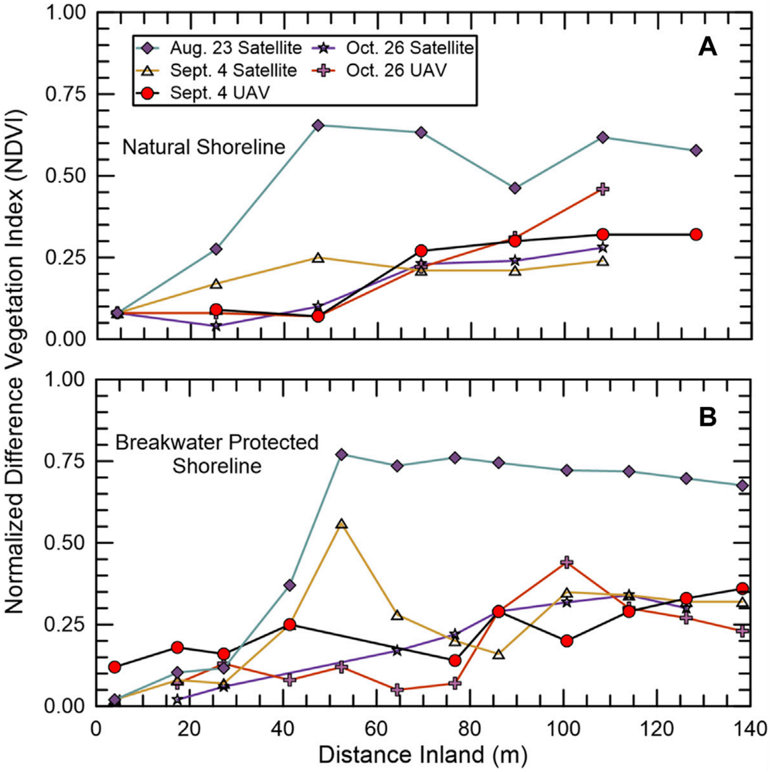

FIGURE 13 | NDVI from satellite and UAV on 23 August 2020, 04 September 2020, 26 October 2020, and for the natural **(A)** and breakwater protected **(B)** shorelines.

the breakwater-protected transect may be due to the protection provided to the inland wetlands here from smaller-scale inundation events in which higher-salinity waters from the Gulf of Mexico may stress and decrease the health of the inland vegetation of the natural transect. The furthest inland tests, **Figure 14C**, display similar resistance curves with depth, and a single, sharp peak in the upper soil column. The shape of the resistance with depth curve is similar to other Louisiana wetlands, where the vegetative root depth extends to depths of approximately 20–30 cm (Jafari et al., 2019a; Jafari et al., 2019b; Harris B. D. et al., 2020; Cadigan et al., 2020). The identical profiles, and singular-peaks of the resistance curves, indicate that the furthest inland sites are likely unaffected by the storms to a significant degree as compared to the sites closer to the shoreline. The profiles would also indicate, unlike those in **Figure 14B**, that the protection afforded to more typical inundation events by the breakwater system to interior wetlands is negated at the distances inland of the shoreline that these tests were taken.

OBSERVATIONS OF THE MUD DEPOSIT AT ROLLOVER BAYOU

The storm driven sediment deposition on the interior of the wetlands (**Figures 8**, **9**) is also of great interest as wetland elevation is strongly tied to vegetative health and wetland stability (Cahoon et al., 2006; Chambers et al., 2019; Cadigan et al., 2020). The highest accretion values in RWR by far were found at the mouth of Rollover Bayou, which experienced a major depositional event consisting of a very large lens (in the order of 2.5 km^2) of fine grained mud deposit with a thickness of approximately 1800 mm (1.8 m or 6 ft) in the middle and tapering off towards the edges. Surrounding sites had accretion ranging from 1.0 ± 0.1 mm to 446.7 ± 3.3 mm. These observations are similar to previous observations of storm-driven mud deposits on the Chenier Plain. Hurricane Audrey made landfall in June 1957, near the Texas-Louisiana border and generated a 3–4 m storm surge in the study area. Morgan et al. (1958) reported about "a mass of fluid mud that was transported by the storm tide and deposited as a unit". In the mid-1960s, Coleman (1966) found little change with respect to the distribution of mud in the study area, but added much new information on the physical and biological properties of the mudflat sediments (Kemp, 1986). Coleman (1966) X-rayed mudflat cores which, to the unaided eye, appeared almost featureless and found multiple sets of parallel laminations relatively undisturbed by biological reworking.

Kemp (1986) studied fluid mud dynamics along a 30 km section of the Louisiana coast west of the Southwest Pass of Vermilion Bay on the eastern margin of the Louisiana chenier plain about 10 miles east of Rollover Bayou. There Kemp reported a depositional feature of highly fluid mud with

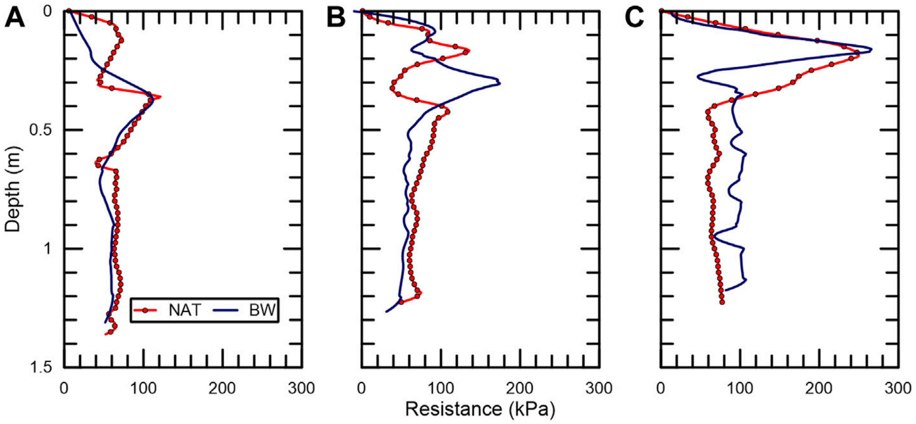

FIGURE 14 | Modified cone-penetrometer resistance values with depth for **(A)** sites closest to the shoreline, **(B)** the locations at the midpoint between shoreline and furthest inland site, and **(C)** furthest inland site.

dimensions of 300 m × 1,500 m and a maximum thickness of 2 m. Initial measurements of the elevation of the deposit at Rollover Bayou indicated elevations ranging between 0.44 and 1.8 m. The soil had a bulk density of 1.1 g/cm^3, moisture content of 32.7%, and was 10.2% organic matter. Previous observations of fluid mud deposits on the Chenier Plain by Kemp (1986) indicate bulk densities of 1.2 g/cm^3 at the surface to 1.4 g/cm^3 a meter below. More recent surveys conducted after Hurricane Rita in 2005 by Turner et al. (2006) reported an average bulk density of the newly deposited material of 0.37 g/cm^3 with a range of zero to 1.78 g/cm^3, which was highest near the coastline and decreased inland. Turner et al. (2006) reported that Hurricane Rita deposited mud with a thickness of 5.18 cm, with deposition greatest near the center of the storm track and along the eastern side of the hurricane path. The western side of the storm track had lower sediment deposition thicknesses corresponding to the lower surge and inundation times from west to east. The observations of Kemp (1986), together with the sedimentological data provided by Coleman (1966), and the observations presented here, indicate that chenier plain mudflats are deposited rapidly under the highest energy conditions this coast experiences (Kemp, 1986).

CONCLUSION

The results of multi-institutional and multi-disciplinary field observations made in Rockefeller Refuge during the intense 2020 hurricane season indicate key differences and similarities between a section of wetlands protected by a breakwater system and a natural, unprotected section. In addition, observations of a storm-driven fluidized mud deposit in Rockefeller Refuge provide key insight into the energy required for the wetlands along the Chenier Plain to receive sediment deposition which may allow for the maintenance of interior wetland stability. Several differences in the response of the protected and natural shorelines to major hurricanes became apparent over the 2020 hurricane season:

- The breakwater protected shoreline drained more slowly following the passage of Hurricane Laura. The difference in drainage times may be due to the engineered water features in the breakwater transect, however a numerical model is required to fully understand the processes and causes behind this observed difference.
- On both transects, once the waves reach the interior wetlands, the wave height reduction rate per meter is essentially identical and seems to be controlled primarily by vegetation.
- The difference in inundation period between the two transects may have implications for long-term marsh health, as prolonged flooding and exposure to sea-strength saltwater may negatively impact plant productivity and marsh elevation.

Several similarities in the response of the protected and natural shorelines to major hurricanes became apparent over the 2020 hurricane season:

- The storm induced surge on the wetlands reached similar values at the same time on both the protected and natural shorelines.
- Vegetative health measured remotely using NDVI seem to have responded similarly in both the breakwater protected and natural shorelines. However as there may be a latent effect caused by differing inundation periods, long-term NDVI measurements are required to confirm this conclusion.
- NDVI analysis the following years which may show greater differences among the natural and hybrid transects as some vegetation effects are latent. For example, if vegetation roots were killed by prolonged inundation in the breakwater transect, vegetation regrowth the following year may be

less extensive and make the area more susceptible to erosion/ponding/etc.
- No significant difference is present between the CPT resistance profiles with depth at each site between the two transects.
- Double-peaks in the CPT resistance curve with depth may be indicative of reworked vegetation or storm deposition atop the now-buried, previous wetland surface.
- Furthest inland sites show curves characteristic of vegetated Louisiana wetlands, though are much higher than sites in the Terrebonne Basin.

Observations of the fluid mud deposit at Rollover Bayou in Rockefeller Refuge indicates that:

- Massive deposits of fluid mud are driven onto the wetland platform on the more energetic, western side of hurricanes.
- The effect of breakwater systems on the deposition of this fluidized mud is still unclear.
- The majority of mudflat deposits, and interior deposits which control the elevation and in turn the health of the sediment-starved wetland system in the Chenier Plain, are deposited by only the highest energy storm events which strike the coastline.

DATA AVAILABILITY STATEMENT

The raw data supporting the conclusion of this article will be made available by the authors, without undue reservation.

AUTHOR CONTRIBUTIONS

JC: Selection of study site, supervision, methodology, field deployment, data collection, data analysis, writing; JB: Selection of study site, design of instrumentation transects, methodology, data analysis, writing; NJ: Selection of study site, supervision, methodology, field deployment, data collection, writing—review and editing; LZ: Wave and surge data analysis, data curation, writing—review and editing; AB: Selection of study site, design of instrumentation transects, methodology, resources, writing, reviewing and editing; QC: Selection of study site, design of instrumentation transects, methodology, resources, writing—review and editing; BR: Selection of study site, design of instrumentation transects, methodology, resources, writing—review and editing; BH: Methodology, resources, writing—review and editing; CO: Selection of study site, design of instrumentation transects, methodology, resources, writing—review and editing; RL: Selection of study site, design of instrumentation transects, methodology, resources, writing—review and editing; GPK: Selection of study site, design of instrumentation transects, methodology, resources, writing—review and editing; JND: Selection of study site, design of instrumentation transects, methodology, resources, writing—review and editing; JWD: Selection of study site, design of instrumentation transects, methodology, resources, writing—review and editing; HU: Selection of study site, design of instrumentation transects, field deployment.

FUNDING

Funding for the study has been partially provided by the National Science Foundation through grants NSF 2139882, 2139883, 1829136, 1848650, and 1939275, as well as through the United States Army Corps of Engineers Regional Sediment Management program. Student support provided through the National Science Foundation Graduate Research Fellowship Program and the Louisiana Coastal Science Assistantship Program.

ACKNOWLEDGMENTS

The authors are grateful to T. Baker Smith for providing boat and logistical support, to the NSF RAPID instrumentation depot and team, and to Phillip “Scooter” Trosclair for facilitating access to Rockefeller Wildlife Refuge.

REFERENCES

Balaguru, K., Foltz, G. R., and Leung, L. R. (2018). Increasing Magnitude of Hurricane Rapid Intensification in the Central and Eastern Tropical Atlantic. *Geophys. Res. Lett.* 45, 4238–4247. doi:10.1029/2018gl077597

Cadigan, J., Stagg, C. L., Jafari, N., Harris, B., and Laurenzano, C. (2020). December)Geotechnical Characterization of a Saline Wetland with Implications towards Quantifying Peat Collapse. *AGU Fall Meet. Abstr.* 2020, 0577–B106.

Caffey, R., Wang, H., Niu, H., Froeba, J., and Isaacs, J. (2022). *Projected Infrastructure, Revenue and Resource Losses to Louisiana Fisheries from the Hurricanes of 2020 and 2021*. Baton Rouge, United States: Louisiana State University, Louisiana Sea Grant & Louisiana Department of Wildlife and Fisheries.

Cahoon, D. R., Hensel, P. F., Spencer, T., Reed, D. J., McKee, K. L., and Saintilan, N. (2006). “Coastal Wetland Vulnerability to Relative Sea-Level Rise: Wetland Elevation Trends and Process Controls,” in *Wetlands and Natural Resource Management* (Berlin, Heidelberg: Springer), 271–292.

Campbell, T., Benedet, L., and Finkl, C. W. (2005). Regional Strategies for Coastal Restoration along the Louisiana Chenier Plain. *J. coastal Res.*, 268–283.

Cangialosi, J. P., and Berg, R. (2021). *National Hurricane Center Tropical Cyclone Report: Hurricane Delta*. Miami, FL: National Hurricane Center.

Chambers, L. G., Steinmuller, H. E., and Breithaupt, J. L. (2019). Toward a Mechanistic Understanding of “Peat Collapse” and its Potential Contribution to Coastal Wetland Loss. *Ecology* 100 (7), e02720. doi:10.1002/ecy.2720

Cohen, M. C. L., De Souza, A. V., Liu, K.-B., Rodrigues, E., Yao, Q., Pessenda, L. C. R., et al. (2021). Effects of Beach Nourishment Project on Coastal Geomorphology and Mangrove Dynamics in Southern Louisiana, USA. *Remote Sensing* 13, 2688. doi:10.3390/rs13142688

Coleman, J. M. (1966). *RECENT COASTAL SEDIMENTATION: CENTRAL LOUISIANA COAST*. Baton Rouge, LA, United States: LOUISIANA STATE UNIV BATON ROUGE COASTAL STUDIES INST.

Eley, E. N., Subrahmanyam, B., and Trott, C. B. (2021). Ocean-Atmosphere Interactions during Hurricanes Marco and Laura (2020). *Remote Sensing* 13, 1932. doi:10.3390/rs13101932

Gary, D. L. (1979). *Recreational Dwellings in the Louisiana Coastal Marsh*. Baton RougeCenter for Wetland Resources: Louisiana State University.

Geesey, B. L., Heilman, D. J., and Mcpherson, R. L. (20112011). "Rockefeller Refuge Gulf Shoreline protection Demonstration," in *Coastal Engineering Practice*, 658–671. doi:10.1061/41190(422)55

Harris, B. D., Day, D. J., Cadigan, J. A., Jafari, N. H., Bailey, S. E., and Tyler, Z. J. (2021). Establishment of Soil Strength in a Nourished Wetland Using Thin Layer Placement of Dredged Sediment. *PLoS ONE* 16, e0251420. doi:10.1371/journal.pone.0251420

Harris, B. D., Cadigan, J., Day, D., and Jafari, N. (2020b). "Geotechnical Characterization of an Eroding Wetland," in *Geo-Congress 2020*, 740–748. doi:10.1061/9780784482810.077

Harris, B. D., Johnson, C., Jafari, N. H., Chen, Q., and Ozdemir, C. E. (2020a). Effects of Coupled Consolidation and Overwash Processes on a Low-Lying headland System. *Coastal Eng.* 160, 103746. doi:10.1016/j.coastaleng.2020.103746

Hill, S., and Belhadjali, K. (2005). "Rockefeller Refuge Gulf Shoreline Stabilization Ecological Review (ME-18)," in *Cwppra* (Baton Rouge: Louisiana Department of Natural Resources Restoration Technology Section).

Jafari, N. H., Chen, Q., and Cadigan, J. (2020). Rapid Deployment and post-storm Reconnaissance of hurricane Laura. *Int. Conf. Coastal. Eng.*, 60. doi:10.9753/icce.v36v.waves.60

Jafari, N. H., Harris, B. D., Cadigan, J. A., and Chen, Q. (2019a). Piezocone Penetrometer Measurements in Coastal Louisiana Wetlands. *Ecol. Eng.* 127, 338–347. doi:10.1016/j.ecoleng.2018.12.012

Jafari, N. H., Harris, B. D., Cadigan, J. A., Day, J. W., Sasser, C. E., Kemp, G. P., et al. (2019b). Wetland Shear Strength with Emphasis on the Impact of Nutrients, Sediments, and Sea Level Rise. *Estuarine, Coastal Shelf Sci.* 229, 106394. doi:10.1016/j.ecss.2019.106394

Karimpour, A., and Chen, Q. (2017). Wind Wave Analysis in Depth Limited Water Using OCEANLYZ, A MATLAB Toolbox. *Comput. Geosciences* 106, 181–189. doi:10.1016/j.cageo.2017.06.010

Kemp, G. P. (1986). Mud Deposition at the Shoreface: Wave and Sediment Dynamics on the Chenier Plain of Louisiana, LSU Historical Dissertations and Theses. Avaliable At: https://digitalcommons.lsu.edu/gradschool_disstheses/4305.

LACPRA (2017). *Coastal Master Plan (Louisiana's Coastal Protection and Restoration Authority).* Avaliable at: https://coastal.la.gov/our-plan/2017-coastal-master-plan/ (Accessed November 1, 2021).

Louisiana Department of Wildlife and Fisheries (2021). Rockefeller Wildlife Refuge. Available: https://www.wlf.louisiana.gov/page/rockefeller-wildlife-refuge.

Martin Associates (2021). *The Economic Impacts of the Calcasieu Ship Channel conducted for the Port of Lake Charles*. Avaliable at: https://portlc.com/wp-content/uploads/2021/12/PORT.Executive-Summary-2021-POLC-Economic-Impact-Study.pdf

Mcbride, R. A., Anderson, J. B., Buynevich, I. V., Cleary, W., Fenster, M. S., Fitzgerald, D. M., et al. (2013). "10.8 Morphodynamics of Barrier Systems: A Synthesis," in *10.8 Morphodynamics of Barrier Systems: A SynthesisTreatise on Geomorphology*. Editor J. F. Shroder (San Diego: Academic Press), 166–244. doi:10.1016/b978-0-12-374739-6.00279-7

Mcbride, R. A., Taylor, M. J., and Byrnes, M. R. (2007). Coastal Morphodynamics and Chenier-Plain Evolution in Southwestern Louisiana, USA: A Geomorphic Model. *Geomorphology* 88, 367–422. doi:10.1016/j.geomorph.2006.11.013

Morton, R. A., and Barras, J. A. (2011). Hurricane Impacts on Coastal Wetlands: A Half-Century Record of Storm-Generated Features from Southern Louisiana. *J. Coastal Res.* 275, 27–43. doi:10.2112/jcoastres-d-10-00185.1

Oscar, K. H., Walker, N. D., and Christopher, M. (2001). Sedimentation along the Eastern Chenier Plain Coast: Down Drift Impact of a Delta Complex Shift. *J. Coastal Res.* 17, 72–81.

Pasch, R. J., Berg, R., Roberts, D. P., and Papin, P. P. (2021). *National Hurricane Center Tropical Cyclone Report: Hurricane Laura.* Miami, FL: N.H. Center. NOAA.

Penland, S., Connor, P. F., Beall, A., Fearnley, S., and Williams, S. J. (2005). Changes in Louisiana's Shoreline: 1855–2002. *J. Coastal Res.* 21, 7–39.

Reid, R. L. (2021). Protecting a Refuge. *Civ. Eng.* 91, 62–67. doi:10.1061/ciegag.0001554

Roberts, H. H. (1997). Dynamic Changes of the Holocene Mississippi River delta plain: The delta Cycle. *J. Coastal Res.* 13, 605–627.

Seabrook, S. R., and Hall, K. R. (1998). Wave Transmission at Submerged Rubble mound Breakwaters. *Coastal Eng. Proc.* 1, 26. doi:10.9753/icce.v26.%25p

Selman, W., Salyers, B., Salyers, C., Perry, G., Elsey, R., Hess, T., et al. (2011). in *Rockefeller Wildlife Refuge Management Plan*. Editor L. D. O. W. A. Fisheries (Grand Chenier, LA: Rockefeller Wildlife Refuge).

Shiner Moseley and Associates (2002). *Geotechnical Study (Part I of II) Gulf Shoreline Stabilization Project, Rockefeller Refuge*. Cameron Parish, Louisiana: Corpus Christi, TX: Fugro South.

Shows, H. (2019) Living Shorelines as Alternative Methods of Shoreline Protection. Baton Rouge, LA: Louisiana State University. MS Thesis.

Snedden, G. A., Cretini, K., and Patton, B. (2015). Inundation and Salinity Impacts to above- and Belowground Productivity in Spartina Patens and Spartina Alterniflora in the Mississippi River Deltaic plain: Implications for Using River Diversions as Restoration Tools. *Ecol. Eng.* 81, 133–139. doi:10.1016/j.ecoleng.2015.04.035

Turner, R. E., Baustian, J. J., Swenson, E. M., and Spicer, J. S. (2006). Wetland Sedimentation from Hurricanes Katrina and Rita. *Science* 314 (5798), 449–452. doi:10.1126/science.1129116

Willoughby, H. E. (1998). Tropical Cyclone Eye Thermodynamics. *Mon. Wea. Rev.* 126 (12), 3053–3067. doi:10.1175/1520-0493(1998)126<3053:tcet>2.0.co;2

Wise, L. A., Mclellan, T. N., and Byrnes, M. R. (2004). "Feasibility Analysis of Shore Protection Alternatives for Rockefeller Wildlife Refuge in the Chenier Plain of Southwestern Louisiana (USA)," in Coastal Structures 2003, Portland Oregon, 2003-8-26 to 2003-8-30 (United States: American Society of Civil Engineers), 1142–1154. doi:10.1061/40733(147)94

Xi, D., and Lin, N. (2021). Sequential Landfall of Tropical Cyclones in the United States: From Historical Records to Climate Projections. *Geophys. Res. Lett.* 48, e2021GL094826. doi:10.1029/2021gl094826

Yao, Q., Liu, K.-B., and Ryu, J. (2018). Multi-proxy Characterization of Hurricanes Rita and Ike Storm Deposits in the Rockefeller Wildlife Refuge, Southwestern Louisiana. *J. Coastal Res.* 85, 841–845. doi:10.2112/si85-169.1

Zhou, S., Kan, P., Huang, Q., and Silbernagel, J. (2021). A Guided Latent Dirichlet Allocation Approach to Investigate Real-Time Latent Topics of Twitter Data during Hurricane Laura. *J. Inf. Sci.* doi:10.1177/01655515211007724

Zhu, L., Chen, Q., Wang, H., Capurso, W., Niemoczynski, L., Hu, K., et al. (2020). Field Observations of Wind Waves in Upper Delaware Bay with Living Shorelines. *Estuaries and Coasts* 43 (4), 739–755. doi:10.1007/s12237-019-00670-7

Zhu, Y. J., Collins, J. M., and Klotzbach, P. J. (2021). Nearshore Hurricane Intensity Change and Post-Landfall Dissipation along the United States Gulf and East Coasts. *Geophys. Res. Lett.* 48, e2021GL094680. doi:10.1029/2021gl094680

Conflict of Interest: Authors RL and JD were employed by Comite Resources, Inc.

The remaining authors declare that the research was conducted in the absence of any commercial or financial relationships that could be construed as a potential conflict of interest.

frontiers | Frontiers in Built Environment

REVIEW
published: 27 April 2022
doi: 10.3389/fbuil.2022.814180

Innovations in Coastline Management With Natural and Nature-Based Features (NNBF): Lessons Learned From Three Case Studies

Cindy M. Palinkas[1]*, Philip Orton[2], Michelle A. Hummel[3], William Nardin[1], Ariana E. Sutton-Grier[4], Lora Harris[5], Matthew Gray[1], Ming Li[1], Donna Ball[6,7], Kelly Burks-Copes[8], Meri Davlasheridze[9], Matthieu De Schipper[10], Douglas A. George[11], Dave Halsing[7], Coraggio Maglio[8], Joseph Marrone[12], S. Kyle McKay[13], Heidi Nutters[14], Katherine Orff[15], Marcel Taal[16], Alexander P. E. Van Oudenhoven[17], William Veatch[18] and Tony Williams[19]

[1]Horn Point Laboratory, University of Maryland Center for Environmental Science, Cambridge, MD, United States, [2]Stevens Institute of Technology, Hoboken, NJ, United States, [3]Department of Civil Engineeering, University of Texas at Arlington, Arlington, TX, United States, [4]Earth System Science Interdisciplinary Center, University of Maryland, College Park, College Park, MD, United States, [5]Chesapeake Biological Laboratory, University of Maryland Center for Environmental Science, Solomons, MD, United States, [6]San Francisco Estuary Institute, Richmond, CA, United States, [7]South Bay Salt Pond Restoration Project, San Francisco, CA, United States, [8]US Army Corps of Engineers, Galveston, TX, United States, [9]Texas A&M University atGalveston, Galveston, TX, United States, [10]Delft University of Technology, Delft, Netherlands, [11]National Oceanic and Atmospheric Administration (NOAA), San Francisco, CA, United States, [12]Arcadis, Long Island City, NY, United States, [13]US Army Engineer Research and Development Center, Vicksburg, MS, United States, [14]San Francisco Estuary Partnership, San Francisco, CA, United States, [15]Graduate School of Architecture, Planning, and Preservation, Columbia University, New York, NY, United States, [16]Deltares, Delft, Netherlands, [17]Institute of Environmental Sciences CML, Leiden University, Leiden, Netherlands, [18]US Army Corps of Engineers, New Orleans, LA, United States, [19]Texas General Land Office, Austin, TX, United States

OPEN ACCESS

Edited by:
Tori Tomiczek,
United States Naval Academy,
United States

Reviewed by:
Steven Scyphers,
Northeastern University, United States
Edgar Mendoza,
National Autonomous University of
Mexico, Mexico

***Correspondence:**
Cindy M. Palinkas
cpalinkas@umces.edu

Specialty section:
This article was submitted to
Coastal and Offshore Engineering,
a section of the journal
Frontiers in Built Environment

Received: *12 November 2021*
Accepted: *25 March 2022*
Published: *27 April 2022*

Citation:
Palinkas CM, Orton P, Hummel MA, Nardin W, Sutton-Grier AE, Harris L, Gray M, Li M, Ball D, Burks-Copes K, Davlasheridze M, De Schipper M, George DA, Halsing D, Maglio C, Marrone J, McKay SK, Nutters H, Orff K, Taal M, Van Oudenhoven APE, Veatch W and Williams T (2022) Innovations in Coastline Management With Natural and Nature-Based Features (NNBF): Lessons Learned From Three Case Studies. Front. Built Environ. 8:814180. doi: 10.3389/fbuil.2022.814180

Coastal communities around the world are facing increased coastal flooding and shoreline erosion from factors such as sea-level rise and unsustainable development practices. Coastal engineers and managers often rely on gray infrastructure such as seawalls, levees and breakwaters, but are increasingly seeking to incorporate more sustainable natural and nature-based features (NNBF). While coastal restoration projects have been happening for decades, NNBF projects go above and beyond coastal restoration. They seek to provide communities with coastal protection from storms, erosion, and/or flooding while also providing some of the other natural benefits that restored habitats provide. Yet there remain many unknowns about how to design and implement these projects. This study examines three innovative coastal resilience projects that use NNBF approaches to improve coastal community resilience to flooding while providing a host of other benefits: 1) Living Breakwaters in New York Harbor; 2) the Coastal Texas Protection and Restoration Study; and 3) the South Bay Salt Pond Restoration Project in San Francisco Bay. We synthesize findings from these case studies to report areas of progress and illustrate remaining challenges. All three case studies began with innovative project funding and framing that enabled expansion beyond a sole focus on flood risk reduction to include multiple functions and benefits. Each project involved stakeholder engagement and incorporated feedback into the design process. In the Texas case study this dramatically shifted one part of the project design from a more traditional, gray approach to a more natural hybrid solution. We also identified common challenges related to permitting and funding, which often arise as a consequence of uncertainties in performance and long-term sustainability for diverse NNBF approaches. The Living Breakwaters project is helping to address these uncertainties by using detailed computational and physical modeling and a variety of experimental morphologies to help facilitate learning while monitoring future performance. This paper informs and improves future sustainable coastal resilience projects by learning from these past innovations, highlighting the need for integrated and robust monitoring plans for projects after implementation, and emphasizing the critical role of stakeholder engagement.

Keywords: coastal resiliency, restoration, stakeholder engagement, NNBF design, NNBF monitoring

1 INTRODUCTION

There is a growing need to protect shorelines from coastal flooding due to accelerating numbers of floods due to sea-level rise (Sweet et al., 2018) and a rapid increase in billion-dollar coastal storm disasters (NRC 2014; Smith 2020). Sea-level rise in particular is predicted to have much larger impacts to coastal communities during the remainder of this century and into the future (IPCC 2021). Traditional approaches to coastal protection largely have relied on "gray" infrastructure, such as seawalls, levees, and breakwaters, which may reduce the risk of flooding but may have adverse ecological impacts (Bilkovic and Mitchell 2013) and alter physical dynamics resulting in downstream erosion (de Schipper et al., 2020). In response, management strategies in the United States (US) and elsewhere have evolved and often incorporate natural, or "green," approaches such as living shorelines (Gittman et al., 2014; Sutton-Grier et al., 2015). Interest in infrastructure projects with natural and nature-based features (NNBF) for tackling these coastal resilience challenges is rapidly expanding. New initiatives are helping address this demand, including Engineering with Nature (EWN) from the US Army Corps of Engineers (USACE), "Building with Nature" in Europe (Van Slobbe et al., 2013), and the World Association for Waterborne Transport Infrastructure (PIANC; The World Association for Waterborne Transport Infrastructure, 2018). The EWN Atlas volumes 1 and 2 (Bridges et al., 2018; Bridges et al., 2021) present over 100 projects from around the world that integrate natural processes with engineering approaches. Project descriptions emphasize operational efficiencies, the use of natural processes to maximize benefits, and collaborations with partners and stakeholders.

Coastal ecosystem restoration, often with a goal of restoring fisheries, water quality benefits, and/or key habitat features has been occurring for decades, some of it at quite large scales (DeAngelis et al., 2020). More recent NNBF efforts (which are also sometimes called "hybrid" infrastructure approaches) on the other hand differ in that they tend to have a focus on providing specific coastal resilience benefits, typically involving both habitat restoration components to the design as well as other engineering components (Sutton-Grier et al., 2015). These NNBF projects are innovative in that they are not attempting to restore a fully functioning ecosystem, but instead are designed to restore very specific ecosystem functions for coastal resilience (such as erosion reduction and/or flood protection) while potentially providing some additional benefits. Additional NNBF hallmarks include a limited geographic setting, often near large human populations dependent on anticipated coastal resilience benefits, and constraints on budget. The critical human dimension involved in NNBF projects translates to community engagement in the outcomes and designs of the projects. Together, these NNBF characteristics are much more likely to push a project towards meaningful risk mitigation while also enhancing ecological and/or social resilience.

However, there are still many unknowns about the broader enterprise of NNBF-based coastal resilience, spanning design, funding, policy, co-production, implementation, and long-term monitoring and learning. Traditional gray infrastructure has been used to prevent flooding and erosion for decades and, as a result, there are standard design criteria for projects and a permitting system that is designed to easily and quickly provide project approval (Sutton-Grier et al., 2015). In contrast to traditional coastal gray infrastructure, NNBF projects are more complex and challenging to design and implement, since they tend to be multifunctional with several goals and are often more dynamic due to the natural components of the projects (e.g., shifting sediments, vegetation changes) rather than being a static structure, and key questions remain as to how to design, fund, and permit projects. This is particularly important as communities and agencies increasingly look to incorporate NNBF into their shoreline management plans. In fact, the USACE has recently been given guidance for "equal consideration" of economic, social and environmental categories in their project planning and evaluation (US Army Corps of Engineers, 2021).

One particular shortcoming of past NNBF projects has been limited stakeholder engagement. A great deal of the literature focused on community engagement in the context of coastal resilience has centered around disaster preparedness, rather than the specific conditions relevant to NNBF efforts. More than 2 decades ago, Mileti (1999) documented the challenges of externally designed hazard-mitigation strategies. Mileti (1999)

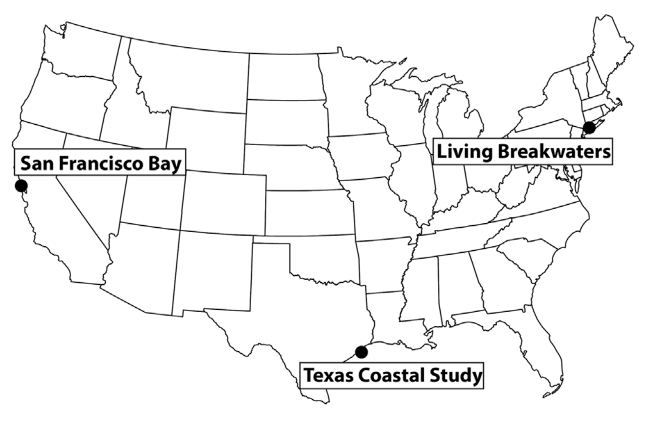

FIGURE 1 | Overview map of project locations.

noted the significant shift in understanding that these projects are not just a combination of the physical environment with engineering and infrastructure mitigation, but that communities are also central to identifying and implementing successful solutions. This shift towards less hierarchical planning was evident in varying degrees following the devastating impacts of Hurricanes Katrina and Harvey on the Gulf Coast and extended to participatory modeling (Hemmerling et al., 2020), appreciation for multi-stakeholder participatory planning efforts (Dunning 2020), and the critical value of local and traditional ecological knowledge in prioritizing data collection and modeling and decision-making frameworks (Nichols et al., 2019). Stakeholder engagement that reaches "hard-to-reach" and underrepresented communities is particularly important to avoid unintended consequences of NNBF. For example, there are now several high-profile examples of "green gentrification," such as East Boston Greenway (Anguelovski and Connolly 2021), Chicago's 606 rails-to-trails (Rigolon and Németh 2018), and New York High Line (Wolch et al., 2014). These projects led to rapid commercial and property development, escalating property values and eventual displacement of vulnerable community members. NNBF solutions can be more equitable when engagements reach vulnerable communities, infrastructure is designed with these communities' input, and funds are distributed among these communities along with other tangential communities (Heckert and Rosan, 2016). The examples presented here highlight the growing role of stakeholder engagement in disaster preparedness and planning, even though examples of community involvement are more limited in the case of NNBF focused projects.

In this study, we analyze three case studies of innovative NNBF coastal resilience projects on different US coastlines and coming from widely contrasting initiatives and sources of funding. These examples showcase the diverse ways that NNBF projects are imagined and implemented, with different features, designs, engineering strategies, funding sources, and stakeholder engagement. Our goal is to synthesize insights and lessons learned from these projects to inform future efforts and add to a growing knowledge base for NNBF implementation (e.g., Narayan et al., 2016; Morris et al., 2018; Vuik et al., 2018) similar to guidance for gray infrastructure.

The case studies were presented at a series of web panels from which we developed the case study descriptions and assessed keys to success and remaining challenges. The three case studies are 1) Living Breakwaters in New York (NY) Harbor, 2) the Coastal Texas Protection and Restoration Feasibility Study (Coastal Texas (TX) Study), and 3) South Bay Salt Pond Restoration Project in San Francisco Bay, California (CA) (**Figure 1**). We begin by summarizing these innovative projects, all of which have created or will create in-water habitat within coastal natural/human resilience projects. We focus on the innovations to coastal design, the important role of stakeholder engagement in all three projects, and funding implementation for each project and then assess common themes that emerged. Within each theme, we discuss tips for success and/or areas of progress, as well as remaining challenges and knowledge gaps for future work.

2 METHODS

A series of web panels was held in October and November 2020 entitled "Innovations in Nature-Based Systems for Coastal Protection" as part of Coastlines & People (CoPe) Research Coordination Network (RCN) funded by the US National Science Foundation. The web panels were recorded and can be accessed at https://www.umces.edu/cope/events. The final list of web panel titles and panelists, and Steering Committee members, is provided in **Table 1**. The focus of these panels was initially developed by the Steering Committee, with the intention of featuring one project along each of the continental US's ocean coastlines (East, West, Gulf) and one international project. Steering Committee members identified potential projects in each geographic region and contacted relevant partners to help select panelists. The goal was to select large-scale projects with diverse approaches that were not yet completely constructed and had willing panel participants. While there are many other projects we could have selected, we feel that the insights gained from three case studies selected highlight emerging themes that are broadly applicable to other NNBF projects.

The Steering Committee and panelists co-developed the focus and initial content of each panel, which followed the same structure of ~30 min of introductory presentations by panelists followed by ~45 min of discussion moderated by a Steering Committee member and including attendees as active participants. We focused these discussions on implementation and design, funding, and stakeholder engagement; from our perspective, these aspects make NNBF projects unique relative to gray infrastructure and are often the most challenging. We used a structured analysis approach and asked panelists to comment on these aspects, highlighting successes and challenges, as well as lessons learned from their experiences. More than 700 people registered for the series, with ~200–300 attending the live sessions, from a variety of fields (e.g., academia; local, state, and federal agencies; non-profits; private industry) and geographies.

Using content shared prior to and during the panels, the Steering Committee developed descriptions for each case study and synthesized lessons learned across all panels. These were

TABLE 1 | Steering Committee Members: Cindy Palinkas [University of Maryland Center for Environmental Science (UMCES)]; Philip Orton (Stevens Institute of Technology); Michelle Hummel (University of Texas at Arlington); William Nardin, Matthew Gray, Ming Li, Lora Harris (UMCES); Ariana Sutton-Greir (University of Maryland College Park).

Date	Title	Moderator	Panelists
8 October 2020	Beach replenishments in sand motor (Netherlands)	William Nardin (University of Maryland Center for Environmental Science)	Matthieu de Schipper (Delft University of Technology Alexander van Oudenhoven (Leiden University) Marcel Taal (Deltares) William Veatch (US Army Corps of Engineers)
20 October 2020	Wetland restoration in San Francisco Bay	Cindy Palinkas (University of Maryland Center for Environmental Science)	Dave Halsing (South Bay Salt Pond Restoration Project) Donna Ball (San Francisco Estuary Institute, South Bay Salt Pond Restoration Project) Heidi Nutters (San Francisco Estuary Partnership) Doug George (NOAA)
5 November 2020	Living breakwaters in NY Harbor	Philip Orton (Stevens Institute of Technology)	Kate Orff (Columbia University) Joseph Marrone (Arcadis) Kyle McKay (US Army Corps of Engineers)
17 November 2020	Texas Coastal Spline in Houston/ Galveston	Michelle Hummel (University of Texas at Arlington)	Coraggio Maglio (US Army Corps of Engineers Galveston) Kelly Burks-Copes (US Army Corps of Engineers Galveston) Tony Williams (Texas General Land Office) Meri Davlasheridze (Texas A&M University-Galveston)

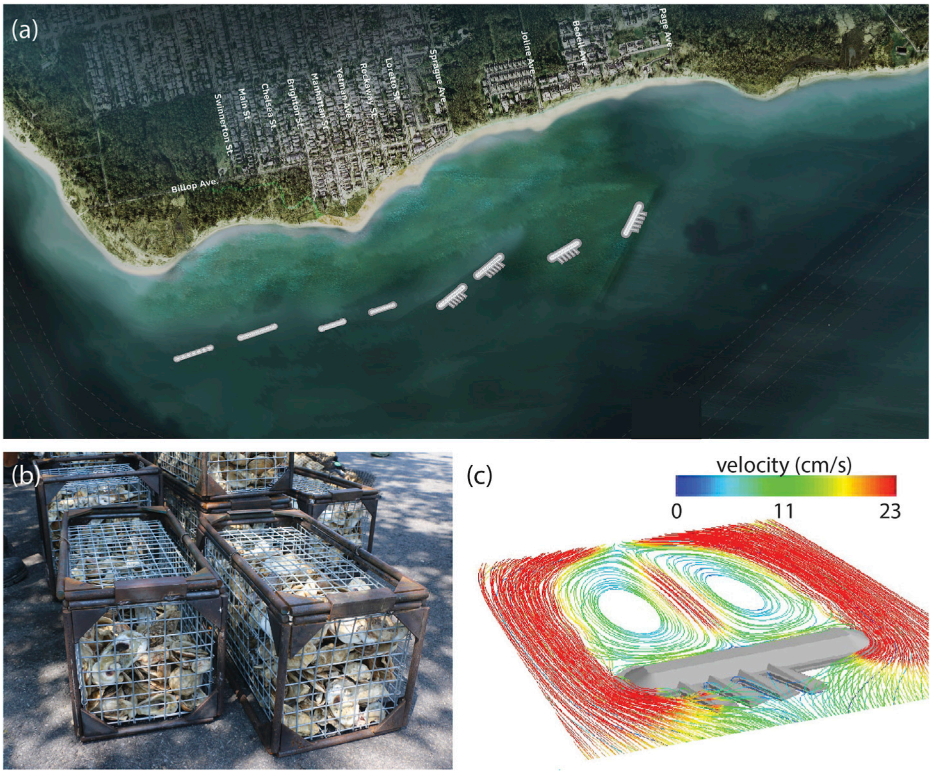

FIGURE 2 | (A) The Living Breakwaters project will construct a series of breakwaters in Raritan Bay, offshore of Staten Island. **(B)** The breakwaters are designed to provide habitat for marine life, including oysters. **(C)** Sample breakwaters (shown in gray) include a main breakwater plus "reef streets" angled outward. These were tested using computational fluid dynamics modeling to evaluate and optimize designs for avoiding scour and sedimentation.

refined during a meeting that included all panelists and the Steering Committee and informed the rest of the paper. The first panel focused on the Sand Motor project in Netherlands, which is well described in the first volume of the EWN Atlas (Bridges et al., 2018) and other publications (e.g., Stive et al., 2013; Brière et al., 2018; Luijendijk and van Oudenhoven 2019; de

Schipper et al., 2020). Rather than repeating those details, we have chosen to omit it as a specific case study and instead focus on the other three projects. These three projects (described below) are in different phases of development. The Living Breakwaters project in New York Harbor has obtained funding and worked with stakeholders to refine the design plan; its construction began in August 2021. The Coastal Texas Protection and Restoration Project in the Gulf of Mexico is still in the study phase, awaiting submission to Congress for authorization of federal funding. If authorized, it will then proceed to the design and implementation phases. South Bay Salt Ponds in San Francisco Bay is the most mature project, having completed the initial phase of implementation in 2014. This project has a robust adaptive management plan, so that results from the first phase informs project designs and the science program for subsequent phases, including an established program for stakeholder engagement and long-term plans for monitoring and performance assessments.

3 CASE STUDY DESCRIPTIONS

3.1 Living Breakwaters—New York Harbor

The Living Breakwaters project is being built in the waters of Raritan Bay (Lower New York Harbor) along the southernmost part of Staten Island's eastern shoreline (**Figure 2**). The project area is a shallow estuary that has historically supported commercial fisheries and shell fisheries. The area was heavily impacted by Hurricane Sandy in October 2012, which damaged or destroyed an unprecedented number of homes and businesses and caused loss of life and significant harm to the local economy. In response, a design competition, Rebuild by Design, was launched by the Hurricane Sandy Rebuilding Task Force to "couple innovation and global expertise with community insight to develop implementable solutions to the region's most complex needs" (Grannis et al., 2016) (http://www.rebuildbydesign.org/our-work/sandy-projects). The Living Breakwaters project resulted from a winning entry to this competition, with the competition and initial design phase occurring in 2013–2014.

3.1.1 Innovative Coastal Design

The Living Breakwaters project innovates by integrating risk reduction, ecological enhancement, and social resilience (Tschirky et al., 2018). The project consists of approximately 2,500 linear feet (~760 m) of nearshore "breakwaters," or partially submerged rubble-mound structures located between 790 and 1,800 ft (~240 and 550 m, respectively) from shore (**Figures 2A,B**). With regards to risk reduction, the project addresses both event-based and long-term shoreline erosion to preserve or increase beach width and provides wave attenuation to improve safety and prevent damage to buildings and infrastructure. The breakwaters are designed to reduce the height of wind-driven waves reaching buildings and roads to less than 3 ft (~1 m) during a 100-year storm event with up to 18 inch (~45 cm) of sea-level rise (SLR). They are not designed to reduce storm surge but instead cause wind waves to break further offshore, reducing wave run-up onto land and potentially also reducing the effect of waves on the surge (termed "wave setup"). Even as the breakwaters are more frequently submerged by storm surges with higher SLR, hydrodynamic modeling indicates that they will continue to provide wave attenuation (Marrone et al., 2019). The project also includes one-time sand replenishment to enhance beach width along the narrowest stretch of shoreline. Extensive computational fluid dynamics modeling and scaled physical laboratory modeling was utilized to optimize design, ranging from evaluation of the effectiveness of the entire set of breakwaters to reduce erosion and accrete beach over time, down to design of individual breakwaters to avoid scour and sediment accretion (**Figure 2C**; Marrone et al., 2019).

In addition to risk reduction, the project is also meant to increase the diversity of aquatic habitats, especially hard-structured habitats that can function much like the historical oyster reefs that once existed in Raritan Bay. In particular, the breakwaters were designed as rubble-mound structures with outer layers consisting of armor stones of varying sizes and ecologically enhanced concrete armor units that provide textured surfaces to promote biological activity and species recruitment. The structures also include "reef streets," narrowly-spaced rocky protrusions on the ocean side of the breakwaters, to increase habitat diversity (Marrone et al., 2019).

The benefits of detached breakwaters for coastal protection have been known for decades (e.g., Chasten et al., 1993), and oyster reefs have been gaining appreciation as a new NNBF option (e.g., Piazza et al., 2005; Reguero et al., 2018). However, their combination, the urban setting, and the social components of LB are innovations on these concepts. The project uses education, outreach, and workforce training to spread awareness about harbor restoration activities and to encourage stewardship of the harbor. It also aims to increase physical and visual access to the shoreline and nearshore waters for enhanced recreational use.

3.1.2 Stakeholder Engagement

The community-based design process engaged a range of stakeholders such as regional experts, government entities, elected officials, issue-based organizations, local groups and individuals. Stakeholder engagement during the Rebuild by Design Competition led to improved understanding of current vulnerability and future threats, while at the same time raising public expectations about grantees meeting grand challenges with constrained budgets (Grannis et al., 2016). After LB was selected as winner of the Rebuild by Design Competition, the Citizens Advisory Committee (CAC) formed in 2015. The CAC intended to serve in a community-based advisory role to the project while leaving additional input from the public during public engagements and workshops. The NY Governor's Office of Storm Recovery "encouraged applications from all variety of individuals and organizations in order to represent the diverse community of Staten Island and the region who the project will serve" (https://stormrecovery.ny.gov/LBWCAC). There were nine CAC meetings between July 2015 to July 2018.

Stakeholder input led to many adjustments to the project, including the project location, breakwater height, and an initial

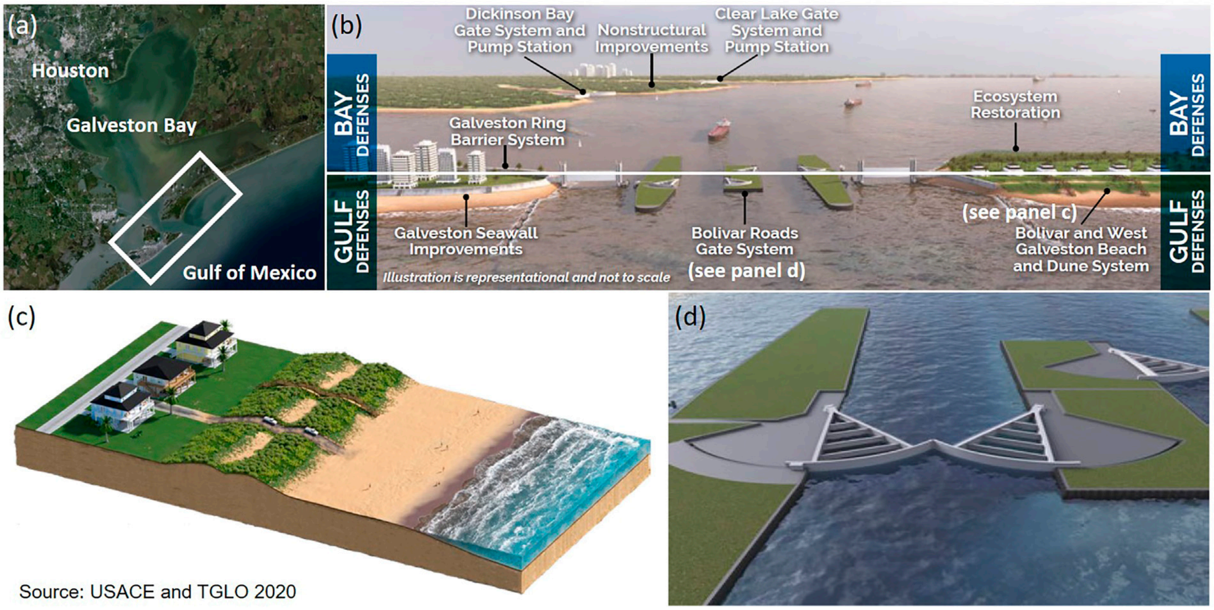

Source: USACE and TGLO 2020

FIGURE 3 | (A) Overview of the Coastal Texas Study area. **(B)** The study proposes a multiple lines of defense approach for Galveston Bay that includes gulf defenses along the outer barrier island coast as well as bay defenses to provide residual risk reduction within the bay. The gulf defenses include **(C)** restored beach and dune systems along Bolivar Peninsula and **(D)** a gate system at Bolivar Roads, the primary connection between Galveston Bay and the Gulf of Mexico.

land-based “water hub” concept evolved and eventually changed form altogether to become a floating hub. Moreover, stakeholder input also informed project priorities and helped ensure the retention of critical features of the project, including ecological elements, through the design process when budgetary concerns often lead to loss of non-protective features of NNBF projects. Additionally, the iterative process of reviewing and updating designs with public input garnered greater public support for the projects over time.

3.1.3 Funding and Implementation

The project was implemented using $60M of Community Development Block Grant Disaster Recovery (CDBG-DR) funding as well as $14M of funding from the State of New York. An environmental impact statement (EIS) was completed in 2018, and necessary state and federal permits were secured soon thereafter. The project construction began in August 2021 with a projected completion date of Fall 2024.

3.1.4 Ecosystem Services and Connectivity

Given that a fundamental goal of the project is ecological enhancement, several ecosystem service benefits are part of the design. Ecosystem service values for the project were estimated using a biome-based spatial approach, using the net change in habitat area with areal habitat dollar values obtained from published literature sources (NYS-GOSR 2021). Biomes with positive net change in value included oyster habitat/reef sustainability, increased productivity of commercial finfish and crustaceans, shoreline stabilization, water quality improvements (nitrogen removal and SAV enhancement), and refugia. The only negative (gross) ecosystem services were related to loss of relatively lower-value sandy subtidal habitat under the footprint of the breakwater structures (NYS-GOSR 2021). Also, there were hopefully limited negatives with regard to ecological connectivity, since the breakwaters could cause increased long-term sedimentation and reduced circulation behind them.

3.2 Coastal Texas Protection and Restoration Study—Gulf of Mexico

The Coastal Texas Study was undertaken to address habitat loss and the range of hazards faced by coastal areas in the state, including erosion, sea-level rise, and storm surge (**Figure 3**). It seeks to determine the feasibility of Coastal Storm Risk Management (CSRM) and Ecosystem Restoration (ER) measures to protect the state’s communities, critical economic functions, and environmental assets (US Army Corps of Engineers and Texas General Land Office, 2020; https://coastalstudy.texas.gov). The scope of the project covers the entire Texas coast, from the Sabine River to the Rio Grande River, including all coastal areas and interconnected ecosystems in the state’s 18 Gulf Coast counties.

3.2.1 Innovative Coastal Design

The project aims to minimize economic damage from coastal storm surge, inland and Gulf shoreline erosion, and restore threatened and endangered critical habitats hydrology to key lagoons. This is accomplished through a multiple-lines-of-defense strategy that combines structural, nature-based, and non-structural features to provide coastal resilience through implementation of robust and redundant protective features similar to the “double-insurance” framework of Andersson et al. (2017). A tentatively selected plan was identified in May 2018, followed by draft reports integrating feasibility and environmental impacts for public, policy, and peer review, with the goal of advancing the project to Congress for authorization of construction funding in 2022. The comprehensive plan consists of 1) an ER component that covers 6,600 acres (~27 km^2) of the coast to restore fish and wildlife habitat, improve hydrologic connectivity, and create and restore oyster reefs, marshes, dunes, and islands that provide protection for communities and infrastructure; 2) a CSRM component for 2.9 miles (~4.7 km) of beach nourishment on South Padre Island along the lower Texas coast; and 3) a final CSRM component for the Houston-Galveston region spanning 63 miles (~101 km) of the upper Texas coast to reduce storm surge entering Galveston Bay. This largest component, referred to as the Galveston Bay Storm Surge Barrier System, deploys a multiple-lines-of-defense approach intended to offer redundancy with the goal of mitigating storm surge impacts and improving the resilience for residents, industry, and ecosystems in the Houston-Galveston region. It includes a 2.8-mile (~4.5-km) long gated surge barrier system across the Galveston Bay entrance, improvements to the existing Galveston Seawall, and 43 miles (~69 km) of beach and dune systems on Galveston Island and Bolivar Peninsula, as well as strategies to mitigate residual risk from bay water surges, including additional gate closures and pumping stations at Clear Lake and Dickinson Bay on the mainland, a ring barrier for the backside of the City of Galveston, and additional nonstructural improvements on the mainland including floodproofing and raising of at-risk structures. The ER components target eight locations along the coast and include the construction of 114 miles (~183.5 km) of breakwaters, 15.2 miles (~24.5 km) of bird rookery islands, 2,052 acres (~8.3 km^2) of marsh, 12.3 miles (~19.8 km) of oyster reef, and 19.5 miles (~31.4 km) of beach and dune restoration (US Army Corps of Engineers and Texas General Land Office, 2020).

3.2.2 Stakeholder Engagement

The scoping process included federal, state, and local agencies and tribal nations, which met monthly to discuss study details and progress. Additional interagency and international workshops were held to discuss alternatives, performance metrics, and adaptive management approaches, among other aspects. Prior to the COVID-19 pandemic, a series of face-to-face public hearings and outreach meetings were held to solicit public comments on the plan and to inform the public regarding project updates (recordings are available at https://coastalstudy.texas.gov/get-involved/public-meetings/index.html). Community feedback led to changes to the plan, which originally included a floodwall over 17 ft (~5.2 m) high to protect the barrier islands along Galveston Bay's Gulf of Mexico shoreline. Local communities objected to this floodwall solution for a variety of reasons. After the USACE received more than 13,000 negative comments to this effect, they revised their plans and moved toward a more nature-based solution of beach and dune systems on the fronts of the barrier islands. It should be noted that this modification came with an increase of potential residual risks, but the tradeoffs offered an opportunity to better balance engineering performance, costs, benefits (i.e., returns on investment), and fewer environmental impacts resulting in a more socially acceptable solution. During the COVID-19 pandemic, the study team could not host face-to-face public outreach activities, and as a fallback developed an interactive GIS-based driven StoryMap system to offer the public an opportunity to engage with the study team virtually and explore the recommended plan through an interactive experience medium (https://coastal-texas-hub-usace-swg.hub.arcgis.com/).

3.2.3 Funding and Implementation

The US Congress appropriated $20.6 million to USACE over the course of the study in cooperation with the Texas General Land Office (TGLO), the non-federal cost-share sponsor, to complete the study effort. The estimated construction first-cost (in 2021 dollars) for the recommended plan is $28.9 billion, with 69% of the cost for Gulf Coast defense in Houston-Galveston and South Padre Island, 22% for bayshore defense in Houston-Galveston, and 9% for ecosystem restoration. The estimated average annual operation, maintenance, repair, replacement, and rehabilitation costs are $131 million, which must be shouldered solely by the construction sponsor. Recent scholarly research demonstrated economic benefits of a coastal barrier for the communities along the upper Texas coast to outweigh its engineering costs (Davlasheridze et al., 2019) and also looked at its significance in terms of buffering negative ripple effects on the economies of other states and the nation as a whole (Davlasheridze et al., 2021). To proceed to construction, funding must be authorized and appropriated by Congress, and cost-share sponsors must be identified. The recent Senate Bill 1160, passed on 16 June 2021, authorized a creation of the "Gulf Coast Protection District," a five-county taxing authority (https://legiscan.com/TX/drafts/SB1160/2021) and corresponds to the latest developments towards realization of the coastal-defense system for upper Texas coast communities. The bill creates a formal mechanism for the district to partner with USACE and contribute towards funding, construction, and maintenance of a coastal barrier by taxing, issuing bonds, and other financial instruments. In addition, the Texas General Land Office will serve as an additional cost-share sponsor for the ER and South Padre Island components.

Design is expected to take 2–5 years to complete (per component), and construction is expected to take an additional 10–15 years after that. The project will be maintained for a minimum of 50 years by local sponsors. The average annual costs for operation, maintenance, repair, rehabilitation, and replacement during this period are estimated at $131 million. This includes funding for periodic nourishment of restored beaches and dunes on Bolivar Peninsula and West Galveston Island every 6–7 years. As the project moves into the next phase, the project team will continue to engage with stakeholders and the public at large through the interactive StoryMap tool.

3.2.4 Ecosystem Services and Connectivity

A main goal of the Coastal Texas Study is to improve hydrologic connectivity while restoring or creating fish and wildlife habitat and natural features to provide coastal protection for communities and infrastructure. Specifically,

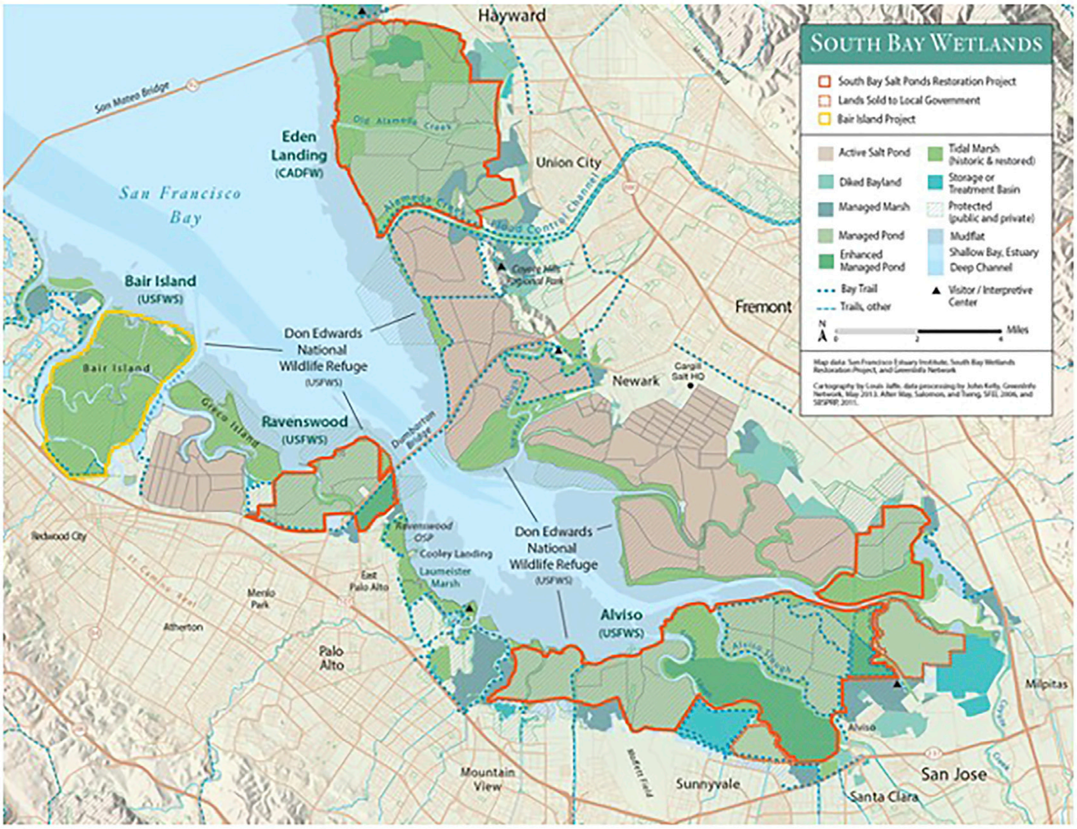

(Source: https://www.southbayrestoration.org/maps/Display%20map%20v46.pdf)

FIGURE 4 | Map of the South Bay Salt Pond Restoration Project in San Francisco Bay.

this includes a designed system to reduce storm surge entering Galveston Bay. The full project incorporates several types of restoration actions including marsh restoration, island creation/restoration, dune and beach restoration, oyster reef creation/restoration, and hydrologic restoration. Each proposed ER action was evaluated by simulating the change in number of habitat units available for target species, compared to the no-project condition. Tools such as the Habitat Evaluation and Assessment Tool (HEAT), Habitat Suitability Index (HSI), and the Wetland Value Assessment (WVA) were used based on the ecosystem type and species. Average annual habitat units calculated across the project planning period were then used to develop the final suite of ER actions described in **Section 3.2.1**.

Together, the ER components of the project are designed to provide a range of ecosystem services for Texas coastal communities. They contribute to the primary risk-reduction goals of the project by preventing shoreline erosion and reducing inundation of populated areas. In addition, these projects can enhance local water quality and provide habitat for a variety of species of commercial and recreational value, including brown shrimp, brown pelican, Kemp's Ridley sea turtle, oyster, and spotted seatrout.

3.3 South Bay Salt Ponds—San Francisco Bay, California

This panel had a wider focus than the others, since restoration in San Francisco Bay often occurs within a regional context. The panel included experts from the NOAA National Estuarine Research Reserve System (NERRS), San Francisco Estuary Partnership, California State Coastal Conservancy, and San Francisco Estuary Institute, providing perspectives from federal, state, local, and non-profit stakeholders. Many San Francisco Bay projects take regional strategies into consideration as part of their planning and implementation. These strategies include the San Francisco Bay Subtidal Habitat Goals Project (Subtidal Goals 2010), Baylands Habitat Goals Update (Goals Project 2015), Comprehensive Conservation and Management Plan for the San Francisco Estuary (2016), the San Francisco Bay Shoreline Adaptation Atlas (Beagle et al., 2019), and the recent effort to establish a regional monitoring program through the Wetlands Regional Monitoring Program (WRMP; https://www.sfestuary.org/wrmp). The WRMP Program Plan was released in April 2020, with the intention of full program implementation by 2022. The development of the WRMP included a process that engaged hundreds of experts around the Bay Area in designing the overall plan and the science framework. We focus on one specific project for the case study—South Bay Salt Pond Restoration Project (SBSP; https://www.southbayrestoration.org)—and provide insights from regional collaborations in the discussion of common themes below (**Figure 4**). While the SBSP Restoration Project has been featured in other publications (Chapple and Dronova 2017; Gies 2018; DeAngelis et al., 2020; also see https://www.southbayrestoration.org/news-items), the project continues to evolve and has entered its second phase of construction.

3.3.1 Innovative Coastal Design

The SBSP Restoration Project is the largest tidal wetland restoration project on the US West Coast (15,100 acres, ~60.7 km^2), seeking to restore multiple former salt-production ponds back to natural conditions like tidal marshes and other aquatic habitats (Valoppi 2018). In addition to restoration, the project will provide regional flood risk reduction by absorbing tidal energy instead of reflecting it, reducing tidal amplitudes far beyond the project, to varying degrees across all of San Francisco Bay (Holleman and Stacey 2014).

The project integrates three main goals: 1) habitat restoration that focuses on a range of special-status species, primarily tidal-marsh species but also species (mainly birds) that used ponded areas during the salt production era; 2) protection from tidal flows brought closer to developed areas as leveed salt ponds are opened up; and 3) addition of wildlife-compatible public access features to connect people with the Bay while providing wildlife access and habitat. The SBSP Restoration Project is implemented on lands within a state ecological reserve (Eden Landing Ecological Reserve) and a national wildlife refuge (Don Edwards San Francisco Bay National Wildlife Refuge), and it is located in three counties, underscoring the importance of a regional approach to coastal management. Phase 1 occurred from 2007–2014, restored 3,000 (~12.1 km^2) acres of tidal marsh, made improvements to >700 acres (~2.8 km^2) of managed ponds to target pond-dependent wildlife, built islands and installed water management structures, and added 7 miles (~11.3 km) of trails, mostly on levees, viewing platforms, a kayak launch, and historical exhibits. The project is in the earliest phases of Phase 2, which seeks to return tidal flows to additional areas, enhance pond habitat in other places, add trails, and integrate flood-protection projects with several external partner agencies. The SBSP Restoration Project includes an adaptive management program that uses a "restoration staircase" concept to address questions of adaptation and resilience, inserting intentional pauses to evaluate how habitats are evolving and how wildlife are responding. For example, before moving to Phase 2, the program worked with scientists to evaluate past performance and suggest possible adaptation measures to adjust project designs and refine the science program for Phase 2. These measures include anticipated effects of climate change and emerging technologies, as well as potential funding and communication mechanisms. Insights from this process and other regional planning efforts such as the Adaptation Atlas (developed by the San Francisco Estuary Institute; Beagle et al., 2019) help to identify types of adaptation strategies for consideration at specific sites.

Both the regional WRMP and the SBSP Restoration Project face potential challenges to success. For the WRMP, the biggest challenge is serving such a broad community of interest while remaining technically rigorous. There is a constant driving need to produce great science, but the process can overpower a Program like this one if all interested parties are at the table. For example, balancing trade-offs of serving such a broad community of stakeholders and of inclusion and focus when it comes to program development can be difficult. For the SBSP Restoration Project, challenges include climate change and other environmental changes that affect flooding and sediment supply to sustain the establishing tidal marshes. Project actions have the potential to increase bioavailable mercury and negatively impact the food web, as well as invasive species expansion. South Bay Salt Pond Restoration Project Adaptive Management Plan, (2007) is specifically designed to address these, and many other, uncertainties as the project continues, directly informing design and implementation of each phase of the project.

The marsh restoration areas are meant to have an indefinite/permanent useful life, as they are primarily habitat features in an obviously dynamic and ever-changing environment. They are not necessarily intended to provide any specific degree of coastal resilience or flood protection on their own. The public access features such as levee-top trails, boardwalks, viewing platforms, etc. have useful lives of 30–50 years, with the 30 being the official "intended" useful life of those features. The water control structures and pond levees/berms used in the managed pond enhancements usually need constant maintenance and/or repair/replacement on the order of a decade or so.

3.3.2 Stakeholder Engagement

The Wetland Regional Monitoring Plan (WRMP) uses a collaborative, consensus-based approach for regulators, land managers, and scientists making decisions together, starting with management questions that drive monitoring down to the level of metrics, protocols, and indicators, then bringing in new questions to update metrics and protocols. It is a prime example of combining the technical foundation for the work with public engagement, listening to the underserved communities that are adjacent to restoration projects and any other interested community members. Indeed, extensive community engagement is becoming a basic foundational practice for designing restoration projects and is one of the core best management practices.

For the SBSP Restoration Project, outreach and stakeholder engagement efforts are led by the California State Coastal Conservancy and the Consensus and Collaboration Program at California State University Sacramento. Outreach is a critical part of the entire project, since it is one of the largest restoration projects in the US and takes place in one of the most densely populated regions of California with many different user groups, interests, neighboring landowners, and stakeholders. The major venue for the public to provide advice and recommendations to the Project Management Team is through the Stakeholder Forum, a group of 25 individuals representing local businesses, advocacy groups, elected officials, recreational groups, and others. Input from extensive interviews with a wide range of stakeholders prior to implementation resulted in the current stakeholder process that provides opportunities for input at each phase of planning (California State University Sacramento, 2003). This feedback, and recognition of the additional challenges of climate change on this system, led to recent recommendations to increase regional coordination and engagement to enhance adaptive management moving forward. This is recognized as an important theme for all regional planning. Indeed, the Baylands Goals Science Update for the San Francisco Bay area (Goals Project 2015; https://www.sfei.org/projects/baylandsgoals) made several recommendations for climate planning in the region that included centralizing data for better coordination and facilitating dialogue to promote information diffusion among stakeholder groups.

3.3.3 Funding and Implementation

In 2003, 15,100 acres (~61.1 km^2) of commercial salt ponds were acquired from Cargill, Inc. for $100 million, funded by federal and state resource agencies and several private foundations. Funds for implementation of the South Bay restoration, flood management, and public access plan to date have come from a mix of sources, including local, state, and federal funds, as well as private funds from foundations or other non-governmental organizations. The largest sources of ongoing funding for restoration planning, design, permitting, and construction are competitive federal, state, and regional grant programs, matched by in-kind contributions from the project partner agencies.

The South Bay project is being implemented in multiple phases over 50 years, using a robust adaptive management plan (AMP) to determine how far the system can move toward full tidal action and associated tidal habitats, while still meeting the other Project Objectives (Trulio et al., 2007). The AMP identifies restoration targets as well as triggers that may necessitate management actions. The organizational strategy includes an Executive Project Manager and Executive Leadership Group and a Project Management Team that regularly interacts with the Science Team, Regulatory and Trustee Agency Group, and Stakeholder Forum to ensure oversight and coordinate planning and implementation throughout the project (https://www.southbayrestoration.org/page/who-we-are-collaborative-team).

3.3.4 Ecosystem Services and Connectivity

The SBSP Restoration Project highlights the need to make sure habitats are not created for a single species but rather consider competing species' needs. Indeed, one of the main goals of the SBSP Restoration Project is habitat restoration for a range of special-status species. While the focus is mostly on tidal marsh species, there is also a need to protect the many types of wildlife (mainly birds) that used the ponded areas during salt production. So, the project design needed to restore tidal marsh species while also providing for pond-dependent wildlife species and while connecting habitat *via* wildlife corridors. Another goal is to add wildlife-compatible public access features like trails and viewing areas to connect people with SF Bay and help them understand why restoration is needed. These goals and associated ecosystem services are not always compatible, making some trade-offs potentially necessary. For example, opening up the salt ponds and restoring tidal flows brought water closer to developed areas, resulting in a need to maintain or improve current levels of flood protection for those areas. This has entailed working with local flood protection agencies to incorporate their projects into the landscape with the restored sites.

Beyond the challenge of managing the competing goals for the project and the challenges of predicted effects of sea-level rise, the project provides an array of ecosystem services and greatly improved connectivity along the shoreline. The restoration supports baseline services and functions such as photosynthesis, nutrient cycling and provides habitat and nursery areas, increases biodiversity, and the transition zones designed into the project provide high tide refugia. Much of the habitat along the shoreline of San Francisco Bay has been reduced in size and suffered from fragmentation due to urban development. Increasing the area of tidal marshes is an important part of the design and will help to create larger, more connected patches of marsh habitat in the South Bay to allow movement of not only wildlife species, but of water, sediment and nutrients between the Bay and ponds that were previously restricted by berms and levees. Social and economic services are services that are especially important to people for cultural and social development and the Bay area will benefit from increased access to trails for hiking and biking, and birdwatching. This is a key issue for the region, and so it follows that evaluating how wetland restoration provides benefits to humans is one of the five guiding questions of the regional WRMP. This task will work to ensure that diverse voices are at the table in the WRMP process, and their interests are reflected in the suite of indicators monitored by the WRMP. Enhancing community engagement and ecosystem services evaluation will improve the ability of the WRMP to advance environmental justice and improve environmental conditions for communities disproportionately impacted by climate change and the loss of wetlands.

4 DISCUSSION OF EMERGING THEMES

Several common themes emerged from the three case studies that highlight factors contributing to and/or hindering success of innovative coastline management projects, depending on the context. We have organized the themes into two sections—areas of progress and remaining challenges. It is important to note that there have been advancements and challenges in every theme; the groupings are intended to guide readers rather than represent a hard boundary. Our goal is to glean lessons learned within each theme to inform future NNBF coastal resilience projects.

4.1 Areas of Progress

4.1.1 Moving Beyond Single-Benefit Projects

Historical approaches to coastal protection have focused on reducing potential damages from hazards such as flooding and erosion *via* gray infrastructure (e.g., levees, seawalls, and bulkheads) (Griggs 2005; Spalding et al., 2014). Despite the immediate and often substantial risk-reduction benefits provided by these structures, they offer minimal co-benefits and can even cause loss of coastal habitat and associated ecosystem services (Sutton-Grier et al., 2015). NNBF and hybrid approaches to coastal protection represent a promising alternative to gray infrastructure because of the many co-benefits that can be achieved, including wildlife habitat, recreation, water quality, and carbon/nutrient sequestration (Bridges et al., 2015). Additionally, the USACE has determined that NNBF projects that involve very collaborative, multi-disciplinary partnerships including landscape architects, engineers, and applied scientists, not only result in improved NNBF projects, but also improved communication and support for these types of projects (King et al., 2022). Hence, projects with multiple goals and multiple collaborators have many benefits.

Each case study started with an innovative framing, enabled through the funding sources themselves. The Rebuild by Design competition that resulted in the Living Breakwaters project encouraged innovation and broad interdisciplinary teams, with the goal of "promoting innovation by developing regionally scalable but locally contextual solutions that increase resilience in the region" (https://stageipk.es.its.nyu.edu/initiatives/rebuild-by-design/). The competition awarded projects that included strong engagement of local communities and government stakeholders, driving projects to target a wider range of benefits than simple flood-damage reduction. In the case of the Coastal Texas Study, the authorization for the study was explicitly for "flood damage reduction" and "ecosystem restoration," in contrast to other more typical feasibility studies (e.g., US Army Corps of Engineers, 2015; US Army Corps of Engineers, 2019) that were only authorized for damage reduction. The SBSP Restoration Project initiative sought co-benefits from the initial stages of planning for restoration, flood reduction and wildlife-friendly public access.

By leveraging nature-based and hybrid infrastructure, all three case studies move beyond a sole focus on safety and flood reduction to include multiple functions and benefits (Van Veelen et al., 2015; O'Shaughnessy et al., 2020). Complete elimination of risk is not the goal, nor is it realistic given anticipated increases in the rate of sea-level rise and storm intensity; instead, each project provides meaningful risk mitigation while also enhancing ecological and/or social resilience. For example, in addition to providing wave attenuation and erosion reduction, the Living Breakwaters project also aims to increase biodiversity, enhance shoreline recreational opportunities, and raise awareness of coastal resiliency and ecological health. The Coastal Texas Study includes numerous components aimed at creating or restoring natural features that provide habitat in addition to acting as barriers to storm surge or waves. The SBSP Restoration Project and other regional projects in San Francisco Bay are focused on ecological restoration rather than an explicit risk reduction component, although projects do include measures to ensure that flood risk for adjacent communities and infrastructure does not increase as a result of restoration actions. Also, enhancing recreation opportunities can be an important aspect for community buy-in and obtaining funding from multiple sources. For example, the SBSP Restoration Project has public access as one of its main goals and includes trails and viewpoints in almost all of the project sites.

Multi-functional projects such as these can address the needs of a variety of stakeholders and enable multiple pathways for a project to be successful, even if some aspects of the project do not end up working as well as others. For example, there has been increasing awareness by the public that the restoration of ponds at the edge of SF Bay may provide some protection against sea level rise for critical infrastructure, global technology companies, and other Silicon Valley businesses. As these case studies demonstrate, communities and stakeholders value natural habitats and the services they provide and may be more willing to support coastal resilience projects that include co-benefits such as maintaining ecosystem integrity and recreational access. An example of increased public awareness and support of wetland restoration includes the passage of Measure AA (San Francisco Bay Clean Water, Pollution Prevention and Habitat Restoration Measure)—the nine counties of San Francisco Bay voted for a 20-year, $12/year parcel tax that will raise $500 million for restoration projects in the Bay. The personal connection to the Bay by voters was one of the major factors for its success (https://www.sfbayrestore.org/overview). Given the multifaceted and interdisciplinary nature of NNBF projects, successful design and implementation requires expertise and cooperation across a variety of fields and sectors. Local system knowledge is critical to apply successful strategies from other projects, adapting them to address site-specific conditions. The projects described here include teams spanning a broad range of participants from architecture, engineering, ecology, economics, and/or social science representing state/federal agencies, consulting firms, and academia. These multidisciplinary teams reflect the importance of integrated thinking that considers the physical hazards alongside ecological and social responses.

4.1.2 Creating Opportunities for Natural and Nature-Based Features Through Co-Production of Project Designs

Input from the public is critically important since coastal resilience projects not only affect local communities and the environment but also people's lives. As a result of the potential negative side effects of protecting coasts with gray infrastructure, including degraded habitat, loss of shoreline access, and impacts on neighboring properties, gray projects have faced opposition from stakeholders and the public in the past (Griggs 2005). For example, a project in Ventura, California to prevent shoreline erosion by constructing a seawall was opposed by local stakeholders, including the Surfrider Foundation and the California State Coastal Conservancy, in the 1990s. Instead, the interested parties agreed upon a managed retreat approach (Surfer's Point Managed Shoreline Retreat; https://ventura.surfrider.org/surfers-point/) that allowed for habitat restoration and did not interfere with local hydrodynamics (Judge et al., 2017).

In contrast, coastal resilience projects that have stakeholder engagement as one of their explicit goals can incorporate feedback early and often as the project progresses. The Coastal

Texas Study is an excellent example of feedback shifting the project design from a more traditional, gray approach to a more natural/hybrid solution. That project initially proposed a floodwall that was opposed by local residents, who sent thousands of negative comments to USACE. As a result, the project was redesigned to use a beach and dune system to reduce flooding from the Gulf instead. This solution provides fewer risk-reduction benefits but is more acceptable to the local community and provides more NNBF co-benefits.

Frequent and effective communication between the project team, stakeholders, and the public can contribute to a more transparent process that includes opportunities for input and adjustments, helping to build trust and buy-in (Paul et al., 2018). The case studies here, especially Living Breakwaters and the Coastal Texas Study, highlight the importance of clear communication. For example, in the Living Breakwaters project, being transparent in the process about what the project could and could not do was critical for developing trust with everyone involved. This project made it clear from the beginning that the goal was not to keep flood waters out of the area but rather to restore ecological systems, reduce the risk of erosion and wave damage, and enhance social outreach and education. The project team specifically engaged with stakeholders before truly beginning the design to establish project goals and trade-offs, ultimately producing hundreds of pages of information for the Environmental Impact Statement (EIS). For the Coastal Texas Study, following the release of the first Draft EIS, there was widespread misunderstanding among locals about the proposed plan, and misinformation was spread on social media. The project team learned from this experience and conducted a much more extensive outreach and public education campaign prior to the release of the revised Draft EIS, which resulted in more productive exchanges between the project team and the public.

4.1.3 Managing Uncertainty in Project Performance

Unlike engineered structures that have a set of well-defined design criteria, there are uncertainties in quantifying the capacity of nature-based systems to withstand extreme events and determining the breakpoints at which such a system is expected to either fail to provide its required engineering service or itself be destroyed due to the environmental conditions. This requires a flexible design approach that can not only satisfy short-term needs but also allow for future adjustments to meet long-term goals. It also requires a post-construction monitoring program to document the performance of these systems and may require a greater commitment to ongoing maintenance to achieve a desired level of protection than traditional approaches. Since these systems are innovative, guidance on expected outcomes (e.g., amount of sediment accretion that will occur over time) is lacking, especially compared to decades of experience with gray infrastructure, and engineers may have more comfort with materials that have documented factors of safety. It can also be a challenge to predict the long-term evolution of NNBF and to scale up from small-scale to larger-scale applications. For example, in the Sand Motor project in Netherlands, the uncertainty in the predicted evolution is a mixture of both uncertainty in model formulations in current state of the art models and the uncertainty in future (wave) forcing (Kroon et al., 2020). This is especially important since there is a large natural variability in ecology and still many unknowns on how habitat attributes result in changes in biodiversity and species richness.

Thus, it is critical that learning from NNBF projects also be one of the multi-functional goals, so that we can learn as much as possible from every project. For example, because there is no "one-size-fits-all" natural infrastructure design for all contexts (Sutton-Grier et al., 2015) and the coastal resilience ecosystem services provided by natural infrastructure vary by geomorphic setting and event conditions (Saleh and Weinstein 2016), one main research focus that is still greatly needed is better understanding of what approaches and strategies work well in which conditions (Smith et al., 2020). Additionally, we need to know how to effectively implement NNBF projects for coastal resilience, and how projects can address uncertainties and evaluate or weigh different components (e.g., using Ecosystem Services framework). Projects should define goals for long-term adaptability in the planning of the project and establish specific performance metrics and clearly defined goals (Arkema et al., 2017; Bayulken et al., 2021). In the Living Breakwaters project, modeling of waves, storm surge, and sediment movement in water and then onshore was a critical component to developing the design, and monitoring the project will be key to understanding how well the project is functioning for both ecological and risk reduction goals. In the SBSP Restoration Project, understanding how salt pond restoration would impact flooding and flood risk to human development has been key to planning to maintain or improve flood protection for those communities as part of the restoration design.

There is a general focus on "no-regrets" strategies by assessing adaptability to climate change *via* stress tests under higher sea levels. The Coastal Texas Study evaluated project alternatives under low, intermediate, and high SLR scenarios through 2,135 and includes a plan for monitoring and adaptively managing the ecosystem restoration components of the project to ensure that project objectives are met across the lifetime of the project. It also utilizes a multiple-lines-of-defense approach to provide redundancy in coastal protection and address possible failure modes. For example, possible breaching of the dune barrier system during large storms is addressed by including bay-side defenses and by elevating structures. The SBSP Restoration Project explicitly includes adaptive management, so that lessons learned from Phase 1 can be incorporated into Phase 2 plans and future phases along with new insights from emerging science and technology. Adaptive management *via* engaging scientists and stakeholders is a key part of the WRMP in San Francisco Bay, in which lessons learned from designing, implementing, and monitoring for one project will inform other projects at local and regional scales.

4.1.4 Expanding Beyond the Project Scale to a Regional Perspective

Possibly because of the stakeholder engagement and the focus on multiple benefits of each project, as well as the need to design multiple features to achieve many aspects of resilience, NNBF projects are often part of a suite of projects to build resilience across a broad region. This is a strength of the NNBF approach, because there can be a larger focus on how individual projects fit together into a coastal system designed for resilience. Connectivity of multiple projects along a coastline can be part of the design of NNBF projects particularly in urban settings in order to counter past loss of coastal ecosystems and biodiversity (Aguilera et al., 2020). For example, in the Coastal Texas Study, there are many different resilience approaches across an entire region that are combined into one larger project with multiple goals—restoring fish and wildlife habitat; improving hydrologic connectivity; creating and restoring oyster reefs, marshes, dunes, and islands that provide protection for communities and infrastructure; renourishing beaches; installing a new tidal gate; and improving a seawall. In the SF Bay, once developed, the WRMP would integrate monitoring, reporting, and data-sharing across a wide range of projects to improve uniformity, consistency, currency, and other aspects of data. The project itself is also taking into account that as a result of the restoration of tidal flows, flood risk on different parts of the landscape is changing, and so maintaining and improving flood protection is part of the design of the project to help address the changes taking place across the landscape as restoration reconnects parts of the landscape that were previously separated by the salt ponds. Taking a regional approach to resilience and incorporating NNBF projects is a critical, forward-looking step in improving coastal resilience.

4.2 Remaining Challenges

4.2.1 Navigating Permitting and Policy Barriers

A significant barrier to the widespread implementation of innovative NNBF projects is the permitting process for new designs, which is often complex and may need quite a lot of lead time. Permits may be required at the local, state, and/or federal level. There may be many steps, and regulators may be seeing this type of innovative project for the first time. Again, the importance of being transparent and doing outreach and education as part of these projects applies to getting regulatory and community buy-in. For example, a key to facilitating the permitting process for the Living Breakwaters project was to have a clear purpose and need statement that included all of the project benefits (risk reduction, ecological enhancement, and social resilience) and to have a robust and transparent dialog with the regulatory community early and often to help craft a permitting path that was appropriate for the project's innovative approaches.

Many panelists described the frustrations and challenges with regulatory barriers that made projects more difficult. Oftentimes the policies are well-meaning environmental regulations that aim to protect people and ecosystems, and yet make it challenging to be innovative in the coastal resilience setting. For example, regulations around the use of "fill" (e.g., sand or silt dredged from a location often for maintenance needs such as navigable shipping channels) in wetlands were initially designed to protect wetlands and generally did not include anticipated effects of climate change or potential opportunities to use fill to enhance or restore coastal environments when they were implemented. Because they are legal requirements, regulatory agencies may have to undergo a lengthy legal process to grant permits to allow use of fill in wetlands. Even given the challenges of addressing this barrier, it is important to change the conversation on fill from seeing it only as a pollutant to considering it as a possible asset to NNBF projects. Restrictions on fill use was a challenge to the Living Breakwaters project design. In San Francisco Bay, the Bay Conservation and Development Commission, the regional body charged with managing the Bay coastline, is doing just that and changing its policy to allow the use of fill for restoration and environmental enhancement projects while still maintaining restrictions on the use of fill for development projects. At the federal level, USACE is increasingly exploring opportunities to incorporate NNBF into coastal risk-reduction projects, as evidenced by the Coastal Texas Study and EWN efforts, including the use of fill for beneficial reuse. However, there are still limitations in the use of dredged material across multiple projects that will require innovations in policy and blending of funds. Thus, more research on the appropriate use of fill is needed to inform potential changes in regulations that could facilitate more NNBF projects. This type of innovation in the policy space is going to continue to be needed to support more NNBF projects.

Successful permitting and implementation of multi-objective projects may also require a rethinking of how project planning is conducted within and between mission-focused agencies, as projects that move outside of the stated mission may be difficult to justify and fund. This siloing of projects within existing agency boundaries to avoid "mission creep" may miss out on opportunities to achieve multiple benefits across a range of objectives. Thus, while there has already been some progress to address these barriers, they will likely continue to be a challenge for innovative coastal resilience projects until these innovations become more of the "norm."

4.2.2 Funding

Several panelists identified funding as a critical need for both project development and long-term monitoring after implementation. This is a continuing challenge, especially in the US, where funding for resilience projects is primarily often tied to the disaster-response cycle (NRC, 2014). The Living Breakwaters project is an excellent example of a project that arose after a major disaster; if it had been implemented before Hurricane Sandy, it may have protected the coastline from some damages. It is important as a society that we start making investments in resilience projects that are not tied to the disaster-response cycle. We need to be anticipatory and fund the development and implementation of these projects during "blue-sky" periods before the next big storm (e.g., Reguero et al., 2020). This would allow projects to not be rushed and to have more certainty about funding opportunities.

When NNBF projects are funded in a post-disaster context, there is often a firm and short timeline on funds, prohibiting post-installation monitoring. Yet such monitoring can help define "success" of a project and inform other projects or other phases of the existing projects. In response to a vacuum of long-term

TABLE 2 | Potential services provided by NNBF (Bridges et al., 2015).

Type of service	Example
Risk reduction	Erosion control, storm surge reduction, wave attenuation, flood peak reduction
Economic	Fisheries, property values, raw materials production, tourism/recreation
Social	Aesthetics, cultural heritage, educational/scientific opportunities
Environmental	Biodiversity, carbon sequestration, water quality, wildlife habitat, sediment management, nutrient sequestration, groundwater storage, hazard material reduction, threatened and endangered species protection

monitoring of NNBF projects after Hurricane Sandy, a New York State-funded team and stakeholders recently co-created a state-level monitoring program (Wijsman et al., 2021).

An ongoing monitoring program can be planned during project design that is rigorous but not so much that it becomes onerous or burdensome to fund and/or conduct over the years. For example, the Living Breakwaters project was designed to enable long-term monitoring to learn more about which specific breakwater designs and parameters are more likely to be effective to help inform adaptive management efforts and future projects. However, future funding will still be required for the actual research and measurements in this project. The SBSP Restoration Project offers a success story in which the investment of funding for long-term monitoring in the first phase of the project has informed the planning for the next phase, as well as providing valuable insights for other projects in the region.

Cost-sharing requirements can also place a limitation on the long-term maintenance and monitoring of NNBF projects. For example, in the Coastal TX Study, the ecosystem restoration alternatives were initially meant to include funding for nourishment if needed in response to changing conditions and sea-level rise. However, the cost of maintaining ecosystem restoration measures, which are required to be self-sustaining, could not be cost-shared, so this was later removed from the recommended plan. If nourishment is deemed necessary during the post-project monitoring period, the required work will have to be authorized separately at that time. Without proper funding to maintain ecosystem restoration components, the long-term survival and performance of these systems may be constrained. In contrast, features that also included a risk-reduction component, such as the beach and dune restoration, do include funding for periodic nourishment to maintain protective benefits.

4.2.3 Defining and Assessing Project Costs and Benefits

There is also a need to broaden the thinking on cost-benefit analyses. These studies are commonly used to assess options and trade-offs for project alternatives, and yet have traditionally only included the costs of construction and the benefits of reducing flood risks provided by projects (e.g., Aerts 2018; Reguero et al., 2018; Waryszak et al., 2021). With the burgeoning of innovative NNBF projects with multi-functional goals, it is key that cost-benefit analyses include all the benefits these projects provide, including ecological, recreational, and other benefits, although these co-benefits can be hard to quantify in monetary terms (Sutton-Grier et al., 2015; Seddon et al., 2020). Each of our case studies addressed more than benefit-cost ratios for risk reduction, often in response to community input. In the Coastal Texas Study for example, the cost-benefit analysis included benefits to wildlife in addition to risk reduction benefits. For Living Breakwaters, the project team is specifically planning to monitor fish productivity on the underwater portions of the breakwaters to quantify the ecological benefits. In some cases, data may be lacking or very limited to inform cost-benefit analyses of these multiple benefits; however, this is one of the reasons why monitoring many aspects of these NNBF projects is key. We will learn from these projects and that new understanding of co-benefits can help inform cost-benefit analyses of future projects and address some of the hesitancy to give permits.

One of the unique elements of the Coastal Texas Study and Living Breakwaters project is a focus on co-benefits in the provision of dune habitat and oyster reefs, respectively. Without the context of serving as engineering structures, these elements alone might be considered ecosystem restoration. Here, the NNBF context reimagines a practical approach to incorporating these elements into levees and breakwaters and asks us to consider the phenomenological roots of "restoration" (see Hilderbrand et al., 2005; Hobbs et al., 2009; Hertog and Turnhout 2018). Certainly, these efforts are not restoring the system back to some historical state, but they replace lost restoration functions, and in this way, they lie in a grey area of restoration (e.g., "novel ecosystems"; Hobbs et al., 2013).

One recommendation for future projects and efforts in coastal resilience is to think specifically about what we can learn from each of these innovative projects because additional data on the performance, community outreach/stakeholder engagement, and socioeconomic components of NNBF projects is key to improving future projects (Smith et al., 2020; Bayulken et al., 2021). Collecting similar types of data from these and future projects would enable us to learn as much as possible from each project. We have included recommendations for the types of benefits or ecosystem services that NNBF projects should consider including in their monitoring plans (**Table 2**).

This is not a comprehensive list by any means, but is a good starting point for thinking about the types of data we should collect across projects to help with project comparisons and to inform future planning and analyses. Considering a consistent and more complete set of services across NNBF projects could facilitate the evaluation, selection, and permitting of similar future projects. The goal of this case-study analysis, as well as the suggestions for data collection for future projects, is to facilitate additional innovative coastal resilience projects across the US and around the world.

AUTHOR CONTRIBUTIONS

This paper was co-developed by the Steering Committee members and Panelists listed in **Table 1**. The Steering Committee wrote the first draft of the paper, led by CP, after which it was reviewed for feedback and input by the Panelists. All authors participated in subsequent rounds of revisions and editing. All authors have read and agreed to the published version of the manuscript.

FUNDING

We acknowledge funding support from National Science Foundation through the CoPe (Coastlines and People) RCN (Research Coordination Network): Advancing Interdisciplinary Research to Build Resilient Communities and Infrastructure in the Nation's Estuaries and Bays CoPe RCN grant: ICER 1940273. CP was partially supported by the Grayce B. Kerr Fund. The funders had no role in the design of the study; in the collection, analyses, or interpretation of data; in the writing of the manuscript, or in the decision to publish the results.

ACKNOWLEDGMENTS

The authors would like to thank many colleagues, students, and staff for fruitful discussions on this topic. We especially thank the attendees of the web panel series, particularly those who actively participated *via* questions and comments in the chat and brought out additional facets of the projects beyond our initial panel planning. Constructive comments from 2 reviewers helped improve the original manuscript. This is contribution #6113 of the University of Maryland Center for Environmental Science.

REFERENCES

Aerts, J. (2018). A Review of Cost Estimates for Flood Adaptation. *Water* 10, 1646. doi:10.3390/w10111646

Aguilera, M. A., Tapia, J., Gallardo, C., Núñez, P., and Varas-Belemmi, K. (2020). Loss of Coastal Ecosystem Spatial Connectivity and Services by Urbanization: Natural-to-Urban Integration for bay Management. *J. Environ. Manage.* 276, 111297. doi:10.1016/j.jenvman.2020.111297

Andersson, E., Borgström, S., and McPhearson, T. (2017). "Double Insurance in Dealing with Extremes: Ecological and Social Factors for Making Nature-Based Solutions Last," in *Nature-Based Solutions to Climate Change Adaptation in Urban Areas*. Editors N. Kabisch, H. Korn, J. Stadler, and A. Bonn (Cham: Springer International Publishing), 51–64. Theory and Practice of Urban Sustainability Transitions. doi:10.1007/978-3-319-56091-5_4

Anguelovski, I., and Connolly, J. J. T. (2021). "Addressing green and Climate Gentrification in East Boston," in *The Green City and Social Injustice: 21 Tales from North America and Europe*. 1st ed. (London: Routledge), 14.

Arkema, K. K., Griffin, R., Maldonado, S., Silver, J., Suckale, J., and Guerry, A. D. (2017). Linking Social, Ecological, and Physical Science to advance Natural and Nature-Based protection for Coastal Communities. *Ann. N.Y. Acad. Sci.* 1399, 5–26. doi:10.1111/nyas.13322

Bayulken, B., Huisingh, D., and Fisher, P. M. J. (2021). How Are Nature Based Solutions Helping in the Greening of Cities in the Context of Crises Such as Climate Change and Pandemics? A Comprehensive Review. *J. Clean. Prod.* 288, 125569. doi:10.1016/j.jclepro.2020.125569

Beagle, J., Lowe, J., McKnight, K., Safran, S. M., Tam, L., and Jo Szambelan, S. (2019). *San Francisco Bay Shoreline Adaptation Atlas: Working with Nature to Plan for Sea Level Rise Using Operational Landscape UnitsSFEI Contribution No. 915*. Richmond, CA: SFEI & SPUR, 255. Available at: https://www.sfei.org/documents/adaptationatlas.

Bilkovic, D. M., and Mitchell, M. M. (2013). Ecological Tradeoffs of Stabilized Salt Marshes as a Shoreline protection Strategy: Effects of Artificial Structures on Macrobenthic Assemblages. *Ecol. Eng.* 61, 469–481. doi:10.1016/j.ecoleng.2013.10.011

Bridges, T., Bourne, E. M., King, J., Kuzmitski, H., Moynihan, E., and Suedel, B. (2018). *Engineering with Nature : An Atlas*. Vicksburg, MS: US Army Corps of Engineers. Engineer Research and Development Center Special Report ERDC/EL SR-18-8. doi:10.21079/11681/27929

Bridges, T., Bourne, E., Suedel, B., Moynihan, E., and King, J. (2021). *Engineering with Nature: An Atlas*, 2. Vicksburg, MS: US Army Corps of Engineers. Engineer Research and Development Center Special Report ERDC/EL SR-21-2. doi:10.21079/11681/40124

Bridges, T. S., Burks-Copes, K. A., Bates, M. E., Collier, Z., Fischenich, C. J., Piercy, C. D., et al. (2015). *Use of Natural and Nature-Based Features (NNBF) for Coastal Resilience*. Washington, D.C.: US Army Corps of Engineers.

Brière, C., Janssen, S. K. H., Oost, A. P., Taal, M., and Tonnon, P. K. (2018). Usability of the Climate-Resilient Nature-Based Sand Motor Pilot, The Netherlands. *J. Coast Conserv* 22, 491–502. doi:10.1007/s11852-017-0527-3

California State University (CSU) Sacramento. 2003. Stakeholder and Organizational Assessment Findings and Recommendations by Center for Collaborative Policy. Available at: https://www.southbayrestoration.org/pdf_files/stakeholder_assess/Final_Assessment_Report.pdf.. (Accessed April 4, 2022).

Chapple, D., and Dronova, I. (2017). Vegetation Development in a Tidal Marsh Restoration Project during a Historic Drought: a Remote Sensing Approach. *Front. Mar. Sci.* 4, 243. doi:10.3389/fmars.2017.00243

Chasten, M. A., Rosati, J. D., McCormick, J. W., and Randall, R. E. (1993). "Engineering Design Guidance for Detached Breakwaters as Shoreline Stabilization Structure," in *DTIC Document*. Available at: http://oai.dtic.mil/oai/oai?verb=getRecord&metadataPrefix=html&identifier=ADA275241.

Comprehensive Conservation and Management Place for the San Francisco Estuary (2016). Available at: https://www.sfestuary.org/wp-content/uploads/2021/05/CCMPFinalOct2016.pdf. (Accessed April 4, 2022).

Davlasheridze, M., Atoba, K. O., Brody, S., Highfield, W., Merrell, W., Ebersole, B., et al. (2019). Economic Impacts of Storm Surge and the Cost-Benefit Analysis of a Coastal Spine as the Surge Mitigation Strategy in Houston-Galveston Area in the USA. *Mitig Adapt Strateg. Glob. Change* 24, 329–354. doi:10.1007/s11027-018-9814-z

Davlasheridze, M., Fan, Q., Highfield, W., and Liang, J. (2021). Economic Impacts of Storm Surge Events: Examining State and National Ripple Effects. *Climatic Change* 166, 1–20. doi:10.1007/s10584-021-03106-z

de Schipper, M. A., Ludka, B. C., Raubenheimer, B., Luijendijk, A. P., and Schlacher, T. A. (2020). Beach Nourishment Has Complex Implications for the Future of sandy Shores. *Nat. Rev. Earth Environ.* 2, 70–84. doi:10.1038/s43017-020-00109-9

DeAngelis, B., Sutton-Grier, A., Colden, A., Arkema, K., Baillie, C., Bennett, R., et al. (2020). Social Factors Key to Landscape-Scale Coastal Restoration: Lessons Learned from Three U.S. Case Studies. *Sustainability* 12, 869. doi:10.3390/su12030869

Dunning, K. H. (2020). Building Resilience to Natural Hazards through Coastal Governance: a Case Study of Hurricane Harvey Recovery in Gulf of Mexico Communities. *Ecol. Econ.* 176, 106759. doi:10.1016/j.ecolecon.2020.106759

Gies, E. (2018). Fortresses of Mud: How to Protect the San Francisco Bay Area from Rising Seas. *Nature* 562, 178–180. doi:10.1038/d41586-018-06955-4

Gittman, R. K., Popowich, A. M., Bruno, J. F., and Peterson, C. H. (2014). Marshes with and without Sills Protect Estuarine Shorelines from Erosion Better Than Bulkheads during a Category 1 hurricane. *Ocean Coastal Manag.* 102, 94–102. doi:10.1016/j.ocecoaman.2014.09.016

Goals Project (2015). *The Baylands and Climate Change: What We Can Do. Baylands Ecosystem Habitat Goals Science Update 2015 Prepared by the San*

Francisco Bay Area Wetlands Ecosystem Goals Project. Oakland, CA: California State Coastal Conservancy. Available at: https://www.sfei.org/documents/baylandsgoalsreport.

Grannis, J., Arroyo, V., Hoverter, S., Goetz, M., Bennett, A., DeWeese, J., et al. (2016). *Rebuilding with Resilience: Lessons from the Rebuild by Design Competition after Hurricane Sandy*. Washington, DC. USA: Georgetown Climate Center.

Griggs, G. (2005). "California's Retreating Coastline: where Do We Go from Here," in California and the World Ocean. '97 Conference Proceedings Editors Magoon, O. T., Converse, H., Baird, B., and Miller-Henson, M.. American Society of Civil Engineering, 2 121–125.

Heckert, M., and Rosan, C. D. (2016). Developing a Green Infrastructure Equity Index to Promote Equity Planning.. *Urban Forest. Urban Green.* 19, 263–270.

Hemmerling, S. A., Barra, M., Bienn, H. C., Baustian, M. M., Jung, H., Meselhe, E., et al. (2020). Elevating Local Knowledge through Participatory Modeling: Active Community Engagement in Restoration Planning in Coastal Louisiana. *J. Geogr. Syst.* 22, 241–266. doi:10.1007/s10109-019-00313-2

Hertog, I. M., and Turnhout, E. (2018). Ideals and Pragmatism in the Justification of Ecological Restoration. *Restor Ecol.* 26, 1221–1229. doi:10.1111/rec.12680

Hilderbrand, R. H., Watts, A. C., and Randle, A. M. (2005). The Myths of Restoration Ecology. *Ecol. Soc.* 10, 19. doi:10.5751/es-01277-100119

Hobbs, R. J., Higgs, E., and Harris, J. A. (2009). Novel Ecosystems: Implications for Conservation and Restoration. *Trends Ecol. Evol.* 24, 599–605. doi:10.1016/j.tree.2009.05.012

Hobbs, R. J., Higgs, E. S., and Hall, C. M. (2013). "Defining Novel Ecosystems," in *Novel Ecosystems: Intervening in the New Ecological World Order*. Editors R. J. Hobbs, E. Higgs, and C. M. Hall (Chichester, West Sussex, Hoboken, NJ: John Wiley & Sons), 58–60. doi:10.1002/9781118354186.ch6

Holleman, R. C., and Stacey, M. T. (2014). Coupling of Sea Level Rise, Tidal Amplification, and Inundation. *J. Phys. Oceanography* 44, 1439–1455. doi:10.1175/jpo-d-13-0214.1

Judge, J., Newkirk, S., Leo, K., Heady, W., Hayden, M., Veloz, S., et al. (2017). *Case Studies of Natural Shoreline Infrastructure in Coastal California: A Component of Identification of Natural Infrastructure Options for Adapting to Sea Level Rise (California's Fourth Climate Change Assessment)*. Arlington, VA: The Nature Conservancy, 38.

King, J., Holmes, R., Burkholder, S., Holzman, J., and Suedel, B. (2022). Advancing Nature-based Solutions by Leveraging Engineering with Nature Strategies and Landscape Architectural Practices in Highly Collaborative Settings. *Integr. Envir Assess. Manag.* 18, 108–114. doi:10.1002/ieam.4473

Kroon, A., de Schipper, M. A., van Gelder, P. H. A. J. M., and Aarninkhof, S. G. J. (2020). Ranking Uncertainty: Wave Climate Variability versus Model Uncertainty in Probabilistic Assessment of Coastline Change. *Coastal Eng.* 158, 103673. doi:10.1016/j.coastaleng.2020.103673

Luijendijk, A., and van Oudenhoven, A. (2019). *The Sand Motor: A Nature-Based Response to Climate Change: Findings and Reflections of the Interdisciplinary Research Program NatureCoast*. Delft: Delft University Publishers - TU Delft Library.

Marrone, J., Zhou, S., Brashear, P., Howe, B., and Baker, S. (2019). "Numerical and Physical Modeling to Inform Design of the Living Breakwaters Project, Staten Island, New York," in *Coastal Structures 2019*. Editors N. Goseberg and T. Schlurmann (Karlsruhe: Bundesanstalt für Wasserbau), 1044–1054. doi:10.18451/978-3-939230-64-9_105

Mileti, D. (1999). *Disasters by Design: A Reassessment of Natural Hazards in the United States*. Washington, DC: Joseph Henry Press. doi:10.17226/5782

Morris, R. L., Konlechner, T. M., Ghisalberti, M., and Swearer, S. E. (2018). From Grey to green: Efficacy of Eco-Engineering Solutions for Nature-Based Coastal Defence. *Glob. Change Biol.* 24, 1827–1842. doi:10.1111/gcb.14063

Narayan, S., Beck, M. W., Reguero, B. G., Losada, I. J., van Wesenbeeck, B., Pontee, N., et al. (2016). The Effectiveness, Costs and Coastal protection Benefits of Natural and Nature-Based Defences. *PLOS ONE* 11, e0154735. doi:10.1371/journal.pone.0154735

Nichols, C. R., Wright, L. D., Bainbridge, S. J., Cosby, A., Hénaff, A., Loftis, J. D., et al. (2019). Collaborative Science to Enhance Coastal Resilience and Adaptation. *Front. Mar. Sci.* 6, 404. doi:10.3389/fmars.2019.00404

NRC (2014). *Reducing Coastal Risk on the East and Gulf Coasts*. Washington, D.C.: National Academies Press. doi:10.17226/18811

NYS-GOSR (2021). *New York State Governor's Office of Storm Recovery, Living Breakwaters Benefit Cost Analysis*. New York, NY: Wisp USA Solutions, Inc. Project No.: LSC2043436.07.

O'Shaughnessy, K. A., Hawkins, S. J., Evans, A. J., Hanley, M. E., Lunt, P., Thompson, R. C., et al. (2020). Design Catalogue for Eco-Engineering of Coastal Artificial Structures: a Multifunctional Approach for Stakeholders and End-Users. *Urban Ecosyst.* 23, 431–443. doi:10.1007/s11252-019-00924-z

Paul, J. D., Buytaert, W., Allen, S., Ballesteros-Cánovas, J. A., Bhusal, J., Cieslik, K., et al. (2018). Citizen Science for Hydrological Risk Reduction and Resilience Building. *Wiley Interdiscip. Rev. Water* 5, e1262. doi:10.1002/wat2.1262

Piazza, B. P., Banks, P. D., and La Peyre, M. K. (2005). The Potential for Created Oyster Shell Reefs as a Sustainable Shoreline protection Strategy in Louisiana. *Restor Ecol.* 13 (3), 499–506. doi:10.1111/j.1526-100x.2005.00062.x

Reguero, B. G., Beck, M. W., Bresch, D. N., Calil, J., and Meliane, I. (2018). Comparing the Cost Effectiveness of Nature-Based and Coastal Adaptation: a Case Study from the Gulf Coast of the United States. *PLOS ONE* 13, e0192132. doi:10.1371/journal.pone.0192132

Reguero, B. G., Beck, M. W., Schmid, D., Stadtmüller, D., Raepple, J., Schüssele, S., et al. (2020). Financing Coastal Resilience by Combining Nature-Based Risk Reduction with Insurance. *Ecol. Econ.* 169, 106487. doi:10.1016/j.ecolecon.2019.106487

Rigolon, A., and Németh, J. (2018). "We're not in the Business Of Housing:" Environmental Gentrification And The Nonprofitization Of Green Infrastructure Projects. *Cities* 81, 71–80.

Saleh, F., and Weinstein, M. P. (2016). The Role of Nature-Based Infrastructure (NBI) in Coastal Resiliency Planning: a Literature Review. *J. Environ. Manage.* 183, 1088–1098. doi:10.1016/j.jenvman.2016.09.077

Seddon, N., Chausson, A., Berry, P., Girardin, C. A. J., Smith, A., and Turner, B. (2020). Understanding the Value and Limits of Nature-Based Solutions to Climate Change and Other Global Challenges. *Phil. Trans. R. Soc. B* 375, 20190120. doi:10.1098/rstb.2019.0120

Smith, A. (2020). *2010–2019: A Landmark Decade of US Billion-Dollar Weather and Climate Disasters*. National Oceanic and Atmospheric Administration. Available at: https://www.climate.gov/news-features/blogs/beyond-data/2010-2019-landmark-decade-us-billion-dollar-weather-and-climate. (Accessed April 4, 2022).

Smith, C. S., Rudd, M. E., Gittman, R. K., Melvin, E. C., Patterson, V. S., Renzi, J. J., et al. (2020). Coming to Terms with Living Shorelines: a Scoping Review of Novel Restoration Strategies for Shoreline protection. *Front. Mar. Sci.* 7, 434. doi:10.3389/fmars.2020.00434

South Bay Salt Pond Restoration Project Adaptive Management Plan. South Bay Salt Pond Restoration Project Adaptive Management Plan. 2007. Available at: https://www.southbayrestoration.org/sites/default/files/documents/appendix_d_final_amp.pdf.. (Accessed April 4, 2022).

Spalding, M. D., Ruffo, S., Lacambra, C., Meliane, I., Hale, L. Z., Shepard, C. C., et al. (2014). The Role of Ecosystems in Coastal protection: Adapting to Climate Change and Coastal Hazards. *Ocean Coastal Manag.* 90, 50–57. doi:10.1016/j.ocecoaman.2013.09.007

Stive, M. J. F., de Schipper, M. A., Luijendijk, A. P., Aarninkhof, S. G. J., van Gelder-Maas, C., Van Thiel de Vries, J. S. M., et al. (2013). A New Alternative to Saving Our Beaches from Sea-Level Rise: The Sand Engine. *J. Coastal Res.* 290, 1001–1008. doi:10.2112/jcoastres-d-13-00070.1

Subtidal Goals. 2010. San Francisco Bay Subtidal Habitat Goals Report: Conservation Planning for the Submerged Areas of the Bay. Available at: https://www.sfbaysubtidal.org/PDFS/Full%20Report.pdf. (Accessed April 4, 2022).

Sutton-Grier, A. E., Wowk, K., and Bamford, H. (2015). Future of Our Coasts: the Potential for Natural and Hybrid Infrastructure to Enhance the Resilience of Our Coastal Communities, Economies and Ecosystems. *Environ. Sci. Pol.* 51, 137–148. doi:10.1016/j.envsci.2015.04.006

Sweet, W. V., Dusek, G., Obeysekera, J., and Marra, J. J. (2018). *Patterns and Projections of High Tide Flooding along the U.S. Coastline Using a Common Impact Threshold*. Technical Report, NOAA NOS CO-OPS 086.

The World Association for Waterborne Transport Infrastructure (PIANC) (2018). *Guide for Applying Working with Nature to Navigation Infrastructure Projects*. Brussels: Environmental Commission, PIANC, 97. Working Group 176.

Trulio, L., Clark, D., Richie, S., and Hutzel, A. (2007). *Adaptive Management Plan: Science Team Report for the South Bay Salt Pond Restoration Project*.

Tschirky, P., Brashear, P., Sella, I., and Manson, T. (2018). Living Breakwaters: Designing for Resiliency. *Int. Conf. Coastal. Eng.* 36, 50. doi:10.9753/icce.v36.risk.50

US Army Corps of Engineers (USACE) and Texas General Land Office (2020). *Coastal Texas Protection and Restoration Feasibility Study: Draft Report*Galveston District; Galveston: US Army Corps of Engineers. Available at: https://coastalstudy.texas.gov/draft-proposal/index.html.

US Army Corps of Engineers (USACE) (2021). *International Guidelines on NNBF for Flood Risk Management*. Vicksburg, MS: US Army Engineer and Research Center.

US Army Corps of Engineers (USACE) (2019). *New York – New Jersey Harbor and Tributaries Coastal Storm Risk Management Feasibility Study Interim Report*. Available at: https://www.nan.usace.army.mil/Portals/37/docs/civilworks/projects/ny/coast/NYNJHAT/NYNJHAT%20Interim%20Report%20-%20Main%20Report%20Feb%202019.pdf?ver=2019-02-19-165223-023.

US Army Corps of Engineers (USACE) (2015). *North Atlantic Comprehensive Coast Study*. USACE, North Atlantic Division.

Valoppi, L. 2018. *Phase 1 Studies Summary of Major Findings of the South Bay Salt Pond Restoration Project*, South San Francisco Bay, California. US Geological Survey Open-File Report 2018-1039. 68pp.

Van Slobbe, E., de Vriend, H. J., Aarninkhof, S., Lulofs, K., de Vries, M., and Dircke, P. (2013). Building with Nature: in Search of Resilient Storm Surge protection Strategies. *Nat. Hazards* 66, 1461–1480. doi:10.1007/s11069-013-0612-3

Van Veelen, P., Voorendt, M., and Van Der Zwet, C. (2015). Design Challenges of Multifunctional Flood Defences. *Res. Urbanism Ser.* 3, 275–292. doi:10.7480/RIUS.3.841

IPCC (2021). in *Climate Change 2021: The Physical Science Basis. Contribution of Working Group I to the Sixth Assessment Report of the Intergovernmental Panel on Climate Change*. Editors V. Masson-Delmotte, P. Zhai, A. Pirani, S. L. Connors, C. Péan, S. Berger, et al. (Cambridge: Cambridge University Press). In Press.

Vuik, V., van Vuren, S., Borsje, B. W., van Wesenbeeck, B. K., and Jonkman, S. N. (2018). Assessing Safety of Nature-Based Flood Defenses: Dealing with Extremes and Uncertainties. *Coastal Eng.* 139, 47–64. doi:10.1016/j.coastaleng.2018.05.002

Waryszak, P., Gavoille, A., Whitt, A. A., Kelvin, J., and Macreadie, P. I. (2021). Combining gray and green Infrastructure to Improve Coastal Resilience: Lessons Learnt from Hybrid Flood Defenses. *Coastal Eng. J.* 63, 335–350. doi:10.1080/21664250.2021.1920278

Wijsman, K., Auyeung, D. S. N., Brashear, P., Branco, B. F., Graziano, K., Groffman, P. M., et al. (2021). Operationalizing Resilience: Co-creating a Framework to Monitor Hard, Natural, and Nature-Based Shoreline Features in New York State. *E&S* 26 (3), 10. doi:10.5751/ES-12182-260310

Wolch, J. R., Byrne, J., and Newell, J. P. (2014). Urban green Space, Public Health, and Environmental justice: The challenge of Making Cities 'just green Enough'. *Landscape Urban Plann.* 125, 234–244. doi:10.1016/j.landurbplan.2014.01.017

Conflict of Interest: JM is employed by Arcadis.

The remaining authors declare that the research was conducted in the absence of any commercial or financial relationships that could be construed as a potential conflict of interest. The funders had no role in the design of the study; in the collection, analyses, or interpretation of data; in the writing of the manuscript, or in the decision to publish the results.

frontiers | Frontiers in Built Environment

ORIGINAL RESEARCH
published: 08 June 2022
doi: 10.3389/fbuil.2022.893664

Experimental Study of Wave Attenuation Across an Artificial Salt Marsh

Scott Baker[1]*, *Enda Murphy*[1], *Andrew Cornett*[1,2] *and Paul Knox*[1]

[1]*Ocean, Coastal, and River Engineering Research Centre, National Research Council, Ottawa, ON, Canada,* [2]*Department of Civil Engineering, University of Ottawa, Ottawa, ON, Canada*

Scaled laboratory experiments were conducted to investigate the effectiveness of marsh vegetation in dissipating wave energy and reducing wave overtopping discharges at the crest of a dyke located immediately landward of the marsh. Model dyke and marsh platform features, loosely based on archetypes found in Atlantic Canada, were constructed in a wave basin at 1:20 scale and exposed to a broad range of waves and water level conditions. The 2D experiments were conducted using idealized surrogate vegetation (both rigid and flexible), and the model setup featured four parallel flumes which enabled four alternative configurations to be investigated simultaneously. The experiments investigated the sensitivity of wave attenuation and overtopping to the length of the vegetation field, vegetation characteristics (stem density, height, and flexibility) and varying water levels and wave conditions. The study outputs have helped to address knowledge gaps and provide evidence to support and inform broader use of hybrid marsh-dyke systems and managed dyke realignment to help manage flood and erosion risk and improve coastal resilience in Canada and internationally. This research confirmed the benefit of tidal flats hosting coastal marshes for attenuating waves, reducing overtopping volumes and lessening damage to dyke structures. As expected, taller and denser marshes were more effective in attenuating wave energy for a given marsh width.

Keywords: wave attenuation by vegetation, salt marsh, physical modelling, artificial vegetation, flood and erosion risk

Edited by:
Tori Tomiczek,
United States Naval Academy,
United States

Reviewed by:
M. Luisa Martinez,
Instituto de Ecología (INECOL),
Mexico
Mireille Escudero,
National Autonomous University of
Mexico, Mexico
Jord J. Warmink,
University of Twente, Netherlands

****Correspondence:***
Scott Baker
scott.baker@nrc-cnrc.gc.ca

Specialty section:
This article was submitted to
Coastal and Offshore Engineering,
a section of the journal
Frontiers in Built Environment

Received: *10 March 2022*
Accepted: *17 May 2022*
Published: *08 June 2022*

Citation:
Baker S, Murphy E, Cornett A and
Knox P (2022) Experimental Study of
Wave Attenuation Across an Artificial
Salt Marsh.
Front. Built Environ. 8:893664.
doi: 10.3389/fbuil.2022.893664

1 INTRODUCTION

The global risk associated with coastal flooding and erosion has increased substantially over the past several decades, as a consequence of population growth, development in coastal zones and climate change effects including sea-level rise (Jongman, 2018). Projections for the 21st century suggest that these trends will continue (Muis et al., 2020), and, in the absence of intervention or adaptation, the exposure of people and valued assets to episodic coastal flooding could increase by nearly half (Kirezci et al., 2020). There is a large and growing body of evidence surrounding the benefits of natural and nature-based solutions (NBS) as viable alternatives or complements to conventional (hard) engineering shore protection measures (Browder et al., 2019; Bridges et al., 2014; Spalding et al., 2014; Sutton-Grier et al., 2015; Moudrak et al., 2018; Sutton-Grier et al., 2018; Bridges et al., 2021). In particular, the value provided by coastal wetlands or marshes in supporting flood and erosion risk management objectives has been well demonstrated (Costanza et al., 2008; Arkema et al., 2013; Narayan et al., 2017; Piercy et al., 2021).

Coastal marsh systems deliver flood and erosion risk management benefits by attenuating waves and storm surges (Barbier et al., 2011), attracting and retaining sediment (Shepard et al., 2011), and by providing hydraulic storage (Barbier et al., 2011; Shepard et al., 2011; Webb et al., 2018); while at the same time providing a host of co-benefits (Spalding et al., 2014; Pontee et al., 2016; Piercy et al., 2021). Unlike hard structures, coastal marshes can self-adapt to rising sea levels under the right settings (Spalding et al., 2014; Piercy et al., 2021). For example, if sediment supply and accretion rates exceed sediment losses caused by erosion or other mechanisms, marsh growth can offset relative sea-level rise (Barbier et al., 2011; Pontee et al., 2016). Nature-based solutions for coastal hazard risk management that incorporate marsh systems can be implemented through conservation and restoration of existing or degraded marsh systems, landward realignment of hard defences resulting in restoration or generation of new marshes (e.g., managed dyke realignment), and construction of new wetland features (Piercy et al., 2021). The latter two forms of intervention (managed realignment and marsh construction) typically involve hybrid solutions (Spalding et al., 2014; Sutton-Grier et al., 2015; Pontee et al., 2016; Vuik et al., 2016; Jongman, 2018; Vuik et al., 2018), whereby hard structures are integrated with marsh and other vegetation features to provide flood and erosion risk management function. In the case of hybrid dyke-marsh systems, the presence of a foreshore salt marsh can reduce the failure probability of a landside dyke (Vuik et al., 2018), and reduce the costs of dyke maintenance and upgrades (Jongman, 2018). However, the lack of data and rigorous analyses demonstrating the performance and limitations of such hybrid NBS under a variety of environmental settings and metocean conditions remains a barrier to uptake (Sutton-Grier et al., 2015; Morris et al., 2018).

Coastal communities and infrastructure in Canada are vulnerable to flooding and erosion caused by water level and wave extremes (Lemmen et al., 2016), and the risks are expected to increase over the coming decades due to urbanization, rising sea levels, declining sea ice cover, and shifting weather patterns associated with climate change (Bush and Lemmen, 2019). The risk to coastal communities, including damage to infrastructure, is one of the top climate change risks facing Canada (Council of Canadian Academies, 2019). Some coastal regions of Canada have a legacy of dyke construction, which has facilitated settlement, population growth and agricultural activities in low-lying coastal regions (van Proosdij et al., 2013; Sherren et al., 2019). Many of these older dykes now provide a certain level of protection to communities, valued land and assets from coastal hazards (Barron et al., 2012; van Proosdij et al., 2013; Doberstein et al., 2019), although many have been poorly maintained and are in need of repair (van Proosdij et al., 2013). The resources demanded to maintain and upgrade this ageing infrastructure stock are substantial (Barron et al., 2012; Doberstein et al., 2019; Sherren et al., 2019), particularly in the face of rising relative sea levels. In some places, the dykes have contributed to loss of valued salt marsh ecosystems (Virgin et al., 2020). Over-reliance on dykes as a sole flood protection strategy can also introduce vulnerabilities, for example by creating a false perception of risk and encouraging development in flood-prone areas, or leading to catastrophic consequences in the event of a dyke breach or failure (Jongman, 2018). Natural or nature-based features, such as marshes and barrier islands, can act in concert with dykes as part of multiple-lines-of-defence strategies to increase engineering redundancy, enhance the level of flood protection provided, and reduce the costs of dyke maintenance or upgrades (Barron et al., 2012; Jongman, 2018). Empirical field evidence of the effectiveness of hybrid dyke-marsh systems is being developed for a number of managed realignment pilot projects in Atlantic Canada, which were typically implemented by: (i) constructing new dykes landward of legacy agricultural dykes, and (ii) breaching the old dykes to restore tidal flows and facilitate marsh restoration (Sherren et al., 2019; Virgin et al., 2020). Although managed dyke realignment and hybrid-dyke marsh systems are common approaches to flood and erosion risk management in many of the world's coastal regions, such solutions still pose some risk in the Canadian context. This is due, in part, to uncertainty surrounding the performance of these nature-based solutions in diverse Canadian coastal environmental settings, which are characterized by extreme variability in regional climates, tidal ranges, rates of relative sea-level rise, and exposure to wave energy. An improved understanding of the performance of hybrid dyke-marsh systems under a broad range of conditions is needed to guide applications in Canada, and in other regions where uptake has been relatively low.

This paper describes a series of scaled laboratory experiments conducted to investigate the hydraulic performance of hybrid marsh-dyke systems, and in particular examine the effectiveness of coastal marshes in dissipating wave energy and reducing wave overtopping under a broad range of wave and water level conditions representative of Canadian coastal regions. The experiments used physical modelling to investigate dyke and marsh platform features typically found in the Tantramar Marsh on the Chignecto Isthmus in the upper Bay of Fundy, shared by the Canadian provinces of New Brunswick and Nova Scotia, which features *Spartina alterniflora* (smooth cordgrass) vegetation. It is worth noting that the upper Chignecto Bay can be characterized as a macro-tidal environment where high tide typically reaches from 9.5 to 14 m above chart datum. In these experiments, the marsh vegetation was represented using both rigid and flexible artificial or surrogate vegetation designed to approximate the effect of real vegetation on wave attenuation. The experimental study is unique in several respects:

- Testing was conducted with identical wave conditions in four identical flumes arranged side-by-side, so that the effect of controlled changes in various marsh properties including surrogate plant density, stem height, stem flexibility and marsh width (in the direction of wave propagation) could be directly assessed by comparing data and observations obtained at the same time from neighbouring flumes.
- In contrast with many previous studies which focused on wave-plant interaction at full scale or near full scale, this study focused on assessing the changes in wave properties across a 4.75 m wide (95 m wide at full scale) artificial coastal marsh and their interaction with a dyke located

immediately landward of the marsh. The effect of various marsh properties and characteristics on the wave attenuation, the volume of wave overtopping and extent of damage (to the dyke) was assessed.
- The artificial marsh's effect on wave attenuation was investigated over a broad range of significant wave height (H_{m0}), peak period (T_p) and local water depth (h) or plant submergence.
- Although the experiments were conducted at 1/20 scale, the wave conditions included significant wave heights and periods up to 0.15 m and 3.35 s, representing full scale conditions with H_{m0} = 3 m and T_p = 15 s, which are believed to be more energetic than those considered in previous experimental research involving coastal marshes.

This study used an artificial marsh to provide new information on the performance of marsh-dyke systems in a broad range of wave and water level conditions, and the sensitivity of wave attenuation, wave overtopping and damage to variables such as plant density, plant height (submergence), stem flexibility, marsh width, significant wave height, peak period and local water depth. The methods and results described in the paper may be useful to others interested in representing coastal marshes in physical or numerical models of coastal processes and shoreline developments incorporating natural and nature-based features.

Section 2 summarizes the results from a literature review on how marsh vegetation has been represented in past laboratory experiments, while **Section 3** introduces the existing theory and formulae for predicting wave attenuation by marsh vegetation. New 2D experiments conducted at 1/20 scale with coastal marshes comprised of surrogate vegetation fronting dyke structures are described in **Section 4**. **Section 5** presents an analysis and discussion of the new experimental data, in which many of the formulae presented in **Section 3** are used, while the main conclusions from this work are summarized in **Section 6**.

2 PAST REPRESENTATION OF MARSH VEGETATION IN PHYSICAL EXPERIMENTS

The experiments discussed in the present work were conducted using idealized surrogate vegetation representing *S. alterniflora*. The stem densities, heights and diameters of the model vegetation were selected based on findings in literature (Percy, 2000; Lightbody and Nepf, 2006; Cranford et al., 2008; Anderson and Smith, 2014; Nepf et al., 2017; Feagin et al., 2019; Pinsky et al., 2021). For this study, the average stem diameter and height of *S. alterniflora* was taken as 8.7 mm and 1.80 m respectively, though these values depend on the season, the geographic location, and a number of environmental factors.

Some species of vegetation may be successfully represented using rigid elements such as aluminum rods (mangroves) or wooden dowels (salt marsh), despite demonstrating some degree of flexibility in reality (Wu et al., 2011; Arkema et al., 2013; Maza et al., 2019; van Veelen et al., 2020). A combined field-numerical study demonstrated that *S. alterniflora* can be reasonably modelled as a rigid cylinder (Jadhav et al., 2013). Similarly, Augustin et al. (2009) modelled *S. alterniflora* using both rigid and flexible elements and found that the two models produced similar attenuation effects for the tested flow conditions. Thus, the appropriate selection of rigid versus flexible elements may depend on the experimental hydrodynamic conditions.

These elements are often selected to mimic the geometric parameters of the target vegetation, including stem/blade length, width, diameter and planting density (Arkema et al., 2013; Anderson and Smith, 2014; Ozeren et al., 2014; Maza et al., 2019). For small-scale physical models with surrogate vegetation, stem diameters should only be downscaled if flows remain in the rough-turbulent range, as overly small stem diameters can lead to overly small stem Reynolds numbers and significant distortions in drag coefficient (Blackmar et al., 2012).

Table 1 presents a concise summary of previous experimental studies conducted with both real and surrogate marsh vegetation.

Markov (2021) conducted an extensive review of state-of-the-art physical and numerical modelling research in the use of vegetation for coastal protection. Based on the reviewed body of literature, a number of knowledge gaps and recommendations for future research were identified, in particular: developing knowledge of species-specific attenuation capacity considering seasonal variation in biomass and plant characteristics; comparing small- and large-scale models to quantify scaling effects, addressing uncertainties associated with modelling NBS at a small-scale and thus allowing practitioners to better interpret the results of small-scale testing for the design of NBS; testing a wider ranger range of hydrodynamic conditions to determine the impact of wave period on attenuation capacity, with the aim to address presently conflicting results from previous experimental works; perform further testing on stem density and arrangement.

In summary, although there have been numerous previous experimental studies of wave-vegetation interaction, the majority of studies were conducted at prototype or near-prototype scale, and therefore considered processes over a rather limited spatial extent and with a narrow range of conditions (waves and water levels). In addition, much of the previous work dealt only with the effect of vegetation itself, without looking at the broader application of combined systems (e.g., vegetation fronting coastal dykes). While this approach limits or eliminates model scaling effects, knowledge gaps remain surrounding application of the results to real-world situations and larger spatial extents. The absence of studies covering a broad range of environmental conditions and longer sections of marsh is a barrier to understanding how salt marsh creation or restoration can be practically implemented to provide optimal flood and erosion risk management function. As described above, a number of challenges exist for using live vegetation in experimental studies. Real vegetation cannot be used for assessing performance at model scale, whereas the use of surrogate vegetation provides the ability to change the model scale as needed and study processes over larger areas. In this work, a scaled physical modelling approach in a large wave basin facility is used to address some of these gaps and better inform design of hybrid marsh-dyke systems.

TABLE 1 | Summary of previous experimental studies with marsh vegetation.

Study	*Species*, model material	Testing variables	Observed variables	Key findings
Anderson and Smith (2014)	*Spartina alterniflora,* polyolefin tubing	• Stem density • Submergence • Wave height • Wave period	• Wave attenuation	• Wave attenuation appeared most dependent on stem density and ratio of stem length to water depth • Wave attenuation increased slightly with wave height, no clear trend with respect to wave period
Lightbody and Nepf (2006)	*Spartina alterniflora*	• Field measurements	• Stem frontal area • Velocity • Vertical diffusion • Longitudinal dispersion	• Vegetation volumetric frontal area peaked ~10 cm from bed • Velocity profile varied inversely with canopy drag (i.e., velocity is min. where frontal area is max.)
Augustin et al. (2009)	*Spartina alterniflora,* wooden dowels, polyethylene foam tubing	• Water depth • Stem density • Wave height • Wave period	• Wave attenuation	• Laboratory data analyzed using linear wave theory to quantify bulk drag coefficients and with nonlinear Boussinesq model to determine numerical friction factors to better represent wetland vegetation
Koftis et al. (2013)	*Posidonia oceanica*, PVC stem and leaves	• Stem density • Submergence	• Wave attenuation • Wave-induced velocities	• Calculated vs. measured wave heights found to be in agreement • Wave orbital velocities shown to be significantly attenuated inside the meadow and just above flume bed • Submerged vegetation attenuated mostly longer waves
Pinsky et al. (2013)	Kelp, mangrove, marsh and seagrass species	• Re-analysis of existing wave attenuation studies	• Wave attenuation	• Much of the variation in wave attenuation explained by differences in vegetation characteristics and change in bulk drag with flow conditions • Vegetation can exert substantial drag on passing waves, but bulk drag coefficient declines in flow conditions characterized by high Reynolds numbers
Ozeren et al. (2014)	*Spartina alterniflora* and *Juncus roemerianus*, live plants, wooden dowels, EPDM foam-rubber cords	• Vegetation type • Stem density • Plant height • Wave height • Wave period	• Wave attenuat ion	• C_D did not depend significantly on the relative submergence • Drag coefficients were higher for live vegetation species than for rigid and flexible surrogate vegetation • Vertical variation of plant density strongly influenced the drag coefficient
Lara et al. (2016)	*Puccinellia maritima* and *Spartina anglica*, live plants	• Wave height • Wave period • Currents • Water depth • Stem density	• Wave attenuation	• Challenges of employing live vegetation: selection of appropriate species; source, quantity and survivability of selected plants; suitability of substrate; experimental setup to simulate natural conditions; plant degradation throughout the experiment; hydraulic characteristics to be tested and measurement techniques; plant response to hydraulic loading; plant characteristics; logistics and operation to conduct a large-scale experiment using real vegetation

(Continued on following page)

TABLE 1 | (*Continued*) Summary of previous experimental studies with marsh vegetation.

Study	*Species*, model material	Testing variables	Observed variables	Key findings
Houser et al. (2015)	*Thalassia testudinum*, wooden dowels, cable ties, polyethylene ribbon	• Blade rigidity • Wave height • Wave period • Water depth	• Wave attenuation	• Drag coefficient exhibited strong dependency on the flexibility of individual blades • Flexible vegetation had relatively small drag coefficient compared to rigid vegetation • Flexible vegetation provides little to no shoreline protection, except where the vegetation field is extensive and high density
Wu and Cox (2015a); Wu and Cox (2015b)	wooden dowels (no specific species)	• Vertical variation in vegetation density • Wave nonlinearity	• Wave attenuation	• Damping factor dependent on the wave steepness • Damping factor can increase by a factor of two when the wave steepness approximately doubles • Highlighted the effect of vertical biomass distribution which can result in changes in C_D
Losada et al. (2016)	*Spartina anglica* and *Puccinellia maritime*, live vegetation	• Wave height • Wave period • Plant density • Water depth • Currents	• Wave attenuation	• New analytical formulation for evaluation of wave damping under combined effect of waves and both following and opposing currents, suggested for implementation in phase-averaged and phase-resolving numerical models of wave propagation
Vuik et al. (2016)	*Spartina anglica* and *Scirpus maritimus*	• Field measurements • Numerical modelling	• Wave attenuation	• Numerical model appeared capable of reproducing the observed decay in wave height over the salt marsh, applied to compute the reduction of incident wave height on a dyke for various foreshore configurations • Vegetated foreshores can be considered promising supplement to conventional engineering methods for dyke reinforcement
Sonnenwald et al. (2019)	rigid cylinders (no specific species)	n/a	• Evaluated several practical engineering functions for estimating bulk drag coefficient	• Estimates of C_D were compared to a range of experimental data from previous studies wherein a frontal area approach was used for selecting the stem diameter and spacing • Estimates of C_D utilizing the re-parametrization presented match the experimental data better than estimates of C_D made using the other functions evaluated
Lei and Nepf (2019)	*Various seagrass species*, LDPE film	• Plant morphology • Plant flexibility • Stem density • Water depth • Wave height • Wave period	• Wave attenuation	• Validated new model to predict dissipation of wave energy over submerged meadow of flexible plants • Vegetation drag and thus wave decay are diminished relative to that for a fully rigid blade of the same geometry
Keimer et al. (2021)	rigid PVC rods (no specific species)	• Wave height • Wave period • Water depth • Plant height	• Wave attenuation • Wave run-up	• Vegetated foreshores contribute to a mean wave attenuation of 9% • Wave run-up reduction up to 16.5% observed with decreasing water depths and increasing vegetation heights • Authors noted a number of topics for further investigation regarding the eco-hydraulic effects of foreshore vegetation

3 PREDICTION OF WAVE ATTENUATION BY VEGETATION

As described in many previous studies [e.g., 1,35,44], the prediction of wave attenuation over a coastal marsh can be based on the energy conservation equation. Assuming a flat bed, linear wave theory, invariant quantities with depth, and rigid vegetation (no swaying motion), the regular wave height profile along the vegetation field can be written as (Dalrymple et al., 1984):

$$\frac{H}{H_i} = \frac{1}{1 + \beta x} \tag{1}$$

where H_i is the incident wave height; H is the wave height within the vegetation field (at location x); and β is the damping coefficient for regular wave trains. Mendez and Losada (2004) extended this formulation for non-breaking random waves over constant depth assuming a Rayleigh distribution and deriving the wave height evolution as a function of the root-mean-square wave height as :

$$\frac{H_{rms}}{H_{rms,i}} = \frac{1}{1 + \beta' x} \tag{2}$$

And

$$\beta' = \frac{1}{3\sqrt{\pi}} H_{rms,i} C_D a k_p \frac{\sinh\left(k_p s h\right)^3 + 3\sinh\left(k_p s h\right)}{\sinh\left(k_p h\right)\left[\sinh\left(2k_p h\right) + 2k_p h\right]} \tag{3}$$

where $H_{rms,i}$ is the root-mean-square (RMS) height of the incident waves; H_{rms} is the RMS wave height inside the vegetation field (at location x); C_D is the depth-averaged spatial mean bulk drag coefficient; $a = D_v N_v$ is the total frontal plant area per unit volume; D_v is the stem diameter; N_v is the vegetation stem density; h_v is the vegetation height; $k_p = 2\pi / L_p$ is the wave number; L_p is the wavelength associated with the peak period (T_p); h is the water depth; and $s = h_v / h$ for submerged ($h_v < h$) and unity for emergent ($h_v > h$) vegetation.

Drag coefficients, energy dissipation and wave attenuation are a strong function of Reynolds number and Keulegan–Carpenter number (Keulegan and Carpenter, 1958). The stem Reynolds number is calculated as :

$$\text{Re} = \frac{u_c D_v}{v} \tag{4}$$

where v is the kinematic viscosity of seawater ($1.44\,\text{E}^{-6}\,\text{m}^2/\text{s}$ at 8°C, the average temperature of Atlantic Canadian waters); and u_c is the characteristic velocity acting on the plant. The characteristic velocity is defined as :

$$u_c = \frac{\bar{H}_{rms}}{2} \omega_p \frac{\cosh(ksh)}{\sinh(kh)} \tag{5}$$

where $\bar{H}_{rms}$ is the average root-mean-square wave height across the vegetation field; and ω_p is the peak wave angular frequency.

The Keulegan–Carpenter number :

$$\text{KC} = \frac{u_c T_p}{D_v} \tag{6}$$

Describes the relative importance of drag forces versus inertia forces for objects in an oscillatory fluid flow. For relatively small values of KC, the water particle displacements become comparable to the stem diameter, and inertia force dominates. For larger values of KC, water particle displacements are much larger than the stem diameter, leading to flow separation and vortex shedding, and drag force becomes increasingly important. Some researchers (Ozeren et al., 2014; Wu and Cox, 2015b) have shown dependence on the KC number. Following Sonnenwald et al. (2019), the drag coefficient can be written as :

$$C_D = 2\left(\frac{6475 D_v + 32}{\text{Re}} + 17 D_v + 3.2\phi + 0.50\right) \tag{7}$$

where ϕ is the solid volume fraction $= a D_v \pi / 4$.

4 EXPERIMENTAL METHODS AND MATERIALS

4.1 Experimental Setup

The present study was conducted in the National Research Council of Canada's (NRC) 63 m long by 14 m wide by 1.5 m tall Coastal Wave Basin (CWB). The CWB is equipped with a computer-controlled wave machine capable of generating irregular long-crested waves with significant wave heights up to ~0.35 m (at model scale). The active wave absorption feature was not enabled during this study.

A length scale of 1/20 was adopted for the experiments, and Froude scaling was used to relate most (but not all) conditions in the model to corresponding conditions at full scale. The 1/20 scale factor, together with the chosen wave conditions and the fact that the surrogate plant stems in the model were purposely over-sized, ensured that the wave-driven flows around the model vegetation and model armour stones on the dyke surface remained rough-turbulent at all times, as in nature. Preserving rough-turbulent flow in the model was essential to minimizing scale effects and preserving the realism of the wave-plant and wave-structure interactions in the physical model.

The 14 m wide CWB was subdivided into four separate 1.22 m wide flumes by erecting parallel masonry block walls (see **Figure 1**). This setup created four identical test flumes and allowed four different marshes to be built and evaluated at the same time, one per flume, with identical incident wave conditions in front of each marsh. Each flume included an identical scaled reproduction of the typical sloping foreshore along the edge of the Tantramar Marsh on the Chignecto Isthmus, as well as an idealized model dyke structure (see **Figure 2**). A ~1V:11H foreshore slope followed by a 4.75 m long (95 m at full scale) horizontal tidal flat was created by rigidly securing thick plywood sheets to the flume walls.

The floor of the wave basin at the toe of the sloping foreshore was assigned an elevation of −0.18 m (corresponding to −3.50 m at full scale), while the tidal flat elevation was +0.27 m (+5.40 m at full scale). Water depths on the tidal flat in this study ranged from 0.05 to 0.12 m (1.0–2.4 m at full scale). The bathymetry helped to ensure that wave conditions at the edge of the marsh in the physical model, including the distribution of wave heights and the percentage of breaking and broken waves, was similar to head-on wave conditions at the edge of typical marshes in upper Chignecto Bay.

Marshes comprised of *S. alterniflora* were simulated on the 4.75 m long tidal flat using idealized surrogate vegetation fixed to the plywood. During the study, several different marshes with different plant characteristics could be modelled in each flume by

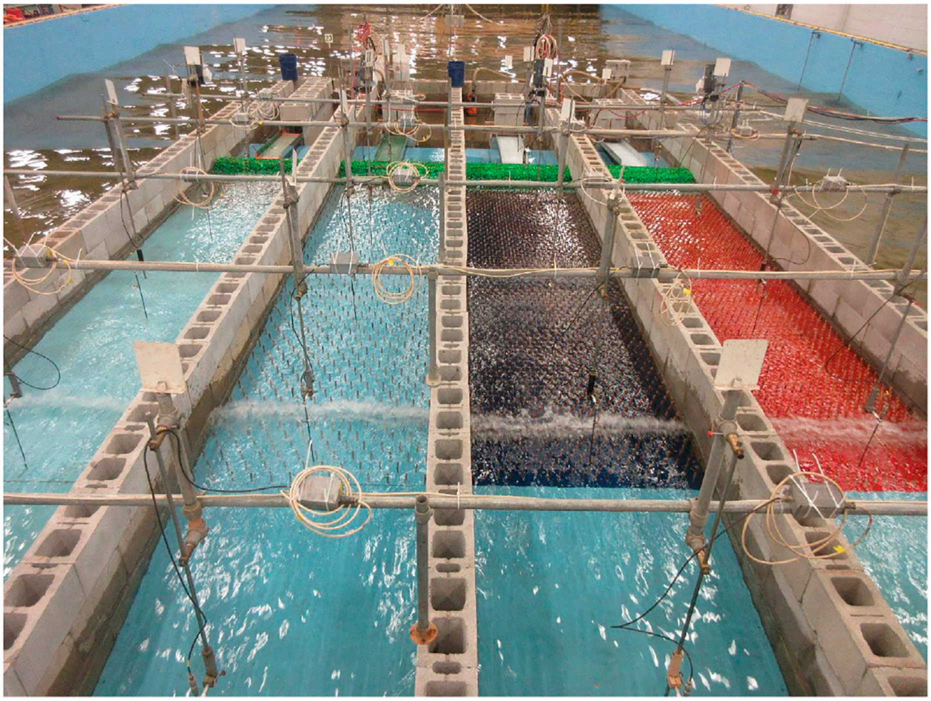

FIGURE 1 | Simultaneous parallel testing of wave attenuation across four coastal marshes with different densities of surrogate vegetation (onshore view).

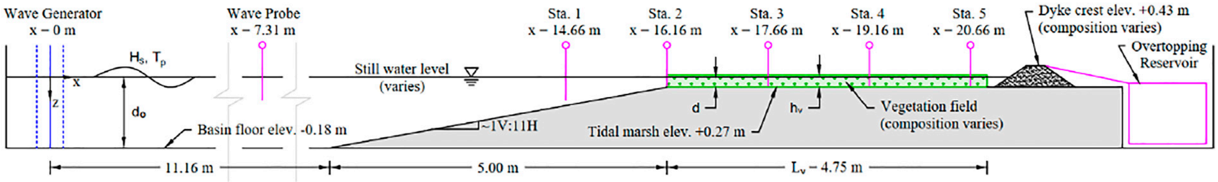

FIGURE 2 | Definition sketch of the experimental setup (Scale 1V:0.5H).

swapping the vegetated plywood panels between tests. The sensitivity to plant density, plant height (and submergence), stem stiffness and marsh cross-shore width were investigated in this way.

4.2 Idealized Vegetation

These experiments were conducted using idealized surrogate vegetation representing *S. alterniflora*. Several configurations of rigid (cylindrical birch dowels) and flexible (Tygon polymer tubing) model vegetation were used during the experiments. The birch dowels were 3/8 inch (9.5 mm) in diameter, while the flexible tubing had outer and inner diameters of 5/16 inch (7.9 mm) and 1/4 inch (6.4 mm) respectively. It should be noted that vertical variability in stem diameter (tapering) or frontal area was not captured in this study. A tensile strength test indicated that Young's modulus of the Tygon tubing was approximately 4.5 MPa, equivalent to ~90 MPa at full scale.

Vegetated meadows were constructed by inserting dowels or tubing into 19 mm thick plywood sheets following a staggered arrangement. These vegetated panels were pre-constructed and easily interchangeable so that different vegetation conditions could be investigated during the experiments. The staggered arrangement of model plant stems shown in **Figure 3** corresponds to the following relationship between stem spacing, λ, and the vegetation density [from Ozeren et al., 2014]:

$$N_v = \frac{2}{\sqrt{3}}\lambda^{-2} \tag{8}$$

Scaling the stem diameter according to the model length scale was impractical since it would involve replicating hundreds of thousands of wire-thin stems. Moreover, this approach would cause the stem Reynolds number in the model to be significantly smaller than in prototype. Previous studies suggest wave attenuation is predominately associated with vegetation drag, which is proportional to the vegetation frontal area. Therefore the stems were scaled to maintain an equivalent solid volume fraction, ϕ, where $\phi = ad\pi/4$, d is the cylinder diameter and a is the frontal facing area (the cylinder area perpendicular to the direction of flow per unit volume, m^2m^{-3}). Following this approach, three different

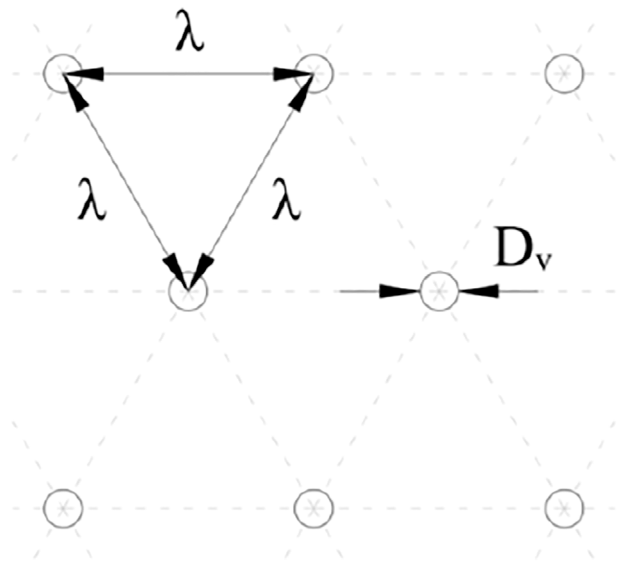

FIGURE 3 | Arrangement of vegetation stems.

meadows of *S. alterniflora* stems were simulated in the experiments using a reduced number of oversized cylinders. The stem densities of these scaled meadows were N_v = 125, 295, and 450 stems/m^2, representing meadows with low-, medium-, and high-densities, equivalent to 150, 350, and 550 stems/m^2 of live vegetation (see **Figure 4**). Two stem heights, h_v = 0.090 and 0.025 m were investigated in the experiments, representing *S. alterniflora* meadow heights of 1.8 and 0.5 m respectively, nominally representing two different periods of the growth season.

4.3 Dyke Design and Construction

The performance of four different dyke designs located at the leeward end of the model test flumes was examined in these experiments (see **Figure 5**). The first design was considered typical for dykes throughout Atlantic Canada and featured an impermeable dyke core with two layers of riprap on the seaside only (herein referred to as a simply reinforced dyke). Three additional designs, representing various potential methods for upgrading the simply reinforced dyke, were also studied. The second design (armoured dyke) was created by adding two layers of riprap on the crest and leeside of the structure while maintaining the same crest elevation. The third design

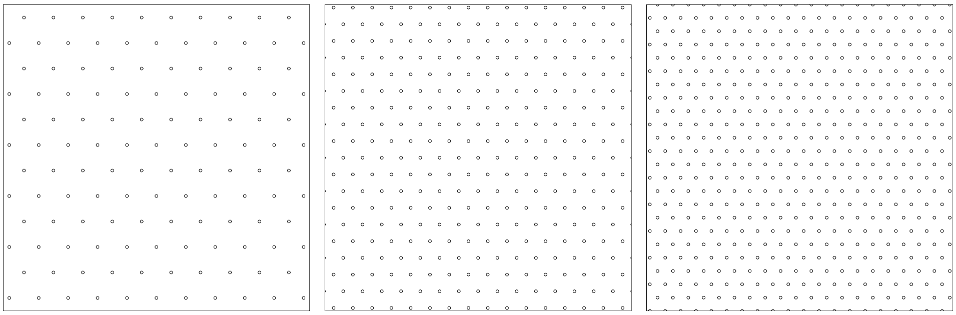

FIGURE 4 | Comparative 1 m^2 sections of surrogate meadows with 125, 295, and 450 stems/m^2.

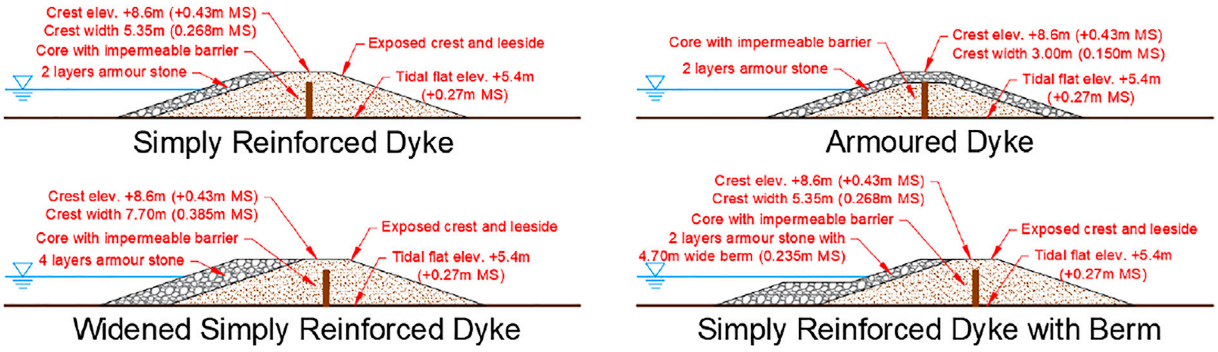

FIGURE 5 | Cross-section drawings for the four dyke structures investigated.

TABLE 2 | Experiment setup for Test Series 1–5.

Test series	Flume	Structure type	Marsh width, L_v (m)	Vegetation density, N_v (stems/m^2)	Vegetation height, h_v (m)	Vegetation type
TS1	1	Armoured dyke	4.75 (95)	0	0	No Veg
41[a]	2			125	0.090 (1.8)	Rigid
	3			295		
	4			450		
TS2	1	Gravel beach	4.75 (95)	0	0	No Veg
17[a]	2			125	0.090 (1.8)	Rigid
	3			295		
	4			450		
TS3	1	Armoured dyke	4.75 (95)	295	0.090 (1.8)	Rigid
21[a]	2	Simply reinforced dyke				
	3	Simply reinforced dyke with berm				
	4	Widened simply reinforced dyke				
TS4	1	Armoured dyke	0	0	0	No Veg
31[a]	2		2.30 (46)	295	0.090 (1.8)	Rigid
	3	Simply reinforced dyke with berm	4.75 (95)		0.025 (0.5)	
	4	Armoured dyke		125	0.090 (1.8)	Flexible
TS5	1	Armoured dyke	2.30 (46)	0	0	No Veg
31[a]	2			450	0.090 (1.8)	Rigid
	3	Simply reinforced dyke with berm		295	0.025 (0.5)	
	4	Widened simply reinforced dyke	4.75 (95)	125	0.090 (1.8)	Flexible

[a] *Indicates the number of wave height, wave period, and water level combinations per test series. Values in brackets indicate corresponding full scale values.*

(widened reinforced dyke) was created by doubling the thickness of the seaside armour layer. The fourth design (simply reinforced dyke with berm) was created by adding a berm of armour stone on the seaside that was half the height of the structure and four armour stones in thickness. All four model dyke designs featured a crest elevation of +0.43 m (corresponding to +8.6 m above mean sea level at full scale), a typical crest elevation of older dykes in the Tantramar area (Lieske and Bornemann, 2012).

Each model dyke was constructed using carefully prepared stone materials and construction methods. The dyke cores were constructed using a fine gravel with low permeability, but also included impermeable wooden barriers which prevented water from seeping through the dykes into the inland areas. Furthermore, a thin, flexible plastic membrane was placed between the core and armour materials to prevent water from flowing into the core. This method of construction allowed overtopping flows to pass through or above the armour stone on the dyke crest as would occur in the prototype situation. The landward end of each test flume was sealed off so that the water level behind each model structure could be kept lower (using submersible pumps), thereby simulating the situation where the inland area behind the dyke structure is not flooded, which is expected to be the most critical condition for rear slope stability.

The sizing of armour stone was based on Hudson formula calculations and also informed by Nova Scotia Department of Transportation Guidelines. The required armour stone mass M_{50} was calculated as 136 kg at full scale. The armour stone was assumed to have a wide gradation such that $M_{15} = M_{50}/2$ and $M_{85} = M_{50} \times 2$. The corresponding values of M_{15}, M_{50}, and M_{85} at model scale, accounting for the density difference between the freshwater used in the model and the seawater in prototype, were 7.5, 15.1, and 30.2 g. Model stone materials were prepared to closely replicate the gradation and characteristics of the prototype material. During construction of the various dyke structures, due care was taken to ensure that stones with aspect ratios greater than 3:1 were not used (i.e., stones where either the length, width or height was more than three times larger than any other dimensions). This was important since flatter stones are more likely to move or overturn under wave action.

4.4 Test Conditions and Instrumentation

Particulars of the marsh-dyke system in each test flume during each test series are given in **Table 2**. Each setup was chosen in order to obtain results needed to independently assess the influence of key variables including: vegetation density, vegetation (stem) height, cross-shore marsh width, type of vegetation (rigid or flexible), and dyke structure type. For Test Series 2, the dyke structures were replaced with gently sloping gravel beaches featuring less than 5% wave reflectance, so that wave conditions across the artificial marshes could be measured with minimal influence of reflected waves. Hence, much of the analysis concerning wave attenuation presented in the following Section is based on data gathered during Test Series 2.

The wave conditions and water levels selected for testing were generally representative of conditions along the Canadian Atlantic coast where marsh-dyke systems exist (see **Table 3**), with a particular focus on storm conditions (higher water levels and energetic waves) that could overtop and/or damage the

TABLE 3 | Range of irregular wave parameters.

Water depth at tidal flat, *d* (m)	Significant Wave Height, H_{m0} (m)	Peak wave period, T_p (s)	Keulegan-Carpenter #	Reynolds #
0.05 (1.0)	0.05 (1.0) 0.075 (1.5) 0.10 (2.0)	0.67, 1.34, 2.01, 2.68 (3, 6, 9, 12) 1.34, 2.01, 2.68 (6, 9, 12) 1.34, 2.01, 2.68 (6, 9, 12)	12–152 (243–3,044)	1,133–3,553 (5,067–15,889)
0.075 (1.5)	0.05 (1.0) 0.075 (1.5) 0.10 (2.0)	0.67, 1.34, 2.01, 2.68 (3, 6, 9, 12) 1.34, 2.01, 2.68 (6, 9, 12) 1.34, 2.01, 2.68 (6, 9, 12)	13–212 (268–4,248)	1,249–4,959 (5,587–22,176)
0.10 (2.0)	0.05 (1.0) 0.075 (1.5) 0.10 (2.0)	0.67, 1.34, 2.01, 2.68 (3, 6, 9, 12) 1.34, 2.01, 2.68 (6, 9, 12) 1.34, 2.01, 2.68 (6, 9, 12)	14–173 (273–3,464)	1,273–4,432 (5,694–19,821)
0.12 (2.4)	0.05 (1.0) 0.075 (1.5) 0.10 (2.0) 0.15 (3.0)	0.67, 1.34, 2.01, 2.68 (3, 6, 9, 12) 1.34, 2.01, 2.68, 3.35 (6, 9, 12, 15) 1.34, 2.01, 2.68 (6, 9, 12) 1.34, 2.01, 2.68, 3.35 (6, 9, 12, 15)	12–168 (241–5,359)	1,124–5,170 (5,026–23,121)

(Values in brackets indicate corresponding full scale values).

dykes. **Table 2** specifies the number of wave height, wave period, and water level combinations investigated in each test series. Overall, the testing program consisted of 141 unique tests.

The wave signals for tests with irregular waves were synthesized from a family of JONSWAP-type spectra with a 3.3 peak enhancement factor approaching from a single direction. However, due to the shallow water conditions in the CWB and the natural growth of sub- and super-harmonics, the spectral shapes, and the distribution of energy with frequency in the experiments were typical of shallow water conditions. The test program included significant wave heights (H_{m0}) ranging from 0.05 to 0.15 m (corresponding to 1.0–3.0 m at full scale) and peak wave periods (T_p) ranging from 0.63 to 3.35 s (corresponding to 3–15 s at full scale). These conditions respect the guidance of Hughes (1993) and Heller (2011) for minimizing scale effects on wave propagation caused by surface tension. Water depths on the tidal flat ranged from 0.05 to 0.12 m (corresponding to 1.0–2.4 m at full scale). Each wave signal featured a non-repeating sequence of approximately 1,000 irregular waves, thus the duration of each wave signal and test varied depending on the peak wave period, ranging from ~10.9 to 38.9 min long (corresponding to ~0.8–2.9 h at full scale). One-thousand waves was selected to ensure that each signal included a statistically representative distribution of larger wave heights and crest elevations, since wave overtopping and armour stone stability are typically sensitive to the few largest waves in a sea state. Water levels were adjusted in the model by filling or draining the basin until the desired level was reached.

Twenty-two capacitance-type probes were used to measure water surface displacement at several locations of interest in each test flume. Two probes were located in deeper water near the wave generator to measure offshore wave conditions, while the others were positioned such that five probes were deployed inside each flume as shown in **Figure 2** (one above the sloping foreshore and the other four distributed across the artificial marsh). The probes were configured to record water levels at a sampling frequency of 50 Hz and were (re)calibrated before each test series by changing their elevation with respect to a fixed (known) water level. The wave probes featured a highly linear and stable response, with calibration errors typically less than 0.5% over their calibration range. Comprehensive time-domain and frequency-domain analysis algorithms were applied to analyze the wave conditions measured in the model in detail.

Four simple, accurate and reliable overtopping measurement systems were deployed, one in each test flume. Each overtopping measurement system consisted of a collection tray positioned to collect water passing over the dyke crest and convey it to a water storage reservoir fitted with a capacitance water level gauge located on the leeside of the dyke. Wave overtopping was quantified as a volumetric flow rate per unit width passing over the top of the dyke crest. This overtopping measurement system was best suited for measuring moderate-to-heavy overtopping flows (e.g., greater than 1 L/s/m at full scale); measuring smaller volumes of splash and spray was less precise. The overtopping collection trays were positioned at the rear slope break of the dyke crest atop nominally two layers of armour stone. Small overtopping events in which the wave runup reached the crest elevation, generating overtopping flows through the armour stone on the dyke crest, were not captured by the overtopping measurement system. It is noted that typical dykes have a drainage ditch along their leeside which can handle some degree of overtopping flow. Only larger overtopping events featuring green water flowing over the crest and reaching the rear slope break were captured by the overtopping measurement systems in these experiments.

A photographic damage analysis system comprising four remotely-operated digital cameras was used to monitor the stability of the armour stones on each of the four dyke structures. Since each camera remained fixed throughout a test series, by comparing photographs taken before and after each test segment, damage could be assessed and quantified based on the number of individual stones that were displaced during each test

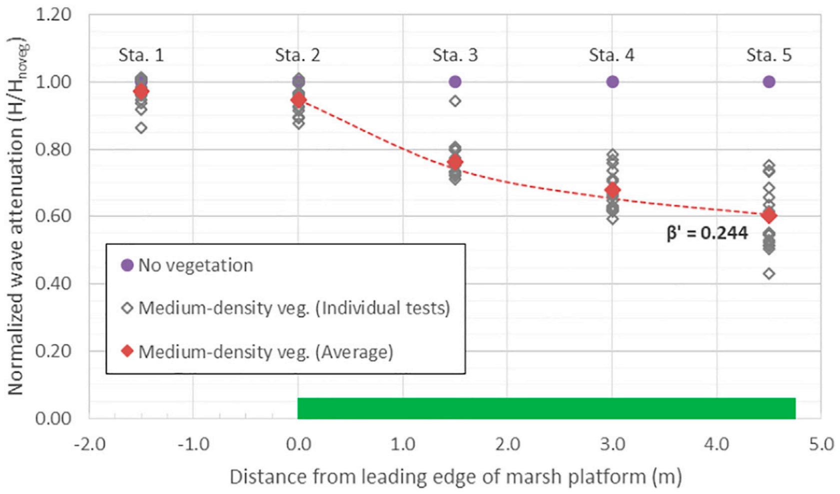

FIGURE 6 | Wave attenuation across the artificial marsh for medium-density vegetation only. Data is normalized by the case with no vegetation to remove the effects of wave transformation and breaking due to the sloping foreshore and shallow depths, and highlight the role of vegetation in wave attenuation. Open symbols (◇) show the observed attenuation across a wide range of wave heights, periods, and water depths, while filled symbols (◆) denotes the average with fitted damping coefficient β'. Refer to **Figure 2** for the location of the measurement stations.

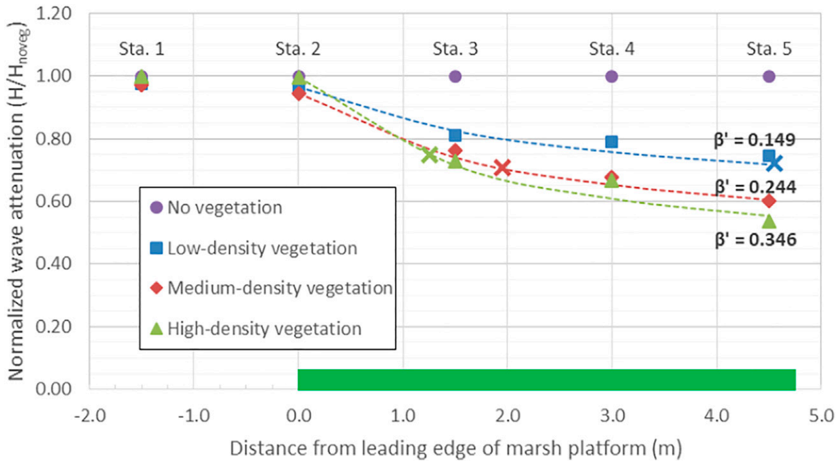

FIGURE 7 | Wave attenuation across the artificial marsh for different vegetation densities. Data is normalized by the case with no vegetation to remove the effects of wave transformation and breaking due to the sloping foreshore and shallow depths, and highlight the role of vegetation in wave attenuation. Data points denote average measurements across a wide range of wave heights, periods, and water depths. Dashed lines denote predicted (fitted) curves and corresponding β' values. The bold **X** denotes the distance from the leading edge of the model vegetation canopy encompassing 700 surrogate stems for each vegetation density. Refer to **Figure 2** for the location of the measurement stations.

segment. The effect of marsh vegetation on armour stone stability will be discussed briefly in the next section.

5 RESULTS AND DISCUSSION

5.1 Effect of Vegetation Density

Previous research has identified a strong correlation between vegetation density and wave damping, and this correlation was further confirmed in these experiments. Not only did the rate of wave attenuation increase with increasing vegetation density, but the amount of wave overtopping recorded at the dyke, and the damage to the dyke itself was reduced as well. **Figure 6** shows relative wave heights (wave height with vegetation normalized by corresponding wave height without vegetation) measured across the tidal flat comprised of medium-density vegetation for a range of wave conditions and water levels. Measurement locations are shown in **Figure 2**. This normalization of wave height is necessary to isolate the effects of vegetation, since the wave conditions across the artificial marshes in these experiments were generally

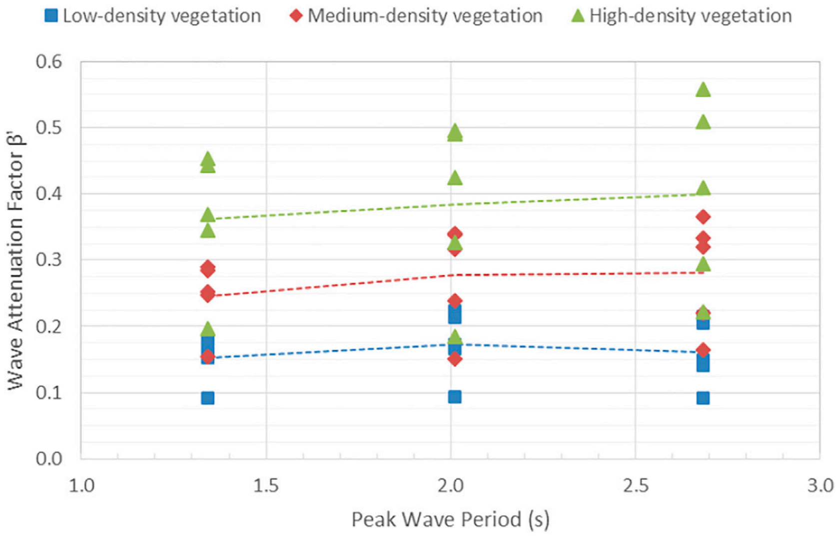

FIGURE 8 | Variation in wave attenuation factor β' with wave peak period for artificial marshes with different vegetation densities. Symbols denote results from individual tests spanning a range of wave heights and water depths. Dashed lines connect average β' values at each wave period.

strongly influenced by the effects of shoaling and depth-limited wave breaking, and, to a lesser extent, flume friction effects (Maza et al., 2019). For test flumes with vegetation, measured significant wave heights at each probe were normalized by H_{m0} values measured at corresponding locations in the flume with no vegetation (i.e., Flume 1 in Test Series 2; refer to **Table 2**). **Figure 6** shows the spread of observed wave attenuation for individual tests spanning a broad range of significant wave heights, peak wave periods, and water depths. For each test, the damping coefficient β' (**Eq. 3**) was evaluated by least squares regression to the significant wave heights measured across the model marsh canopy. Values from individual tests were averaged to permit comparison across different vegetation densities (discussed below).

Similarly, **Figure 7** shows relative wave heights (wave height with vegetation normalized by corresponding wave height without vegetation) measured across the tidal flat as a function of vegetation density. Average β' values (derived by averaging results from multiple tests with different wave conditions and water depths) for the three different artificial marshes considered in these experiments are shown in **Figure 7**. Although different plant species were investigated by Maza et al. (2015), the β' values derived from the present experiments (0.149–0.346) are similar to those observed by Maza et al. at lower water depths (0.124–0.286), which involved submergence ratios similar to the present study (1.0 in Maza et al. compared to an average of 0.92 in the present experiments).

As shown in **Figure 7**, significant wave heights in the low-density, medium-density and high-density vegetation were 28, 40 and 46% lower (respectively) than those in the flume with no vegetation for the same test conditions. Therefore, higher vegetation density does lead to increased wave attenuation, as expected, but there appears to be a diminishing return on additional bio-mass leading to additional wave attenuation, at least for the range of densities tested in this study.

Looking at the data points along each individual curve in **Figure 7**, the majority of the wave damping occurs in the first third of the marsh (i.e., between Stations 2 and 3). Averaging over the full range of water level and sea state conditions investigated, there was a 19% reduction in significant wave height across the first 1.5 m of the low-density marsh, compared to a further 9% reduction across the following 3.25 m of marsh. For the high-density marsh, there was a 27% reduction across the first 1.5 m long section versus a further 19% reduction across the remainder.

Stakeholders looking to make use of vegetated tidal flats to augment shore protection should consider creating expansive marshes wherever possible, not only from a wave attenuation and flood risk reduction perspective but also for the environmental co-benefits they bring. Where expansive marshes are not possible, this data suggests that denser vegetation is preferred from a wave attenuation perspective, as opposed to sparser vegetation. **Figure 7** shows that narrower denser marshes can be considered roughly equivalent to wider marshes with sparser vegetation. For example, 700 dowels placed in the low-density configuration (denoted by the blue ╳ in **Figure 7**) spans X = 4.55 m and yields ~28% wave attenuation on average. However, 700 dowels placed in the medium-density configuration (denoted by the red ╳) occupies X = 1.95 m of horizontal distance and yields ~29% attenuation on average across a broad range of wave conditions and water depths, while the same number of dowels in the high-density configuration (denoted by the green ╳) spans X = 1.25 m and yields ~25% attenuation on average.

Figure 8 shows the observed variation in wave attenuation factor β' with peak wave period based on the present experiments. In this figure, symbols denote results for individual tests and dashed lines connect average wave attenuation factors for each wave period. For the range of conditions investigated in these

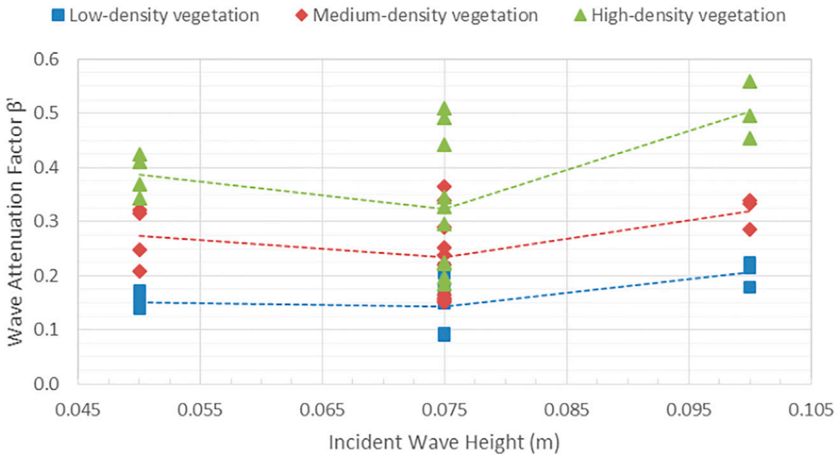

FIGURE 9 | Variation in wave attenuation factor β' with significant wave height for artificial marshes with different vegetation densities. Symbols denote results from individual tests spanning a range of wave periods and water depths. Dashed lines connect average β' values for each significant wave height.

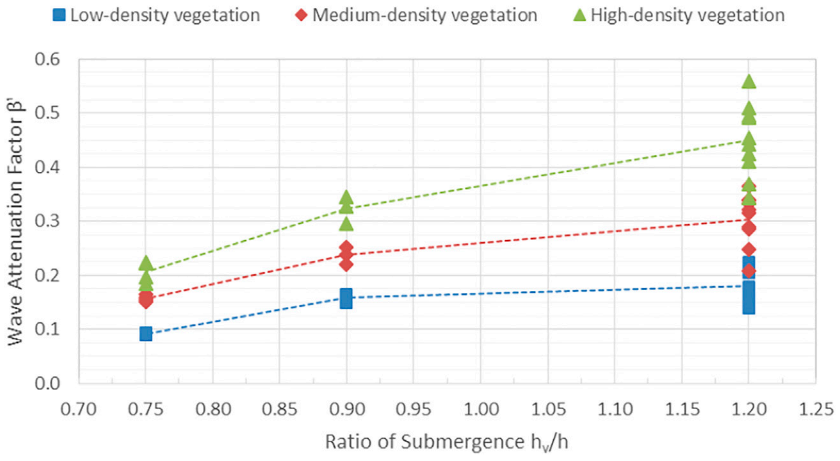

FIGURE 10 | Variation in wave attenuation factor with submergence ratio for artificial marshes with different vegetation densities. Symbols denote results from individual tests spanning a range of wave conditions. Dashed lines connect average values for each submergence ratio.

tests, no clear dependence of attenuation factor on wave period was identified. While some wave period dependency was identified for specific test conditions (particular combinations of water depth and wave height), the trend was not consistent across all test conditions.

Contrary to the findings of Wu and Cox (2015b), no significant correlation between wave steepness and wave attenuation was observed across the range of conditions investigated in this study.

Based on a study by Maza et al. (2019), damping coefficients determined for various water depths, wave heights and wave periods indicated that, in general, higher damping coefficients are associated with higher wave heights and shorter wave lengths (i.e., smaller wave periods). In addition, higher correlations were found between the damping coefficient and wave height than with wave steepness, indicating that wave height has greater control than wave period in terms of attenuation capacity.

Figure 9 shows the variation in wave attenuation factor (β') with incident wave height based on data from Test Series 2, where the dykes in each flume were replaced by absorbing gravel beaches with low wave reflectance. The results show that wave attenuation is, on average, greatest (largest β') for the highest incident waves investigated in this study, which is consistent with the results of Maza et al. (2019). However, further analysis (presented and discussed below) makes it clear that submergence ratio plays a more significant role and helps to explain the degree of scatter seen in **Figure 9**. Analysis to detect correlations between wave attenuation factor and wave steepness were undertaken, but no clear trends were evident for the range of conditions in Test Series 2.

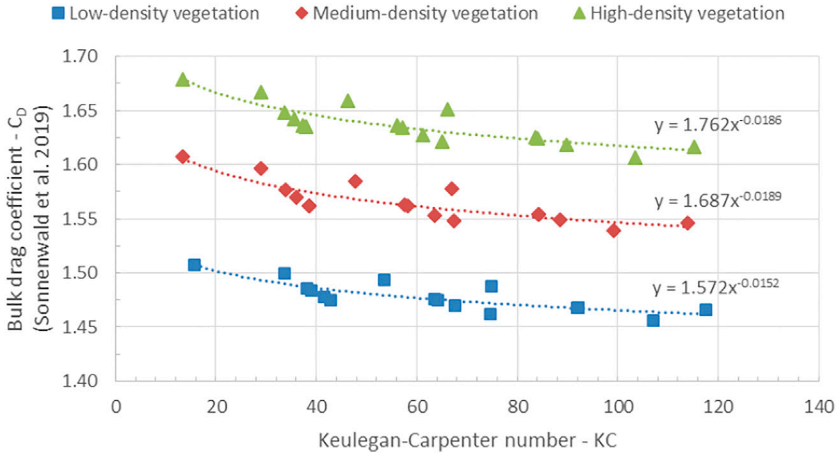

FIGURE 11 | Bulk drag coefficient versus Keulegan-Carpenter number for artificial marshes with low, medium, and high vegetation densities.

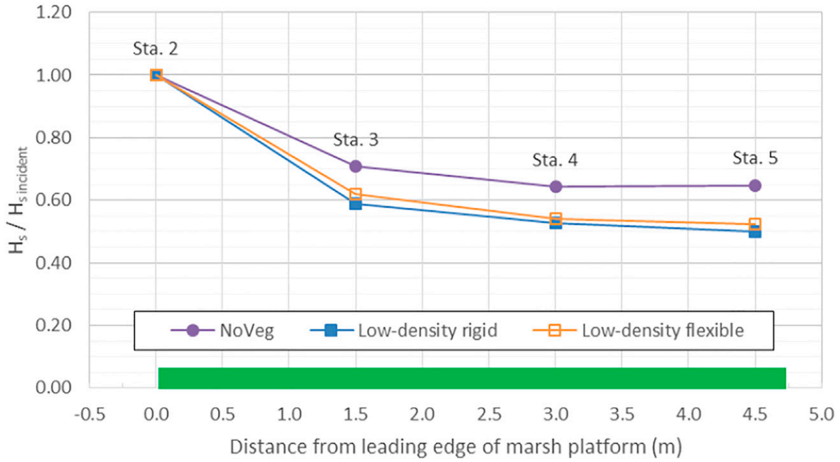

FIGURE 12 | Wave attenuation across similar artificial marshes comprised of rigid and flexible vegetation. Data is normalized by the incident wave height at the edge of the marsh (@ Station 2). Note that this figure includes wave height attenuation due to depth-limited breaking.

The relationship between wave attenuation factor (β') and the ratio of submergence derived from the present experiments is presented in **Figure 10**, where symbols denote results from individual tests spanning a range of wave conditions, while dashed lines connect average values for each submergence ratio. As seen in many previous studies, wave attenuation clearly increases as plant height (submergence) increases relative to the local water depth. Although results for only three submergence ratios are available from this dataset, the data suggests that the rate of increase with submergence ratio is greater for submergence ratios less than 0.9, decreasing as the vegetation becomes emergent in still water.

Using data from Test Series 2, the bulk drag coefficient, C_D, was calculated according to the formula proposed by Sonnenwald et al. (2019), see **Eq. 7**. **Figure 11** shows the resulting relationship between the bulk drag coefficient and the KC number defined in **Eq. 6**. These results suggest that for larger KC number ($KC > 80$), the low-, medium-, and high-density marshes studied in these experiments are associated with bulk drag coefficients of approximately 1.47, 1.55, and 1.63, respectively, and that bulk drag coefficients for all three marshes increase gradually as KC number decreases towards $KC \sim 10$. These results are generally consistent with the findings of Ozeren et al. (2014), who found that C_D was dependent on KC when $KC < 10$. In these experiments, $12 < KC < 268$, suggesting all were in the range where drag forces dominate and the drag coefficient is weakly dependent on KC. At field (full) scale, $268 < KC < 2{,}351$ would be typical for the same range of wave and water level conditions, assuming stem diameters of 9.5 mm, and therefore bulk drag coefficients observed in the present experiments are expected to slightly over-predict field conditions.

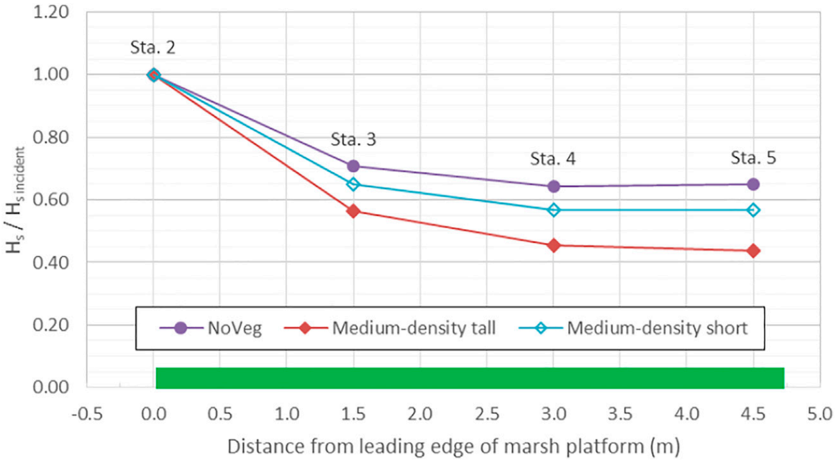

FIGURE 13 | Wave attenuation across similar artificial marshes featuring different vegetation heights. Data is normalized by the incident wave height at the edge of the marsh (@ Station 2). Note that this figure includes the effect of wave transformation and breaking due to the sloping foreshore.

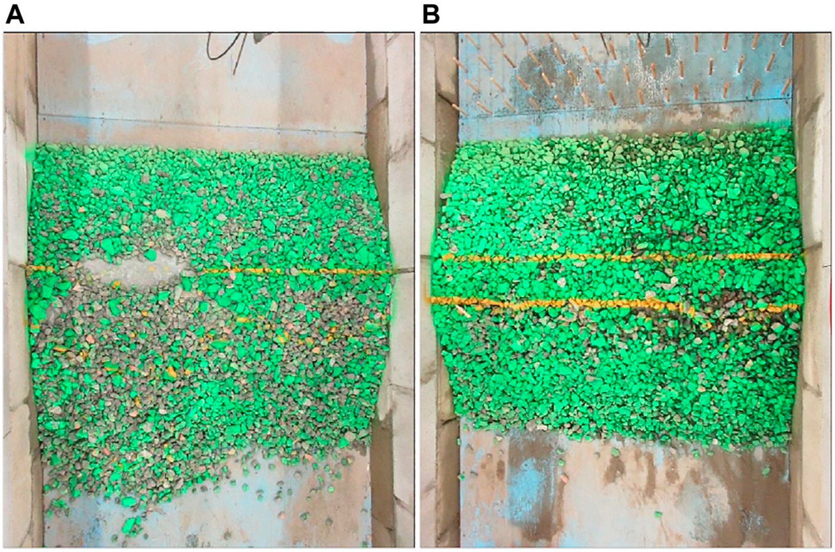

FIGURE 14 | Comparison of damage to identical dykes built behind a salt marsh platform; without vegetation **(A)** and with vegetation **(B)**. Waves approached from the top in these images.

5.2 Effect of Vegetation Flexibility and Submergence

Test Series 4 was conducted to investigate the effects of vegetation height (or submergence ratio) and stem flexibility on the resulting wave attenuation. **Figure 12** compares wave attenuation across the model marsh for otherwise identical marshes comprised of rigid and flexible vegetation. In this figure, the wave height attenuation across the marsh platform for the no vegetation (NoVeg) case is primarily due to depth-limited wave breaking. Across the wide range of significant wave heights, peak wave periods and water depths investigated, the additional wave attenuation due to flexible vegetation is roughly 90% of the additional attenuation due to comparable rigid vegetation. Although plant stiffness was not the main focus of these tests, and plant flexibility was not modelled with strict parametric specificity, these results are consistent with the findings of Maza et al. (2015), where increased plant rigidity was shown to correlate with increased wave attenuation.

The influence of plant submergence ratio on wave height attenuation is plotted in **Figure 10** and discussed briefly in the previous section, where it is shown that wave attenuation capacity increases with increasing submergence ratio. In a similar vein, **Figure 13** shows the effect of plant submergence (or height) on wave attenuation across otherwise similar model marshes. As in **Figure 12**, the wave height attenuation curves in this figure are based on averaging results from several tests with different wave

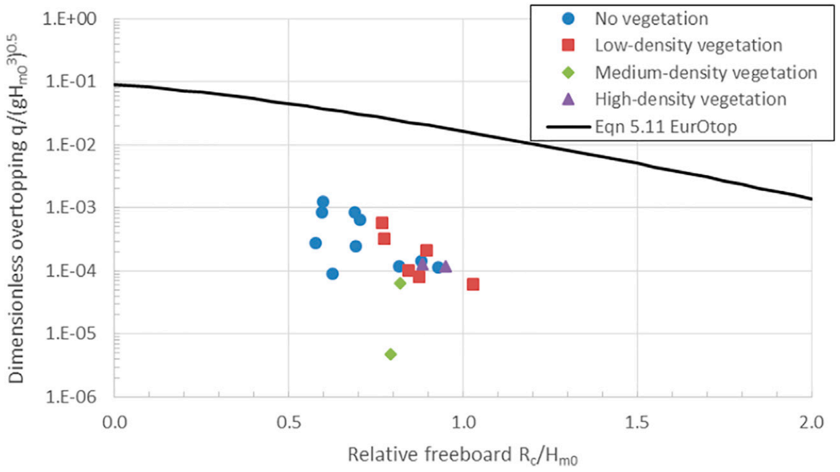

FIGURE 15 | Wave overtopping at four identical dykes for different vegetation densities.

conditions, and include the effects of depth-limited wave breaking. Stems in the tall marsh were simulated using 0.09 m tall rigid dowels, whereas 0.025 m tall dowels were used in the short marsh (28% of the tall plant height). **Figure 13** shows that the additional wave height attenuation due to the short stems (relative to the NoVeg case) was roughly 1/3rd of the additional attenuation due to the taller ones. These results are consistent with the results shown in **Figure 10** and the findings by other authors (Arkema et al., 2013; Anderson and Smith, 2014) who investigated the effect of water depth on wave attenuation capacity and found a significant influence on wave height decay, specifically that emergent conditions led to higher amounts of wave attenuation. Wave attenuation due to shorter, broken stems is an important topic, particularly for higher latitude regions where marsh plants tend to die off following the summer growing season, thus reducing their capacity to dissipate wave energy and limit flood risk.

5.3 Effect of Vegetation on Dyke Performance

The presence (or absence) of vegetation was a strong function of dyke performance. **Figure 14** shows a comparison of two identical dykes built in the lee of salt marsh platforms subject to the same series of increasingly harsh sea states and water levels. At the end of the test series, the dyke without protective vegetation (shown on the left) suffered significant damage, exposing the core at the seaside crest and causing significant scouring on the leeside. In stark contrast, the dyke fronted by a 4.75 m length of low-density marsh (shown on the right) sustained only minor damage to the leeside crest. Identical dykes protected by medium-density and high-density marshes (not pictured) showed effectively no damage following exposure to identical test conditions. **Figure 15** shows a comparison of the overtopping measured at four identical dykes fronted by varying vegetation fields. Out of the 41 sea states examined in Test Series 1, the dykes typically only experienced overtopping as a result of the largest wave heights in combination with extreme water levels. From **Figure 15**, it is clear that the NoVeg case not only saw overtopping in a greater number of these sea states, but that the overtopping volumes were also significantly larger. It is noted that these overtopping results are notably smaller than predicted by Equation 5.11 from EurOtop (Van der Meer et al., 2018), however this formula likely does not consider a dyke fronted by a long tidal flat. These results emphasizes the potential effectiveness of coastal salt marshes in dissipating wave energy, lessening overtopping and reducing damage of adjacent coastal infrastructure in storm conditions, provided that the marsh itself is able to survive the storm without being damaged.

5.4 Effect of Dyke Structure Design

A detailed investigation of wave overtopping and damage to the dyke structures was not the primary focus of this study; however, some general commentary based on observations made during the testing program is presented herein. Four different dyke structure designs (see **Figure 5**) were modelled and investigated in Test Series 3 with identical foreshore marshes to help inform decisions concerning potential upgrading of older dyke structures. Analysis of the wave data measured on the tidal flats suggests that the level of wave reflection was similar in each flume, and that the degree of wave attenuation across the model marsh was also similar in each flume.

However, clear differences in overtopping flowrates (and damage) were measured in each flume, depending on the dyke design (see **Figure 16**). The armoured dyke (requiring a rock armour volume of 15.4 m^3 per linear metre of full-scale structure), will be considered as a base case for comparison. The mean overtopping discharge for the armoured dyke, averaged across a broad range of test conditions, was 1 L/s/m. Despite this overtopping, the armour on the leeside crest and slope sustained negligible damage. In comparison, the simply reinforced dyke, with a slightly wider crest but requiring only 7.5 m^3/m of rock armouring, saw a 36% reduction in overtopping discharge. However the unprotected leeside crest and slope saw

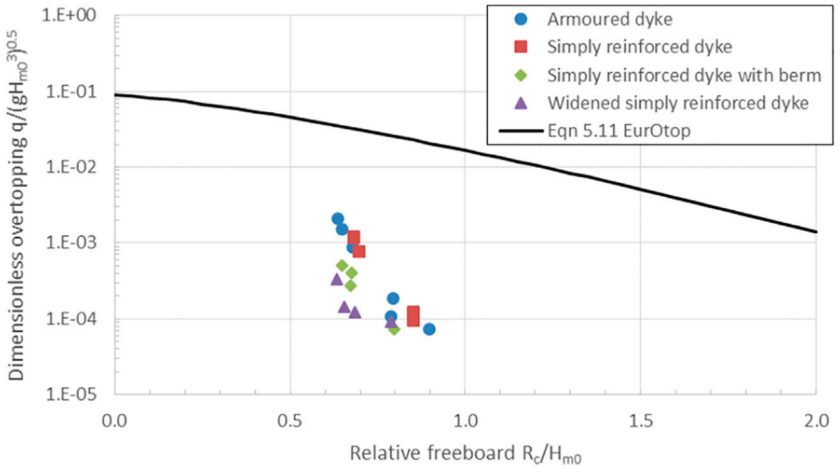

FIGURE 16 | Wave overtopping at four different dyke structures with identical marsh platforms.

comparatively greater damage, though not serious enough to jeopardize the overall integrity of the dyke.

In comparison, significantly fewer overtopping events and smaller flowrates were measured at the simply reinforced dyke with berm and the widened simply reinforced dyke (74 and 86% reductions in mean overtopping discharge, respectively). Each of these dyke designs requires 15.0 m^3 of armour stone per linear metre of structure. The berm was observed to trigger earlier wave breaking, and the additional volume of porous rock in the widened dyke was effective at reducing run-up and overtopping. In both cases, despite the lower overtopping volumes, damage to the leeside crest and slope was similar to that observed on the simply reinforced dyke (without berm), which may point to the high mobility of the impermeable core material under the conditions tested. Overall, the widened simply reinforced dyke was most effective in reducing mean overtopping discharge, however the armoured dyke provided the best protection in terms of leeside stability.

In all four cases, the seaside armouring saw only minor damage, in the form of rocking and/or small displacements. It should be noted that all four dykes saw effectively zero overtopping (or damage to the leeside) in all but the most energetic test conditions featuring the highest water levels combined with the largest wave heights. These results provide information on the relative ability of the upgraded structures to reduce overtopping and limit damage in extreme conditions. The relative benefits of each potential dyke upgrade must be balanced against the relative cost of implementation, which can be assumed to be roughly proportional to the volume of armour stone required.

6 CONCLUSION

A series of scaled laboratory experiments were conducted to investigate the function of coastal salt marshes as part of a coastal marsh and dyke system, and to determine the effectiveness of marsh vegetation in dissipating wave energy and reducing wave overtopping and damage under a broad range of wave and water level conditions, including harsh conditions, representative of Canadian coastal regions. A secondary goal was to assess the feasibility and efficacy of using simple, low-cost scale model surrogates to represent salt marsh vegetation in scale model testing. The model dyke and marsh platform features investigated in this study were based on archetypes found in Atlantic Canada, in particular the Tantramar Marsh on the Chignecto Isthmus between New Brunswick and Nova Scotia where *Spartina alterniflora* (smooth cordgrass) dominates.

This study addressed several of the research knowledge gaps highlighted by Markov (2021). In particular, two different plant heights were investigated as a proxy to the seasonal variation in marsh plant posture and stature typical of higher latitude regions, and tests were conducted across a much broader range of wave heights, periods, and water levels than previously seen in full scale (or near full scale) experiments using live or surrogate vegetation.

This research confirmed the benefit of tidal flats hosting coastal marshes for attenuating waves, reducing overtopping volumes and lessening damage to dyke structures. As expected, taller and denser marshes were more effective in attenuating wave energy for a given marsh width. From a wave attenuation perspective, the study results show that narrow, densely vegetated marshes (i.e., 25 m wide marsh with ~450 stems/m^2) provide similar wave attenuation capacity as wider marshes with sparser vegetation (i.e., ~90 m wide marsh with ~150 stems/m^2). Of course, stakeholders looking to make use of vegetated tidal flats to augment shore protection should consider creating expansive marshes wherever possible, not only from a wave attenuation perspective but also for the ancillary environmental co-benefits they bring.

This study is certainly limited by the use of artificial plants to represent coastal marshes. As noted by Tinoco et al. (2019), several authors have shown that simplifications in experimental setup, such as the use of rigid elements, a single stem diameter, a single element height, and a regular or staggered layout, can bias study outcomes, by either hiding or amplifying some of the relevant physical processes found in natural conditions. However, representing coastal marshes in a simple manner at reduced scale made it possible to study wave interaction with entire marsh-dyke systems in controlled laboratory conditions, efficiently study the effect of numerous changes in marsh properties and dyke characteristics, and study relatively high-energy wave conditions; investigations that would be impractical or highly demanding and expensive using live plants at full scale. Despite its limitations, it is believed that the present study contributes useful new information leading to greater understanding of the behaviour of marsh-dyke systems, the wave attenuation over wide marshes in a broad range of depths and wave conditions, and the sensitivity of these processes to various marsh characteristics and properties, such as plant density, plant height (submergence), stem flexibility and marsh width. Moreover, results from the present study can be used to inform the representation of coastal marshes in physical and numerical models.

It is noted that Webb et al. (2018) highlighted that *S. alterniflora* marsh vegetation in southern Alabama was stable when significant wave heights are less than 0.2 m 80 percent of the time and less than 0.3 m 95 percent of the time. In comparison, some of the wave heights investigated in this study were considerably larger (up to H_s = 3 m at full scale) and may have been sufficient to cause erosion and/or damage in natural settings. In reality, it is likely that at least the seaward edge of the marsh may have experienced some erosion as a result of these energetic conditions, though conceivably some sort of soil stabilization measures could be applied to reduce erosion in vulnerable areas. When reviewing the results of this study and assessing the performance and efficacy of salt marshes, it is important to consider the potential for soil erosion, plant damage and loss of wave attenuation capacity in high-energy conditions, although these processes were not included in the present study.

Although several researchers have conducted experiments with live plants in test facilities, further research is required to better understand wave attenuation caused by vegetation. Topics where further research is needed include examining wave attenuation capacity over the plant life cycle (spring growth, summer, and winter dormancy periods), understanding erosion and plant damage processes in high-energy wave conditions, and understanding how to best protect and establish young plants early in their life cycle or in more exposed locations. Additional research, especially in connection with field studies, is recommended and encouraged. Future work by the authors will focus on extending the analysis of the data obtained in the current study (particularly with respect to overtopping and stability of the dyke structures), developing and validating improved approaches for representing other types of coastal vegetation in scale model studies and investigating the behaviour and performance of other types of nature-based coastal infrastructure.

DATA AVAILABILITY STATEMENT

The raw data supporting the conclusions of this article will be made available by the authors, without undue reservation.

AUTHOR CONTRIBUTIONS

SB designed and led the experiments described in the paper and is the primary author of this paper. EM, AC, and PK acted in an advisory role before and during the experiments, and are secondary authors of this paper.

FUNDING

This research was supported by the Climate-Resilient Buildings and Core Public Infrastructure Initiative through Infrastructure Canada and by the Nature-Based Infrastructure for Coastal Resilience and Risk Reduction project through the Canadian Safety and Security Program (CSSP-2019-CP-2444).

ACKNOWLEDGMENTS

The NRC-OCRE technical staff, in particular Alistair Rayner, are recognized for their efforts in model construction and testing.

REFERENCES

Anderson, M. E., and Smith, J. M. (2014). Wave Attenuation by Flexible, Idealized Salt Marsh Vegetation. *Coast. Eng.* 83, 82–92. doi:10.1016/j.coastaleng.2013.10.004

Arkema, K. K., Guannel, G., Verutes, G., Wood, S. A., Guerry, A., Ruckelshaus, M., et al. (2013). Coastal Habitats Shield People and Property from Sea-Level Rise and Storms. *Nat. Clim. Change* 3 (10), 913–918. doi:10.1038/nclimate1944

Augustin, L. N., Irish, J. L., and Lynett, P. (2009). Laboratory and Numerical Studies of Wave Damping by Emergent and Near-Emergent Wetland Vegetation. *Coast. Eng.* 56, 332–340. doi:10.1016/j.coastaleng.2008.09.004

Barbier, E. B., Hacker, S. D., Kennedy, C., Koch, E. W., Stier, A. C., and Silliman, B. R. (2011). The Value of Estuarine and Coastal Ecosystem Services. *Ecol. Monogr.* 81 (2), 169–193. doi:10.1890/10-1510.1

Barron, S., Canete, G., Carmichael, J., Flanders, D., Pond, E., Sheppard, S., et al. (2012). A Climate Change Adaptation Planning Process for Low-Lying, Communities Vulnerable to Sea Level Rise. *Sustainability* 4 (9), 2176–2208. doi:10.3390/su4092176

Blackmar, P. J., Cox, D. T., and Wu, W.-C. (2014). Laboratory Observations and Numerical Simulations of Wave Height Attenuation in Heterogeneous Vegetation. *J. Waterw. Port. Coast. Ocean. Eng.* 140 (1), 56–65. doi:10.1061/(asce)ww.1943-5460.0000215

Bridges T. S., King J. K., Simm J. D., Beck M.W., Collins G., Lodder Q., et al. (Editors) (2021). *International Guidelines on Natural and Nature-Based Features for Flood Risk Management* (Vicksburg, MS: U.S. Army Engineer Research and Development Center).

Bridges, T. S., Wagner, P. W., Burks-Copes, K. A., Bates, E. M., and Collier, Z. (2014). *Use of Natural and Nature-Based Features (NNBF) for Coastal Resilience*. Vicksburg: U.S. Army Engineer Research and Development Center. Report ERDC SR-15-1.

Browder, G., Ozment, S., Rehberger Bescos, I., Gartner, T., and Lange, G. M. (2019). *Integrating Green and Gray: Creating Next Generation Infrastructure*. Washington: World Bank and World Resources Institute.https://openknowledge.worldbank.org/handle/10986/31430.

Bush, E., and Lemmen, D. S. (2019). *Canada's Changing Climate Report*. Ottawa: Government of Canada.

Costanza, R., Pérez-Maqueo, O., Martinez, M. L., Sutton, P., Anderson, S. J., and Mulder, K. (2008). The Value of Coastal Wetlands for Hurricane Protection. *AMBIO A J. Hum. Environ.* 37 (4), 241–248. doi:10.1579/0044-7447(2008)37[241:tvocwf]2.0.co;2

Council of Canadian Academies (2019). *Canada's Top Climate Change Risks: the Expert Panel on Climate Change Risks and Adaptation Potential*. Ottawa: Council of Canadian Academie.

Cranford, P. J., Gordon, D. C., and Jarvis, C. M. (1989). Measurement of Cordgrass, Spartina Alterniflora, Production in a Macrotidal Estuary, Bay of Fundy. *Estuaries* 12 (1), 27–34. doi:10.2307/1351447

Dalrymple, R. A., Kirby, J. T., and Hwang, P. A. (1984). Wave Diffraction Due to Areas of Energy Dissipation. *J. Waterw. Port, Coast. Ocean Eng.* 110 (1), 67–79. doi:10.1061/(asce)0733-950x(1984)110:1(67)

Doberstein, B., Fitzgibbons, J., and Mitchell, C. (2019). Protect, Accommodate, Retreat or Avoid (PARA): Canadian Community Options for Flood Disaster Risk Reduction and Flood Resilience. *Nat. Hazards* 98 (1), 31–50. doi:10.1007/s11069-018-3529-z

Feagin, R. A., Irish, J. L., Möller, I., Williams, A. M., Colón-Rivera, R. J., and Mousavi, M. E. (2011). Short Communication: Engineering Properties of Wetland Plants with Application to Wave Attenuation. *Coast. Eng.* 58, 251–255. doi:10.1016/j.coastaleng.2010.10.003

Heller, V. (2011). Scale Effects in Physical Hydraulic Engineering Models. *J. Hydraulic Res.* 49 (3), 293–306. doi:10.1080/00221686.2011.578914

Houser, C., Trimble, S., and Morales, B. (2015). Influence of Blade Flexibility on the Drag Coefficient of Aquatic Vegetation. *Estuaries Coasts* 38, 569–577. doi:10.1007/s12237-014-9840-3

Hughes, S. (1993). *Physical Models and Laboratory Techniques in Coastal Engineering*. Singapore: World Scientific.

Jadhav, R. S., Chen, Q., and Smith, J. M. (2013). Spectral Distribution of Wave Energy Dissipation by Salt Marsh Vegetation. *Coast. Eng.* 77, 99–107. doi:10.1016/j.coastaleng.2013.02.013

Jongman, B. (2018). Effective Adaptation to Rising Flood Risk. *Nat. Commun.* 9 (1), 1986. doi:10.1038/s41467-018-04396-1

Keimer, K., Schürenkamp, D., Miescke, F., Kosmalla, V., Lojek, O., and Goseberg, N. (2021). Ecohydraulics of Surrogate Salt Marshes for Coastal Protection: Wave–Vegetation Interaction and Related Hydrodynamics on Vegetated Foreshores at Sea Dikes. *J. Waterw. Port. Coast. Ocean. Eng.* 147 (6). doi:10.1061/(asce)ww.1943-5460.0000667

Keulegan, G. H., and Carpenter, L. H. (1958). Forces on Cylinders and Plates in an Oscillating Fluid. *J. Res. Natl. Bur. Stan.* 60 (5), 423–440. doi:10.6028/jres.060.043

Kirezci, E., Young, I. R., Ranasinghe, R., Muis, S., Nicholls, R. J., Lincke, D., et al. (2020). Projections of Global-Scale Extreme Sea Levels and Resulting Episodic Coastal Flooding over the 21st Century. *Sci. Rep.* 10 (1), 11629. doi:10.1038/s41598-020-67736-6

Koftis, T., Prinos, P., and Stratigaki, V. (2013). Wave Damping over Artificial *Posidonia Oceanica* Meadow: a Large-Scale Experimental Study. *Coast. Eng.* 73, 71–83. doi:10.1016/j.coastaleng.2012.10.007

Lara, J. L., Maza, M., Ondiviela, B., Trinogga, J., Losada, I. J., Bouma, T. J., et al. (2016). Large-scale 3-D Experiments of Wave and Current Interaction with Real Vegetation. Part 1: Guidelines for Physical Modeling. *Coast. Eng.* 107, 70–83. doi:10.1016/j.coastaleng.2015.09.012

Lei, J., and Nepf, H. (2019). Wave Damping by Flexible Vegetation: Connecting Individual Blade Dynamics to the Meadow Scale. *Coast. Eng.* 147, 138–148. doi:10.1016/j.coastaleng.2019.01.008

Lemmen, D. S., Warren, F. J., James, T. S., and Mercer Clarke, C. S. L. (2016). *Canada's Marine Coasts in a Changing Climate*. Ottawa: Government of Canada.

Lieske, D. J., and Bornemann, J. (2012). *Coastal Dykelands in the Tantramar Area: Impacts of Climate Change on Dyke Erosion and Flood Risk*. Canada: Mount Allison University.

Lightbody, A. F., and Nepf, H. M. (2006). Prediction of Velocity Profiles and Longitudinal Dispersion in Salt Marsh Vegetation. *Limnol. Oceanogr.* 51 (1), 218–228. doi:10.4319/lo.2006.51.1.0218

Losada, I. J., Maza, M., and Lara, J. L. (2016). A New Formulation for Vegetation-Induced Damping under Combined Waves and Currents. *Coast. Eng.* 107, 1–13. doi:10.1016/j.coastaleng.2015.09.011

Markov, A. (2021). *Nature-based Solutions for Coastal Erosion ProtectionLiterature Review*. Ottawa, Canada: University of Ottawa.

Maza, M., Lara, J. L., and Losada, I. J. (2019). Experimental Analysis of Wave Attenuation and Drag Forces in a Realistic Fringe Rhizophora Mangrove Forest. *J. Adv. Water. Resour.* 131, 103376. doi:10.1016/j.advwatres.2019.07.006

Maza, M., Lara, J. L., Losada, I. J., Ondiviela, B., Trinogga, J., and Bouma, T. J. (2015). Large-scale 3-D Experiments of Wave and Current Interaction with Real Vegetation. Part 2: Experimental Analysis. *Coast. Eng.* 106, 73–86. doi:10.1016/j.coastaleng.2015.09.010

Mendez, F. J., and Losada, I. J. (2004). An Empirical Model to Estimate the Propagation of Random Breaking and Nonbreaking Waves over Vegetation Fields. *Coast. Eng.* 51, 103–118. doi:10.1016/j.coastaleng.2003.11.003

Morris, R. L., Konlechner, T. M., Ghisalberti, M., and Swearer, S. E. (2018). From Grey to Green: Efficacy of Eco-Engineering Solutions for Nature-Based Coastal Defence. *Glob. Change Biol.* 24 (5), 1827–1842. doi:10.1111/gcb.14063

Moudrak, N., Feltmate, B., Venema, H., and Osman, H. (2018). "Combating Canada's Rising Flood Costs: Natural Infrastructure Is an Underutilized Option," in *Intact Centre on Climate Adaptation* (Canada: University of Waterloo).

Muis, S., Apecechea, M. I., Dullaart, J., de Lima Rego, J., Madsen, K. S., Su, J., et al. (2020). A High-Resolution Global Dataset of Extreme Sea Levels, Tides, and Storm Surges, Including Future Projections. *Front. Mar. Sci.* 7, 263. doi:10.3389/fmars.2020.00263

Narayan, S., Beck, M. W., Wilson, P., Thomas, C. J., Guerrero, A., Shepard, C. C., et al. (2017). The Value of Coastal Wetlands for Flood Damage Reduction in the Northeastern USA. *Sci. Rep.* 7 (1), 9463. doi:10.1038/s41598-017-09269-z

Nepf, H. M. (1999). Drag, Turbulence, and Diffusion in Flow through Emergent Vegetation. *Water Resour. Res.* 35 (2), 479–489. doi:10.1029/1998wr900069

Ozeren, Y., Wren, D. G., and Wu, W. (2014). Experimental Investigation of Wave Attenuation through Model and Live Vegetation. *J. Waterw. Port. Coast. Ocean. Eng.* 140 (5). doi:10.1061/(asce)ww.1943-5460.0000251

Percy, J. A. (2000). *Salt Marsh Saga: Conserving Fundy's Marine Meadows*. Canada: Bay of Fundy Ecosystem Partnership.

Piercy, C. D., Pontee, N., Narayan, S., Davis, J., and Meckley, T. (2021). "Chapter 10: Coastal Wetlands and Tidal Flats," in *International Guidelines on Natural and Nature-Based Features for Flood Risk Management*. Editors T. S. Bridges, J. K. King, J. D. Simm, M. W. Beck, G. Collins, Q. Lodder, et al. (Vicksburg, Mississippi, United States: U.S. Army Engineer Research and Development Center). MS.

Pinsky, M. L., Guannel, G., and Arkema, K. K. (2013). Quantifying Wave Attenuation to Inform Coastal Habitat Conservation. *Ecosphere* 4 (8), 95. doi:10.1890/es13-00080.1

Pontee, N., Narayan, S., Beck, M. W., and Hosking, A. H. (2016). Nature-based Solutions: Lessons from Around the World. *Proc. Institution Civ. Eng. - Marit. Eng.* 169 (1), 29–36. doi:10.1680/jmaen.15.00027

Shepard, C. C., Crain, C. M., and Beck, M. W. (2011). The Protective Role of Coastal Marshes: A Systematic Review and Meta-Analysis. *PLoS One* 6 (11), e27374. doi:10.1371/journal.pone.0027374

Sherren, K., Bowron, T., Graham, J. M., Rahman, H. M. T., and van Proosdij, D. (2019). "Coastal Infrastructure Realignment and Salt Marsh Restoration in Nova Scotia, Canada," in *Responding to Rising Seas: Comparing OECD Countries' Approach to Coastal Adaptation* (Paris, France: Organization for Economic Collaboration and Development), 75–108.

Sonnenwald, F., Stovin, V., and Guymer, I. (2019). Estimating Drag Coefficient for Arrays of Rigid Cylinders Representing Emergent Vegetation. *J. Hydraulic Res.* 57 (4), 591–597. doi:10.1080/00221686.2018.1494050

Spalding, M. D., McIvor, A. L., Beck, M. W., Koch, E. W., Möller, I., Reed, D. J., et al. (2014). Coastal Ecosystems: a Critical Element of Risk Reduction. *Conserv. Lett.* 7 (3), 293–301. doi:10.1111/conl.12074

Sutton-Grier, A. E., Wowk, K., and Bamford, H. (2015). Future of Our Coasts: the Potential for Natural and Hybrid Infrastructure to Enhance the Resilience of Our Coastal Communities, Economies and Ecosystems. *Environ. Sci. Policy* 51, 137–148. doi:10.1016/j.envsci.2015.04.006

Sutton-Grier, A., Gittman, R., Arkema, K., Bennett, R., Benoit, J., Blitch, S., et al. (2018). Investing in Natural and Nature-Based Infrastructure: Building Better along Our Coasts. *Sustainability* 10 (2), 523. doi:10.3390/su10020523

Tinoco, R. O., San Juan, J. E., and Mullarney, J. C. (2019). Simplification Bias: Lessons from Laboratory and Field Experiments on Flow through Aquatic Vegetation. *J. Earth Surf. Process. Landforms* 45, 121–143. doi:10.1002/esp.4743

Van der Meer, J. W., Allsop, N. W. H., Bruce, T., De Rouck, J., Kortenhaus, A., Pullen, T., et al. (2018). *EurOtopManual on Wave Overtopping of Sea Defences and Related Structures. An Overtopping Manual Largely Based on European Research, but for Worldwide Application*. EurOtop. www.overtopping-manual.com.

van Proosdij, D., Perrott, B., and Carrol, K. (2013). Development and Application of a Geo-Temporal Atlas for Climate Change Adaptation in Bay of Fundy Dykelands. *J. Coast. Res.* 65, 1069–1074. doi:10.2112/si65-181.1

van Veelen, T. J., Fairchild, T. P., Reeve, D. E., and Karunarathna, H. (2020). Experimental Study on Vegetation Flexibility as Control Parameter for Wave Damping and Velocity Structure. *J. Coast. Eng.* 157, 103648. doi:10.1016/j.coastaleng.2020.103648

Virgin, S. D., Beck, A. D., Boone, L. K., Dykstra, A. K., Ollerhead, J., Barbeau, M. A., et al. (2020). A Managed Realignment in the Upper Bay of Fundy: Community Dynamics during Salt Marsh Restoration over 8 Years in a Megatidal, Ice-Influenced Environment. *J. Ecol. Eng.* 149, 105713. doi:10.1016/j.ecoleng.2020.105713

Vuik, V., Jonkman, S. N., Borsje, B. W., and Suzuki, T. (2016). Nature-based Flood Protection: the Efficiency of Vegetated Foreshores for Reducing Wave Loads on Coastal Dikes. *Coast. Eng.* 116, 42–56. doi:10.1016/j.coastaleng.2016.06.001

Vuik, V., Van Vuren, S., Borsje, B. W., van Wesenbeeck, B. K., and Jonkman, S. N. (2018). Assessing Safety of Nature-Based Flood Defenses: Dealing with Extremes and Uncertainties. *Coast. Eng.* 139, 47–64. doi:10.1016/j.coastaleng.2018.05.002

Webb, B., Douglass, S., Dix, B., and Asam, S. (2018). *Nature-based Solutions for Coastal Highway Resilience*. Report FHWA-HEP-18-037. Washington, DC: U.S. Federal Highway Administration (Accessed February 13, 2018).

Wu, W.-C., and Cox, D. T. (2015). Effects of Vertical Variation in Vegetation Density on Wave Attenuation. *J. Waterw. Port. Coast. Ocean. Eng.* 142 (2). doi:10.1061/(ASCE)WW.1943-5460.0000326

Wu, W.-C., and Cox, D. T. (2015). Effects of Wave Steepness and Relative Water Depth on Wave Attenuation by Emergent Vegetation. *Estuar. Coast. Shelf Sci.* 164, 443–450. doi:10.1016/j.ecss.2015.08.009

Wu, W.-C., Ozeren, Y., Wren, D., Chen, Q., Zhang, G., Holland, M., et al. (2011). Phase I Report for SERRI Project No. 80037: Investigation of Surge and Wave Reduction by Vegetation, SERRI Report 80037-01, (Accessed January 16, 2011)

Conflict of Interest: The authors declare that the research was conducted in the absence of any commercial or financial relationships that could be construed as a potential conflict of interest.

frontiers | Frontiers in Built Environment

ORIGINAL RESEARCH
published: 09 June 2022
doi: 10.3389/fbuil.2022.885298

The Emerald Tutu: Floating Vegetated Canopies for Coastal Wave Attenuation

Julia Hopkins[1]*, *Nicholas Lutsko*[2], *Gabriel Cira*[3], *Louiza Wise*[3] and *Jena Tegeler*[3]

[1]Northeastern University, Boston, CA, United States, [2]University of California, San Diego, San Diego, CA, United States, [3]The Emerald Tutu, Boston, MA, United States

Nature-based solutions (NBS) have been broadly defined in coastal resilience as the restoration of natural environments or as civil infrastructure with natural elements, with examples ranging from marsh restoration and new oyster beds to artificial reefs and living shorelines. The multiplicity of NBS types makes it difficult to quantify and model their effectiveness as a whole in coastal flood reduction and environmental co-benefits. Specific types of NBS operate under a variety of physical and ecological regimes: oyster beds care about the benthic environment and can be modeled as bed roughness elements, while living shorelines are a combination of emergent/submerged vegetation elements located in the dynamic swash zone. As such, NBS cannot be investigated as a monolith and their evaluation will be intervention-specific. Here, we present the evaluation of an engineered NBS called the Emerald Tutu, a series of interlinked vegetated mats which leverage known physical and ecological properties of marsh environments and combine them in networked formats for rapid deployment around shoreline environments. The Tutu takes inspiration from marsh canopies, but aims to transport the physical protection of these canopies to urban areas using the wave attenuation properties of floating vegetation elements and network effects. Prototype Tutu units were deployed in the OH Hinsdale Wave Lab at Oregon State University in summer 2021 to test the physical efficacy of the mat networks. The results show the effect of network arrangement, mat canopy size, and Tutu unit density on wave attenuation. We show how these results can be used to design the Tutu for a variety of coastal environments, and discuss the impact of submerged vegetation dynamics on Tutu effectiveness and what research gaps remain for the implementation of these kinds of engineered NBS.

Keywords: coastal resilience, nature-based solutions, vegetated solutions, wave attenuation, floating canopy, climate change

Edited by:
Brian C McFall,
U.S. Army Engineer Research and Development Center, United States

Reviewed by:
Longhuan Zhu,
Michigan Technological University, United States
Ravindra Jayaratne,
University of East London, United Kingdom

****Correspondence:***
Julia Hopkins
j.a.hopkins@northeastern.edu

Specialty section:
This article was submitted to Coastal and Offshore Engineering, a section of the journal Frontiers in Built Environment

Received: *27 February 2022*
Accepted: *06 May 2022*
Published: *09 June 2022*

Citation:
Hopkins J, Lutsko N, Cira G, Wise L and Tegeler J (2022) The Emerald Tutu: Floating Vegetated Canopies for Coastal Wave Attenuation. Front. Built Environ. 8:885298. doi: 10.3389/fbuil.2022.885298

INTRODUCTION

Coastal environments and coastal communities are vulnerable to climate change impacts such as sea level rise, higher rates of erosion, and more intensified storms. These effects will increase flooding and expose more inhabited land to the ocean, damaging livelihoods, infrastructure, and ecological systems. Historically, issues of erosion and flooding have been mitigated in populated areas using “hard” infrastructure such as seawalls, groins, jetties, and other concrete- or steel-based structures (Smallegan et al., 2016; Morris et al., 2018). Eroding beaches along more natural coasts have been

FIGURE 1 | Aerial view of a rendering of the Emerald Tutu (green circles) surrounding East Boston, MA. The white strips represent walkways through the mat which can be used by community members during calm weather.

managed with nourishments as well as hard structures to encourage sand accumulation (van Duin et al., 2004; Stive et al., 2013; de Schipper et al., 2020). These traditional measures are being challenged by the uncertain impacts of climate change both in terms of sea level rise and weather patterns, as hard infrastructure is difficult to design or adapt to uncertain climate futures (Sutton-Grier et al., 2015). Nature-based solutions (NBS) offer alternative coastal resilience measures which have the potential to adapt to a changing climate.

NBS leverage aspects of the natural environment to buffer against negative effects of climate change. Coastal examples include efforts to restore marshes and mangrove forests (Quartel et al., 2007; Howard et al., 2017), and designs to deploy oyster reefs near urban areas (Morris et al., 2018). These examples attempt to build natural barriers of vegetation and benthic organisms between ocean forces (e.g., storm waves) and coastal communities. The physical premise for the effectiveness of these NBS is reasonably well-understood. Research into seagrass and mangrove forests shows that their effectiveness at damping wave energy comes from forcing complex vortical structures in the landward flow (Quartel et al., 2007; Crooks et al., 2011; Howard et al., 2017; Bergstrom et al., 2019; Menendez et al., 2020). Similarly, submerged oyster reefs and even submerged artificial reefs operate under the principle of enhanced bed roughness, increasing the friction between the bed and incoming waves or surge and reducing the energy of the flow before it reaches the shoreline (Morris et al., 2018). NBS are organic, living entities and as such have the potential to adjust to, and mitigate, climate change effects like sea level rise and storm intensity.

These natural types of NBS require a significant amount of space to be effective: mangrove forests and marshes demand shoreline real estate and the research into the footprint of an oyster reef needed to fully damp a storm wavefield is ongoing, but likely in the range of hundreds of meters to kilometers. In urban environments, the necessary real estate may not be readily available. This presents both a challenge and an opportunity to develop new types of NBS which are engineered to incorporate natural features in infrastructure designed for urban environments and flexible enough to evolve as the climate changes. The research presented here focuses on one such engineered NBS, the Emerald Tutu, as a model for how these types of solutions may operate and be evaluated for effective deployment in urban environments.

The Emerald Tutu consists of floating vegetated mats that are interlinked and anchored to the seafloor to provide a modular network of protective canopies encircling urban coastlines (**Figure 1**). The Tutu was developed through collaboration between landscape architects, coastal engineers, climate scientists, and water resource specialists to provide flood mitigation as well as ecological and social co-benefits to coastal communities. Floating wetlands similar to the Tutu have been used thus far as individual elements in quiescent water bodies such as wastewater treatment plants, rivers, and lakes to improve water quality (Faulwetter et al., 2011; Hwang and LePage, 2011; Bi et al., 2019). Isolated vegetated canopies seeded with emergent and submerged vegetation have also been tested in laboratory conditions, showing that vegetated canopies have the potential to damp incident wave energy (Chen et al., 2016; Zhu et al., 2021). The Tutu extends the floating canopy concept to increase robustness for exposed coastal conditions, and adds the element of network effects to damp storm wave energy.

The modular, floating nature of the Tutu design makes it ideal for deployment in areas where land real estate is difficult to use for coastal resilience. Its structural reliance on vegetation provides benefits to native plants and animals. However, the efficacy of the Tutu, or any similarly engineered NBS, needs to be carefully evaluated to determine its optimal design and deployment. At present, there are few site-specific examples of NBS performance and few studies which dive into the physical underpinnings of NBS operations to the extent that coastal scientists could use them to improve existing numerical models or create new models which accurately predict and quantify NBS effects (Chen et al., 2016; Sarabi et al., 2019; Chausson et al., 2020; Zhu et al., 2021). The Emerald Tutu is an opportunity to begin to bridge this knowledge gap between NBS ideation and performance.

In this paper, we report on initial tests of the physical effectiveness of the Tutu system. The objective of the study was to evaluate the efficacy of an interlinked network of floating mats in attenuating nearshore waves. We designed and built scaled physical analogues of the Tutu and observed their behavior under a variety of wave conditions in the Natural Hazards Engineering Research Infrastructure (NHERI) O.H. Hinsdale Wave Basin at Oregon State University. In particular, we tested the hypothesis that the attenuation of waves owing to a network of Tutu mats is a function of mat network geometry, wavelength, and mat density. Our results show the existence of a relationship between network geometry and incident wavelength, as opposed to network density and incident wave conditions. Further, our results support the idea that a truly effective NBS requires a significant footprint along either the shoreline or the nearshore environment, suggesting that approaches to NBS which incorporate multiple, tiered solutions may be optimal for urban coastal communities in the face of climate change.

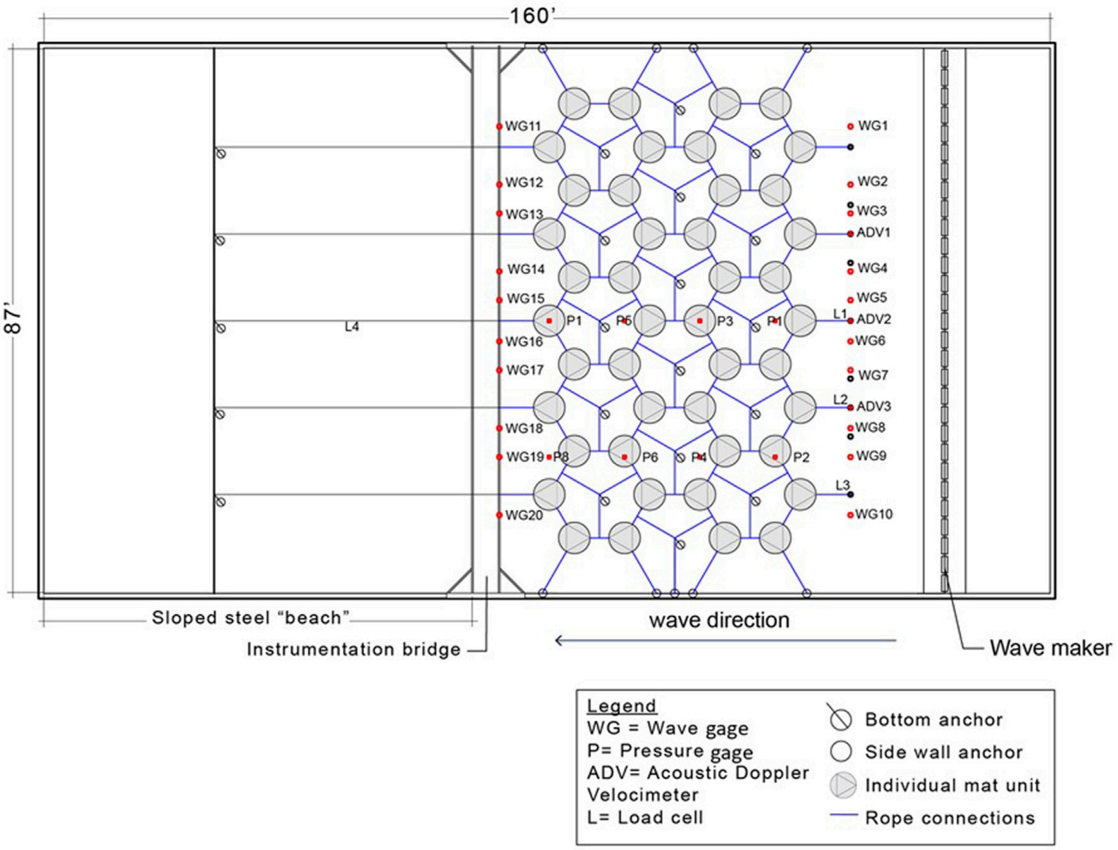

FIGURE 2 | Aerial view of the "sparse" Tutu network in the wave basin, with the wavemaker on the right and the beach on the left. The 5 ft diameter Tutu mats are show in grey, the dark blue lines are nylon connections between the mats and the anchors to the beach and side walls, empty circles with lines show bottom anchors, and the red dots show the location of instruments measuring hydrodynamic properties. The 1:10 sloped beach begins to the left of the instrumentation bridge. The instruments are labeled as shown in the legend to the bottom right.

METHODS

Experimental Setup

This initial study tests the physical behavior of the Emerald Tutu, focused on the abilities of individual mats and the network as a whole to damp incident wave energy. The facility we used was the NHERI O.H. Hinsdale Directional Wave Basin at Oregon State University, a lab capable of simulating both regular and random wavefields for a range of heights and directions. The basin is 48.8 m by 26.5 m in the horizontal, and 2.1 m deep with a 1:10 sloped steel beach for wave energy dissipation set opposite a series of wave paddles (**Figure 2**). The basin's capabilities, most importantly its width, make it an ideal setting to focus on understanding the wave dissipation properties of a floating dense mat network.

We deployed a scaled physical replica of the Tutu network according to the spatial limitations of the lab setup. The mats were designed to be half the diameter of what we would expect in a field deployment (thus 1.5 m diameter in the lab). We built and deployed 44 mats in the basin (**Figure 2**) to allow for sufficient space between the wavemaker, the network, and the beach slope for wave development. The mats consisted of canvas shells, stuffed with discarded wood fragments from a nearby forestry service in Corvallis, OR, and a large piece of pink insulation foam (cut into a hexagon with 1.4 m length diagonals) for buoyancy (**Figure 3**). The wood fragments are used in the Tutu design because they are an abundant, reliable, cheap, and ubiquitous biomass sources (and wood lignin takes longer to break down than biomass alternatives). The wood fragments also have a large surface area, which for the field means that they get covered with slime and algae and jumpstart the food chain to encourage vegetation. In the real mat design, we mix sharp wood fragments with coconut fiber (**Figure 3**), which makes a substrate able to hold its shape and encourages Spartina roots to grow in these nooks.

For the lab prototype, the canvas shells had two components, a top and a bottom circular piece stitched together at the edges by hand. The outer canvas shell and the inner wood fragments are identical to the proposed field design. The buoyant insulation foam made the draft of each unit (0.3 m draft for 150 lbs) such that only the top of the yellow canvas shell was exposed once water had soaked into the mats (see **Figures 3**, **4E**,F).

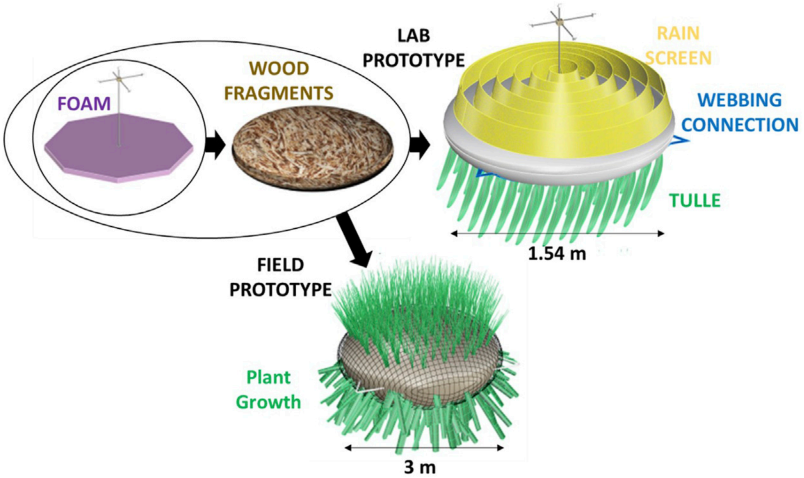

FIGURE 3 | Flow chart of the components of the wave basin prototype and the field prototype. Both contain foam (purple) and wood fragments from local forestry services (brown), but the Field Prototype (bottom) is made from burlap and coconut fiber to encourage natural plant growth (e.g., *Spartina*) while the Lab Prototype (top right) is made from lightweight canvas, a rain screen sewn to the top (yellow), strands of tulle sewn to the bottom (green), and webbing also sewn to the bottom in a triangle with the corners stick out (blue) to provide connection points to other mats and basin anchors.

FIGURE 4 | Construction of the individual mats and the network, from **(A)** cutting and marking canvas to 5 ft diameter, **(B)** sewing rain screen (yellow) to the top canvas piece and tulle (light green) with a webbing triangle (light blue) to the bottom piece, **(C)** using wood discard fragments to stuff the units, **(D)** lifting a stuffed and sewn unit into the basin where **(E)** it is tied to other units using nylon rope (dark blue) to finally set the **(F)** completed network in 1.37 m of water depth.

Material was sewn onto the canvas shells to represent light vegetation, with a rigid and porous rain screen sewn on the top and flimsier, more flexible strands of tulle sewn to the bottom (**Figure 3**). The rains screen was chosen as an analog for Spartina grass vegetation because: 1) its suppleness matches marsh grass, 2) it is porous/fiber-based and dense (which makes it omnidirectional), and 3) is available in a "surface" (roll) format which made it easy to sew onto the top of the units. The submerged vegetation (tulle) was chosen so it could move/sway in a similar manner to actual seaweed strands. Also sewn to each bottom piece were triangles of webbing that served as anchor points for the network connections (blue in **Figures 3**, **4E**).

The mats were anchored together using nylon rope (blue in all figures) that was spliced together at webbing anchor points on the mats and eye bolts between mats set into the floor of the basin and the basin walls. The webbing anchor points on the mats were from three corners of webbing triangles that were otherwise sewn into the bottom half of the canvas shell (the corners extended beyond the shell diameter, see **Figure 3**). Nylon rope was chosen to connect the mats and the wave basin anchors because it has similar resistance to tension as rigid shipping line, which we used in the field deployment, while being simpler to work with in the lab.

We tested wave conditions within the range of what was feasible given the facility and the strength of connections

TABLE 1 | List of wave conditions tested on the 50% scaled Tutu mat network.

Wave Period (s)										
Wave Height (m)	—	1	1.2	1.4	1.6	1.8	2	3	4	6
	0.1	S,D	D	D	D	D	S,D	S,D	S,D	S,D
	0.2	—	—	—	—	—	S,D,R	S,D,R	—	S,D
	0.3	—	—	—	—	—	—	S,D,R	—	S,D
	0.4	—	—	—	—	—	—	—	S,D	S,D
	0.45	—	—	—	—	—	—	—	S,D	S,D

S = sparse network, D = dense network, R = random waves, JONSWAP spectra with $\gamma = 3.3$

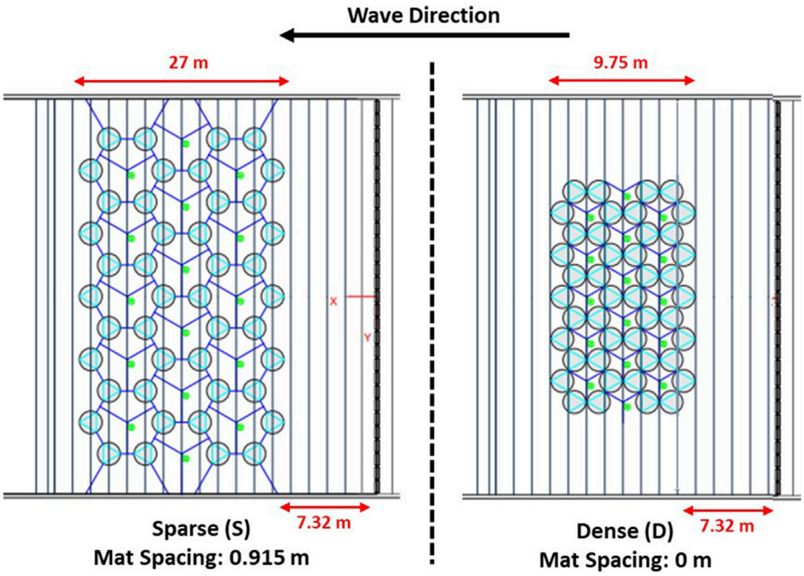

FIGURE 5 | Aerial view sketches of the two mat network configurations (Sparse, left, and Dense, right) inside the basin. The vertical lines represent divots in the bottom of the basin where eyelets (light green) were placed as anchor points. The spacing between these lines is 1.22 m. The wavemaker is to the right, the beach is to the left. The dark blue lines are interconnections between the mats (circles), with the light blue lines within the circles indicating the webbing sewn into the canvas.

between the mats. The weak point in the mat construction was the hand-sewn canvas around the webbing anchors, where the bulk of the force on the mats was being applied by incident waves. This limited the intensity of waves and meant we discarded our highest wave height of 0.5 m over the duration of the experiment. Despite this, we were able to test a representative range of waves (**Table 1**), in both regular and random regimes. The conditions were repeated for two mat network configurations, one where the mats were spread out in a “sparse” configuration (S, **Table 1** and **Figure 5**) and another where the mats were pulled together to eliminate the spacing between them in a “dense” configuration (D, **Table 1** and **Figure 5**). The networks are arranged in hexagons according to the Tutu design for the field, intended to accommodate multi-directional wave fields. We chose the sparse configuration to fill the possible width provided by the wave basin (0.915 m spacing between the mats), and the dense configuration to test the extreme of no space between the mats (0 m spacing between the mats).

The wave basin was outfitted with a number of instruments to track mat behavior and hydrodynamic conditions before and after the mat network (**Figure 2**). The primary measurements of interest for this paper are: 1) the wave attenuation measured by wave gages set before and after the mat network, and 2) the pressure gages scattered within the network. As seen in **Figure 2**, there were ten wave gages deployed between the mats and the wavemaker, and ten deployed between the mats and the beach. The first set of gages (wavemaker-to-mats) were deployed on steel struts anchored to eyebolts in the bed of the basin. The second set of gages (mats-to-sloped beach) were deployed on the gantry (instrument bridge) above the basin and suspended in the water. The eight pressure gages deployed within the network were placed at the bed along the unistrut supports running alongshore relative to the wave direction. All gages collected data at 100 Hz.

In addition to the tests conducted with sparse and dense mat networks (**Table 1**), we ran all of the “Dense” wave conditions for a basin with no mats. This gave us a baseline for wave behavior measured by the gages and the pressure sensors, and also allowed us to determine wave reflectance from the sloped beach and the side wall to remove any confounding factors in our analysis.

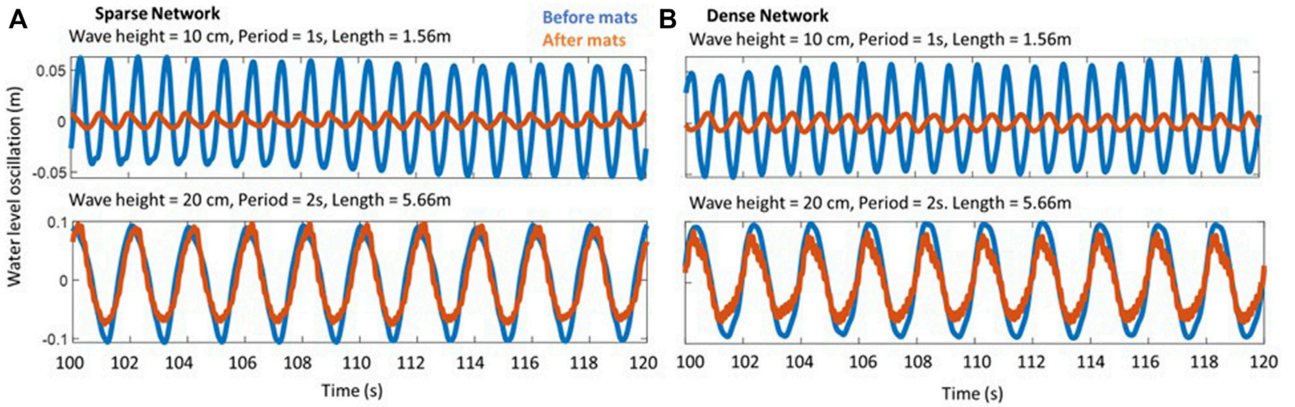

FIGURE 6 | Sample wave gage signals from the sparse network **(A)** and the dense network **(B)** for wave heights of 10 cm (top) and 20 cm (bottom). Incident wave conditions (blue) are higher than wave conditions after the network (red) but the damping effect of the network changes depending on the wave conditions and network configuration. The gages used here are located in the middle of the basin in the direction of wave propagation.

Experimental Procedure and Data Analysis

Initial results focus on the wave attenuation properties of the mat network. Regular wave tests were about 3 min long to allow for steady state in the basin. The timeseries of wave height and pressure measured within these 3 minutes was analyzed at each wave and pressure gage location to determine time-averaged wave behavior in space around the mat network for the full set of tests. The signals were analyzed with Fourier transforms to isolate the wave height (water oscillation amplitude) and wave period. Wavelengths were calculated using the intermediate depth wave dispersion relationship $\omega^2 = gktanh(kh)$, where $h = 1.36\,m$ is the basin depth, the wave frequency is $\omega = \frac{2\pi}{T}$, the wave period T is measured by the wave gages, the wave number $k = \frac{2\pi}{L}$ where L is the wavelength, and $g = 9.81\,m/s^2$ is gravitational acceleration.

We calculated the time-averaged energy of the waves at each gage location using $E = \frac{1}{2}\rho g a^2$, where E is the wave energy, ρ is the water density (1,000 kg/m^3), g is gravitational acceleration ($9.81 m/s^2$), and a is the wave amplitude ($\frac{1}{2}H$ where H is the wave height). We also calculated how the wave energy progressed through the mats using the wave amplitude measured at the pressure sensors embedded within the mat network. We calculated the variance in wave energy between pressure sensors (a variance in space) as a standard deviation around the mean energy measured within the mat network. This value shows how, and if, the wave energy changes between pressure sensors as the wave propagates through the mat network.

RESULTS

Wave Gages

The wave gages before and after the mat network were compared to determine the attenuation for the network as a whole. **Figure 6** demonstrates the signal before and after the mats at the centerline of the flume. The mat network performance depends on the incident wave conditions.

To be consistent in the analysis despite the different spatial extents of the network configurations (the sparse network extends to the edges of the tank, dense does not, see **Figure 5**), and to reduce erroneous measurements owing to wall effects, we focus on the gages aligned with the center of the network in the cross-shore in this analysis. The resulting wave attenuation patterns are shown in **Figure 7**, averaged over the three gages closest to the centerline of the basin in the direction of wave propagation. **Figure 7A** shows the attenuation compared to the wave steepness, a non-dimensional quantity calculated by dividing wave height by wavelength (calculated using the dispersion relationship). **Figure 7B** shows the same attenuation broken up between wavelength (x-axis, **Figure 7B**) and wave height (colors, **Figure 7B**).

Pressure Sensors and Velocities

The pressure sensors were strategically located throughout the mat network and occasionally returned a staccato signal indicating that they were not measuring perfect wave shapes. This signal is owing to the fact that the pressure gages were measuring both pressure from the water and occasionally pressure from a mat passing over the gage in response to wave action. As a result, a point-by-point comparison in time between the pressure gages was not possible, and we focused on relating the incident wave conditions to the spatial variance in the average wave measurements from the pressure sensors (how much the wave energy kept moving through the network). A low variance suggests that either the wave energy did not change throughout the mat network, or that it was all dissipated by the initial line of mats. **Figure 8A** shows that the variance in space has a dependency on wave height more so than wavelength. Similarly, the velocity measurements from the ADVs placed before the mat network show a relationship between velocity and wave height, as expected from linear wave theory since larger waves generate higher wave orbital velocities (**Figure 8B**).

We used the pressure sensors and the wave experiments run without Tutu units in the basin to calculate wave reflection for all the regular wave conditions, following the method of using three

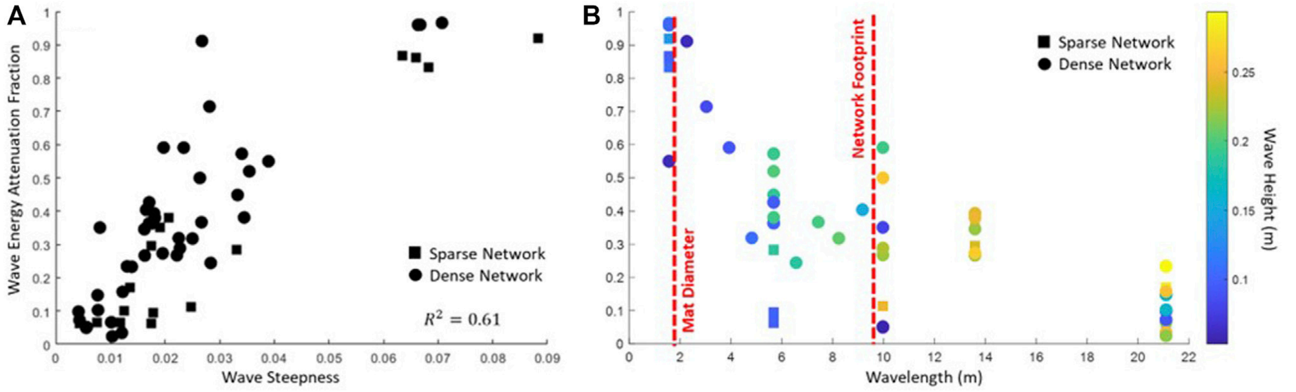

FIGURE 7 | (A) Wave steepness (x-axis) versus wave attenuation (y-axis) where 0 is no attenuation and 1 is full attenuation. Symbols represent the network configuration (square is sparse, circles are dense). **(B)** Wavelength (x-axis) versus wave attenuation (y-axis). Color indicates wave height (yellow is higher, blue is lower) and symbol represents the network configuration (square is sparse, circles are dense). The red dotted lines indicate the size of the mat diameter and of the network footprint in the direction of wave propagation (specifically for the dense network configuration).

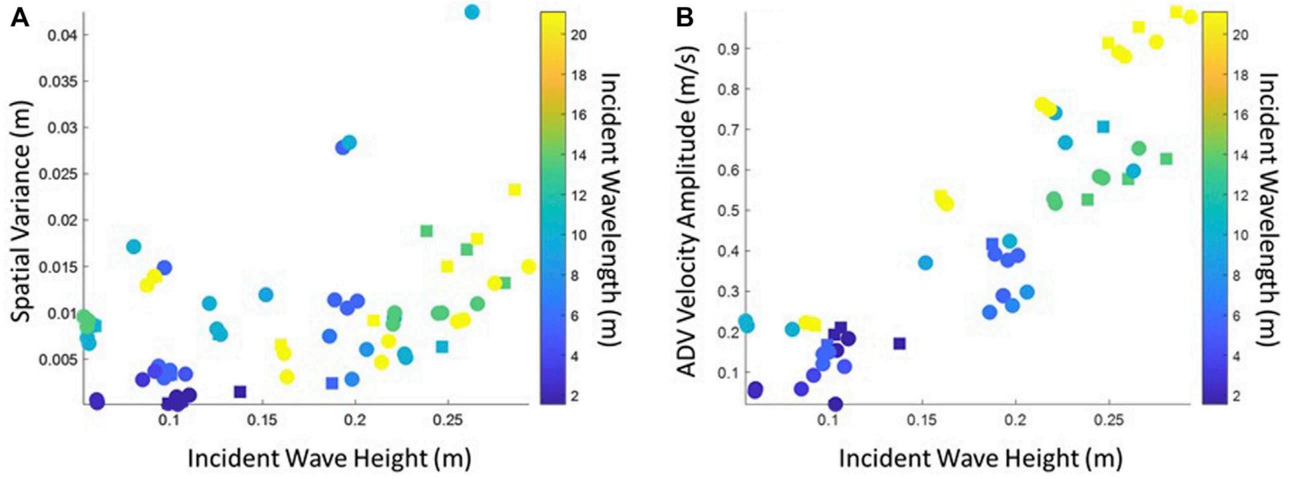

FIGURE 8 | (A) The spatial variance of wave height within the mat network as measured by the pressure gages (y-axis), and **(B)** wave height (x-axis) versus velocity (y-axis) measured before the mats by the ADV. Color shows the associated wavelength with lighter colors indicating longer waves, and darker colors indicating shorter waves. Higher incident wave height translates to higher velocities before the mats, as expected, and higher variance of pressure within the mat network indicates greater changes in wave height as the waves penetrate the network.

gages in the direction of wave propagation as outlined in Isaacson (1991). This method shows that reflection increases as the wavelength increases, yet the reflection coefficient remains less than 0.1 for most wave conditions tested. Experiments with reflections over this threshold were not considered in our analysis, hence the results presented here are not contaminated by significant wave reflection either before or after the mat network.

Random Wave Tests

The three random wave tests using the Dense configuration were run for 10 minutes to allow for a fully random sea state. The results from the wave gage measurements in the random tests were analyzed in frequency space to determine the reduction in wave energy before and after the mat network. The results show a similar picture to the regular wave cases across the frequency spectrum (**Figure 9**) with more detail of how the attenuation behaves at different frequencies (lower frequencies = longer wavelengths). We considered only frequencies which had measurable wave energy density generated by the wavemaker, excluding frequencies below 0.05 Hz and above 1.5 Hz.

DISCUSSION

These lab experiments show the potential for a modular network of floating mats to reduce incident wave energy. We see a strong

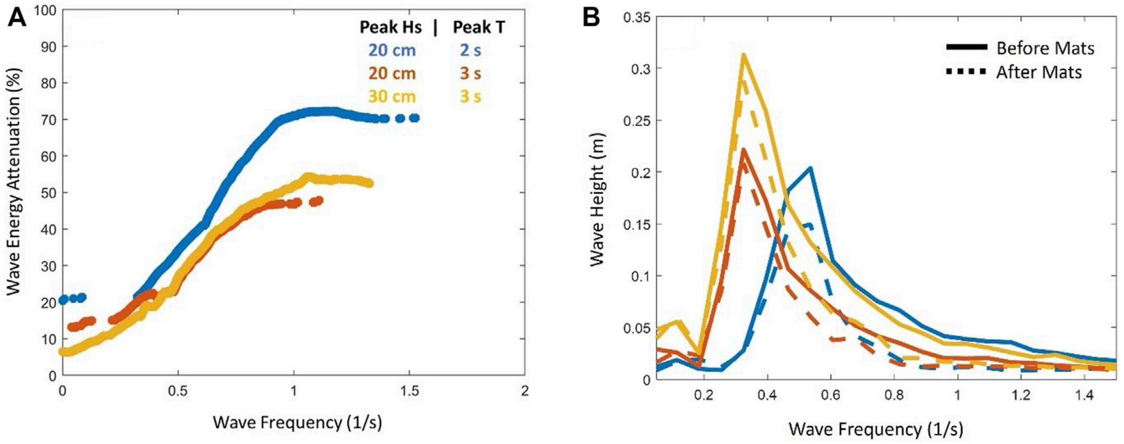

FIGURE 9 | (A) Wave frequency (x-axis) versus wave attenuation (y-axis) for the three random cases (colors and legend) centered on varying peak wave heights and peak periods around a JONSWAP spectra with $\gamma = 3.3$. **(B)** The resulting spectra measured by the wave gages located along the centerline of the mat network (in the direction of wave propagation) are shown to peak at the prescribed frequencies (x-axis) and wave heights (y-axis), with the incident wave height (solid line) higher than the resulting wave height (dashed line) in all cases. The distinction between solid and dashed lines is greater at higher frequencies (shorter waves), which aligns with results using regular wave conditions (see **Figure 7**).

relationship between the wave steepness and the attenuation, where steeper waves are more attenuated than shallower ones (**Figure 7A**). We divide this into wavelength and wave height (**Figure 7B**) to better understand this relationship, and find that wavelength is a primary indicator of wave attenuation. The test conditions with both regular waves and random waves suggest that the geometry of the network relative to the incident wavelength drives wave attenuation. The majority of the wave attenuation occurs at wavelengths shorter than or equal to the length of individual mats, though wave energy continues to be reduced until the wavelengths grow beyond the cross-shore footprint of the entire mat network. Further, the results show that wave attenuation is not appreciably different between sparse and dense network layouts (**Figure 7**, squares versus circles). Instead, the size of individual mats and the network footprint relative to the wavelength (**Figure 7**, red dashed lines) have a stronger impact on wave attenuation than the separation between mats.

The mechanics of wave orbital velocity explains some of this dependence. The dissipation of wave velocity in the vertical water column scales with wavelength, with shorter (longer) wavelengths losing energy at shallower (deeper) water depths. A generalization from linear wave theory describes the depth of the wave velocity dissipation as half of the wavelength. The Tutu network is suspended at the surface with a draft of about 0.3 m maximum, thus we would expect the Tutu canopies to impact the shortest waves more than longer waves. To explain the dependence relative to the network footprint (**Figure 7B**, red dashed lines), we note that if a wave is shorter than the diameter of the Tutu mats then the crest and trough of the wave encounter a mat simultaneously which leads to dissipation. If the wave is longer than an individual mat, but shorter than the network, its crest and trough encounters two or more mats linked together, and energy dissipates owing to tension between them as the wave moves the mats in opposition. If the wave is longer than the entire network, however, the network rides along the wave and dissipation is negligible.

Our initial hypothesis was that the network spacing–sparse and dense–would be a significant factor in wave attenuation, with the denser cluster of mats dampening more wave energy than the sparse cluster. Our results show that there is not a significant difference between the mat spacing in the network for these two configurations, suggesting that the mechanism of mats moving in opposition to dissipate wave energy can work even if that tension is transferred on a rope between them. We cannot generalize to larger spacings between mats than tested here, though we anticipate that at the extreme a Tutu design with too much space between mats will not be in enough tension to dissipate energy. The comparisons between sparse and dense networks, however, do suggest that a field deployment of the Tutu could attenuate waves while allowing space for light to penetrate the water (a concern for ecological systems in the water column and in the benthic region of shallow areas) and space for small craft to move between the network (for maintenance and leisure).

Whether or not the wave energy dissipates at the initial row of mats or after several rows appears to depend on wave height rather than wavelength (**Figure 8A**). The spatial variance of wave energy within the mat network, calculated using the pressure sensors, shows how much the waves change in the direction of wave propagation. A higher (lower) variance indicates that the wave energy changes within (at the first row of) the network. In this experiment, we found that smaller incident waves had little energy variance within the mat network, suggesting that the first row of mats dissipate the bulk of the energy. Higher energy waves often had more energy variance within the mat network, suggesting that the waves change as they moved through the network. The wavelength does not appear to be as relevant as the wave height in determining where within the network the waves dissipate. Wavelength indicates whether dissipation will happen at all, and wave height directly correlates to the wave velocity

(**Figure 8B**). the amount of energy in a wave, and thus likely the number of mat rows the wave needs to encounter for that energy to attenuate.

The results presented here are relevant for dense floating mats with minimal, short, stiff "emergent vegetation" represented by the rain screen, but not for mats with submerged vegetation. We found that the strips of tulle sewn to the bottom were not influencing the wave attenuation. We tested this by flipping the mats and re-running the Dense network regular waves, which produced similar results. At most 12 bunches of tulle were sewn onto each mat, and the bunches extended down to less than 20% of the water depth, so it is perhaps unsurprising that the effect was small. Observations from cameras placed underwater around the mats showed that the tulle was moving freely with the waves, and thus had little rigidity to contribute to energy attenuation. However, a concurrent full-scale prototype of a Tutu mat deployed in East Boston in summer 2021 showed dense vegetation undergrowth after 2 months in the water, which would have translated to a column of vegetation at least a meter deep in our wave basin experiments. Previous studies with kelp suggest that this type of submerged vegetation will enhance the dissipation of waves. These studies measured and modeled the dissipation of waves by suspended canopies of submerged kelp (fixed to a rigid platform above the water surface) (Zhu et al., 2021; Zhu et al., 2022) and suggest that the wave attenuation would improve with more realistic submerged vegetation structures, possibly extending the wavelengths at which the scaled Tutu is effective.

Our results build on previous work studying wave attenuation by floating individual canopies, notably experiments simulating floating shellfish farms in the field (Zhu et al., 2020). These experiments focused on dense buoys tethered individually to the sea floor and subjected to random wave attack. Attenuation measured from these tests using random waves are similar to **Figure 9**, with suspended canopies attenuating waves at higher frequencies better than at lower frequencies and plateauing at high frequencies. The plateau evident in **Figure 9A** occurs at wave frequencies greater than 1 Hz, which for a basin water depth of 1.36 m translates to a wavelength of 1.5m, which is also the diameter of our mats. The plateau appears to occur when the wavelength is at or smaller than the mat diameter. Zhu et al. (2020) further shows that the number of floating elements within the canopy influences attenuation, with more floating elements providing greater attenuation. This suggests that adding more mats to a Tutu network will improve performance at longer wavelengths.

In particular, Zhu et al. (2020) test the potential of combining floating shellfish farms (buoyant elements on individual tethers) with submerged seagrass or other vegetation patches anchored to the seafloor. Their results suggest that the floating farms can attenuate short waves and the submerged vegetation can attenuate longer waves (whose wave orbital velocities are more likely to penetrate the water column to the bed). This supports the idea that a tiered NBS approach to coastal protection should be used to protect against storm waves, with floating elements tackling higher wave frequencies and submerged elements tackling lower wave frequencies. The results presented above suggest that we can extend the frequency range attenuated by floating elements through interconnections between dense mats and network geometry. Future work will investigate how dense, suspended undergrowth from the mats impacts wave attenuation, and will likely expand the range of wave frequencies that a floating structure such as the Emerald Tutu can dissipate.

CONCLUSION

We tested the efficacy of a new NBS called the Emerald Tutu to attenuate waves in nearshore environments. Physical analogues of the mats were tested in the OH Hinsdale Wave Basin at Oregon State University for both regular and random wave conditions. Results from these tests show that wave attenuation depends on the geometry of the mat system, notably mat size and network size relative to the wavelength. These results are in line with previous work studying wave attenuation in the field owing to individually anchored floating shellfish farms. Both results suggest that floating nearshore networks of mats have the potential to protect the coastline from wave attack. Future research into the Tutu will include testing the impact of submerged vegetation, suspended from the mats, on additional wave attenuation, and developing a non-hydrostatic numerical model to replicate these lab results and scale them to the field.

DATA AVAILABILITY STATEMENT

The datasets presented in this study can be found in online repositories. The names of the repository/repositories and accession number(s) can be found below: https://www.designsafe-ci.org/data/browser/public/designsafe.storage.published/PRJ-3283.

AUTHOR CONTRIBUTIONS

JH, JT, and GC collected data for the experiment. JH and LW processed the data. JH wrote the manuscript, while LW and NL collaborated on revisions.

FUNDING

NSF SBIR Phase 1: funds for the experiment and the prototypes of the Tutu deployed and studied in 2021. This work was funded by a Phase 1 grant from the NSF Small Business Innovation Research (SBIR) program.

ACKNOWLEDGMENTS

We are forever grateful to the staff of the OH Hinsdale Wave Basin, who were invaluable in helping us to set up the instrumentation around the mat network, troubleshooting wave maker functionality issues, determining the best sets of regular and random waves to prioritize for our time in the facility, and being an amazing crew who fostered an excellent scientific environment. In particular, we would like to thank Pedro Lomonaco and Tim Maddux for being patient with us as we filled the space with wood chips, sewing machines, and colorful playmats. We also thank the REU students who helped us build and monitor the mats, Chelsea Wilhite, Alexis Lipovich, and Carter Howe.

REFERENCES

Bergstrom, E., Silva, J., Martins, C., and Horta, P. (2019). Seagrass Can Mitigate Negative Ocean Acidification Effects on Calcifying Algae. *Sci. Rep.* 9 (1), 1–11. doi:10.1038/s41598-018-35670-3

Bi, R., Zhou, C., Jia, Y., Wang, S., Li, P., Reichwaldt, E. S., et al. (2019). Giving Waterbodies the Treatment They Need: A Critical Review of the Application of Constructed Floating Wetlands. *J. Environ. Manag.* 238, 484–498. Academic Press. doi:10.1016/j.jenvman.2019.02.064

Chausson, A., Turner, B., Seddon, D., Chabaneix, N., Girardin, C. A. J., Kapos, V., et al. (2020). Mapping the Effectiveness of Nature-based Solutions for Climate Change Adaptation. *Glob. Change Biol.* 26 (11), 6134–6155. Blackwell Publishing Ltd. doi:10.1111/gcb.15310

Chen, X., Chen, Q., Zhan, J., and Liu, D. (2016). Numerical Simulations of Wave Propagation over a Vegetated Platform. *Coast. Eng.* 110, 64–75. Elsevier. doi:10.1016/j.coastaleng.2016.01.003

Crooks, S., Herr, D., Tamelander, J., Laffoley, D., and Vandever, J. (2011). *Marine Ecosystem Series Mitigating Climate Change through Restoration and Management of Coastal Wetlands and Near-Shore Marine Ecosystems Challenges and Opportunities*. Washington, DC: World Bank. Available at: www.worldbank.org/environment/publications (Accessed December 10, 2020).

de Schipper, M. A., Ludka, B. C., Raubenheimer, B., Luijendijk, A. P., and Schlacher, T. A. (2020). Beach Nourishment Has Complex Implications for the Future of Sandy Shores. *Nat. Rev. Earth Environ.* 2, 70–84. doi:10.1038/s43017-020-00109-9

Faulwetter, J. L., Burr, M. D., Cunningham, A. B., Stewart, F. M., Camper, A. K., and Stein, O. R. (2011). Floating Treatment Wetlands for Domestic Wastewater Treatment. *IWA Publ.* 64 (10), 2089–2095. doi:10.2166/wst.2011.576

Howard, J., Sutton-Grier, A., Herr, D., Kleypas, J., Landis, E., Mcleod, E., et al. (2017). Clarifying the Role of Coastal and Marine Systems in Climate Mitigation. *Front. Ecol. Environ.* 15 (1), 42–50. Wiley Blackwel. doi:10.1002/fee.1451

Hwang, L., and LePage, B. A. (2011). "Floating Islands-An Alternative to Urban Wetlands," in *Wetlands* (Dordrecht: Springer Netherlands), 237–250. doi:10.1007/978-94-007-0551-7_14

Isaacson, M. (1991). Measurement of Regular Wave Reflection. *J. Waterw. Port, Coast. Ocean Eng. (ASCE)* 117 (6), 553–569. doi:10.1061/(asce)0733-950x

Menéndez, P., Losada, I. J., Torres-Ortega, S., Narayan, S., and Beck, M. W. (2020). The Global Flood Protection Benefits of Mangroves. *Sci. Rep.* 10, 4404. doi:10.1038/s41598-020-61136-6

Morris, R. L., Konlechner, T. M., Ghisalberti, M., and Swearer, S. E. (2018). From Grey to Green: Efficacy of Eco-Engineering Solutions for Nature-Based Coastal Defence. *Glob. Change Biol.* 24 (5), 1827–1842. Blackwell Publishing Ltd. doi:10.1111/gcb.14063

Quartel, S., Kroon, A., Augustinus, P. G. E. F., Van Santen, P., and Tri, N. H. (2007). Wave Attenuation in Coastal Mangroves in the Red River Delta, Vietnam. *J. Asian Earth Sci.* 29 (4), 576–584. Pergamon. doi:10.1016/J.JSEAES.2006.05.008

Sarabi, S., Han, Q., Vries, de, and Wendling, L. A. (2019). Key Enablers of and Barriers to the Uptake and Implementation of Nature-Based Solutions in Urban Settings: A Review. *Resources* 8 (3), 121. doi:10.3390/resources8030121

Smallegan, S. M., Irish, J. L., Van Dongeren, A. R., and Den Bieman, J. P. (2016). Morphological Response of a Sandy Barrier Island with a Buried Seawall during Hurricane Sandy. *Coast. Eng.* 110, 102–110. Elsevier B.V. doi:10.1016/j.coastaleng.2016.01.005

Stive, M. J. F., de Schipper, M. A., Luijendijk, A. P., Aarninkhof, S. G. J., van Gelder-Maas, C., van Thiel de Vries, J. S. M., et al. (2013). A New Alternative to Saving Our Beaches from Sea-Level Rise: The Sand Engine. *J. Coast. Res.* 290, 1001–1008. The Coastal Education and Research Foundation. doi:10.2112/JCOASTRES-D-13-00070.1

Sutton-Grier, A. E., Wowk, K., and Bamford, H. (2015). Future of Our Coasts: The Potential for Natural and Hybrid Infrastructure to Enhance the Resilience of Our Coastal Communities, Economies and Ecosystems. *Environ. Sci. Policy* 51, 137–148. doi:10.1016/j.envsci.2015.04.006

van Duin, M. J. P., Wiersma, N. R., Walstra, D. J. R., van Rijn, L. C., and Stive, M. J. F. (2004). Nourishing the Shoreface: Observations and Hindcasting of the Egmond Case, The Netherlands. *Coast. Eng.* 51 (8–9). Elsevier, 813–837. doi:10.1016/j.coastaleng.2004.07.011

Zhu, L., Huguenard, K., Fredriksson, D. W., and Lei, J. (2022). Wave Attenuation by Flexible Vegetation (And Suspended Kelp) with Blade Motion: Analytical Solutions. *Adv. Water Resour.* 162, 104148. Elsevier. doi:10.1016/j.advwatres.2022.104148

Zhu, L., Huguenard, K., Zou, Q.-P., Fredriksson, D. W., and Xie, D. (2020). Aquaculture Farms as Nature-Based Coastal Protection: Random Wave Attenuation by Suspended and Submerged Canopies. *Coast. Eng.* 160, 103737. Elsevier B.V. doi:10.1016/j.coastaleng.2020.103737

Zhu, L., Lei, J., Huguenard, K., and Fredriksson, D. W. (2021). Wave Attenuation by Suspended Canopies with Cultivated Kelp (Saccharina Latissima). *Coast. Eng.* 168, 103947. Elsevier B.V. doi:10.1016/j.coastaleng.2021.103947

Conflict of Interest: The authors declare that the research was conducted in the absence of any commercial or financial relationships that could be construed as a potential conflict of interest.

frontiers | Frontiers in Built Environment

ORIGINAL RESEARCH
published: 16 June 2022
doi: 10.3389/fbuil.2022.926662

Delft3D as a Tool for Living Shoreline Design Selection by Coastal Managers

Thomas P. Huff, Rusty A. Feagin and Jens Figlus*

Texas A&M University, College Station, TX, United States

Coastal risk reduction features are often built to protect infrastructure and ecosystems from damaging waves, sea level rise, and shoreline erosion. Engineers often use predictive numerical modeling tools, such as Delft3D to help design optimal intervention strategies. Still, their use by coastal managers for optimizing the design of living shorelines in complex geomorphic environments has been limited. In this study, the Delft3D modeling suite is used to help select the optimum living shoreline structure for a complex inlet and bay system at Carancahua Bay, Texas. To achieve this goal, an extensive array of sensors was deployed to collect hydrodynamic and geotechnical data in the field, and historical shoreline changes were assessed using image analysis. The measured data were then used to parameterize and validate the baseline Delft3D model. Using this validated model, the hydrodynamics resulting from a series of structural alternatives were simulated and compared. The results showed that the mouth of this complex inlet has widened greatly since the 1800s due to wave erosion and sea level rise. The analysis of the structural alternatives showed it was not advisable to attempt a return of the inlet to its historical extent, but rather to create a hybrid design that allowed for limited flow to continue through a secondary inlet. The numerical modeling effort helped to identify how to best reduce wave and flow energy. This study provides a template for the application of Delft3D as a tool for living shoreline design selection under complex shallow-estuary and inlet dynamics.

Keywords: Delft3D flow, living shorline, erosion control, flow modeling, sea level rise

Edited by:
Rodolfo Silva,
National Autonomous University of Mexico, Mexico

Reviewed by:
Debora Lithgow,
Instituto de Ecología (INECOL), Mexico
Valeria Chávez,
National Autonomous University of Mexico, Mexico

****Correspondence:***
Thomas P. Huff
thomas.huff@agnet.tamu.edu

Specialty section:
This article was submitted to Coastal and Offshore Engineering, a section of the journal Frontiers in Built Environment

Received: *22 April 2022*
Accepted: *27 May 2022*
Published: *16 June 2022*

Citation:
Huff TP, Feagin RA and Figlus J (2022) Delft3D as a Tool for Living Shoreline Design Selection by Coastal Managers. Front. Built Environ. 8:926662. doi: 10.3389/fbuil.2022.926662

INTRODUCTION

Around the globe, many estuarine basins are adjusting morphologically to maintain equilibrium with sea level rise (Morris et al., 2002; Passeri et al., 2015). Their adjustment often results in increases in depth or width to inlets, changes to tidal prism, shoreline erosion, and changes to aquatic species communities (Hoyt, 1967; White et al., 2006; Huff and Feagin, 2017). A common mitigating response is placement of erosion reduction structures such as sea walls, sand engines, or living shorelines (Williams et al., 2018). However, selection of the appropriate structure is a complex task that requires extensive knowledge of system dynamics.

One wave abatement structure that has gained popularity has been the living shoreline (Miller et al., 2016; Smith et al., 2020). This building concepts seeks to balance erosion control with long term habitat and sediment management goals. Often living shorelines are constructed in a manner to promote self healing and vertical accretion by the continued growth of oysters. Weaver et al. (2017) outlined eight ecosystem services living shorelines can provide: sediment accretion, self healing, improved water quality, improved carbon sequestration, refuge habitat, improved recreational and commercial fishing, wave energy reduction, and improved durability and resiliency over traditional

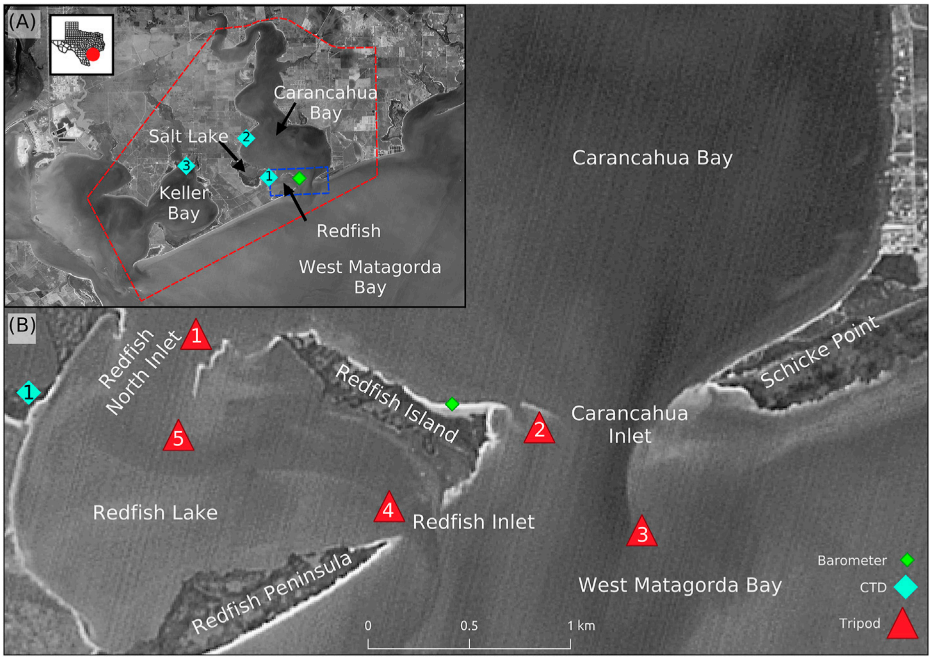

FIGURE 1 | Study area map. **(A)** indicates the study area outlined in red with the blue box indicating the extent shown in **(B)**.

structures during tropical events. These concepts have further been supported by Smith et al. (2020) and Smith (2006).

Modern management goals for living shorelines often dictate that such structures must provide aquatic habitat, reduce sediment loss through scouring, allow for safe navigation, and reduce shoreline erosion (Vona et al., 2021). Moreover, they can be expensive to construct and demand extensive input from stakeholders to appropriately balance objectives (Cooper and McKenna, 2008; Williams et al., 2018). Delft3D gives scientists a tool to quickly test potential erosion abatement designs using computer modeling. Created by Deltares, Delft3D has proven to be a powerful tool for modeling estuarine flow behavior (Elias et al., 2000; Sutherland et al., 2004). One of its more recent upgrades includes the option of flexible meshes (Deltares Flexible Mesh Suite HM 2021.03) (Delft3D [computer software], 2021) which was utilized in this study. This software allows for the flexibility to work at various spatial resolutions and is now widely used in coastal and estuarine environments (Horstman et al., 2013; Bennett et al., 2020; Muñoz et al., 2022). However, its use has been primarily restricted to traditional engineering structures, and it has not yet been widely used within the context of living shorelines.

As part of this study an attempt was made to balance between two competing interests in living shoreline design—to protect against wave erosion while avoiding an unnecessary restriction to flow to surrounding aquatic habitats. The design that maximized these two metrics was deemed to produce a positive outcome. Other factors such as sediment entrapment or habitat creation were still considered, however they were not directly quantified. Thus, sediment entrapment and habitat creation were secondary factors to wave reduction and flow velocity mitigation. To improve the chances of a positive outcome, seven design alternatives were compared in terms of their effects on hydrodynamics. The main goal of this study was to answer the following question: How will living shoreline designs alter waves and flow velocities, within the context of a complex dual inlet system that is adjusting to sea level rise?

METHODS

Study Area

The study area encompasses Carancahua Bay and parts of Matagorda Bay which lies along the Central Texas Coast in the Gulf Prairies and Marshes ecoregion. Carancahua Bay is a secondary bay to the much larger West Matagorda Bay, with distinct circulation patterns and biological production (**Figure 1A**). The bay is fed by East and West Carancahua Creeks. Redfish Lake and Salt Lake are tertiary geomorphic basins that are located near the Carancahua inlet. During the late 1980s a breach formed between Matagorda Bay and into Redfish Lake. This breach was permanent and resulted in the formation of a double inlet into Carancahua Bay (**Figure Figure1B**).

Carancahua Bay is an ideal location to explore questions about living shorelines and morphologic change, as it is at a tipping point in its geological history. The bay inlet has more than doubled in size over the last 20 years (ten-fold increase since 1872), critical habitat has been lost due to ensuing wave erosion, and the bay will soon cease to exist as a distinct circulatory unit from the adjacent Matagorda Bay. As the mouth widens, the entire bay is increasingly exposed to wave erosion and an altered hydrological,

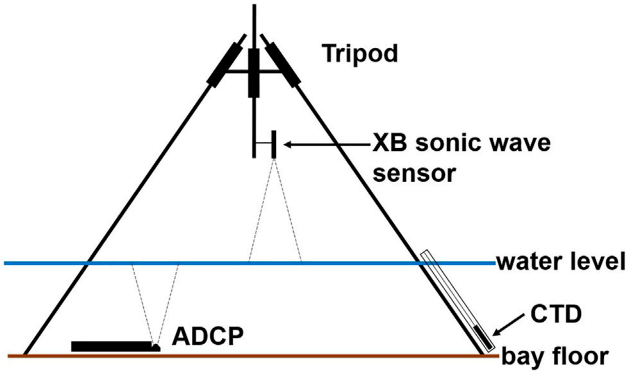

FIGURE 2 | The configuration of the sensor tripods and how the XB, ADCP, and CTD sensors were arranged.

salinity, and biological regime. Its unique role as a nursery and refuge, off-limits to commercial fishing and shrimping, is at great risk. Moreover, the large oyster reef and marsh complex at its mouth, supporting mountain laurel and migratory songbird habitat, recreational anglers, and oyster production, is rapidly eroding.

Additionally, the widening at the Carancahua Bay inlet has enhanced wave erosion and threatens public safety (Tompkins and Tresaugue, 2017). As the bay mouth proceeds to widen, the significant wave fetch across West Matagorda Bay will begin to impact the community of Port Alto. A previous living shoreline was placed at Schicke Point to mitigate erosion by an engineering firm funded by a private landowner (Freese and Nichols, 2019). This action proved to be effective at reducing shoreline erosion and encouraged sediment accumulation behind the barrier. Due to the success of the Schicke Point structure, similar structures were proposed to help mitigate erosion at Carancahua inlet. However, the placement of such a structure is complicated by a breach from West Matagorda Bay into Redfish Lake that formed in the late 1980s. This breach continues to widen and has resulted in a dual inlet mouth of Carancahua. The dual inlet system further complicates the hydrologic processes being measured and modeled.

Historic Trends

We conducted both short-term and long-term shoreline change analyses to examine the evolution of Carancahua Bay. All imagery was obtained from the Texas Natural Resources Information System (TNRIS, 2022), the US Geological Survey EarthExplorer interface (USGS, 2022), or digitized nautical maps (NOAA, 2022a).

For the short-term analysis, the shorelines were digitized by hand using aerial imagery for the dates of 1996 and 2018. The rate of shoreline retreat over this date range was then estimated along the entire shoreline. Because of the multi-directional and non-linear nature of shoreline retreat around the geomorphic features of the landscape, the rate was calculated by converting the line data shapefiles into point data with a 10 m spacing. A nearest neighbor analysis was employed to find the points in the direction with the shortest distance.

TABLE 1 | Sensors deployed on each tripod. See **Figure 1** for placement locations.

Tripod	1	2	3	4	5
XB	X	X	X	X	X
CTD			X		X
ADCP	X	X		X	

The long-term analysis assessed change between 1872 and 2018. An 1872 nautical map was georeferenced to the 2018 imagery, and then digitized. Changes from the 1872 to 2018 shoreline were referenced only qualitatively.

The shoreline change data was further examined using related bathymetric sounding datasets (NOAA, 2022a; NOAA, 2022b) and a bathymetric dataset collected in 2020. Historical soundings from 1872 to 1935 were manually entered into a Geographic Information System (GIS) as point data, then interpolated into raster using a standard Inverse Distance Weighting method. Inlet cross-section comparisons were conducted between the years 1872, 1935, and 2020, respectively.

In-Situ Data Collection

In-situ hydrodynamic and sedimentary datasets were collected for two purposes: 1) to understand the general principles of how this multiple-inlet system works, and 2) serve as validation datasets for modeling purposes.

Five sensor tripods were deployed across Carancahua Bay and West Matagorda Bay (**Figure 2**; **Table 1**) to collect hydrodynamic and environmental data. Tripods included conductivity temperature and depth (CTD) sensors (VanEssen CTD), wave sensors [Ocean Sensor Systems Sonic Xbees (XB)], and Acoustic Doppler Current Profilers (ADCP) (Nortek Aquadopp Profilers). The sensors were deployed continuously from 18 February 2020 to 2 June 2020.

The XB sensors were used to gather both wave and water level data. An initial sensor deployment on 18 February 2020 was followed up with two more deployments of radio relay stations to improve sensor range and reliability. The sensors were set to record data at 16 Hz for 2 minutes at the start of every hour. Significant wave height (H_s) was extracted from the XB wave data using the zero-up-crossing method over 120 s data segments to determine individual waves before averaging over the largest third of these waves. Tidal currents were simultaneously monitored passing through the Carancahua inlet, the southern inlet of Redfish Lake, and the connection between Carancahua and Redfish Lake, thus a total of three ADCPs were deployed at once (**Table 2**). ADCP1 was deployed in an upward-looking configuration used to measure water velocity through the water column. The barometrically compensated pressure transducer data from CTD1 was used to reference the water level to ADCP1. Both ADCP2 and ADCP4 were deployed horizontally, or side-looking, allowing them to gaze across the mouths of their respective channels and better sample a wider range of flow behavior. The side looking ADCP's were mounted on steel frames which positioned the sensor head approximately 45 cm from the bay bottom. The upward-looking ADCP was deployed on a steel frame that set into the soft bay bottom, and positioned so that the

TABLE 2 | ADCP configuration.

	Model	Hz	Range in meters	Sampling bins	Bin size (meters)	Deployment orientation
ADCP1	Nortek Aquadopp HR	2 MHz	2	20	0.1	Up-looking
ADCP2	Nortek Profiler	600 KHz	40	40	1	Side-looking
ADCP4	Nortek Profiler	100 KHz	25	25	1	Side-looking

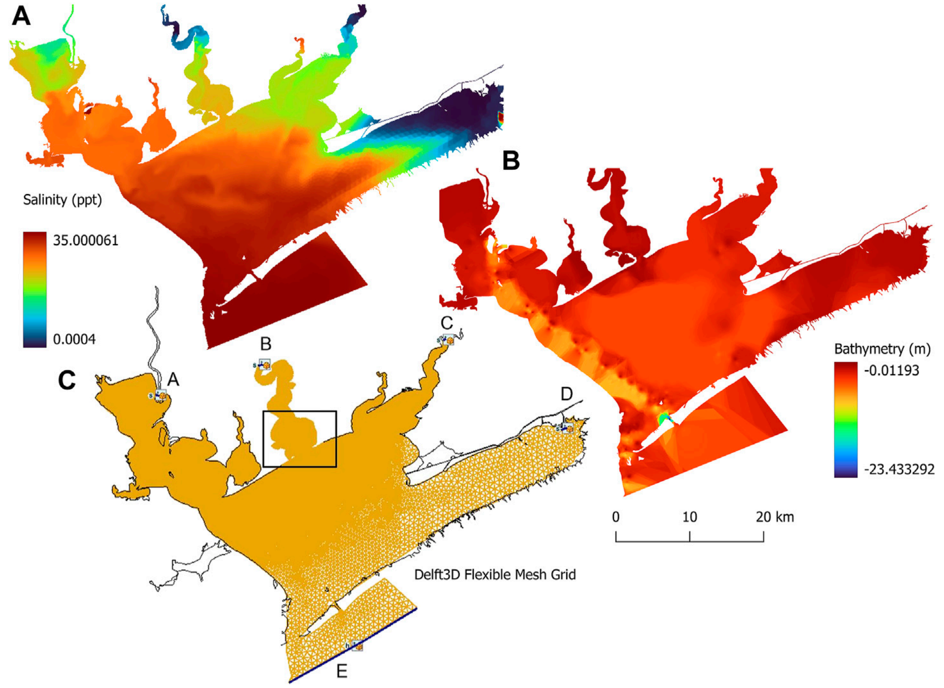

FIGURE 3 | (A) The initial salinity input map at the start date, and the integrated bathymetric map. Vertical units for bathymetry are meters (NAVD88). **(B)** Salinity units are in parts per thousand. Flow model mesh. **(C)** Input forcing locations are shown for: (A) Lavaca River input boundary, (B) Carancahua Creek input boundary, (C) Tres Palacios River input boundary, (D) Colorado River input boundary, and (E) Gulf of Mexico input boundary. The black box indicates the main area of interest were observation points and barriers were placed.

bottom of the ADCP casing just touched the bay bottom. All ADCPs were set to sample at 1 Hz for 120 s, at the beginning of every hour.

Sediment grab samples were collected from the upper 5 cm of bed sediment for sensor stands one through 5. Each sample was weighed in a dish of known volume, dried in an oven at 65°C, and reweighed in its dry condition to obtain a measure of bulk density (g/cm^3). Each sample was then sieved by using sieves ranging from 2 mm to 15.6 μm (from gravel granules to fine silt and finer). Each subset of sieved particles was weighed and standardized by the total weight of the sample. This procedure yielded the percentage of each sample that was of a given grain size. The mean sediment size was then compared to Hjulstrom-Sundborg diagram to determine settling and erosion velocities (Earle, 2019).

Modeling

The flexible mesh for the Delft3D model was created first as a grid of varying density that acts as the foundation on which all calculations are performed (**Figure 3**). All model input data is either interpolated to, or applied to, this grid.

For inputs to the models, the bathymetry was measured using a custom system composed of a linked depth finder (Matrix 12 by Humminbird) and a survey-grade Global Navigations Satellite System (GNSS) system (Trimble R10). This product was integrated with a coarser Texas Parks and Wildlife Department (TPWD) product, to retain the high resolution for the primary study areas (**Figure 3**) (TPWD, 2022). The combined bathymetry was then imported into Delft3D and interpolated to the mesh grid.

The inputs to the models included wind direction and velocity, water level, river and creek discharge, and salinity. Wind inputs were sourced from NOAA (NOAA #8773259, Port Lavaca) and applied consistently across the model (NOAA, 2022b). The winds forced the wave generation, using the Hurdle-Stive Fetch/Depth limited model available in Delft3D. Water level data were sourced from NOAA station #8775241 (Port Aransas) and used as forcing condition from 24 January 2020 through 9 July 2020 (boundary E

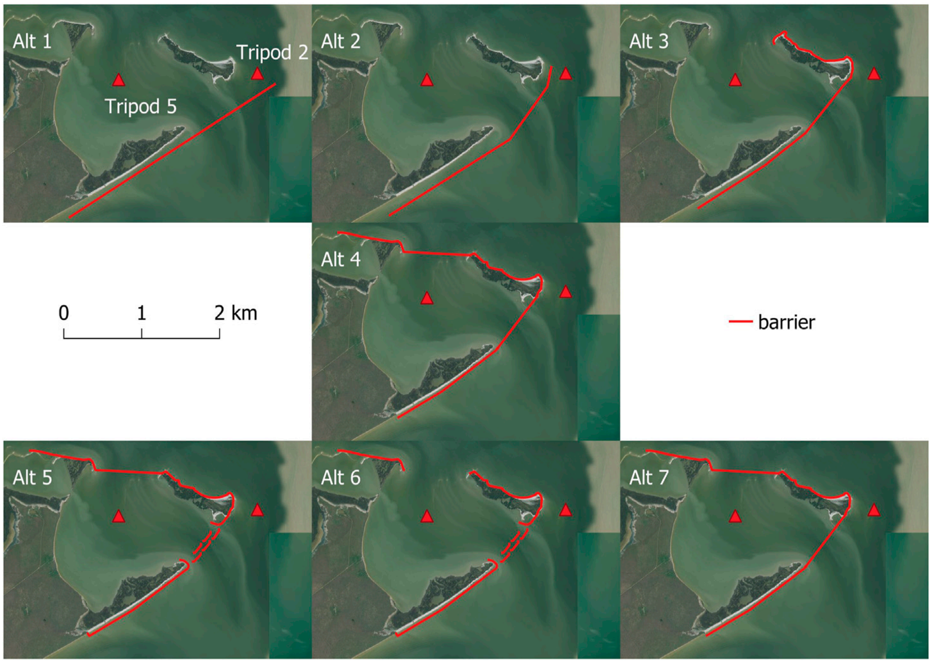

FIGURE 4 | Alternatives 1 to 4 are enclosed living shoreline designs and Alternatives 5 to 7 are hybrid living shoreline designs. See text for detailed descriptions of each. Model observation points at tripods 2 and 5 are depicted as red triangles.

TABLE 3 | Major aspects of tested design alternatives.

	Enclosed				Hybrid		
	Alt 1	**Alt 2**	**Alt 3**	**Alt 4**	**Alt 5**	**Alt 6**	**Alt 7**
Redfish Lake inlet blocked	X	X	X	X			
Redfish northern connection blocked				X	X		
Redfish Island blocked			X	X	X	X	X

in **Figure 3**). Salinity was initially set at 35 ppt at the Gulf of Mexico input location. Salinity for all freshwater inflows was set to 0 ppt. River and creek discharge volumes were gathered from USGS river flow gauges (USGS #08162501 for the Colorado river, #08164000 for the Lavaca River, and #08162600 for Carancahua Creek and Tres Palacios River) (USGS, 2022). In order to properly model salinity, an initial version of the flow model was run (with no structural designs) to properly distribute salinity across the basin (**Figure 3**). This baseline salinity output was then fed back into subsequent models to act as the starting salinity value for each node of the mesh.

The flow model simulations were run to cover dates from 24 January 2020 to 9 July 2020. Model runs typically completed in approximately 12 h on an Intel I9-10900F 10 core 20 thread CPU.

Several living shoreline designs were tested using the numerical model to meet the overall objective of protecting and enhancing habitat in Carancahua Bay, Redfish Lake, and Salt Lake. Living shoreline performance was assessed based on the structures effects on: significant wave heights, water velocity, salinity, reduction of erosion, and potential for habitat creation.

Eight separate models were run, to include seven unique design alternatives and one baseline scenario. The design alternatives can be grouped into two general categories "enclosed" versus "hybrid" as explained below and presented in **Figure 4**; **Table 3**. Unless otherwise noted below, the structures' vertical height was infinite, they were immovable, and they were modeled as "Thin Dams" in Delft3D. The purpose was to simulate the effects of wall-like structures that extended above the maximum water level, at a 30% engineering design phase.

The enclosed alternatives sought to restore the historic nature of the single inlet at Carancahua Bay inlet by extending a wall-like structure across the inlet of Redfish Lake. The main goal was to shelter Redfish Lake from southerly aspect waves and flow. Considered alternatives included:

Alt 1: "Short". This alternative tested the general effect of protecting the Redfish Lake area by blocking the Redfish inlet from waves entering from a southerly direction.

Alt 2: "Curved". This tested effects of curving the structure and more closely hugging the shorelines, while also protecting the Redfish Lake area.

FIGURE 5 | Shoreline retreat rates in the southern portion of Carancahua Bay.

Alt 3: "Extended". This tested benefits of extending the structure around Redfish Island.
Alt 4: "Full". This alternative tested benefits of fully blocking all major entrances into Redfish Lake.

The hybrid alternatives sought to retain the dual inlet system at the Carancahua Bay inlet and Redfish Lake by placing perforated structures across the Redfish Lake inlet. The main goal was to shelter Redfish Lake from southerly aspect waves, while also allowing for continued tidal exchange through it.

Alt 5: "Full Perforated". This alternative tested benefits of protecting Redfish Lake from waves using a perforated structure, through which tidal currents could flow.
Alt 6: "Full Perforated with North Open". This alternative tested benefits of a perforated structure, while the northern entrance to Redfish Lake remained open.
Alt 7: "Full V-Notch with North Open". This alternative tested benefits of a V-shaped structure across Redfish Lake inlet, while the northern entrance to Redfish Lake remained open. The structure was emergent 100% of the time in front of Redfish Peninsula and Redfish Island, but partially submerged across the Redfish Lake inlet, grading down in a V-shape to the center of the inlet. The minimum height in the center was 1 m above the bathymetric depth.

RESULTS

Historic Trends

Shoreline retreat between 1996 and 2018 averaged 27 m (median of 15 m) in Carancahua Bay, with a maximum of 293 m and a standard deviation of 37 m. On average, Carancahua Bay shorelines retreated at a rate of 1.22 m/yr. However, large stretches of the southern portion of the bay exceeded this erosion rate. Much of Redfish Peninsula averaged 7 m/yr (**Figure 5**).

From 1872 to 2018, there visually appeared to be a significant amount of change to Redfish Lake, Salt Lake, and at the Carancahua Bay inlet. Most notably, Redfish Lake was fully breached and created a southern entrance and the Redfish Peninsula shoreline retreated northward. The width of the Carancahua inlet grew from 160 m to 2,025 m (**Figure 6**). In textual notes from a related 1935 survey, the surveyor remarked that there had been significant changes in this area from the 1800s to the 1930s (from 160 to 610 m, respectively; NOAA, 2022b). A clear relationship was found between the width and relative sea level rise (0.0065 m/yr from NOAA #8771450) over this time period (**Figure 7**). The average widening rate was 12 m/yr.

Extrapolating the historical rate at which the bay mouth widened using data points from 1872, 1935, and 2020, the Carancahua inlet will erode all the way to its upland banks by 2082. This calculation used the historical relative sea level rise rate since 1904 (0.0065 m/yr), which differs from the future rate used by the model (0.0076 m/yr). The difference between these two rates is only 17% (as this area had high relative sea level change in the past due to hydrocarbon extraction-induced subsidence, which has since slowed; counter to that, future eustatic change is expected to accelerate; generally, the two offset, albeit with this 17% future increase).

Historically, the Carancahua inlet was narrower, but also considerably deeper, than it is today (**Figure 8**). Initially it was hypothesized that the inlet changes were the product of increased

FIGURE 6 | Shoreline change from 1872 to 2018.

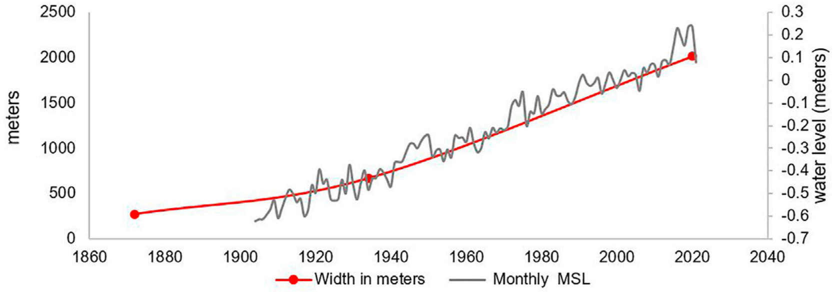

FIGURE 7 | The width of the Carancahua Bay inlet and relative water level change over time.

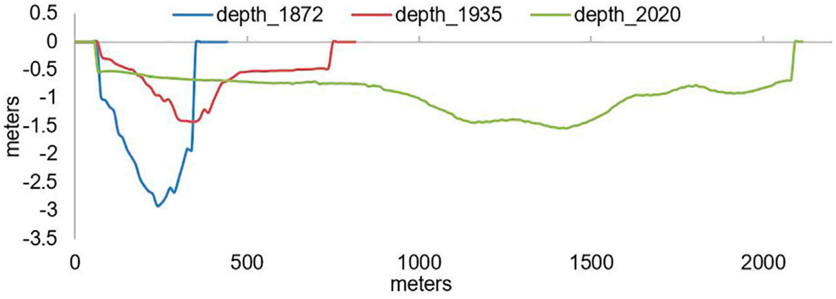

FIGURE 8 | Cross-section of the Carancahua Bay inlet over time (NE-SW direction).

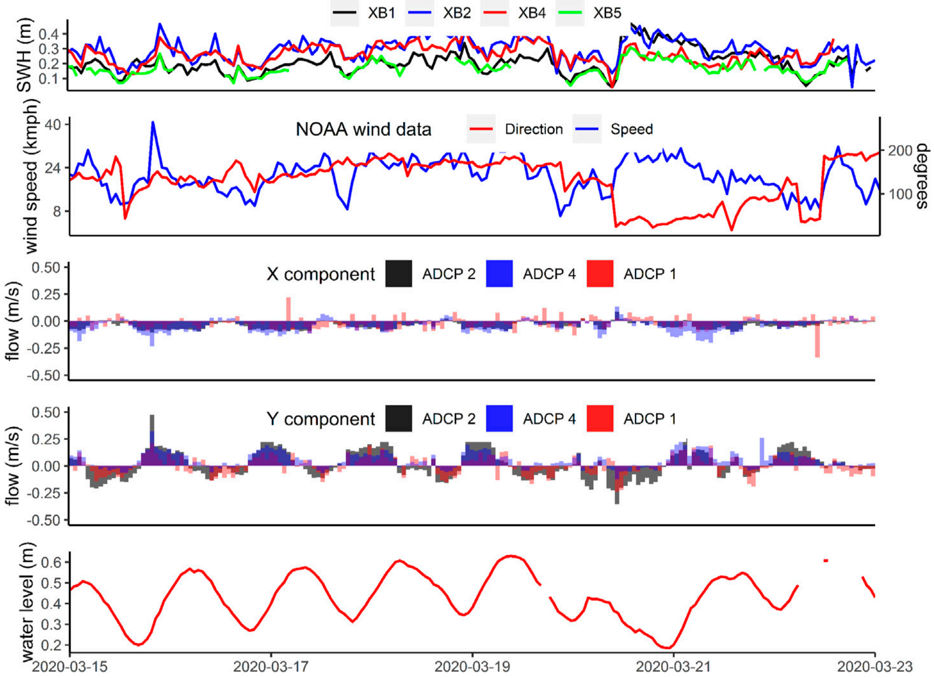

FIGURE 9 | Significant wave heights (H_2) at XB1, XB2, XB4, and XB5; NOAA wind speed and direction; ADCP1 (upward-looking, depth averaged), ADCP2 (side-looking, averaged over 20 m across bins 10–20), ADCP4 (side-looking but different model, averaged over 2 m across bins 10–20) flow direction and velocity in X and Y components; and CTD1 water level. Subplot C and D are the Cartesian coordinate components of flow with the X component corresponding to east/west flow. Positive values in subplot C indicate flow towards the east while positive values for subplot D indicate flow to the north.

flow velocities. After calculation of volumetric change over the three dates using the bathymetry and the historical relative sea level rise rate, it was found that the actual volume change could not explain the magnitude of the increase in cross-sectional opening. Additional support for the rejection of this hypothesis is that the mouth shallowed—if the disequilibrium was caused by the volume of tidal pumping alone, one would expect the depth to also increase or at least remain the same.

In-Situ Data Collection

The *in-situ* data showed that waves were similar at both the Redfish and Carancahua inlets during southerly winds (~0.3 m for gauges XB2 and XB4) wile gauges XB1 and XB5 showed lower wave heights at ~0.2 m. However, during northerly winds, gauge XB1 and XB2 showed similar wave heights at 0.3 m while XB4 was more sheltered from the waves (**Figure 9**).

The ADCP data showed average flow velocities were 0.03 m/s faster through Carancahua inlet and 0.007 m/s slower through Redfish Lake inlet than through the northern connection of Redfish Lake with Carancahua (**Figure 9**). We also found that Redfish Lake inlet (ADCP4) experienced velocities 0.06 m/s greater during the flood tide than the ebb tide. This is likely the result of the unique behavior of the dual inlet system of Carancahua Bay and Redfish Lake. Water often flowed out of Carancahua inlet (ADCP2) and into Redfish Lake during ebb tides, and the flow velocity was stronger going into Redfish (ADCP4) than coming out (**Figure 10**). A temporal shift was also seen with ADCP4 where northern flows started before and extended later than the northern flows through Carancahua inlet. This resulted in a circular flow south out of Carancahua and north into Redfish (**Figure 10**).

The sedimentary data showed a mean erosion velocity of the subtidal bottom sediments [0.35 m/s, mean grain size (mm) of 0.20] and along the unconsolidated shorelines [0.40 m/s mean grain size (mm) of 0.08] are near the peak velocities seen during the tidal cycle. Under the current wave and flow conditions at the Carancahua inlet, the mean erosion velocity of 0.35 m/s was exceeded 5.76% of the time.

Modeling

To validate the models, wave, flow velocity, water level, and salinity predictions were compared against observations. The focus was on validating the model performance against the baseline *in-situ* data across 24 January 2020 to 9 July 2020. Visual comparisons of the results at finer time scales, for example from 15 March 2020 to 23 March 2020 indicated acceptable model agreement with the field data (**Figure 11**).

Due to the tidal boundary input data not matching the location of the modeled boundary, the baseline model was tuned further using an iterative process. The tidal amplitude and timing at the Gulf of Mexico boundary was adjusted to reduce the mean error between the modeled and observed values to levels below 10% (5.22% measured deviation, mean error of 0.022 m). Mean water levels were the same between the model and observed data with the model overpredicting mean significant wave height by 0.03 m and underpredicting mean flow velocities by 0.003 m/s.

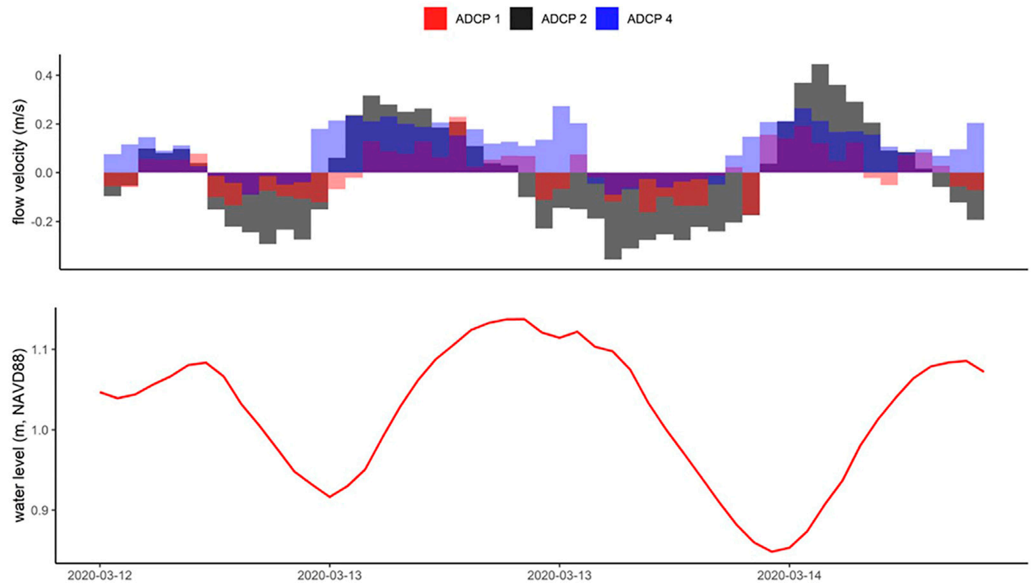

FIGURE 10 | Temporal shifts in the water flow direction at the Redfish Lake inlet (ADCP4) are both delayed and lag behind those at the Carancahua inlet (ADCP2). For several hours of the record, they flow in opposite directions.

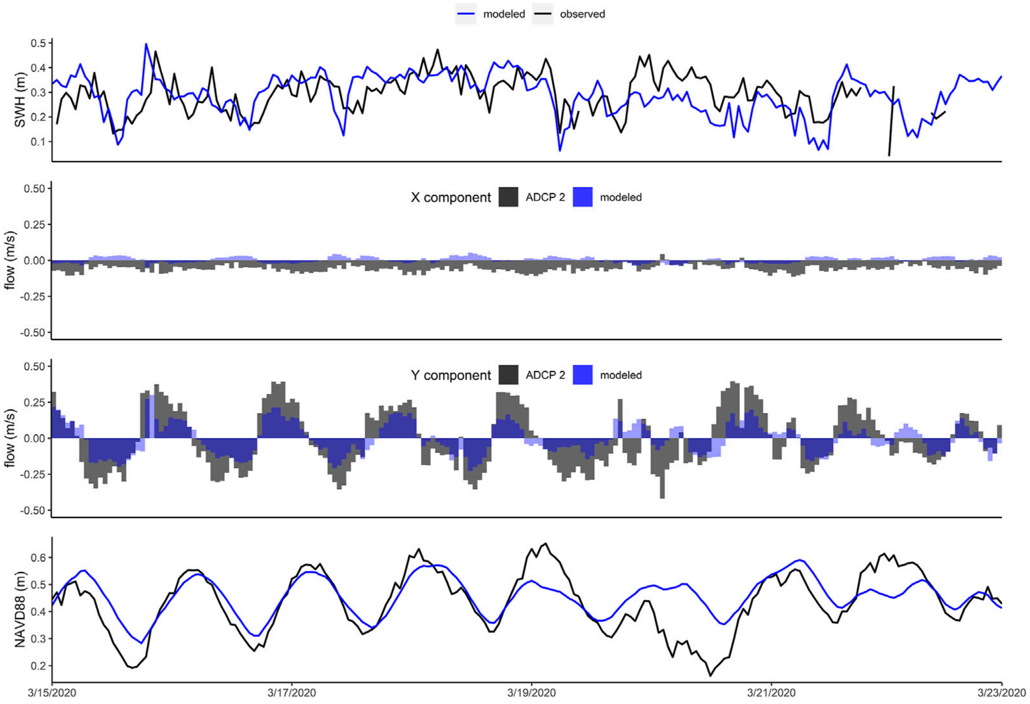

FIGURE 11 | Comparison of measured and modeled hydrodynamics at Carancahua inlet.

The largest discrepancies were found for maximum flow velocities in the north-south direction, with the model under-predicting values by 43%. At the Carancahua inlet (Tripod #2 location), the average velocities were 0.089 m/s slower in the modeled product than the ADCP data in the *Y* direction and 0.041 m/s slower in the *X* direction (**Figure 11**). The apparent differences were likely due to an incomplete representation of the intersection of Redfish Lake, Carancahua Bay, and Matagorda Bay in the Delft3D model resulting from the need for higher resolution bathymetry.

TABLE 4 | The effect of various design alternatives on existing waves and flow velocities.

	Change at the Carancahua bay Inlet (tripod 2 location)			Change in the center of redfish lake (tripod 5 location)		
	H_s	N-S velocity	E-W velocity	H_s	N-S velocity	E-W velocity
Alt 1	0%	+67%	+80%	−9%	−34%	−67%
Alt 2	0%	+33%	0%	−9%	−34%	−67%
Alt 3	0%	+33%	0%	−9%	−34%	−67%
Alt 4	0%	+20%	0%	−25%	−75%	−75%
Alt 5	0%	+20%	0%	−17%	−75%	−50%
Alt 6	0%	+13%	0%	−8%	−50%	−25%
Alt 7	0%	+27%	0%	−8%	−75%	−50%

**Percent changes are based on the design effect relative to the baseline, at the location of Tripod 2 in the Carancahua Bay inlet and Tripod 5 in the center of Redfish Lake.*

Compared to the baseline scenario, no alternatives reduced the wave energy impacting Carancahua Bay or Redfish Lake by more than 25%, in immediate terms for the year 2020 (**Table 4**).

Secondly, structures that blocked tidal flows at Redfish Lake inlet proportionally increased flows through the other side of this dual inlet. For example, Alt 2: “Curved” and Alt 3: “Extended” increased the average north-south flow velocities at the Carancahua inlet by 33% (**Table 4**).

Hybrid, perforated structures also increased velocities in the Carancahua inlet, but to a lesser extent on average (**Table 4**), for example Alt five increased them in the north-south direction by 20%. This partial blocking was deemed more acceptable in terms of quantity of time that flow exceeded the erosion threshold.

Thirdly, alternatives that avoided blocking the northern entrance to Redfish Lake relieved a portion of the energy created when partially blocking the inlet to Redfish Lake. For example, Alt six increased north-south velocities in the Carancahua inlet by only 13%, while also reducing them in Redfish Lake by −50%.

DISCUSSION

The shoreline change analysis and field datasets showed that flows through the Redfish Lake inlet were primarily generated by wave action, while those through the Carancahua inlet were primarily tidal, and this behavior is related to both tidal flow direction and wind-driven wave direction (**Figures 9**, **10**). It is likely that relative sea level rise promoted the conditions under which the waves accessed and excavated the sediments on the Redfish Peninsula; the perforation of the Peninsula was likely the direct result of wave erosion as opposed to tidal current scouring (Schwartz, 1967). Once the sediments were eroded by the waves, tidal currents then moved them out into a submerged ebb tidal shoal in West Matagorda Bay as well as entrained them into the littoral drift moving to the southwest of the Redfish Peninsula. Accordingly, it is likely the case that the widening and shallowing over time of the inlet at the Carancahua inlet is indirectly related to relative sea level rise, as waves gained access to higher sections of shoreline. These waves then loosened the sediments and tidal flow exported them.

Generally, a wall-like structure across the Redfish Lake inlet or Carancahua Bay will not greatly reduce wave heights within these basins in 2020. The fetch length within the Redfish Lake basin is sufficient to re-build the maximum wave heights that are allowable given its depths. Thus, adding a barrier to its mouth will not materially change the ability of waves larger than these heights to make it into the basin, at least in the present day under existing conditions. The same effects can be seen for Carancahua Bay (**Table 4**). However, as shown by the shoreline change analysis, waves in these basins will completely erode the Redfish Peninsula and Redfish Island by 2082. Although the results are not shown here, further modeling work corroborated this finding and showed that waves should be expected to increase three-fold between 2020 and the year 2100 in Redfish Lake and Carancahua Bay.

While many other studies examine much larger engineered structures, it has been well demonstrated that placement of hardened structures can cause unintended erosion (Toso et al., 2019). Structure placement will alter flow velocities, and closing the Redfish Lake inlet will result in a proportional increase in flow velocities in Carancahua inlet. As velocities are already exceeding the mean erosion threshold approximately 5% of the time at Carancahua inlet, any increase in velocity will further accelerate sediment transport. This situation presents challenges with any ‘enclosed’ design as increased scour at Carancahua is unavoidable. Conversely the ‘hybrid’ structures allowed for some flow relief while still providing protection long term (Khojasteh et al., 2020). The hybrid structures showed only an average of 20% increase in velocity at Carancahua inlet compared to the 38% increase with the enclosed designs. The hybrid designs offer a greater margin of safety especially when considering the added erosive energy tropical events could exert on the bay system. Moreover, our validation datasets showed that the Delft3D models underpredicted the velocities that were observed. Thus, it is likely that real-world velocities will exceed our predictions. The “enclosed” designs have the potential to cause erosion that is beyond the predictive ability covered by the current research. For this reason, the safest decision is for coastal managers to use a “hybrid” design alternative. This narrows down the possible structures to Alternatives 5–7. All three designs reduce wave heights and water velocities in the center of Redfish Lake, however, Alternatives 5 and 7 increase water velocities within Carancahua inlet by 20% or more while Alternative 6 only increased velocities 13%. A major goal was to not increase erosive velocities, therefore Alternative 6 was selected for further analysis.

CONCLUSION

Without intervention the Carancahua inlet will erode completely to the edge of the uplands to the west of the Redfish Peninsula by 2082. Carancahua Bay will fully merge with West Matagorda Bay, with detrimental consequences for wave generation, shoreline erosion, and impacts to properties and aquatic habitats.

A living shoreline structural design that allows the maintenance of the existing dual inlet system will help maintain acceptable flow velocities through the Carancahua inlet, while still creating a barrier to wave energy and reducing sediment export velocities out of Redfish Lake. For this reason, we contend that Alt 6: “Full Perforated with North Open” best mitigates wave heights, reduces erosion, and reduces risks. The selected Alt 6 design will need to undergo further analysis by a modeling specialist before implementation. The future work should include the addition of morphology in the evaluation of Alt 6 in addition to the utilization of a SWAN model to drive the wave calculations. However, this study shows the utility of Delft3D in helping to design living shorelines, particularly within the context of a complex dual inlet system that is adjusting to sea level rise.

DATA AVAILABILITY STATEMENT

The raw data supporting the conclusion of this article will be made available by the authors, without undue reservation.

AUTHOR CONTRIBUTIONS

RF acquired project funding in conjunction with JF with TH aiding in experimental design of and sensor selection. TH handled computer computation analysis with guidance of both RF and JF. TH conceived and created the figures and written material. Both JF and RF assisted with revisions and paper scope.

FUNDING

This work was supported in part by funds provided by the Texas General Land Office (20-106-000-C051) to TH, RF, and JF; US Fish and Wildlife Service to RF (FWS/R2/ES/F17AC00461); National Science Foundation (1756477) to RF; National Institute of Food and Agriculture (91380) to RF.

ACKNOWLEDGMENTS

We would like to thank the TAMU Coastal Ecology and Management Lab graduate students (Rachel Innocenti and Mathew “Jake” Madewell) for their assistance in data collection and processing. We also appreciate the help provided by Bill Balboa from the Matagorda Bay Foundation and Dave Buzan from Freese and Nichols.

REFERENCES

Bennett, W. G., van Veelen, T. J., Fairchild, T. P., Griffin, J. N., and Karunarathna, H. (2020). Computational Modelling of the Impacts of Saltmarsh Management Interventions on Hydrodynamics of a Small Macro-Tidal Estuary. *J. Mar. Sci. Eng.* 8, 373. doi:10.3390/jmse8050373

Cooper, J. A. G., and McKenna, J. (2008). Social Justice in Coastal Erosion Management: The Temporal and Spatial Dimensions. *Geoforum* 39, 294–306. doi:10.1016/j.geoforum.2007.06.007

Delft3D [computer software] (2021). Deltares. Retrieved from https://oss.deltares.nl. (Accessed May 13, 2021).

Earle, S. (2019). *Physical Geology*. 2nd Edition. Victoria, BC: BCcampus.

Elias, E. P. L., Walstra, D. J. R., Roelvink, J. A., and Stive, M. J. F. (2000). “Hydrodynamic Validation of Delft3D with Field Measurements at Egmond,” in 27th International Conference on Coastal Engineering. Sidney Australia, July 16-21, 2000.

Freese and Nichols (2019). A Living Shoreline. Available at: https://www.freese.com/a-living-shoreline/(Accessed 17 5, 2022).

Horstman, E., Dohmne-Janssen, M., and Hulscher, S. (2013). “Modeling Tidal Dynamics in a Mangrove Creek Catchment in Delft3D,” in *Coastal Dynamics*. Editors P. Bonneton and T. Garlan (Bordeaux: Bordeaux University), 833–844.

Hoyt, J. H. (1967). Barrier Island Formation. *Geol. Soc. Am. Bull.* 78, 1125–1136. doi:10.1130/0016-7606(1967)78[1125:bif]2.0.co;2

Huff, T. P., and Feagin, R. A. (2017). Hydrological Barrier as a Cause of Salt Marsh Loss. *J. Coast. Res.* 77, 88–96. doi:10.2112/si77-009.1

Khojasteh, D., Hottinger, S., Felder, S., De Cesare, G., Heimhuber, V., Hanslow, D. J., et al. (2020). Estuarine Tidal Response to Sea Level Rise: The Significance of Entrance Restriction. *Estuar. Coast. Shelf Sci.* 244, 106941. doi:10.1016/j.ecss.2020.106941

Miller, J. K., Rella, A., Williams, A., and Sproule, E. (2016). Living Shorelines Engineering Guidelines. Stevens Institute of Technology. Available at: http://stewardshipcentrebc.ca/PDF_docs/GS_LocGov/BkgrdResourcesReports/living-shorelines-engineering-guidelines.pdf.

Morris, J. T., Sundareshwar, P. V., Neitch, C. T., Kjerfve, B., and Cahoon, D. R. (2002). Response of Coastal Wetlands to Rising Sea Level. *Ecology* 83 (10), 2869–2877. doi:10.1890/0012-9658(2002)083[2869:ROCWTR]2.0.CO;2

Muñoz, D. F., Yin, D., Bakhtyar, R., Moftakhari, H., Xue, Z., Mandli, K., et al. (2022). Inter-Model Comparison of Delft3D-FM and 2D HEC-RAS for Total Water Level Prediction in Coastal to Inland Transition Zones. *J Am. Water Resour. Assoc.* 58, 34–49. doi:10.1111/1752-1688.12952

NOAA (2022a). Coast Chart #107 Matagorda Bay Texas. Historical Map and Chart Collection. Available at: https://historicalcharts.noaa.gov/image=AR22-00-1869 (Accessed 0218, 2022).

NOAA (2022b). NOAA Tides and Currents. Available at: https://tidesandcurrents.noaa.gov (Accessed 0216, 2022).

Passeri, D. L., Hagen, S. C., Medeiros, S. C., and Bilskie, M. V. (2015). Impacts of Historic Morphology and Sea Level Rise on Tidal Hydrodynamics in a Microtidal Estuary (Grand Bay, Mississippi). *Cont. Shelf Res.* 111, 150–158. doi:10.1016/j.csr.2015.08.001

Schwartz, M. L. (1967). The Bruun Theory of Sea-Level Rise as a Cause of Shore Erosion. *J. Geol.* 75, 76–92. doi:10.1086/627232

Smith, C. S., Rudd, M. E., Gittman, R. K., Melvin, E. C., Patterson, V. S., Renzi, J. J., et al. (2020). Coming to Terms with Living Shorelines: A Scoping Review of Novel Restoration Strategies for Shoreline Protection. *Front. Mar. Sci.* 7, 434. doi:10.3389/fmars.2020.00434

Smith, K. (2006). "Management, Policy, Science, and Engineering of Nonstructural Erosion Control in Chesapeake Bay: Proceeding of the 2006 Living Shoreline Summit," in Integrating Habitat and Shoreline Dynamics Into Living Shoreline Applications. Williamsburg, Virginia: Chesapeake Bay National Estuarine Research Reserve

Sutherland, j., Walstra, D. J. R., Chester, T. J., Van Rijn, L. C., and Southgate, H. N. (2004). Evaluation of Coastal Area Modelling Systems at an Estuary Mouth. *Coast. Eng.* 51 (2), 119–142. doi:10.1016/j.coastaleng.2003.12.003

TNRIS (2022). Texas Natural Resources Information System. Available at: https://tnris.org (Accessed 22 3, 2022).

Tompkins, S., and Tresaugue, M. (2017). Death of Three Hunters a Cautionary Tale. Available at: https://www.houstonchronicle.com/sports/outdoors/article/Death-of-three-hunters-a-cautionary-tale-10851671.php (Accessed 17 5, 2022).

Toso, C., Madricardo, F., Molinaroli, E., Fogarin, S., Kruss, A., Petrizzo, A., et al. (2019). Tidal Inlet Seafloor Changes Induced by Recently Built Hard Structures. *PLoS One* 14, e0223240. doi:10.1371/journal.pone.0223240

TPWD (2022). Texas Parks and Wildlife Geographic Information Systems. Available at: https://tpwd.texas.gov/gis/(Accessed 22 3, 2022).

USGS (2022). United States Geological Survey. Available at: https://waterdata.usgs.gov/nwis/rt (Accessed 22 3, 2022).

Vona, I., Palinkas, C. M., and Nardin, W. (2021). Sediment Exchange between the Created Saltmarshes of Living Shorelines and Adjacent Submersed Aquatic Vegetation in the Chesapeake Bay. *Front. Mar. Sci.* 8, 727080. doi:10.3389/fmars.2021.727080

Weaver, R. J., Stehno, A., Bonanno, N., Sager, A., Kenny, A., Zehnder, J. A., et al. (2017). Scale Model Design of Oyster Reef Structures as Part of a Showcase Living Shoreline Project. *Shore Beach* 85, 41–54.

White, W. A., Tremblay, T. A., Waldinger, R. L., and Calnan, T. R. (2006). *Status and Trends of Wetland and Aquatic Habitats on Texas Barrier Islands, Coastal Bend*. Austin, Texas: The University of Texas at Austin, Bureau of Economic Geology Final Report Prepared for Texas General Land Office and National Oceanic and Atmospheric Administration Under Contract 05-041, 65.

Williams, A. T., Rangel-Buitrago, N., Pranzini, E., and Anfuso, G. (2018). The Management of Coastal Erosion. *Ocean Coast. Manag.* 156, 4–20. doi:10.1016/j.ocecoaman.2017.03.022

Conflict of Interest: The authors declare that the research was conducted in the absence of any commercial or financial relationships that could be construed as a potential conflict of interest.

The handling editor RS declared a past co-authorship with the author RF.

Frontiers in Built Environment

ORIGINAL RESEARCH
published: 17 June 2022
doi: 10.3389/fbuil.2022.884849

Assessing Wave Attenuation With Rising Sea Levels for Sustainable Oyster Reef-Based Living Shorelines

Reza Salatin[1], *Hongqing Wang*[2], *Qin Chen*[1,3]* *and Ling Zhu*[1]

[1]Department of Civil and Environmental Engineering, Northeastern University, Boston, MA, United States, [2]U.S. Geological Survey, Wetland and Aquatic Research Center, Baton Rouge, LA, United States, [3]Department of Marine and Environmental Sciences, Northeastern University, Boston, MA, United States

In densely populated coastal areas with sea-level rise (SLR), protecting the shorelines against erosion due to the wave impact is crucial. Along with many engineered structures like seawalls and breakwaters, there are also green structures like constructed oyster reefs (CORs) that can not only attenuate the incident waves but also grow and maintain pace with SLR. However, there is a lack of data and understanding of the long-term wave attenuation capacity of the living shoreline structures under SLR. In this study, we used the phase-resolving Boussinesq model, FUNWAVE-TVD, to examine the hydrodynamics including wave height and wave-induced currents around the CORs in the Gandys Beach living shoreline project area in the upper Delaware Bay, United States. Waves were measured at six locations (offshore to onshore, with and without CORs) in the Gandys Beach living shoreline project area for two winter months, during which four nor'easters occurred. We selected three cases that represent prevailing wind, wave, and tide conditions to examine the fine spatial and temporal changes in wave height and current velocity by the construction of the reefs. Wave heights and wave energy spectra generated from FUNWAVE-TVD were then validated with field observations. It is found that FUNWAVE-TVD is capable of simulating waves and associated hydrodynamic processes that interact with CORs. The model results show that wave attenuation rates vary with the incident wave properties and water depth, and wave-induced circulation patterns are affected by the CORs. The wave attenuation capacity of CORs over the next 100 years was simulated with the incorporation of the oyster reef optimal growth zone. Our study found that sustainable wave attenuation capacity can only be achieved when suitable habitat for COR is provided, thus it can vertically grow with SLR. Suitable habitat includes optimal intertidal inundation duration, current velocity for larval transport and settlement, on-reef oyster survival and growth, and other environmental conditions including salinity, temperature, and nutrient availability. Furthermore, the model results suggest that it would take CORs approximately 9 years after construction to reach and maintain the maximum wave attenuation capacity in sustainable living shorelines.

Keywords: constructed oyster reef, current velocity, FUNWAVE-TVD model, living shoreline, optimal growth zone, sea-level rise, wave attenuation

Edited by:
Jane McKee Smith,
Engineer Research and Development
Center (ERDC), United States

Reviewed by:
Matt Malej,
Engineer Research and Development
Center (ERDC), United States
Alec Torres-Freyermuth,
Instituto de Ingeniería, Universidad
Nacional Autónoma de México,
Mexico

****Correspondence:***
Qin Chen
q.chen@northeastern.edu

Specialty section:
This article was submitted to
Coastal and Offshore Engineering,
a section of the journal
Frontiers in Built Environment

Received: *27 February 2022*
Accepted: *09 May 2022*
Published: *17 June 2022*

Citation:
Salatin R, Wang H, Chen Q and Zhu L
(2022) Assessing Wave Attenuation
With Rising Sea Levels for Sustainable
Oyster Reef-Based Living Shorelines.
Front. Built Environ. 8:884849.
doi: 10.3389/fbuil.2022.884849

INTRODUCTION

Wind waves are one of the critical forces that cause shoreline erosion and retreat along coasts (Marani et al., 2011; Leonardi et al., 2016). With climate change and increasing sea levels, the threat of erosion and flooding along the coastlines is looming (Morris, et al., 2018). To prevent coastal shoreline retreat, traditional methods, such as seawalls, bulkheads, groins, and revetments have been used. These structures may not be sustainable because they are likely to be either overtopped or submerged as the sea-level rises and consequently lose their functionality as shoreline protection structures. An increasing number of green infrastructure or living shoreline structures (LSS) have been proposed and applied in coastal shoreline protection (Manson et al., 2018; Chowdhury et al., 2019; Morris et al., 2021; Polk et al., 2022). The specific LSS types include coastal vegetation, oyster reefs, seagrass, and coral reefs. These nature-based approaches can provide not only shoreline protection but also improve habitat suitability for fish and native wildlife species.

However, there is a lack of data on wave attenuation by LSS. Our understanding of LSS effects on wave processes and the controlling factors of sustainability remains incomplete, thus limiting the effectiveness of living shoreline projects for adaptive monitoring and management (Wang et al., 2021). Such data gaps and incomplete understanding of wave dynamics along living shorelines can be attributed to 1) insufficient wave monitoring stations along the shoreline to measure wave processes such as wave shoaling, reflection, refraction, diffraction, and breaking across LSS and detect local wave energy changes induced by individual structures over the project area with varying topography and bathymetry, and 2) short wave monitoring period (e.g., hours to a few days) that may not cover the critical wind, wave, and tide conditions (e.g., storms). Therefore, the project level and long-term effects of LSS on wave attenuation, or the sustainable wave attenuation capacity of LSS under climate change, could not be robustly assessed.

Oyster reef-based living shorelines are becoming increasingly popular because they can provide both wave attenuation and suitable habitats for oysters, fish, and other species (Rodriguez et al., 2014; Morris et al., 2019; Wang et al., 2021). They can artificially be built by stacking concrete blocks and letting the oysters grow on these blocks (Theuerkauf et al., 2015; Wang et al., 2021). Moreover, they are believed to be an effective alternative to the traditional and unsustainable coastal erosion defense structures (Morris et al., 2018, 2019). However, a growing number of coastal scientists and managers have noted the value of both engineering and ecological benefits in the design and implementation of living shoreline projects to achieve sustainable living shorelines (Morris et al., 2019; Fivash et al., 2021; Morris et al., 2021). Because, on one hand, constructed oyster reefs (CORs) need to maintain their height at an emergent elevation to ensure maximum wave attenuation, since wave attenuation capacity is closely related to the freeboard (the difference between water surface elevation and COR crest elevation) (Wiberg et al., 2019; Zhu et al., 2020). On the other hand, COR needs to grow vertically to maintain pace with SLR and maintain its crest elevation in the optimal growth zone (OGZ), which is the elevation range for oyster reefs with inundation duration of 60–80% (or 20–40% exposure) of the time (Ridge et al., 2015; Morris et al., 2021). Ridge et al. (2015) found that oyster reef growth is unimodal, relative to emergence with greatest growth rates occurring at 60–80% inundation duration, and zero-growth at >90% and <45% inundation duration. Thus, oyster life cycles including larval movement, recruitment, on-reef growth, reproduction, and mortality are considerations in these restoration plans (La Peyre et al., 2021).

In addition to the OGZ, current velocity is closely associated with LSS and would affect the oyster life cycle from larval transport, and settlement to on-reef survival and growth Currents affect sediment transport, eventually leading to sediment deposition and erosion along the shorelines. In addition, current velocity was found to be a critical factor affecting oyster larval transport and settlement, nutrient availability, oyster filtration, and oyster growth and mortality (Harsh and Luckenbach, 1999; Smith et al., 2009; Campbell and Hall, 2019; Theuerkauf et al., 2019; La Peyre et al., 2021; Lipcius et al., 2021). LSS-induced circulation patterns and current velocity changes are rarely investigated in assessing the effectiveness of oyster reef-based living shoreline projects. Although the impact of current velocities on various oyster life stages is still debated, it is found that a current velocity below 15 cm/s would be optimal for required nutrient delivery and oyster filtration (Theuerkauf et al., 2019).

Overall, the effectiveness of CORs as an alternative to traditional breakwaters is unclear due to the potential disconnects between the ecological and engineering functions of the reefs which may result in failure to optimize either of these goals (Morris et al., 2019). Moreover, the processes and mechanisms of oyster reef–induced wave attenuation are still not clear and therefore put a constraint on the assessment of their effectiveness for shoreline protection (Zhu et al., 2020; Wang et al., 2021). Zhu et al. (2020) and Wang et al. (2021) conducted field observations and analyzed the effectiveness of CORs based on field data. They obtained valuable insights into the wave attenuation capacity of CORs along a specific transect with a few *in situ* measurements for 2 months in 2018. Wang et al. (2022a) used the scientific machine learning techniques to extend the 2-month field observations in Gandys Beach to multiple years, allowing for an estimate of annual wave power to correlate with marsh edge erosion. No physics-based numerical model was used in their study. This study investigates the effectiveness of CORs through numerical modeling using FUNWAVE-TVD and quantifies the wave height changes in the entire simulation domain, including the area protected by CORs, under representative wave conditions. Field measurements are necessary and extremely valuable albeit at a limited number of locations. However, the phase-resolving model results provide insights into both the wave and current fields at any point of the domain with and without the presence of CORs. The validated numerical model can be used as a tool to isolate the effects of local bathymetric changes or structures like CORs on wave processes from other factors like wave shoaling and diffraction and thus,

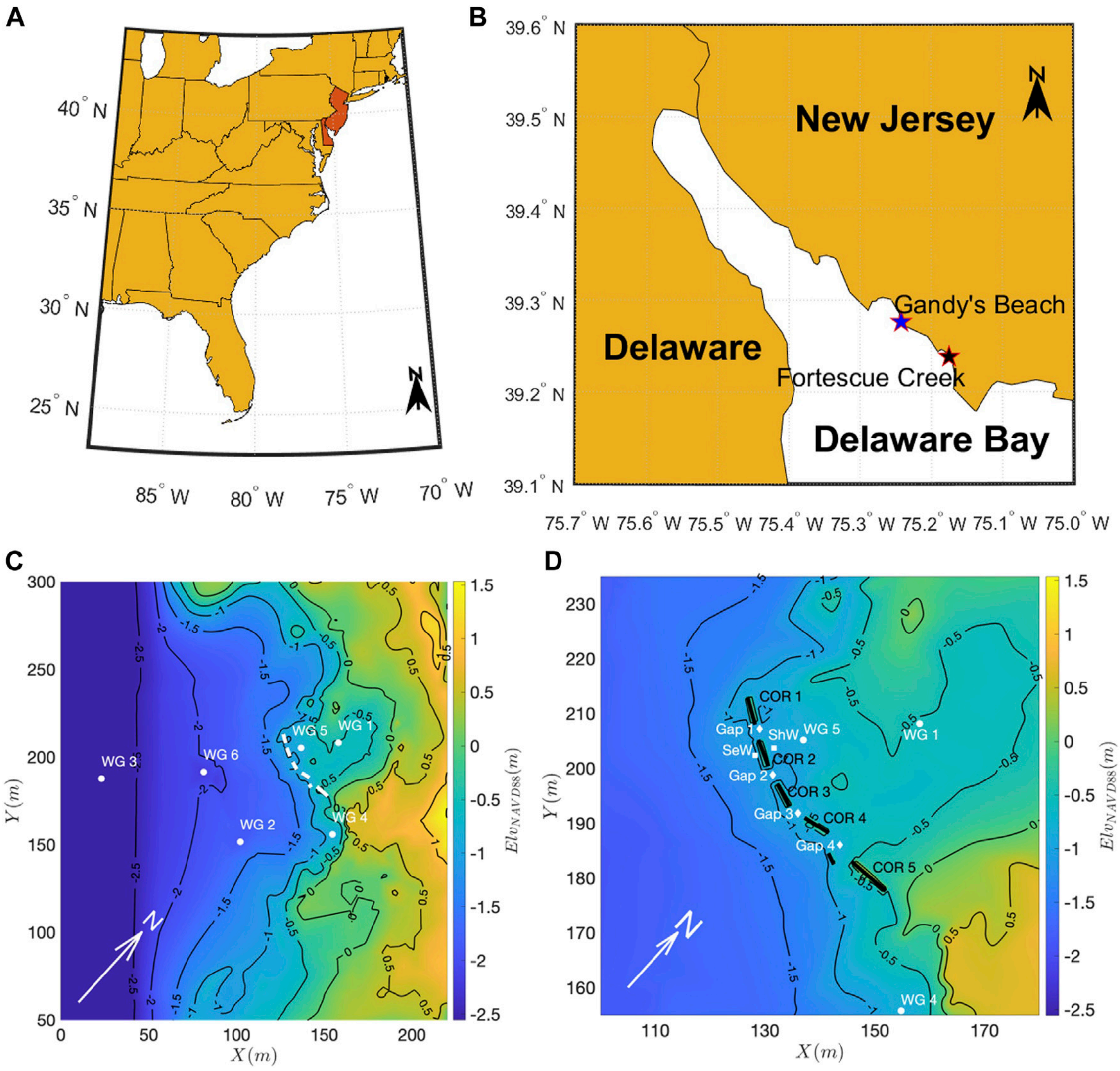

FIGURE 1 | (A) Map showing the location of Delaware Bay between New Jersey and Delaware in the United States, **(B)** map showing the location of Gandys Beach and the Fortescue Creek station in Delaware Bay, **(C)** topography of Gandys Beach (NAVD88) and location of six wave gauges, and **(D)** detailed view of the CORs in Gandys Beach. CORs are named COR 1 to COR 5 from the uppermost COR downward. Six additional numerical wave gauges are placed around the CORs including Gap1–4, SeW, and ShW in FUNWAVE-TVD. Gap 1 to Gap 4 refer to the gaps between the COR segments, SeW is seaward of COR 2, and ShW is behind COR 2.

provide a holistic view of wave attenuation capacity of CORs compared to field measurements.

In this study, our objectives are to 1) calibrate and validate a numerical wave model with high spatial and temporal resolution for wave and current simulations in the Gandys Beach living shoreline area within upper Delaware Bay, United States; 2) quantify local wave attenuation with and without CORs; 3) examine wave-induced circulation patterns and current velocity changes with and without CORs; and 4) determine if the wave attenuation capacity of COR can be maintained under SLR by taking the OGZ and current velocity into consideration. Data and information from this study could be helpful for adaptive monitoring and management of the design and implementation of sustainable living shorelines under climate change and rising sea levels.

MATERIALS AND METHODS

Study Area

A total of 914 m of living shoreline was constructed in 2016 to withstand future storms and reduce erosion along the shoreline between Money Island Marina and Gandys Beach, New Jersey, in upper Delaware Bay, United States (Wang et al., 2021). The study site is located near Gandys Beach as shown in **Figures 1A,B**. CORs (also called oyster castles, made of prefabricated concrete blocks) were constructed as a critical part of the living shoreline project. The CORs provide a segmented line of protection (**Figures 1C,D**) for the shoreline with blocks of 2.4–7.0 m in length, 0.5–0.9 m in width, 0.4–0.8 m in height, and an average gap of 3.9 m between the segments (Zhu et al., 2020). Fortescue Creek, NJ (Station ID:

8536931) is the closest tide station located 7 km to the southeast of the site. Considering the mean low water (MLW) as the datum, elevations of mean sea level (MSL), North American Vertical Datum (NAVD88), and mean high water (MHW) are 0.92, 0.93, and 1.78 m, respectively. Thus, the mean tidal range at this site is 1.78 m and the average elevation of the COR base is −0.01 m (MLW), meaning that CORs are emergent only in low tide conditions.

Field Data and Test Cases

Six wave gauges (Ocean Sensors Systems Inc., OSSI-010-003C) were deployed on the bed at the study site in 2018 (Wang et al., 2020). As illustrated in **Figure 1C**, wave gauge 3 (WG3) was the most offshore wave gauge used as the offshore boundary condition for the numerical experiment. Wave gauge 6 (WG6) was midway between WG3 and concrete blocks. Wave gauge 5 (WG5) was immediately behind the COR and was lying on the mud floor to assess the change in the energy of the waves passing over the concrete blocks. Wave gauge 1 (WG1) was also located shoreward of the concrete blocks on a marsh platform and was the least submerged wave gauge at the site. Wave gauge 2 (WG2) and wave gauge 4 (WG4) formed a reference transect parallel to the monitoring transect across CORs. Topography of the study area and the COR geometry were also surveyed during the deployment, checkup, and retrieval phases with a static global navigation satellite system (GNSS). The horizontal and vertical accuracies of the survey are 0.015 and 0.03 m, respectively.

Water pressure was recorded in 20-min bursts once every 30 min with a sampling frequency of 10 Hz. The pressure data were then converted to wave energy spectra using OCEANLYZ (Karimpour and Chen, 2017). The spectra computed from the measured data were used to obtain the zero-moment wave height (H_{m0}) and peak period (T_p) of the waves during the selected timestamps as follows:

$$H_{m0} = 4\sqrt{m_0} = 4\sqrt{\int_{f_{min}}^{f_{max}} S_{\eta\eta}(f)df}, \quad (1)$$

$$T_p = \frac{1}{f_p}, \quad (2)$$

where m_0 is the zero-moment or area under the wave energy spectrum, $f_{min} = 0.04Hz$ and $f_{max} = 0.4\,Hz$ are the energy spectrum frequency cutoffs, $S_{\eta\eta}(f)$ is the energy spectrum value corresponding to frequency f, and df is the frequency discretization resolution. f_p is also the peak wave period of the output energy spectrum.

We selected three cases that represent prevailing wind, wave, and tide conditions to examine the fine spatial and temporal changes in wave height and current velocity by the construction of reefs. The three representative cases are selected from the measured time series in 2018 with nor'easters and are provided in **Table 1**. The peak wave period (T_p), zero-moment wave height (H_{m0}), MWL, freeboard (R_c), and mean wave direction (θ_m) of the representative cases at the offshore WG3 are listed in this table. Because the offshore wave direction was not measured, the third-generation wind wave model, Simulating WAves Nearshore (SWAN) (Booij et al., 1999) coupled with Delft3D-FLOW (Deltares, 2013) was employed to simulate the wave characteristics at WG3 and provide the mean wave direction (θ_m) of the wave field and directional spreading (σ_θ) in different frequency ranges for the selected cases. A three-level nesting approach is implemented in the coupled models. The mesh size gradually reduces from 40 km in deep basins and flat shelves in the North Atlantic Ocean (in the first level mesh), to 1.8 km in the adjacent continental shelf outside of Delaware bay (in the second level mesh), and eventually to 3 m near CORs at the study site (in the third level mesh). The computational domains of the Delft3D-FLOW and SWAN-coupled model and the FUNWAVE-TVD model are provided in **Supplementary Figure S1**. The time series of the modeled and measured H_{m0} and T_p is also plotted in **Figure 2**. At the selected timestamps, modeled H_{m0} and T_p are, respectively, 0.19 m and 16 s for Case 1, 0.46 m and 3.5 s for Case 2, and 0.53 m and 3 s for Case 3. Overall, the coupled model results achieve good agreement with measurements for the selected cases except that the T_p is overestimated for Case 1. The measured wave spectrum at WG3 of Case 1, demonstrated in **Supplementary Figure S2**, shows that the peak energy density of swell and wind sea are close. It is very possible that SWAN modeled larger swell energy at this timestamp and picked the swell peak frequency to calculate the peak wave period.

The selected cases are from March 2018, where energetic waves are due to nor'easters with heavy precipitation, destructive winds, and coastal flooding. The cumulative distribution functions for the zero-moment wave height as well as the peak wave period for the year 2018 are depicted in **Figure 3**. The selected H_{m0} are in 46th, 92nd, and 97th percentile for the year 2018 for Cases 1–3, respectively. For selected T_p in Cases 1–3, the percentiles are 98th, 99th, and 90th, respectively. The freeboard, which is one of the main factors impacting the COR-induced wave attenuation, is similar in Case 1 and Case 3, meaning that CORs in these cases are nearly emergent, whereas in Case 2 the freeboard is lower, making the corresponding COR completely submerged for Case 2. For all cases, COR 2, which is the most adjacent COR segment to WG5 as marked in **Figure 1D**, is submerged. However, all cases have different mean wave directions, making each case unique. Waves propagate approximately from the south in Case 1, from the west in Case 2, and from the southwest in Case 3. In addition, the stability and accuracy of the Boussinesq model, which depends on the offshore wave properties like wave height, wave period, and water depth (Suanda et al., 2016), were also considered in selecting the representative cases.

FUNWAVE-TVD

For living shorelines, wave processes interact with LSS (e.g., CORs), resulting in complex wave and current dynamics that occur across multiple temporal and spatial scales. Previous studies on wave attenuation along living shorelines (Wiberg et al., 2019; Wang et al., 2020; Zhu et al., 2020; Wang et al., 2021) did not provide detailed information on wave dynamics and circulation patterns affected by the living shoreline (e.g., salt marshes and oyster reefs). This is mainly due to the lack of data in field measurements. In the current study, we provide high spatial and temporal resolution information and analyses on nearshore wave processes along the living shoreline in Gandys Beach to understand the complicated flow field near CORs using the total variation diminishing (TVD) version of the fully nonlinear Boussinesq wave model, FUNWAVE-TVD (Shi et al., 2012). FUNWAVE-TVD integrates high-fidelity Boussinesq-type

TABLE 1 | Representative study cases.

Case	Date and time	T_p	H_{m0} (WG3)	MWL[a]	R_c (COR 2)[b]	R_c/H_{m0}	θ_m[c]
1	2018-03-07, 08:00	3.79 s	0.13 m	0.90 m	–0.24 m (S)	–1.85	194°
2	2018-03-13, 19:30	4.05 s	0.38 m	1.74 m	–1.08 m (S)	–2.84	273°
3	2018-03-15, 10:30	3.23 s	0.49 m	0.86 m	–0.20 m (S)	–0.41	232°

[a] *Mean water level (mean low water as the reference datum).*

[b] *Crest freeboard (vertical distance from the water surface to the crest of COR 2).*

[c] *Mean wave direction (clockwise from true north).*

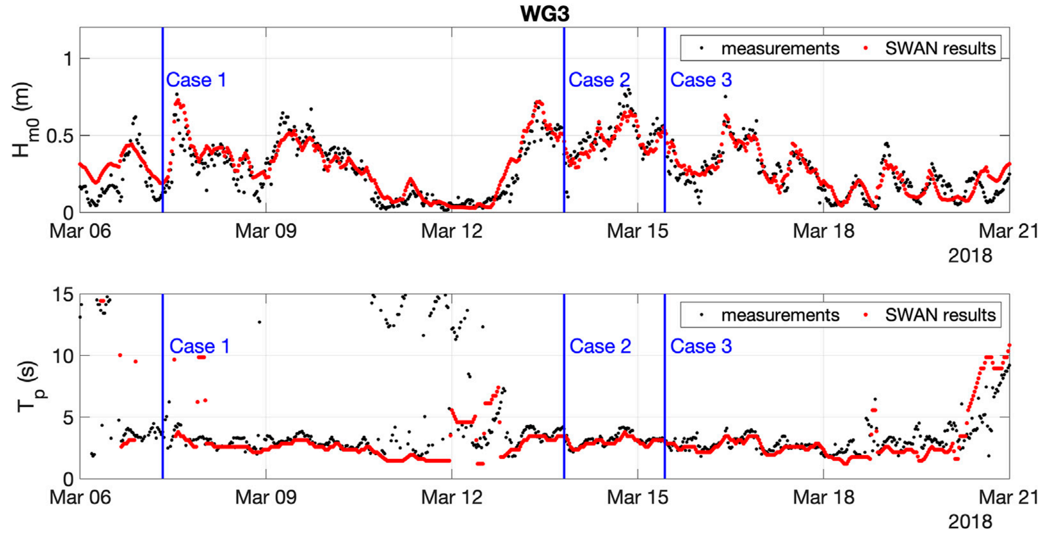

FIGURE 2 | Time series of the measured and modeled (SWAN) H_{m0} and T_p at offshore wave gauge (WG3). Three representative cases are denoted by the blue lines.

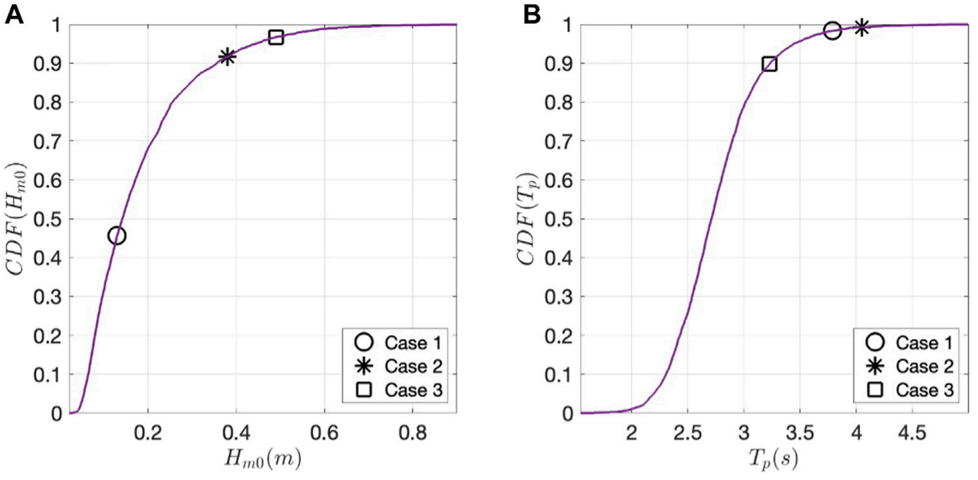

FIGURE 3 | Cumulative probability distribution functions (CDF) for the **(A)** zero-moment wave height and **(B)** peak wave period for the year 2018 with the representative cases marked on the figure.

modeling of wave transformation, interaction, and response with a range of coastal structure properties; thus, it can be a robust and computationally efficient tool for the design of LSS in the context of wave and current energy attenuation. In this study, FUNWAVE-TVD is used to simulate the three representative cases.

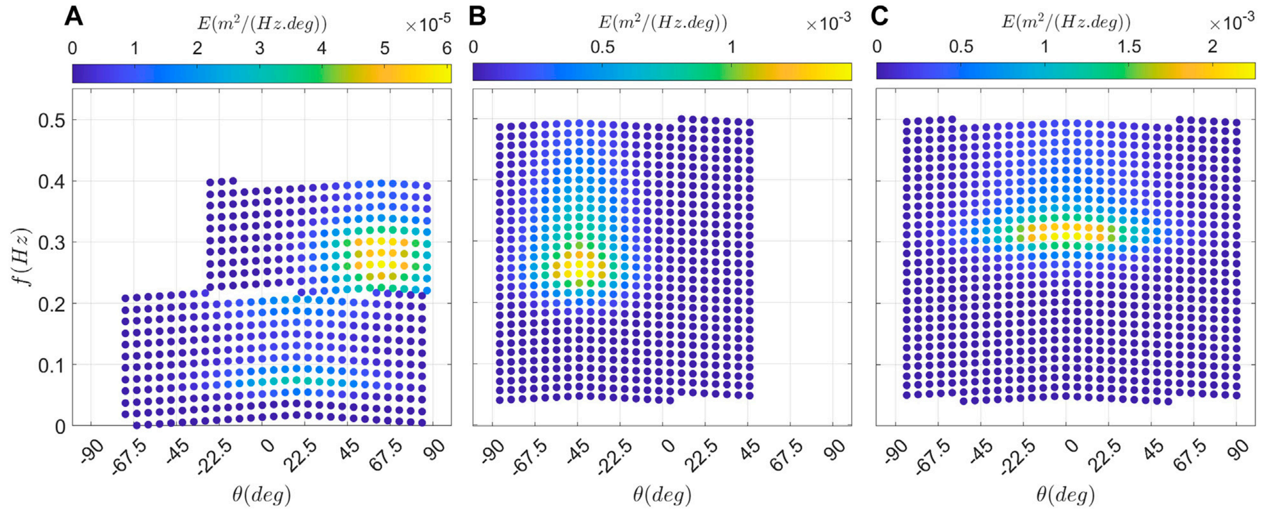

FIGURE 4 | Wave energy spectra at the offshore boundary for **(A)** Case 1, **(B)** Case 2, and **(C)** Case 3.

The depth-integrated continuity equation of FUNWAVE-TVD is given as follows:

$$\eta_t + \nabla \cdot \mathbf{M} = 0, \qquad (3)$$

where η is the water surface elevation and $\mathbf{M}$ is the horizontal volume flux. The depth-averaged horizontal momentum equation is as follows:

$$\mathbf{u}_{\alpha,t} + (\mathbf{u}_\alpha \cdot \nabla)\mathbf{u}_\alpha + g\nabla\eta + \mathbf{V}_1 + \mathbf{V}_2 + \mathbf{V}_3 + \mathbf{R} = 0, \qquad (4)$$

where $\mathbf{u}_{\alpha,t}$ and $\mathbf{u}_\alpha$ are the local acceleration and velocity at the reference level (α), respectively, η is the surface elevation, g is the gravitational acceleration, $\mathbf{V}_1$ and $\mathbf{V}_2$ are the dispersive Boussinesq terms, $\mathbf{V}_3$ is a second-order term of vertical vorticity, and $\mathbf{R}$ represents the diffusive and dissipative terms like wave breaking, bottom friction, and subgrid lateral turbulent mixing (Chen et al., 2003; Chen, 2006; Shi et al., 2012).

The outputs from FUNWAVE-TVD include high temporal and spatial resolution water surface elevation, wave height, and current field. The model inputs for this study were taken from the offshore wave gauge (WG3) deployed in Gandys Beach to record wave data over 2 months in the year 2018. This nearly 2-month period from February to March had four nor'easters (Zhu et al., 2020), allowing us to investigate the wave processes in the presence of CORs under storm conditions. Directional wave energy spectra for the representative cases are shown in **Figure 4**. These spectra are given as input to FUNWAVE-TVD. The input wave spectra are discretized with the method described in Salatin et al. (2021), which is a modified version of the Wei et al. (1999) wavemaker to avoid longshore variation of wave height due to wave coherence in the wave field.

In FUNWAVE-TVD, the simulation domain uses the bathymetry surveyed during the deployment and retrieval phases, which also includes the CORs as impermeable bathymetric features. The bathymetry is discretized with a grid size of 0.2 m in both directions. Lateral boundaries are set to periodic and the offshore boundary behind the wavemaker is equipped with sponges of 15 m length to dissipate the outgoing waves and prevent them from reflecting into the domain. Friction sponge with $C_{d_{\max}} = 1.0$ and L-D type sponge (Larsen and Dancy, 1983) with free parameters $\gamma_s = 0.85$ and $\alpha_s = 2.0$ (Chen et al., 1999) are used for wave absorption. To suppress the artificial longshore currents forming at the wavemaker, a localized higher bottom friction factor ($C_d = 0.2$) is used, as opposed to a lower bottom friction factor ($C_d = 0.002$) used at the rest of the domain. The eddy viscosity-based parameterization of wave breaking (Kennedy et al., 2000) is used with $C_1 = 0.45$ and $C_2 = 0.35$. The wavemaker width parameter (δ) is equal to 0.6 for all cases. The CFL number for Case 1 and 2 is 0.3, and for Case 3 is 0.1, which were selected through trial and error based on stability and efficiency of the numerical simulations.

The numerical simulation of FUNWAVE-TVD is run for 30 min for each case. The first 10 min of the simulation is considered as the spin-up to let the high-frequency waves arrive at the shoreline. Moreover, nearshore circulation also matures within the spin-up interval as the wave field becomes fully developed, thus giving a more accurate mean current field at the end of the simulation. Then, mean properties are obtained in the last 20 min of simulation, and that is equal to 317, 296, and 371 peak periods for Case 1, 2, and 3, respectively. In addition, to replicate the physical field setup of actual wave gauges, six numerical wave gauges are also included in the numerical model domain to obtain the water surface elevation and orbital velocities at the same locations of WG1-6. Like the field wave gauges, model wave gauges are also set to a sampling frequency of 10 Hz. The model results, including output wave energy spectra and wave heights, are then compared to field measurements for model validation. Since the current velocity in the field is composed of tidal- and wave-induced currents, and FUNWAVE-TVD only generates wave-induced currents, current velocity is not considered in model validation.

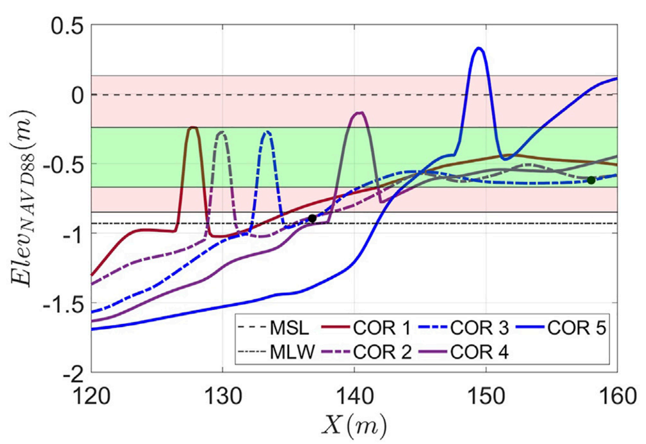

FIGURE 5 | Cross-sectional view of the five COR segments, water levels (MSL and MLW), OGZ (green area), and the interval between OGZ and CEB (red area). Black dots denote the locations of WG5 (left) and WG1 (right).

To investigate the effects of CORs on wave attenuation and the wave-induced current fields upon model validation against the measured field data, numerical experiments are conducted under the same offshore wave conditions and modified bathymetries, in which the CORs are intentionally removed. The two bathymetry settings are analyzed and wave heights and current fields in both bathymetry settings are compared. FUNWAVE-TVD's ability to resolve the CORs and the wave-structure interaction with high resolution makes it possible to assess the wave height variations around CORs. Because FUNWAVE-TVD outputs the wave height and current field all over the domain with a high spatial and temporal resolution, it helps to understand the potential of CORs in wave height attenuation and nearshore circulation variations in a way that is not possible through *in situ* measurements with wave gauges and current meters deployed at a few locations.

FUNWAVE-TVD provides the spatial distributions of water surface elevation and wave-induced current in the whole domain. Root mean square wave height (H_{rms}) can be obtained at each grid point with the zero crossing of the water surface elevation time series. The mean current field is also obtained by averaging each horizontal component of the instantaneous orbital velocity over the last 20 min of the simulations.

Optimal Growth Zone of Oyster Reefs

The OGZ is the best vertical elevation for the placement of COR for a successful growth of the oysters (Ridge et al., 2015; Morris et al., 2021). **Figure 5** illustrates five cross-shore transects of the bathymetry with the COR segments. The green-shaded area refers to the OGZ (60–80% inundation duration) based on the water level data in 2018 (Wang et al., 2020). Pink-shaded areas refer to the range between the OGZ and critical exposure boundary (CEB), beyond which no oyster growth is expected (Ridge et al., 2015). CEB limits are 50 and 95% inundation time. MSL and MLW are also depicted with dash and dash-dotted lines, respectively. Based on the water level data in 2018, the upper half of CORs 1–4 and the lower half of COR 5 are within the OGZ.

To assess the wave attenuation capacity of CORs in 100 years with rising sea levels, multiple one-dimensional simulations using FUNWAVE-TVD are carried out with the bathymetry transect for COR 5 as shown in **Figure 5**. The simulations are carried out with the offshore wave properties of Case 3, since it has the largest wave height among the cases. Moreover, three water levels are used for the simulations, MSL, MHW, and the water level between MSL and MHW. Three different water levels help to assess the wave height attenuation capacity of COR with different freeboards. Since in one-dimensional simulations, waves would be completely blocked by COR under MLW conditions, this water level is not considered here. Then, to assess the effects of SLR on wave attenuation capacity of COR, these water levels are increased by the SLR rate of 0.5 cm/year (Rahmstorf, 2010) for 100 years. Each year's simulation is run separately with constant wave properties, but with increased static water levels.

In addition, an alternative design for COR 5 is also proposed. In this design, COR 5 is removed from the bathymetry transect and a low-lying COR base with a height of 15 cm and width of three times COR 5's width is placed in COR 5's location. This alternative COR base is completely within the OGZ. According to Rodriguez et al. (2014), this alternative COR base would be an ideal location for the larval settlement and will allow the oysters to grow and flourish by itself. This COR base is designed to imitate the low-lying wide natural reefs. The water level and the new COR segment's height and width increase each year in 100 years in the new bathymetry configuration. It is believed that the proposed oyster reef configuration would grow fast with a vertical growth rate of 9 cm/year in the initial year of construction and would reach the MSL in about 8 years (Rodriguez et al., 2014). Then, COR would vertically grow at the rate of the SLR (Rodriguez et al., 2014).

RESULTS

Model Validation

To investigate the accuracy of the modeled result, measured wave data are compared to the FUNWAVE-TVD outputs of the three representative cases. The wave energy spectra obtained from the measured data and FUNWAVE-TVD are illustrated in the **Supplementary Figures S2–S4** for Case 1–3, respectively. Moreover, the wave height to offshore wave height ratio for measured and modeled data in three cases are demonstrated in **Figure 6**. These wave heights correspond to the swell ($0.04 < f < 0.14$ Hz) and wind sea ($0.14 < f < 0.5$ Hz) bands of the spectra. In addition, the wave height to offshore wave height ratio for infragravity ($0.004 < f < 0.04$ Hz), swell, and wind sea bands of the spectra are also decomposed and shown in **Supplementary Figure S5**. For Case 1, the simulated wave heights are overestimated at WG1, 3, 5, and 6, by 19, 8, 29, and 16%, respectively, due to higher swell energy in the numerical model. Modeled wave heights at WG2 and 4 are underestimated by 6 and 22%, respectively, because of underestimated wind seas. For Case 1, the infragravity band is underestimated for all wave gauges. In Case 2, WG1 and WG5 are underestimated by 18, and 30%, respectively. WG2 and WG6 are overestimated by 7 and 40%, respectively. The inaccuracy in the

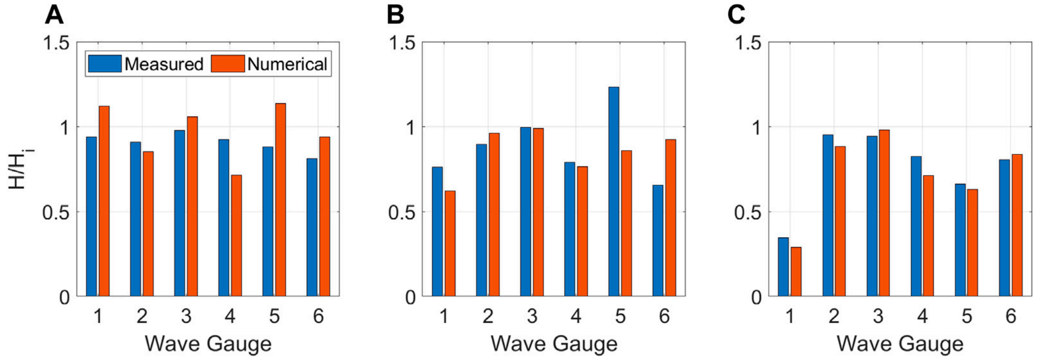

FIGURE 6 | Comparison of wave height to offshore wave height ratio at WG1–6 between measured and modeled data for **(A)** Case 1, **(B)** Case 2, and **(C)** Case 3.

modeled results is mainly because of the wind sea energy band. For Case 2, infragravity and swell band energies are underestimated in all wave gauges. Finally, in Case 3, wave energy in WG1, 2, 4, and 5 are underestimated by 16, 7, 13, and 4%, respectively. In this case, WG3 and WG6 are also overestimated by 4%.

It should be noted that the mean wave direction and directional spreading of the input wave spectrum play an important role in nearshore wave processes. For this study, these properties were not gathered in the field work and thus, they are obtained from the SWAN model and might not be accurate. Recently, there have been some attempts to improve SWAN modeling with artificial neural networks (e.g., Wang et al., 2022b). The discrepancy between wave directions in field conditions and SWAN outputs can be one of the reasons for the difference between the measured and Boussinesq model wave heights. Measuring the wave directional spreading during the field work and using it as model inputs can increase the accuracy of the model in simulating the measured wave data.

Effects of COR on Wave Field

The original bathymetry used in this study includes CORs as impermeable bathymetric features. To better evaluate the effects of CORs on nearshore wave processes, the original topography is modified, and the CORs are removed from the bathymetry. The model is run with both bathymetries (original bathymetry and modified bathymetry without the CORs) and the results are illustrated in **Figures 7–9**. **Figures 7A–C** demonstrate the water surface elevation snapshots in the presence of CORs, whereas **Figures 7D–F** depict the water surface elevation snapshots in the absence of CORs at the end of 30-min simulation. Dark red lines in water surface elevation snapshots denote wave breaking. For Case 1, because wave height is small, waves do not break in the vicinity of CORs, and therefore, there is no significant difference between the two scenarios. In Case 2, due to higher water levels, waves do not break before reaching the shallower area close to WG4. Case 3 shows a notable difference between the two scenarios. For Case 3 with the CORs, as illustrated in **Figure 7C**, wave breaking is delayed compared to the same case without CORs in **Figure 7F**.

Field measurements show that wave attenuation strongly depends on the ratio between crest freeboard and the offshore wave height (Zhu et al., 2020). This ratio is illustrated for the three test cases in **Table 1**. For cases with ratios lower than -1.6, either a wave attenuation of 35% or wave amplification of 70% was observed from WG3 to WG5 in the field measurements since both wave breaking and wave shoaling concurrently occur. From WG5 to WG1, further wave attenuation also happened owing to depth-limited wave breaking. For the cases with the freeboard ratio larger than −1.6, an average wave attenuation of 41% was measured from WG3 to WG5 because of wave breaking and reflection. In this modeling study, Cases 1 and 2 fall within the first category with the ratios of −1.85 and −2.84, respectively. Case 3 corresponds to the latter with a ratio of −0.41. Note that Zhu et al. (2020) used the measured data along two cross-shore transects to estimate the wave attenuation rates from offshore to the nearshore, like the assumption made in simple one-dimensional (1D) models. Such an assumption is valid when the wave direction is parallel to the transects. However, if the incident waves propagate in a direction different from the monitoring and reference transects, a direct comparison of the wave height variations along the monitoring and reference transects might not give a correct estimation of the CORs' efficacy in wave attenuation. The present modeling study reveals the complexity of the wave and current fields around the CORs.

Instead of assessing the CORs' efficacy along cross-shore transects, wave height changes in an area with and without CORs are investigated in this study. **Figures 8A–F** demonstrate the spatial distributions of wave heights in the modeling area for Case 1–3. **Figures 8G–I** illustrate the ratio of the wave height change in the presence of CORs to the wave height in the absence of CORs in the study area. The red and blue colors mean an increase and decrease in wave height, respectively, when the CORs are present in the modeling domain. For Case 1 in **Figure 8G**, among the five COR segments, four of them have resulted in wave height increases in the protected area. The wave height amplifications at WG5 and WG1 locations are 10 and 5%, respectively. However, incident waves to COR 5, which was

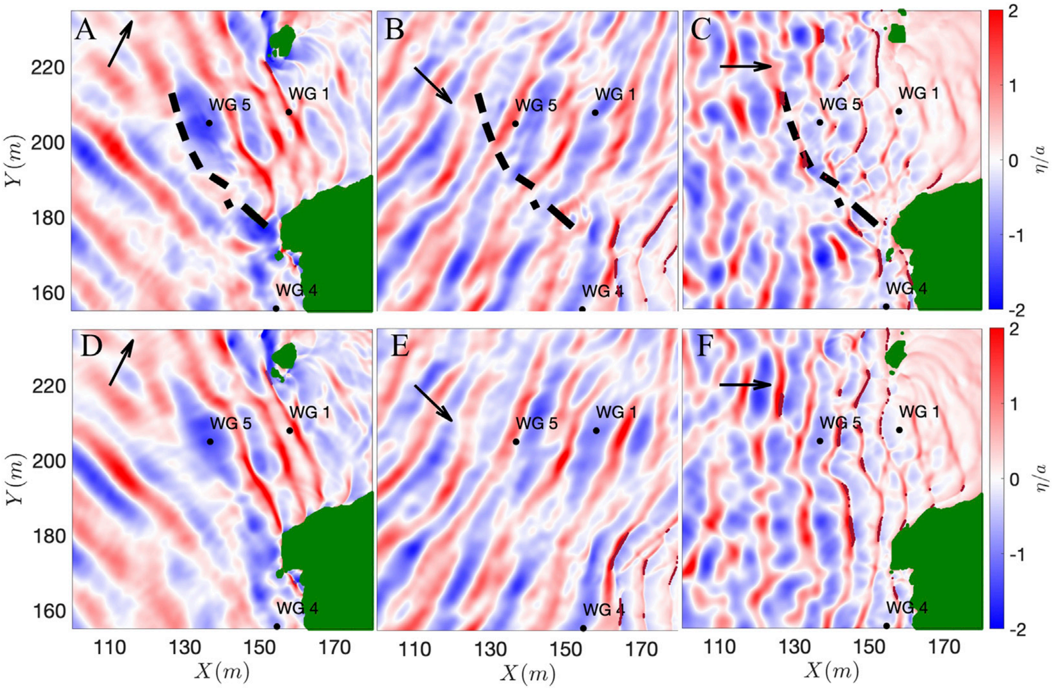

FIGURE 7 | Water surface elevation snapshot to wave amplitude ratio for **(A,D)** Case 1, **(B,E)** Case 2, and **(C,F)** Case 3. In panels **(A–C)** CORs are present in the domain, while in panels **(D–F)** CORs are removed from the domain. Dark red lines on the figures denote wave breaking at those locations.

emergent, were reflected, and therefore, a 40% decrease in wave height behind it is seen. For Case 2 in **Figure 8H**, there is a 16% increase in wave height at WG5. However, at WG1, wave height decreases at a similar rate. In this case, wave direction is obliquely incident to the monitoring transect. Therefore, estimating the wave attenuation along the monitoring transect can lead to inaccurate attenuation rates. This illustrates the limitation of simple 1D models under field conditions. For Case 3 in **Figure 8I**, the COR reflects the incident waves and results in a 17% decrease of wave height at WG5. Wave height at WG1 remains roughly unchanged and behind COR 5, a 50% of wave height reduction is seen. Overall, the phase-resolving model validated by the *in situ* measurements provides a holistic estimation of the CORs' efficacy in wave attenuation. In addition, the model can isolate the effect of CORs on the wave field from other nearshore processes included in the field data, such as wave refraction, reflection, diffraction, and depth-limited breaking. However, a larger number of cases will need to be simulated, which requires considerable computational costs.

Effects of COR on Current Field

Figure 9 depicts the current field for three cases in two bathymetries with and without CORs. The colors of the figures denote the current velocity, and the arrows show the current velocity with directions. Current velocity plays an important role in the growth of the oysters. However, excessive current velocity might damage the oysters. Therefore, the threshold of 15 cm/s (Theuerkauf et al., 2019) is considered the limit of current velocity in **Figure 9**, and current velocities above this limit are shown with the same color as the limit.

For Case 1 in **Figure 9A**, CORs have resulted in the formation of a clockwise circulation pattern inside the protected area. For Case 1 in **Figure 9D**, current would flow seaward in the absence of CORs. Therefore, CORs increase the wave-induced current velocity inside the protected area close to WG5 and WG1 and decrease the wave-induced current velocity seaward of CORs as shown in **Figure 9G**. For Case 2 in **Figure 9B**, CORs have resulted in a similar clockwise circulation pattern with increased current velocity inside the protected area. From the current velocity change in **Figure 9H**, COR 5 blocks the current flow, and other COR segments generate the circulation pattern. However, negligible change of current velocity can be observed around the COR segments. Case 3 with flow patterns illustrated in **Figure 9C** and **Figure 9F** is complicated because of higher current velocities around CORs. Like Case 2, COR 5 again redirects the flow field into the protected area. Moreover, current velocity for Case 3 potentially exceeds the current velocity threshold for optimal oyster reefs growth. It is interesting to note that the wave-driven circulation behind CORs is clockwise regardless of different wave directions and water levels in the three cases.

While **Figure 9** provides an overview of the current field, to better understand the effects of the CORs on the current velocity and circulation patterns in the protected area behind CORs, some numerical current meters are defined in addition to the numerical current meters at the locations of WG1 and WG5. These current meters are named Gap 1–4,

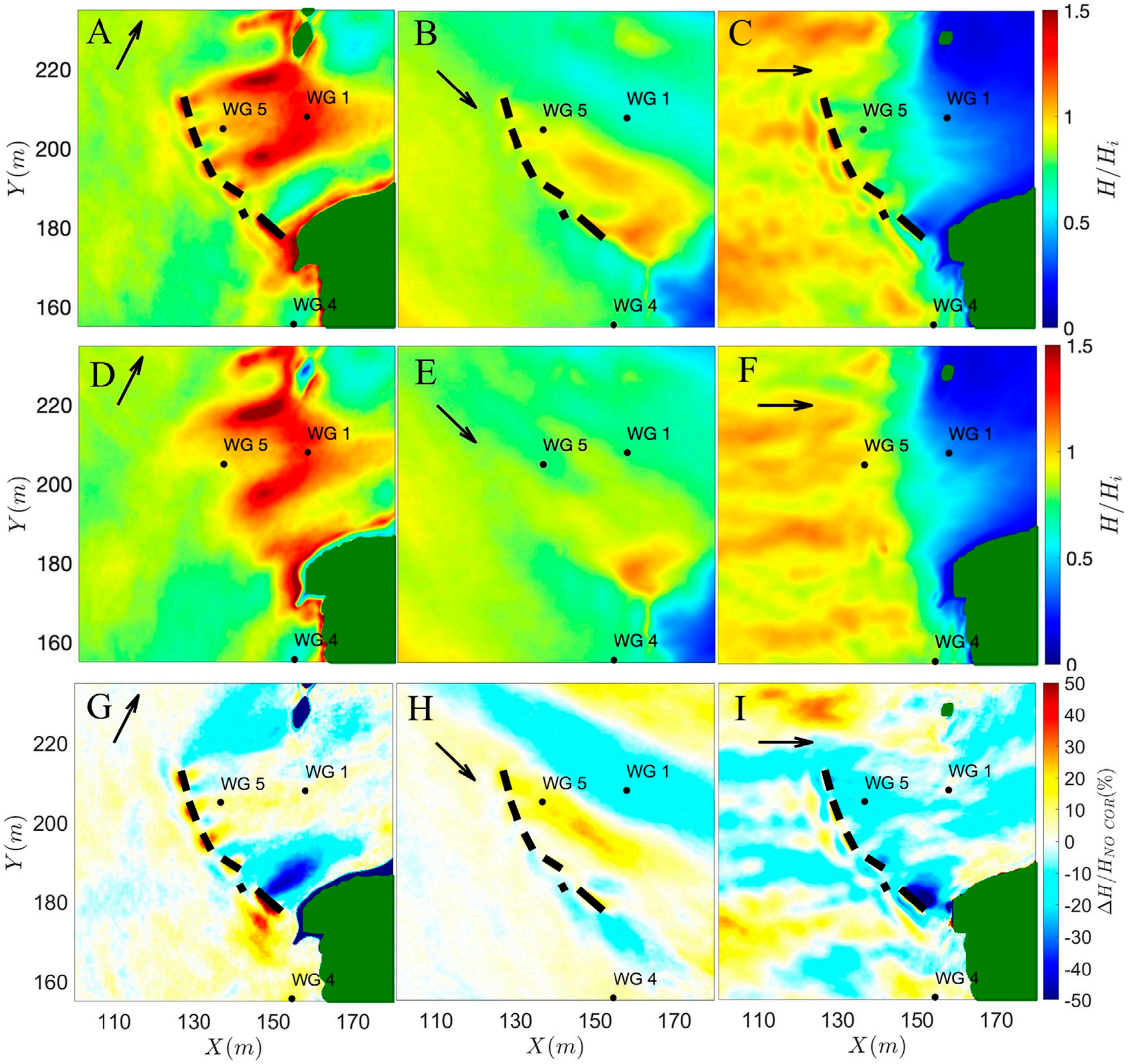

FIGURE 8 | Wave height to offshore wave height ratio for **(A,D)** Case 1, **(B,E)** Case 2, and **(C,F)** Case 3. In panels **(A–C)** CORs are present in the domain, while in panels **(D–F)** CORs are removed from the domain. Panels **(G–I)** illustrate the change of root mean square wave height due to CORs.

SeW, and ShW, and are marked in **Figure 1D**. Gaps 1–4 refer to the current meters in gaps between COR segments and demonstrate the velocity of current flowing out of the protected area through the gaps. The high current velocity at these locations can damage the oysters settling in the vicinity of the gaps between COR segments. SeW and ShW refer to the current meters on seaward and shoreward of COR 2, respectively and illustrate the current velocity change in both sides of COR 2.

Figure 10 provides the current velocity for the three representative cases at these numerical current meters for two bathymetry configurations (with and without CORs). For Case 1 in **Figure 10A**, while CORs have increased current velocity in SeW, ShW, and Gap 1–3, compared to the bathymetry without CORs, current velocity hardly exceeds 15 cm/s limit. For Case 2 in **Figure 10B**, except for WG1 and WG2, current velocity is less than 5 cm/s for all other current meters. For WG1 and WG2, current velocity is higher than 10 cm/s but does not exceed the limit like Case 1. Moreover, CORs have not affected the current velocity at these locations significantly. For Case 3 in **Figure 10C**, current velocities in the gaps vary between 5 and 45 cm/s and can potentially be destructive to the oysters. In fact, except Gap 1 and WG5, current velocity exceeds the limit at all other current meters. At these locations, CORs have increased the current velocity. For example, in WG1 current velocity has doubled. Overall, CORs can either increase or decrease the wave-induced current velocity at different locations and sometimes, this increase can be large, harming the oyster reefs.

Long-Term Wave Attenuation With SLR

To assess the long-term protection provided by the CORs, COR 5's wave attenuation capability over 100 years with changing water

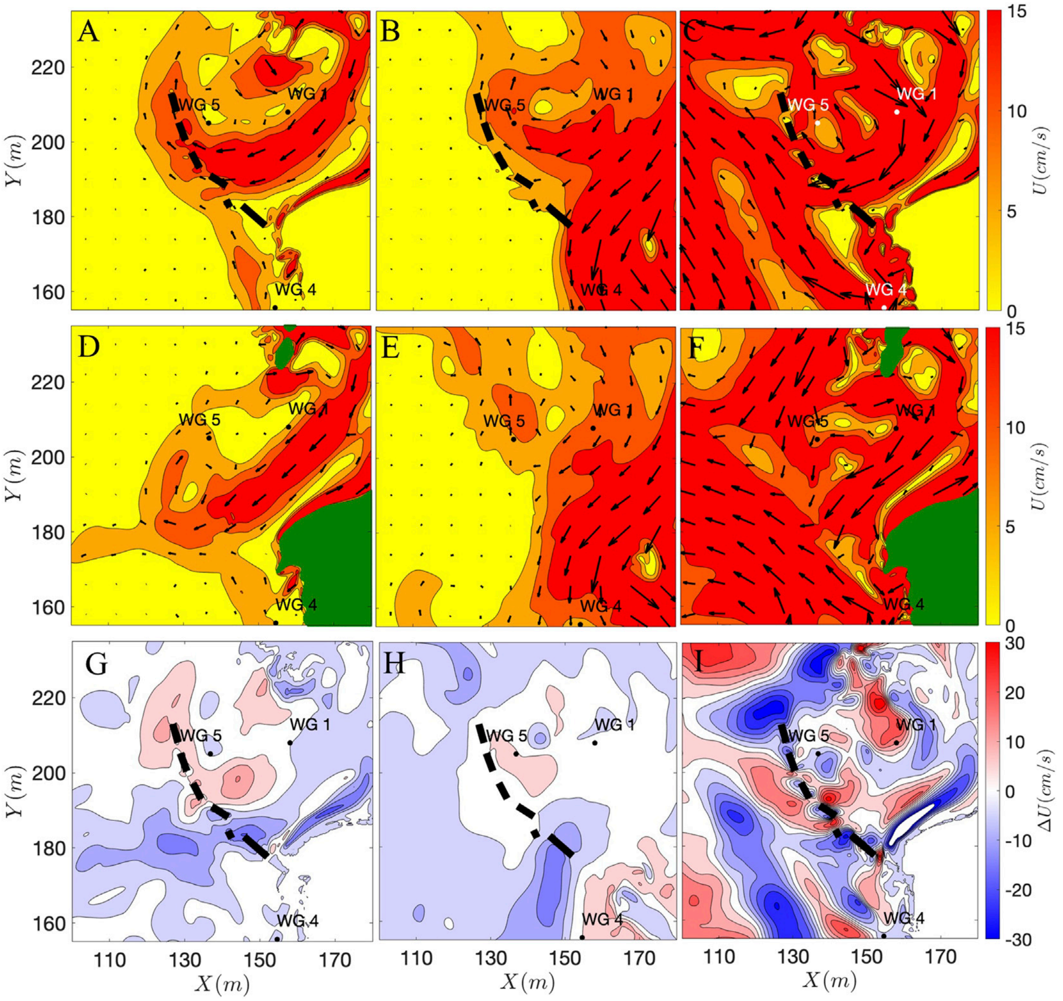

FIGURE 9 | Wave-driven current velocity for **(A,D)** Case 1, **(B,E)** Case 2, and **(C,F)** Case 3. In panels **(A–C)** CORs are present in the domain, while in panels **(D–F)** CORs are removed from the domain. Panels **(G–I)** illustrate the change of wave-driven current velocity due to CORs.

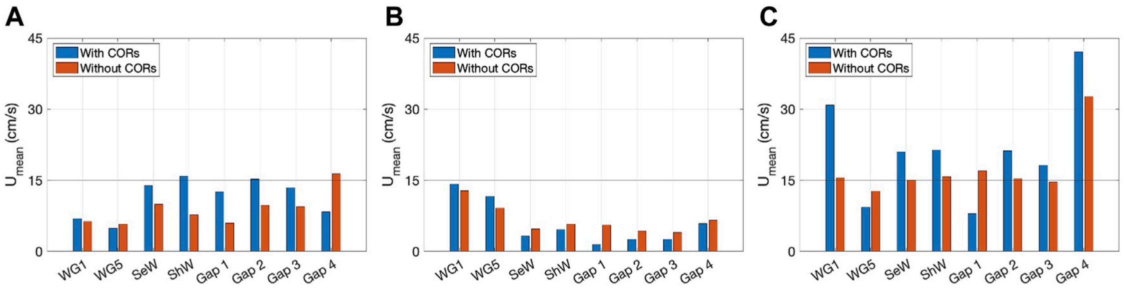

FIGURE 10 | Comparison of the wave-driven current velocity averaged for 20 min for **(A)** Case 1, **(B)** Case 2, and **(C)** Case 3 for two bathymetry configurations.

levels is investigated. Moreover, an alternative reef configuration, as a sustainable design, is also proposed and is illustrated in **Supplementary Figure S6**. As mentioned earlier, sustainability of CORs is determined based on its ability to grow and maintain pace with SLR. Thus, it can maintain its efficacy in shoreline protection in the future. The wave attenuation capability of each reef design under different water levels is demonstrated in **Figure 11**. Wave attenuation is calculated by the wave height difference at both sides of COR 5. For the MSL in **Figure 11A**, since COR 5 is emergent for the unsustainable design with limited

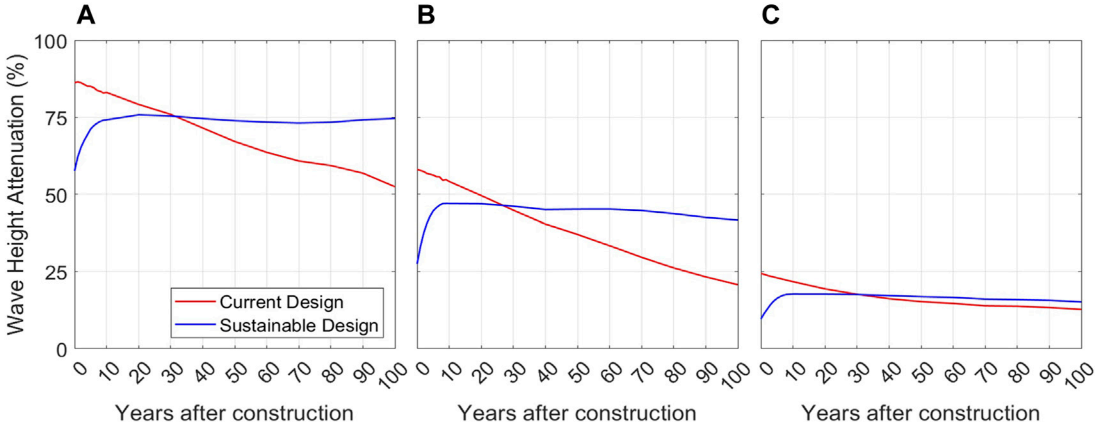

FIGURE 11 | Long-term wave height attenuation with the sustainable and current design of CORs under SLR for three water levels **(A)** MSL, **(B)** between MSL and MHW, and **(C)** MHW.

potential of oyster growth, a good degree of protection at about 80% of wave height reduction is seen under current conditions. However, it would lose its protection in about 30 years after getting submerged. The sustainable design for this water level, though, takes about 10 years to reach a constant level of protection of about 75%. This level of protection is then maintained for the next 90 years. For the water level between the MSL and MHW illustrated in **Figure 11B**, the unsustainable design has initial protection of 60% and loses its protection in about 25 years, while the sustainable design also gains about 45% protection in approximately 8 years. For the MHW in **Figure 11C**, the previous design has 25% protection at the initial phase and then its protection is gradually reduced to less than 20%. The sustainable design also reaches 20% protection in about 8 years. For the MHW, both designs provide limited protection in the long term and the only difference between the two designs is a slight loss of protection in the unsustainable design. This suggests that CORs, regardless of their sustainability, do not provide significant wave attenuation benefits if they are deeply submerged under extreme water level conditions.

DISCUSSION

High Spatial and Temporal Variability of Wave Processes Along Living Shorelines

Our modeling results indicate that wave height change by CORs in Gandys Beach is complex. Wave height in the protected area can decrease or increase compared to the wave height without CORs depending on the offshore wave height, mean wave direction, and water depth conditions. Previous studies might likely overestimate the wave attenuation capacity of living shorelines if only simple 1D models or limited data were used. This could be attributed to 1) a lack of wave measurements under the representative wind, wave, and water depth conditions (e.g., measurements were short and taken from non-storm conditions), 2) a large model domain in wave modeling with a coarse grid size or obsolete bathymetry data that could not represent the local bathymetry conditions, and 3) making wave height and current comparisons between locations with false equivalence.

The present study is among the first investigations to address these issues by 1) using the bathymetry data which is a combination of the comprehensive U.S. Geological Survey Coastal National Elevation Database (CoNED, 1 m resolution) and our field survey in this project, 2) employing the phase-resolving wave model with high temporal and spatial resolution as well as an updated bathymetry from CoNED and recent survey carried out during 2017–2018 after oyster castle construction at Gandys Beach living shoreline, and 3) comparing the wave height and the current field between a bathymetry with CORs and a bathymetry without CORs. The rich field data and the state-of-the-art phase-resolving wave model reveal the changes in the wave field and the wave-driven flow field due to CORs. Wave models with high spatial and temporal resolution are therefore recommended for the study of wave attenuation by CORs. Thus, we can determine the difference in the flow field and wave height caused by CORs using the high-resolution phase-resolving wave model that can appropriately resolve the bathymetric and geometric features of CORs.

Local Wave-Induced Current Pattern Changes Across Living Shorelines

For the modeling part, three representative wind–wave conditions were selected from a series of combinations of wind and wave data for Gandys Beach. For Case 1 with the lowest wave energy among the cases and with near emergent CORs, we found that CORs increase wave height behind them. Circulation patterns inside the protected area may also increase wave height if the current is opposite to the wave direction. For Case 1, COR 5 is emergent with the negligible current behind it and attenuates the incident waves. For Case 2, with intermediate wave energy and with the highest water level among the three cases, CORs increase the wave height in the protected area as well.

For this case, waves are roughly parallel to CORs. Since waves are not blocked by CORs, a possible reason for the modeled wave height increase can also be the current pattern behind CORs in the protected area like Case 1. For Case 3, with the highest wave energy and with a water level like Case 1, we found that the wave height is blocked by CORs. Looking at the wave energy spectra for Case 3, a reduction of wave energy in higher frequencies and a transfer of energy to the lower frequencies can be observed. Thus, one can infer that the swell energies have passed through CORs, though most of the higher frequency waves are blocked, which has also been observed by Zhu et al. (2020).

There is a lack of simultaneous measurements of wave and current dynamics in existing studies on wave attenuation by LSS. This numerical study simultaneously examines both wave and current dynamics across LSS under representative wave conditions including strong nor'easters along the upper Delaware Bay. By having an accurate map of the current pattern inside the protected area, we can confirm the role of CORs on the formation of a circulation pattern behind CORs. This circulation can trap the incoming sediment in the protected area behind the oyster castles and increase the total suspended solids concentration around the CORs. It can also result in sediment deposition and reduction of vertical and horizontal erosion of shorelines (Colden et al., 2016; Wang et al., 2021).

It should be noted that the current field simulated by our model is purely wave-driven and does not take the tidal currents into account. The current velocity measured in the field is a combination of wave-induced and tidal currents, and the Boussinesq model only provides us with the wave-induced current velocity fields. Thus, more work on the separation of tidal- and wave-induced current in the measured data is needed to make a reasonable comparison between the simulated and measured current data. Simulated wave-induced current velocities in the vicinity of CORs varied with the incident waves and water levels. While the current velocities were less than 15 cm/s for Case 1 and 2, they exceeded the threshold value for Case 3. In some cases, these wave-driven currents may not be suitable for oyster optimal growth, even though oyster filtration and food ingestion will not stop (Wang et al., 2017, 2021).

Sustainable Living Shorelines Under Sea-Level Rise

The existing CORs in this study are slanted tall structures composed of five stacked layers of concrete blocks. It has been reported that the oyster settlement on these blocks has not been successful (Wang et al., 2021). While salinity, temperature, and nutrient concentrations are in the range for oyster survival and growth in Gandys Beach, engineering factors like the placement of these blocks in the OGZ as well as their geometrical design could be among the reasons for the low oyster settlement and growth on these oyster castles. Moreover, current velocity behind CORs and through the gaps was seen to be over the optimal range for oyster growth under energetic wave conditions.

Generally, existing LSS designs do not consider long-term (>5 years) environmental factors. Though these structures might trap some sediment inside the protected area, attenuate the wave height (Zhu et al., 2020; Wang et al., 2021), and consequently reduce the shoreline erosion, their protection will likely diminish with SLR. Thus, the design of sustainable LSS that can maintain pace with SLR can help to achieve long-term benefits (Rodriguez et al., 2014; Ridge et al., 2017; Morris et al., 2019). To achieve this, engineering aspects, ecological benefits, and their interaction are design considerations. For oyster reef living shorelines like Gandys Beach, oyster reef's vertical growth *via* shell and biomass growth is needed to maintain the wave attenuation capacity of oyster castles in the future.

Future Studies

While this study provides valuable information on the sustainability of living shoreline structures, it can be further improved. The oyster growth rates should be site-specific and applying the oyster growth rates of Rodriguez et al. (2014) on Gandys Beach might not yield accurate results. In addition, these analyses were made in 1D settings with only one COR segment. The results would be more reliable if a 2D bathymetry was run with two bathymetry configurations (with and without CORs in the domain). Thus, in addition to the wave height, current field could also be obtained. Current fields can also affect the wave height, and therefore, a 2D analysis would give more reliable information on the efficacy of the sustainable oyster design. However, 2D analyses would significantly increase the computational time. Another shortcoming of the current design is the lack of information on the projection of future wave and water level conditions. The mean sea level is assumed to rise 0.5 cm/year due to SLR; however, wave properties can also change with the changing climate. Thus, wave height changes in the 100-years range should be considered for the COR's long-term sustainability analyses.

Results of wave modeling incorporating the OGZ under SLR indicate that sustainable living shorelines can be achieved if the living shorelines were designed for the oysters with long-term vision instead of designing them for just wave attenuation to protect the shoreline from erosion. Incorporating oyster reef vertical growth into the sustainable living shoreline design is a critical component in sustaining long-term wave attenuation under future SLR. We found that it will take about 8–10 years for a sustainable oyster reef-based shoreline to reach its maximum wave attenuation capacity. Then, it will maintain this maximum wave attenuation capacity by growing at the same pace as SLR. It was found that it will take approximately 9 years for oyster reefs in Winyah Bay, South Carolina, United States, to grow from establishment to maximum reef height from shells and live oysters based on oyster reef mechanics and self-organization theory (Yurek et al., 2021). Therefore, maintaining CORs wave attenuation capacity with reef vertical growth to maintain pace with SLR, suggests prolonged protection of the shoreline and habitat maintenance without human intervention or additional investments.

Though our model results demonstrate the current field altered by the CORs with high spatial and temporal resolution, it is limited to simulating wave-driven currents. Models could be further refined by including tidal currents. In addition, natural oyster reefs are wider and lower in height than the man-made oyster castle substrates. Replicating similar designs to the natural reefs in numerical models with an appropriate roughness coefficient for the increased friction may shed new light on the optimal design of oyster reefs for better protection of the shorelines. Furthermore, continuous monitoring of wave data including mean wave direction, sediment concentration, and sediment budget (deposition and erosion on the shoreline with oyster castle protection) could provide a rich bank of measured data for future modeling. Oyster biological studies, including transport and settlement of larvae and growth of oysters with different sizes (spat, juvenile, and markable) at the crest and base of the reefs under various current velocity conditions could also help to improve model accuracy. An integrated modeling system of hydrodynamics and ecology of oyster growth could help to predict the shoreline morphology and to better understand the oyster population dynamics under future climate change and rising sea levels.

SUMMARY AND CONCLUSION

Living shorelines need to be sustainable both in terms of wave energy attenuation to protect the shoreline from erosion and maintaining native species habitat under future climate change and SLR. In this study, wave dynamics around CORs, in Gandys Beach, New Jersey, in the upper Delaware Bay, United States were examined using the phase-resolving Boussinesq wave model, FUNWAVE-TVD. To our knowledge, this is the first study on assessing wave and current dynamics along living shorelines using fine temporal and spatial resolution wave modeling. Field wave data collected from six wave gages across the CORs for two winter months in 2018 with four nor'easters were used to calibrate some of the input parameters and validate the wave model, showing good agreement between simulated and observed wave heights and wave energy spectra. To assess the effects of CORs on the wave and current fields, using simulations with oyster castles on and off the bathymetric data, three cases that represent the prevailing wind, wave, and tide conditions along the Gandys Beach shoreline based on field measurements and phase-averaged wave model outputs were selected.

It was found that oyster castles do not always attenuate the waves, and in some special events, oyster castles even result in wave height amplification, as well. Wave attenuation capacity of living shorelines including constructed oyster reefs tends to be overestimated by one-dimensional empirical formulas for submerged breakwaters or phase-averaged wave models with coarse spatial resolutions. These models neither resolve local bathymetry variations across the LSS nor the local wave processes such as wave reflection, diffraction, and breaking over the narrow reef crest. Furthermore, it was found that oyster castles alter the wave-driven flow and generate a circulation pattern behind them, which increases current velocity at and near the oyster castles. This affects oyster larval transport and settlement, nutrient delivery, and oyster filtration. Current velocity adjacent to the oyster castles under some representative cases exceeds the threshold of 15 cm/s for nutrient delivery and oyster filtration, indicating that the current oyster castle design might not provide suitable current velocity for on-reef oyster growth.

The COR's wave attenuation capacity along Gandys Beach shoreline under future SLR conditions in the next 100 years was evaluated in current and sustainable designs. In a sustainable design, oyster reef vertical growth within the OGZ was incorporated in a representative case. It was found that the COR's wave attenuation capacity can be maintained over the next 100 years, but this long-term benefit can only be achieved when the COR is placed inside the OGZ and grows at the same rate as SLR. It was found that one of the COR segments in Gandys Beach living shoreline may not be designed for long-term protection and may lose its protection with SLR because of being located outside the OGZ. The model results suggest that it would take approximately 9 years for a sustainably designed COR after the construction to reach and maintain the maximum wave attenuation capacity. Within this period, the oyster reef grows fast, reaches its maximum elevation, and eventually evolves at an equilibrium stage with the physical environment like natural oyster reefs.

DATA AVAILABILITY STATEMENT

The raw data supporting the conclusion of this article will be made available by the authors, without undue reservation.

AUTHOR CONTRIBUTIONS

RS: conceptualization, software, formal analysis, validation, visualization, and writing—original draft; HW: conceptualization, supervision, methodology, resources, and writing—review and editing; QC: conceptualization, supervision, methodology, writing—review and editing, and project administration; LZ: conceptualization, resources, data curation, software, formal analysis, validation, visualization, and writing—review and editing.

FUNDING

Funding for the study has been provided by the U.S. Coastal Research Program (USCRP, W912HZ-20-2-0046) and the National Fish and Wildlife Foundation (NFWF, Project #55032).

ACKNOWLEDGMENTS

We would like to thank Cody Johnson and two reviewers for their constructive reviews of an earlier version. Any use of trade, firm, or product names is for descriptive purposes only and does not imply endorsement by the U.S. Government.

SUPPLEMENTARY MATERIAL

The Supplementary Material for this article can be found online at: https://www.frontiersin.org/articles/10.3389/fbuil.2022.884849/full#supplementary-material

REFERENCES

Booij, N., Ris, R. C., and Holthuijsen, L. H. (1999). A Third-Generation Wave Model for Coastal Regions: 1. Model Description and Validation. *J. Geophys. Res.* 104 (C4), 7649–7666. doi:10.1029/98jc02622

Campbell, M. D., and Hall, S. G. (2019). Hydrodynamic Effects on Oyster Aquaculture Systems: a Review. *Rev. Aquacult* 11 (3), 896–906. doi:10.1111/raq.12271

Chen, Q. (2006). Fully Nonlinear Boussinesq-type Equations for Waves and Currents over Porous Beds. *J. Eng. Mech.* 132 (2), 220–230. doi:10.1061/(asce)0733-9399(2006)132:2(220)

Chen, Q., Kirby, J. T., Dalrymple, R. A., Shi, F., and Thornton, E. B. (2003). Boussinesq Modeling of Longshore Currents. *J. Geophys. Res. Oceans* 108 (C11). doi:10.1029/2002jc001308

Chen, Q., Madsen, P. A., and Basco, D. R. (1999). Current Effects on Nonlinear Interactions of Shallow-Water Waves. *J. Waterw. port, Coast. ocean Eng.* 125 (4), 176–186. doi:10.1061/(asce)0733-950x(1999)125:4(176)

Chowdhury, M. S. N., Walles, B., Sharifuzzaman, S. M., Shahadat Hossain, M., Ysebaert, T., and Smaal, A. C. (2019). Oyster Breakwater Reefs Promote Adjacent Mudflat Stability and Salt Marsh Growth in a Monsoon Dominated Subtropical Coast. *Sci. Rep.* 9 (1), 1–12. doi:10.1038/s41598-019-44925-6

Colden, A. M., Fall, K. A., Cartwright, G. M., and Friedrichs, C. T. (2016). Sediment Suspension and Deposition across Restored Oyster Reefs of Varying Orientation to Flow: Implications for Restoration. *Estuaries coasts* 39 (5), 1435–1448. doi:10.1007/s12237-016-0096-y

Deltares, D. (2013). *Delft3D-FLOW Simulation of Multi-Dimensional Hydrodynamic Flows and Transport Phenomena, Including Sediments*. Delft: Delft Hydraulics.

Fivash, G. S., Stüben, D., Bachmann, M., Walles, B., van Belzen, J., Didderen, K., et al. (2021). Can We Enhance Ecosystem-Based Coastal Defense by Connecting Oysters to Marsh Edges? Analyzing the Limits of Oyster Reef Establishment. *Ecol. Eng.* 165, 106221. doi:10.1016/j.ecoleng.2021.106221

Harsh, D. A., and Luckenbach, M. W. (1999). *Materials Processing by Oysters in Patches: Interactive Roles of Current Speed and Seston Composition*.

Karimpour, A., and Chen, Q. (2017). Wind Wave Analysis in Depth Limited Water Using OCEANLYZ, A MATLAB Toolbox. *Comput. Geosciences* 106, 181–189. doi:10.1016/j.cageo.2017.06.010

Kennedy, A. B., Chen, Q., Kirby, J. T., and Dalrymple, R. A. (2000). Boussinesq Modeling of Wave Transformation, Breaking, and Runup. I: 1D. *J. Waterw. port, Coast. ocean Eng.* 126 (1), 39–47. doi:10.1061/(asce)0733-950x(2000)126:1(39)

La Peyre, M. K., Marshall, D. A., and Sable, S. E. (2021). *Oyster Model Inventory: Identifying Critical Data and Modeling Approaches to Support Restoration of Oyster Reefs in Coastal US Gulf of Mexico Waters (No. 2021-1063)*. Reston, VA: US Geological Survey. doi:10.3133/ofr20211063

Larsen, J., and Dancy, H. (1983). Open Boundaries in Short Wave Simulations - A New Approach. *Coast. Eng.* 7 (3), 285–297. doi:10.1016/0378-3839(83)90022-4

Leonardi, N., Ganju, N. K., and Fagherazzi, S. (2016). A Linear Relationship between Wave Power and Erosion Determines Salt-Marsh Resilience to Violent Storms and Hurricanes. *Proc. Natl. Acad. Sci. U.S.A.* 113 (1), 64–68. doi:10.1073/pnas.1510095112

Lipcius, R. N., Zhang, Y., Zhou, J., Shaw, L. B., and Shi, J. (2021). Modeling Oyster Reef Restoration: Larval Supply and Reef Geometry Jointly Determine Population Resilience and Performance. *Front. Mar. Sci.* 8, 1395. doi:10.3389/fmars.2021.677640

Manson, T., Gilman, J. F., Perkol-Finkel, S., Sella, I., and Marrone, J. F. (2018). "Multi-Purpose Breakwaters," in *Coasts, Marine Structures and Breakwaters 2017: Realising the Potential* (London, United Kingdom: ICE Publishing), 449–458. doi:10.1680/cmsb.63174.0449

Marani, M., D'Alpaos, A., Lanzoni, S., and Santalucia, M. (2011). Understanding and Predicting Wave Erosion of Marsh Edges. *Geophys. Res. Lett.* 38 (21). doi:10.1029/2011gl048995

Morris, R. L., La Peyre, M. K., Webb, B. M., Marshall, D. A., Bilkovic, D. M., Cebrian, J., et al. (2021). Large-scale Variation in Wave Attenuation of Oyster Reef Living Shorelines and the Influence of Inundation Duration. *Ecol. Appl.* 31 (6), e02382. doi:10.1002/eap.2382

Morris, R. L., Bilkovic, D. M., Boswell, M. K., Bushek, D., Cebrian, J., Goff, J., et al. (2019). The Application of Oyster Reefs in Shoreline Protection: Are We Over-engineering for an Ecosystem Engineer? *J. Appl. Ecol.* 56 (7), 1703–1711. doi:10.1111/1365-2664.13390

Morris, R. L., Konlechner, T. M., Ghisalberti, M., and Swearer, S. E. (2018). From Grey to Green: Efficacy of Eco-Engineering Solutions for Nature-Based Coastal Defence. *Glob. Change Biol.* 24 (5), 1827–1842. doi:10.1111/gcb.14063

Polk, M. A., Gittman, R. K., Smith, C. S., and Eulie, D. O. (2022). Coastal Resilience Surges as Living Shorelines Reduce Lateral Erosion of Salt Marshes. *Integr Envir Assess Manag* 18 (1), 82–98. doi:10.1002/ieam.4447

Rahmstorf, S. (2010). A New View on Sea Level Rise. *Nat. Clim. Change* 1 (1004), 44–45. doi:10.1038/climate.2010.29

Ridge, J. T., Rodriguez, A. B., Joel Fodrie, F., Lindquist, N. L., Brodeur, M. C., Coleman, S. E., et al. (2015). Maximizing Oyster-Reef Growth Supports Green Infrastructure with Accelerating Sea-Level Rise. *Sci. Rep.* 5 (1), 14785–14788. doi:10.1038/srep14785

Ridge, J. T., Rodriguez, A. B., and Fodrie, F. J. (2017). Evidence of Exceptional Oyster-Reef Resilience to Fluctuations in Sea Level. *Ecol. Evol.* 7 (23), 10409–10420. doi:10.1002/ece3.3473

Rodriguez, A. B., Fodrie, F. J., Ridge, J. T., Lindquist, N. L., Theuerkauf, E. J., Coleman, S. E., et al. (2014). Oyster Reefs Can Outpace Sea-Level Rise. *Nat. Clim. Change* 4 (6), 493–497. doi:10.1038/nclimate2216

Salatin, R., Chen, Q., Bak, A. S., Shi, F., and Brandt, S. R. (2021). Effects of Wave Coherence on Longshore Variability of Nearshore Wave Processes. *J. Geophys. Res. Oceans* 126 (11), e2021JC017641. doi:10.1029/2021jc017641

Shi, F., Kirby, J. T., Harris, J. C., Geiman, J. D., and Grilli, S. T. (2012). A High-Order Adaptive Time-Stepping TVD Solver for Boussinesq Modeling of Breaking Waves and Coastal Inundation. *Ocean. Model.* 43-44, 36–51. doi:10.1016/j.ocemod.2011.12.004

Smith, K. A., North, E. W., Shi, F., Chen, S.-N., Hood, R. R., Koch, E. W., et al. (2009). Modeling the Effects of Oyster Reefs and Breakwaters on Seagrass Growth. *Estuaries Coasts* 32 (4), 748–757. doi:10.1007/s12237-009-9170-z

Suanda, S. H., Perez, S., and Feddersen, F. (2016). Evaluation of a Source-Function Wavemaker for Generating Random Directionally Spread Waves in the Sea-Swell Band. *Coast. Eng.* 114, 220–232. doi:10.1016/j.coastaleng.2016.04.006

Theuerkauf, S. J., Burke, R. P., and Lipcius, R. N. (2015). Settlement, Growth, and Survival of Eastern Oysters on Alternative Reef Substrates. *J. Shellfish Res.* 34 (2), 241–250. doi:10.2983/035.034.0205

Theuerkauf, S. J., Eggleston, D. B., and Puckett, B. J. (2019). Integrating Ecosystem Services Considerations within a GIS-Based Habitat Suitability Index for Oyster Restoration. *PloS one* 14 (1), e0210936. doi:10.1371/journal.pone.0210936

Wang, H., Capurso, W. D., Chen, Q., Zhu, L., Niemoczynski, L., and Snedden, G. (2021). *Assessment of Wave Attenuation, Current Patterns, and Sediment Deposition and Erosion during Winter Storms by Living Shoreline Structures in Gandys Beach*. New Jersey: US Geological Survey. (No. 2021-1040). doi:10.3133/ofr20211040

Wang, H., Chen, Q., La Peyre, M. K., Hu, K., and La Peyre, J. F. (2017). Predicting the Impacts of Mississippi River Diversions and Sea-Level Rise on Spatial Patterns of Eastern Oyster Growth Rate and Production. *Ecol. Model.* 352, 40–53. doi:10.1016/j.ecolmodel.2017.02.028

Wang, H., Zhu, L., Chen, Q., Capurso, W., Niemoczynski, L., Hu, K., et al. (2020). *Field Observations and Spectral Evolution of Wind Waves in Upper Delaware Bay with Living Shorelines*. Reston, VA: U.S. Geological Survey data release. doi:10.5066/P9YEUNTM

Wang, N., Chen, Q., Zhu, L., and Sun, H. (2022b). Integration of Data-Driven and Physics-Based Modeling of Wind Waves in a Shallow Estuary. *Ocean. Model.* 172, 101978. doi:10.1016/j.ocemod.2022.101978

Wang, N., Chen, Q., Zhu, L., and Wang, H. (2022a). Data-driven Modeling of Wind Waves in Upper Delaware Bay with Living Shorelines. *Ocean. Eng.* In press.

Wei, G., Kirby, J. T., and Sinha, A. (1999). Generation of Waves in Boussinesq Models Using a Source Function Method. *Coast. Eng.* 36 (4), 271–299. doi:10.1016/s0378-3839(99)00009-5

Wiberg, P. L., Taube, S. R., Ferguson, A. E., Kremer, M. R., and Reidenbach, M. A. (2019). Wave Attenuation by Oyster Reefs in Shallow Coastal Bays. *Estuaries Coasts* 42 (2), 331–347. doi:10.1007/s12237-018-0463-y

Yurek, S., Eaton, M. J., Lavaud, R., Laney, R. W., DeAngelis, D. L., Pine, W. E., III, et al. (2021). Modeling Structural Mechanics of Oyster Reef Self-Organization Including Environmental Constraints and Community Interactions. *Ecol. Model.* 440, 109389. doi:10.1016/j.ecolmodel.2020.109389

Zhu, L., Chen, Q., Wang, H., Capurso, W., Niemoczynski, L., Hu, K., et al. (2020). Field Observations of Wind Waves in Upper Delaware Bay with Living Shorelines. *Estuaries Coasts* 43 (4), 739–755. doi:10.1007/s12237-019-00670-7

Conflict of Interest: The authors declare that the research was conducted in the absence of any commercial or financial relationships that could be construed as a potential conflict of interest.

frontiers | Frontiers in Built Environment

ORIGINAL RESEARCH
published: 22 June 2022
doi: 10.3389/fbuil.2022.884795

Observations of Wave Height Amplification Behind an Oyster Castle Breakwater System in a High-Energy Environment: Gandys Beach, NJ

Amy L. Bredes*, Jon K. Miller, Laura Kerr and Dana Rose Brown

Department of Civil, Environmental and Ocean Engineering, Coastal Engineering Research Group (CERG), Stevens Institute of Technology, Hoboken, NJ, United States

This study reports findings of an analysis of modifications to the incident wave field caused by constructed Oyster Castle® breakwater systems at Gandys Beach Preserve in Downe Township, NJ. The Nature Conservancy's (TNC) Gandys Beach Preserve is a one-mile stretch of beach located along with intertidal mud flats, sandy beaches, tidal creeks, and salt marshes. Gandys Beach can be classified as a high-energy environment, with open water fetches exceeding 30 miles, and a tidal range on the order of 2 m. The Gandys Beach living shoreline project was designed and constructed by TNC in partnership with the United States Fish and Wildlife Service (USFWS) to investigate the effectiveness of various natural and nature-based features (NNBFs) in protecting and enhancing salt marshes and beaches in high (er) energy environments. Many of the NNBF techniques used at Gandys Beach, such as Oyster Castle® block breakwaters (Oyster Castles), had only been implemented at smaller scales in New Jersey prior to the project. Stevens was contracted by USFWS/TNC to evaluate the impact of the breakwater systems on incident waves. Four breakwater sections along the beach were selected to monitor wave attenuation. Month-long deployments of wave staffs and pressure sensors occurred in the summer and winter of 2019. Analysis of the data indicates that when crests of the Oyster Castles are exposed the breakwater system effectively attenuates waves. However, when the structures are submerged, wave height attenuation decreases, and under certain conditions wave heights behind Oyster Castles can be amplified more than 80%. These results are troubling, especially in areas experiencing sea level rise where the frequency of submergence will likely increase in the future. Due to the complex nature of Gandys Beach, exact mechanisms causing this amplification remain uncertain. Furthermore, transmission coefficients (K_t) above 1 are not typically modeled in existing empirical equations. Seabrook and Hall (Coast. Eng. Proc., 1998, 1 (26), 2000) is the only studied empirical formula that indicated an amplification of the H_s as observed during these field deployments and therefore was used to model K_t. However, poor agreement between the modeled and observed K_t was found and a better predictive tool is needed.

Keywords: living shorelines, NNBF, oyster castle, breakwater, wave amplification, wave transmission

OPEN ACCESS

Edited by:
Tori Tomiczek,
United States Naval Academy,
United States

Reviewed by:
Qin Chen,
Northeastern University, United States
Meagan Wengrove,
Oregon State University, United States

****Correspondence:***
Amy L. Bredes
abredes1@stevens.edu

Specialty section:
This article was submitted to
Coastal and Offshore Engineering,
a section of the journal
Frontiers in Built Environment

Received: *27 February 2022*
Accepted: *23 May 2022*
Published: *22 June 2022*

Citation:
Bredes AL, Miller JK, Kerr L and Brown DR (2022) Observations of Wave Height Amplification Behind an Oyster Castle Breakwater System in a High-Energy Environment: Gandys Beach, NJ.
Front. Built Environ. 8:884795.
doi: 10.3389/fbuil.2022.884795

INTRODUCTION

The coastal areas of New Jersey are highly exposed to waves and storm surge during extreme weather events such as hurricanes or Nor'easters. Erosion is a large component of storm-related damage to both natural and built environments. Storm surges, tides, and heightened water levels can impact coastal marshlands by the uprooting and removal of vegetation, scouring and erosion, and folding, tearing, and compression of the marsh (Guntenspergen et al., 1995). Coastal marshes provide important ecosystem services such as buffering the negative impact of storms by protecting inland areas from erosion and storm surge, making their degradation problematic (Costanza et al., 2006). In fact, coastal wetlands prevented approximately $625 million in direct flood damage alone during Hurricane Sandy (Narayan et al., 2017). However, marshes require large extents to achieve flood and storm protection in inland areas, and marsh edge erosion can reduce marsh size and thus the protectiveness of the marsh (Koch et al., 2009; Gedan et al., 2011).

Delaware Bay wetlands are thought to be more resilient to sea level rise due to their large tidal and plant growth range, sediment supply, low slope, and the availability of open space to migrate inland. At the same time, the Delaware Bay marsh edges are eroding and converting to open water with marsh loss rates of 1.1%–1.9% per decade (Weis et al., 2021). This marsh edge erosion appears to be worsening with sea level rise. An increase of storm frequency and intensity in conjunction with increased water levels will subject marsh edges to increased attack by wave action; in extreme cases this may result in erosion rates of 5–20 m per year (Elsey-Quirk et al., 2019). Given the inland protection and habitat provided by these marshes, it is imperative to reduce the erosion of marshes and the sand areas within them (Niles et al., 2013). Living shoreline projects can provide a more ecologically sensitive approach to reducing marsh edge erosion compared to traditional coastal shoreline protection.

Living shoreline projects, or natural and nature-based features (NNBF), have become an increasingly popular method of shoreline stabilization throughout the United States. Living shoreline projects provide the same protection benefits as traditional coastal protection (i.e., wave attenuation, storm surge, and wave action buffering), maintain natural coastal processes, and provide valuable ecosystem services, while having reduced initial and maintenance costs (O'Donnell, 2017). In some cases, living shoreline projects are more protective than traditional shoreline protection (Gittman et al., 2014; Smith et al., 2018) while enhancing ecosystem services such as carbon sequestration, wave attenuation, and fish nursey habitat (Scyphers et al., 2011; Davis et al., 2015; Gittman et al., 2016).

Oyster reefs and oyster reef structures like Oyster Castles have increasingly been the target of research for use in living shoreline projects. It has been long known that oyster reefs stabilize intertidal sediment and influence hydrodynamics within estuaries (Dame and Patten, 1981). The primary appeal of oyster reefs are their wave attenuation and erosion reduction characteristics. Oyster reefs are currently being investigated for their ability to protect both natural habitat and human infrastructure from wave action. An Oyster Castle installation in Alabama effectively attenuated waves, as well as provided additional ecological benefit including the appearance of some economically important species such as blue crabs; further, it was found that at one of the study locations vegetation retreat was mitigated by more than 40% over two years (Scyphers et al., 2011). Another study on oyster reefs in Virginia found that they can be effective at reducing wave energy, and thusly marsh edge erosion, however; their effectiveness is a function of freeboard (Wiberg et al., 2019).

While some engineering guidance exists for the design of living shoreline projects (Miller et al., 2015; Hardaway et al., 2017) more research is necessary to improve upon this guidance. Living shorelines projects are often designed with minimal budgets so simple empirical formulas are often used in lieu of complex physical or numerical modeling. For this reason, it is crucial that these simple formulas be as robust as possible to ensure adequate design. Adding to the complexity of the problem, even where design formulas exist the variability in the way living shorelines are constructed makes evaluating these formulas in a field setting difficult. **Table 1** shows a selection of laboratory and mathematically derived equations for submerged and low-crested breakwater structures along with applicable ranges for various parameters of each equation which might be expected to apply to living shorelines. Numerous publications exist describing design criteria or installations of living shoreline projects, yet there is seldom long-term monitoring data collection associated with these projects; this monitoring data is needed to evaluate the effectiveness of each design.

SITE DESCRIPTION

TNC's Gandys Beach Preserve (Gandys Beach) is located on Delaware Bay on the Southwestern coast of New Jersey and has been experiencing loss of marsh through edge erosion since measurement began in 1930 (Conrad, 2015; Weis et al., 2021). The site has large intertidal mud flats, sandy beaches, tidal creeks, and salt marshes. Gandys Beach is a relatively high-energy environment, with recorded wave heights in excess of 0.6 m and a tidal range of 1.72 m (Conrad, 2015). The site is located relatively close to the mouth of the Delaware Bay and is exposed to both wind-wave generated across the local fetch and to ocean waves propagating into and through the bay (Kukulka et al., 2017). Field observations and historic images at the Gandys Beach Preserve indicate significant shoreline erosion with reduced acreage of beach and salt marshes (Conrad, 2015; Weis et al., 2021). Marsh edges have sharp scarps at this site, another indicator of marsh retreat (Mariotti and Fagherazzi, 2010). Estimated shoreline retreat at Gandys Beach is about 500 feet between 1930 and 2007 (Conrad, 2015; Weis et al., 2021). Superstorm Sandy accelerated marsh edge erosion in 2012 causing significant loss of wetlands and shoreline regression in this area (Walling et al., 2017).

The Gandys Beach Preserve living shoreline project (**Figure 1**) was designed and constructed by The Nature Conservancy (TNC) in collaboration with the United States Fish and Wildlife Service (USFWS) to mitigate the effects of marsh edge erosion at the

TABLE 1 | Empirical equations to describe the transmission coefficient for waves over low-crested or submerged breakwater structures and the ranges these equations are valid.

Equation	Applicability	Structure	Reference
$K_t = -0.4\frac{F}{H_{si}} + 0.64\left(\frac{B}{H_{si}}\right)^{-0.31} \times \left(1 - e^{-0.5\xi}\right)$	$B/H_i < 10$ $0.075 < K_t < 0.80$	Low-crested breakwaters	d'Angremond et al. (1996)[a,b]
$K_t = -0.35\frac{F}{H_{si}} + 0.51\left(\frac{B}{H_{si}}\right)^{-0.31} \times \left(1 - e^{-0.41\xi}\right)$	$B/H_i > 10$ $0.075 < K_t < 0.80$	Low-crested breakwaters	d'Angremond et al. (1996); van der Meer et al. (2005)[a,b]
$K_t = \frac{1}{1.18\left(\frac{H_{si}}{F}\right)^{0.12} + 0.33\left(\frac{H_{si}}{F}\right)^{1.5}\frac{B}{\sqrt{H_{si}L_p}}}$	$2 \geq \left(\frac{F}{H_{si}}\right) \geq 0.83$	Low-crested breakwaters	Buccino and Calabrese (2007)
$K_t = \left[\min\left(0.74; 0.62\xi^{0.17}\right) - 0.25\min\left(2.2; \frac{B}{\sqrt{H_{si}L_p}}\right)\right]^2$	$\left(\frac{F}{H_{si}}\right) = 0$	Low-crested breakwaters	Buccino and Calabrese (2007)
$K_t = 1 - e^{0.65\left(\frac{F}{H}\right) - 1.09\left(\frac{H}{B}\right)} - 0.047\left(\frac{BF}{LD_{n50}}\right) + 0.067\left(\frac{FH}{BD_{n50}}\right)$	$0 \leq BF/LD_{n50} \leq 7.08$ $0 \leq FH/BD_{n50} \leq 2.14$	Submerged rubble mound breakwaters	Seabrook (1997); Seabrook and Hall (1998)
$K_t = -0.4969e^{\left(\frac{F}{H_{moi}}\right)} - 0.0292\left(\frac{B}{d_s}\right) - 0.4257\left(\frac{h}{d_s}\right) - 0.0696\log\left(\frac{B}{L}\right) + 0.1359\left(\frac{F}{B}\right) + 1.0905$	$-8.696 \leq F/H_{moi} \leq 0$ $0.286 \leq B/d_s \leq 8.750$ $0.440 \leq h/d_s \leq 1.000$ $0.024 \leq B/L \leq 1.890$ $-1.050 \leq F/B \leq 0.000$	Submerged breakwaters	Friebel and Harris (2003)[c]
$K_t = -0.4\frac{R_c}{H_i} + 0.64\left(\frac{B}{H_i}\right)^{-0.31}\left(1 - e^{-0.5\xi_{op}}\right)$	$0.075 < K_t < 0.8$	Rough and permeable breakwaters	van der Meer et al. (2005)[d]
$K_t = \frac{1.0}{1 + \left(\frac{h}{d}\right)^{1.188}\left(\frac{A}{dL}\right)^{0.261} e^{\left(0.529\left(\frac{F}{H}\right) + 0.00551\left(\frac{A^{\frac{3}{2}}}{D_{n50}^2 L}\right)\right)}}$	$F/H < 1.0$	Reef breakwaters	Ahrens (1987)

[a] For values $8 < B/H_i > 12$, the values of the transmission coefficient are interpolated linearly.
[b] Irribaren number: $\xi = tg\alpha / \left(\frac{H_{si}}{L_p}\right)^{0.5}$.
[c] d_s = Water level from the offshore toe of the structure.
[d] Surf Parameter: $\xi_{op} = \tan\theta / \sqrt{\frac{2\pi H}{gT^2}}$.

preserve. TNC installed a variety of living shoreline structures paralleling the marsh line along an approximately half-mile stretch of shoreline. These techniques include shell bag breakwaters, coir logs, spartina alterniflora plantings, and Oyster Castle® breakwaters constructed of interlocking blocks to encourage oyster growth (**Figure 2**). The Gandys Beach living shoreline project originated as a trial or "living laboratory" project to test the use of large-scale living shoreline projects in New Jersey after the marsh was damaged during Superstorm Sandy. At the time of its conception, few of the techniques implemented had ever been attempted in New Jersey or were used infrequently or at much smaller scales and typically at lower energy sites (Conrad, 2015).

Sites A, B, C, and D were selected as areas of study as they represent the variety of shoreline at Gandys Beach and are depicted in the orthomosaic in **Figure 3**. Each site has several Oyster Castles constructed of 30 cm (1 foot) rough hollow blocks with a variety of crest heights and crest widths of 60 cm (2 feet) with gaps ranging from 2 to 5 m between each structure. Each structure was designed to be seven blocks high (3.66 feet from bottom) with the offshore toe along the mean low water line (−3.1 feet NAVD88). However, the oyster castles were largely built by volunteers, so the structures may have settled unevenly or not have been placed exactly where designed. It should be noted that Sites A and D were constructed parallel to the marsh while Sites B and C run parallel to a tombolo. By summer 2019 deployment (S19) the tombolo was mostly eroded; however during the winter 2019 deployment (W19) adaptive management occurred to attempt to reduce erosion. During higher water levels, the tombolo is completely submerged and depending on wave direction, waves can approach breakwaters from both sides.

The Oyster Castle breakwaters are the primary focus of technical studies at this site, most specifically wave attenuation. In 2018 the USGS deployed wave gages and current meters at Gandys Beach along a profile which crossed one of the constructed breakwaters (Stevens' Site D). During their deployment four Nor'easters occurred. It was observed that wave attenuation initiated by the breakwater was strongly dependent on the ratio between the freeboard of the structure and the offshore wave heights (Wang et al., 2021). This is consistent with laboratory experiments relating breakwaters and the wave attenuation coefficient (Ahrens, 1987; d'Angremond et al., 1996; Seabrook, 1997; Seabrook and Hall, 1998; van der Meer et al., 2005; Buccino and Calabrese, 2007). Swell waves were not found to be dampened effectively by the Oyster Castle breakwaters but wind waves were effectively reduced in height, although occasionally waves were amplified on the leeward side of the breakwaters (Zhu et al., 2020; Wang et al., 2021). Numerous studies have demonstrated the relationship between wind waves and marsh edge erosion, leading to a focus on reducing wind wave heights rather than swell for erosion control (Marani et al., 2011; Leonardi et al., 2016). Overall USGS observed less marsh edge erosion in the area protected by Oyster Castles compared to the control area (Wang et al., 2021).

Data collected from Stevens' initial wave attenuation studies in 2019 indicate that the Oyster Castle breakwaters were effective at dissipating waves in both summer and winter; the majority of the wave heights were reduced by over 50% on the leeward side of the breakwaters (Kerr and Miller, 2020). However, it was also found that under certain conditions waves were amplified, indicating that the relationship between breakwaters and wave height reduction is not as simple as the relationship between

FIGURE 1 | Photograph of Gandys Beach preserve near Site A, October 2019.

structure freeboard and wave heights as was initially expected (Kerr and Miller, 2020). The current work focuses on identifying the conditions during which these amplification events occur and comparing the observed field data to existing empirical formulations which are based primarily on laboratory data.

FIELD METHODS AND DATA PROCESSING

Stevens deployed instruments at Gandys Beach twice in 2019 as part of this study; the first deployment was in summer 2019 (S19) (August 29 thru 3 October 2019) and the second in winter 2019 (W19) (November 21 thru 20 December 2019). Each deployment included four 4-m Ocean Sensor Systems Wave Logger III (WL3) capacitance wave staffs, four RBRsolo[3] D wave16 high-frequency pressure sensors (RBR), and a 1,200 kHz Teledyne Workhorse Sentinel Acoustic Doppler Current Profiler (ADCP). The ADCP was deployed approximately 170 m offshore of the Preserve in 3–5 m of water depending on tide and the RBR and WL3 sensors were deployed in pairs at each of four breakwater locations designated Sites A, B, C, and D (**Figure 3**). WL3 sensors were placed 2–3 m inshore of the Oyster Castles to measure transmitted wave characteristics and the RBR sensors were placed 2–3 m offshore of the structures to measure incident wave characteristics. Two-meter WL3 were deployed as data quality checks collocated with RBRs at Site A in W19 and Site D in S19 and W19 to ensure measurement consistency.

Wave data were sampled hourly on the hour by the WL3s, RBRs, and ADCP. The ADCP combines pressure data readings with acoustically measured water velocities to extract directional wave climate data. This data was collected using standard 17-min wave bursts. The WL3s measured and recorded water levels at 10 Hz for 20-min bursts. The RBRs measured and recorded pressure at 16 Hz for 17.1-min bursts. The data from the WL3s and RBRs are the basis of this wave data analysis. A real-time kinematic global positioning system (RTK GPS) was used to measure the crest elevation and extent of each Oyster Castle breakwater in NAVD88.

During the S19 deployment some data was lost due to several disruptions to data collection. The RBR at Site A had a firmware issue resulting in data loss between August 29 and 19 September 2019; simultaneously, the WL3 at Site A also experienced intermittent dropouts. Therefore, S19 Site A is completely excluded from analysis due minimal data overlap. At Site B, the WL3 was knocked over on 10 September 2019, resulting in a partial dataset for S19. Data loss was minimal, so this dataset is included in this analysis.

These data collection efforts are part of a four-year study for TNC which includes additional winter and summer deployments in 2021 and 2022. In addition to water level, wave data, and breakwater crest elevations, bathymetric and topographic datasets were collected during the 2019 deployments and will be collected again during the 2021/2022 deployments. Analysis of

FIGURE 2 | Photograph of Oyster Castle® breakwaters, August 2019.

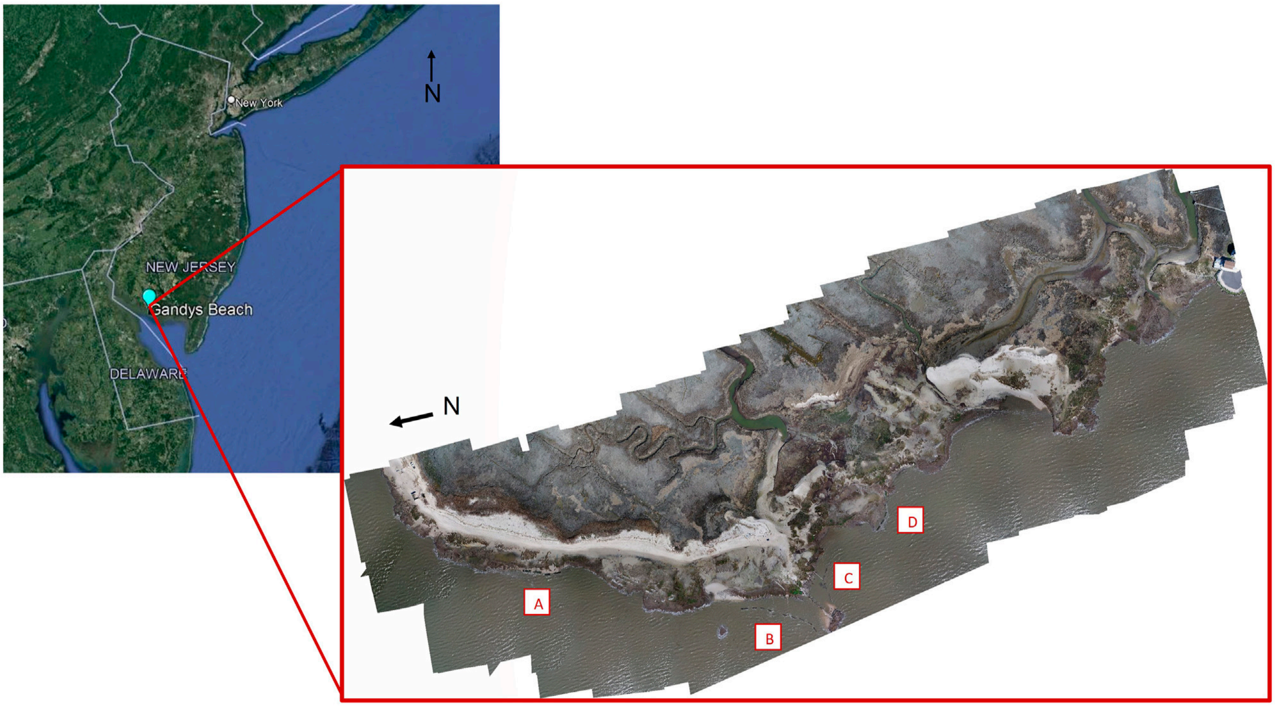

FIGURE 3 | Orthomosaic created from drone imagery of Gandys Beach Preserve with Sites A, B, C, and D labelled, April 2020.

TABLE 2 | Average significant wave height and period during S19 and W19 for both incident and transmitted waves during instances of amplification ($K_t > 1$) and reduction ($K_t < 1$).

		S19				W19			
		Incident		Transmitted		Incident		Transmitted	
		$K_t > 1$	$K_t < 1$	$K_t > 1$	$K_t < 1$	$K_t > 1$	$K_t < 1$	$K_t > 1$	$K_t < 1$
Wave height (m)	A	N/A[a]	N/A[a]	N/A[a]	N/A[a]	0.28	0.19	0.37	0.21
	B	0.16	0.16	0.14	0.08	0.54	0.22	0.54	0.16
	C	0.26	0.16	0.23	0.07	0.26	0.20	0.34	0.17
	D	0.17	0.16	0.08	0.07	0.31	0.20	0.39	0.20
Period (s)	A	N/A[a]	N/A[a]	N/A[a]	N/A[a]	2.9	2.8	2.6	2.8
	B	3.7	3.4	2.4	2.8	3.3	3.0	1.8	2.7
	C	2.7	3.4	2.7	3.1	2.9	3.0	3.1	2.7
	D	3.6	3.4	3.1	2.8	3.0	3.0	2.7	2.7

[a] *Insufficient data.*

temporal trends will continue as additional data is collected and processed.

WL3 data were processed using a moving average filter in MATLAB to remove tidal variations (detrend) from the water level data. A zero up-crossing wave analysis was performed using the MACE toolbox to determine individual wave heights and periods (Barker et al., 2012) of the detrended data; significant wave height and mean period were then calculated for each resultant 17-min burst of detrended water level. RSKtools, provided by RBR Ltd., was used to extract wave statistics from the raw RBR datasets; this software uses a similar zero-crossing methodology for analysis and accounts for pressure attenuation with depth. For both RBR and WL3 data, significant wave heights less than 5 cm were considered "too small" to be reliably compared and removed from further analysis. Bulk statistics comparing RBR and WL3 data sets were then calculated over a 20-min period. Additionally, reflected waves were not separated in this analysis due to the limited number of gauges (Grønbech et al., 1997). The ADCP data was initially processed using Teledyne's WaveMons software and then extracted to MATLAB for further analysis.

The effectiveness of the Oyster Castles at reducing wave heights was evaluated in terms of a wave transmission coefficient (K_t) calculated using the following formula:

$$K_t = \frac{H_t}{H_i} \tag{1}$$

where H_t is the transmitted wave height as measured by the WL3 inside the Oyster Castle structure and H_i is the incident wave height as measured by the RBR outside of the Oyster Castle. A K_t value greater than 1 indicates that the transmitted wave height is larger than the incident wave height.

As discussed previously, wave transmission can also be related to the freeboard of the structure. Freeboard is calculated using the crest height of each structure and the water level as measured by the WL3 and is adjusted to account for the height of the instrument. Freeboard (F) is calculated as follows:

$$F = h - d \tag{2}$$

where h is the Oyster Castle crest height and d is the water depth at the Oyster Castle. Negative freeboard values indicate breakwater submergence while positive values indicate that the breakwater crest is exposed.

Wave steepness (S) is known to indicate the potential for a wave to be erosional or accretional and is calculated as follows:

$$S = \frac{H_i}{L} \tag{3}$$

where H_i is incident significant wave height, and L is wavelength. Limited research on wave steepness erosion thresholds exist in marsh environment; the majority of wave steepness erosion research is along sandy coastlines with a steepness threshold ranging from 0.01 to 0.03, and a typical value of 0.025 (King and Williams, 1949; Kana, 1977; Masselink et al., 2010; Lemke and Miller, 2020). Due to the lack of literature on erosional wave steepness for marshes, a wave steepness threshold of 0.017 was selected by averaging the wave steepness of the measured incident waves associated with transmission coefficients > 1. This value does not reflect true erosional conditions in marshes; however, it does provide a basis for beginning to analyze the erosional or accretional behavior of waves at a marsh edge.

Observed wave transmission coefficients were compared to the wave transmission coefficient modeled with Seabrook and Hall (1998). The Seabrook and Hall formula was selected because of all the formulas presented in **Table 1**, the Seabrook and Hall formula is the only one that produces instances of $K_t > 1$ and that was tested under 3-D conditions. The Seabrook and Hall (1998) formula is as follows:

$$K_t = 1 - e^{0.65\left(\frac{F}{H_i}\right) - 1.09\left(\frac{H_i}{B}\right)} - 0.047\left(\frac{BF}{LD_{n50}}\right) + 0.067\left(\frac{FH_i}{BD_{n50}}\right) \tag{4}$$

where F is freeboard, H is incident significant wave height, B is crest width, L is wavelength, and D_{n50} is nominal stone diameter. For all sites, D_{n50} is 30 cm and the constructed crest width is 0.5 m. The Seabrook and Hall formula is most sensitive to relative freeboard (F/H_i) and relative crest width (B/H_i), the dimensionless ratios of freeboard and crest width, respectively, with incident significant wave height.

RESULTS

Wave data were collected during two seasonal deployments at Gandys Beach. During S19 and W19 conditions varied, with larger incident wave heights and shorter periods being measured in W19 as summarized in **Table 2**. This reflects differences in seasonal storminess typical in the area. No storms occurred during the S19 deployment, while a large storm and multiple smaller storms occurred during W19, as seen in the elevated water levels depicted in **Figure 4**.

The hourly, 20-min burst sampled wave gauge data collected during S19 and W19 were analyzed to determine the significant wave height, mean wave period (period), and mean water level. These data were then used to calculate wave steepness and wave transmission

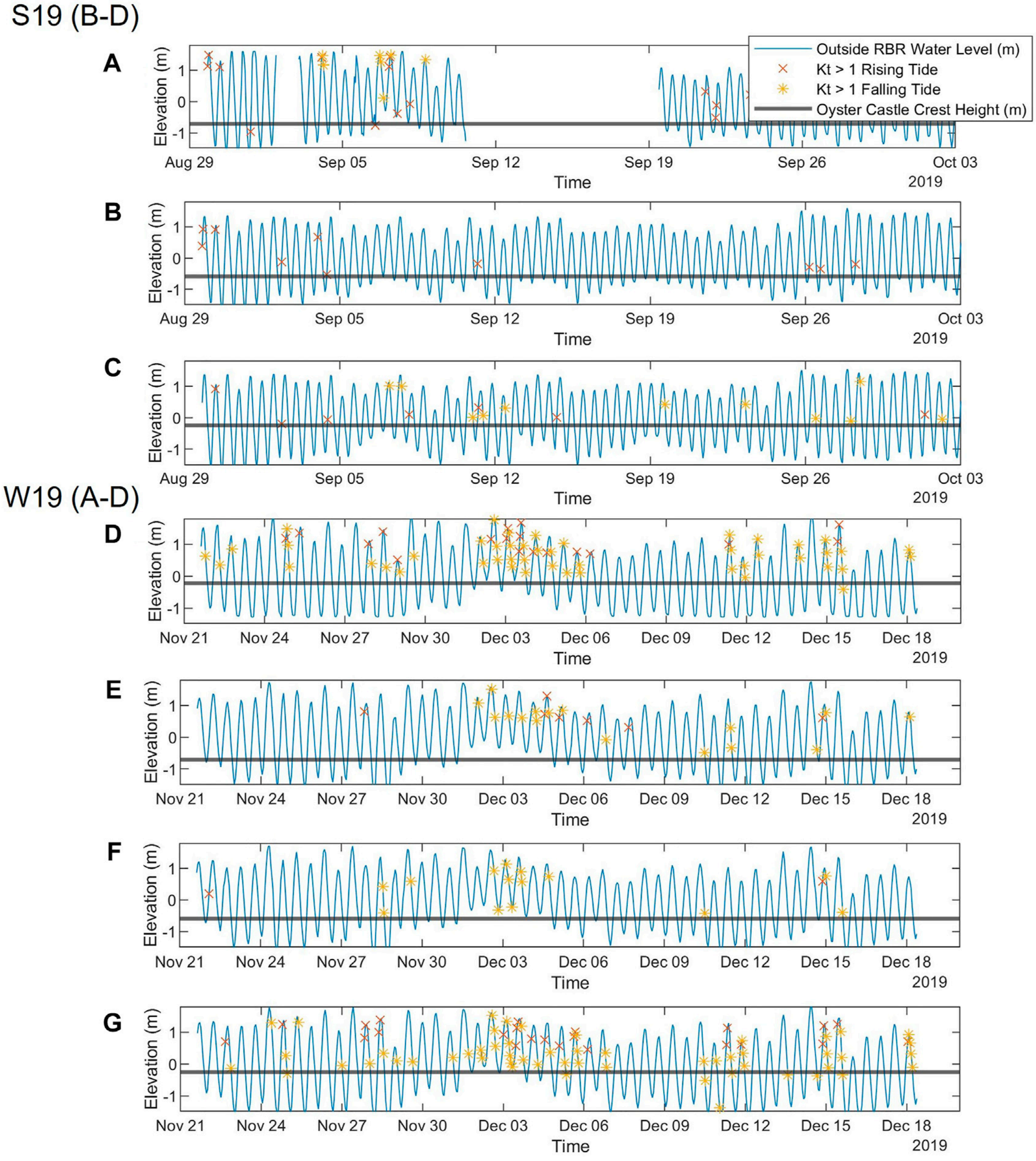

FIGURE 4 | Water levels during S19 **(A–C)** and W19 **(D–G)** at Site A **(D)**, B **(A,E)**, C **(B,F)**, and D **(C,G)**. Amplificated wave height ($K_t > 1$) is indicated by stars and x's. Yellow stars and red x's indicate if amplification is on the falling or rising tide, respectively. The bold horizontal line indicates the Oyster Castle crest elevation at that Site.

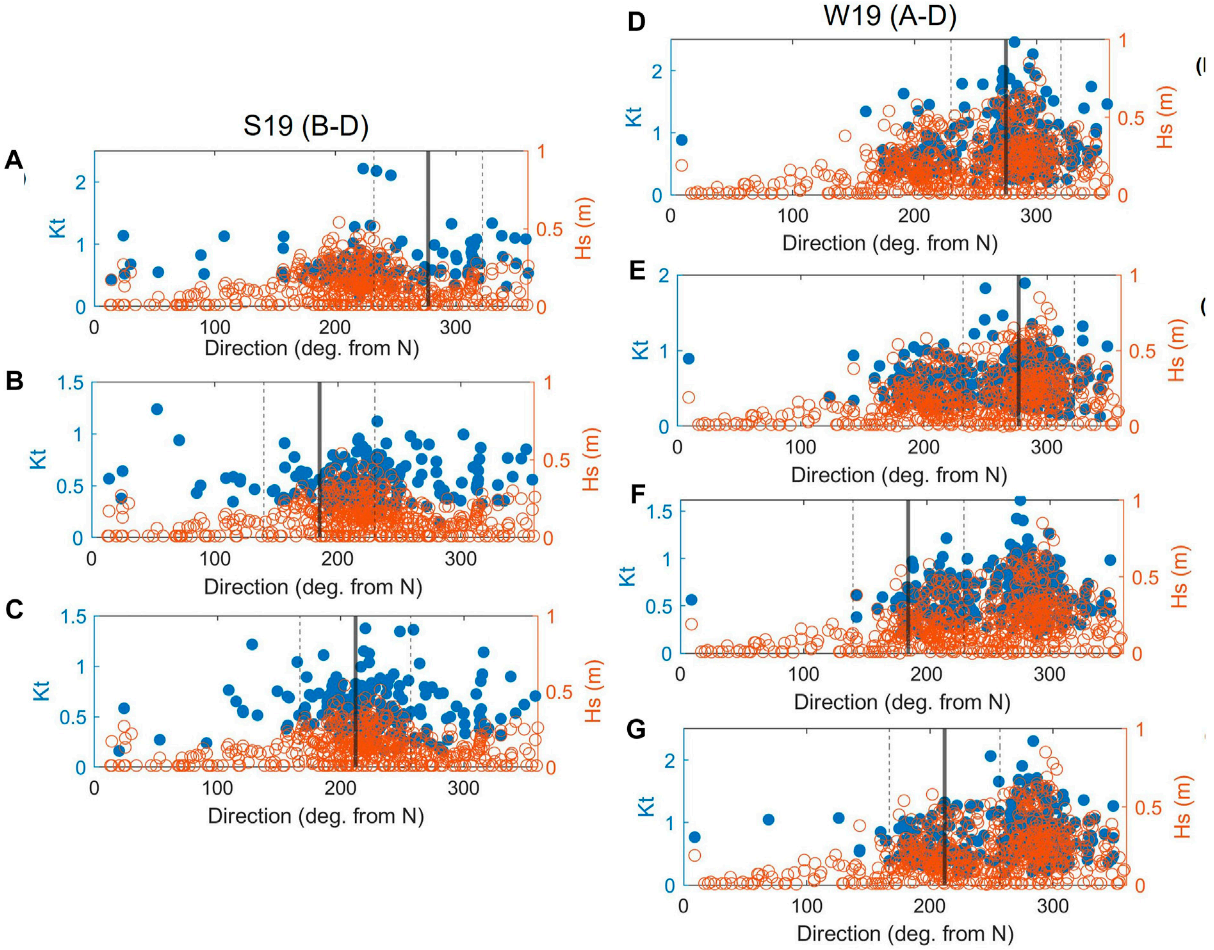

FIGURE 5 | Incident wave direction and significant wave height (open red circle) from offshore ADCP and transmission coefficient (K_t) (filled blue circle) during S19 **(A–C)** and W19 **(D–G)** and at Site A **(D)**, B **(A,E)**, C **(B,F)**, and D **(C,G)**. Direction of structure perpendicular is indicated with vertical lines and have a ± 45° range. Direction of approach does not appear to have a meaningful impact on transmission coefficient.

coefficients. Significant wave heights ranged from 0.05 to 0.7 m over the two deployments, with the average significant wave height higher during the W19 deployment (0.20 m) than during the S19 deployment (0.15 m). Wave periods ranged from around 2 s to just over 6 s over the deployments; average wave period longer in the S19 deployment (3.4 s) than in the W19 deployment (2.9 s). Variations in significant wave height and wave period were observed between the four sites. It should be noted that Sites B and C are separated by a predominantly submerged tombolo while Sites A and D both front the marsh. The average calculated K_t value was also slightly larger during the W19 deployment (0.7) than during the S19 deployment (0.6).

Regardless of season, structure orientation relative to the incident wave field was found to have minimal impact on the transmission coefficient. In **Figure 5**, the direction of wave approach (degrees from North) is plotted against K_t and H_i. Structure perpendicular is indicated by a bold vertical line with a 45° buffer indicated by dashed vertical lines on each side to indicate the wave directions that are considered "directly approaching" each structure. Transmission coefficient displayed similar behavior at each breakwater site, independent of incident wave direction.

While the majority of waves appear to be attenuated by the structures, periods of wave height amplification were observed in both seasonal datasets. In the S19 data, amplification events were more limited, and tended to occur during a small number of individual events. On the contrary, in the W19 dataset, wave amplification occurred throughout the record with amplification events more clustered during storms (**Figure 4**). Incident wave heights tended to be larger during cases of amplification during W19, but not necessarily during S19. Incident wave periods were relatively similar regardless of wave transmission coefficient, however transmitted mean wave periods tended to be shorter than incident mean periods (**Table 2**). This observed decrease in mean period is likely due to the variety of complex processes occurring at this site; waves transmitting over, around, and through structures, waves breaking or shoaling on structures, waves reflecting off the marsh, and the influence of currents.

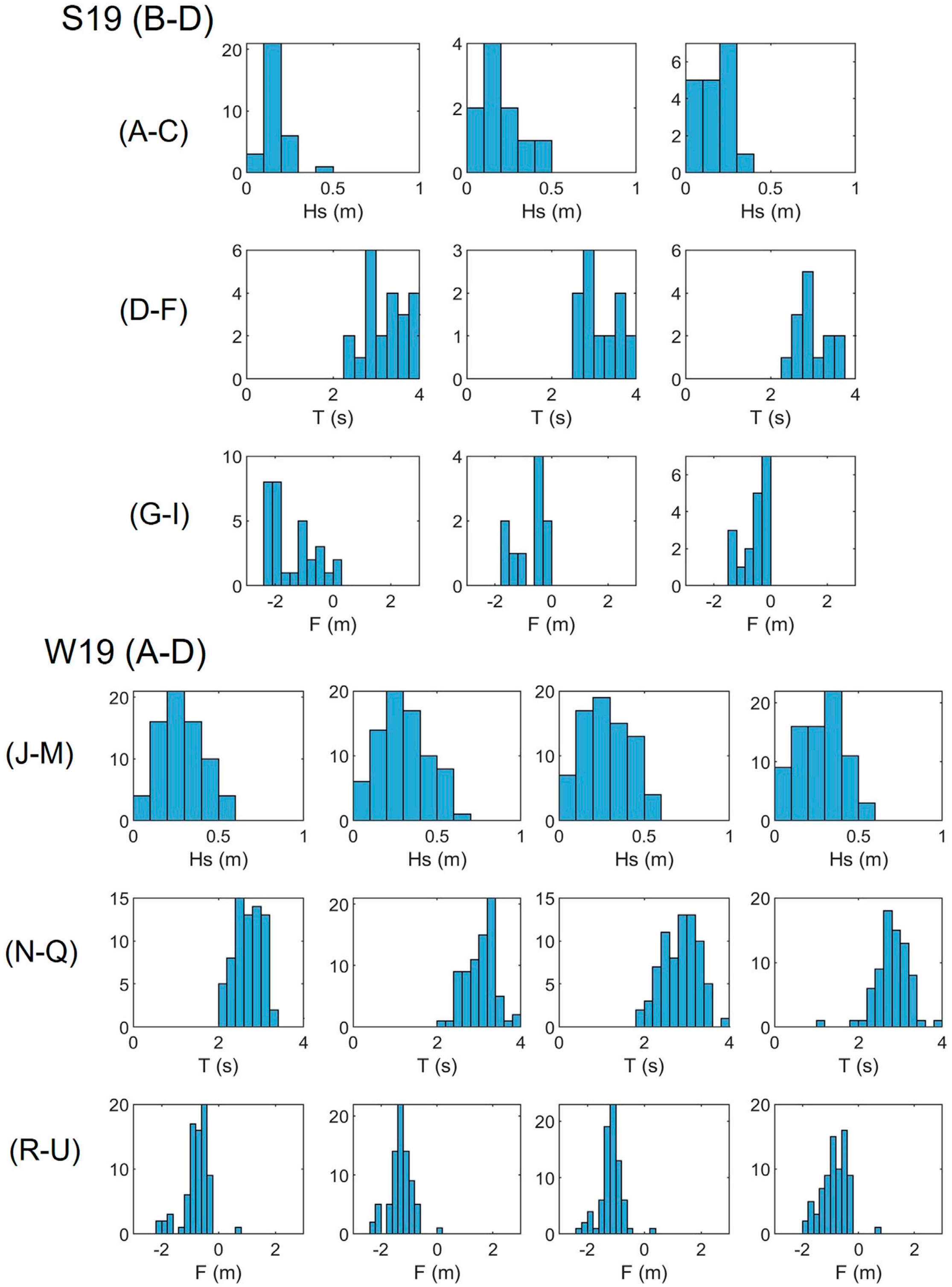

FIGURE 6 | Histograms of incident significant wave height **(A–C,J–M)**, period **(D–F,N–P)**, and freeboard **(G–I,Q–T)** during S19 **(A–I)** and W19 **(J–T)** for cases of $K_t > 1$ at Site A **(J,N,R)**, B **(A,D,G,K,O,S)**, C **(B,E,H,L,P,T)**, D **(C,F,I,M,Q,U)**. Each histogram represents the entire deployment at the corresponding location.

TABLE 3 | Average change in significant wave height and wave period between the incident and transmitted wave heights at Sites A, B, C, and D. Negative percentages indicate a decrease of period or wave height of the transmitted wave as compared to the incident wave.

		S19		W19	
		$K_t > 1$	$K_t < 1$	$K_t > 1$	$K_t < 1$
Wave height change (m)	A	N/A[a]	N/A[a]	43%	−38%
	B	38%	−41%	21%	−44%
	C	17%	−46%	19%	−42%
	D	15%	−42%	27%	−41%
Period change (s)	A	N/A[a]	N/A[a]	−11%	1%
	B	−27%	−9%	−7%	−8%
	C	−11%	0%	0%	−6%
	D	−4%	−13%	5%	−8%

[a] *Insufficient data.*

TABLE 4 | Occurrences of amplification during each 20-min calculated bulk statistic at each site during rising or falling tides.

	S19		W19	
	Rising	Falling	Rising	Falling
A	N/A[a]	N/A[a]	18	47
B	22	9	7	16
C	10	0	2	14
D	7	11	23	54

[a] *Insufficient data.*

The significant wave height and mean wave period of the incident waves, along with the freeboard were examined during instances of wave amplification ($K_t > 1$) (**Figure 6**). Overall, for $K_t > 1$, mean wave heights ranged from 0.05 to 0.6 m, mean wave periods ranged from 2 s to 4 s, and freeboard ranged from −2.5 to 0.5 m. The most frequent amplification events occurred when wave heights were between 0.1 and 0.3 m, periods were between 2.5 and 3.5 s, and freeboard was between −1.5 m and −0.5 m. In 8 out of 240 recorded instances of amplification, structures were emergent. These occurrences may be due to waves transmitting through the gaps between structures, waves reflecting off the marsh edge, waves interacting with strong localized currents as the marsh drains and fills, or a combination of the above.

The percent change in wave height between the incident and transmitted waves was found to be consistent between W19 and S19. During periods of amplification, average transmitted wave height was 14%–42% greater than incident wave height, while during times of wave reduction the average transmitted wave height was 38%–46% less than the incident wave height (**Table 3**). Amplification occurred when the structures were submerged, with eight exceptions (**Figure 4**). During the W19 deployment, amplification events occurred during falling tides 72% of the time and were clustered near storm events, possibly due to interactions with currents during marsh drainage. Conversely, during the S19 deployment, amplification events occurred during rising tides 66% of the time and no large storm events occurred (**Table 4**).

There are many possible physical explanations for this wave amplification that further research will attempt to uncover in order to provide more thorough guidance on oyster castle design. The large tidal range at Gandys Beach provides a unique opportunity to analyze wave attenuation of structures front such a marsh. The tidal range and fetch at Gandys Beach in combination with the relatively small oyster castle breakwaters and complex geography of the area provide a rich set of results for analysis.

DISCUSSION

This study was not the first to document increased wave heights behind one of the Oyster Castle breakwaters at Gandys Beach. In a 2021 study, USGS observed both wave height amplification and reduction associated with Oyster Castle breakwaters at Site D (the only site in their study) (Wang et al., 2021). This is consistent with the observations made during S19 and W19 at all four oyster castle breakwaters studied; however, the USGS study noted that wave height amplification mostly occurred during small wave heights. This result is inconsistent with the findings of this study, where wave height amplification was observed over a range of incident wave conditions. In fact, many of the observed wave amplification events during W19 and S19 correlate with storm conditions during which elevated water levels and large wave heights were recorded. Most notably, a large storm event occurred during the W19 deployment from December 1–5, 2019. During these storm events, the wave heights were large, the wave periods remained consistent, and wave amplification was more frequent, particularly during falling tides (**Figure 4**). When storm surge fills the marsh, large volumes of water can drain from marsh behind the structures during falling tides, interacting with the incoming wave field, likely contributing to the observed wave amplification during some falling tides.

The ability to model wave transmission across a living shoreline structure designed for wave attenuation is tantamount for designing and constructing successful projects that provide desired outcomes at a site. As briefly discussed, several empirical models exist for predicting wave attenuation across low-crested/submerged structures (**Table 1**). While formulas differ, all contain freeboard, crest width, and wave height, highlighting the importance of these structure and wave field characteristics. Nearly all of these models were tested in simplified laboratory conditions and largely have not been validated by field data. Notably, only Seabrook and Hall, Friebel and Harris, and Ahrens specifically describe submerged structures, and only Seabrook is capable of producing transmission coefficient was greater than one. Field data collected at Gandys Beach provides the opportunity to evaluate the applicability of these models during more complicated, real-world conditions.

USGS compared their observations to the empirical models of (d'Angremond et.al.,1996; van der Meer et.al.,2005) but found that the modeled amplification was considerably lower than the

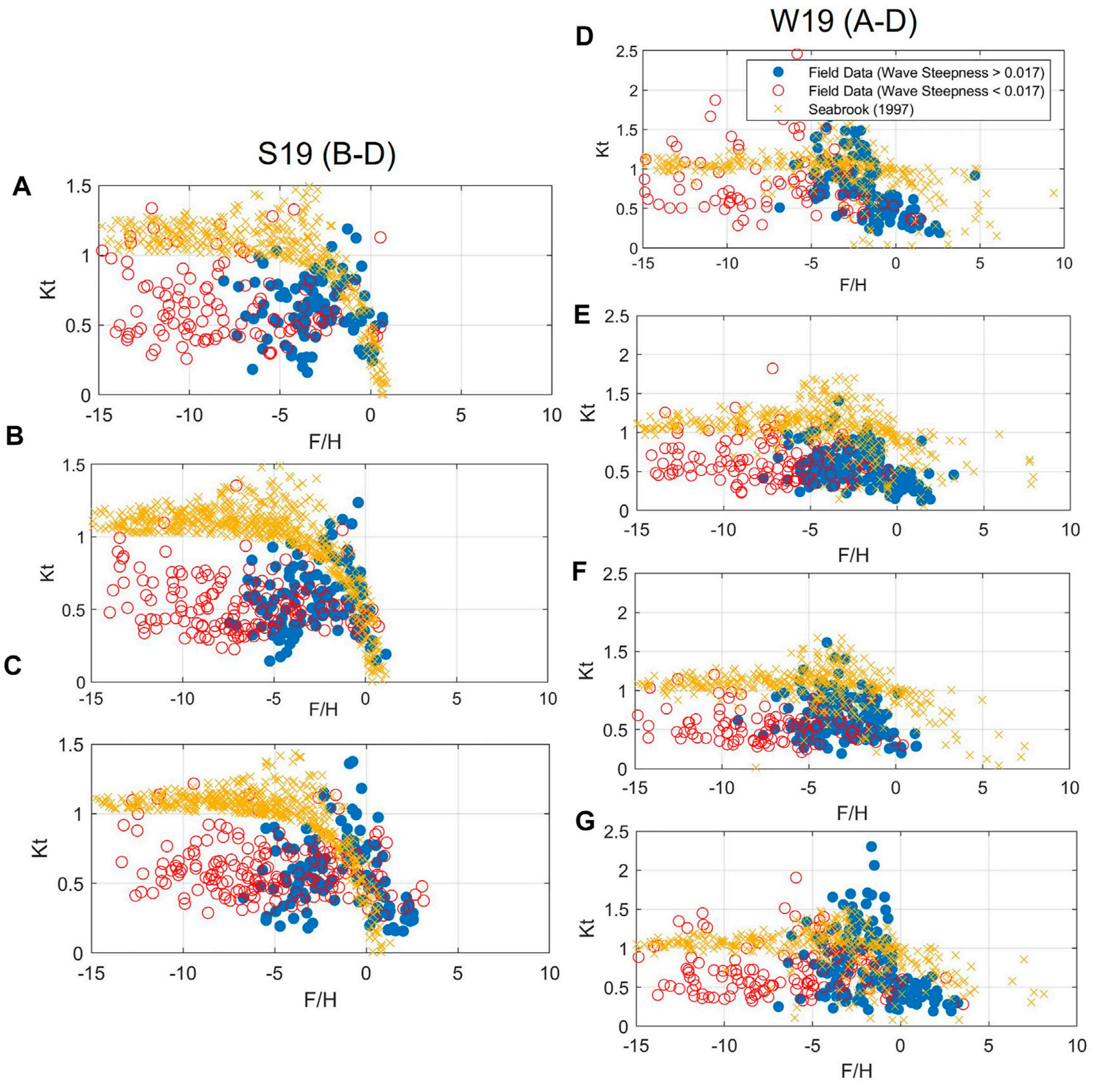

FIGURE 7 | Wave transmission coefficient (K_t) vs. relative freeboard (F/H_i) as observed in field data and modeled by Seabrook and Hall (1998) during S19 **(A–C)** and W19 **(D–G)** and at Site A **(D)**, B **(A,E)**, C **(B,F)**, and D **(C,G)**. F/H_i values greater than 0 indicate structure emergence and values less than 0 indicate submergence. Observed data is grouped by incident wave steepness threshold of greater than 0.017. Waves with a steepness greater than the threshold are more likely to be erosional and potentially contribute more to marsh edge erosion.

observed amplification during emergent structure conditions. We hypothesize that this was potentially due to the gaps between the individual Oyster Castles reducing the effectiveness of the structures. USGS also identified periods during which the measured transmission coefficient was >1. Neither of the empirical equations selected by USGS can reproduce this result as they predict maximum transmission coefficients below 1.

In the current study, the observed transmission coefficients were compared against the empirical model by Seabrook and Hall (1998). Of the models considered (listed in **Table 2**), Seabrook and Hall is the only one capable of producing $K_t > 1$ and was one of the few tested in oblique wave conditions. In our analysis, the transmission coefficient was calculated with field observations and modeled using Seabrook and Hall and incident wave data. Results of the W19 and S19 deployments are plotted in **Figure 7** along with the transmission coefficient predicted by the Seabrook and Hall equation. While there is significant scatter in the data, a similar relative freeboard region of amplification was produced in the modeled and observed K_t. In cases of $K_t < 1$ Seabrook and Hall (1998) does not perform well compared to measured K_t. This scatter is not unexpected as there are significant differences and poor agreement between the continuous low-crested breakwater structure modeled by Seabrook and Hall under controlled laboratory conditions and the highly irregular non-continuous structures and varied wave conditions observed in the field, making Seabrook and Hall (1998) an inadequate predictive tool for structures and conditions such as those at Gandys Beach. Living shorelines structures are often constructed of non-traditional materials, irregular, non-continuous, and change significantly over time with shellfish colonization or

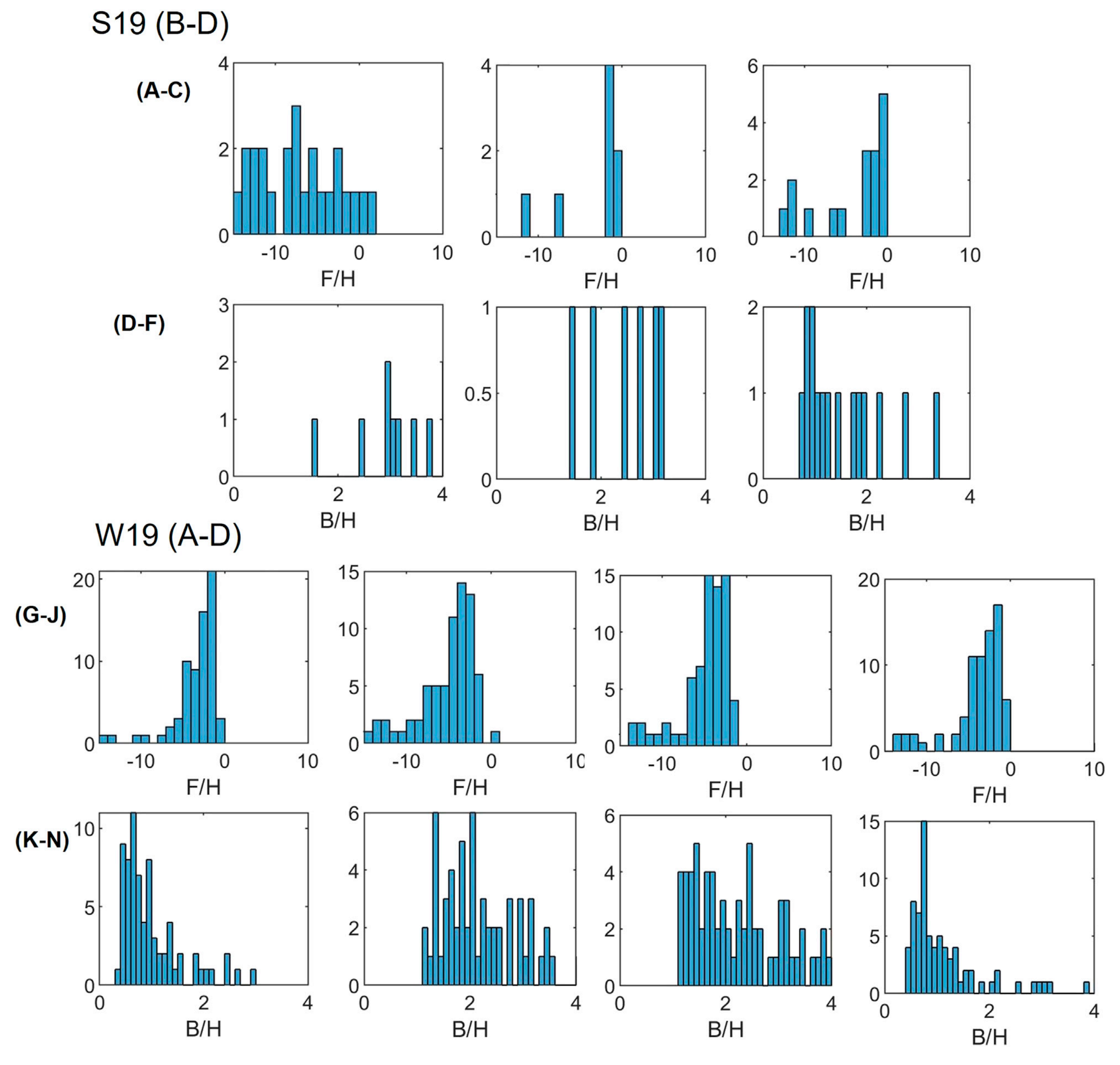

FIGURE 8 | Histograms of relative freeboard (F/H_i) and relative crest width (F/B) during S19 **(A–F)** and W19 **(G–N)** at Site A **(G,K)**, B **(A,D,H,L)**, C **(B,E,I,M)**, and D **(C,F,J,N)**.

vegetation growth, and as habitat created by the living shoreline becomes more developed. These changes will alter porosity, roughness, effective stone size, dimensions of structures, relative crest width, and relative freeboard. Formulas that only represent the structures at the state of construction are inadequate to describe living shorelines and novel empirical formulas need to be developed that can estimate living shoreline wave transmission over the life of the structure.

Relative freeboard (F/H_i) and relative crest width (B/H_i) are parameters that appear in many of the empirical equations for wave transmission coefficient over submerged breakwaters, including Seabrook and Hall (1998) (d'Angremond et al., 1996; Seabrook, 1997; Seabrook and Hall, 1998; van der Meer et al., 2005; Buccino and Calabrese, 2007) (**Table 1**). Relative freeboard and relative crest width were examined for all observed amplification events in the W19 and S19 field data and it was found that most of these events occur when the relative freeboard is between −1 and −6 (submerged) (**Figure 8**), with very few events occurring when the relative freeboard was above −1 (minorly submerged to emergent). One possible explanation for wave amplification when the relative freeboard is between −1 and −6 (submerged) is wave shoaling. The waves "feel the bottom" (in this case, the oyster castle structure) and begin to shoal, but do not break, leading to an increase in transmitted height. When the relative freeboard is > −1 (minorly submerged to emergent) the depth over the structures becomes shallow enough that the waves begin to break, leading to wave height reduction in this region. Wave amplification and reduction observed when the structure is submerged (relative freeboard less than −6), may be the result of waves reflecting off the marsh or interacting with water draining from the marsh.

The majority of waves where relative freeboard was between −1 and −6 (submerged) have an incident wave steepness above 0.017, the basis wave steepness threshold applied in this analysis (**Figure 7**). Several wave amplification events occurred when relative freeboard was less than −6 (significantly submerged) and waves in this range tended to be below the wave steepness threshold. There is no clear correlation between wave steepness and wave amplification in the data collected at Gandys Beach. However, steeper waves are more likely to erode shorelines in sandy areas, some of which are present at Gandys Beach (**Figure 2**) and may also be a factor in marsh edge erosion and worth investigating in future research.

The Seabrook and Hall equation, consistent with most submerged breakwater relationships, suggests that wave transmission decreases as the relative crest width increases and increases as relative freeboard decreases when structures are submerged. When modeling wave transmission using Seabrook and Hall and relative freeboard is between −1 and −6 (submerged), the amplification events are very sensitive to decreases in crest width. Most amplification events at Sites A and D were clustered around relative crest widths between 0.4 and 1.5 and were skewed to the right. It is clear from this analysis that at Sites A and D relative crest width is a predictor of wave amplification. At Sites B and C, the observed amplification events occurred more evenly across a range of relative crest widths. This may be related to the position of the breakwaters, as noted in the site description. Increasing crest width during structure design may mitigate the likelihood of wave amplification. Designing to minimize instances where relative crest width is less than 0.4–1.5 may reduce these events. Additional considerations should be taken when considering future adaptability of structures to ensure that crest width remains sufficiently large when inevitable structure modifications are made to maintain structure effectiveness with sea level rise.

It is clear that wave heights are more likely to amplify at Gandys Beach Preserve when structures are submerged, relative crest width is 0.4–1.5, and relative freeboard is −1 to −6 (submerged). These results are troubling especially in areas experiencing sea level rise where the frequency of submergence is likely to increase in the future. However, the field data collected at Gandys Beach does not create a clear picture of mechanisms causing wave height amplification due to the complexity of the site. Reflection of waves off the marsh edge, wave shoaling on structure crests during certain relative crest width and relative freeboard conditions, wave transmission through gaps between Oyster Castles, and currents resulting from marsh drainage during falling tides are all possible mechanisms amplifying wave heights at the sites studied. All of these factors complicate the identification of the most appropriate empirical formula to aid design of Oyster Castle breakwaters. Additional datasets are being collected at Gandys Beach that aim to resolve some of the hypotheses and questions identified in this analysis regarding wave amplification to help inform robust guidance on living shoreline design.

DATA AVAILABILITY STATEMENT

The raw data supporting the conclusions of this article will be made available by the authors, without undue reservation.

AUTHOR CONTRIBUTIONS

Conceptualization, AB; field deployment, DB, LK, and JM; formal analysis, AB and DB; data curation, AB; writing—original draft preparation, AB; writing—review and editing, JM. and LK.; visualization, AB; supervision, JM and LK; project administration, JM. All authors have read and agreed to the published version of the manuscript.

FUNDING

This research was funded by National Fish and Wildlife Foundation and the Nature Conservancy. Amy Bredes work on this project was supported by a Provost's Doctoral Fellowship awarded by Stevens Institute of Technology. A portion of DanaRose Brown's work on the project was supported by the New Jersey Department of Environmental Protection (NJDEP) through the New Jersey Coastal Protection Technical Assistance Service (N.J.S.A. 18A:64L-1).

ACKNOWLEDGMENTS

The writers wish to gratefully acknowledge the contributions of The Nature Conservancy (TNC) and United States. Fish and Wildlife Service (USFWS), with special thanks to Adrianna Zito-Livingston (TNC) and Danielle McCulloch (USFWS).

REFERENCES

Ahrens, J. (1987). *Characteristics of Reef Breakwaters*. Vicksburg, MS: Coastal Engineering Research Center. [Preprint].

Barker, C., Day, C. M., Johnson, D., Liu, P., Brennan, M., Martinez, G. R., et al. (2012). *MACE*. Kyoto, Japan: Kyoto University. Available at: http://www.oceanwave.jp/softwares/mace/index.php?MACE%20is.

Buccino, M., and Calabrese, M. (2007). Conceptual Approach for Prediction of Wave Transmission at Low-Crested Breakwaters. *J. Waterw. Port. Coast. Ocean. Eng.* 133 (3), 213–224. doi:10.1061/(asce)0733-950x(2007)133:3(213)

Conrad, K. (2015). *Final Environmental Assessment for the Gandys Beach/Money Island Living Shoreline Project*. Pleasantville, N.J.: U.S. Fish and Wildlife Service. Available at: https://www.fws.gov/hurricane/sandy/pdf/GandysBeachEA.pdf.

Costanza, R., Wilson, M., Troy, A., Voinov, A., Liu, S., and Agostino, J. (2006). *'The Value of New Jersey's Ecosystem Services and Natural Capital'*. Trenton, NJ: New Jersey Department of Environmental Protection. [Preprint].

d'Angremond, K., Van Der Meer, J. W., and De Jong, R. J. (1997). "Wave Transmission at Low-Crested Structures," in *Coastal Engineering*. 25th International Conference on Coastal Engineering (Orlando, Florida, United States: American Society of Civil Engineers), 2418–2427. doi:10.1061/9780784402429.187

Dame, R., and Patten, B. (1981). Analysis of Energy Flows in an Lntertidal Oyster Reef. *Mar. Ecol. Prog. Ser.* 5, 115–124. doi:10.3354/meps005115

Davis, J. L., Currin, C. A., O'Brien, C., Raffenburg, C., and Davis, A. (2015). Living Shorelines: Coastal Resilience with a Blue Carbon Benefit. *PLoS ONE* 10 (11), e0142595. doi:10.1371/journal.pone.0142595

Elsey-Quirk, T., Mariotti, G., Valentine, K., and Raper, K. (2019). Retreating Marsh Shoreline Creates Hotspots of High-Marsh Plant Diversity. *Sci. Rep.* 9 (1), 5795. doi:10.1038/s41598-019-42119-8

Friebel, H. C., and Harris, L. E. (2003). *Re-evaluation of Wave Transmission Coefficient Formulae from Submerged Breakwater Physical Models*. Melbourne, Fl 32901, USA: Department of Marine and Environmental Systems, Florida Institute of Technology.

Gedan, K. B., Kirwan, M. L., Wolanski, E., Barbier, E. B., and Silliman, B. R. (2011). The Present and Future Role of Coastal Wetland Vegetation in Protecting Shorelines: Answering Recent Challenges to the Paradigm. *Clim. Change* 106 (1), 7–29. doi:10.1007/s10584-010-0003-7

Gittman, R. K., Peterson, C. H., Currin, C. A., Joel Fodrie, F., Piehler, M. F., and Bruno, J. F. (2016). Living Shorelines Can Enhance the Nursery Role of Threatened Estuarine Habitats. *Ecol. Appl.* 26 (1), 249–263. doi:10.1890/14-0716

Gittman, R. K., Popowich, A. M., Bruno, J. F., and Peterson, C. H. (2014). Marshes with and Without Sills Protect Estuarine Shorelines from Erosion Better Than Bulkheads During a Category 1 Hurricane. *Ocean Coast. Manag.* 102, 94–102. doi:10.1016/j.ocecoaman.2014.09.016

Grønbech, J., Jensen, T., and Andersen, H. (1997). "Reflection Analysis with Separation of Cross Modes," in *Coastal Engineering 1996*. 25th International Conference on Coastal Engineering (Orlando, Florida, United States: American Society of Civil Engineers), 968–980. doi:10.1061/9780784402429.076

Guntenspergen, G. R., Cahoon, D. R., Grace, J. B., Steyer, G. D., Fournet, S., Townson, M. A., et al. (1995). Disturbance and Recovery of the Louisiana Coastal Marsh Landscape from the Impacts of Hurricane Andrew. *J. Coast. Res.* 21, 324–339.

Hardaway, C. S., Jr, Milligan, D. A., Duhring, K., and Wilcox, C. A. (2017). *Living Shoreline Design Guidelines for Shore Protection in Virginia's Estuarine Environments*. Gloucester Point, VA: Virginia Institute of Marine Science.

Kana, T. W. (1977). Beach Erosion During Minor Storm. *J. Wtrwy., Port, Coast., Oc. Div.* 103 (4), 505–518. doi:10.1061/JWPCDX.0000056

Kerr, L., and Miller, J. K. (2020). *'Gandy's Beach Living Shoreline Project, Wave Attenuation Monitoring Interim Report'*. Hoboken, NJ: Stevens Institute of Technology, Davidson Labroratory. [Preprint], (TR SIT-DL-20-9-CV1).

King, C. A. M., and Williams, W. W. (1949). The Formation and Movement of Sand Bars by Wave Action. *Geogr. J.* 113, 70. doi:10.2307/1788907

Koch, E. W., Barbier, E. B., Silliman, B. R., Reed, D. J., Perillo, G. M., Hacker, S. D., et al. (2009). Non-Linearity in Ecosystem Services: Temporal and Spatial Variability in Coastal Protection. *Front. Ecol. Environ.* 7 (1), 29–37. doi:10.1890/080126

Kukulka, T., Jenkins, R. L., Kirby, J. T., Shi, F., and Scarborough, R. W. (2017). Surface Wave Dynamics in Delaware Bay and its Adjacent Coastal Shelf. *J. Geophys. Res. Oceans* 122 (11), 8683–8706. doi:10.1002/2017JC013370

Lemke, L., and Miller, J. K. (2020). Evaluation of Storms Through the Lens of Erosion Potential Along the New Jersey, USA Coast. *Coast. Eng.* 158, 103699. doi:10.1016/j.coastaleng.2020.103699

Leonardi, N., Ganju, N. K., and Fagherazzi, S. (2016). A Linear Relationship Between Wave Power and Erosion Determines Salt-Marsh Resilience to Violent Storms and Hurricanes. *Proc. Natl. Acad. Sci. U.S.A.* 113 (1), 64–68. doi:10.1073/pnas.1510095112

Marani, M., D'Alpaos, A., Lanzoni, S., and Santalucia, M. (2011). Understanding and Predicting Wave Erosion of Marsh Edges: Marsh Edge Erosion. *Geophys. Res. Lett.* 38 (21), L21401. doi:10.1029/2011gl048995

Mariotti, G., and Fagherazzi, S. (2010). A Numerical Model for the Coupled Long-Term Evolution of Salt Marshes and Tidal Flats. *J. Geophys. Res.* 115 (F1), F01004. doi:10.1029/2009JF001326

Masselink, G., Russell, P., Blenkinsopp, C., and Turner, I. (2010). Swash Zone Sediment Transport, Step Dynamics and Morphological Response on a Gravel Beach. *Mar. Geol.* 274 (1–4), 50–68. doi:10.1016/j.margeo.2010.03.005

Miller, J. K., Rella, A., Williams, A., and Sproule, E. (2015). *Living Shorelines Engineering Guidelines*. Hoboken, NJ: Stevens Institute of Technology. SIT-DL-14-9-2942.

Narayan, S., Beck, M. W., Wilson, P., Thomas, C. J., Guerrero, A., Shepard, C. C., et al. (2017). The Value of Coastal Wetlands for Flood Damage Reduction in the Northeastern USA. *Sci. Rep.* 7 (1), 9463. doi:10.1038/s41598-017-09269-z

Niles, L. J., Smith, J. A., Daly, D. F., Dillingham, T., Shadel, W., Danihel, M. S., et al. (2013). *Restoration of Horseshoe Crab and Migratory Shorebird Habitat on Five Delaware Bay Beaches Damaged by Superstorm Sandy*. Bordentown: L.J. Niles Associates.

O'Donnell, J. E. D. (2017). Living Shorelines: A Review of Literature Relevant to New England Coasts. *J. Coast. Res.* 33 (2), 435–451. doi:10.2112/JCOASTRES-D-15-00184.1

Scyphers, S. B., Powers, S. P., Heck, K. L., and Byron, D. (2011). Oyster Reefs as Natural Breakwaters Mitigate Shoreline Loss and Facilitate Fisheries. *PLoS ONE* 6 (8), e22396. doi:10.1371/journal.pone.0022396

Seabrook, S. R., and Hall, K. R. (1998). Wave Transmission at Submerged Rubblemound Breakwaters. *Coast. Eng. Proc.* 1 (26), 2000.

Seabrook, S. R. (1997). *Investigation of the Performance of Submerged Rubblemound Breakwaters*. Ontario, Canada: Queen's University.

Smith, C. S., Puckett, B., Gittman, R. K., and Peterson, C. H. (2018). *Living Shorelines Enhanced the Resilience of Saltmarshes to Hurricane Matthew (2016)*. Dryad Morehead City, NC: Dryad. doi:10.5061/DRYAD.NH71T5C

van der Meer, J. W., Briganti, R., Zanuttigh, B., and Wang, B. (2005). Wave Transmission and Reflection at Low-Crested Structures: Design Formulae, Oblique Wave Attack and Spectral Change. *Coast. Eng.* 52 (10–11), 915–929. doi:10.1016/j.coastaleng.2005.09.005

Walling, K., Gaffney, D., and Moses, K. (2017). *Wave Attenuation and Sediment Transport Monitoring of Living Shorelines in the Delware Bay*. U.S.: Mott MacDonald.

Wang, H., Capurso, W., Chen, Q., Zhu, L., Niemoczynski, L., and Snedden, G. (2021). *Assessment of Wave Attenuation, Current Patterns, and Sediment Deposition and Erosion During Winter Storms by Living Shoreline Structures in Gandys Beach, New Jersey*. Reston, Virginia: U.S. Geological Survey, 37. [Preprint].

Weis, J. S., Watson, E. B., Ravit, B., Harman, C., and Yepsen, M. (2021). The Status and Future of Tidal Marshes in New Jersey Faced with Sea Level Rise. *Anthr. Coasts* 4 (1), 168–192. doi:10.1139/anc-2020-0020

Wiberg, P. L., Taube, S. R., Ferguson, A. E., Kremer, M. R., and Reidenbach, M. A. (2019). Wave Attenuation by Oyster Reefs in Shallow Coastal Bays. *Estuaries Coasts* 42 (2), 331–347. doi:10.1007/s12237-018-0463-y

Zhu, L., Chen, Q., Wang, H., Capurso, W., Niemoczynski, L., Hu, K., et al. (2020). Field Observations of Wind Waves in Upper Delaware Bay with Living Shorelines. *Estuaries Coasts* 43 (4), 739–755. doi:10.1007/s12237-019-00670-7

Conflict of Interest: The authors declare that the research was conducted in the absence of any commercial or financial relationships that could be construed as a potential conflict of interest.

frontiers | Frontiers in Built Environment

ORIGINAL RESEARCH
published: 01 July 2022
doi: 10.3389/fbuil.2022.891612

Wave Attenuation by Vegetation: Model Implementation and Validation Study

Ali Abdolali[1,2,3]*, *Tyler J. Hesser*[4], *Mary Anderson Bryant*[4], *Aron Roland*[5], *Arslaan Khalid*[6], *Jane Smith*[4], *Celso Ferreira*[6], *Avichal Mehra*[1] *and Mathieu Dutour Sikiric*[7]

[1]NWS/NCEP/Environmental Modeling Center, National Oceanic and Atmospheric Administration (NOAA), College Park, MD, United States, [2]I.M. Systems Group, Inc. (IMSG), Rockville, MD, United States, [3]University of Maryland, College Park, MD, United States, [4]US Army Engineer Research and Development Center, Coastal and Hydraulics Laboratory, Vicksburg, MS, United States, [5]BGS IT & E, Darmstadt, Germany, [6]Civil, Environmental and Infrastructure Engineering, George Mason University, Fairfax, VA, United States, [7]Laboratory for Physic of the Sea and Chemistry of Water Systems, Rudjer Bošković Institute, Zagreb, Croatia

Wave–vegetation interaction is implemented in the WAVEWATCH III (WW3) model. The vegetation sink term followed the early formulations of Dalrymple et al. (Journal of Waterway, Port, Coastal, and Ocean Engineering, 1984, 110, 67–79), which focused on monochromatic waves and vegetation approximated as an array of rigid, vertical cylinders, and was later expanded by Mendez and Losada (Coastal Engineering, 2004, 51, 103–118) for random wave transformations over mildly sloping vegetation fields under breaking and nonbreaking conditions assuming a Rayleigh distribution of wave heights. First, validation is carried out for 63 laboratory cases (Anderson and Smith, 2014) with homogeneous vegetation fields for single and double-peak wave spectra. Then, a field case application is conducted to assess the wave attenuation in a wetland environment with spatially variable vegetation fields during stormy conditions. The case study uses data collected at the Magothy Bay located in the Chesapeake Bay, United States, during Hurricanes Jose and Maria in 2017. The domain decomposition parallelization and the implicit scheme have been used for the simulations to efficiently resolve complex shorelines and high-gradient wave zones, incorporating dominant physics in the complicated coastal zone, including wave breaking, wave–current interaction, bottom friction and scattering, wave–vegetation interaction, and nonlinearity (Abdolali et al., 2020). The lab validation and field application demonstrate that WW3 is an effective tool for evaluating the capacity of wetland natural or nature-based features to attenuate wave energy to achieve coastal flood risk reduction.

Keywords: wave–vegetation interaction, spectral wave model WAVEWATCH III, wetland hydrodynamics, hurricane, marshland

Edited by:
Spyros Hirdaris,
Aalto University, Finland

Reviewed by:
Edgar Mendoza,
National Autonomous University of Mexico, Mexico
Giovanni Besio,
University of Genoa, Italy

****Correspondence:***
Ali Abdolali
ali.abdolali@noaa.gov

Specialty section:
This article was submitted to Coastal and Offshore Engineering, a section of the journal Frontiers in Built Environment

Received: *08 March 2022*
Accepted: *03 May 2022*
Published: *01 July 2022*

Citation:
Abdolali A, Hesser TJ, Anderson Bryant M, Roland A, Khalid A, Smith J, Ferreira C, Mehra A and Sikiric MD (2022) Wave Attenuation by Vegetation: Model Implementation and Validation Study. Front. Built Environ. 8:891612. doi: 10.3389/fbuil.2022.891612

1 INTRODUCTION

Wetlands are key natural and nature-based features used to dissipate wave energy and reduce flood risk. Historically, the operational practice to account for wave energy reduction due to wetland vegetation was through bottom friction sink terms implemented in nearshore wave models. The formulations most often applied use Manning's roughness coefficients n, which

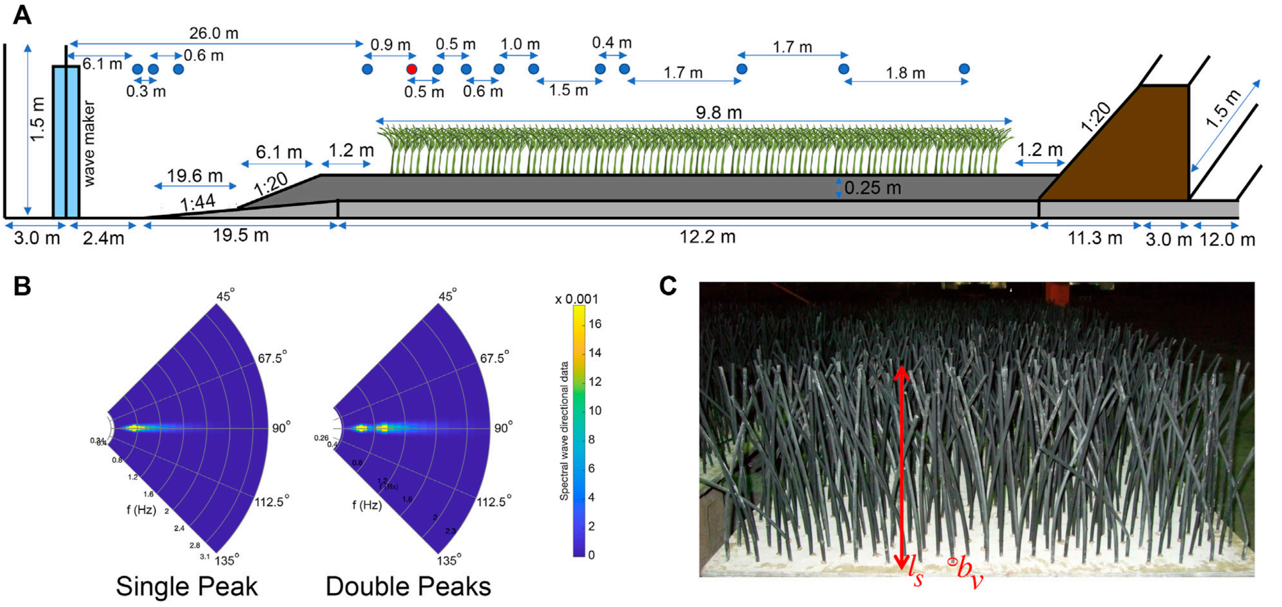

FIGURE 1 | (A) Schematic view of Anderson and Smith (2014) wave flume. **(B)** Single-peak and double-peak spectral density data for boundary forcing at the wave-maker in the flume and numerical model (red dot in panel (a)). **(C)** Installed idealized vegetation (vegetation height l_s and vegetation thickness b_v).

traditionally described bottom roughness in uniform flows for open channels and floodplains (Chow, 1959). These Manning's coefficients n account for spatial variations tied to local terrain and roughness, and many numerical studies, particularly those coupling phase-averaged wave models to hydrodynamic models such as the ADvanced CIRCulation model (ADCIRC), select Manning's n based on land-cover databases and standard hydraulic literature (Dietrich et al., 2011; Bender et al., 2013; Hope et al., 2013; Lawler et al., 2016; Bryant and Jensen, 2017). Controlled laboratory experiments continue to highlight the complexity of wave–vegetation interactions, most notably the effect of vegetation properties such as rigidity, height, density, and diameter on wave attenuation (Anderson and Smith, 2014; Ozeren et al., 2014; Luhar et al., 2017; Jacobsen et al., 2019; Phan et al., 2019; van Veelen et al., 2020). These studies suggest there are key physics

TABLE 1 | Wave condition at the beginning of vegetation zone (5th gauge from wave-maker).

Case	Wave type	h (m)	H_0 (cm)	T_p (s)	λ_p (m)	l_s/h	H_0/h	h/λ_p
1	Single peak	53.3	11.1 ± 0.07	1.5	2.89	0.78	0.21	0.18
2		53.3	11.0 ± 0.10	1.75	3.53	0.78	0.21	0.15
3		53.3	11.2 ± 0.06	2.0	4.16	0.78	0.21	0.13
4		45.7	8.1 ± 0.03	1.5	2.74	0.91	0.18	0.17
5		45.7	10.9 ± 0.05	1.5	2.74	0.91	0.24	0.17
6		45.7	13.9 ± 0.07	1.5	2.74	0.91	0.30	0.17
7		45.7	5.0 ± 0.03	2.0	3.91	0.91	0.11	0.12
8		45.7	10.7 ± 0.04	2.0	3.91	0.91	0.23	0.12
9		45.7	15.3 ± 0.10	2.0	3.91	0.91	0.33	0.12
10		45.7	19.2 ± 0.14	2.0	3.91	0.91	0.42	0.12
11		30.5	11.3 ± 0.09	1.25	2.88	1.36	0.37	0.16
12		30.5	11.0 ± 0.11	1.5	2.36	1.36	0.36	0.13
13		30.5	11.2 ± 0.10	1.75	2.82	1.36	0.37	0.11
14		30.5	11.1 ± 0.16	2.0	3.28	1.36	0.36	0.09
15		30.5	11.2 ± 0.13	2.25	3.73	1.36	0.37	0.08
16	Double peaks	53.3	13.7 ± 0.04	1.25/2.0	-	0.78	0.26	-
17		53.3	10.9 ± 0.03	1.25/2.0	-	0.78	0.20	-
18		45.7	13.6 ± 0.04	1.25/2.0	-	0.91	0.30	-
19		45.7	10.7 ± 0.05	1.25/2.0	-	0.91	0.23	-
20		30.5	13.0 ± 0.18	1.25/2.0	-	1.36	0.43	-
21		30.5	10.7 ± 0.14	1.25/2.0	-	1.36	0.35	-

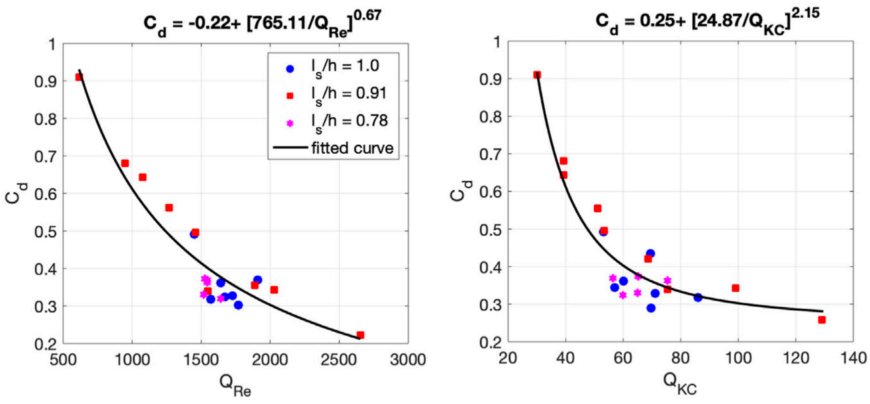

FIGURE 2 | Bulk drag coefficient C_d as a function of (left) modified stem Reynolds number Q_{Re} and (right) modified Keulegan–Carpenter number Q_{KC} accounting for stem submergence ratio for Anderson and Smith (2014) dataset. Different symbols represent different values of l_s/h.

that Manning's *n* does not properly represent, such as the drag force exerted on the water column due to temporally and spatially varying immersed vegetation. These potential shortfalls of Manning's *n* led to the derivation and subsequent implementation of vegetation-dissipation sink terms in widely used nearshore wave models, such as WWM-III (Roland, 2008), SWAN (Suzuki et al., 2012), STWAVE (Anderson and Smith, 2015), and XBEACH (Van Rooijen et al., 2015). These vegetation-dissipation sink terms are a function of the local hydrodynamic conditions and account directly for measurable vegetation characteristics. Both Smith et al. (2016) and Baron-Hyppolite et al. (2019) reported an underestimation of wave dissipation using enhanced Manning's *n* to represent vegetation compared to vegetation-dissipation formulations that explicitly account for plant properties.

The fundamental formulation for wave dissipation through vegetation was derived by Dalrymple et al. (1984) for monochromatic waves using the conservation of energy flux equation, where the horizontal force F_x acting on the vegetation per unit volume is expressed in terms of a Morison-type equation neglecting swaying motion and inertial force:

$$F_x = \frac{1}{2}\rho C_d b_v N u|u| \tag{1}$$

where ρ is water density, C_d is the depth-averaged bulk drag coefficient, b_v is stem diameter, N is plant density ($stems/m^2$), and u is horizontal velocity due to wave motion.

Although plant motion is neglected, **Eq. 1** may still be applied to swaying plants because the bulk drag coefficient C_d accounts for our ignorance of plant motion, interactions between stems, and other unresolved processes. Indeed, Mendez et al. (1999) stated that using the relative velocity between the fluid and plant required a higher value of C_d to obtain the same amount of attenuation. Mendez and Losada (2004) expanded upon Dalrymple et al. (1984) and derived an analytical solution for random wave transformations over mildly sloped vegetation fields under breaking and nonbreaking conditions by assuming a Rayleigh distribution of wave heights. The modification by Mendez and Losada (2004) is incorporated into several phase-averaged nearshore wave models similar to Suzuki et al. (2012), with verification largely focused on laboratory studies, albeit field applications are now gaining traction (Garzon et al., 2019). As an alternative to field surveys to collect vegetation properties, Figueroa-Alfaro et al. (2022) proposed a modified parameterization using a leaf area index-based measurement that can be readily derived from satellite imagery, but its application is limited to emergent vegetation. While these developments are advancing wave–vegetation modeling, continued research into the drag coefficient C_d, which directly affects the dissipation rate, is critical given the growing concerns regarding its assumptions and derivations (Tempest et al., 2015).

This study is arranged as follows: a summary of the implementation of Mendez and Losada (2004) in WAVEWATCH III (WW3) is presented in **Section 2**; **Section 3** provides a brief overview of the validation studies using laboratory data of homogeneous vegetation fields and field case application with observations in Virginia during Hurricanes Jose and Maria in 2017; and concluding remarks are provided in **Section 4**.

2 FORMULATION

In spectral wave models such as WW3, the waves are defined in terms of wave action density spectrum $N(\sigma, \theta)$ as a function of angular wave frequency and wave direction:

$$\frac{\partial}{\partial t}N + \nabla_x\left(c_g + \mathbf{U}\right)N + \frac{\partial}{\partial\sigma}c_\sigma N + \frac{\partial}{\partial\theta}c_\theta N = \frac{S}{\sigma} \tag{2}$$

where $N(k, \theta)$ is the wave action density spectrum related to the wave energy density spectrum $F(k, \theta)$, where $N(k, \theta) = F(k, \theta)/\sigma$ and c_g, $\mathbf{U}$, c_σ, and c_θ are the group velocity, the current velocity depth-time averaged over the scales of individual waves, propagation velocity in frequency σ, and direction θ spaces, respectively.

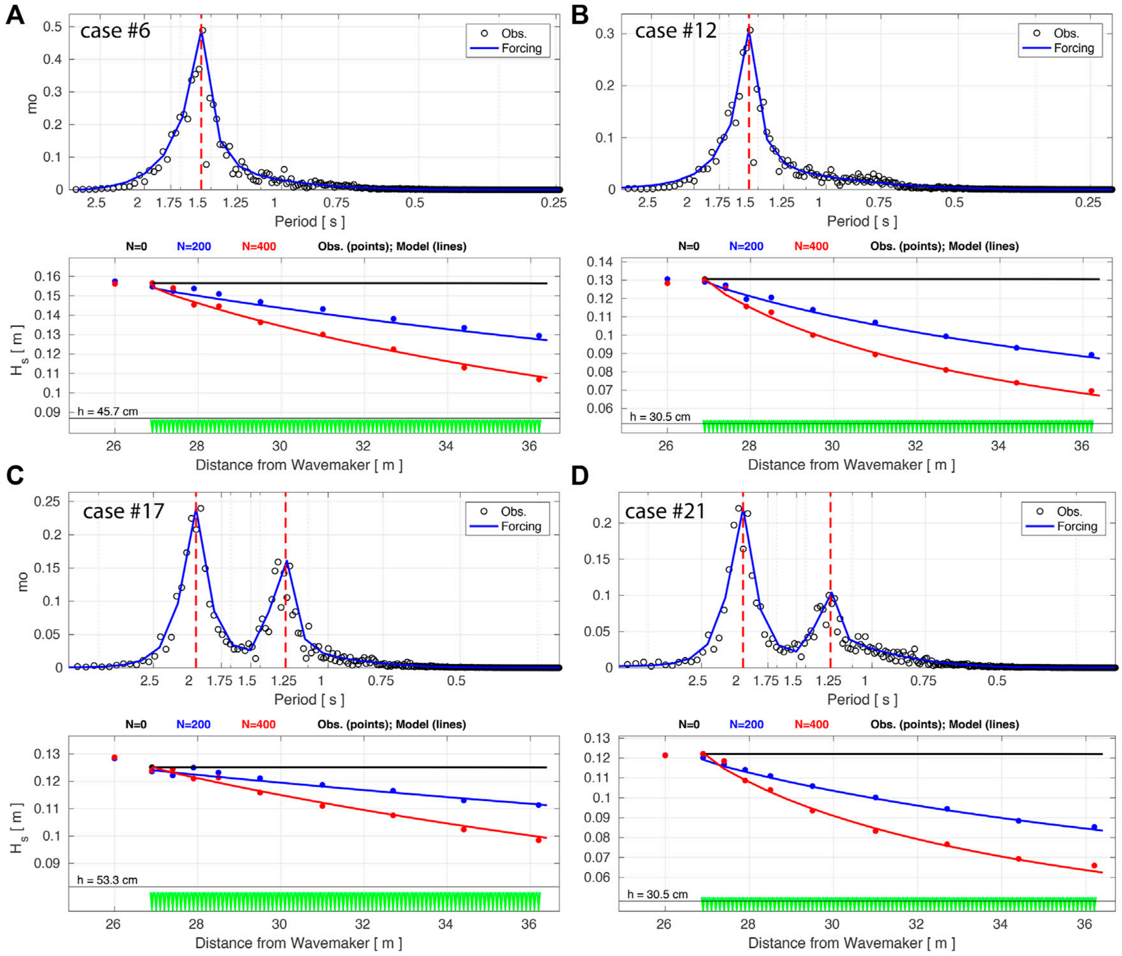

FIGURE 3 | Upper panels) Spectral density for single-peak **(A,B)** and double-peak **(C,D)** waves at the 5th gauge in the flume (black circles) and boundary forcing in the WW3 model (solid blue). The dashed red lines show the peak(s). (Lower panels) Significant wave height observed in the lab (circles) and from the WW3 model (solid) for no vegetation (black), N =200 stems/m^2 (blue) and N =400 stems/m^2 (black). Wave conditions for Cases 6 **(A)**, 12 **(B)**, 17 **(C)**, and 21 **(D)** are provided in **Table 1**.

The terms on the left-hand side of **Equation 2** represent wave action density change in time, propagation in geographical space, shifting of the relative frequency due to changes in current and depth, and depth and current-induced refraction, respectively.

The energy density source term S is placed on the right-hand side of **Eq. 2** and accounts for generation (i.e., by wind), dissipation (i.e., whitecapping, bottom friction, depth induced breaking), and nonlinear wave–wave interaction.

Without vegetation, wave energy flux remains constant if no energy is lost or gained. In the presence of vegetation, the wave energy flux, following Dalrymple et al. (1984), Kobayashi et al. (1993)m and Mendez and Losada (2004) becomes

$$\frac{\partial F}{\partial x} = -\epsilon_v \rightarrow \frac{\partial}{\partial x}\left[E.c_g\right] = -\epsilon_v \tag{3}$$

where wave energy is defined as

$$E = \frac{1}{8}\rho g H^2 \tag{4}$$

and ϵ_v is a function of the drag force F_x (**Equation 1**) integrated over the height of the vegetation

$$\epsilon_v = \overline{\int_{-h}^{-h+\alpha h} F_x u dz} \tag{5}$$

Assuming linear wave theory is valid to calculate u, the horizontal velocity due to wave motion, the mean rate of energy dissipation per unit horizontal area ϵ_v due to wave damping by vegetation becomes

$$\epsilon_v = \frac{1}{2\sqrt{\pi}}\rho C_d b_v N\left(\frac{kg}{2\sigma}\right)^3 \frac{\sinh^3(k\alpha h) + 3\sinh(k\alpha h)}{3k\cosh^3(kh)} H_{rms}^3 \tag{6}$$

where k is wave number, α is the ratio of plant height l_s to water depth h (L_s/h), and H_{rms} is root mean square wave height.

Combining **Eqs (3)–(6)**,

$$\frac{\partial H_{rms}^2}{\partial x} = \frac{-\epsilon_v}{\frac{1}{8}\rho g c_g} = \frac{2}{3\sqrt{\pi}} C_d b_v N k \frac{\sinh^3(k\alpha h) + 3\sinh(k\alpha h)}{[\sinh(2kh) + 2kh]\sinh(kh)} H_{rms}^3 \tag{7}$$

A spectral version implemented in WW3 is divided by $-\rho g$ and written in a spectral/directional form:

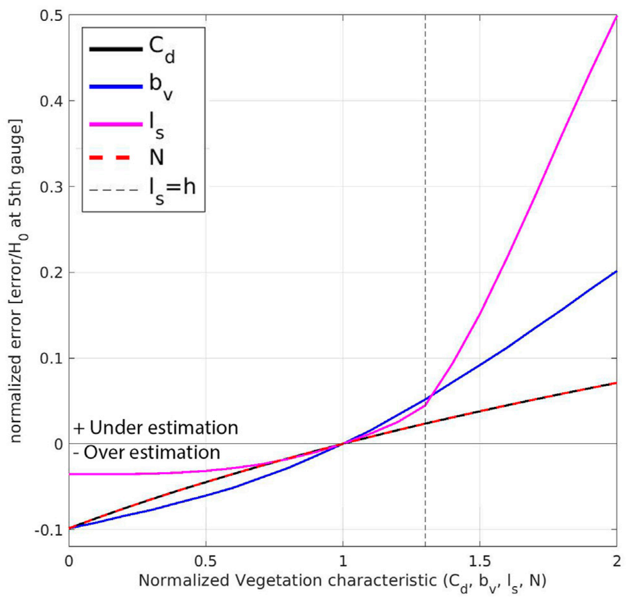

FIGURE 4 | Sensitivity of the model to vegetation characteristics (C_d, b_v, l_s, and N, normalized by the observed values) for Case 1 (see **Table 1**) in terms of mean error normalized by the significant wave height value at the 5th gauge.

$$S_{veg}(\sigma,\theta) = \frac{D_{tot}}{E_{tot}} E(\sigma,\theta) \tag{8}$$

$$D_{tot} = -\frac{1}{2g\sqrt{\pi}} C_d b_v N \left(\frac{\bar{k}g}{2\bar{\sigma}}\right)^3 \frac{\sinh^3(\bar{k}\alpha h) + 3\sinh(\bar{k}\alpha h)}{3\bar{k}\cosh^3(\bar{k}h)} H_{rms}^3 \tag{9}$$

where the mean frequency $\bar{\sigma}$, mean wave number $\bar{k}$, and total wave energy E_{tot} are given by

$$\bar{\sigma} = \left(\frac{1}{E_{tot}} \int_0^{2\pi} \int_0^{\infty} \frac{1}{\sigma} E(\sigma,\theta) d\sigma d\theta\right)^{-1} \tag{10}$$

$$\bar{k} = \left(\frac{1}{E_{tot}} \int_0^{2\pi} \int_0^{\infty} \frac{1}{\sqrt{k}} E(\sigma,\theta) d\sigma d\theta\right)^{-2} \tag{11}$$

$$E_{tot} = \int_0^{2\pi} \int_0^{\infty} E(\sigma,\theta) d\sigma d\theta \tag{12}$$

Finally, substituting $H_{rms}^2 = 8E_{tot}$, the wave–vegetation sink term becomes (Suzuki et al., 2012)

$$S_{d,veg} = -\sqrt{\frac{2}{\pi}} g^2 C_d b_v N \left(\frac{\bar{k}}{\bar{\sigma}}\right)^3 \frac{\sinh^3(\bar{k}\alpha h) + 3\sinh(\bar{k}\alpha h)}{3\bar{k}\cosh^3(\bar{k}h)} \sqrt{E_{tot}} E(\sigma,\theta) \tag{13}$$

Although not currently in WW3, the spectral wave–vegetation sink term formulated by Suzuki et al. (2012) may consider different densities and stem widths between trunks and roots (i.e., mangrove trees) by considering layer schematization. Recent developments by Dalrymple et al. (1984) and Mendez and Losada (2004) include implementation into mild slope equation models (Tang et al., 2015) and the incorporation of wave–current interactions for both following and opposing currents (Losada et al., 2016).

3 VALIDATION

After implementing the vegetation sink term in WW3, we verified for idealized laboratory experiments, consisting of 63 cases with homogeneous vegetation fields. Then, we progressed to the large-scale field test case for Hurricanes Jose and Maria (2017).

3.1 Laboratory Experiments (Anderson and Smith, 2014)

The Anderson and Smith (2014) experiments were performed at the U.S. Army Engineer Research and Development Center in Vicksburg, Mississippi, in a 63.4 m long, 1.5 m wide, and 1.5 m deep wave flume equipped with a piston-type wave-maker (**Figure 1**). A 9.8 m long vegetation zone, populated with idealized *Spartina alterniflora* vegetation, was located 29.3 m from the wave-maker. The idealized vegetation was constructed of b_v = 6.4 mm diameter and l_s = 41.5 cm tall flexible polyolefin tubing considering two stem densities of N = 200 and 400 stems/m^2 (corresponding to an element spacing of 7.1 and 5 cm, respectively). Given the inherent complexities live vegetation introduces to the laboratory, Anderson and Smith (2014) selected polyolefin tubing similar in dimension and rigidity to *Spartina alterniflora* measured along the Louisiana coast (Chatagnier, 2012) in order to best approximate biomechanical properties of the real vegetation. The water depths of the experiments were h = 30.5, 45.7, and 53.3 cm, simulating both submerged (l_s/h = 0.78, 0.91) and emergent (l_s/h = 1.0) conditions. The periods and significant wave heights for the the incident irregular waves with single- and double-peak periods vary between T_p = 1.25–2.25 s and H_{m0} = 5–19.2 cm, respectively. Wave attenuation by the vegetation was assessed relative to a bare control run (no vegetation) for each wave condition. A summary of the wave conditions tested by Anderson and Smith (2014) for each vegetation density is provided in **Table 1**.

The bulk drag coefficient (C_d) is a function of wave parameters and vegetation species/characteristics. The relationship between C_d and flow parameters is given by

$$C_d(Re) = \alpha_1 + \left(\frac{\alpha_2}{Re}\right)^{\alpha_3} \tag{14}$$

for flow characteristics defined by Reynolds number:

$$Re = \frac{u_c b_v}{\nu} \tag{15}$$

where $\nu = 10^{-6}$ m^2/s is kinematic viscosity of water and u_c is the characteristic velocity acting on the plant. The characteristic velocity is defined here as the maximum horizontal velocity immediately in the front of the vegetation field as shown by red circle in **Figure 1**:

$$u_{max} = \frac{\sigma a}{\tanh(kh)} \tag{16}$$

where H_s and T_p correspond to monochromatic wave train characteristics and the depth is $z = h\ (1 - \alpha)$. The

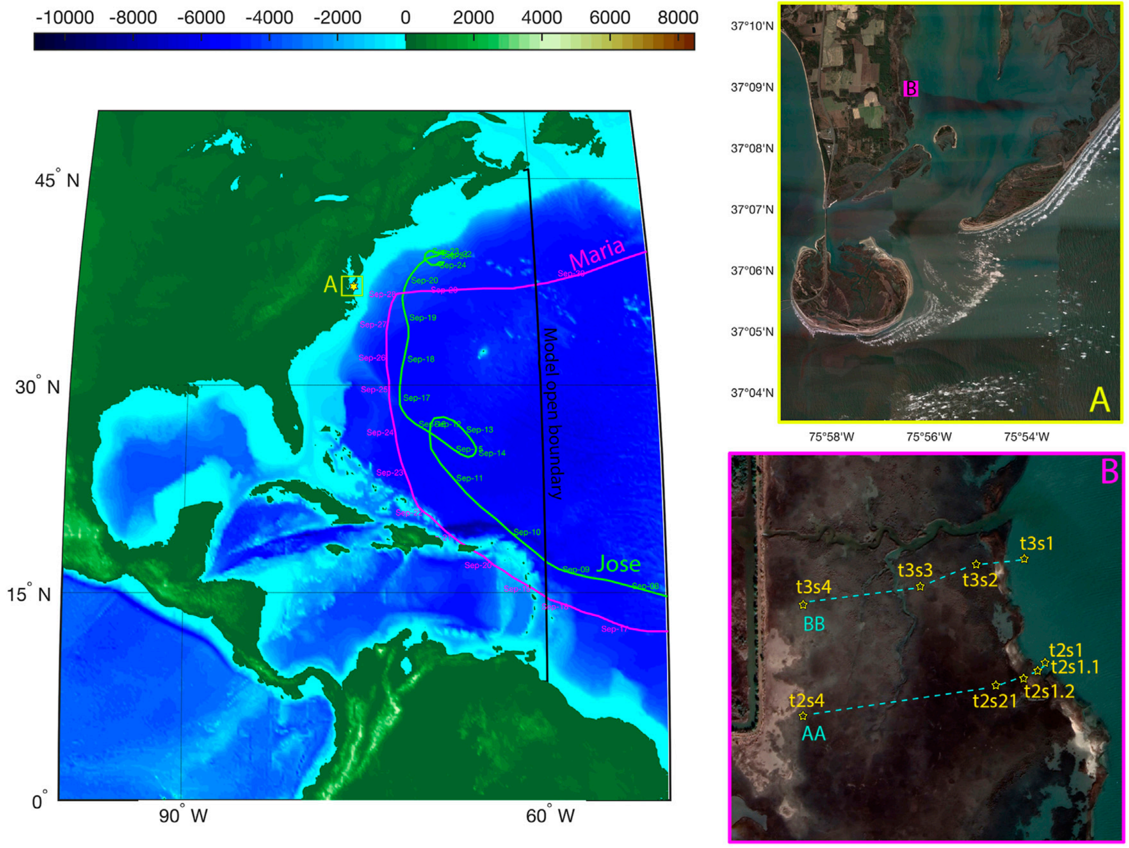

FIGURE 5 | Numerical domain extent for the east coast of the United States. The black line shows the open boundaries. The best tracks with time tags of hurricanes Maria and Jose (2017) are shown by magenta and green lines, respectively. The zoom-in windows in Magothy Bay and the locations of wave and water level gauges are shown in the left-hand side panels.

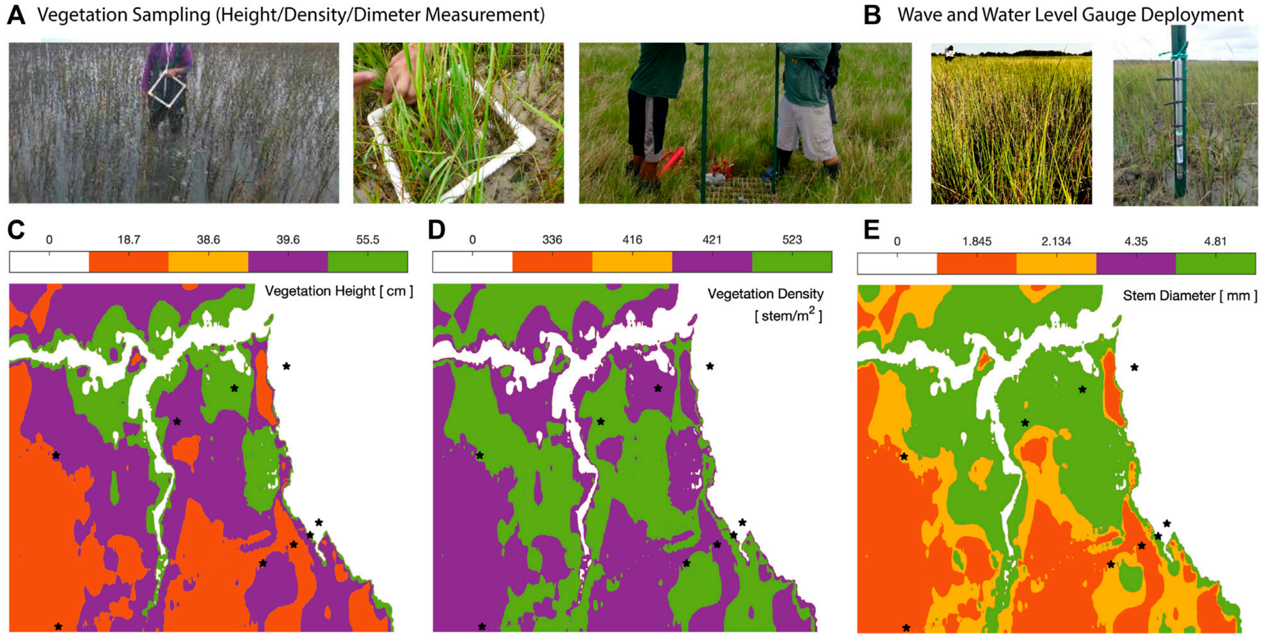

FIGURE 6 | Field measurements for vegetation sampling **(A)** and wave and water level gauges deployment/survey **(B)**. Spatial distribution of vegetation height **(C)**, vegetation density **(D)**, and stem diameters **(E)** in Magothy Bay.

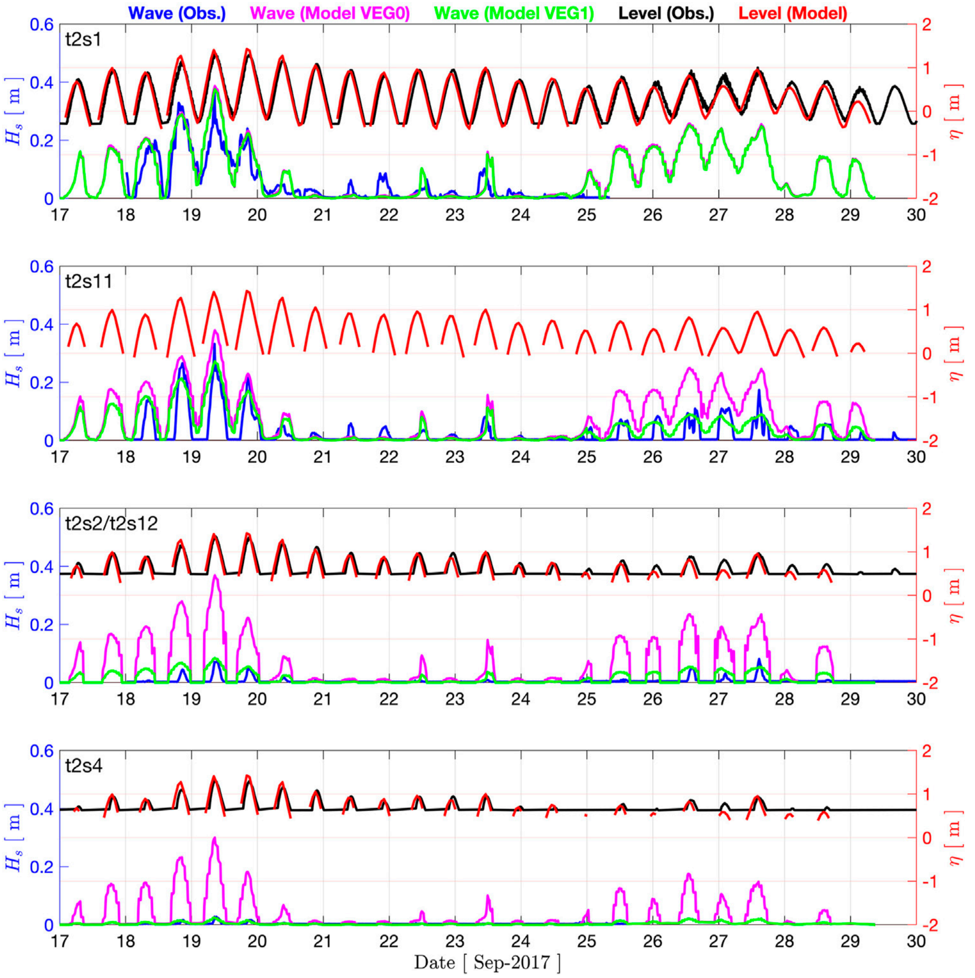

FIGURE 7 | Wave and storm surge Models' validation at the wave and water level gauges locations (transect AA) for significant wave height H_s(observation: blue; WW3 without wave–vegetation interaction: magenta; and WW3 with wave–vegetation interaction: green) and water level elevation η (observation: black; and ADCIRC: red).

Keulegan–Carpenter number is a dimensionless number that describes the relative importance of the drag force over inertia for a vertical obstacle in an oscillating flow:

$$KC = \frac{u_{max} T_p}{b_v} \tag{17}$$

The relation between C_d and KC number is evaluated based on experiments.

Following Kobayashi et al. (1993) and Mendez and Losada (2004) and considering the correction due to the canopy submergence (Ls/h), the empirical relationship between C_d and the nondimensional numbers Q_{Re} and Q_{KC} is shown in **Figure 2** and given by

$$C_d\left(Q_{Re}\right) = \theta_1 + \left(\frac{\theta_2}{Q_{Re}}\right)^{\theta_3}; \quad C_d\left(Q_{KC}\right) = \lambda_1 + \left(\frac{\lambda_2}{Q_{KC}}\right)^{\lambda_3} \tag{18}$$

where $[\theta_1, \theta_2, \theta_3] = [-0.22, 765.11, 0.67]$, $[\lambda_1, \lambda_2, \lambda_3] = [0.25, 24.87, 2.15]$, and

$$Q_{Re} = \frac{Re}{\left(l_s/h\right)^{1.5}}; \quad Q_{KC} = \frac{KC}{\left(l_s/h\right)^{1.5}} \tag{19}$$

The results are shown in **Figure 3** for two-single-peak (#6 and #12) and two-double-peak (#17 and #21) wave spectra. The spectra density observed at the 5th gauge in the flume and the corresponding forcing boundary condition at the WW3 wave-maker are shown in the upper panels. The time series of the significant wave heights extracted from the model (solid) is compared with the observations (dashed), shown in the lower panels for no vegetation (black), N = 200 (blue) and N = 400 stems/m^2 (black). The outputs of the model show a good agreement with the laboratory measurement for the wave attenuation due to wave–vegetation as a function of distance from the wave-maker.

The sensitivity of the model to vegetation characteristics (normalized by the observed values, for Case 1 from **Table 1**, C_d = 0.369, b_v = 0.0064 m, l_s = 0.415 m, and N = 400 stem/m^2) is investigated in terms of mean error normalized by the significant wave height value at the 5th gauge (H_0 = 11.1 cm). As is shown in

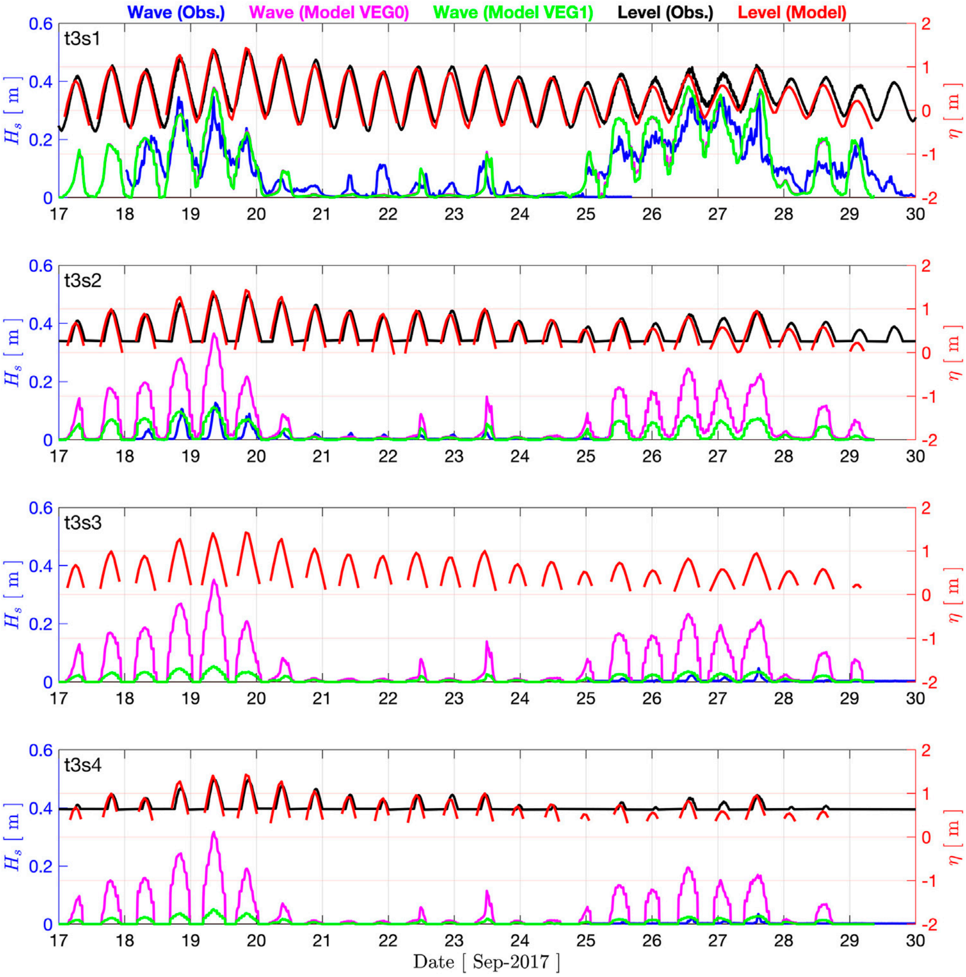

FIGURE 8 | Wave and storm surge Models' validation at the wave and water level gauges locations (transect BB) for significant wave height H_s(observation: blue; WW3 without wave–vegetation interaction: magenta; and WW3 with wave–vegetation interaction: green) and water level elevation η (observation: black; and ADCIRC: red).

Figure 4 and **Eq. 13**, the model sensitivity to stem density and drag coefficient is linear. On the contrary and for stem diameter (b_v), the drag coefficient (C_d) is a function of b_v (**Eq. 17**). Therefore, the error varies non-linearly with respect to changes in step diameter. Similarly, for step height (L_s), the drag coefficient (C_d) is a function of l_s (**Eq. 19**) and the parameter is in the sin term (**Eq. 13**). Overall, the wave attenuation due to vegetation is less sensitive to step height. The role of stem diameter is more important than other parameters.

3.2 Field Case (September 17–30, 2017)

A field case study was performed using data collected in Magothy Bay, located in Northampton County, Virginia, United States. The Magothy Bay Natural Area Preserve encompasses woodlands, forested wetlands, and extensive salt marshes. The location of the study area (A) is shown in **Figure 5**. Eight low-frequency water level gauges and eight high-frequency (4 Hz) wave gauges were deployed along two transects, as shown in box B. The transects are perpendicular to the coastline. The first gauges on each transect are deployed bayward of the marsh; therefore, they remain submerged and measure the entire tidal cycles. On each transect, three more water levels and three wave gauges were on the marsh surface, so they become wet during high tides or in stormy conditions. The vegetation characteristics, including stem height, density, and diameter, were measured across the marsh in a field campaign led by George Mason University. **Figure 6** shows vegetation sampling, including height, density, and diameter. Additional details on the field data collection can be found in Garzon et al. (2019). We have selected hurricanes Jose and Maria (2017) to verify the wave–vegetation sink term implementation in the WW3 model due to the availability of observations and atmospheric forcing and proximity of hurricane tracks to the study area.

3.2.1 Hurricane Jose (5–22 September 2017)

On 5 September, a week after the genesis of a tropical wave near the west coast of Africa, Jose developed into a tropical storm. Jose was a classic, long-lived Cape Verde hurricane that reached Category 4 strength (on the Saffir–Simpson Hurricane Wind Scale) east of the

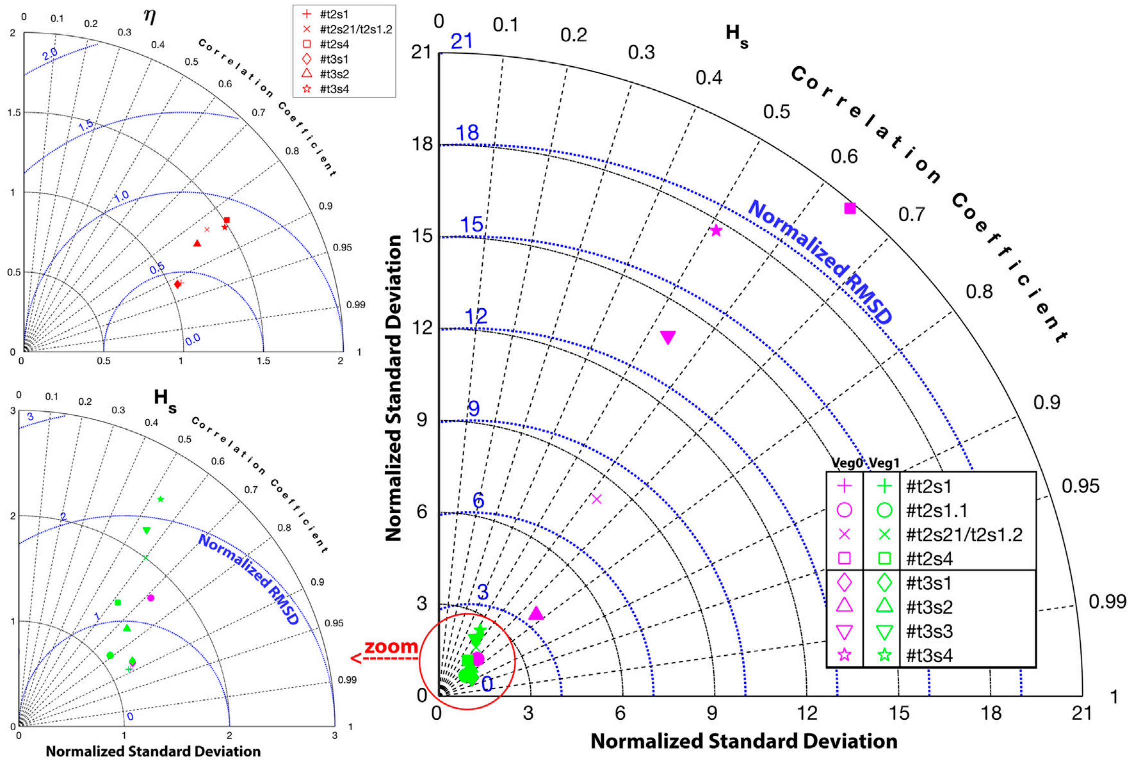

FIGURE 9 | Taylor diagrams for water level (η: top left); and significant wave height (H_s: right and bottom left (zoom in) representing modeled and collected data at gauges locations (red: ADCIRC; magenta: WW3 without wave–vegetation interaction; and green: WW3 with wave–vegetation interaction) in terms of the Pearson correlation coefficient, the normalized root mean square deviation (RMSD), and the normalized standard deviation σ.

Leeward Islands on 8 September, but fortunately, it spared the Irma-ravaged islands of the northeastern Caribbean Sea. Jose made a clockwise loop over the southwestern Atlantic and then meandered off the coast of New England as a tropical storm for several days. Jose produced tropical-storm-force winds and minor coastal flooding along portions of the mid-Atlantic and southern New England coastline. Jose was directly responsible for one death, with damage of $2.84 million (2017 USD). It was the 10th named storm, fifth hurricane, and third major hurricane of the 2017 Atlantic hurricane season.

3.2.2 Hurricane Maria (16–30 September 2017)

On 12 September, a Cape Verde tropical wave later named Hurricane Maria was generated on the west coast of Africa, swept westward over the Atlantic, and formed a tropical depression about 580 nautical miles east of Barbados on 16 September (49.7°W, 12.2°N), reaching Category 5 intensity (Saffir–Simpson Hurricane Wind Scale) just before making landfall on Dominica on 18 September and high-end Category 4 hurricane by the time it struck Puerto Rico on 20 September. Maria gradually weakened over the Bahamas, swept eastward over the open Atlantic, and dissipated by 2 October. Maria was directly responsible for 3,059 deaths and indirectly responsible for further 82 fatalities, with damage of $91.61 billion (2017 USD), mostly in Puerto Rico. Maria was the most intense tropical cyclone worldwide in 2017, the 13th named storm, 8th consecutive hurricane, 4th major hurricane, 2nd Category 5 hurricane, and deadliest storm of the extremely active 2017 Atlantic hurricane season. The best tracks of the Jose and Maria path are given in **Figure 5**.

We have used the Hurricane Weather Research and Forecasting (HWRF) model (Ma et al., 2020) to provide winds and atmospheric pressures to force ADCIRC (Luettich et al., 1992) and WW3 models. HWRF has movable multilevel nesting technology and is designed for extreme events such as hurricanes. The model runs on a stationary parent and two movable nest domains. The parent domain covers 77.2° × 77.2° with 13.5 km resolution on a rotated latitude/longitude E-staggered grid. The middle nest domain, of about 17.8° × 17.8° with 4.5 km resolution, and the inner nest domain, of about 5.9° × 5.9° with 1.5 km resolution, move along with the storm using two-way interactive nesting. The hourly data are extracted for wind speed at 10 m elevation and pressure at MSL (see Abdolali et al. (2020) and Abdolali et al. (2021) for more information on the HWRF model and forcing data preparation).

The extent of an unstructured grid is shown in **Figure 5**. This grid is generated in accordance with enhancement in grid resolution and size in the study area down to 20 ~ m coastal resolution. Such a resolution is required to represent complex marsh geometry (Deb et al., 2022b). We first conducted simulations with the ADCIRC model to prepare water level and current fields for WW3. Then, two sets of WW3

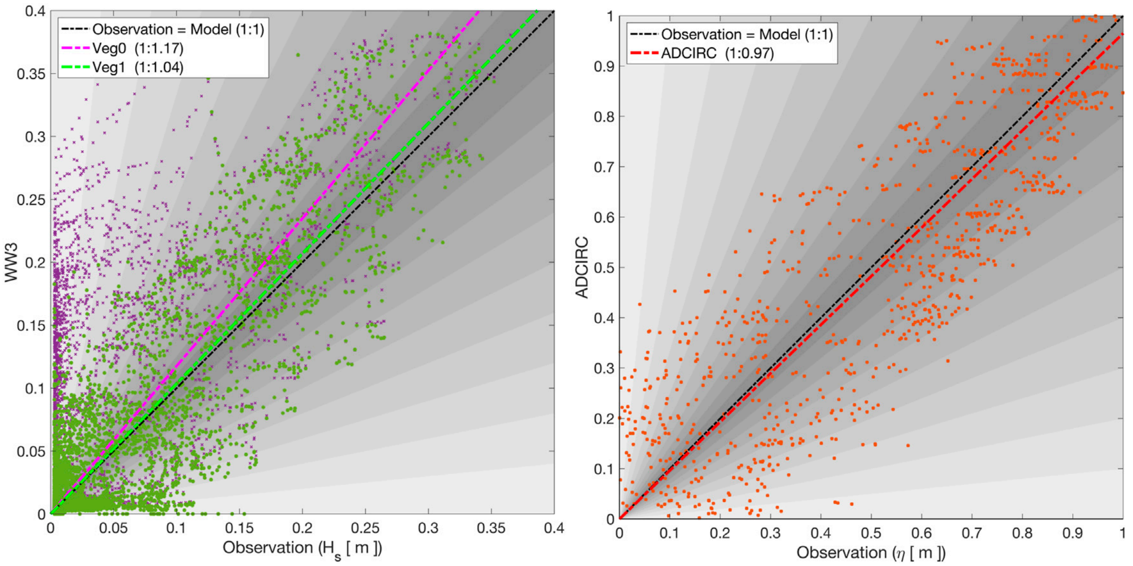

FIGURE 10 | Linear regression comparison between collected data *versus* WW3 (significant wave height H_s: left) and ADCIRC (water elevation η: right) models. The linear regression (dotted-dashed lines) is shown in each subplot.

simulations were performed, forced by a wind from HWRF, water level, and current from the ADCIRC model. In the first simulation, the wave–vegetation sink term was deactivated (VEG0). In the second simulation, the VEG1 sink term was activated. For this simulation, spatially variable vegetation characteristics were used in the model.

In the wave model simulations, the model resolves the source spectrum with frequencies between 0.05 and 0.9597 Hz, divided into 32 spectral bands with an increment factor of 1.1 and 36 directions with a 10° increment. The boundary conditions are imposed at the eastern open boundary nodes of the unstructured mesh to include the effect of a distantly generated swell extracted from a global simulation on a structured grid with 0.5°, forced by the GFS wind field. In addition (Ardhuin et al., 2010), source term parameterizations (ST4), nonlinear wave-wave interaction using the discrete interaction approximation, DIA (Hasselmann et al., 1985), moving bottom friction (SHOWEX-BT4) (Ardhuin et al., 2003), depth-limited breaking based on Battjes–Janssen formulation (DB1) (Battjes and Janssen, 1978), nonlinear triad interactions (Lumped Triad Interaction method LTA) (Eldeberky and Battjes, 1996), and reflection by the coast (REF1) (Ardhuin and Roland, 2012) have been used for computations. The domain decomposition parallelization and the implicit numerical scheme are utilized for these simulations to avoid small time step in the explicit scheme, mandated by small grid resolution in the Magothy bay area (~20 m) (Abdolali et al., 2020).

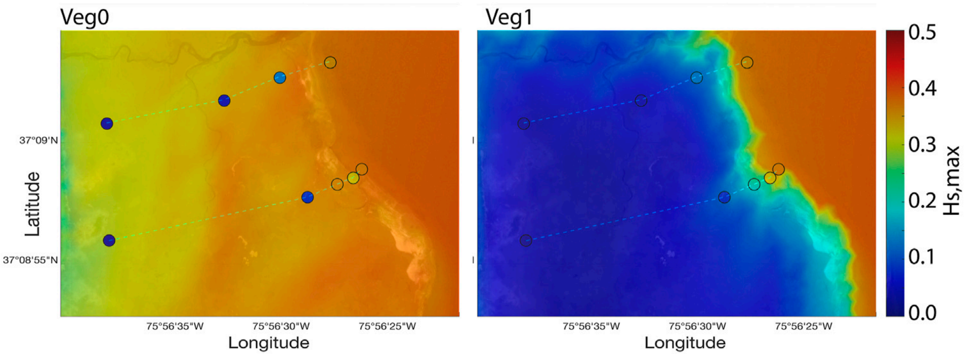

FIGURE 11 | Wave model sensitivity to wave–vegetation interaction in terms of the spatial distribution of the envelope of significant wave height H_s, extracted from the model without wave–vegetation interaction (left) with wave–vegetation interaction (right). The observed maximum values at wave gauge locations are shown with the circles.

We compared the time series of storm surge and wave model outputs at pressure gauge locations (**Figure 5D**). The results are shown in **Figure 7** for transect AA and **Figure 8** for transect BB as time series of water level (η) from the storm surge model and significant wave height (H_s) from WW3. The gauges are sorted by proximity to the bay from top to bottom for each transect. In each panel, the observed and modeled water levels are shown by black and red lines, respectively. Wave observations and model outputs without vegetation sink term (VEG0) and with vegetation sink term (VEG1) are shown by blue, magenta, and green lines, respectively. Overall performance at pressure gauge locations is shown in the Taylor diagrams presented in **Figure 9**, combining standard deviation (σ), the root mean square deviation (RMSD), and correlation coefficient (*CC*) for the observation and model outputs. For water level η, the normalized standard deviation (σ) varies between 1.05 and 1.51, whereas the RMSD range is 0.42–0.87. The correlation coefficient *(CC)* range is 0.83–0.92. A similar correlation coefficient is observed for the significant wave height time series at wave gauge locations within the ranges of 0.51–0.88 and 0.52–0.89 for VEG0 and VEG1 sink terms, respectively. However, a substantial improvement is achieved with the activation of the vegetation sink term for the standard deviation from the range of 1.19–20.81 to 1.09–2.54. Similarly, the RMSD improved from 0.55–20.18 to 0.54–2.18.

From the linear regression analysis, a slight underestimation of water level by ADCIRC is observed with a skill of 0.97, whereas WW3 overestimates the significant wave height with skills of 1.17 without the vegetation sink term and 1.04 with the vegetation sink term (**Figure 10**).

Wave height significantly improved due to wave–vegetation interaction. **Figure 11** represents the maximum wave height during the whole simulation (17–30 September) between VEG0 and VEG1 cases.

4 SUMMARY AND CONCLUSION

This study implemented wave–vegetation interaction in the WW3 model. The application is examined using a standard laboratory flume case for wave dissipation due to homogeneous vegetation fields. Different submergence ratios, densities were examined for single and double-peaks incident waves. The drag coefficients C_d were calculated using the empirical relationship based on Keulegan–Carpenter *KC* and Reynolds Re numbers, considering the correction due to the canopy submergence.

In addition to controlled laboratory experiments, we validated the model for a field application with spatially variable vegetation fields in a vegetated marshland during Hurricanes Jose and Maria, 2017. A well-known atmospheric model designed for hurricane modeling (HWRF) is used to drive the storm surge model (ADCIRC) to provide water level and current fields and the spectral wave model (WW3). These wind, current, and water level inputs were used to drive WW3 on a high-resolution triangular mesh with a ~1 km resolution near the coast of the East Coast of the United States and a nominal resolution of ~ 20 m in the Magothy Bay where wave height observations were available for validation. Such a resolution is required for resolving wave action in complex marsh environments (Deb et al., 2022a). WW3 simulations were conducted with the domain decomposition parallelization algorithm and the implicit numerical solver (Abdolali et al., 2020), making it possible to run the model on a high-resolution grid efficiently. The model skills and improvement due to the vegetation sink terms were examined and discussed using time series of high-frequency pressure gauges. We conclude that the wave attenuation due to vegetation is significant in marsh environments, and neglecting the vegetation sink term leads to a significant bias in the model outputs and observations. It is shown that WW3 skills are improved over areas with vegetation, with sufficient grid resolution and proper representation of spatially variable vegetation fields. Designing and evaluating wetlands as nature-based flood risk reduction features require accurate modeling of wave dissipation by vegetation. Updated WW3 with the vegetation sink term coupled with a storm surge provides the necessary capability to model wave attenuation in wetlands. Such implementation provides an opportunity to investigate the effect of seasonal variability of vegetation coverage on wave characteristics. Organic protection methodologies can be designed for beach and wetland erosion mitigation purposes. In addition, the changes in the stem characteristic (diameter, height, and density) and hydrodynamics can be investigated to identify the role of dry/wetland cover before, during, and after the occurrence of severe storm surges. Further improvement can be achieved by a two-way coupling between the storm surge and wave models, where depth-integrated wave radiation stresses in the presence of vegetation affect the storm surge model. In return, the updated water level and current fields derive the wave model dynamically. In this way, the model components interact with each other representing what occurs in nature (Moghimi et al., 2020).

DATA AVAILABILITY STATEMENT

The datasets presented in this study can be found in online repositories. The names of the repository/repositories and accession number(s) can be found at https://github.com/NOAA-emc/ww3.

AUTHOR CONTRIBUTIONS

AA: conceptualization, methodology, code development, data curation, visualization, validation, writing—original draft. TH: conceptualization, methodology, code development, writing—review and editing. MA: laboratory experiments, writing—original draft. AR: code development, writing—review and editing. AK: field case observation collection and simulation. JS: methodology, program management, review and editing. CF: field case observation collection, review and editing. AM: program management, methodology. MS: Software.

ACKNOWLEDGMENTS

The author wishes to thank Drs. Saeideh Banihashemi and Matthew Masarik for fruitful discussions. AA and AM acknowledge the support of the Consumer Option for an Alternative System to Allocate Losses (COASTAL Act) Project within National Oceanic and Atmospheric Administration (NOAA).

SUPPLEMENTARY MATERIAL

The Supplementary Material for this article can be found online at: https://www.frontiersin.org/articles/10.3389/fbuil.2022.891612/full#supplementary-material

REFERENCES

Abdolali, A., Roland, A., van der Westhuysen, A., Meixner, J., Chawla, A., Hesser, T. J., et al. (2020). Large-scale Hurricane Modeling Using Domain Decomposition Parallelization and Implicit Scheme Implemented in Wavewatch Iii Wave Model. *Coast. Eng.* 157, 103656. doi:10.1016/j.coastaleng.2020.103656

Abdolali, A., van der Westhuysen, A., Ma, Z., Mehra, A., Roland, A., and Moghimi, S. (2021). Evaluating the Accuracy and Uncertainty of Atmospheric and Wave Model Hindcasts during Severe Events Using Model Ensembles. *Ocean. Dyn.* 71. doi:10.1007/s10236-020-01426-9

Anderson, M. E., and Smith, J. M. (2015). *Implementation of Wave Dissipation by Vegetation in Stwave*. Vicksburg, MS. ERDC/CHL CHETN-I-5.

Anderson, M. E., and Smith, J. (2014). Wave Attenuation by Flexible, Idealized Salt Marsh Vegetation. *Coast. Eng.* 83, 82–92. doi:10.1016/j.coastaleng.2013.10.004

Ardhuin, F., O'reilly, W., Herbers, T., and Jessen, P. (2003). Swell Transformation across the Continental Shelf. Part I: Attenuation and Directional Broadening. *J. Phys. Oceanogr.* 33, 1921–1939. doi:10.1175/1520-0485(2003)033<1921:statcs>2.0.co;2

Ardhuin, F., Rogers, E., Babanin, A. V., Filipot, J.-F., Magne, R., Roland, A., et al. (2010). Semiempirical Dissipation Source Functions for Ocean Waves. Part I: Definition, Calibration, and Validation. *J. Phys. Oceanogr.* 40, 1917–1941. doi:10.1175/2010JPO4324.1

Ardhuin, F., and Roland, A. (2012). Coastal Wave Reflection, Directional Spread, and Seismoacoustic Noise Sources. *J. Geophys. Res. Oceans* 117. doi:10.1029/2011JC007832

Baron-Hyppolite, C., Lashley, C. H., Garzon, J., Miesse, T., Ferreira, C., and Bricker, J. D. (2019). Comparison of Implicit and Explicit Vegetation Representations in Swan Hindcasting Wave Dissipation by Coastal Wetlands in Chesapeake Bay. *Geosciences* 9, 1–22. doi:10.3390/geosciences9010008

Battjes, J. A., and Janssen, J. (1978). "Energy Loss and Set-Up Due to Breaking of Random Waves," in *Coastal Engineering 1978*, 569–587. doi:10.1061/9780872621909.034

Bender, C., Smith, J. M., Kennedy, A., and Jensen, R. (2013). Stwave Simulation of Hurricane Ike: Model Results and Comparison to Data. *Coast. Eng.* 73, 58–70. doi:10.1016/j.coastaleng.2012.10.003

Bryant, M. A., and Jensen, R. E. (2017). Application of the Nearshore Wave Model Stwave to the North Atlantic Coast Comprehensive Study. *J. Waterw. Port, Coast. Ocean Eng.* 143, 04017026. doi:10.1061/(asce)ww.1943-5460.0000412

Chatagnier, J. (2012). *The Biomechanics of Salt Marsh Vegetation Applied to Wave and Surge Modeling*. Baton Rouge, LA: Louisiana State University. Ph.D. thesis.

Chow, V. T. (1959). *Open-channel Hydraulics*. McGraw-Hill Book Company, Inc.

Dalrymple, R. A., Kirby, J. T., and Hwang, P. A. (1984). Wave Diffraction Due to Areas of Energy Dissipation. *J. Waterw. Port, Coast. Ocean Eng.* 110, 67–79. doi:10.1061/(asce)0733-950x(1984)110:1(67)

Deb, M., Abdolali, A., Kirby, J. T., Shi, F., Guiteras, S., and McDowell, C. (2022b). Sensitivity of Tidal Hydrodynamics to Varying Bathymetric Configurations in a Multi-Inlet Rapidly Eroding Salt Marsh System: A Numerical Study. *Earth Surf. Process. Landforms* 47, 1157–1182. doi:10.1002/esp.5308

Deb, M., Abdolali, A., Kirby, J. T., and Shi, F. (2022a). Hydrodynamic Modeling of a Complex Salt Marsh System: Importance of Channel Shoreline and Bathymetric Resolution. *Coast. Eng.* 173, 104094. doi:10.1016/j.coastaleng.2022.104094

Dietrich, J. C., Westerink, J. J., Kenney, A. B., Smith, J. M., Jensen, R. E., Zijlema, M., et al. (2011). Hurricane Gustav (2008) Waves and Storm Surge: Hindcast, Synoptic Analysis, and Validation in Southern louisiana. *Mon. Weather Rev.* 139, 2488–2522. doi:10.1175/2011MWR3611.1

Eldeberky, Y., and Battjes, J. A. (1996). Spectral Modeling of Wave Breaking: Application to Boussinesq Equations. *J. Geophys. Res. Oceans* 101, 1253–1264. doi:10.1029/95JC03219

Figueroa-Alfaro, R. W., van Rooijen, A., Garzon, J. L., Evans, M., and Harris, A. (2022). Modelling Wave Attenuation by Saltmarsh Using Satellite-Derived Vegetaion Properties. *Ecol. Eng.* 176, 106528. doi:10.1016/j.ecoleng.2021.106528

Garzon, J. L., Miesse, T., and Ferreira, C. M. (2019). Field-based Numerical Model Investigation of Wave Propagation across Marshes in the Chesapeake Bay under Storm Conditions. *Coast. Eng.* 146, 32–46. doi:10.1016/j.coastaleng.2018.11.001

Hasselmann, S., Hasselmann, K., Allender, J., and Barnett, T. (1985). Computations and Parameterizations of the Nonlinear Energy Transfer in a Gravity-Wave Specturm. Part II: Parameterizations of the Nonlinear Energy Transfer for Application in Wave Models. *J. Phys. Oceanogr.* 15, 1378–1391. doi:10.1175/1520-0485(1985)015<1378:CAPOTN>2.0.CO;2

Hope, M. E., Westerink, J. J., Kennedy, A. B., Kerr, P. C., Dietrich, J. C., Dawson, C., et al. (2013). Hindcast and Validation of Hurricane Ike (2008) Waves, Forerunner, and Storm Surge. *J. Geophys. Res. Oceans* 118, 4424–4460. doi:10.1002/jgrc.20314

Jacobsen, N. G., Bakker, W., Uijttewaal, W. S. J., and Uittenbogaard, R. (2019). Experimental Investigation of the Wave-Induced Motion of and Force Distribution along a Flexible Stem. *J. Fluid Mech.* 880, 1036–1069. doi:10.1017/jfm.2019.739

Kobayashi, N., Raichle, A. W., and Asano, T. (1993). Wave Attenuation by Vegetation. *J. Waterw. port, Coast. ocean Eng.* 119, 30–48. doi:10.1061/(asce)0733-950x(1993)119:1(30)

Lawler, S., Haddad, J., and Ferreira, C. M. (2016). Sensitivity Considerations and the Impact of Spatial Scaling for Storm Surge Modeling in Wetlands of the Mid-atlantic Region. *Ocean Coast. Manag.* 134, 226–238. doi:10.1016/j.ocecoaman.2016.10.008

Losada, I. J., Maza, M., and Lara, J. L. (2016). A New Formulation for Vegetation-Induced Damping under Combined Waves and Currents. *Coast. Eng.* 107, 1–13. doi:10.1016/j.coastaleng.2015.09.011

Luettich, R. A., Westerink, J. J., Scheffner, N. W., et al. (1992). *Adcirc: An Advanced Three-Dimensional Circulation Model for Shelves, Coasts, and Estuaries. Report 1, Theory and Methodology of Adcirc-2dd1 and Adcirc-3dl.* Vicksburg, MS.

Luhar, M., Infantes, E., and Nepf, H. (2017). Seagrass Blade Motion under Waes and its Impact on Wave Decay. *J. Geophys. Res. Oceans* 122, 3736–3752. doi:10.1002/2017jc012731

Ma, Z., Liu, B., Mehra, A., Abdolali, A., van der Westhuysen, A., Moghimi, S., et al. (2020). Investigating the Impact of High-Resolution Land–Sea Masks on Hurricane Forecasts in Hwrf. *Atmosphere* 11. doi:10.3390/atmos11090888

Mendez, F. J., and Losada, I. J. (2004). An Empirical Model to Estimate the Propagation of Random Breaking and Nonbreaking Waves over Vegetation Fields. *Coast. Eng.* 51, 103–118. doi:10.1016/j.coastaleng.2003.11.003

Mendez, F. J., Losada, I. J., and Losada, M. A. (1999). Hydrodynamics Induced by Wind Waves in a Vegetation Field. *J. Geophys. Res. Oceans* 104, 18383–18396. doi:10.1029/1999jc900119

Moghimi, S., Van der Westhuysen, A., Abdolali, A., Myers, E., Vinogradov, S., Ma, Z., et al. (2020). Development of an Esmf Based Flexible Coupling Application of Adcirc and Wavewatch Iii for High Fidelity Coastal Inundation Studies. *J. Mar. Sci. Eng.* 8. doi:10.3390/jmse8050308

Ozeren, Y., Wren, D. G., and Wu, W. (2014). Experimental Investigation of Wave Attenuation through Model and Live Vegetation. *J. Waterw. Port, Coast. Ocean Eng.* 140, 04014019. doi:10.1061/(asce)ww.1943-5460.0000251

Phan, K. L., Stive, M. J. F., Zijlema, M., Truong, H. S., and Aarninkhof, S. G. J. (2019). The Effects of Wave Non-linearity on Wave Attenuation by Vegetation. *Coast. Eng.* 147, 63–74. doi:10.1016/j.coastaleng.2019.01.004

Roland, A. (2008). *Development of WWM II: Spectral Wave Modelling on Unstructured Meshes*. Darmstadt, Germany: Technische Universität Darmstadt, Institute of Hydraulic and. Ph.D. thesis, Ph. D. thesis.

Smith, J. M., Bryant, M. A., and Wamsley, T. V. (2016). Wetland Buffers: Numerical Modeling of Wave Dissipation by Vegetation. *Earth Surfaces Process. Landforms* 41, 847–854. doi:10.1002/esp.3904

Suzuki, T., Zijlema, M., Burger, B., Meijer, M. C., and Narayan, S. (2012). Wave Dissipation by Vegetation with Layer Schematization in Swan. *Coast. Eng.* 59, 64–71. doi:10.1016/j.coastaleng.2011.07.006

Tang, J., Shaodong, S., and Wang, H. (2015). Numerical Model for Coastal Wave Propagation through Mild Slope Zone in the Presence of Rigid Vegetation. *Coast. Eng.* 97, 53–59. doi:10.1016/j.coastaleng.2014.12.006

Tempest, J. A., Moller, I., and Spencer, T. (2015). A Review of Plant-Flow Interactions on Salt Marshes: The Importance of Vegetation Structure and Plant Mechanical Characteristics. *WIREs Water* 2, 669–681. doi:10.1002/wat2.1103

Van Rooijen, A. A., Van Thie de Vries, J. S. M., McCall, R. T., Van Dongeren, A. R., Roelvink, J. A., and Reniers, A. J. H. M. (2015). “Modeling of Wave Attenuation by Vegetation with Xbeach,” in *E-proceedings of the 36th IAHR World Congress*. Hague, Netherlands.

van Veelen, T. J., Fairchild, T. P., Reeve, D. E., and Karunarathna, H. (2020). Experimental Study on Vegetation Flexibility as Control Parameter for Wave Damping and Velocity Structure. *Coast. Eng.* 157, 103648. doi:10.1016/j.coastaleng.2020.103648

Conflict of Interest: AA was employed by the company I.M. Systems Group, Inc.

The remaining authors declare that the research was conducted in the absence of any commercial or financial relationships that could be construed as a potential conflict of interest.

frontiers | Frontiers in Built Environment

ORIGINAL RESEARCH
published: 12 July 2022
doi: 10.3389/fbuil.2022.904837

The Unique Ability of Fine Roots to Reduce Vegetated Coastal Dune Erosion During Wave Collision

Jens Figlus[1]*, Jacob M. Sigren[2], Rusty A. Feagin[3] and Anna R. Armitage[2]

[1]Department of Ocean Engineering, Texas A&M University, Galveston, TX, United States, [2]Department of Marine Biology, Texas A&M University at Galveston, Galveston, TX, United States, [3]Department of Ecology and Conservation Biology, Texas A&M University, College Station, TX, United States

Vegetated coastal sand dunes can be vital components of flood risk reduction schemes due to their ability to act as an erosive buffer during storm surge and wave attack. However, the effects of plant morphotypes on the wave-induced erosion process are hard to quantify, in part due to the complexity of the coupled hydrodynamic, morphodynamic, and biological processes involved. In this study the effects of four vegetation types on the dune erosion process under wave action was investigated in a wave flume experiment. Sand dune profiles containing real plant arrangements at different growth stages were exposed to irregular waves at water levels producing a collision regime to simulate storm impact. Stepwise multivariate statistical analysis was carried out to determine the relationship of above- and below-ground plant variables to the physical response. Plant variables included, among others, fine root biomass, coarse root biomass, above-ground surface area, stem rotational stiffness, and mycorrhizal colonization. Morphologic variables, among others, included eroded sediment volume, cross-shore area centroid shift, and scarp retreat rate. Results showed that vegetation was able to reduce erosion during a collision regime by up to 37%. Although this reduction was found to be related to both above- and belowground plant structures and their effect on hydrodynamic processes, it was primarily accounted for by the presence of fine root biomass. Fine roots increased the shear strength of the sediment and thus lowered erosional volumes and scarp retreat rates. For each additional 100 mg/L of fine roots (dry) added to the sediment, the erosional volume was reduced by 6.6% and the scarp retreat rate was slowed by 4.6%. Coarse roots and plant-mediated mycorrhizal colonization did not significantly alter these outcomes, nor did the apparent enhancement of wave reflection caused by the fine roots. In summary, fine roots provided a unique ability to bind sediment leading to reduced dune erosion.

Keywords: dune, erosion, vegetation, physical model, mycorrhizal fungi, multivariate statistics

Edited by:
Rodolfo Silva,
National Autonomous University of Mexico, Mexico

Reviewed by:
Itxaso Odériz,
Environmental Hydraulics Institute (IHCantabria), Spain
M. Luisa Martinez,
Instituto de Ecología (INECOL), Mexico

****Correspondence:***
Jens Figlus
figlusj@tamu.edu

Specialty section:
This article was submitted to Coastal and Offshore Engineering, a section of the journal Frontiers in Built Environment

Received: *25 March 2022*
Accepted: *22 June 2022*
Published: *12 July 2022*

Citation:
Figlus J, Sigren JM, Feagin RA and Armitage AR (2022) The Unique Ability of Fine Roots to Reduce Vegetated Coastal Dune Erosion During Wave Collision.
Front. Built Environ. 8:904837.
doi: 10.3389/fbuil.2022.904837

INTRODUCTION

Coastal sand dunes form a protective buffer for many coastal communities around the world, protecting infrastructure and homes from damaging storm surges and waves. The economic storm protection benefits of dunes are substantial (e.g., Sigren et al., 2016; Sigren, 2017), warranting investment in restoring and maintaining these coastal ecosystems. This is in line with most published work on wave erosion of vegetated dunes suggesting reduced erosion due to the presence of plants (e.g., Silva et al., 2016; Feagin et al., 2019; Maximiliano-Cordova et al., 2019 and 2021). However, questions remain on whether dune vegetation is meaningful to dune storm protection beyond promoting long term accretional processes (i.e., building up dune size over time) (Feagin et al., 2015) since the potential for enhanced scouring due to accelerated flow around plant stems or uprooting of entire plants exists. Small-scale flume studies have indicated the potential for dune vegetation to reduce wave-induced erosion (e.g., Sigren et al., 2014; Silva et al., 2016), lending support to the idea that dune vegetation could play an active role in erosion resistance during storm surges. However, only few studies have addressed the specific biophysical mechanisms and interactions between vegetation, sediment, and water that drive this erosion resistance and storm protection. Mendoza et al. (2017) for example, studied implications of the dune plant *Ipomoea pes-caprae* at various densities and under various hydrodynamic forcing conditions on dune morphology evolution in a sediment wave flume, showing that the vegetation slowed the erosion process by adding small, localized perturbations to the flow. Both above- and belowground vegetation aspects likely play a role, enhancing complexity of the problem. The objective of this paper is to analyze and assess the specific interactions between vegetation, sediment, and hydrodynamics in a controlled flume setting to form statistical models for the role of vegetation in dune erosion resistance. Quantifiable information on effects of vegetation parameters on physical processes associated with dune erosion could help optimize the practice of dune restoration and the management of vegetated dune systems.

The above- and belowground components of vegetation affect hydrodynamics and sediment properties in multiple transitional and coastal ecosystems (e.g., marshes, mangroves, seagrass and kelp beds, riparian banks), reducing erosion in the process (Thampanya et al., 2006; Gedan et al., 2011; Coops et al., 1996). Though coastal dunes in some ways differ from these other ecosystems (e.g., different shore geometries/morphology, sediment characteristics, swash and surf zone/wave breaking dynamics), the interactions observed in other ecosystems can provide context for the kinds of interactions that may occur between dune vegetation and sediment/water during direct wave impact. Aboveground interactions are hydrodynamic in nature, occurring between moving water and plant stems and leaves. In marshes, aboveground plant structures reduce tidal flow and turbulent velocities (Leonard and Luther, 1995). Such reductions in velocities lower the overall amount of energy in the water column that is available to entrain and move sediments, tending to promote the settling of sediments and reduce erosion. Other energy dissipation by plant structures has been observed in coastal ecosystems in the form of wave energy dissipation (e.g., Ysebaert et al., 2011; Yang et al., 2012). The amount of energy dissipation that occurs depends on the type of vegetation and the rigidity and surface area/density of the aboveground plant structures (Augustin et al., 2009; Bouma et al., 2010). Similar hydrodynamic interactions may occur between aboveground dune plant structures, water flow, and waves during elevated water levels where wave breaking and runup affect the dune face.

Belowground, plant roots and their associated microbial communities bind sediments and strengthen sediment structure. Soil binding and aggregation influences the general erodability of sediment and can take place over decades in dune sediment (Forster and Nicholson, 1981). The process involves bacterial and fungal decomposition, secretion of adhesive compounds, and entanglement of sediment particles by root hairs and fungal hyphae (Miller & Jastrow, 1990). The ratio of surface area and mass is reduced in water-stable conglomerates, conceivably causing behavior under hydrodynamic stresses comparable with larger particles. The described soil binding would therefore increase the dune sediment's "effective grain size" and resistance to movement *via* water-borne forces. Potentially, higher amounts of mycorrhizal activity and roots present in a soil could increase this binding of sediment and erosion resistance.

De Baets et al. (2008) and Fan & Su (2008) point out the increased shear strength for sediments interspersed with roots from vegetation. In dunes, certain surge and wave collision scenarios (Sallenger, 2000) cause a dune scarp (cliff) to form as waves erode the base of the dune (Roelvink et al., 2009). Gravity acts on the overhanging sand of the dune scarp, inducing cantilever action and shear stress across the dune sediment and potentially causes slumping. Genet et al. (2007) pointed out that the tensile strength of roots can help delay the slumping process through the provided increased resistance to shear stress. It is hypothesized that, to a certain extent, as root density increases, so does the resistance of vegetated dunes to erosion.

These above- and belowground processes provide a conceptual framework for how dune vegetation could influence erosion but depend on observations made about plants in other ecosystems. To fill this knowledge gap concerning coastal dunes, the overall objective of the research in this paper was to determine the importance of dune vegetation in erosion resistance and to explore which aspects of vegetation (e.g., surface area and rigidity of plant stems, root biomass, mycorrhizal activity) are linked to various physical processes in the coastal zone (e.g., turbulence, swash velocity, wave reflection, shear stress reinforcement, sediment binding, erosion, dune scarp retreat). Controlled flume experiments were conducted varying both above- and belowground vegetation parameters to accomplish the objective. Four specific dune plant morphotypes at different growth stages were embedded into the dune face of a model sand dune and subjected to elevated water levels and irregular waves to simulate the dune collision impact regime. This approach allowed the physical interactions between waves, the dune substrate, and vegetation to be statistically modeled (multivariate regression). Understanding these biophysical linkages could inform dune restoration and management practices and allow for the optimization of protective aspects of vegetation for the use in Engineering with Nature™ projects. Furthermore, optimized vegetation strategies may be a valuable tool to combat climate change threats to coastal areas, such as increased erosion resulting from future elevated water levels and more intense or frequent storms.

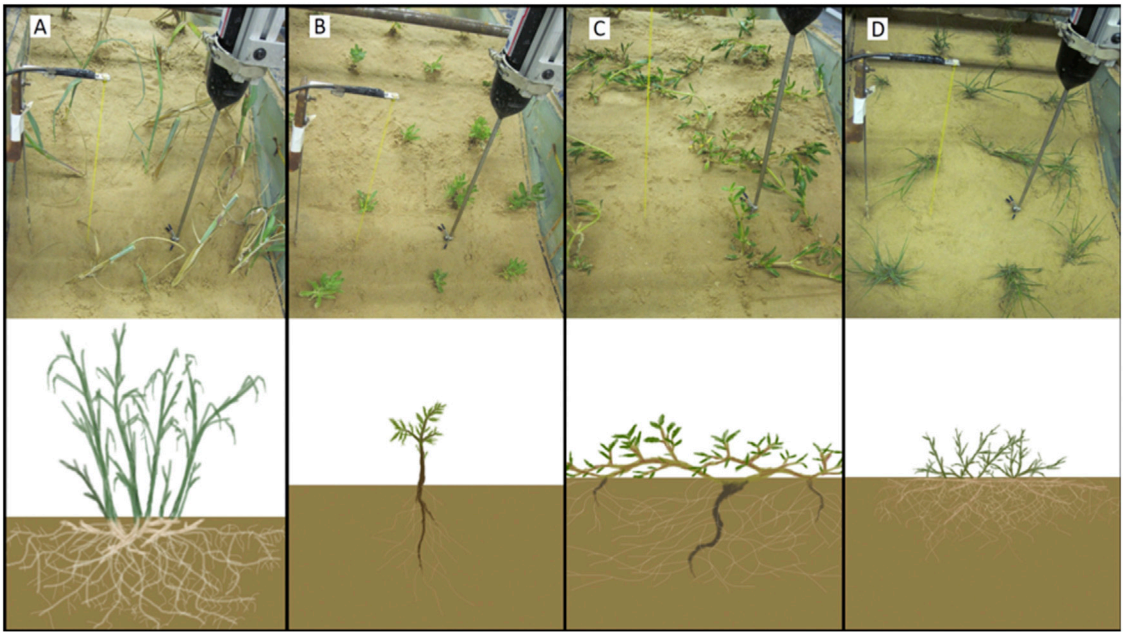

FIGURE 1 | Photos (top panels) and schematics (bottom panels) of plants used in sediment wave flume experiment. Four species/morphotypes of plants were used for this experiment: A tall grass (**A**: *P. amarum*), a small forb (**B**: *R. phyllocephala*), a spreading vine (**C**: *S. portulacastrum*), and a short grass (**D**: *S. virginicus*). Photos depict initial dune profile conditions for vegetated trials using 3-week-old transplants. Schematics highlight differences in above- and below-ground structure of the four different plant morphotypes.

METHODOLOGY

The overarching approach taken for this experiment was to generate variation in plant characteristics that may be relevant to dune swash hydrodynamics, sediment properties, and erosion and to test those variable plant characteristics in a simulated storm surge and wave attack while measuring physical response variables. This variation in plant characteristics was generated by testing four different species of dune plants at three different growth intervals (time allotted for the plants to grow in a greenhouse). Five plant metrics were measured through these tests: above-ground plant surface area, plant stem rotational stiffness/rigidity, fine root biomass, coarse root biomass, and mycorrhizal colonization. Six physical response metrics were also measured: near-bed swash flow velocity, turbulent kinetic energy (TKE), wave reflection (proxy for wave energy dissipation), sediment shear strength, sediment aggregation/effective grain size, and morphodynamic evolution of the vegetated dune profile. The influence of plant metrics on physical response variables was statistically evaluated using multivariate regression analysis. Several confounding variables were also analyzed and are thoroughly detailed in the Appendix.

Plant Growth and Setup

Four different species of plants, each a unique morphotype (tall grasses, shrubs, vines, and short grasses–each representative of plants that live throughout the US Gulf Coast), were tested in different flume trials (**Figure 1**). *Panicum amarum (P. amarum)* represented the morphotype of tall dune grasses (**Figure 1A**). This plant features relatively rigid stems and can grow in excess of 1 m in vertical extent. However, most of the plant did not interact with waves because it was taller than the maximum water depth of the swash zone of the wave flume. This species also has a dense, adventitious root system featuring large rhizomes (>1 cm in diameter). Dune forbs/shrubs were represented by *Rayjacksonia phyllocephala (R. phyllocephala).* For flume testing seedlings between 5 and 10 cm in height were transplanted, but it is common for this plant to grow up to 50 cm in height in nature. This species has a woody stem and tap root with few fine roots (**Figure 1B**). The species *Sesuvium portulacastrum (S. portulacastrum)* represents the morphotype of spreading dune vines in this experiment (**Figure 1C**). This species forms a dense matrix of structures close to the ground (typically not higher than 5 cm) but is flexible compared to the other species. *S. portulacastrum* grows primary roots from nodes on stolons. Moderately dense networks of fine roots radiate from these larger primary roots. The last represented morphotype was *Sporobolus virginicus (S. virginicus).* This dune plant is characterized as a short grass with relatively low stem rigidity and a dense network of adventitious fine roots (**Figure 1D**). Its typical growth height ranges from 5 to 15 cm.

In addition to the variations in plant morphotype, transplant age at the time of flume testing was varied as a measure of the length of time a plant has had to grow and develop. The procedure to grow and transplant the vegetation into the sand dune of the wave flume is described next. Cylindrical plastic pots,

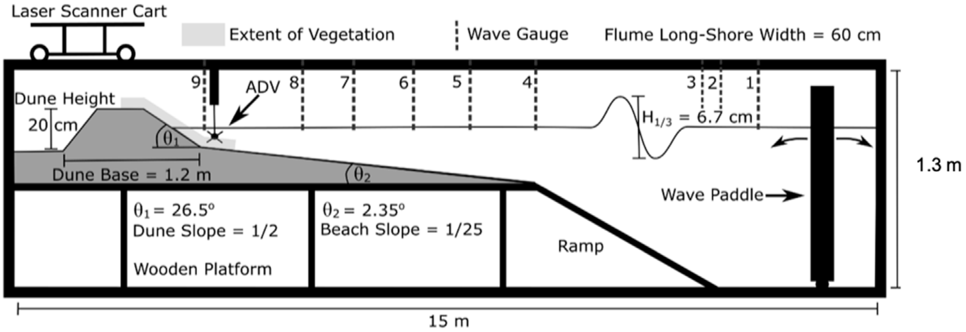

FIGURE 2 | Schematic of sediment wave flume setup including the area of vegetation plantings.

16 cm in both diameter and height, were filled with the same sediment that was used to form the dune in the wave flume. Over the spring and summer months, cuttings from each plant species were watered and fertilized in an identical fashion in a nearby greenhouse to allow for the development of above- and belowground plant features. After set growth periods of 3, 6, and 9 weeks the entire content of the respective pots was transplanted into the dune for testing. This was accomplished by removing an identical cylindrical volume of sediment from an initial bare dune in the flume and replacing it with the content of a pot. The sediment surface was then smoothed by hand to provide a seamless dune surface. Once transplanted, the contents from the pots (15 per trial) formed a staggered grid of five rows and three columns (*see* **Figure 1**). A total of 15 wave flume trials were conducted, three controls trials without plants and 12 trials with plants (4 species × 3 growth intervals).

Sediment Wave Flume Setup

All tests were conducted in a 15 m long × 1.3 m deep × 0.6 m wide wave flume (**Figure 2**). Sediment within the flume consisted of sand from a Texas sand pit with a median grain diameter of 152 microns. The sediment's grain size distribution resembles that of native material along upper Texas coast beaches (*see* **Sections 2.4**, **2.5** for more details) and was determined using sieve analysis. The seaward facing dune slope was 1/2 (= tan θ_1) and the beach slope was 1/25 (= tan θ_2). A plywood ramp of 2.45 m cross-shore length connected the sand profile to the base elevation of the flume. The initial dune was trapezoidal with a 120 cm base width, a 30 cm crest width, and a height of 20 cm. The initial dune and beach morphology were maintained constant for all trials using cross-shore acrylic templates positioned along the inside walls of the wave flume. This template allowed initial sediment elevations to be consistent at the start of each trial, though some slight variation between initial dune morphologies did occur. The initial dune morphology was parameterized so it could be modeled as a confounding variable in multivariate statistical analysis. Nine capacitance wave gauges (WG) measured the free surface elevation of water within the flume and were positioned at select cross-shore locations throughout the flume (**Figure 2** and **Table 1**). WG1 was used as the cross-shore coordinate origin and was located 1.9 m from the wave paddle in a water depth of $h = 103$ cm. The wave gauge data were used to calculate wave statistics (wave height, wave period, spectral energy density) and are described in more detail in subsequent sections. Additionally, a side-looking Nortek Vectrino Plus (a type of acoustic Doppler velocimeter or ADV) was placed near the dune base within the swash zone. This instrument recorded water velocities at 200 Hz and these data were used to calculate TKE and average swash velocity (additional details also in subsequent sections). Each trial consisted of 12 irregular wave runs, each wave run lasting 210 s to accommodate enough individual waves to complete the statistical analysis but at the same time provide the opportunity for frequent profile scans in between wave runs. Three control trials (C1, C2, C3) with the same initial bare dune and 12 vegetated trials (four species at three respective maturity levels) were conducted. No replicate tests of the vegetated trials were performed. This was a deliberate decision primarily due to logistical constraints related to available greenhouse space and time. The decision was made to focus on various plant morphotypes and transplant age rather than replicates under the given constraints. Before each trial, still water level elevation was maintained for about 1 h to allow for comparable sediment moisture conditions to establish throughout the dune interior before starting the waves. Additionally, the dune surface was sprayed with water before each trial using a spray bottle to attain comparable sediment moisture conditions but also to mimic more realistically the dune surface conditions during storms. An irregular, JONSWAP wave spectrum with a 6.7 cm significant wave height and a peak period of 0.53 s formed the basis for each run for which identical incident wave time series were used. A summary of all experiment parameters is provided in **Table 1**.

Plant Measurements

Data on above- and belowground vegetation parameters were obtained for each plant that had been part of the wave flume experiment. Once each trial had been completed, all included plants were carefully removed from the flume followed by a thorough wash to remove any attached sediment. Further processing involved separation into aboveground and belowground components and determination of dry biomass. The total aboveground vegetation surface area

TABLE 1 | Summary of wave flume experiment parameters.

Plant species	None (control)	*P. amarum* (tall grass)	*R.* phyllocephala (short shrub)	*S. portulacastrum* (vine)	*S. virginicus* (short grass)
Trial ID	C1, C2, C3	PA1, PA2, PA3	RP1, RP2, RP3	SP1, SP2, SP3	SV1, SV2, SV3
Maturity (weeks)	N/A	3, 6, 9	3, 6, 9	3, 6, 9	3, 6, 9
No. of plants	0	15			
Plant density	0	28 plants/m^2			
Total duration	42 min				
H_s, T_p, h, D_{50}	6.7 cm, 1.9 s, 103 cm, 0.14 mm (**Figure 3**)				
Profile scan times	0, 3.5, 7, 14, 28, 42 min				
WG and ADV x-positions	WG: 0.0, 0.2, 1.0, 3.5, 6.6, 8.7, 9.7, 10.4, 11.6 m ADV: 11.6 m (all relative to WG1)				

(stems and leaves) interacting with wave up- and downrush on the dune face was quantified *via* spectral image analysis. Based on measured water depth time series on the dune face, only the lowest 5 cm of the aboveground plant structure were deemed to contribute to flow-vegetation interactions in this experiment. Stems and leaves from five of the used plants in each trial were photographed against a white background with length scale markings. Care was taken to make sure no plant structures were stacked on top of one another. Images were then spectrally analyzed in ArcMap where any non-white pixel was considered plant area. Total plant surface area was then calculated by converting the sum of all vegetation pixels up to 5 cm in plant height to an actual surface area value. Both average surface area per plant as well as total surface area per wave flume trial were determined. Belowground plant parameters were divided into two categories and included fine roots with a diameter less than 1 mm and coarse roots with a diameter larger than 1 mm.

Rotational stiffness (*RS*) of plant stems was determined *via* a cantilever beam setup by measuring the angle of deflection (θ) resulting from applying a force (F) at a distance (D) from the fixed anchor point (**1**):

$$RS = \frac{F \times D}{\theta} \tag{1}$$

Where:

RS = Rotational stiffness
F = Magnitude of the force applied to the plant stem
D = Distance of the applied force from the anchor of the plant stem
θ = Angle of deflection caused by applied force

Five different stems for each plant species were used to determine the respective average *RS*. The level of mycorrhiza presence on roots was quantified using Trypan Blue to stain the fine roots of each plant species following Morton & Amarasinghe (2006). By examining the roots under a microscope (magnification factor 200) in 1-cm length increments, the percentage of root length showing signs of mycorrhiza was recorded. Each 1-cm increment of roots displaying either hyphae, spore structures, arbuscule, or vacuole was taken to have active mycorrhiza.

Hydrodynamics

The swash zone water velocity was collected for every wave run and trial at 200 Hz sampling frequency with a Nortek Vectrino Plus acoustic Doppler velocimeter (ADV) in “side-looker” configuration. The ADV relies on Doppler shifts in reflected acoustic bursts to determine the velocity of particles moving in water. When exposed to air, the ADV records only noise. Therefore, bubbles in the water column or backwash occurrences that exposed the ADV would cause erroneous readings. Both sources of error were filtered out. Because the ADV sensor head was placed in the swash zone, good data were logged intermittently during full sensor submergence. Based off each ADV dataset’s collocated wave gauge data, velocity data were removed when the local water free surface elevation was less than 0.5 cm below the still water level. As reference, the center of the ADV head was roughly 1 cm above the initial sediment bed and the tips of the top-most receiver prongs were roughly at the surface of the water (**Figure 3**). The 0.5 cm below still-water mark was the minimum level at which the ADV sensor head could record data. This technique filtered out the noise generated by air exposure for the ADV data so that turbulence and velocity calculations could be made. It should be noted that even though the center of the ADV sensor head was on average around 1 cm above the sediment bed over the course of all trials and wave runs, the sediment bed would shift slightly at this location (+/− 1 cm). For this reason, the distance from the sediment bed to the ADV sensor-head was used as a confounding variable for multivariate modeling of swash velocity and turbulent kinetic energy.

Turbulent velocity fluctuations (u', v', w') were computed by subtracting the mean flow velocity from the measured velocity signal for each dimension, respectively. The mean flow velocity was calculated as a running average over 21 adjacent points (i.e., a 0.1 s window) in the 200-Hz data set. The cross-shore and alongshore location of the velocity measurements remained the same for each trial (only the vertical position was adjusted to maintain similar distance to the bed at the beginning of each trial): The sensor head was positioned along the center axis of the flume just landward of

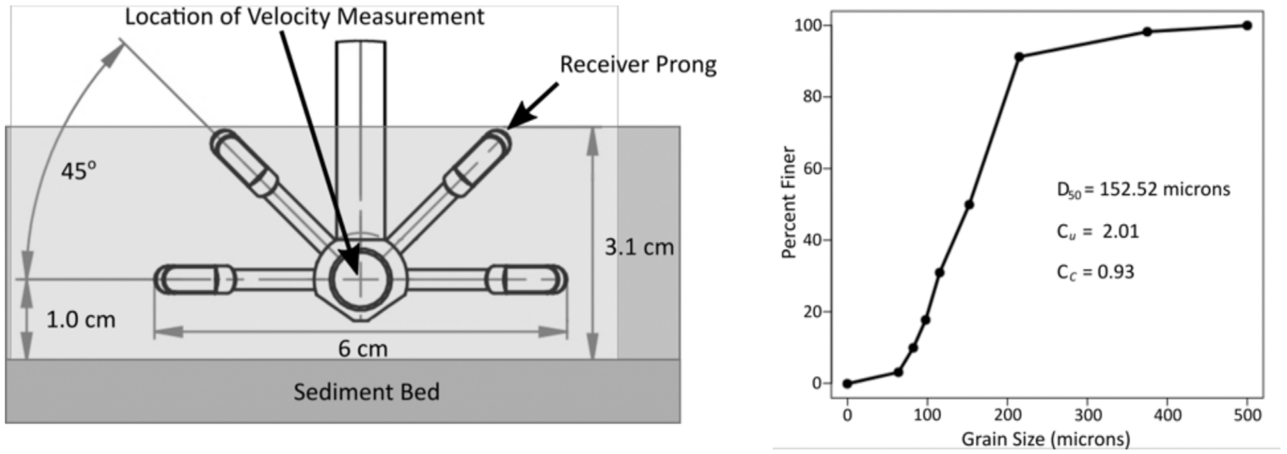

FIGURE 3 | Schematic side view of ADV sensor head placement relative to the initial sediment bed (left panel). Cumulative grain size distribution of the sediment used to build the dunes in the sediment wave flume (right panel). D_{50} is the median grain size, C_u is the coefficient of uniformity, and C_c is the coefficient of curvature.

the first row of plants approximately at the transition point between erosion and accretion of the dune profile. Various filtering mechanisms (i.e., acceleration, amplitude return, correlation, and signal-to-noise ratio filters) were applied to the raw velocity data to remove outliers that could occur due to the presence of bubbles, for example.

Turbulent kinetic energy (TKE) was calculated using the post-processed data of each wave run **(2)** where time-averaging is denoted by overbars. The absolute value of the mean flow velocity in the cross-shore direction was taken to be representative of the velocity magnitude of both the uprush and downrush during swash motion.

$$TKE = \frac{1}{2}\left(\overline{u'^2} + \overline{v'^2} + \overline{w'^2}\right) \tag{2}$$

where:

TKE = Mean turbulent kinetic.

u', v', w' = Turbulent velocity fluctuations in the cross-shore, alongshore, and vertical direction, respectively.

Nine capacitance wave gauges collected data for every wave run in every trial at 20 Hz and were used to calculate the wave reflection coefficient and other wave parameters. Wave reflection coefficients were obtained from the records of the three wave gauges furthest offshore (WG1 – WG3, *see* **Figure 2**) following the technique by Mansard and Funke (1980). Wave reflection coefficients were calculated for every 400-s window of wave action.

$$R = \frac{H_r}{H_i} \tag{3}$$

where R is the wave reflection coefficient, and H_r and H_i are the reflected and incident wave height, respectively.

Sediment Properties

Data were collected for two sediment properties: sediment shear strength and sediment aggregation. As these two properties could not be sampled from the wave flume before or after a trial without interrupting the trial or being disrupted by wave action, samples were taken from a harvested pot representative of each plant trial (control samples were simply collected from the flume sediment without plants present). Shear strength was measured by applying shear forcing across a 6 cm long, 7 cm diameter core using a horizontal soil shear apparatus. Cores were sheared at a speed of approximately 1 mm per second over a distance of 2.5 cm. Shear curves were created by video analysis of an attached force gauge display. Both peak shear and cumulative shear (the area under the shear curve) were calculated from the recorded data. In addition, the fine and coarse root biomass from each core was measured. Sediment aggregation was measured from a small sample (~50 g) of sediment obtained from the same harvested plant that was run through a sieve tower submerged in water and placed on an INNOVA 2100 platform shaker at 80 RPM for 20 min. The advantage of using a water submerged tower was that unaltered sediment could be used (not dried, frozen, or ground up). Unaltered sediment is assumed to have binding properties (adhesive compounds, mycorrhizal entanglements, *etc.*) intact. The resulting grain size distribution represents the sediment's effective grain size during a water-based forcing event. The sieve sizes of 63, 125, 180, and 250 microns were used and provided high resolution for this sediment's grain size distribution.

Dune and Beach Morphology Measurements

Three-dimensional dune and beach morphology changes were measured using a combination of a laser line scanner (Acuity AP820-1000) mounted on a movable cart and a laser range finder (Acuity AR 2000). The elevation of the evolving morphology was scanned six times per trial, including the initial scan and subsequent scans following wave runs 1, 2, 4, 8, and 12 (or

3.5, 7, 14, 28, 42 min, respectively). Scans consisted of a 50-cm alongshore swath along the center transect (5 cm were excluded on each side to minimize interference with the walls of the wave flume) at 1-cm cross-shore increments. Plant structures measured by the laser were consistently removed from all profile scans. After filtering out plant elevations, the three-dimensional sediment surfaces were averaged at each cross-shore increment to yield representative 2D cross-shore profiles for calculation of the eroded volume of sediment from the dune area. For every final and initial profile comparison, there is a point near the base of the initial dune which marks the transition between erosion and accretion areas. All erosion that occurred landward of this point was summed and multiplied by the width of the flume.

Statistical Analysis

The correlation between plant characteristics and physical response variables was determined *via* stepwise multivariate regression analysis. However, due to the large number of variables, a dredge algorithm (Barton, 2015) was used to narrow the list of predictor variables from the large pool. This algorithm is a type of automated model selection that creates all possible models (every combination of predictive/independent variables) and produces a ranking of the best possible fit models (based off R^2). Stepwise forwards and backwards modeling techniques along with collinearity assessments (Variable Inflation Factors - VIFS) were then used on the dredge-optimized models to create a coherent model with only significant (α < 0.05) predictive variables. This statistical analysis also accounted for confounding variables which could influence physical response variables. These confounding variables arose due to differential patterns of erosion and sediment redistribution as a trial proceeded and due to slight user-based variation in the initial setup of dune/beach morphology and wave conditions. The Appendix includes additional details on the specific confounding variables that were analyzed in conjunction with the plant metrics.

Some predicted variables were modeled by the number of trials (n = 15) while others were modeled by the number of wave runs (n = 180). This sample size discrepancy is because dune morphological change variables and sediment data (shear strength, aggregation, eroded volume) only had one data point per trial (based off differences between beginning and end profile of each respective run). Alternatively, hydrodynamic data (TKE, swash velocity, wave reflection) were collected for each wave run and though there were repeated vegetation conditions for some wave runs, these hydrodynamic data were independent of each other. For example, measured TKE for any given wave run depends on profile, wave, and vegetation characteristics of that wave run and was modeled as such. It is possible in this type of analysis, however, that a certain variable (vegetation as well as confounding variable) does not show up as a significant predictor for a specific outcome simply because the tested range was not adequate. Additionally, if two plant variables were collinear, the modeling techniques used in this analysis cannot detect the independent importance of each plant variable with respect to a predicted variable.

RESULTS

Wave Flume Observations

As waves approached the shoreline, they shoaled and eventually broke between 40 (for the smallest waves) and 80 cm (for the largest waves) from the toe of the dune. The surf zone transitioned into the swash zone with swash runup passing through the first row of vegetation before reaching the location of the ADV sensor head. Vegetation structures had a visible effect on water flow, forming wakes behind stems indicating turbulence generation and energy dissipation. The average swash zone cross-shore velocity component u at the ADV was reduced from 0.272 m/s for the three control trials (C1 – C3) to an average of 0.238 m/s over all vegetated trials. **Figure 4** shows the cross-shore swash velocity component u as well as the TKE obtained from **(2)** in color matrix form for each wave run and all experiment trials. Swash velocity decreased in all vegetated trials compared to the control trials without vegetation. This is likely caused by increased friction and drag provided by the above-ground plant structure and felt by the flow passing through the vegetation. However, for most of the vegetated trials the velocity increased with increasing plant growth duration. This indicates that while overall vegetation reduces flow velocities at the measurement location, the increased level of flow obstruction in trials with more mature vegetation can lead to localized small relative increases in velocity due to flow acceleration around the plant obstacles. The only exception were the vegetated trials with *S. virginicus* (SV1 – 3) where, on average, velocity decreased with increased plant maturity level. This can be explained by the relatively low rotational stiffness of this plant morphotype where added above-ground biomass *via* leaves may increase overall friction levels, but the lack of rigid stems may lead to negligible plant area reduction perpendicular to the flow (i.e., leaves sway back and forth aligning themselves with the flow direction rather than acting as a rigid object forcing flow acceleration around it). TKE at the ADV measurement location varied from 0.01 J/kg to 0.03 J/kg across all trials where the higher values always occurred during the initial wave run of each trial. For the control trials, TKE reduced to about 0.02 J/kg as profiles adjusted to the wave forcing conditions while all vegetated trials showed further reduction even down to the lowest values of 0.01 J/kg by the end of PA3, RP3, SP2, and SP3 (**Figure 4**). This showed that the more matured vegetation enhanced dissipation due to added above-ground surface structure. Reflection coefficients, R, were 0.27 on average for all control trials, compared to 0.23 on average across all vegetated trials indicating enhanced wave energy dissipation in the vegetated trials. Scour occurred in the sediment bed in front of and along the sides of the vegetation stems. Vegetation structures moved with the swash flow, with the magnitude of the swaying motion seemingly proportional to the rigidity of the plant structures. *P. amarum* motion was minimal while *S. portulacastrum* undulated greatly with each passing uprush and downrush. For all tests, the initial wave run exhibited the most severe morphodynamic changes, as the profile started to adjust toward an equilibrium based on the incoming wave energy. During the first wave run

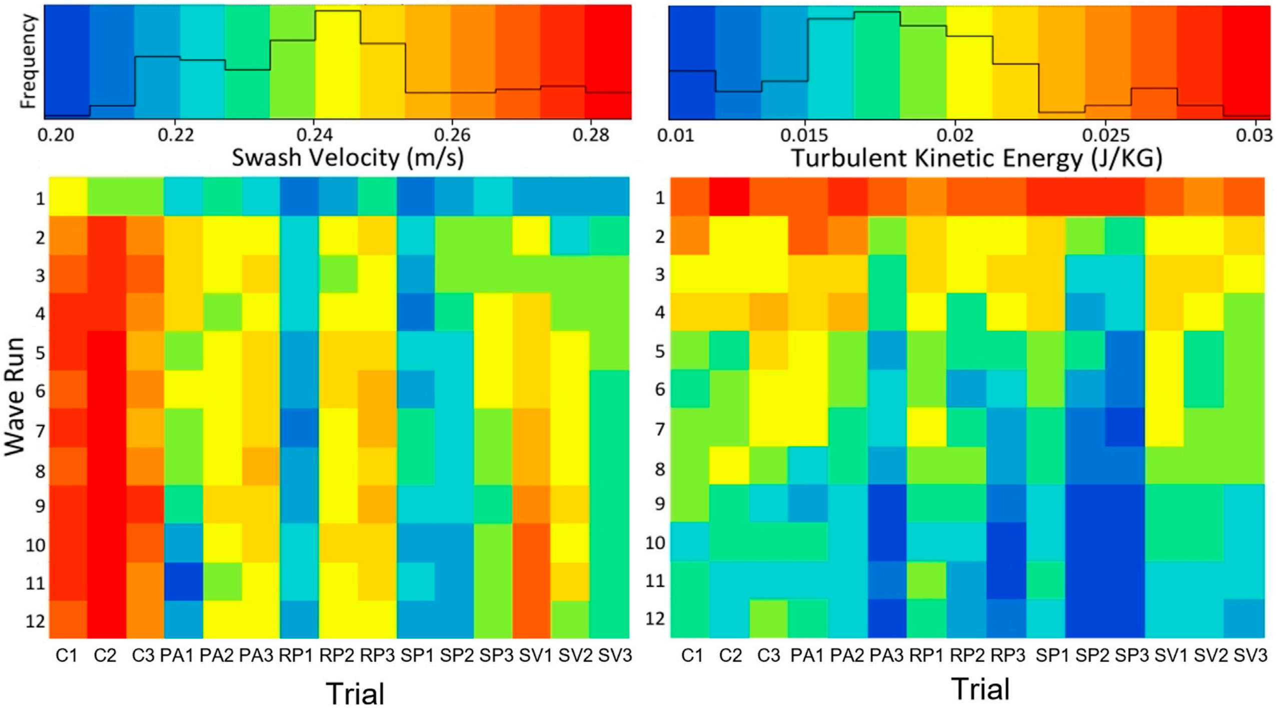

FIGURE 4 | ADV-measured cross-shore swash velocity component *u* (left panels) and computed TKE (right panels) using **Eq. 2** for each wave run and every experiment trial. The top row of panels includes the respective color key maps linking colors to specific parameter value ranges. The bottom row of panels shows the actual data as color matrices. Each column represents a separate trial as indicated by the trial ID (**Table 1**). Each row represents a single wave run (210 s) from top (1) to bottom (12). The frequency of occurrence of specific value bins is indicated by the histograms overlaid on top of the respective color key maps.

of each trial, the runup limit exceeded the first three rows of vegetation and nearly reached the crest of the dune. By design, only the collision regime was tested, so trials were stopped before the dune crest was breached to avoid any overwash. As erosion occurred in the swash zone, roots were exposed along a 20 cm cross-shore segment of shoreline. Roots, when exposed to waves, also had a visible impact on the motion of water in the swash zone that was similar to the above-ground plant structures.

As waves began washing up onto the dune during the first wave run, dune sediment became wet and was pulled offshore into the swash zone by the return flow (downrush). By the end of the first wave run, rapid erosion of the seaward dune face had taken place forming a pronounced vertical scarp. Typically, this dune scarp started between the third and fourth rows of vegetation with a vertical extent between 5 and 6 cm. During the second wave run, the erosion dynamic shifted due to the adjusted profile featuring a growing offshore bar that aided in wave energy dissipation further away from the vegetation line. Thus, smaller waves from the JONSWAP spectrum began having less impact, barely running up to the base of the scarp. Larger waves, however, still interacted with the vegetation and substrate and collided with the base of the dune scarp continuing to erode sediment. This dynamic created a scarp overhang which would eventually slump into the swash zone as the base was undermined by attacking waves. The occurrence of intermittent slumping therefore appeared to be a dominant driver of erosion. When the overhang remained intact, minimal amounts of sediment were carried offshore from the dune. When the overhang collapsed, sediment slumped into attacking waves and the active swash zone. This sediment was then moved offshore by wave action and the previous dynamic of scarp overhang and base erosion commenced.

For trials without plants, two or three major slumping events would take place over the duration of the whole series of wave runs. For plant trials, often no or only one major slumping event occurred. As slumping occurred during plant trials, large cracks formed on the dune crest and plant roots were observed to span these cracks, providing a source of attachment of the slumping sediment to the rest of the dune. Plant trial slumping events would generally be prolonged and less violent than those observed in control trials. The eroded dune volume (E) and the scarp retreat (S) since the start of the respective experiment trial are listed in **Table 2**. Trial IDs correspond to those explained in **Table 1**. For the three bare dune control trials (C1-3) the average values are given. Time in minutes indicates the duration after the start of each trial at which profile scans were conducted.

Variability of Vegetation Aspects

The 5-spoke star plots in **Figure 5** are a tool to visualize variations of a select set of five vegetation parameters across the different

TABLE 2 | Eroded dune volume and scarp retreat.

Trial ID/Time	3.5 min	7 min	14 min	28 min	42 min
C1-3	12281.3	13756.2	15401.3	17103.1	18379.4
	43.3	48.5	54.3	60.3	64.8
PA1	11883.4	14041.3	14588.4	16108.0	15013.8
	39.1	46.2	48	53	49.4
PA2	10559.1	10957.1	12761.2	13689.7	14565.2
	39.8	41.3	48.1	51.6	54.9
PA3	10559.1	11036.7	12655.0	14087.7	14379.5
	39.8	41.6	47.7	53.1	54.2
RP1	12308.9	13281.5	14254.0	15469.7	16989.4
	40.5	43.7	46.9	50.9	55.9
RP2	12187.4	14162.9	15013.8	17080.5	19147.2
	40.1	46.6	49.4	56.2	63
RP3	12521.7	13950.1	15682.5	15773.7	17749.2
	41.2	45.9	51.6	51.9	58.4
SP1	12187.4	13281.5	15257.0	16563.9	17323.7
	40.1	43.7	50.2	54.5	57
SP2	9524.4	10293.8	11620.4	12469.3	12840.8
	35.9	38.8	43.8	47	48.4
SP3	9895.9	10293.8	12097.9	12575.5	12840.8
	37.3	38.8	45.6	47.4	48.4
SV1	13190.3	13494.2	16108.0	18812.9	19147.2
	43.4	44.4	53	61.9	63
SV2	12977.6	14497.2	16563.9	17627.6	17749.2
	42.7	47.7	54.5	58	58.4
SV3	10665.3	10851.0	11142.8	13026.5	13424.4
	40.2	40.9	42	49.1	50.6

The first row of values for each trial is eroded dune volume (cm^3) since the beginning of the respective trial and the second row of values is scarp retreat (cm). C1-3 indicates averages across the three control trials.

plant species and growth durations. The five parameters included are the fine (FR) and coarse (CR) root mass, respectively, percent of roots with mycorrhiza colonization (MC), the plant surface area (SA) in contact with the flow, and the rotational stiffness (RS) of plant stems starting at the top of the star and proceeding in a counterclockwise direction. Parameter values relative to all other trials are indicated on the respective spokes of the star plots where the maximum value observed is shown at the point along the spoke farthest away from the center of the star. Connecting all the values to form a shaded 5-point area allows for easy comparison of dominant vegetation characteristics among various trials and to baseline control tests without vegetation.

The star plots reveal contrasts in plant parameters between vegetation types, but also changes based on growth duration. For example, a substantial increase in fine roots (FR), coarse roots (CR), and rotational stiffness (RS) was observed for *P. amarum* as growth duration increased from 3 (PA1) to 6 (PA2) and eventually 9 (PA3) weeks, while at the same time mycorrhizal colonization (MC) and plant surface area (SA) remained low (**Figure 5**). This behavior can be explained in part by specific plant morphotype growth. *P. amarum* grows relatively tall with individual stems increasing in rigidity over time while maintaining a relatively low stem density (number of stems per unit area). Since most of the stem and leaf growth occurs above the elevation where flow interactions are expected, the aboveground changes in *P. amarum* over time do not significantly affect SA. Both the amount of fine (FR) and coarse (CR) roots of this plant, however, seem to have flourished with increasing growth duration to maximum levels across all tested plant morphotypes. In contrast, the dune forb *R. phyllocephala* did not show significant amounts of change in any of the vegetation parameters over the allotted growth time in this experiment, leading to continued small star plot area for all tests. Fine roots (FR), coarse roots (CR), surface area (SA), as well as stem rotational stiffness (RS) increased less than 5% of the respective maximum value for each parameter. A relatively moderate increase in fine roots (FR) and coarse roots (CR) in combination with the largest increase in surface area (SA) while maintaining low rotational stiffness (RS) was observed for *S. portulacastrum.* These observations make sense as this plant remains low to the ground as it spreads out over time (i.e., increased surface area in contact with the flow) without necessarily increasing its stem rigidity. The plant type *S. virginicus* did also not increase its rotational stiffness (RS) significantly over time but displayed a relatively large value for coarse roots (CR) by the 9-week mark (13.2 g/L for SV3) with only moderate increase in fine root (FR) and plant surface area (SA) values. Mycorrhiza presence remained relatively low for all tested morphotypes and growth durations, varying only between zero and 34.6% with a mean value of 5.4%. In general, the gray area formed by the 5-spoke star plots allows grouping of trial runs into three broad categories: Control trials without any vegetation present (C1, C2, C3), trials with relatively low vegetation influence (PA1, RP1, RP2, RP3, SP1, SV1, SV2), and trials with high vegetation influence (PA2, PA3, SP2, SP3, SV3).

The erosion response of the beach-dune system to hydrodynamic forcing is captured by the 3-spoke star plots shown in **Figure 5**. Parameters displayed include the eroded volume (E), the dune scarp retreat (S), and the cross-shore shift in profile area centroid (CS). A larger black triangle area indicates a more substantial erosion response with individual parameter values relative to all trials shown along the respective parameter spoke of the star. The highest values for erosion response parameters were measured in the bare dune control trials without any vegetation. Average values across all three control trials for E, S, and CS were 18379.4 cm^3, 64.8 cm, and 11.9 cm, respectively. The trials listed above with measurable but still relatively low vegetation influence produced average erosion response values for E, S, and CS of 17588.5 cm^3, 57.9 cm, and 10.7 cm, respectively, a notable reduction across the board. The trials considered to have high vegetation influence further decreased the overall erosion response. For these trials, the average values for parameters E, S, and CS were 13610.1 cm^3, 51.3 cm, and 6.6 cm, respectively.

Multivariate statistical modeling of these vegetation variables with regards to erosion and other physical processes will add specificity to these generalizations and are detailed in the next sections. It should be noted that several of the plant variables were collinear with one another. Fine and coarse root biomass were strongly and positively correlated to one another. Both fine and coarse root biomass were also strongly and positively correlated to rotational stiffness. Lastly, mycorrhizal colonization showed a moderate correlation to plant surface area.

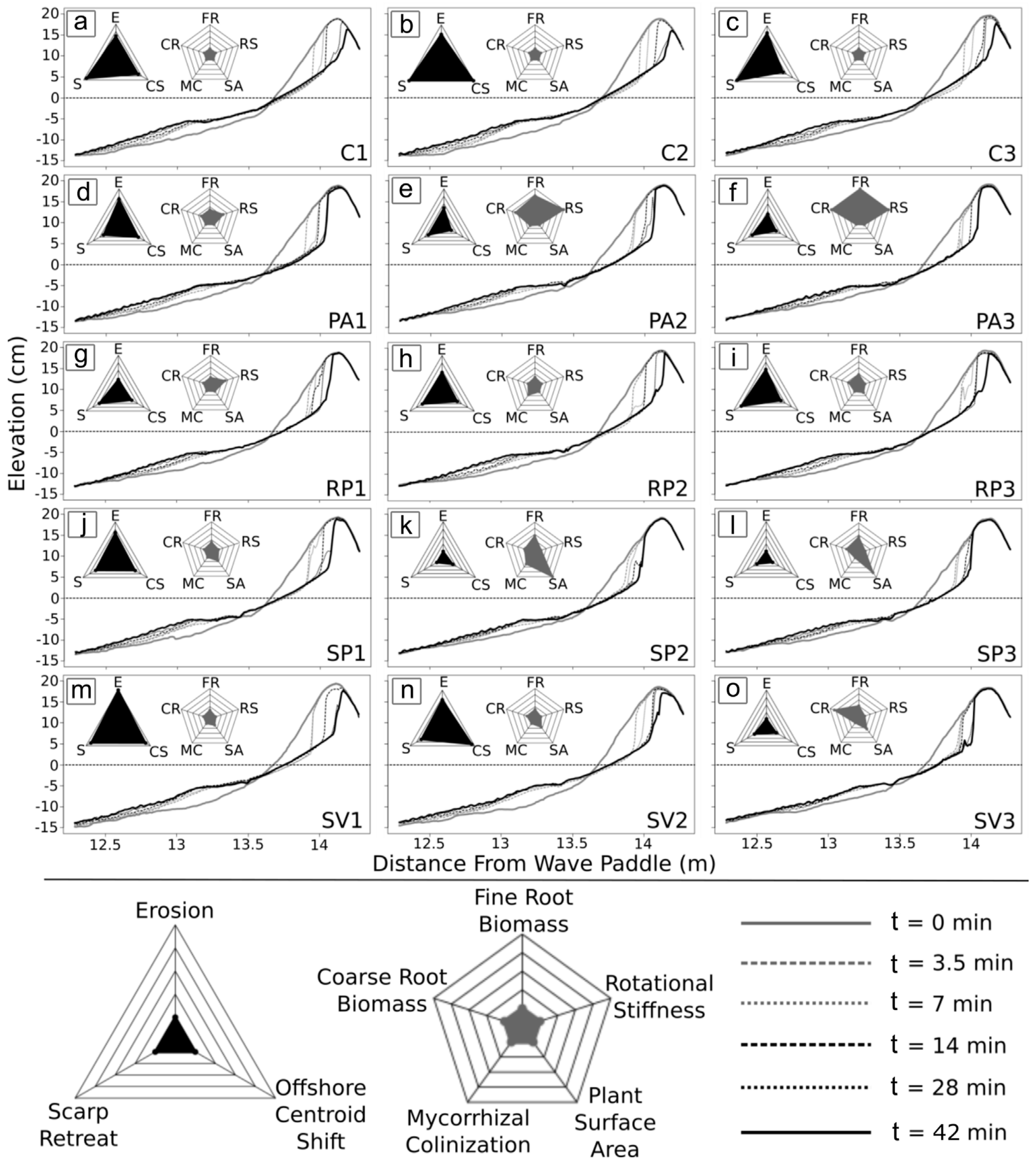

FIGURE 5 | Evolution of beach and dune profiles for all wave runs. Panel letters **(A–O)** indicate each of the 15 individual experiment trials with specific trial ID given in the lower right corner of each panel as detailed in **Table 1**. Profiles are plotted at set times t in minutes as indicated in the legend with the initial profile depicted as a solid gray line and the final profile as a solid black line. Star plots summarizing beach/dune morphological change (three spokes) and plant (five spokes) data between initial and final run for each trial are also shown in each panel with individual spoke parameters explained in the legend at the bottom.

Statistical Model Outcomes

Data were collected over 15 flume trials on plant characteristics (plant surface area, rotational stiffness, fine root biomass, coarse root biomass, and mycorrhizal colonization) as well as physical response variables (average swash velocity, TKE, wave reflection coefficient, shear strength, sediment aggregation, erosion, profile centroid shift, and dune scarp retreat rate). To evaluate whether vegetation aspects affected physical properties during the experiments, multivariate regression analyses were conducted for all predictive and response variables (**Table 3**). Minus signs mark negative relationships and plus signs note positive relationships (asterisks show the level of significance of the relationship based on statistical *p*-values; N/A indicates "not applicable"; N/S indicates "not significant").

TABLE 3 | Summary of all multivariate models.

Predicted variable	Plant surface area	Rotational stiffness	Fine root biomass	Coarse root biomass	Mycorrhizal colonization
Swash Velocity	–***	–***	N/S	N/S	N/S
Turbulent Kinetic Energy	–***	–*	N/S	N/S	N/S
Wave Reflection Coefficient	–***	N/S	–***	N/S	N/S
Cumulative Sediment Shear Strength	N/A	N/A	+**	N/S	N/S
Peak Sediment Shear Strength	N/A	N/A	N/S	N/S	N/S
Sediment Aggregation	N/A	N/A	N/S	N/S	N/S
Erosion	–*	N/S	–*	N/S	N/S
Cross-shore Centroid Shift	–**	N/S	–*	N/S	N/S
Scarp Retreat	–**	N/S	–***	N/S	N/S

Notes on p values: *p ≤ 0.05, **p ≤ 0.01, ***p ≤ 0.001.

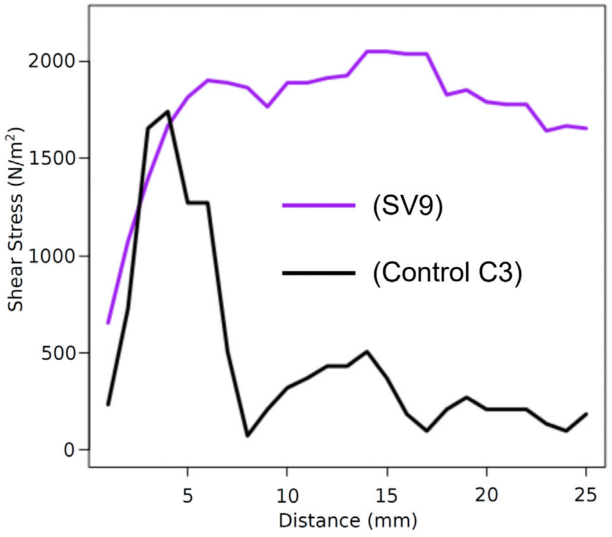

FIGURE 6 | Comparison between shear curves produced from a core of control trial C3 and SV3 (*S. virginicus* at 9 weeks maturity).

Three hydrodynamic parameters were modeled during the flume trials: TKE (**Supplementary Appendix Table SA1**), average swash velocity (cross-shore direction, absolute value, **Supplementary Appendix Table SA2**), and wave reflection (**Supplementary Appendix Table SA3**). The aboveground plant surface area of stems and leaves were negatively and significantly related to swash velocity, TKE, and wave reflection coefficient. In other words, wave runs with more abundant aboveground structures had reduced flow velocities and turbulence in the swash zone. Plant structures also caused less wave energy to be reflected (a more dissipative shoreline). Rotational stiffness also had a similar negative relationship with mean flow velocity and swash zone TKE. Additional statistical model specifications for these models, including the influence of confounding variables, can be found in the Appendix (**Supplementary Appendix Tables SA1–SA3**).

Data were collected on two sediment properties: shear strength and effective grain size (aggregation). For shear testing, both peak shear (**Supplementary Appendix Table SA4**) and cumulative shear, i.e., the area under a shear curve (**Supplementary Appendix Table SA5**), were evaluated for relationships with root properties within tested cores. Fine root biomass was positively and significantly related to peak shear and cumulative shear and displayed a stronger relationship than coarse root biomass or total root biomass. **Figure 6** shows a comparison of sediment shear curves between a core taken from *S. virginicus* at 9 weeks (SV3, the plant/growth increment with the highest cumulative shear as well as the highest fine root density) and a control core from trial C3. The two shear curves have similar peaks (the core with plant roots being slightly higher) but the core with plant material resisted a continuously high shear stress throughout the full length of the shear test, basically providing a more ductile failure mode. In contrast, the control core essentially crumbled when shear stress built up, failing rather rapidly. No significant trend was found between sediment aggregation (effective grain size) and mycorrhizal colonization or fine root biomass. Additional information on sediment shear models can be found in the Appendix (**Supplementary Appendix Tables SA4–SA5**).

The three erosion response parameters (E, S, and CS) all had similar relationships with respect to plant characteristics. Specifically, FR (fine root biomass) and SA (aboveground plant surface area) showed a significant negative correlation with eroded sediment volume (E) in that trials with high parameter values of FR and SA led to significant erosion reduction. For each additional 100 mg/L of fine roots (dry), erosion volume was reduced by roughly 1.2k cm^3 or about 6.6% of the average erosion volume that occurred during the control trials. Erosion volume was reduced by roughly 380 cm^3 (~2.1% of the average erosion volume that occurred during the control trials) for each cm^2 of plant surface area per alongshore centimeter of shoreline (**Supplementary Appendix Table SA6**).

Similarly, the erosion response parameter S (scarp retreat distance) showed a significant negative correlation with FR and SA. For each additional 100 mg/L of fine roots (dry), scarp retreat was reduced by roughly 3 cm or about 4.6% of the average retreat that occurred in the control trials. Scarp retreat was reduced by roughly 1.1 cm (~1.7% of the average scarp retreat that occurred during the control trials) for each cm^2 of plant surface area per alongshore centimeter of shoreline (**Supplementary Appendix Table SA7**). Consistent with the other measures of erosion, offshore centroid shift (CS) was also significantly and negatively correlated with FR and SA (**Supplementary Appendix Table SA7**). In trials with more fine roots, stems, or leaves, the offshore shift of sediment was reduced. For each additional 100 mg/L of fine roots (dry), offshore centroid shift was reduced by roughly 1.1 cm or about 9.6% of the average centroid shift that occurred in the control trials. Cross-shore centroid shift was reduced by roughly 0.2 cm (~1.8% of the average off-shore centroid shift that occurred during the control trials) for each cm^2 of plant surface area per alongshore centimeter of shoreline. Additional details on all three erosion models are given in the Appendix (**Supplementary Appendix Tables SA6–SA7**).

DISCUSSION

Conceptualizing Statistical Models

The presented physical model experiment data indicate that aboveground as well as belowground components of plants contribute to a dune and beach system's resistance against erosion, as has been seen in similar and related studies. For example, the present study found that the rotational stiffness of plant stems and structures contributed to reductions of turbulence and swash flow velocity, though rotational stiffness could not be statistically tied to erosion reduction. This calming effect in both turbulence and flow velocity has been reported from measurements in hydrological settings including emergent vegetation in wetlands (Leonard and Luther, 1995) and beach macroalgae (Innocenti et al., 2018), and related to differing dune plant structures (Maximiliano-Cordova et al., 2019; Oderiz et al., 2020; Innocenti et al., 2021).

The results of the present study also found that the surface area of aboveground plant structures created a more dissipative shoreline and a less energetic swash zone, and that this was indeed related to less erosion. Feagin et al. (2019) similarly found erosion reduction by aboveground structures that are connected to belowground structures, as found in this study and as in the field, but further explained that the belowground structures alone provided still better protection. Their findings implied that while the aboveground structures do dissipate wave energy and reduce velocities, they also provide a cantilever upon which waves can begin to leverage a plant. This cantilever effect can ultimately uproot a plant, extract sediment, and offset the erosion reduction provided by the energy dissipation effect. While the current study did not similarly partition aboveground versus belowground structures into separate treatments, it points to the importance of belowground structures in a novel way.

In particular, the present study shows that the fine roots of plants are a key determinant of erosion reduction. The results show that for erosion reduction, the fine roots are more important than coarse roots, mycorrhizal colonization, or aboveground plant structures. Moreover, these fine roots provide a unique mechanism that binds the sediment grains together and prevents gravity-driving slumping and collapse. Fine roots uniquely enhance the sediment shear strength.

It should be noted that with regards to statistical modeling, beach and dune morphological variables (such as the location and size of the sandbar, or the distance of the ADV head to the sediment surface) were accounted for during the statistical modeling process, implying that plant surface area played a causal role. In other words, it was not some feedback mechanism between plant surface area and shoreline morphology that modified swash hydrodynamics. Rather, plant surface area reduced swash velocity, TKE, and wave reflection independently of confounding shoreline features (*see* Appendix for additional details on the interplay between confounding variables and plant variables). This means that even in the absence of changes in morphological parameters, the surface area of the plants contributes to wave energy dissipation.

Ramifications for Dune Management

The effect of vegetation on erosion was substantial under the presented experiment conditions (based off Model A6, *see* Appendix). Erosion reduction of up to approximately 1/3 (37%) of the erosion experienced by the control trials could be achieved if the aboveground plant surface area of trial SP3 and the biomass of fine roots of trial PA3 were combined. Kobayashi et al. (2013), Sigren et al. (2014), and Silva et al. (2016), among others, have obtained similar values of erosion reduction in physical model studies due to the presence of vegetation (real or surrogate) on the seaward dune face. The temporal aspect of this erosion reduction by vegetation should also enter flood risk management considerations since the time to a complete breach during storm impact is extended. A prolonged dune breach could mean that vegetation will enhance dune storm damage mitigation with regards to homes and infrastructure, though that would depend on the flume results scaling to larger systems (*see* **section 4.3**).

Taking the findings from this study a step further, dune management and restoration practices could consider adopting a combination of multiple native plant morphotypes with specific beneficial characteristics to reduce storm damage and erosion and further enhance the observed effects of vegetation. For example, a combination of species targeting extensive fine root system development as well as substantial low-elevation aboveground surface area may maximize desired benefits. Those plant morphotypes that err on the side of root production would be more important in areas where a scarp forms (i.e., the dune ridge and slopes) because of their contribution to sediment shear strength (at least for a wave collision scenario that is similar to the one that was used in this flume experiment).

Limitations of Experiment and Research Outlook

There were some limitations to the approach taken in this experiment. Due to the usage of a small-scale wave flume, the obtained results are not directly transferrable to larger dune systems or longer temporal events. First, if a comparable amount of *S. portulacastrum* was growing *in situ* as was used in this experiment's *S. portulacastrum* 9 week trial (SP3), it would likely not reduce erosion by the same amount as was observed in the flume (~26%) during a real-life storm surge. This discrepancy occurs because the wave parameters and shoreline profile were scaled down for the experiment, while the plants were not. However, the general trends that were observed in the flume should take place *in situ* (i.e., more roots would reduce more erosion). However, the true magnitude of the erosion reducing effects in scaled up dune and beach systems remains undetermined.

Second, the obtained results do not account for the dynamics that may occur during a longer temporal event, such as during a hurricane. At time scales of hours to days, such events progress through multiple regimes of erosion (Sallenger Jr., 2000), often beginning with swash and runup, then transitioning into collision, and finally resulting in overtopping or inundation of the dune. The obtained results solely apply to the dynamics that occur during the wave collision regime.

Third, the vegetated trials did not include replicates to allow for some form of ensemble averaging or determination of variability. While this is certainly a limitation the choice to run experiments on four different plant morphotypes at three different transplant age levels showed significant trends detailed in the conclusions that would likely not change even if replicate trials were conducted. The minimal variability observed across the three control trial replicates further underscores that point.

There were also some statistical limitations to the approach taken in this experiment. For example, if a variable was not a significant determinant of erosion or a physical process, this does not necessarily mean that it was irrelevant for *in situ* dune systems. Rather, the methodology utilized to model these variables could have tested an inadequate range of variation. For example, sediment aggregation should, in concept, lead to less erosion in sand dunes. If a substantial amount of sediment particles is bound together in a water-stable manner as to shift that sediment's effective grain size distribution, less erosion would take place. Such sediment binding caused by mycorrhizal fungi has been measured in dune systems (Forster and Nicholson, 1981), but may take place over many years as organic materials build up in soil and mycorrhizal fungi increase in abundance. The time allotted for plant growth in this experiment (3–9 weeks) was probably not a long enough time for these soil structures to develop. Therefore, sediment aggregation could be important in dune erosion, but the range of parameters tested in this experiment failed to yield statistically significant results.

Additionally, the collinear relationship of certain plant parameters means that statistical modeling techniques could not verify each variable's independent effect on dependent variables. Fine and coarse roots, for example, were collinear during this experiment. Fine root biomass density was found to be a more significant predictor of dune erosion during statistical modeling but both variables could be important to dune erosion resistance. Further testing of a broader range of variable combinations (a non-collinear dataset) would need to be conducted to parse the independent contribution of these two belowground variables.

CONCLUSION

The physical model experiment conducted in a wave flume led to the conclusion that plant-related parameters that change aboveground as well as belowground properties of a vegetated dune can significantly influence dune erosion. Their net effect was to reduce wave-induced erosion volume by up to 37%. The surface area of aboveground plant structures was related to decreases in turbulence and uprush/backwash velocities, helping create a shoreline that was more effective at dissipating incoming wave energy. Fine roots increased the mechanical strength of sediment, making it more resistant to shearing forces and preventing sediment from slumping into incoming waves. In concept, increasing the quantity of fine roots would create a dune system more resistant to erosive forces. Future research on this topic could expand to larger length and temporal scales, with the aim of guiding coastal dune management and restoration techniques.

DATA AVAILABILITY STATEMENT

The original contributions presented in the study are included in the article/**Supplementary Material**, further inquiries can be directed to the corresponding author.

AUTHOR CONTRIBUTIONS

JF: Experiment design, methodology, supervision, resources and funding, data collection, data analysis, writing, review, editing. JS: Data collection, data analysis, writing. RF: Methodology, review and editing. AA: Resources, methodology, review and editing.

FUNDING

This research was supported in part by the Texas A&M University at Galveston Research and Development Fund. JF was supported in part by National Science Foundation Grant No. OISE-1545837 and an Institutional Grant (NA14OAR4170102) to the Texas Sea Grant College Program from the National Sea Grant Office, National Oceanic and Atmospheric Administration, U.S. Department of Commerce. Rusty Feagin was supported in part by National Science Foundation Grant No. PO-1756477 and the Texas A&M University T3 Fund.

ACKNOWLEDGMENTS

The work presented here is adapted and synthesized from Chapter 2 of the Ph.D. dissertation by co-author Jacob M. Sigren (2017) and has not been previously published in peer-reviewed journal form. Furthermore, the authors would like to thank Robert C. Tyler, Taylor Hennessy, and Melissa D'Amore for their help conducting the wave flume experiments.

SUPPLEMENTARY MATERIAL

The Supplementary Material for this article can be found online at: https://www.frontiersin.org/articles/10.3389/fbuil.2022.904837/full#supplementary-material

REFERENCES

Augustin, L. N., Irish, J. L., and Lynett, P. (2009). Laboratory and Numerical Studies of Wave Damping by Emergent and Near-Emergent Wetland Vegetation. *Coast. Eng.* 56 (3), 332–340. doi:10.1016/j.coastaleng.2008.09.004

Barton, K. (2015). *Mumin: Multi-Model Inference*.

Bouma, T. J., Vries, M. B. D., and Herman, P. M. J. (2010). Comparing Ecosystem Engineering Efficiency of Two Plant Species with Contrasting Growth Strategies. *Ecology* 91 (9), 2696–2704. doi:10.1890/09-0690.1

Coops, H., Geilen, N., Verheij, H. J., Boeters, R., and Velde, G. (1996). Interactions between Waves, Bank Erosion and Emergent Vegetation: an Experimental Study in a Wave Tank. *Aquat. Bot.* 53 (3-4), 187–198. doi:10.1016/0304-3770(96)01027-3

De Baets, S., Poesen, J., Reubens, B., Wemans, K., De Baerdemaeker, J., and Muys, B. (2008). Root Tensile Strength and Root Distribution of Typical Mediterranean Plant Species and Their Contribution to Soil Shear Strength. *Plant Soil* 305 (1-2), 207–226.

Fan, C.-C., and Su, C.-F. (2008). Role of Roots in the Shear Strength of Root-Reinforced Soils with High Moisture Content. *Ecol. Eng.* 33 (2), 157–166. doi:10.1016/j.ecoleng.2008.02.013

Feagin, R. A., Figlus, J., Zinnert, J. C., Sigren, J., Martínez, M. L., Silva, R., et al. (2015). Going with the Flow or against the Grain? the Promise of Vegetation for Protecting Beaches, Dunes, and Barrier Islands from Erosion. *Front. Ecol. Environ.* 13 (4), 203–210. doi:10.1890/140218

Feagin, R. A., Furman, M., Salgado, K., Martinez, M. L., Innocenti, R. A., Eubanks, K., et al. (2019). The Role of Beach and Sand Dune Vegetation in Mediating Wave Run up Erosion. *Estuar. Coast. Shelf Sci.* 219, 97–106. doi:10.1016/j.ecss.2019.01.018

Forster, S. M., and Nicolson, T. H. (1981). Microbial Aggregation of Sand in a Maritime Dune Succession. *Soil Biol. Biochem.* 13 (3), 205–208. doi:10.1016/0038-0717(81)90021-3

Gedan, K. B., Kirwan, M. L., Wolanski, E., Barbier, E. B., and Silliman, B. R. (2011). The Present and Future Role of Coastal Wetland Vegetation in Protecting Shorelines: Answering Recent Challenges to the Paradigm. *Clim. Change* 106 (1), 7–29.

Genet, M., Stokes, A., Salin, F., Mickovski, S. B., Fourcaud, T., Dumail, J. F., et al. (2007). The Influence of Cellulose Content on Tensile Strength in Tree Roots. *Plant Soil* 103, 3–11.

Innocenti, R. A., Feagin, R. A., Charbonneau, B. R., Figlus, J., Lomonaco, P., Wengrove, M., et al. (2021). The Effects of Plant Structure and Flow Properties on the Physical Response of Coastal Dune Plants to Wind and Wave Run-Up. *Estuar. Coast. Shelf Sci.* 261, 107556. doi:10.1016/j.ecss.2021.107556

Innocenti, R. A., Feagin, R. A., and Huff, T. P. (2018). The Role of Sargassum Macroalgal Wrack in Reducing Coastal Erosion. *Estuar. Coast. Shelf Sci.* 214, 82–88. doi:10.1016/j.ecss.2018.09.021

Kobayashi, N., Gralher, C., and Do, K. (2013). Effects of Woody Plants on Dune Erosion and over Wash. *J. Waterw. Port, Coast. Ocean Eng.* 139 (6). doi:10.1061/(asce)ww.1943-5460.0000200

Leonard, L. A., and Luther, M. E. (1995). Flow Hydrodynamics in Tidal Marsh Canopies. *Limnol. Oceanogr.* 40 (8), 1474–1484. doi:10.4319/lo.1995.40.8.1474

Mansard, E. P. D., and Funke, E. R. (1980). The Measurement of Incident and Reflected Spectra Using a Least Squares Method. *Proc. Int. Conf. Coast. Eng.*, 154–172. doi:10.1061/9780872622647.008

Maximiliano-Cordova, C., Martínez, M. L., Silva, R., Hesp, P. A., Guevara, R., and Landgrave, R. (2021). Assessing the Impact of a Winter Storm on the Beach and Dune Systems and Erosion Mitigation by Plants. *Front. Mar. Sci.* 8, 734036. doi:10.3389/fmars.2021.734036

Maximiliano-Cordova, C., Salgado, K., Martínez, M. L., Mendoza, E., Silva, R., Guevara, R., et al. (2019). Does the Functional Richness of Plants Reduce Wave Erosion on Embryo Coastal Dunes? *Estuaries Coasts* 42, 1730–1741. doi:10.1007/s12237-019-00537-x

Mendoza, E., Odériz, I., Martínez, M. L., and Silva, R. (2017). Measurements and Modelling of Small Scale Processes of Vegetation Preventing Dune Erosion. *J. Coast. Res.* 77 (10077), 19–27. doi:10.2112/si77-003.1

Miller, R. M., and Jastrow, J. D. (1990). Hierarchy of Root and Mycorrhizal Fungal Interactions with Soil Aggregation. *Soil Biol. Biochem.* 22 (5), 579–584. doi:10.1016/0038-0717(90)90001-g

Morton, J. B., and Amarasinghe, R. (2006). "Plant and Mycorrhizal Root Lengths. Technical Report," in *International Culture Collection of Vesicular-Arbuscular Mycorrhizal Fungi* (Morgantown, WV: West Virginia University).

Odériz, I., Knöchelmann, N., Silva, R., Feagin, R. A., Martínez, M. L., and Mendoza, E. (2020). Reinforcement of Vegetated and Unvegetated Dunes by a Rocky Core: A Viable Alternative for Dissipating Waves and Providing Protection? *Coast. Eng.* 158, 103675.

Roelvink, D., Reniers, A., van Dongeren, A., van Thiel de Vries, J., McCall, R., and Lescinski, J. (2009). Modeling Storm Impacts on Beaches, Dunes and Barrier Islands. *Coast. Eng.* 56 (11-12), 1133–1152. doi:10.1142/9789814277426_0140

Sallenger, A. H. (2000). Storm Impact Scale for Barrier Islands. *J. Coast. Res.* 16 (3), 890–895.

Sigren, J. M. (2017). *Coastal Dunes and Dune Vegetation: Interdisciplinary Research on Storm Protection, Erosion, and Ecosystem Restoration*. Galveston, TX: Ph.D. Dissertation. Texas A&M University.

Sigren, J. M., Figlus, J., and Armitage, A. R. (2014). Coastal Sand Dunes and Dune Vegetation: Restoration, Erosion, and Storm Protection. *Shore Beach* 82 (4), 5–12.

Sigren, J. M., Figlus, J., Highfield, W., Feagin, R. A., and Armitage, A. R. (2016). The Effects of Coastal Dune Volume and Vegetation on Storm-Induced Property Damage: Analysis from Hurricane Ike. *J. Coast. Res.* 34 (1), 164–173.

Silva, R., Martínez, M. L., Odériz, I., Mendoza, E., and Feagin, R. A. (2016). Response of Vegetated Dune-Beach Systems to Storm Conditions. *Coast. Eng.* 109, 53–62. doi:10.1016/j.coastaleng.2015.12.007

Thampanya, U., Vermaat, J., Sinsakul, S., and Panapitukkul, N. (2006). Coastal Erosion and Mangrove Progradation of Southern thailand. *Estuar. Coast. Shelf Sci.* 68 (1&2), 75–85. doi:10.1016/j.ecss.2006.01.011

Yang, S. L., Shi, B. W., Bouma, T. J., Ysebaert, T., and Luo, X. X. (2012). Wave Attenuation at a Salt Marsh Margin: a Case Study of an Exposed Coast on the Yangtze Estuary. *Estuaries Coasts* 35 (1), 169–182. doi:10.1007/s12237-011-9424-4

Ysebaert, T., Yang, S.-L., Zhang, L., He, Q., Bouma, T. J., and Herman, P. M. J. (2011). Wave Attenuation by Two Contrasting Ecosystem Engineering Salt Marsh Macrophytes in the Intertidal Pioneer Zone. *Wetlands* 31 (6), 1043–1054. doi:10.1007/s13157-011-0240-1

Conflict of Interest: The authors declare that the research was conducted in the absence of any commercial or financial relationships that could be construed as a potential conflict of interest.

frontiers | Frontiers in Built Environment

TYPE Original Research
PUBLISHED 05 August 2022
DOI 10.3389/fbuil.2022.917945

Ship wake forcing and performance of a living shoreline segment on an estuarine shoreline

Cassandra L. Everett[1], Oscar Williams[1], Emma Ruggiero[2], Michael Larner[3], Rachel Schaefer[4], Matt Malej[5], Fengyan Shi[1], Jules Bruck[2] and Jack A. Puleo[1]*

[1]Center for Applied Coastal Research, University of Delaware, Newark, DE, United States, [2]Coastal Resilience Design Studio, University of Delaware, Newark, DE, United States, [3]Sustainable Coastal Solutions, Inc., North Falmouth, MA, United States, [4]Department of Civil and Environmental Engineering, Massachusetts Institute of Technology, Cambridge, MA, United States, [5]Coastal and Hydraulics Laboratory, US Army Engineer Research and Development Center, Vicksburg, MS, United States

Check for updates

OPEN ACCESS

EDITED BY
Tori Tomiczek,
United States Naval Academy,
United States

REVIEWED BY
Cindy Palinkas,
University of Maryland, United States
David Cannon,
University of Michigan, United States

*CORRESPONDENCE
Jack A. Puleo,
jpuleo@udel.edu

SPECIALTY SECTION
This article was submitted to Coastal and Offshore Engineering,
a section of the journal
Frontiers in Built Environment

RECEIVED 11 April 2022
ACCEPTED 01 July 2022
PUBLISHED 05 August 2022

CITATION
Everett CL, Williams O, Ruggiero E, Larner M, Schaefer R, Malej M, Shi F, Bruck J and Puleo JA (2022), Ship wake forcing and performance of a living shoreline segment on an estuarine shoreline.
Front. Built Environ. 8:917945.
doi: 10.3389/fbuil.2022.917945

Investigation of the effectiveness of Natural and Nature-Based Features (NNBF) for protecting shorelines from ship wake is increasingly important with continued development along the coast, especially when combined with sea level rise. Studies that investigate the wave energy dissipation capacity of different techniques and account for variation in context will lead to improvements and innovation in designed NNBF. Few studies have examined the performance of NNBF in protecting shorelines from ship wake. In this study of a low-sloping estuarine shoreline adjacent to a major shipping route, a natural design using coir logs and wooden staking was implemented in a T-head groin configuration. Pressure transducers and electromagnetic current meters were deployed over ~1.5 months to investigate the energy dissipation and velocity attenuation capabilities of the installation. Results indicate that ship wakes account for 25%–50% of the total daily energy impacting the shoreline at the study site. Peak background velocities are typically over 50% smaller than the largest ship wake velocities. Field data and results of the fully nonlinear Boussinesq model, FUNWAVE-TVD, indicate that the installation is capable of decreasing energy impacting the shoreline by 10%–80% and is effective over the lower 50% of the tidal range and when submerged up to twice its height. Elevation surveys of the site indicate accrual of sediment within the installation, suggesting wave diffraction patterns promoting further accretion at the site over time. Observations indicate that coir logs may be effective in reducing wave energy from ship wakes but may fail under storm conditions in a moderate fetch confined channel. Findings from this study illustrate the opportunities and challenges nature-based solutions face in addressing ship wakes, and their ability to protect shorelines under high energy stressors.

KEYWORDS

ship wake, FUNWAVE-TVD, living shoreline, nature-based solution, coir logs, wave attenuation

1 Introduction

Marshes and coastal wetlands along estuaries provide a buffer of protection against hydrodynamic forcing. Natural sediment transport in tidal waterways is affected by the tidal range and controls the development and erosion of marshes and shorelines (Ross et al., 2017). Growing pressures from sea level rise and reductions in sediment supply due to upriver development, combined with effects of ship wakes, influence shoreline morphology and alter the formation and subsistence of coastal wetlands (Syvitski et al., 2005; Brophy et al., 2019; Ezcurra et al., 2019). The inland regions of estuarine waterways lack defense against large wave events because they are primarily subjected to weaker forcing resulting from currents, tides, and small wind waves that are limited by the relatively narrow fetch and shallow bathymetry. The built and natural environment along these waterways will become increasingly susceptible to erosion with an increase in global mean sea level (Neumann et al., 2015). For example, it is estimated that 46%–59% of global coastal wetlands will be lost to 0.5 m of sea level rise, and up to 78% will be flooded by 1.1 m of sea level rise under normal and high projections for sea level rise by 2,100 (Spencer et al., 2016).

Estuarine waterway systems provide valuable shipping routes for inland cities and ports. Increased trade and economic activity (Almaz and Altiok, 2012) has influenced the growth of marine traffic and the necessity for larger ships to transport cargo. Increased large-vessel traffic amplifies the negative impacts of ship-generated waves (Schroevers et al., 2011), hereafter referred to as ship wakes or wakes. Ship movement displaces water, forcing it to flow in front of, around, and under the hull from bow to stern, analogous to a moving surface pressure disturbance (Soomere, 2006). A typical ship wake event consists of a group of low-frequency waves followed by high-frequency large-amplitude waves, and an ultra-low-frequency wave component (Herbert et al., 2018). Vessel length may be an important variable in the development of high amplitude wakes in confined channels (Scarpa et al., 2019).

Ship wakes, due to their higher energy content relative to wind-generated waves in a short fetch environment, have the potential to increase erosion along waterway shorelines (Verney et al., 2007; Soomere et al., 2009; Houser, 2011; Bilkovic et al., 2019; Styles and Hartman, 2019), and cause a variety of negative ecological effects including marsh degradation, wildlife disturbance, and light attenuation for local vegetation (Gabel et al., 2017; Bilkovic et al., 2019). Ship wake events typically produce waves with amplitudes greater than those of wind waves in fetch-limited waters and occur more frequently than storm surge events that produce waves of a similar size (Gabel et al., 2017). Ship wake events can also increase current velocities by an order of magnitude (Rapaglia et al., 2015), and can produce higher near-bottom velocities than wind waves of the same amplitude (Gabel et al., 2017), causing increased sediment suspension. In addition, extreme events and ship wake activity are a known cause of bank failure in fetch-limited environments, and the erosive potential of ship wakes increases with diminishing width in the waterway (De Roo and Troch, 2015). Suspended sediment concentration also increases during ship wake activity as compared to calm conditions before the wake (Safak et al., 2021). The increase in suspension is likely to lead to increased sediment transport under ship wakes relative to background wind-wave forcing (e.g. Safak et al., 2021).

Populations are increasing along coastlines, leading to high density coastal development and a need to protect onshore structures often with hard structures (Douglass and Pickel, 1999). As a conservative estimate, 14% of coastlines in the continental U.S. are hard armored, with the highest concentrations in cities (Gittman et al., 2015). Traditional structures like bulkheads starve estuarine shorelines of sediment (Zabawa et al., 1981) and lead to the loss of intertidal habitat (Douglass and Pickel, 1999). Hard structures prevent physical energy from impacting the shoreline onshore of their placement and help maintain shoreline position. However, they do not decrease the energy or erosion capacity of the wave environment offshore of the structure, allowing for continued erosion and elevation loss. In fact, the reflection of waves, including ship wakes, off of the bulkhead may increase the local energy levels. When compared to natural and restored shorelines, bulkheads may perform worse in protecting shorelines from erosion (Gittman et al., 2014; Smith et al., 2017) and have shown greater and more costly damages during hurricane events (Smith et al., 2017).

Research concerning natural alternatives to hard structure shoreline protection has increased rapidly since the term “living shoreline” was introduced in 2008 (Smith et al., 2020); where living shoreline is generally used to refer to shoreline protection strategies that include an element of habitat restoration (NOAA, 2015). Living shorelines have the potential to dissipate wave energy, stabilize shorelines, reduce flooding, and reduce the impact of large storms while providing co-benefits to ecological and economic systems (Temmerman et al., 2013; Davis et al., 2015; SAGE, 2015; O’Donnell, 2017; Kibler et al., 2019). The value of nature-based solutions is not well understood, especially in terms of coastal defense benefit, due to variations in materials, environment, and desired outcomes, and lack of research of different designs within these contexts (Gedan et al., 2011). Living shorelines are rarely monitored in the long-term for their effectiveness (Polk and Eulie, 2018; Bayraktarov et al., 2019) and those that have been implemented are not always intended to achieve coastal protection outcomes. Other measures of success, such as habitat creation, are often the primary focus of various investigations (Morris et al., 2018).

Living shorelines range widely in their ability to protect shorelines, require careful consideration of ecological components to ensure their sustained success, and may fail in high energy conditions (De Roo and Troch, 2015; SAGE, 2015; Morris et al., 2018), such as ship wakes. The interaction between waves and living shoreline structures has shown successful wave dissipation by different designs (Meyer et al., 1997; Ellis et al., 2002; Dao et al., 2018; Safak et al., 2020a; Safak et al., 2020b; Mai Van et al., 2021), but requires further investigation. Few studies have examined the performance of living shorelines and natural and nature-based features in protecting shorelines from ship wake-induced erosion. However, shipping traffic can significantly alter the wave environment in low-energy waterways. Hydrodynamic processes and tidal depths play a vital role in the success of living shorelines installation such as low-crested brush bundle breakwaters (Ellis et al., 2002). Natural materials are chosen for accessibility, low cost relative to engineered materials, lack of interference with local ecology, biodegradability (impermanence in changing systems), and/or their permeability for wave dissipation as opposed to reflection. However, the applicability of these materials in different contexts is not well researched. In Delaware, and according to the Delaware Department of Natural Resources and Environmental Control (DNREC), “conventional living shorelines” are those employing natural materials, of which coir logs and oyster shell are the most common materials, and are typically constructed in lower energy areas (Delaware Department of Natural Resources and Environmental Control, 2020). Coir logs are accessible, low cost, handleable (low weight), and flexible in terms of application to project configurations. They typically break down in two to five years and are often used to establish a slope of ground elevation through accretion that supports plant material along a gradually sloping shoreline. Oyster shell is used to dissipate wave energy and establish a living breakwater by recruiting live oysters to establish a reef. Therefore, part of this study includes investigating such material recommendations in moderate energy systems. The aim of this study is to quantify the relative importance of ship wakes in the Delaware estuary and develop and test a low-cost nature-based living shoreline in a ship wake-influenced area. Investigating the behavior of such a structure composed of natural materials in an environment with heavy commercial shipping traffic will contribute to the growing body of knowledge surrounding living shoreline design.

2 Ship wake field and numerical study

2.1 Study site

The Delaware River is one of the most commercially navigated estuarine systems on the East Coast, serving as a major artery for over 40 ports and anchorages. About 3,000 ships traverse the waterway each year, supplying and exporting goods to and from major cities such as Camden, Philadelphia, Wilmington, and Trenton (Almaz and Altiok, 2012). The river is subjected to flood dominant semidiurnal tides as far inland as Trenton, limiting the passage of larger and deeper draft ships during low tides. Dredging projects since 2002 have increased the channel depth to 15 m to accommodate larger ships and increased shipping traffic (Cook et al., 2007).

Pea Patch Island is a silt deposit-formed island located on the Delaware River about 1.4 km east of Delaware City and about 1.6 km west of Fort Mott State Park (39°35.67′N, 75°34.35′W, Figure 1A). It has an average elevation of 1.38 m relative to the North American Vertical Datum of 1988 (NAVD88; mean water level is 0.85 m NAVD88) and roughly 95% of the island is less than 2.25 m in elevation. Pea Patch Island has a total area of about 1 km^2, with a length of ~1.9 km and a width of 0.8 km at its widest point. The small island is the site of Fort Delaware, a historic military fort, as well as the largest wading bird nesting area on the East Coast north of Florida. Historically, Pea Patch Island has been susceptible to shoreline erosion due to its location in the middle of the river near the shipping channel and has been the subject of many ongoing shoreline protection efforts to preserve the cultural history of the site and facilitate the roughly 30,000 annual visitors touring the island hosted by the Delaware State Parks (USACE, 2009).

The installation location is on the east side of Pea Patch Island (Figure 1B) adjacent to the main shipping channel, where the shoreline experiences severe erosion as evidenced by exposed tree roots. The river at this location is 1.6 km wide and more than half of this width is spanned by the channel of interest at 900 m wide (Figure 1C). The shipping lane within the channel is approximately 250 m wide and has navigational depths of 10–15 m. The channel runs closest to the shore along the southeastern side of the island and distance between the channel and the island shoreline increases farther north. At the installation location there is a silty-mud tidal flat that spans roughly 140 m between the channel and the shoreline. The tidal flat widens to the northwest and contains sandy shoals offshore.

Wetlands and shorelines are dynamic protection mechanisms for inland areas. A rising concern is whether Pea Patch Island will be able to adapt fast enough to the acceleration of external forces. Increased shipping traffic in the channel, sea level rise and increased storm intensity will result in growth of the mean annual wave power density. Wave power density may be directly proportional to the volumetric retreat of marsh edges (Marani et al., 2011). Shoreline retreat and cross-shore sediment transport result in a decrease in foreshore slope to dissipate wave energy (Dean and Dalrymple, 2002). However, continual dredging of the Delaware River channel decreases frictional forces and increases tidal amplitude resulting in faster tidal (alongshore) currents (van Maren et al., 2015; van Rijn et al., 2018; Ralston et al., 2019). The increase in alongshore currents removes suspended sediment from the local system. The shoreline south of the study site was armored with stone to

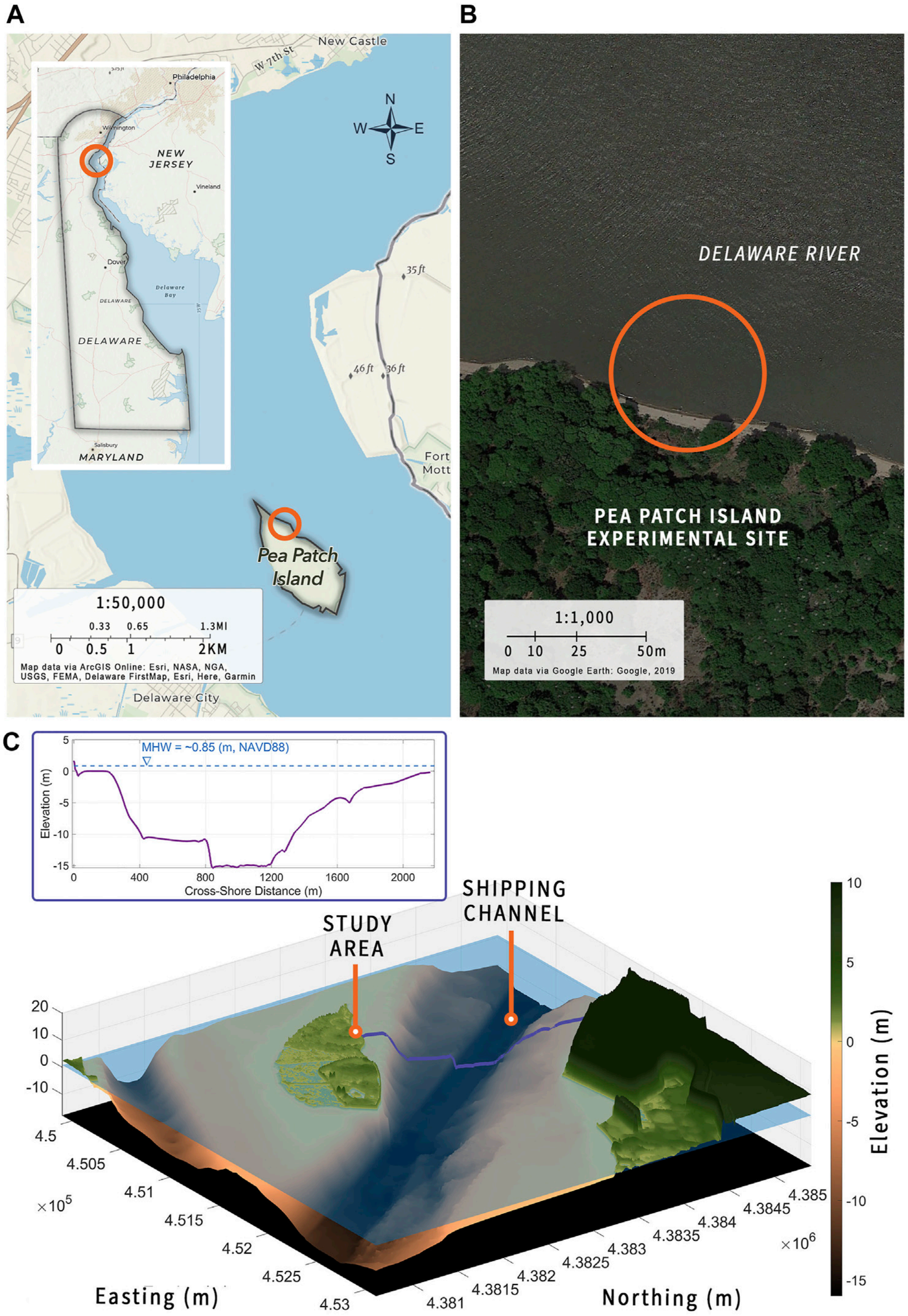

FIGURE 1
(A) Location of Pea Patch Island in the Delaware River. **(B)** Area of living shoreline and field instrumentation deployment. **(C)** Bathymetry in the shipping channel surrounding Pea Patch Island The subplot indicates the elevation of the cross-shore transect from the study site through the shipping channel.

protect the Fort. The protection creates a deficit in downdrift sediment transport upriver, and recent observations have shown erosional flanking at the lateral ends of the structure (Tait and Griggs, 1991; Schaefer, 2019). Moreover, an abrupt change in alongshore sediment transport causes beach erosion (Komar, 1998). The armoring around the Fort induces this type of abrupt

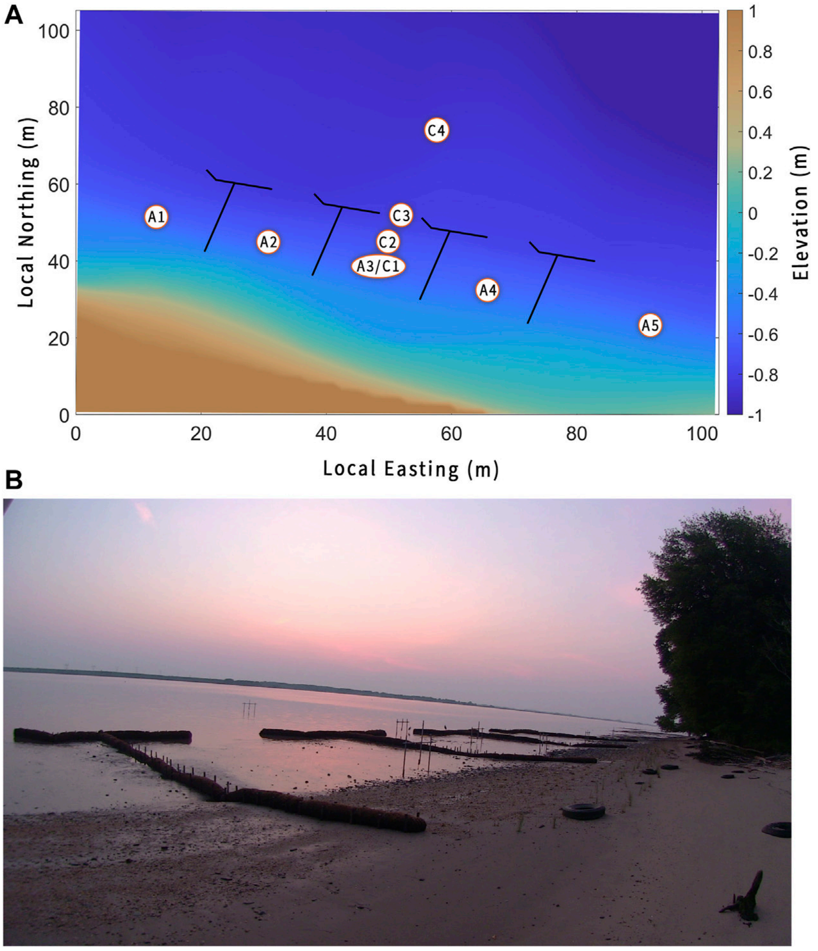

FIGURE 2
(A) Location of the study site in a local coordinate system with the layout of coir log THGs and locations of the deployed sensors. **(B)** Installed coir log THGs at Pea Patch Island. Photograph from Erdman Video Systems, Inc. livestream camera.

change in alongshore sediment transport and disrupts the island's natural ability to keep pace with sea level rise and increased shipping traffic.

2.2 Field study design and deployment

Two pilot field studies were conducted to test the feasibility of using coir logs and matting, wood or branch bundles, and oyster shells as natural materials within the context of the Pea Patch Island wave environment. In October 2020, a week-long pilot test consisting of staked single coir logs and staked modified coir logs with an oyster shell core were installed at the study site. These implements were tested at two different distances from the shoreline to determine qualitatively the depth dependence of a coir log breakwater as a shoreline protection strategy. Pilot testing revealed that the coir logs decreased wave height and wave energy impacting the shoreline (Baldauf, 2021). In November 2020, following these results, a T-head groin (THG) configuration consisting of coir logs with a wood bundle breakwater head was constructed using onsite driftwood. Recycled oyster shell bags were used to line the coir logs. The THG configuration was based on a similarly designed living shoreline in Vietnam composed of bamboo bundles (Albers and Schmitt, 2015). While the brush bundle breakwaters did not perform effectively in the environment at the pilot study site (excessive buoyancy and failure due to repeated rubbing of sisal twine), a THG configuration of coir logs was deemed appropriate for use under these conditions using field data and model simulations. Results of the pilot studies demonstrated dissipation capacity of natural materials, as well as the failure of these materials to stay in place, likely due to insufficient anchoring.

Feedback from pilot studies was incorporated into a final design (Figure 2A) receiving a statewide permit on 8 April 2021 and was installed on 17–18 June 2021. The constructed living shoreline segment (Figure 2B) consisted of four THGs spanning ~65 m of beach. The westernmost coir log of the head of each THG was set at an angle of 45° clockwise from the centerline of the head of the THG. This modification was made to address the visually observed obliquely incident wakes produced by northbound ships. Each groin consisted of two 0.4 m (16 in.) diameter coir logs, placed farthest onshore, and eight 0.5 m (20 in.) diameter high density coir logs. The coir logs at the heads of the THGs were wrapped in jute matting to further protect them from the high-energy ship wakes. All coir logs were anchored using 0.05 m (2 in.) × 0.05 m (2 in.) × 2.44 m (8 ft.) oak stakes driven by a gas-powered post driver and secured with sisal twine using one-way square knots.

A field experiment was conducted from July 2 to 12 August 2021 (Figure 2). A cross-shore transect was established through the center of the installation that spanned from 22.7 m offshore from the heads of the THGs to 6.1 m offshore, at the onshore ends of the THGs (in line with the offshore end of the most onshore coir log). Additionally, an alongshore transect was established from 9.4 m northwest of the installation, with stations halfway between each pair of THGs, extending 18.2 m southeast of the installation. A5 and C4 were located to approximate tidal and wave conditions unaffected by the structure, while A1 was located to approximate the effects of being sheltered by only one THG. Note that ship wakes rarely reach the foreshore/berm during low tides and this study focused primarily on the propagation of waves and dissipation of energy across the THGs. The draft of ships is restricted to less than 12 m during low tides causing larger and more heavily loaded ships to work around the tide or transfer cargo to lightering barges (Almaz and Altiok, 2012). Wind speed and direction data were obtained from National Oceanic and Atmospheric Administration’s (NOAA) National Ocean Service Physical Oceanographic Real Time System Program Station DELD1 Buoy at Delaware City, DE.

Eight stations were occupied and numbered C1–C4 in the cross-shore direction and A1–A5 in the alongshore direction (Figure 2A). C1 doubled as A3. Each station included a structure made from galvanized steel and aluminum pipes pounded into the sediment. Water depths were recorded with RBR Ltd. compact pressure transducers (RBRs). Two additional RBRs were placed above the high-water line to record atmospheric pressure. Fluid velocities at each station were recorded with JFE Advantech Co., Ltd. INFINITY-EM AEM-USB custom two-dimensional electromagnetic current meters (JFEs). RBRs and JFEs were deployed initially at 0.01 and 0.1 m above the bed, respectively. Battery life for the JFEs is approximately three days, resulting in the need for four deployments over the course of the study: July 2–4 July 2021, July 15–17 July 2021, July 20–22 July 2021, and July 29–31 July 2021. Battery life for the RBRs is approximately 30 days, resulting in the need for two deployments over the course of the study: July 2–19 July 2021 and July 20–12 August 2021.

The JFEs sampled continuously at a rate of 5 Hz. Velocity data were used to compare alongshore and cross-shore components and magnitudes among ship wakes and against background forcing. The RBRs sampled continuously at a rate of 2 Hz (A1, A5, C2, C3) or 16 Hz (A2, C1/A3, A4, C4). A Brinno TLC 200 PRO time lapse camera was deployed near the installation to record an image every 10 s. Additionally, a 1080p livestream camera with 3x zoom powered by solar panel from Erdman Video Systems, Inc., was placed on the northwestern end of the site to record an image every 1 min. The cameras captured ship passages, ship wakes, and tidal fluctuations and were used as a preliminary technique for identification of ship wake events.

Elevation surveys of the project area and a cross-shore transect through the center of the installation were collected in May (pre-deployment) and September (post-deployment) 2021 using a Leica Global Navigation Satellite System (GNSS) real-time kinetic global positioning system (RTK GPS), referenced to UTM zone 18 and NAVD88. Measurements were taken at intervals of ~5 m in the alongshore direction and ~1 m in the cross-shore direction. Vertical error in the elevation data is estimated as 0.05 m due to GPS system accuracy and the silty substrate.

2.3 Data processing

2.3.1 Depth and energy flux data

Pressure data were adjusted for atmospheric pressure and then water depth was estimated as:

$$d = \frac{P}{\rho g} \tag{1}$$

where d is local depth in meters, p is the measured pressure in Pascals, g is the gravitational acceleration constant (9.81 m/s^2), and ρ is an average water density for the Delaware River Estuary in kg/m^3 calculated using the International one atmosphere equation of state of seawater (Millero and Poisson, 1981). Salinities in the Delaware River Estuary range from 0.5–19 ppt (PDE, 2012) and the average temperature obtained from the offshore electromagnetic current meter (C4) was ~24°C. A range of densities was established (994.2–1,013.1 kg/m^3) and a typical density for brackish water of 1,013 kg/m^3 was selected. Using the lower bound of the density range increased the depth by 0.01 m, within the error range of the RBRs. Measurements were taken in shallow water, where dispersion is minimal, so Eq. (1) is a reasonable estimate for both long and short waves.

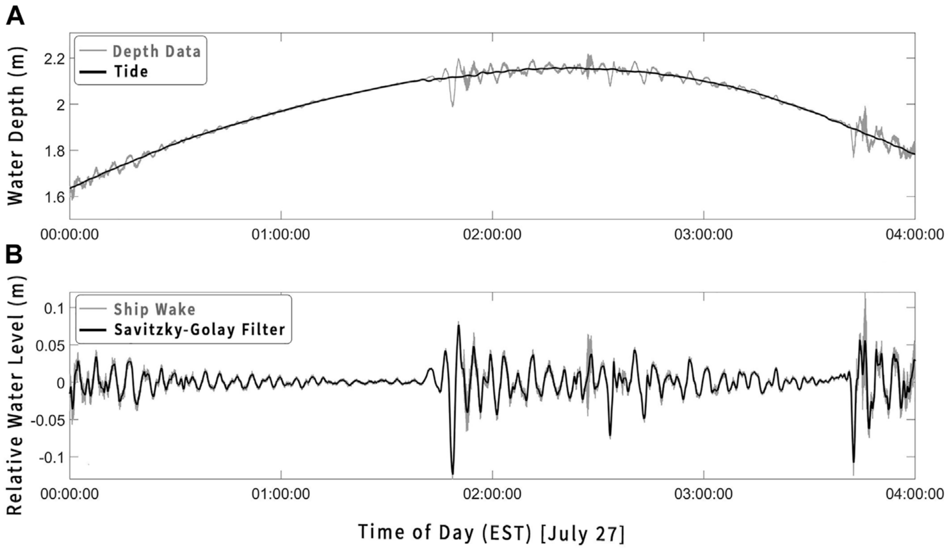

FIGURE 3
(A) Raw depth overlaid with computed tidal signal. **(B)** Depth data after tidal removal overlaid with Savitzky-Golay filtered data.

The tide signal was estimated from a time series of depth measurements using a running average filter with a 15-min window (Figure 3A). The demeaned tidal trend from C4 was used to identify the local water depth for each wake event. The high- and low-frequency signals generated by the ships were isolated by applying a Savitzky-Golay finite impulse response (FIR) convolution filter of polynomial order 10 and a frame length of 100 s to the residual time series (Figure 3B). The Savitzky-Golay filtered data were subtracted from the tide-removed data to separate the high-frequency signal from the low-frequency signal.

Approximate start times for each wake event were identified using time lapse video. The peak water elevation preceding the initial drawdown and a 20-min window of the subsequent data was retained. Data were catalogued chronologically by when the ship travelled past the island for subsequent identification. A 20-min window was chosen by inspection such that only small amplitude seiching on the order of background conditions remained visible in the signal.

Individual wave heights and periods in ship wakes were estimated differently for the low and high-frequency signals, due to the elevated water level in the low-frequency wake. Small amplitude (< 0.02 m) oscillations were neglected based on observations of typical wind wave amplitudes at the site. High-frequency waves (on the order of background conditions, with a typical period of < 5 s) were identified using the zero down-crossing method. Low-frequency waves (typical period of > 100 s) were identified by retaining successive local extrema with differences in water level greater than 0.02 m. Wave periods were taken as the time difference between successive troughs.

Wave energy density per unit surface area (Joules per square meter) can be estimated using small-amplitude linear wave theory as (Kamphuis, 2010):

$$E = \frac{1}{8}\rho g H^2 \tag{2}$$

where E is the energy density and H is the wave height. Wave power, or wave energy flux, per unit crest length (Watts per meter) can be estimated roughly as the energy density per unit surface area multiplied by the group velocity C_g (Kamphuis, 2010):

$$F = EC_g = \frac{1}{2}EC\left(1 + \frac{2kd}{\sinh(2kd)}\right) \tag{3}$$

where F is the wave energy flux, C is the wave celerity (estimated as the wavelength divided by the wave period), and k is the wave number. The wavenumber and wavelength were determined using the Newton-Raphson method to solve the dispersion relationship where the inputs were local water depth and the period identified in the filtered signal. Estimates of wave energy density and wave power using linear wave theory have been used previously to quantify the erosive potential of ship wakes (Gharbi et al., 2008). Percent decrease of energy fluxes between stations was calculated to estimate the relative efficiency of the installation.

2.3.2 Velocity data

Velocity data were removed from the record when the water depth was below 0.35 m, where a conservative 0.35 m rather than 0.1 m cut-off was used to account for the size of the measurement portion of the sensor, sensor hysteresis upon intermittent submergence under wave activity, and the potential for GPS error due to unconsolidated silty-mud (where sensor elevation was determined using bed level elevation from RTK GPS). Acceleration magnitudes were calculated using a forward difference and a 98th percentile cut-off was established. Velocities were removed from the record when acceleration magnitude was greater than this cut-off or the velocity magnitude was greater than 0.5 m/s, which was the upper bound of the remaining ship wake velocities. For each wake, positive (offshore or southerly-directed) and negative (onshore or northerly-directed) velocities were separated and a 98th percentile velocity (peak) and mean velocity were calculated for each in the cross-shore and alongshore direction. The same percentile calculations were performed for background conditions after removing ship wake velocities.

2.4 FUNWAVE-TVD

FUNWAVE-TVD, a nonlinear Boussinesq wave model, was used to simulate wake conditions. This model contains a ship wake module added to the existing Boussinesq formulation, modelling vessels as a moving pressure source (Shi et al., 2018). The model was validated (Shi et al., 2018) using laboratory data (Gourlay, 2001) examining supercritical wake in various flow regimes including slow-moving, large container ships (Forlini et al., 2021). The model was first used to inform installation design by simulating conditions with and without the THGs, comparing maximum velocities and water surface elevations (Williams, Forthcoming 2022). Model bathymetry was collected in 2012 and altered with subsequent data collected in 2018, 2020, and 2021. The data include low tide surveys using GPS and channel bathymetry from the United States Army Corps of Engineers (USACE). The domain spans ~4,812 m in northing and ~3,207 m in easting with grid spacing of 1.3 m (easting) by 1.7 m (northing). Coir logs were added to the bathymetry by raising the bed 0.4 and 0.5 m at the locations where the respective sized coir logs were located. Simulations showed a reduction of maximum velocity and maximum water level onshore of the THGs.

2.4.1 Automatic Identification System data

A log of all large commercial ships that navigated the Delaware River from July 9 to August 12 was provided by the Maritime Exchange for the Delaware River and Bay. The log was generated using the United States Coast Guard's Automatic Identification System (AIS) containing records of ship specifications and time stamps when entering a waterway or port. Each ship will have at least three recordings per visit to the waterway, one upon entry, one for arrival at the port of destination, and one upon exiting the waterway. Often ships will have more than three recordings, accounting for anchorage stops and lightering locations.

Analysis of the timelapse footage revealed 680 ships passing the area (341 northbound and 339 southbound) during the study period, at a rate of ~16 ship passages per day. AIS data were filtered to retain nonstationary commercial vessels by neglecting vessels with a speed of 0 m/s, a draft less than 5 m, or a length less than 100 m. The timelapse footage results and AIS data were compared to match vessel data to individual wake events. Events during which the wake signal would be significantly altered, such as a second vessel passing within the 20-min analysis window, were neglected for the subsequent analysis, leaving 147 wake events.

AIS data including vessel length, width (or beam), draft, and course were then used to force individual ship passages in the model. However, AIS data report maximum vessel drafts. So, the drafts were adjusted to optimize model performance. Simulations lasted for 20 min of field time, a typical time from the start of a wake event to the return to background conditions.

2.4.2 Model validation

The model was validated using measured water levels. Key factors in model validation are the magnitude of maximum drawdown and subsequent surge (commonly referred to as the transverse stern wave) and the amplitude of the Kelvin wake. The phasing of the field data was not well modeled using the AIS course data. This mismatch is likely due to incongruencies between the modeled and actual bathymetry. Thus, for validation purposes, the phasing of the events was matched using the point of maximum drawdown as a reference point.

Model tests were performed separately for a chosen northbound and southbound ship wake event, due to the differences in their wake profiles. As previously mentioned the ship draft was adjusted to optimize model performance (Williams, Forthcoming 2022). The model accurately predicted the magnitude of peak drawdown within 4.0%, magnitude of peak subsequent surge within 3.6%, and the amplitude of the seiche within 1.4% for a northbound ship wake (Figure 4). The phasing between drawdown and surge was incorrect by 43 s. However, the south bound wake simulations were less successful (not shown). Drawdown and surge were predicted within 14.9% and 16.9%, respectively, but the southbound ship wake signal contains a higher frequency, high amplitude (~0.18 m) component, representing some of the largest waves observed, that the model does not predict. This component may be due to model inability to account for a tidal current and inconsistencies between the modeled and real bathymetry. For example, sand shoals to the north of the island, not well-represented in the model bathymetry, could alter wave patterns. The unmodeled high-frequency component also

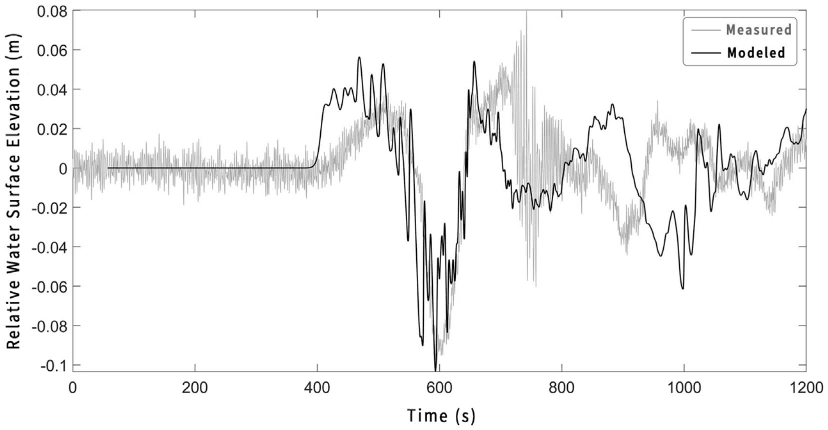

FIGURE 4
Comparison of measured and modeled surface displacements during wake event generated by northbound vessel JS Ineos Intuition.

exists in the northbound case (Figure 4), but with a smaller amplitude relative to the low-frequency drawdown and surge. De Roo and Troch (2015) note that for commercial shipping vessels, the drawdown and surge, rather than the higher frequency Kelvin wake, tend to contain the majority of the wave energy within a ship wake event. The inability to reproduce the high-frequency component is less detrimental to the northbound validation and further numerical analysis was performed only for a northbound ship wake event. The model was subsequently used to test the efficacy of the installation, as well as the effect of water level on the installation performance.

3 Results

3.1 Field conditions

The meteorological conditions during the study period were mild with a maximum wind speed of 11 m/s from the E and an average wind speed of 2.3 ± 1.4 m/s, predominantly from the SW (Figure 5A). The beach was sheltered from most of the wind influence from the SW. Conversely, the strongest wind influences from the E and NE directly impacting the beach had the longest fetch, despite being infrequent and duration limited. Typical background significant wave heights and periods at the site, taken as the significant wave height and period during all periods of no ship activity, range from not detectable to 0.06 m and 1.5 s (C4), respectively.

The beach profile in Figure 5B cross-shore bathymetric transect through the center of the installation, exhibits a slope of ~1:8 shoreward of the toe of the foreshore and a gradual slope of ~1:100 from the toe of the foreshore towards the channel. The profile shows a change in slope at an elevation of −0.51 m (NAVD88). At this location, ~12 m in the local cross-shore coordinate system (Figure 5B), there is also a change in the observed typical grain size from sandy to gravel/cobble to silty-mud. The cross-shore location of the slope break remained approximately the same over the study duration. The tidal range is ~1.7 m for this micro-tidal beach. The average high tide was 1.4 m above the toe of the foreshore (Figures 5B,C), indicating that wave breaking occurs mostly offshore of the installation. The average low tide was 0.3 m below the toe of the foreshore.

Elevation data were interpolated to a uniform grid (Figure 6) using smoothing scales of 5 m (Plant et al., 2002). Changes in elevation over the short timescale of the study were difficult to quantify from the individual surveys (Figures 6A,B). The elevation difference between the May and September surveys (Figure 6C) shows only small magnitude changes. In general, there was erosion directly behind the heads of the THGs (< 0.1 m ± 0.05 m) and accretion of similar magnitude farther onshore. In addition, there was more area of erosion between the two eastern THGs that gradually transitioned, moving west, to more area of accretion between the western THGs. Directly onshore of the three eastern THGs, there was accretion up to ~0.2 ± 0.05 m. There was erosion of a similar magnitude onshore of the western T, which can likely be attributed to the loss of the farthest shoreward coir log in an early September storm (see Section 4).

3.2 Wave characteristics

Data revealed that ships with deep drafts traveling in this confined waterway produce a fairly consistent wave signal

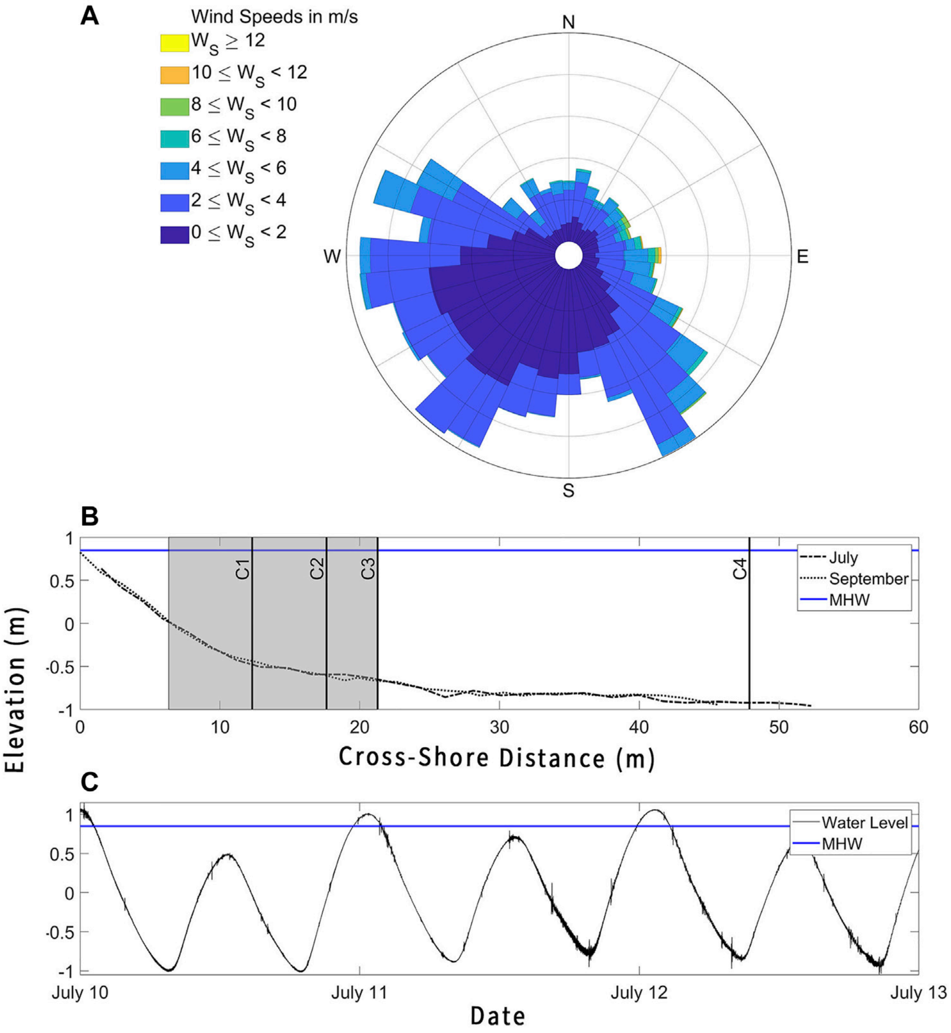

FIGURE 5
(A) Wind rose using data collected 10 times hourly from NOAA buoy DELD1 from 2 July 2021 to 12 August 2021. **(B)** Cross-shore bathymetric transect through the middle of the installation. July (September) denoted by dashed (dotted) black line. Installation delimited by shaded area. Stations denoted by solid lines and labelled. **(C)** Sample water level (NAVD88) data denoted by black line. Mean high water line denoted by blue line in **(B)** and **(C)**.

compared to the wakes generated by other vessels and natural wave conditions (Figure 7). Initially, a slight increase in water level travels along with the passing of the ship. The initial pulse is immediately followed by a substantial drawdown in water level resulting in a surging runup minutes after the ship has passed. The typical period of this drawdown and surge is approximately three to four minutes making it a low-frequency oscillation compared to other ship-induced wakes and wind waves. The low-frequency oscillations are followed by a high-frequency diverging and transverse wave train (Kelvin wake), the amplitude of which is related to ship geometry and speed. The drawdown and surge is followed by low-frequency seiching of smaller magnitude in addition to high-frequency wake. The period of harmonic mode one of the seiche as estimated by Merian's formula (Proudman, 1963) is 200 s–400 s. The seiche gradually decays in wave height due to the frictional forces acting upon the waves (Kamphuis, 2010). The combined drawdown and surge wave can reach heights greater than 0.3 m with seiche wave heights typically less than 0.1 m (Figures 7E,F). High-frequency waves (typical period < 5 s; Figure 7D) can reach heights greater than 0.4 m superimposed on the low-frequency wave heights. Previous studies indicate the wake amplitude is related to ship size and speed (Ng and Byres, 2011; Scarpa et al., 2019). However, observations at Pea Patch Island did not follow a discernable pattern when classified by length (Figure 7E) or average speed

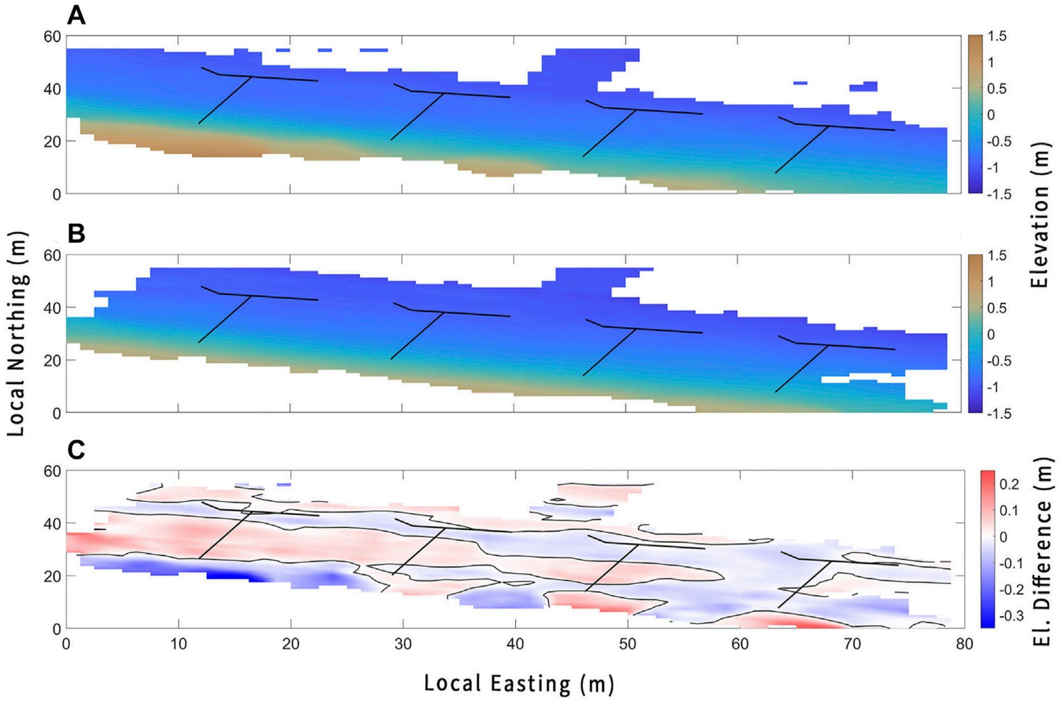

FIGURE 6
Elevation surveys taken in **(A)** May and **(B)** September and **(C)** the difference between the two surveys in **(A)** and **(B)**. THGs are delimited by black lines. In **(C)** the zero-contour line is shown in black.

(Figure 7F). Observed ship wake variation may result from tidal level, distance from sailing line to shore, or ship draft.

A notable difference was observed during northbound and southbound ship wake events. For northbound ship wakes, the orientation of the shoreline with respect to the orientation of the shipping channel creates a strong alongshore component of the wave train. The heads of the THGs were modified to impede the propagation of this alongshore wave train, as noted in Section 2.2. The distinct alongshore component of a northbound ship wake was not present in southbound wake events. As such, northbound and southbound ship wakes events were analyzed separately to examine whether the alongshore component had an effect on the efficiency of the installation.

Velocity data were collected for 52 ship wake events when the JFEs were active (see Section 2.3). Magnitudes of peak offshore ship wake velocities in the cross-shore direction reached ~0.5 m/s and magnitudes of time-averaged (over the 20-min window) offshore cross-shore ship wake velocities reached ~0.2 m/s. In the alongshore direction, magnitudes of peak ship wake velocities reached ~0.4 m/s, and magnitudes of time-averaged (over the 20-min window) alongshore ship wake velocities reached ~0.2 m/s. Ranges of peak northbound and southbound ship wake cross-shore and alongshore velocities are shown as gray lines in Figures 8A–D. Peak velocities of all ship wake events were averaged to obtain the peak velocities of a typical ship passing the site (delineated by circles in Figure 8) and 98% confidence interval (black lines in Figure 8), where solid markers/lines represent positive (offshore or north-directed) velocities and dotted lines/open markers represent negative (onshore or south-directed) velocities. Cross-shore velocities decayed as the waves propagated through the installation from the offshore (C4) to onshore (C1) station (Figures 8A,C). Over the range of ship wake events, the trend of cross-shore velocity decay through the installation is more obvious for northbound ship wake events. However, for southbound ship wake events, the decrease in cross-shore velocity between the offshore station (C4) and the start of the installation (C3) indicates an installation-induced cross-shore velocity decay. For the typical northbound ship wake event, the peak cross-shore velocity decreased from ~0.08 ± 0.03 m/s (98% confidence interval) at C4 to ~0.05 ± 0.02 m/s (98% confidence interval) at C1. For the typical southbound ship wake event, the peak cross-shore velocity decreased from ~0.08 ± 0.03 m/s (98% confidence interval) at C4 to ~0.07 ± 0.01 m/s (98% confidence interval) at C1. Regardless of ship wake presence or direction, the net alongshore current is northerly directed (Figures 8B,D). The presence of a north-directed alongshore velocity for a southbound ship or a south-

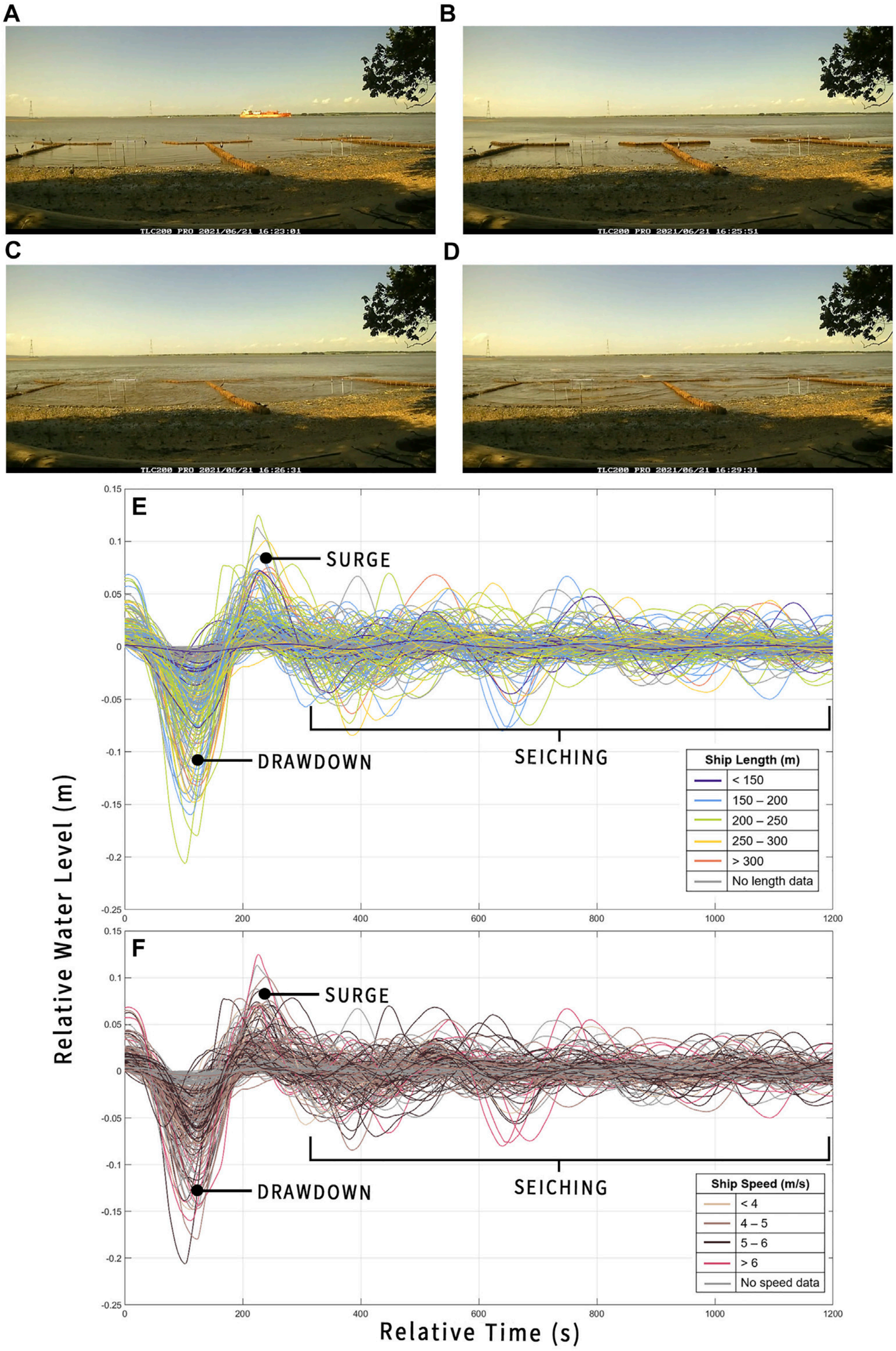

FIGURE 7
Snapshots of signature ship wake event structure: **(A)** elevated water level with ship path, **(B)** drawdown, **(C)** surge, and **(D)** high-frequency wave train. The low-frequency water level follows the graph of each event in **(E)** and **(F)** with notable features called out. Events are organized by ship length in **(E)** and average ship speed in **(F)**.

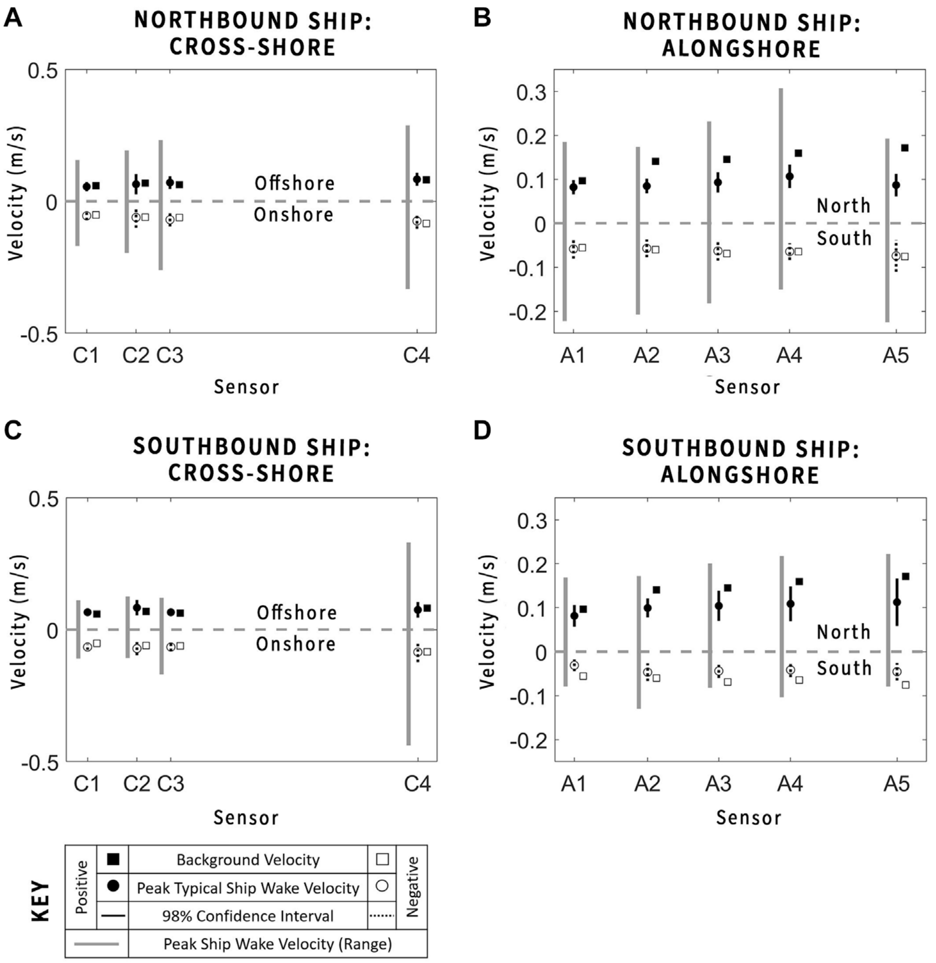

FIGURE 8
Peak (98th percentile) velocities in the cross-shore **(A,C)** and alongshore **(B,D)** directions for northbound **(A,B)** and southbound **(C,D)** ship wake events. Solid black lines/markers denote positive (offshore or north-directed) velocities and dotted lines/open markers denote negative (onshore or south-directed) velocities. Gray lines denote the ranges for ship wakes, black lines denote 98th percent confidence interval, circles are the ensemble-average for ship wakes, and squares are background conditions.

bound alongshore velocity for a northbound ship may be attributed to a dominant tidal current which exceeded the ship wake-induced alongshore current (Figure 8).

Velocity data were removed from the record for the 20-min period following all wake events (including those not analyzed) and the remaining data were taken as background conditions (represented by squares in Figure 8), which includes wind wave-induced velocities as well as tidal current velocities. Background conditions, unaffected by ship wake, are the same for the northbound and southbound ship wake event plots. Peak background velocities in the cross-shore (0.05–0.08 m/s) and alongshore (0.06–0.17 m/s) directions were, on average, ~74% and ~54% smaller, respectively, than the largest peak ship wake velocities (0.08–0.4 m/s; Figure 8). Peak background velocities are within ~10% of *typical* peak ship wake velocities (0.04–0.08 m/s; Figure 8). However, peak north-directed background velocities are ~51% greater than average peak north-directed ship wake velocities (0.08–0.1 m/s), indicating net flow in a northerly direction regardless of ship wake events at the site (Figures 8B,D).

3.3 Wave energy flux

Linear wave theory can be used to provide a rough estimate of energy dissipation through the installation. Changes in wave height, as opposed to other variables, are

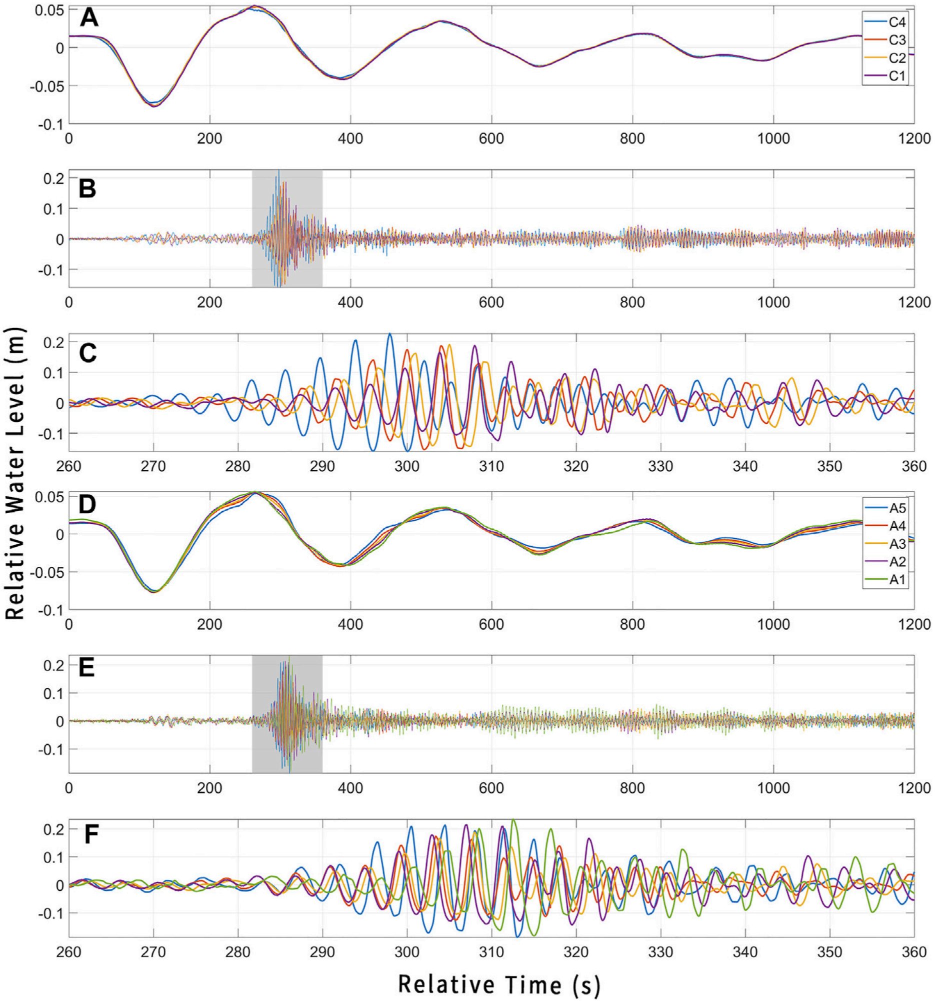

FIGURE 9
Propagation of a sample southbound wake event through the installation, where **(A–C)** show the cross-shore sensor array and **(D–F)** show the alongshore sensor array. **(A)** and **(D)** are the low-frequency signal; **(B)** and **(E)** are the high-frequency signal; and **(C)** and **(F)** are the high-frequency signal contained in the shaded area in **(B)** and **(E)**, respectively.

addressed first because the energy flux is a function of the wave height squared.

Water levels for sample southbound and northbound events are displayed in Figures 9, 10, respectively, where subplots A-C show the cross-shore component and subplots D-F show the alongshore component of the wake. In Figures 9, 10, subplots A and D show the low frequency (typical periods > 100 s) while subplots B and E show the high-frequency signal (typical period < 5 s) over the 20-min event duration. Subplots C and F show the same high-frequency signal over the time duration shaded in subplots B and E. Cross-shore sensors are denoted as C1–C4, onshore to offshore, and alongshore sensors are denoted as A1–A5, left to right (North to South), where C1 and A3 are the same station. Northbound wakes first reach C4 and A5, and southbound wakes first reach C4, lacking a significant alongshore wave component. It should be noted that the sample southbound event, which occurred on August 11, beginning at 13:09:43, represents some of the largest waves at the site over the course of the study, while the sample northbound event, which occurred on July 25, beginning at 9:22:17, had relatively small waves for a typical event at the site.

The installation tended to have a minimal impact on the low-frequency waves of the ship wake event (Figures 9A, 10A), but reduction of wave height is more significant for the high-frequency waves (Figures 9C, 10C) in the cross-shore direction. However, in the case of a northbound ship wake

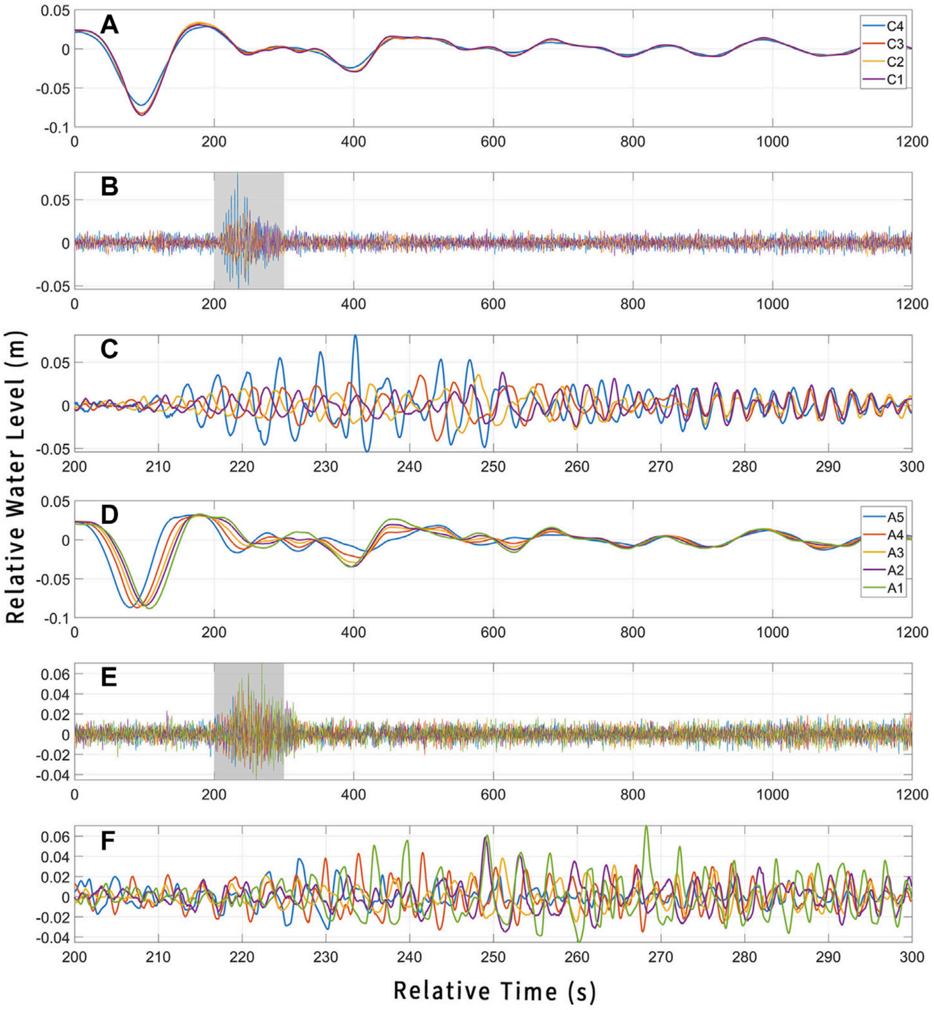

FIGURE 10
Propagation of a sample northbound wake event through the installation, where **(A–C)** show the cross-shore sensor array and **(D–F)** show the alongshore sensor array. **(A)** and **(D)** are the low frequency signal; **(B)** and **(E)** are the high-frequency signal; and **(C)** and **(F)** are the high-frequency signal contained in the shaded area in **(B)** and **(E)**, respectively.

event, the orientation of the shoreline with respect to the orientation of the shipping channel creates a strong alongshore component of the wave train. As expected, in the case of a northbound ship wake event, there was a time delay between arrival of the wake event at successive sensors (Figure 10D) due to the propagation of the alongshore waves through the installation. The time delay was not observed in the case of a southbound ship wake event (Figure 9D) due to the lack of a strong alongshore wave component. For a southbound ship wake event, the waves were approximately shore-normal, so the wave train reached the alongshore sensor array at approximately the same time. As in the case of the cross-shore signals, there was little effect of the installation on the wave height of the low-frequency alongshore portion of the wake event (Figures 9D, 10D). In contrast to the cross-shore signals, there is no discernable positive or negative effect of the installation on the high-frequency signal in the alongshore direction (Figures 9F, 10F).

The total ship wake energy flux for an event was calculated as a summation of energy fluxes for individual waves in the low- and high-frequency signals. Ship wake data were removed from the signal, and flux calculations were performed over the remainder of the signal to obtain background energy conditions. The collected ship wake energy fluxes were averaged per day and compared to the daily averaged background energy experienced across the cross-shore transect. The study area is impacted by 11,000–25,000 N/m of wave power per day, 2,700–12,000 N/

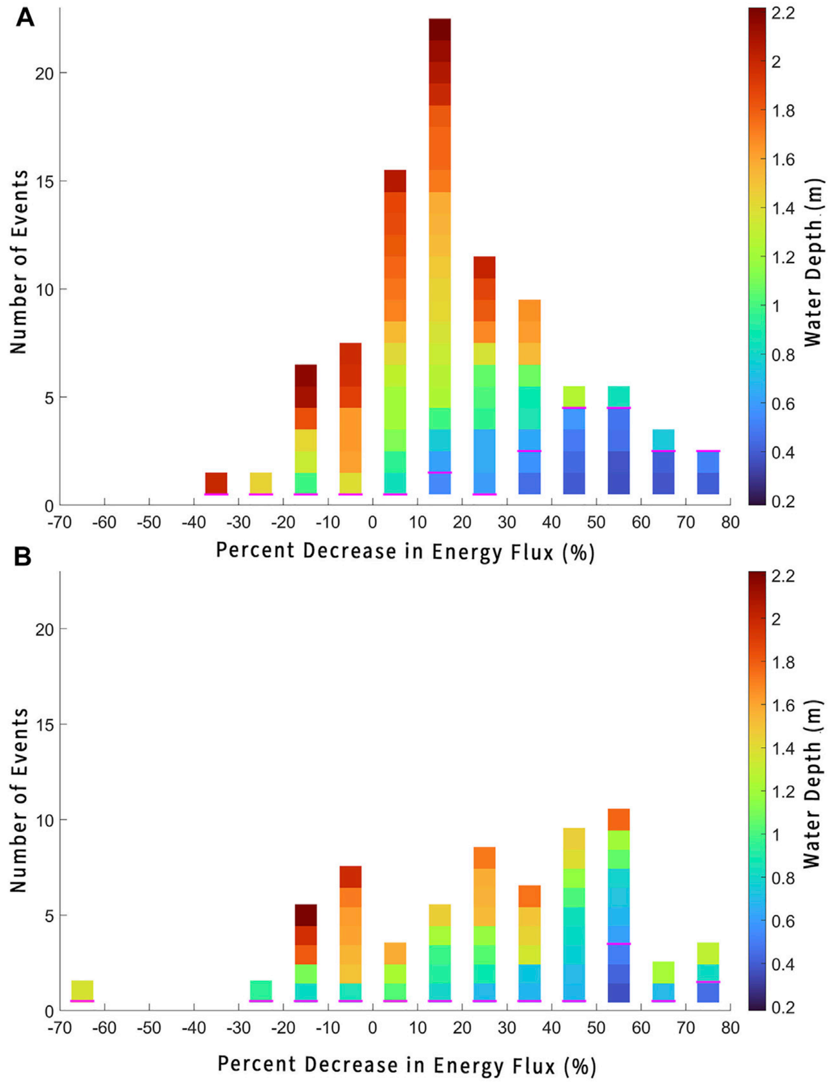

FIGURE 11
Histograms of percent decrease in energy flux from C4 to C1 for **(A)** southbound and **(B)** northbound ship wake events. Color represents water depth at sensor C4 for the event. Events above the magenta line take place with the heads of the THGs submerged.

m of which is ship wake-generated (depending on station and tidal level). Notably, ship wake events account for 25–50% of the energy flux impacting the area each day, but only account for roughly 22% of the duration of each day (~320 min). It is important to note that the overall energy flux imposed on the onshore regions of the beach was noticeably smaller than the offshore stations due to tidal influences resulting in varying water depth. The reduced exposure to natural hydrodynamic forces subsequently reduces the risk of ship-induced impacts.

Northbound and southbound ship wake events were analyzed separately to determine percent decrease in energy flux between C4 (offshore) and C1 (onshore). Decreases in energy flux were analyzed for trends over portions of the tidal cycle, and average ship speed, ship length, and water depth (Everett, Forthcoming 2022). Trends in the decrease in energy flux were most compelling in relation to water depth (Figure 11). The larger decreases in energy flux are represented by blue colors corresponding to shallower water depths. Similarly, in general, smaller decreases in energy flux (and amplifications of energy flux, see Section 4) are represented by red colors, corresponding to greater water depths. While the trend is more evident for southbound ship wake events, it is similar regardless of direction of ship travel. Events above the magenta line for each bin occurred when the heads of the THGs were submerged. Nineteen events (15 southbound and 4 northbound) occurred at shallower depths and had greater than a 10% decrease in

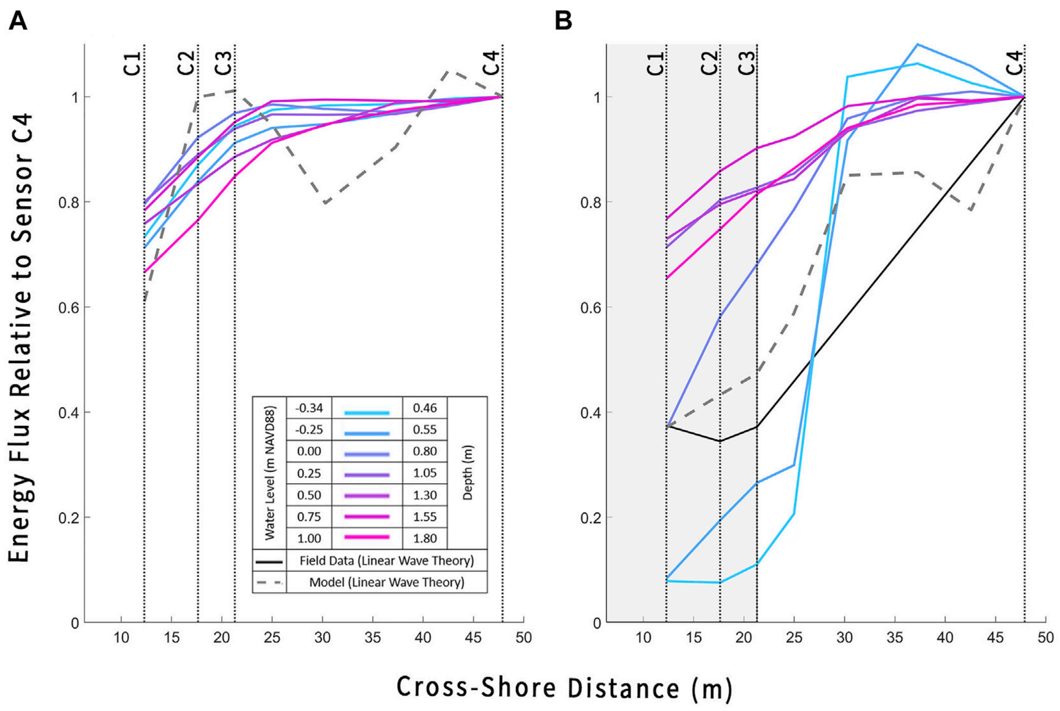

FIGURE 12
Modeled total energy flux normalized relative to C4 for simulations **(A)** with installation and **(B)** without installation. Dotted vertical lines denote labeled field sensor locations. Shaded area delineates the installation area.

energy flux and an average decrease in energy flux of ~50% (Figure 11).

Out of 87 southbound ship wake events, roughly a quarter had a decrease in energy flux between 10% and 20%. The distribution of percent decrease in energy flux is roughly Gaussian around this mean (Figure 11A). Nearly 11% of these events had greater than a 50% decrease in energy flux. The 60 northbound events do not have a similar distribution (Figure 11B). The largest bin of events (10) had a decrease of energy flux between 50% and 60%, larger than for the southbound events. However, these events represent only ~17% of the northbound wakes. Nearly a quarter of the northbound wakes had greater than a 50% decrease in energy flux.

3.4 Model Results

Energy dissipation has previously been shown to have a depth dependence for living shorelines designed to dissipate wave energy (Ellis et al., 2002; Chowdhury et al., 2019; Safak et al., 2020a). As such, FUNWAVE-TVD was used to simulate energy fluxes during wake conditions for water levels from −0.25 m to +1.0 m (NAVD88) at 0.25 m intervals, and the previously tested water level of −0.34 m. At water levels of approximately −0.4 m, the heads of the THGs are just submerged. JS INEOS INTUITION, a large oil tanker travelling northbound at ~7 m/s was used for the simulation. The length, width, and draft of the simulated vessel are 180, 26, and 6 m, respectively, where the draft was estimated through parameter studies (Williams, Forthcoming 2022).

Model simulations were performed first to estimate energy flux without the installation present. Depth-integrated energy flux, normalized to that at C4, was defined using the general definitions of kinetic and potential energy. Regardless of water level, the energy flux calculated at C1 was 60%–80% of the energy flux calculated at C4 (Figure 12A). An additional estimate was made for a water level of −0.34 m using linear wave theory with moderate comparison (10%–20% difference) to estimates based on kinetic and potential energy. Simulations with the THGs present (Figure 12B) show variation depending on water level. Linear wave theory estimates from the model (gray dashed line) and field data (solid black line) show similar trends but differences in the cross-shore decrease in energy flux. At C1, the energy flux decreases to ~40% of the energy flux at C4 and the linear wave theory estimates of energy flux are in good agreement. Modeled energy flux at C1 decreased to ~10% of the flux at C4 for −0.34 m and −0.25 m water levels (Figure 12B). At a water level of 0.0 m, the energy flux at C1 was ~40% of the energy flux at C4, similar to the linear wave theory estimates at a water level of −0.34 m (Figure 12B). Reduction in energy flux to this extent did not occur for higher water level simulations, suggesting that the installation effectiveness decreases sharply between water levels of 0.0 and 0.25 m. For the highest water levels (0.75 and 1.0 m), indicative of high tides and storm surge, simulations with and without the THGs yielded similar results, indicating little to no installation-induced energy dissipation when the installation is submerged in a depth greater than 1.5 m. While estimates of energy flux using linear wave theory indicated that the installation is less effective when submerged, model results indicate that the installation may still be effective when submerged up to approximately twice its height. The simulations indicate that the installation could perform optimally for the lower 50% of the tidal range (up to 0.0 m NAVD88).

4 Discussion

Decreases in energy flux across the installation indicate a depth dependence in agreement with studies on oyster reefs (Taube, 2010; Chowdhury et al., 2019; Wiberg et al., 2019; Safak et al., 2020a), brush bundle breakwaters, (Ellis et al., 2002), coastal fringe marshes (Knutson et al., 1982), and laboratory studies (van der Meer et al., 2005) and numerical simulations (Ting et al., 2004) on porous breakwaters. Morris et al. (2018) note that there is likely an optimal depth for living shorelines, and at greater depths, there is a decoupling of the interaction between surface waves and the habitat or structure. Over the lower 25% of the tidal range (up to −0.4 m elevation), the full impact of the THG was expected to be realized and was supported by field observations. During the surge and successive waves, water would impinge the heads of the THGs, often filtering through the gaps between THGs and eventually overtopping the heads of the THGs. A clear diffraction pattern was visible when water moved through the gaps, indicating a potential for additional energy dissipation. The natural trenching extending onshore from the gaps between the heads of the THGs noted in similar living shorelines (Dinh et al., 2013) was absent at the Pea Patch Island study site. However, the sediment accumulation between comparable emergent THGs (Dinh et al., 2013) is similar to that behind the heads of the three western THGs on the Pea Patch Island site (Figure 6C). The accretion observed at the three western THGs was approximately twice the expected error in elevation measurements, indicating that the actual change in elevation may have been between 0.05 and 0.15 m.

Kraus et al. (1994) recommend that groins not be used in environments where overpassing may occur at high tides. When overpassing occurred at the present study site, the installation may behave akin to a submerged breakwater where wave attenuation of the structure deceases with increased depth of the crest of the structure (Dean et al., 1994). When the installation was submerged approximately twice its height (over ~50% of the tidal range), little to no effect on the energy flux was identified (Figure 12B), similar to oyster reefs (Wiberg et al., 2019) and segmented breakwaters (Dean et al., 1994). In fact, the greatest energy flux reduction occurred when the THGs were submerged between 50%–138% of their height, in agreement with the optimal water level range of ± 0.25 m of the crest of the structure reported by Wiberg et al. (2019). In addition, breakwaters submerged in depths 100%–125% of their height tend to display a specific circulation pattern dominated by a pumping mechanism rather than background alongshore currents (Dean et al., 1994). Water becomes trapped onshore of the structure and cannot form a typical undertow current. Rather, water travels as alongshore currents diverging from the center of the structure along the onshore side until it reaches a gap in the structure and forms a roughly shore normal offshore flowing current (Dean et al., 1994). The alongshore current generated by the pumping mechanism can be up to five times as strong as the undertow current in a control condition (Dean et al., 1994), which can cause increased sediment motion and potential erosion onshore of the structure. This circulation pattern, observed during lower tide levels and wakes from southbound ships, is a likely explanation for the small-scale erosion evident onshore of the heads of the THGs (Figure 6C).

The structure-induced flow alteration can lead to enhanced sediment motion. Critical bottom shear stresses, $\tau_{b,cr}$, for fine-grained sediment on a similar tidal flat ranged from 0.10 to 2.0 N/m^2 (Lanuru, 2008). Bottom shear stress can be estimated through the quadratic drag law as

$$\tau_b = \frac{1}{2}\rho f u^2 \tag{4}$$

where u is the magnitude of the instantaneous velocity and f is a friction factor. Friction factors depend on Reynolds number and grain characteristics and can vary widely. A friction factor of 0.05 is used here (Lacy and MacVean, 2016). Inverting Eq. (4) provides a range of critical velocities u_{cr} for motion of fine-grained sediment as

$$u_{cr} = \sqrt{\frac{2\tau_{b,cr}}{\rho f}} = 0.06 - 0.3\text{m/s} \tag{5}$$

Near bed velocities were not collected behind the heads of the THGs. However, near bed velocities at C3, between the heads of the THGs, indicate, based on this simple analysis, that critical velocities for sediment motion are exceeded under ship wake conditions over 50% of the time. These simple estimates are supported by visual observation of turbid water during ship wake events near the heads of the THGs during low tides.

In the case of obliquely incident waves, the interaction of the alongshore current with pumping-induced return flow can lead to accretion on the downdrift end of the structure (Ranasinghe and Turner, 2006). Northbound wakes, due to the orientation of the channel and shoreline, produced obliquely incident waves at the study site. The increased accretion on the downdrift (western) end of the installation as compared to the updrift (eastern) end indicates the dominance of northbound ship wake activity in combination with a net north-directed flow (flood dominance) at the site. Notably, higher overall energy dissipation occurred for northbound ship wake events. The greater effect by the structure on the northbound ship wakes is further supported by the decay of the alongshore current down-drift of the eastern THG. Further understanding of the circulation patterns within the installation would require additional investigation and more spatially resolved velocity data.

Interestingly, in both directions of ship wake propagation, there are outliers with an *increase* in energy flux (Figure 11). All increases in energy flux occurred when the installation was fully submerged, which may indicate wave reflection and constructive convergence due to limited offshore wave breaking in deeper water. Amplification of energy flux may be attributed to sensor noise and the assumption of linear wave theory for events with an increase of energy flux up to 10%. For the remaining 15 events, many of which occurred at night, timelapse footage was analyzed, but no discernable disturbance or anomaly was detected. It may be suggested that, for the northbound ship wake events, the shore normal wave train may converge with the alongshore wave train from the south, leading to wave amplification. For southbound ship wake events, there may be some impact of the sand shoals north of the site. Limitations imposed by the experimental layout prevent further investigation.

Further analysis of the effect of the installation on the erosional trend of the northeastern beach on Pea Patch Island would require long-term monitoring of the project. One way to predict potential performance of this living shoreline is to examine the performance over approximately two years of a similarly shaped living shoreline (Albers and Schmitt, 2015). Those structures were able to reduce wave heights up to 80% and performed most effectively when not submerged (Albers and Schmitt, 2015). Additionally, structure-induced sedimentation with similar sediment characteristics as the Pea Patch Island tidal flat allowed floodplain and mangrove forest recovery (Albers and Schmitt, 2015). Notably, the Albers and Schmitt (2015) study reported shorter period higher amplitude waves, and a larger tidal range, than the ship wake forcing studied at Pea Patch Island. As such, the Pea Patch Island wave climate may be less energetic than that studied by Albers and Schmitt (2015), making it a potentially more suitable environment for the success of a living shoreline installation in the absence of storm conditions. Although living shorelines are site specific, it is expected that the general morphological changes (erosion and accretion patterns on the tidal flat) observed at Pea Patch Island could have continued if calm and ship-wake conditions remained similar to those during the study period.

Guidance for the design and use of living shorelines in different environments and under different conditions is still being developed. Most guidance recommends soft solutions (no hard structural component such as rock) only be used in low energy environments, which is typically described as waves heights < 0.3 m or minimal wave and boat action (NOAA, 2015; Miller et al., 2016; Delaware Living Shorelines Committee, 2020). Ship wakes can increase the energy level of the wave climate at a site (Hardaway et al., 2017); at Pea Patch Island, maximum ship wake heights are more typical of an environment with moderate energy levels (wave heights 0.3–0.6 m). In addition, previous reports have indicated that coir logs are not a recommended material for high energy saltwater environments or environments with significant boating activity (Duhring, 2008; Skrabal, 2013). Often when design guidelines refer to wake, the relation is to smaller, recreational boats rather than large container ships and tankers. Despite this prior guidance, results from Pea Patch Island indicate that coir logs arranged in a repeating T-head groin configuration may offer some wave attenuation and erosion protection to a silty-mud tidal flat affected by ship wake energy. However, the installation was not robust under storm conditions. Storms may increase in frequency and severity during winter months when *in situ* data were not available. Review of timelapse footage during the winter season indicated structural failure, coir log damage, and coir log shiftings. As such, it is likely that the installation would not be effective year-round. Thus, a coir log installation may not be suitable under sustained high energy conditions, but may be effective in mitigating intermittent moderate energy activity induced by ship wakes similar to conditions at Pea Patch Island (when storm energy is not a factor). A different design approach, potentially a hybrid solution including some hard features, may be necessary for an effective mitigation scheme at this site and similar sites affected by ship wake forcing and seasonal storms.

5 Conclusion

Results of this investigation indicate the severity of negative outcomes arising from ship wakes reaching the shores of the Delaware River Estuary as well as the ability of living shoreline configuration made up of coir log T-head groins to mitigate the effects of ship wakes.

1) Ship wakes account for 25–50% of the total daily energy impacting the shoreline at the site. Peak background velocities are, on average, ~74% (~54%) smaller than the largest cross-shore (alongshore) ship wake velocities. In a moderate fetch confined compound channel, ship wakes can contribute a considerable amount of energy to the hydrodynamic system and increase nearshore velocities.

2) Northbound and southbound ship wake events had different outcomes in part due to the alongshore component of northbound ship wakes. Approximately 11% of southbound wake events had a decrease in energy flux greater than 50% whereas ~25% of northbound ship wake events displayed a similar decrease in energy flux. Channel and nearshore bathymetry play a significant role in the transformation of ship wakes from offshore to onshore, which has implications for the performance of any structure intended to decrease the total energy impacting the shoreline.
3) The installation displayed a strong depth dependence. Over the lower 25% of the tidal range, the installation induced a wave diffraction pattern between the THGs that resulted in onshore accretion of up to 0.1 m and decreases in energy flux of 10–80%. The installation had potential to reduce wave energy impacting the shoreline over the lower 50% of the tidal range and when submerged up to twice its height. The tidal range at a given site and placement of shoreline protection implements within that range are important variables in the performance and efficacy of a living shoreline installation.
4) Morphological changes are commensurate with observations near submerged breakwaters under oblique wave forcing. Erosion of up to 0.1 m occurred just onshore of the heads of the THGs, likely due to the circulation pattern created by a structure-induced pumping mechanism. Shoreline changes showed a larger area of accretion of up to 0.1 m on the northern side of the installation likely due to the interaction of the circulation pattern and north-directed alongshore current. Elevation changes of up to 0.2 m were observed onshore of the installation area. A natural low-crested breakwater arranged in a THG configuration on an estuarine shoreline can produce circulation patterns and morphological changes comparable to similarly designed hard shoreline protection measures.
5) Coir logs were sustained and secured in place through ship wake, non-storm conditions but were damaged during storm conditions. Monitoring of the installation with the time-lapse footage revealed the dislodging and loss of coir logs from their original position. Coir logs demonstrate an ability to sustain position through ship wake conditions in areas with moderate fetch, allowing accretion to occur. However, coir logs may not be suitable for long-term installations addressing ship wake in moderate fetch areas where increased energy from storms is a factor.

Though living shorelines are generally only recommended for low energy environments, results indicate the potential application of nature-based solutions (including coir logs) in environments with intermittent higher energy activity produced by large vessel shipping traffic. Future research directions may investigate alternate nature-based materials and designs in areas affected by ship wakes, or potential hybrid approaches to address storm events in areas with a similar moderate fetch.

Data availability statement

The raw data supporting the conclusion of this article will be made available by the authors, without undue reservation.

Author contributions

CE: original draft preparation, field data collection and analysis, figure generation, manuscript editing, manuscript preparation; OW: original draft preparation (numerical simulation sections), field data collection, model domain update, model validation, numerical simulation analysis, figure generation; ER: original draft preparation, living shoreline design preparation, figure preparation and formatting; ML: original draft contributions, figure generation, manuscript review; RS: original draft contributions, manuscript review; MM: manuscript review; FS: project conceptualization, funding acquisition, manuscript review; JB: project conceptualization, funding acquisition, project administration and supervision, permit acquisition; JP: project conceptualization, funding acquisition, project administration and supervision, manuscript editing.

Funding

This work was supported by Delaware Sea Grant (NA18OAR4170086) and the University of Delaware.

Acknowledgments

The authors gratefully acknowledge the support of individuals affiliated with the Center for Applied Coastal Research and Coastal Resilience Design Studio for their help in the construction and monitoring of the living shoreline, including Olivia Amante, Erica Beddings, David Bogart, Conner Brown, Nick Bruce, Emily Chapman, Delaney Doran, Maya Eley, Seth Esterly, William Everett, Christopher Fettke von Koeckritz, Heather Fettke von Koeckritz, Andrew Gainey, Joshua Gainey, Manoj Kumar Gangadharan, Mackenzie Hammel, Ben Horney, Temitope Ezekiel Idowu, Evan Mazur, Mohammad Sadegh Nouri, Courtney Olney, Maria Pontiki, Kyle Rumaker, Martha Ryan and Mike Welsh. The authors express the utmost gratitude to John Mercer, Linton Mercer, and Kingfisher Environmental Services, Inc. for providing in-kind services. The authors acknowledge the work of Taira Baldauf in data analysis for pilot studies in conjunction with this investigation. The authors additionally thank the Delaware Department of Natural Resources and Environmental Control (DNREC) for providing site access, transportation, and assistance in initial site location determination. We appreciate the critical reviews that improved clarity of the manuscript. Portions of this work were utilized and acknowledged in a master's thesis for both Cassandra Everett and Oscar Williams.

Conflict of interest

ML was employed by Sustainable Coastal Solutions, Inc.

The remaining authors declare that the research was conducted in the absence of any commercial or financial relationships that could be construed as a potential conflict of interest.

Publisher's note

References

Albers, T., and Schmitt, K. (2015). Dyke design, floodplain restoration and mangrove co-management as parts of an area coastal protection strategy for the mud coasts of the Mekong Delta, Vietnam. *Wetl. Ecol. Manag.* 23 (6), 991–1004. doi:10.1007/s11273-015-9441-3

Almaz, O., and Altiok, T. (2012). Simulation modeling of the vessel traffic in Delaware River: impact of deepening on port performance. *Simul. Model. Pract. Theory* 22, 146–165. doi:10.1016/j.simpat.2011.12.004

Baldauf, T. (2021). *Quantifying the effect of ship wake on commonly used living shoreline treatments.* undergraduate thesis. Newark (DE): University of Delaware.

Bayraktarov, E., Stewart-Sinclair, P. J., Brisbane, S., Boström-Einarsson, L., Saunders, M. I., Lovelock, C. E., et al. (2019). Motivations, success, and cost of coral reef restoration. *Restor. Ecol.* 27 (5), 981–991. doi:10.1111/rec.12977

Bilkovic, D., Mitchell, M., Davis, J., Herman, J., Andrews, E., King, A., et al. (2019). Defining boat wake impacts on shoreline stability toward management and policy solutions. *Ocean Coast. Manag.* 182, 104945. doi:10.1016/j.ocecoaman.2019.104945

Brophy, L., Greene, C., Hare, V., Holycross, B., Lanier, A., Heady, W., et al. (2019). Insights into estuary habitat loss in the Western United States using a new method for mapping maximum extent of tidal wetlands. *PLOS ONE* 14 (8), e0218558. doi:10.1371/journal.pone.0218558

Chowdhury, M. S. N., Walles, B., Sharifuzzaman, S., Shahadat Hossain, M., Ysebaert, T., Smaal, A. C., et al. (2019). Oyster breakwater reefs promote adjacent mudflat stability and salt marsh growth in a monsoon dominated subtropical coast. *Sci. Rep.* 9, 8549. doi:10.1038/s41598-019-44925-6

Cook, T., Sommerfield, C., and Wong, K. (2007). Observations of tidal and springtime sediment transport in the upper Delaware Estuary. *Estuar. Coast. Shelf Sci.* 72 (1-2), 235–246. doi:10.1016/j.ecss.2006.10.014

Dao, T., Stive, M. J. F., Hofland, B., and Mai, T. (2018). Wave damping due to wooden fences along mangrove coasts. *J. Coast. Res.* 34 (6), 1317. doi:10.2112/jcoastres-d-18-00015.1

Davis, J. L., Currin, C. A., O'Brien, C., Raffenburg, C., and Davis, A. (2015). Living shorelines: coastal resilience with a blue carbon benefit. *PLOS ONE* 10, e0142595. doi:10.1371/journal.pone.0142595

De Roo, S., and Troch, P. (2015). Evaluation of the effectiveness of a living shoreline in a confined, non-tidal waterway subject to heavy shipping traffic. *River Res. Appl.* 31 (8), 1028–1039. doi:10.1002/rra.2790

Dean, R., and Dalrymple, R. (2002). *Coastal processes with engineering applications.* Cambridge: Cambridge University Press.

Dean, R. G., Browder, A. E., Goodrich, M. S., and Donaldson, D. G. (1994). *Model tests of the proposed P.E.P. Reef installation at Vero Beach, Florida.* Gainesville: Coastal and Oceanographic Engineering Department, University of Florida. UFL/COEL-94-012FL28 pp. plus 2 appendices. [online] Available at: https://ufdc.ufl.edu/UF00085003/00001 (accessed January 12, 2022).

Delaware Department of Natural Resources and Environmental Control (DNREC) (2020). *SAA for tidal and non-tidal shoreline stabilization.* [online] Available at: http://www.dnrec.delaware.gov/wr/Documents/Shoreline_Stabilization_SAA.pdf (accessed May 20, 2022).

Delaware Department of Natural Resources and Environmental Control (DNREC) (2001). "The Pea Patch island heronry region special management plan. Progress report," in *Three years of strategy implementation.*

Delaware Living Shorelines Committee (2020). *Site evaluation for living shoreline projects in Delaware.* [online] Available at: https://static1.squarespace.com/static/59b69f4f2994caee6bf52abe/t/5ea82bf97189b11145040d10/1588079656882/DelawareLivingShorelineSiteEvaluation_v10.pdf (accessed January 12, 2022).

Dinh, S., Albers, T., and Schmitt, K. (2013). "Shoreline management guidelines coastal protection in the lower mekong delta," in *Deutsche Gesellschaft für Internationale Zusammenarbeit (GIZ) GmbH.*

Douglass, S. L., and Pickel, B. H. (1999). The tide doesn't go out anymore: the effect of bulkheads on urban bay shorelines. *Shore Beach* 67 (2-3), 19–25. [online] Available at: https://www.mobilebaynep.com/assets/pdf/Effect_of_Bulkheads_on_Urban_Shorelines.pdf (accessed January 12, 2022).

Duhring, K. A. (2008). *A comparison of structural and nonstructural methods for erosion control and providing habitat in Virginia salt marshes proceedings of the 2006 living shoreline summit (Williamsburg, Virginia).* Gloucester Point, Virginia: Coastal Resources Commission CRC, 41–47. Publication No. 08-164.

Ellis, J., Sherman, D., Bauer, B., and Hart, J. (2002). Assessing the impact of an organic restoration structure on boat wake energy. *J. Coast. Res.* 36, 256–265. doi:10.2112/1551-5036-36.sp1.256

Everett, C. (Forthcoming 2022). *Performance of a living shoreline under ship wake forcing on an estuarine shoreline.* master's thesis. Newark (DE): University of Delaware.

Ezcurra, E., Barrios, E., Ezcurra, P., Ezcurra, A., Vanderplank, S., Vidal, O., et al. (2019). A natural experiment reveals the impact of hydroelectric dams on the estuaries of tropical rivers. *Sci. Adv.* 5 (3), eaau9875. doi:10.1126/sciadv.aau9875

Forlini, C., Qayyum, R., Malej, M., Lam, M., Shi, F., Angelini, C., et al. (2021). On the problem of modeling the boat wake climate: the florida intracoastal waterway. *J. Geophys. Res. Oceans* 126 (2). doi:10.1029/2020jc016676

Gabel, F., Lorenz, S., and Stoll, S. (2017). Effects of ship-induced waves on aquatic ecosystems. *Sci. Total Environ.* 601-602, 926–939. doi:10.1016/j.scitotenv.2017.05.206

Gedan, K., Kirwan, M., Wolanski, E., Barbier, E., and Silliman, B. (2011). The present and future role of coastal wetland vegetation in protecting shorelines: Answering recent challenges to the paradigm. *Clim. Change* 106 (1), 7–29. doi:10.1007/s10584-010-0003-7

Gharbi, S., Hamdi, G., Valkov, G., and Nistor, I. (2008). *Field measurements of ship waves along the St. Lawrence river waterway.* Canada, 1–10. OCEANS 2008. doi:10.1109/OCEANS.2008.5152138

Gittman, R., Fodrie, F., Popowich, A., Keller, D., Bruno, J., Currin, C., et al. (2015). Engineering away our natural defenses: an analysis of shoreline hardening in the US. *Front. Ecol. Environ.* 13 (6), 301–307. doi:10.1890/150065

Gittman, R., Popowich, A., Bruno, J., and Peterson, C. (2014). Marshes with and without sills protect estuarine shorelines from erosion better than bulkheads during a category 1 hurricane. *Ocean Coast. Manag.* 102, 94–102. doi:10.1016/j.ocecoaman.2014.09.016

Gourlay, T. (2001). The supercritical bore produced by a high-speed ship in a channel. *J. Fluid Mech.* 434, 399–409. doi:10.1017/s002211200100372x

Hardaway, C. S., Jr., Milligan, D. A., Duhring, K., and Wilcox, C. A. (2017). *Living shoreline design guidelines for shore protection in virginia's estuarine environment (SRAMSOE #463).* Gloucester Point, VA: Virginia Institute of Marine Science. doi:10.21220/V5CF1N

Herbert, D., Astrom, E., Bersoza, A., Batzer, A., McGovern, P., Angelini, C., et al. (2018). Mitigating erosional effects induced by boat wakes with living shorelines. *Sustainability* 10 (2), 436. doi:10.3390/su10020436

Houser, C. (2011). Sediment resuspension by vessel-generated waves along the savannah river, Georgia. *J. Waterw. Port. Coast. Ocean. Eng.* 137 (5), 246–257. doi:10.1061/(asce)ww.1943-5460.0000088

Kamphuis, J. W. (2010). Introduction to coastal engineering and management: 2nd edition. *Adv. Ser. Ocean Eng.* 30, 1–564. doi:10.1142/9789812834867_0001

Kibler, K. M., Kitsikoudis, V., Donnelly, M., Spiering, D. W., and Walter, L. (2019). Flow-vegetation interaction in a living shoreline restoration and potential effect to mangrove recruitment. *Sustainability* 11 (11), 3215. doi:10.3390/su11113215

Knutson, P., Brochu, R., Seelig, W., and Inskeep, M. (1982). Wave damping in *Spartina alterniflora* marshes. *Wetlands* 2 (1), 87–104. doi:10.1007/bf03160548

Komar, P. (1998). *Beach processes and sedimentation.* Upper Saddle River (New Jersey): Prentice-Hall.

Kraus, N. C., Hanson, H., and Bomgren, H. S. (1994). "Modern functional design of groin systems," in *Proceedings ICCE 1994*, 1327–1342.

Lacy, J., and MacVean, L. (2016). Wave attenuation in the shallows of san francisco bay. *Coast. Eng.* 114, 159–168. doi:10.1016/j.coastaleng.2016.03.008

Lanuru, M. (2008). Measuring critical erosion shear stress of intertidal sediments with eromes erosion device. *Fak. Ilmu Kelaut. Dan. Perikan. Unhas* 18 (5), 390–397.

Mai Van, C., Ngo, A., Mai, T., and Dao, H. (2021). Bamboo fences as a nature-based measure for coastal wetland protection in Vietnam. *Front. Mar. Sci.* 8. doi:10.3389/fmars.2021.756597

Marani, M., d'Alpaos, A., Lanzoni, S., and Santalucia, M. (2011). Understanding and predicting wave erosion of marsh edges. *Geophys. Res. Lett.* 38 (21). doi:10.1029/2011gl048995

Meyer, D., Townsend, E., and Thayer, G. (1997). Stabilization and erosion control value of oyster cultch for intertidal marsh. *Restor. Ecol.* 5 (1), 93–99. doi:10.1046/j.1526-100x.1997.09710.x

Miller, J., Rella, A., Williams, A., and Sproule, E. (2016). *Living shorelines engineering guidelines.* SIT-DL-14-9-2942. [online] Available at: https://www.nj.gov/dep/cmp/docs/living-shorelines-engineering-guidelines-final.pdf (accessed January 12, 2022).

Millero, F., and Poisson, A. (1981). International one-atmosphere equation of state of seawater. *Deep Sea Res. Part A. Oceanogr. Res. Pap.* 28 (6), 625–629. doi:10.1016/0198-0149(81)90122-9

Morris, R., Konlechner, T., Ghisalberti, M., and Swearer, S. (2018). From grey to green: Efficacy of eco-engineering solutions for nature-based coastal defence. *Glob. Chang. Biol.* 24 (5), 1827–1842. doi:10.1111/gcb.14063

Neumann, B., Vafeidis, A., Zimmermann, J., and Nicholls, R. (2015). Future coastal population growth and exposure to sea-level rise and coastal flooding – a global assessment. *PLOS ONE* 10 (3), e0118571. doi:10.1371/journal.pone.0118571

Ng, M., and Byres, R. (2011). *Vessel wake study prepared for: KM LNG operating general partnership (M&N project No. 7333).* Vancouver, BC: Moffat & Nichol. [online] Available at: https://docs2.cer-rec.gc.ca/ll-eng/llisapi.dll/fetch/2000/90466/94153/552726/657379/657474/670503/686250/B11-7-_2011.05.05.RPT.Vessel.Wake.Study_-_A1Z0S9_.pdf?nodeid=686399&vernum=-2 (accessed May 20, 2022).

NOAA (2015). Guidance for considering the use of living shorelines. [online] Available at: https://www.habitatblueprint.noaa.gov/wp-content/uploads/2018/01/NOAA-Guidance-for-Considering-the-Use-of-Living-Shorelines_2015.pdf (accessed January 12, 2022).

O'Donnell, J. (2017). Living shorelines: A review of literature relevant to new england coasts. *J. Coast. Res.* 332, 435–451. doi:10.2112/jcoastres-d-15-00184.1

Partnership for the Delaware Estuary (PDE) (2012). *Technical report for the Delaware estuary and basin.* PDF Report No. 12-01. 255 pages. [online] Available at: https://www.delawareestuary.org/science_programs_state_of_the_estuary.asp (accessed January 12, 2022).

Plant, N. G., Holland, K. T., and Puleo, J. A. (2002). Analysis of the scale of errors in nearshore bathymetric data. *Mar. Geol.* 191 (1-2), 71–86. doi:10.1016/S0025-3227(02)00497-8

Polk, M., and Eulie, D. (2018). Effectiveness of living shorelines as an erosion control method in North Carolina. *Estuaries Coasts* 41 (8), 2212–2222. doi:10.1007/s12237-018-0439-y

Proudman, J. (1963). *Dynamical oceanography.* London: Methuen.

Ralston, D., Talke, S., Geyer, W., Al-Zubaidi, H., and Sommerfield, C. (2019). Bigger tides, less flooding: effects of dredging on barotropic dynamics in a highly modified estuary. *J. Geophys. Res. Oceans* 124 (1), 196–211. doi:10.1029/2018jc014313

Ranasinghe, R., and Turner, I. (2006). Shoreline response to submerged structures: a review. *Coast. Eng.* 53 (1), 65–79. doi:10.1016/j.coastaleng.2005.08.003

Rapaglia, J., Zaggia, L., Parnell, K., Lorenzetti, G., and Vafeidis, A. (2015). Ship-wake induced sediment remobilization: effects and proposed management strategies for the Venice Lagoon. *Ocean Coast. Manag.* 110, 1–11. doi:10.1016/j.ocecoaman.2015.03.002

Ross, A., Najjar, R., Li, M., Lee, S., Zhang, F., Liu, W., et al. (2017). Fingerprints of sea level rise on changing tides in the chesapeake and Delaware bays. *J. Geophys. Res. Oceans* 122 (10), 8102–8125. doi:10.1002/2017jc012887

Safak, I., Angelini, C., Norby, P., Dix, N., Roddenberry, A., Herbert, D., et al. (2020a). Wave transmission through living shoreline breakwalls. *Cont. Shelf Res.* 211, 104268. doi:10.1016/j.csr.2020.104268

Safak, I., Angelini, C., and Sheremet, A. (2021). Boat wake effects on sediment transport in intertidal waterways. *Cont. Shelf Res.* 222, 104422. doi:10.1016/j.csr.2021.104422

Safak, I., Norby, P., Dix, N., Grizzle, R., Southwell, M., Veenstra, J., et al. (2020b). Coupling breakwalls with oyster restoration structures enhances living shoreline performance along energetic shorelines. *Ecol. Eng.* 158, 106071. doi:10.1016/j.ecoleng.2020.106071

SAGE (2015). *Natural and structural measures for shoreline stabilization.* [online] Available at: http://www.sagecoast.org/docs/SAGE_LivingShorelineBrochure_Print.pdf (accessed January 12, 2022).

Scarpa, G., Zaggia, L., Manfè, G., Lorenzetti, G., Parnell, K., Soomere, T., et al. (2019). The effects of ship wakes in the venice lagoon and implications for the sustainability of shipping in coastal waters. *Sci. Rep.* 9 (1), 19014. doi:10.1038/s41598-019-55238-z

Schaefer, R. (2019). *Impacts and vegetation-induced attenuation of wind- and vessel-generated waves.* undergraduate thesis. Newark (DE): University of Delaware.

Schroevers, M., Huisman, B., van der Wal, M., and Terwindt, J. (2011). in *2011 IEEE/OES 10th current, waves and turbulence measurements (CWTM).* doi:10.1109/CWTM.2011.5759539*Measuring ship induced waves and currents on a tidal flat in the Western Scheldt estuary*

Shi, F., Malej, M., Smith, J., and Kirby, J. (2018). Breaking of ship bores in a boussinesq-type ship-wake model. *Coast. Eng.* 132, 1–12. doi:10.1016/j.coastaleng.2017.11.002

Skrabal, T. (2013). "Living shoreline projects in North Carolina," in *Proceedings of the 2013 mid-atlantic living shorelines summit* (Cambridge, Maryland), 29–30.

Smith, C., Gittman, R., Neylan, I., Scyphers, S., Morton, J., Joel Fodrie, F., et al. (2017). Hurricane damage along natural and hardened estuarine shorelines: using homeowner experiences to promote nature-based coastal protection. *Mar. Policy* 81, 350–358. doi:10.1016/j.marpol.2017.04.013

Smith, C., Rudd, M., Gittman, R., Melvin, E., Patterson, V., Renzi, J., et al. (2020). Coming to terms with living shorelines: a scoping review of novel restoration strategies for shoreline protection. *Front. Mar. Sci.* 7. doi:10.3389/fmars.2020.00434

Soomere, T. (2006). Nonlinear ship wake waves as a model of rogue waves and a source of danger to the coastal environment: a review. *Oceanologia* 48 (S), 185–202.

Soomere, T., Parnell, K. E., and Didenkulova, I. (2009). Implications of fast-ferry wakes for semi-sheltered beaches: a case study at aegna island, baltic sea. *J. Coast. Res.* 56 (1), 128–132.

Spencer, T., Schuerch, M., Nicholls, R. J., Hinkel, J., Lincke, D., Vafeidis, A. T., et al. (2016). Global coastal wetland change under sea-level rise and related stresses: the DIVa wetland change model. *Glob. Planet. Change* 139, 15–30. doi:10.1016/j.gloplacha.2015.12.018

Styles, R., and Hartman, M. (2019). Effect of tidal stage on sediment concentrations and turbulence by vessel wake in a coastal plain saltmarsh. *J. Mar. Sci. Eng.* 7 (6), 192. doi:10.3390/jmse7060192

Syvitski, J., Vörösmarty, C., Kettner, A., and Green, P. (2005). Impact of humans on the flux of terrestrial sediment to the global coastal ocean. *Science* 308 (5720), 376–380. doi:10.1126/science.1109454

Tait, J., and Griggs, G. (1991). *Beach response to the presence of a seawall; comparison of field observations.* Washington, DC: US Army Corps of Engineers.

Taube, S. R. (2010). *Impacts of fringing oyster reefs on wave attenuation and marsh erosion rates.* undergraduate thesis. Charlottesville (VA): University of Virginia.

Temmerman, S., Meire, P., Bouma, T., Herman, P., Ysebaert, T., De Vriend, H., et al. (2013). Ecosystem-based coastal defence in the face of global change. *Nature* 504 (7478), 79–83. doi:10.1038/nature12859

Ting, C., Lin, M., and Cheng, C. (2004). Porosity effects on non-breaking surface waves over permeable submerged breakwaters. *Coast. Eng.* 50 (4), 213–224. doi:10.1016/j.coastaleng.2003.10.003

USACE (2009). Delaware River main stem and channel deepening project environmental assessment. [online] Available at: https://www.nap.usace.army.mil/Portals/39/docs/Civil/Deepening/Environmental/Environmental%20Assessment%20-%20April%202009.pdf (accessed January 12, 2022).

van der Meer, J., Briganti, R., Zanuttigh, B., and Wang, B. (2005). Wave transmission and reflection at low-crested structures: Design formulae, oblique wave attack and spectral change. *Coast. Eng.* 52 (10-11), 915–929. doi:10.1016/j.coastaleng.2005.09.005

van Maren, D., van Kessel, T., Cronin, K., and Sittoni, L. (2015). The impact of channel deepening and dredging on estuarine sediment concentration. *Cont. Shelf Res.* 95, 1–14. doi:10.1016/j.csr.2014.12.010

van Rijn, L., Grasmeijer, B., and Perk, L. (2018). Effect of channel deepening on tidal flow and sediment transport: part I – sandy channels. *Ocean. Dyn.* 68 (11), 1457–1479. doi:10.1007/s10236-018-1204-2

Verney, R., Deloffre, J., Brun-Cottan, J., and Lafite, R. (2007). The effect of wave-induced turbulence on intertidal mudflats: impact of boat traffic and wind. *Cont. Shelf Res.* 27 (5), 594–612. doi:10.1016/j.csr.2006.10.005

Wiberg, P., Taube, S., Ferguson, A., Kremer, M., and Reidenbach, M. (2019). Wave attenuation by oyster reefs in shallow coastal bays. *Estuaries Coasts* 42 (2), 331–347. doi:10.1007/s12237-018-0463-y

Williams, O. (Forthcoming 2022). *Evaluating living shoreline performance and vessel wake using the ship wake module of FUNWAVE-TVD*. master's thesis. Newark (DE): University of Delaware.

Zabawa, C., Kerhin, R., and Bayley, S. (1981). Effects of erosion control structures along a portion of the northern Chesapeake Bay shoreline. *Environ. Geol.* 3 (4), 201–211. doi:10.1007/bf02473504

frontiers | Frontiers in Built Environment

ORIGINAL RESEARCH
published: 08 August 2022
doi: 10.3389/fbuil.2022.877378

Dam-Break Waves' Hydrodynamics on Composite Bathymetry

Hajo von Häfen[1]*, *Clemens Krautwald*[1], *Hans Bihs*[2] *and Nils Goseberg*[1,3]

[1]Leichtweiß-Institute for Hydraulic Engineering and Water Resources, Technische Universität Braunschweig, Braunschweig, Germany, [2]Department of Civil and Environmental Engineering, Norwegian University of Science and Technology, Byggteknisk, Trondheim, Norway, [3]Coastal Research Center, Joint Research Facility of Leibniz Universität Hannover and Technische Universität Braunschweig, Hannover, Germany

Among others, dam-break waves are a common representation for tsunami waves near- or on-shore as well as for large storm waves riding on top of storm surge water levels at coasts. These extreme hydrodynamic events are a frequent cause of destruction and losses along coastlines worldwide. Within this study, dam-break waves are propagated over a composite bathymetry, consisting of a linear slope and an adjacent horizontal plane. The wave propagation on the slope as well as its subsequent inundation of the horizontal hinterland is investigated, by varying an extensive set of parameters, for the first time. To that end, a numerical multi-phase computational fluid dynamics model is calibrated against large-scale physical flume tests. The model is used to systematically alter the parameters governing the hydrodynamics and to link them with the physical processes observed. The parameters governing the flow are the slope length, the height of the horizontal plane with respect to the ocean bottom elevation, and the initial impoundment depth of the dam-break. It is found that the overland flow features are governed by the non-dimensional height of the horizontal plane. Empirical equations are presented to predict the features of the overland flow, such as flow depth and velocities along the horizontal plane, as a function of the aforementioned parameters. In addition, analytical considerations concerning these dam-break flow features are presented, highlighting the changing hydrodynamics over space and time and rising attention to this phenomenon to be considered in future experimental tests.

Keywords: tsunami, dam-break, hydrodynamics, composite bathymetry, slope, overland flow

Edited by:
Jane McKee Smith,
Engineer Research and Development Center, United States

Reviewed by:
Hermann Marc Fritz,
Georgia Institute of Technology, United States
William James Pringle,
Argonne National Laboratory (DOE), United States

****Correspondence:***
Hajo von Häfen
h.von-haefen@tu-braunschweig.de

Specialty section:
This article was submitted to Coastal and Offshore Engineering, a section of the journal Frontiers in Built Environment

Received: *16 February 2022*
Accepted: *24 June 2022*
Published: *08 August 2022*

Citation:
von Häfen H, Krautwald C, Bihs H and Goseberg N (2022) Dam-Break Waves' Hydrodynamics on Composite Bathymetry. Front. Built Environ. 8:877378. doi: 10.3389/fbuil.2022.877378

1 INTRODUCTION

Tsunamis are recurring, devastating natural disasters that vulnerable regions can hardly shelter from. They frequently cause numerous casualties and considerable damage to economic assets, as demonstrated by the Indian Ocean tsunami in 2004 (Borrero et al., 2006; Fritz et al., 2006a; Ghobarah et al., 2006; Goff et al., 2006; Jaffe et al., 2006; Rodriguez et al., 2006; Saatcioglu et al., 2006; Tomita et al., 2006), the Chilean tsunami in 2010 (Fritz et al., 2011; Palermo et al., 2013), the Japanese tsunami in 2011 (von Hippel, 2011; Mikami et al., 2012; Chock et al., 2013; Satake et al., 2013; Mori et al., 2014), or the 2018 Indonesian tsunami (Mikami et al., 2019; Paulik et al., 2019; Aránguiz et al., 2020; Stolle et al., 2020; Krautwald et al., 2021). To improve predictions and estimations as to the damage potential of these extreme hydrodynamic events, research is ongoing and carried out by a large group of scientists all over the world. The overarching ambition is to understand the effects and implications of tsunamis more comprehensively; this happens in order to minimize the severe consequences of a tsunami disaster by optimizing evacuation concepts (e.g., Taubenböck et al., 2009) or refining standards (e.g., Naito et al., 2014).

1.1 Literature Review on Dam-Break Waves as an Analogy to Tsunami Waves

Tsunami waves are often caused by tectonic events, usually originating from seabed displacements at larger water depths. In combination with their wave length, they are predominantly shallow-water waves by definition. While propagating in the deep ocean, tectonic tsunamis have small wave heights and usually cause no damage. They can often be detected by early warning systems facilitating pressure sensors on the seafloor (DART system, Bernard and Titov, 2015). More recent attempts have used satellite altimetry to detect tsunamis in deep water (Ablain et al., 2006). Once reaching shallower waters, shoaling increases the wave height while the wave gets shorter and more devastating. Wave breaking occurs mostly prior to landfall and undular bores might develop (Matsuyama et al., 2007; Grue et al., 2008).

Storm waves, which are much shorter than tsunamis, can be simulated almost in their original scale in the largest wave flumes in the world equipped with flap or piston-type wave makers (Oumeraci, 2010). These facilities are also capable of generating solitary or N-waves, which have been often used in simulating tsunami waves. However, even though leading solitary-like waves might reach the shoreline first, Madsen et al. (2008) revealed in a comprehensive study that solitary waves as a model are inappropriate to represent the bulk tsunami on its geophysical scale by affirming that they are "magnitudes" too short. Later on, in 2010, Madsen and Schäffer (2010) conclude that from its generation in the ocean to its impact at the shore, the relevant length- and time-scales of the bulk tsunami are never defined by the solitary wave tie, that is, given by the ratio of the wave height to the water depth. In 2012, Chan and Liu (2012) relax the statement that a solitary wave is "magnitudes" too short (Madsen et al., 2008) by analyzing the time history of an offshore buoy affected by the Tohoku tsunami. They found that in this case, a solitary wave would be approximately six times too short but not magnitudes. However, generating sufficiently long waves is not (or only on a small scale) possible in common wave flumes due to the limited stroke of these facilities. Hence, pump-driven wave generators are often used to cope with this limitation (Goseberg et al., 2013; Park et al., 2013; Schimmels et al., 2016; Sriram et al., 2016; Tomiczek et al., 2016). In line with Madsen et al. (2008) and Madsen and Schäffer (2010), Chanson (2006) suggested using dam-break waves in analogy to tsunami waves propagating onshore and proposed an analytical two-dimensional (2D) model to calculate dam-break waves of real fluids, including friction. This author found good agreement between calculations and observations made by video cameras during the 2004 Banda Ache tsunami (Chanson, 2006).

Similar to tsunami inundation, dam-break waves are characterized by a quasi-infinite wavelength, increasing water level over time and simultaneously decreasing depth-averaged flow velocities. Ritter (1897) first derived equations to describe the surface, depth-averaged velocity, and wave tip celerity of an ideal fluid dam-break wave in a horizontal, initially dry flume. However, his equations do not consider friction. Addressing this issue, Dressler (1952) used the Chezy resistance coefficient to propose an improved approximation. Whitham and Lighthill (1955) adapted the Ritter (1897) solution to consider friction in the wavefront tip region, where friction and turbulence cause the wavefront to slow down and thicken. A more recent analytical solution was presented by Chanson (2009) who additionally included a variable Darcy friction factor for the wave tip region and successfully validated the model against large-scale experimental data. The latter solution is applicable to horizontal and sloping channels.

In laboratory testing, dam-break waves are commonly generated by lift or swing gates, either driven by rapidly opening actuators (von Häfen et al., 2018; von Häfen et al., 2019) or using the vertical release method where an elevated reservoir is quickly emptied into a lower basin that is again connected to a propagation flume (Wüthrich et al., 2018).

Some authors investigated dam-break waves propagating on sloped bathymetry. Mostly, past studies focused on the wave propagating down an inclined bottom in analogy to a dam-break wave triggered by a bursting river dam in the mountains rushing down into the valley (positively inclined slope), while few others focused their work on dam-break waves propagating up an inclined bottom, this then in analogy to a tsunami wave inundating a site with rising topography (negatively inclined slope). Studies dealing with positively inclined slopes are not in the scope of this thesis. The interested reader is referred to Dressler and Stoneley (1958), Hunt (1983), Hunt (1984), Nsom et al. (2000), Fernandez-Feria (2006), and Chanson (2009), who proposed the previously mentioned analytical solution to describe the dam-break wave celerity and surface in a positively or negatively inclined channel. Among others, studies dealing with dam-break wave propagation on negatively inclined slopes are those of Yeh et al. (1989) and Yeh (1991) who investigated broken bores running up a slope in laboratory experiments. These authors used water on both sides of a lift gate in initial settings and a constant slope angle of 7.5°. Once the gate was opened, the dam-break wave slumped into the resting water downstream of the gate. Yeh et al. (1989) and Yeh (1991) observed a so-called "momentum exchange" between the dam-break wave and the resting water downstream of the gate and found that the resting water is pushed up the slope first, followed by the bore. Lu et al. (2018) conducted experimental tests similar to those of Yeh et al. (1989) and Yeh (1991) but using a larger distance between the gate and the toe of the slope (0.4 m vs. 1.8 m). They found a linear relationship with a uniform gradient between impoundment depth and maximum run-up height. Also, given the same impoundment depth, the run-up height increases with increasing initial water depth downstream of the gate. Hence, run-up height is the smallest for an initially dry flume. Furthermore, Lu et al. (2018) analyzed the spatiotemporal development of the run-up process in detail. Barranco and Liu (2021) generated dam-break waves in a flume with water on both sides of the dam-break gate and used a variable reservoir length to investigate the features of the waves' run-up. They found a dependency between the run-up height and the initial impoundment depth and flood duration. By facilitating a numerical model, they proposed equations to predict the inundation depth, run-up height, and duration of the flood in relation to the bore characteristics (Barranco and Liu, 2021).

Following Chanson (2006) and Madsen et al. (2008), dam-break waves are frequently used by a multitude of authors in the context of tsunami engineering: Derschum et al. (2018), Khan et al. (2000), Stolle et al. (2018), Stolle et al. (2019), Stolle et al. (2020b), Stolle et al. (2020a), and von Häfen et al. (2021) used dam-break waves to study debris transport and debris-induced loadings, and Nistor et al. (2017a), Nistor et al. (2017b), Stolle et al. (2016), and Wüthrich et al. (2020) used the vertical release method to investigate debris motion as well. Al-Faesly et al. (2012), Arnason et al. (2009), Aureli et al. (2015), Cross (1967), Farahmandpour et al. (2020), Moon et al. (2019), Ramsden (1996), Shafiei et al. (2016), Soares-Frazão and Zech (2007), Soares-Frazão and Zech (2008), Winter Andrew et al. (2021), and Xu et al. (2020) used dam-break waves to investigate loads on structures like residential houses, breakwaters or idealized cities, and the associated flow regime. Kuswandi and Triatmadja (2019), Maqtan et al. (2018), and Triatmadja et al. (2011) used dam-break waves to investigate scouring around structures during tsunami inundations.

Since tsunami forecasting is challenging and only allows for a short-term warning, evacuation plans need to be applied rapidly after a tsunami hazard is detected (Taubenböck et al., 2013), and no measuring equipment can be installed before the wave reaches the site. Therefore, very limited measurements of flow depths and velocities of real-world tsunami events exist. Fritz et al. (2006b) analyzed survivor videos taken during the 2004 Banda Aceh tsunami. Both survivors observed sites about 3 km inland; one in downtown Banda Aceh, and one in a residential area. Extensive image processing and referencing allowed for extracting surface velocimetry and flow depth from the camera feeds. Fritz et al. (2006b) calculated the Froude numbers for both sites and found that they are close to F_r = 1.0. Matsutomi et al. (2010) analyzed field data of several tsunami events and calculated Froude numbers in the range of F_r = 0.42–2.0 (also depending on velocity estimation). Chanson (2006) also used camera footage from the Banda Ache tsunami in 2004 to validate his analytical dam-break wave approach and highlights the importance of real-fluid bottom-friction interaction. He reports a wavefront velocity of about 1.5 to 1.6 m/s at a site located about 1.5 to 3.0 km inland. Fritz et al. (2012) conducted field surveys in 2011 in Kesennuma Bay (Japan), which was heavily affected by the Tohoku tsunami. They used video recordings taken during the inundation and calibrated them with real-world coordinates measured in field surveys. Focusing on the hydrodynamics in the Kesennuma Bay narrows, they report a wave trough of −3 m followed by 12 min of flooding with a wave crest height of up to 9 m before the flow direction reverses into an outflow. Observed standing water surface waves within the navigation channel (typical water depth of 10 m) support the finding that the Froude number, extracted from the camera recordings, approached approximately unity.

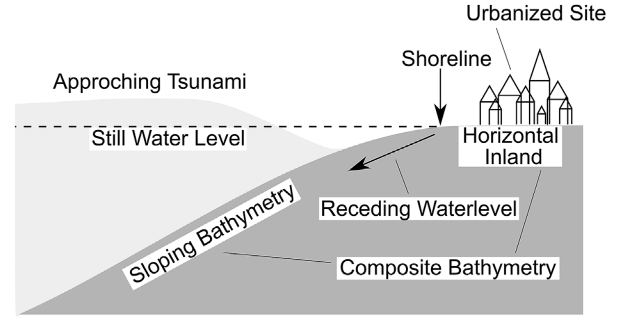

FIGURE 1 | Conceptual sketch of a tsunami wave propagating on a sloped bathymetry while approaching the shore. The inland topography is approximately horizontal (composite bathymetry). The still water line is indicated by a dashed line. Note that a tsunami not necessarily consists of a leading trough, as shown here, when approaching the shore (Fritz et al., 2006a).

1.2 Identified Knowledge Gaps, Objectives, and Aspects of Novelty

Dam-break waves are widely used to simulate tsunami hydrodynamics, both in numerical and physical tests. This is due to their ability to mimic some relevant features that govern tsunami wave hydrodynamics, such as their very long wavelength. In addition to the applications in the field of tsunami-related research, dam-break waves are frequently used in numerical fluid modeling as it is a common test case to validate the accuracy of numerical formulation. Also, numerous publications exist dealing with the obvious analogy to breaking river dams and the associated flood wave. Due to their wide field of application, a multitude of approximations and analytical solutions exists, predicting the surface elevation and flow features of dam-break waves.

However, the aforementioned literature review on tsunami-related applications revealed a lack of knowledge regarding dam-break waves propagation over a sloping bathymetry adjacent to a horizontal plane (composite bathymetry) in analogy to a tsunami wave reaching a sloping bathymetry, approaching a shore, and subsequently inundating a horizontal site (see **Figure 1**). To date, it remains unclear how the dam-break-induced flow evolves after it has climbed the slope and then suddenly being exposed to a change in inclination.

This study, hence, intends to shed light on the features of a dam-break waves' overland flow. Previous studies on tsunami effects, where dam-break waves have been used, did simply set a specific distance between the dam-break gate and their test setup; very rarely was that distance discussed. However, the surface elevation η is a function of space x and time t with the largest gradients for small x (von Häfen et al., 2019). This study, hence, also aims to raise awareness of the fact that the distance parameter x has to be taken into account when planning dam-break-based laboratory tests in analogy to tsunami waves.

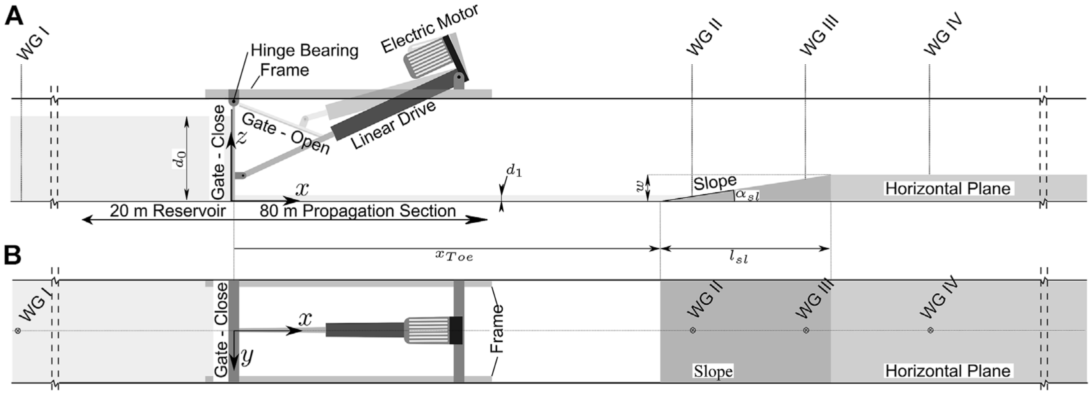

FIGURE 2 | Dam-break facility equipped with a fully controllable gate and four wave gauges in side- **(A)** and top-view **(B)**. The composite bathymetry and the parameters describing its geometry are indicated.

This study presents a unique, novel set of physical large-scale dam-break tests propagating over a composite bathymetry; the data set is subsequently used to calibrate a high-resolution numerical model. That model is then used to analyze the parameters governing the hydrodynamics. The following specific objectives are addressed within this study:

1) To raise awareness of and quantify the dam-break waves' changing hydrodynamics over space and time using simple analytical considerations.
2) To introduce qualitative categories (referred to as classes) to describe types of flow patterns observed and gained through an extensive numerical parameter study.
3) To correlate the classes with the governing parameters varied within the parameter study.
4) To describe the flow features quantitatively (flow depth, velocity, and Froude number) of the dam-break wave affected by the composite bathymetry over space and time and link them to the qualitative categories (classes) to gain knowledge about the underlying physics.
5) To provide empirical equations to predict the overland flow features.

Although there might be additional interest in the sloping region of the composite slope, this study focuses specifically on the flow characteristics along the horizontal plane, as it represents the region where urban siting would typically be present (see **Figure 1**). The authors deem this region mostly important since improving knowledge in this area is of great interest for reducing the number of severe losses caused by a tsunami event.

2 METHODOLOGY

2.1 Laboratory Experiments

Laboratory experiments are conducted to calibrate and validate the numerical model Reef3D (see **Section 2.2**). The test facility is situated at the Leichtweiß-Institute for Hydraulic Engineering and Water Resources, Technische Universität Braunschweig, Germany. The flume used for the dam-break experiments is 2 m wide and approximately 100 m long. A swing gate separates the flume into a 20-m long reservoir section, where water is impounded, and an 80-m long propagation section. The gate is driven by an electric linear drive, which allows a fully controllable movement of the gate. The gate opens within 0.7 s ensuring an unaffected, quasi-instantaneous dam-break (comparable to the ideal numerical dam-break used within this study, see **Section 2-3**), leading to a dam-break bore propagating downstream the flume (von Häfen et al., 2019). The flume is equipped with four wave gauges, capacity type (200 Hz, accuracy ~1%, tailor-made). One of the gauges is located in the reservoir and three downstream the gate in the propagation section of the flume whose positions are indicated in **Figure 2**. Wave gauges and linear drive are synchronized using a data acquisition system (ADLINK DAQe-2206, 64 channel, 16 bit, 250 kS/s). Capacitance wave gauges have been used successfully in accurately detecting aerated flows as occurring during advancing broken bores (Derschum et al., 2018; Ghodoosipour et al., 2019; Stolle et al., 2019a; Stolle et al., 2019b). **Figure 2** shows the flume including a composite bathymetry and measuring devices. Wave reflection at the end of the flume is not recorded by the data acquisition system since the length of the flume is sufficient to stop the measurements before a reflection arrives.

For calibration and validation purposes, four experimental tests are conducted: two with a flat bottom and two with a composite bathymetry installed. Each of these four tests is repeated twice. **Table 1** contains the experimental protocol including the impoundment depth d_0 and the positions of the wave gauges. In the case of an installed composite slope (test nos. 3 & 4), the distance between the gate and toe of the slopes x_{toe} is given, as well as the parameters describing the slope geometry; the height of the horizontal plane w and slope length l_{sl} (see **Figure 2**). A numerical model (see **Section 2.3**) is calibrated using the flat bottom test no. 1 (see **Table 1**) and validated later on against the remaining tests with (no. 2) and without the composite bathymetry (nos. 3 & 4).

2.2 Calibration and Validation of the Numerical Model

Within this study, the software package REEF3D is used. REEF3D is an open-source hydrodynamics framework developed by Bihs

TABLE 1 | Experimental protocol. Variables and coordinates correspond to **Figure 2**. Impoundment depth d_0, the distance between gate and toe of the slope x_{toe}, length of the slope l_{sl}, and height of the horizontal plane w. The positions of the wave gauges are given in the flume's coordinates.

Test no.	Wave type	Repetitions	d_0 [m]	x_{toe} [m]	w [m]	l_{sl} [m]	WG_{pos} [m]			
							WG_1	WG_2	WG_3	WG_4
1	Dam-break	2	0.40	-	-	-	–18.0	12.5	16.5	25.5
2		2	0.60	-	-	-	–18.0	12.5	16.5	25.5
3		2	0.50	10.0	0.30	6.00	–16.6	12.0	14.0	22.0
4		2	0.60	10.0	0.30	6.00	–16.6	12.0	14.0	22.0

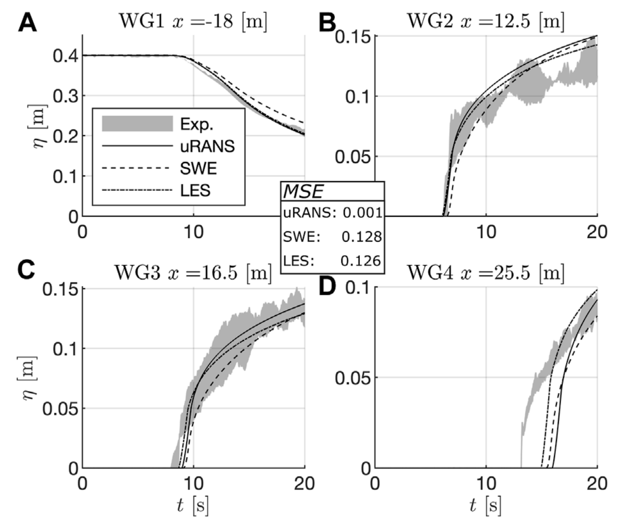

FIGURE 3 | Comparison between three numerical approaches compared against experimental data of a dam-break wave propagating on a flat bottom (test no. 1, see **Table 1**). Four wave gauge time histories are displayed; one in the reservoir section **(A)** and three in the propagation section **(B-D)** of the flume. The mean squared errors (MSE) over all four time histories are given.

et al. (2016), consisting of several numerical modules. The computational fluid dynamics (CFD) solver within REEF3D is used to solve the incompressible unsteady Reynolds-averaged Navier–Stokes (URANS) equations. This approach is selected since the flow is expected to be highly transient, which cannot be represented by the classical RANS formulation. The URANS approach can consider vortices in the front of the dam-break wave and is less costly in terms of computation compared to LES (large eddy simulation, see Iaccarino et al. (2003) for a comparison of the approaches). In addition to these CFD approaches, REEF3D is also used to solve depth-averaged non-hydrostatic shallow water equations (SWE) (Wang et al., 2020), which are much more computationally efficient than CFD calculations and are used by a multitude of authors to approximate dam-breaks; see Brufau and Garcia-Navarro (2000), Liang (2010), Ostapenko (2007), and Ozmen-Cagatay and Kocaman (2010). In order to identify the approach that represents the best compromise between efficiency and accuracy, URANS, SWE, and LES are compared against laboratory data of a flat bottom setup (test no. 1, see **Table 1**). This approach was chosen as the domain was still fairly large to be efficiently computed by the URANS approach. **Figure 3** displays the time histories of the four wave gauges in comparison to the numerical approaches. Deviations in the measured time histories of the wave gauges are small in the reservoir (WG 1), where bottom friction almost does not influence the flow and no turbulences are present. The positive wavefront, however, propagating over the flumes' bottom, results in larger deviations in the measurements. This is due to small imperfections in the flumes' concrete bottom and a highly turbulent flow associated with large fluctuations. Calculations are performed on a regular grid with 0.01 m cell size in a two-dimensional domain and for a duration of 20 s (see **Appendix 6.1** for a convergence study on cell size). The cell size represents the finest resolution, which leads to just acceptable long computing times (approx. 15 h per test in the numerical flume, see **Section 2.3** and **Appendix 6.1**) on the available computing servers (two dual-socket CPU servers with AMD EPYC 7452; in total 128 cores at 2.35 GHz and 128 GB RAM) with the setting of the numerical model summarized in **Appendix 6.2**.

All approaches are in good agreement with the experimentally measured data. However, large eddy simulations are computationally costly, hence, the validation concentrates on the URANS and SWE approaches with the following settings (also summarized in **Appendix 6.2**, showing the control file of REEF3D): for the URANS approach, the WENO (weighted essentially non-oscillatory) scheme (Jiang and Shu, 1996) is used for the convection discretization and the level set method is used to track the free surface (Osher and Sethian, 1988). The scheme can handle large gradients accurately by taking smoothness into account, and it is deemed to be appropriate to handle wet front progress; it was confirmed to be accurate in simulating dam-break scenarios as well (Sun et al., 2012; Cannata et al., 2018; Li et al., 2020). Turbulence is approximated by using the $k-\omega$ turbulence model (Wilcox, 2006), where k is the turbulent kinetic energy and ω is the specific turbulent dissipation. Time stepping for the momentum equation is performed by the TVD Runge–Kutta scheme, which is also applied to the level set and reinitialization method. The pressure is calculated using the projection method (Chorin, 1968). In the case of the SWE approach, the REEF3D:SFLOW implementation is used (Wang et al., 2020), which solves for non-hydrostatic pressure using a quadratic approximation (Jeschke et al., 2017) and uses the WENO scheme for convection. **Figure 4** shows validation runs of the URANS and the SWE approach against wave gauge time histories of the experimental tests 2–4 (see **Table 1**). In analogy to **Figure 3**, the SWE approach shows

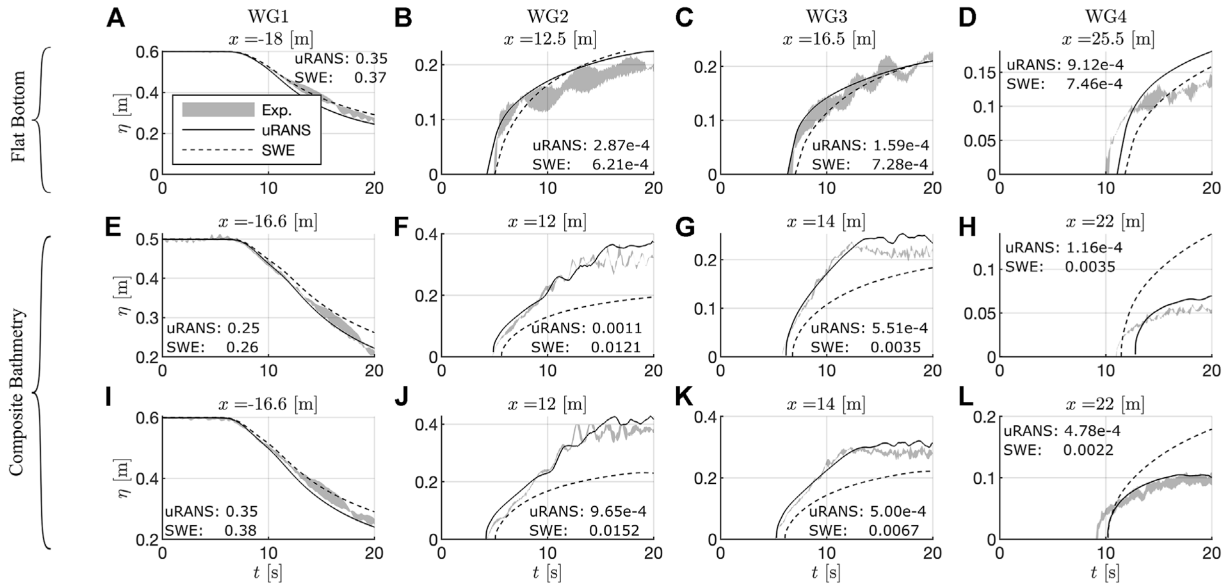

FIGURE 4 | Numerically calculated wave gauge time histories (SWE and URANS approach) compared to laboratory data. Flat bottom test with initial impoundment depth $\boldsymbol{d}_0$ = 0.60 m (**(A–D)**, test no. 2, see **Table 1**), composite bathymetry with $\boldsymbol{d}_0$ = 0.50 m (**(E–H)**, test no. 3, see **Table 1**), and composite bathymetry with $\boldsymbol{d}_0$ = 0.60 m (**(I–L)**, test no. 4, see **Table 1**). Deviations between experimental and numerical data are given as MSE in each subfigure.

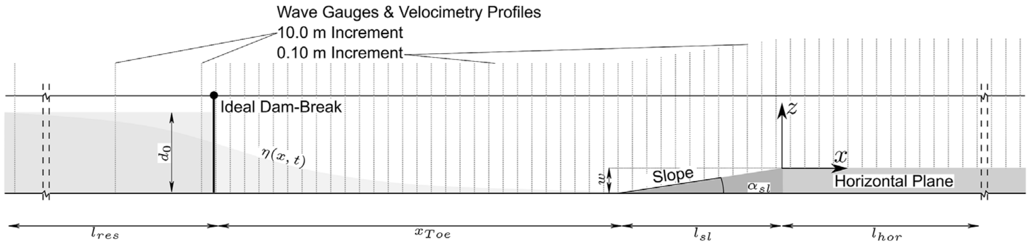

FIGURE 5 | Side-view sketch of the numerical flume. Wave gauges and velocimetry profilers are placed over the entire domain with a spacing of 0.10 **m** and 10.0 **m**. The free surface profile is indicated by $\boldsymbol{\eta}$, the length of the reservoir $\boldsymbol{l_{res}}$, the constant length of the horizontal plane $\boldsymbol{l_{hor}}$ = 10 **m**, the length $\boldsymbol{l_{sl}}$ and the height $\boldsymbol{w}$ of the slope, the distance between the initial water column and slope $\boldsymbol{x_{Toe}}$, and the initial impoundment depth $\boldsymbol{d}_0$.

good results compared to a larger dam-break wave on the horizontal bottom (test 2, see **Table 1**), cp. **Figures 4A–D**. However, once a composite bathymetry is modeled (**Figure 4E-L**), the SWE solution significantly underestimates the water depth along the slope (**Figures 4F, G, J, K**); it also overestimates the water depth on the adjacent horizontal plane (**Figures 4H, L**). The SWE cannot resolve vertical velocities, yet these would become relevant, especially where slope change occurs. Equally, these are also important to resolve reflection processes at and along the slope (see **Section 3.2.1**). However, the URANS approach is in good agreement with the experimental data and will hence be used within this study.

2.3 Numerical Flume and Test Protocol

The two-dimensional (2D) numerical flume (see **Figure 5**) consists of a solid bottom and left boundary, while the right boundary is an outflow to prevent reflections. The sides of the numerical flume are symmetry planes. The length of the reservoir l_{res} equals the length of the propagation section ($l_{res} = x_{Toe} + l_{sl} + l_{hor}$). Since—theoretically and neglecting friction—the negative wavefront, propagating upstream in the reservoir section, is half the celerity of the positive wavefront, a reservoir length equal to the length of the propagation section minimizes the influences of an emptying reservoir on the hydrodynamics on the horizontal plane. The simulation time t_{sim} is hence chosen to be twice the time the negative wavefront needs to reach the end of the flume and is, therefore, a function of the impoundment depth and the reservoir length and reads as follows:

$$\boldsymbol{t_{sim}} = 2\left(\boldsymbol{l_{res}} \middle/ \sqrt{\boldsymbol{g}\boldsymbol{d}_0}\right)\ [\boldsymbol{s}]. \tag{1}$$

The simulation time t_{sim} can be converted into a dimensionless simulation time T_{sim} in analogy to the

TABLE 2 | Values of the parameters varied (left) and normalized parameter range (right).

Parameter	Dimension	Values	Parameter	Dimension	Range
x_{toe}	[m]	2.00, 10.0, and 20.0	$X_{toe} = x_{toe}/d_0$	[-]	2.00–50.0
w	[m]	0.10, 0.20, and 0.30	$W = w/d_0$	[-]	0.10–0.75
l_{sl}	[m]	0.60, 2.00, and 10.0	$L_{sl} = l_{sl}/d_0$	[-]	0.60–25.0
d_0	[m]	0.40, 0.70, and 1.00	$\tan(\alpha)$	[-]	1:2.00–1:100

expression from Wüthrich et al. (2018): $T = t\sqrt{g/d_0}$, so that the dimensionless simulation time T_{sim} reads as follows:

$$\boldsymbol{T_{sim}} = 2\boldsymbol{l_{res}}/\boldsymbol{d}_0\,[-]. \tag{2}$$

An ideal dam-break wave is ensured by an instantaneous release of the water column (starting with the first computational iteration, without simulating any gate). Wave gauges and velocimetry profilers, distributed over the entire domain with increments of 0.1 m in the propagation and 10 m in the reservoir section, yield spatio-temporal information about the flow features and the surface elevation. Simulations are performed on a regular grid with 0.01 m spacing using the URANS approach (see **Section 2.2** for detailed settings and reasoning, as well as **Appendix 6.2**).

The geometry and the position of the composite bathymetry affect the hydrodynamics of the dam-break wave during propagation. To connect the parameters describing the composite bathymetry's geometry with the hydrodynamics and the underlying physical processes, the parameters are systematically varied. Those parameters investigated in this work are (see **Figure 5**) the initial impoundment depth d_0, the distance between the initial water column and the toe of the slope x_{toe}, the length of the slope l_{sl}, and the height of the horizontal plane w. Three values are examined for each of these four parameters. This results in $3^4 = 81$ possible combinations of parameters or a number of tests, respectively. In addition, three reference tests with changing impoundment depth but a horizontal bottom (without composite bathymetry) are performed. Thus, in total, 84 tests are conducted. **Table 2** lists the values of the four parameters being varied systematically (d_0, x_{toe}, l_{sl}, and w). In addition, the table contains the range of these values in dimensionless writing (indicated by capital letters: X_{toe}, L_{sl}, and W) normalized by the initial impoundment depth d_0 as commonly applied in studies on dam-break waves (Lauber and Hager, 1998; Chanson, 2009; Nouri et al., 2010; Oertel and Bung, 2012; Goseberg et al., 2013; Goseberg and Schlurmann, 2014; Hooshyaripor et al., 2017; von Häfen et al., 2018; Wüthrich et al., 2018; von Häfen et al., 2019; von Häfen et al., 2021).

3 RESULTS

3.1 Flow Features over Space and Time–Analytical Considerations

The literature review revealed that in most experimental or numerical studies incorporating dam-break waves, there is little information on how the distance between the test setup and the (idealized) gate is chosen. However, dam-break waves' hydrodynamics change considerably over space and time, which will be briefly highlighted in this section. Based on the analytical approach of Ritter (1897), **Figures 6A–C** show the computed surface elevation (η, panel A), depth-averaged flow velocity (U, panel B), and the Froude number (F_r, panel C) of a dam-break wave over space (abscissa) and time (ordinate). The dam-break location is at $x = 0$ m, the reservoir extends into negative x-direction, whereas the propagation section is positive in x-direction. The positive wavefront is indicated as a red solid line, while the negative wave, propagating in opposite direction within the reservoir, is shown as a red dashed line.

Figure 6 shows that surface elevation, velocity, and, subsequently, also the Froude number always depend on space and time. This is evident from the changing color gradients at constant x in **Figures 6A–C** and is emphasized in **Figures 6D–F**, which show the time series along the transects A and B, shifted to the time of positive wavefront arrival (t_{wf}). The larger the distance between the gate and the location being considered (e.g., the location of the test setup), the

1) lower and flatter the surface elevation time history (see **Figure 6D**),
2) higher the depth-averaged flow velocities over time (see **Figure 6E**), and
3) larger the Froude number time history (see **Figure 6F**).

Hence, the distance between the gate and test setup should preferably be provided in dam-break wave-structure interaction studies; this is to ensure comparability and repeatability of tests. In addition, the distance can be utilized to adjust the local hydrodynamic setting and to achieve conditions as close to *in situ* conditions as possible. Within the subsequently evaluated numerical test program, the distance between the gate and the toe of the slope (x_{toe}) is hence varied (see **Table 2**) to adjust for the gate to compound beach distance effect and to provide just comparisons.

Note that friction is neglected by the analytical approach of Ritter (1897). Even though the approach resembles the overall characteristics of a dam-break wave well, friction significantly influences the waves' tip region (e.g., addressed by Chanson (2009)). Hence, close to the wave tip, the surface elevation will be larger and the depth-averaged velocities and Froude numbers smaller in nature than predicted by Ritter (1897) and presented in **Figure 6**.

3.2 Numerical Investigations

The following sections are using the computational results of the numerical model to investigate the flow features of the dam-break

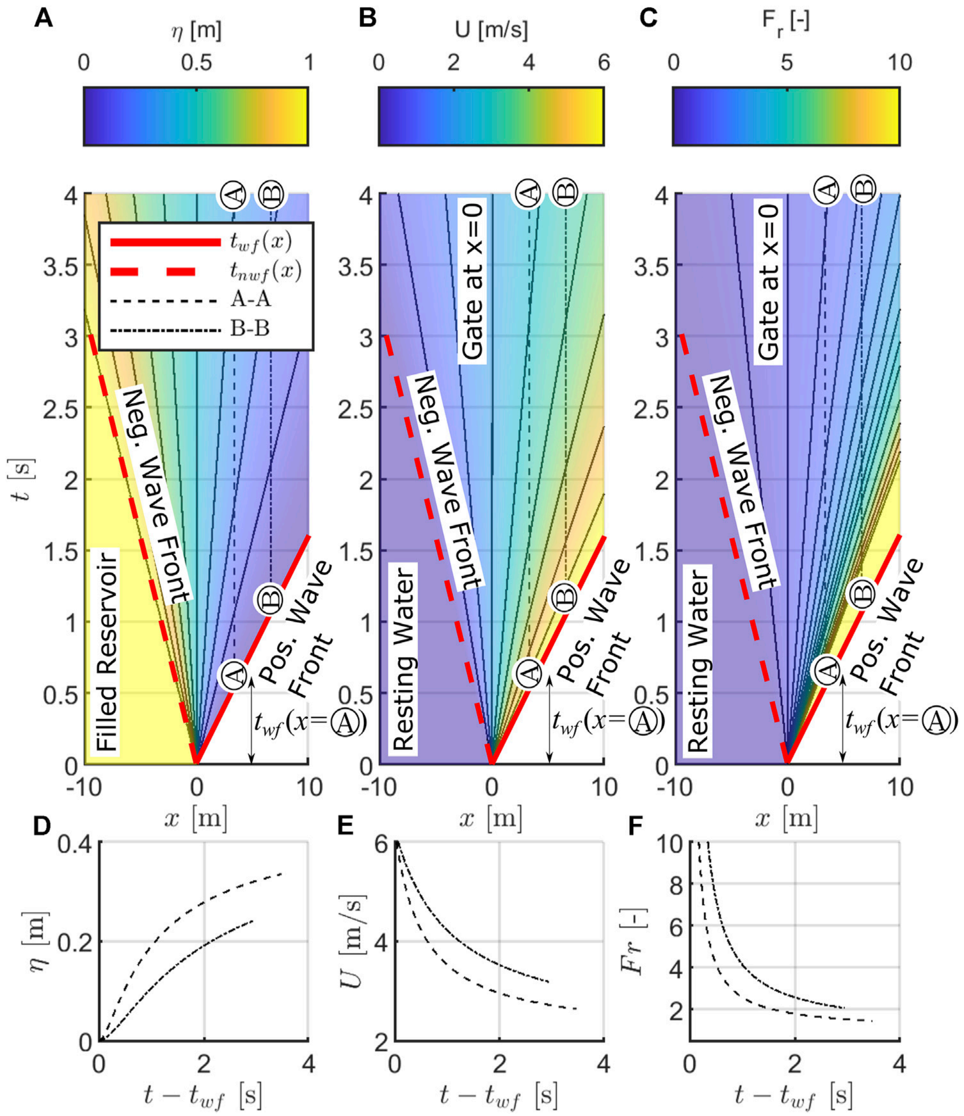

FIGURE 6 | Flow features of a dam-break wave in space and time derived from the analytical approximation by Ritter (1897). Surface elevation **(A)**, depth-averaged velocity **(B)**, and Froude number **(C)** are indicated as colors. Dam-break location at x = 0 m, reservoir spreading in negative *x*-direction. Dry, frictionless propagation section on positive *x*-direction. Positive and negative wavefronts are indicated as solid and dashed red lines. These lines also indicate the time when the positive or negative wave reaches a specific position (***t_{wf}*** and ***t_{nwf}***, respectively). Isolines are displayed as thin black solid lines. Transects over time **(A–A, B–B)** are indicated in each subfigure **(A–C)** as dashed lines. Time histories at these transects are displayed in subfigures **(D–F)**.

waves over compound bathymetries. First, some qualitative observations will be presented before flow depth and velocities as well as Froude numbers are investigated next.

3.2.1 Qualitative Observations

To introduce the data set of computed results with 84 individual tests, all of them with changing domain size, bottom profile, and impoundment depth, a qualitative analysis is performed first. The analysis is based on the velocity field (left column of **Figure 7**) and the turbulent kinetic energy (TKE, right column of **Figure 7**) in the *x-z* plane at two instants in time. The analysis first looks at the time $T(pos_{front} = 9\text{m})$, which is the instant in time when the wavefront reached the end of the computational domain, and afterward at the time $T = T_{sim}$ (see **Eq. 2**) representing the end of the computational time.

Visual inspection of the surface elevation data along with the velocity fields and the TKE in the *x-z* plain has led to a classification of numerical test runs described hereafter in **Table 3**. The classification introduces four classes the authors identified (hereinafter referred to as classes C1 to C4), which are used in the subsequent data evaluation. **Table 3** also indicated whether the surface elevation, front velocity, and Froude number of the classes are typically smaller or larger than the reference tests, where no composite bathymetry is present.

Although the classification presented in **Table 3** is qualitative at this point, the subsequent data analysis of each class presents a

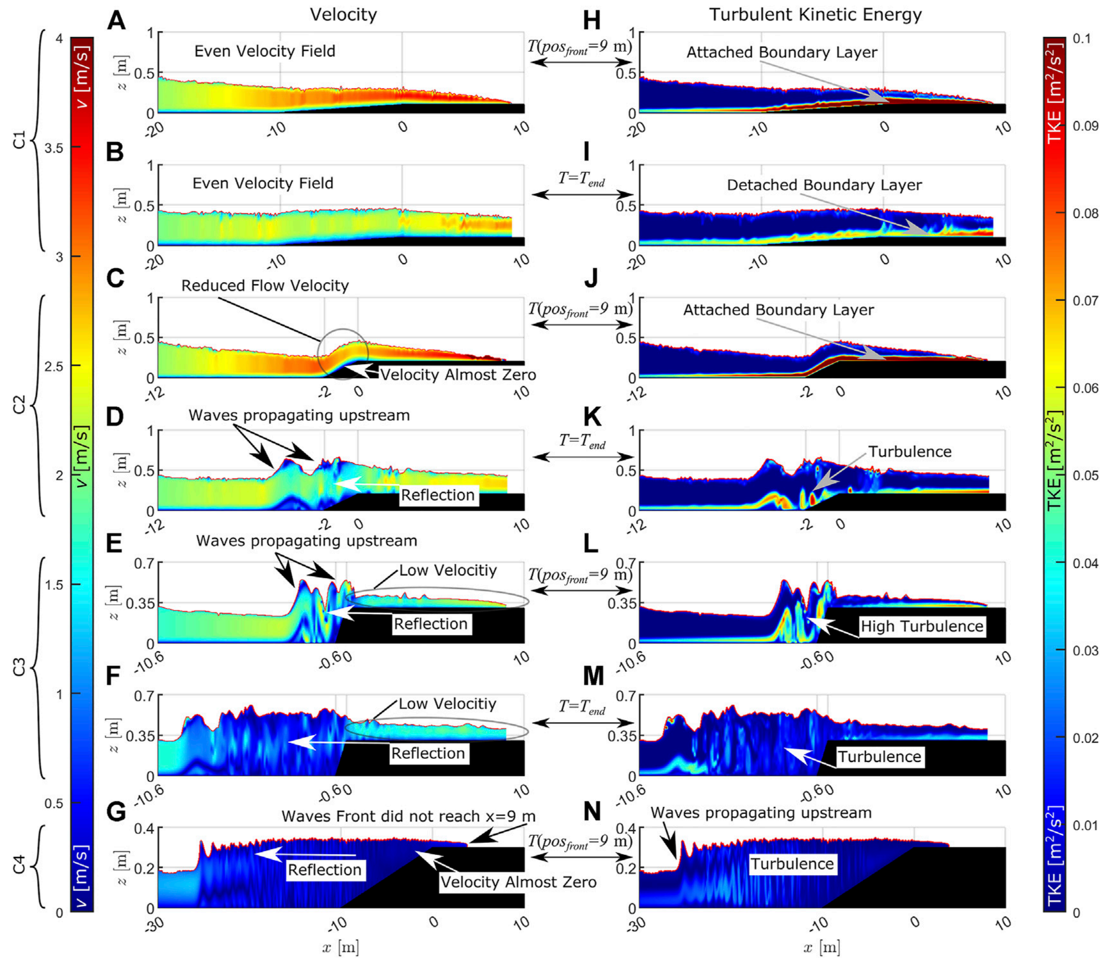

FIGURE 7 | Velocity fields (left column) and turbulent kinetic energy (right columns) of classes C1–C4 (indicated by brackets on the left) at two instants in time (upper and lower row of each class) of class C1 **(A,B,H,I)**, class C2 **(C,D,J,K)**, class C3 **(E,F,L,M)**, and class C4 **(G,N)**. Velocities are given in bolt and the turbulent kinetic energy in **m**^{2}/**s**^{2}. The composite bathymetry is indicated as a black area.

quantitative classification. However, since surface elevations, front velocities, and Froude numbers always depend on space, time, and the initial impoundment depth **(A-C)**, no absolute values can be given per class in **Table 3**.

Looking at the flow visualizations mentioned earlier, it becomes clear that the complex two-dimensional flow patterns observed on the slope in classes C2–C4 cannot be represented well by a depth-averaged numerical approach, such as the shallow water wave equations (SWE). This explains the numerical results observed when validating the model (see **Section 2.2**); the SWE represented tests without a composite bathymetry were accurate and highly efficient in terms of computational time. However, once a composite bathymetry profile is installed, averaging over the water columns is an oversimplification as can be seen in **Figure 7**.

The remainder of this work uses a couple of definitions that are defined next. A "class" describes a group of tests showing similar hydrodynamics, as described earlier. 'Class-averaged' means that all data belonging to a class are averaged (eventually further subdivided into the different impoundment depths). The entire dataset of 81 tests is next classified into the previously defined classes. To link the geometrical parameters of the composite bathymetry with the previously identified classes (C1-C4, **Figure 7**), all tests are analyzed and displayed dimensionless in **Figure 8**.

The dimensionless abscissa of **Figure 8** shows that for large impoundment depth (**Figure 8C**) and $W = 0.3\,[-]$, classes C1–C3 are mostly observed, while for small impoundment depth (**Figure 8A**), only C3 classes occur, comparing the same W -value. Thus, the smaller the impoundment depth, the more pronounced the reflections for the same dimensionless height W of the horizontal plane. Taking the ordinate into account, which displays the dimensionless slope steepness, it is revealed that the steeper the slope (large w/l_{sl} values), the more pronounced the occurrence of reflections (C2–C4 classes). Based on the findings presented in the previous section, an obvious relation between class occurrence and x_{toe}, represented by the triangle, circle, and plus signs, was expected. These symbols always lie on top of each other since each test is performed with each value of x_{toe}. A dependency on x_{toe} would result in changing color coding of the

TABLE 3 | Class definition and relation of flow features to reference tests.

Class	Qualitative observation (Figure 7)	Relation to reference tests		
		Surface elevation (**Figure 10**)	Front velocity (**Figure 11**)	Froude number (**Figure 13**)
C1	The velocity field is uniform at both time steps (**Figures 7A, B**). No turbulence outside the boundary layer can be observed in the first time step (**Figure 7H**), and only minor turbulences in the second one (**Figure 7I**). No reflections can be observed. It is expected that C1 leads to minor energy dissipation. Thus, this class is associated with an *almost unaffected flow*. The ratio $W = w/d_0$ is fairly small (see **Figure 8**), indicating that the impoundment depth or the flow depth of the dam-break wave is large as compared to the change in elevation as a result of the compound beach	Sig. larger	Slightly smaller	Sig. larger
C2	At the instant when the wavefront reaches $x = 9$ m, the velocity field is uniform (**Figure 7C**) and without significant reflections or turbulences (**Figure 7J**) visible. At the end of the computational time, however, reflections, characterized by waves propagating upstream, are observed (**Figure 7D**) as well as turbulences (**Figure 7K**). The energy dissipation is expected to be significantly higher than in C1; **Figure 7C** shows an area of reduced flow velocities and a thicker boundary layer with smaller velocities compared to the flow downstream (on the horizontal plane) and upstream the slopes' toe. This class is associated with a flow *moderately reflected.* This class is also associated with medium numbers for the ratio *W*	Slightly larger	Smaller	Slightly larger
C3	At both instants in time selected for the classification analysis (**Figures 7E, F**), pronounced reflections, along with high turbulences (**Figures 7L, M**), which are associated with high energy dissipation, are observed. This class is associated with *pronounced reflections.* This class is also associated with large numbers for the ratio *W*	Smaller	Sig. smaller	Sig. smaller
C4	Almost the entire reflection leads to very minor or no overland flow at all (**Figure 7G**). Within the computational time, the wavefront did not reach the end of the horizontal plane. This class is associated with a *total reflection.* This class is also associated with large numbers for the ratio *W*	Almost zero	Almost zero	Not calculated

signs laying on top of each other, however, this cannot be seen; a finding being discussed in **Section 4**. In conclusion, the more pronounced the reflections (increasing order of the class numbers):

1) the smaller the initial impoundment depth (d_0),
2) the larger the dimensionless height of the horizontal plane (W), and
3) the steeper the slope (w/l_{sl}).

A dimensionless slope steepness larger than approximately $W \sim 0.55$ is found to be a delimitation criterion above which very minor to no overland flow is observed (class C4; total reflection).

3.2.2 Flow Depth on Horizontal Plane

After classifying the investigated tests, the flow conditions as a result of the dam-break waves are investigated next. To that end, the flow depth at the transition point between the slope and the upper horizontal elevation ($x = 0$ m) is considered. **Figure 9** shows the class-averaged surface elevation time histories at this position. They are normalized over the initial impoundment depth (d_0) and displayed over the dimensionless time ($T = t\sqrt{g/d_0}$) for each impoundment depth separately. Classes are indicated as colored areas which extend plus-minus the standard deviation (σ) above and below the class-averaged time-histories ($\overline{\eta/d_0}$). Lines (solid, dashed, and dotted) represent approximations of the time histories. Coefficients of determination (r^2) between time histories and approximations are given.

Figure 9 shows a dependency of the dimensionless class-averaged surface elevation time-histories on the initial impoundment depth; the larger the initial impoundment depth, the larger the dimensionless flow depth. This observation reveals that flow depth at the transition point is disproportional to the initial impoundment depth. However, it is common practice to normalize the flow depth of a dam-break wave over the initial impoundment depth (see e.g., Lauber and Hager, 1998; Chanson, 2009; Nouri et al., 2010; Oertel and Bung, 2012; Goseberg et al., 2013; Goseberg and Schlurmann, 2014; Hooshyaripor et al., 2017; von Häfen et al., 2018; Wüthrich et al., 2018; von Häfen et al., 2019; von Häfen et al., 2021). This observation is being discussed further in **Section 4**. Considering the classes C1–C3, it becomes apparent that C3 (pronounced reflections) leads to a steeper increasing surface elevation time history than C2 (medium reflections) or C1 (minor/no reflections) (see **Figure 9B** or **Figure 9C**). Thus, the more dominant the reflections in the run-up/overland flow evolution, the faster the surface elevation increases at the beginning of the time histories. Tests associated with pronounced reflections (C3) also lead to larger flow depth than C2 or C1. In addition, the larger the standard deviation, the more pronounced the reflection. To predict the class-averaged surface elevation time history, an approximation is fitted to the data, which is a function of the initial impoundment depth, the dimensionless time, and the class, that follows the form of **Eq. 3** with the coefficients $(a - g)$ given in **Table 4**. **Eq. 3** is an exponential function over dimensionless time with a linear dependency on the initial impoundment depth, and it reads as follows:

$$\frac{\boldsymbol{\eta}}{\boldsymbol{d0}}\left(\boldsymbol{d}_0, \boldsymbol{T}, \boldsymbol{C}\right) = \{\boldsymbol{a}\,\boldsymbol{d}_0 + \boldsymbol{b}\}\boldsymbol{e}^{-\{\boldsymbol{c}\ \boldsymbol{d}_0 + \boldsymbol{d}\}\boldsymbol{T}} + \{\boldsymbol{f}\,\boldsymbol{d}_0 + \boldsymbol{g}\}\,[-]. \qquad (3)$$

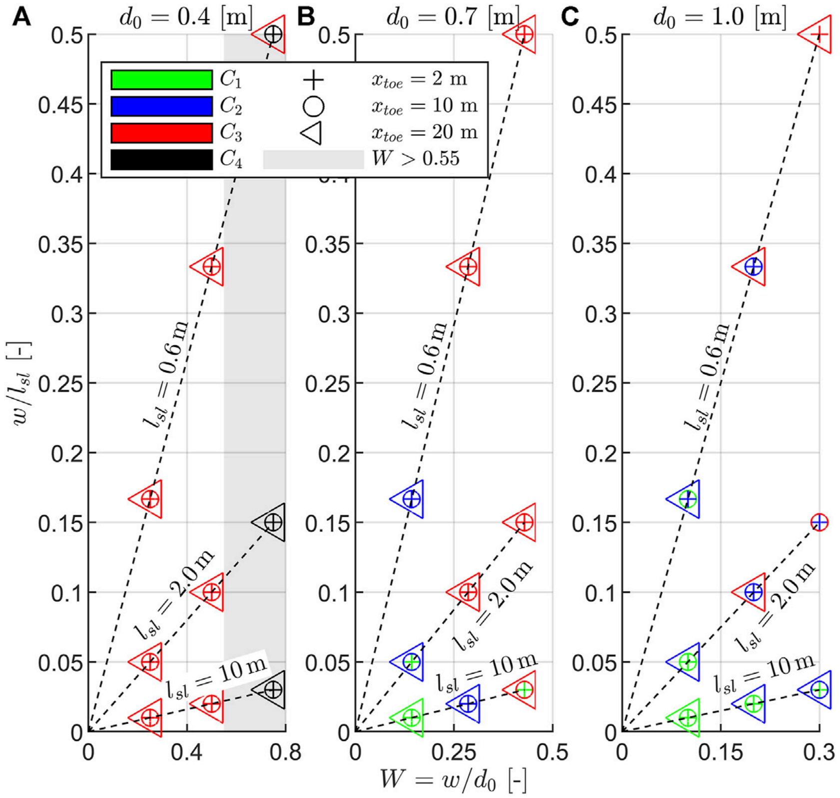

FIGURE 8 | Dimensionless visualization of the observed classes in relation to the composite bathymetries' parameters; slope steepness on the ordinate, dimensionless elevation of the horizontal plane (W) on the abscissa, and x_{toe} indicated by markers and separated by initial impoundment depth **(A-C)**. Dashed lines indicate tests with equal slope length. Classes are indicated by colors. Gray-shaded area covers W-values larger than ~0.55 (only visible in **(A)**), which is found to be a delimitation criterion above which no overland flow is observed (class C4; total reflection).

To obtain information about the class-averaged surface elevation over the entire length of the horizontal plane, surface elevation lines (η over space, referred to as SEL) are calculated at three instants in time. The surface elevation lines are normalized using the reference tests (η_{ref}, plain horizontal bottom, no composite bathymetry present) as displayed in **Figure 10**.

Figure 10A shows SELs for three dimensionless instants in time; the instant when the wavefront reaches the end of the horizontal plane and two later ones (plus $\Delta T = 4$ and $\Delta T = 12$). The following can be extracted from **Figure 10A**:

1) Independent of time and space, tests associated with minor reflections and turbulences (C1) show overall larger normalized flow depths than those tests with more pronounced reflections (C2 and C3).
2) Class C3 shows smaller flow depths than the reference tests. This is due to the significant energy dissipation and reflection associated with this class. Class C2 shows normalized flow depths close to one (except for the peaks at $x = 6$ m), while C1 shows the largest normalized flow depth.
3) Close to the transition point ($x = 0$ m), larger class-averaged normalized flow depths are observed than further downstream (except for the peaks at $x = 6$ m). This is due to the inertia of the flow coming from the slope and evolving over the slope transition into the horizontal plane. This leads to a change in flow direction at the transition point, which is associated with forces (gravity in this case) acting on the flow.
4) Thus, the stronger the effect is, the more pronounced the change in flow direction in relation to flow velocity is. Therefore, this effect is more pronounced for C3 (pronounced reflections due to steep and high slopes, see **Figure 8** for class occurrence with respect to the slope parameters) than for C2. For C1, almost no change in flow depth at the transition point is observed.

Peaks are observed in the class-averaged dimensionless SEL for all classes (C1–C3) and for $\Delta T = 0$. **Figure 10B** reveals the cause of the peaks' occurrence; in some tests, a leading bore front is observed in the surface elevation (solid line in **Figure 10B**) and in the reference SEL too. The dashed vertical line in **Figure 10** indicates that small surface elevation in the reference class (SEL_{ref}) occurs simultaneously with large surface elevation in the concerned tests, leading to the peaks in the normalized surface elevation in **Figure 10A**. This phenomenon, which is discussed in **Section 5**, is typical for dam-break waves. Therefore, velocity time histories are not displayed, but median velocities over space normalized by the velocity of the corresponding reference tests (c_{ref}) are provided in **Figure 11**.

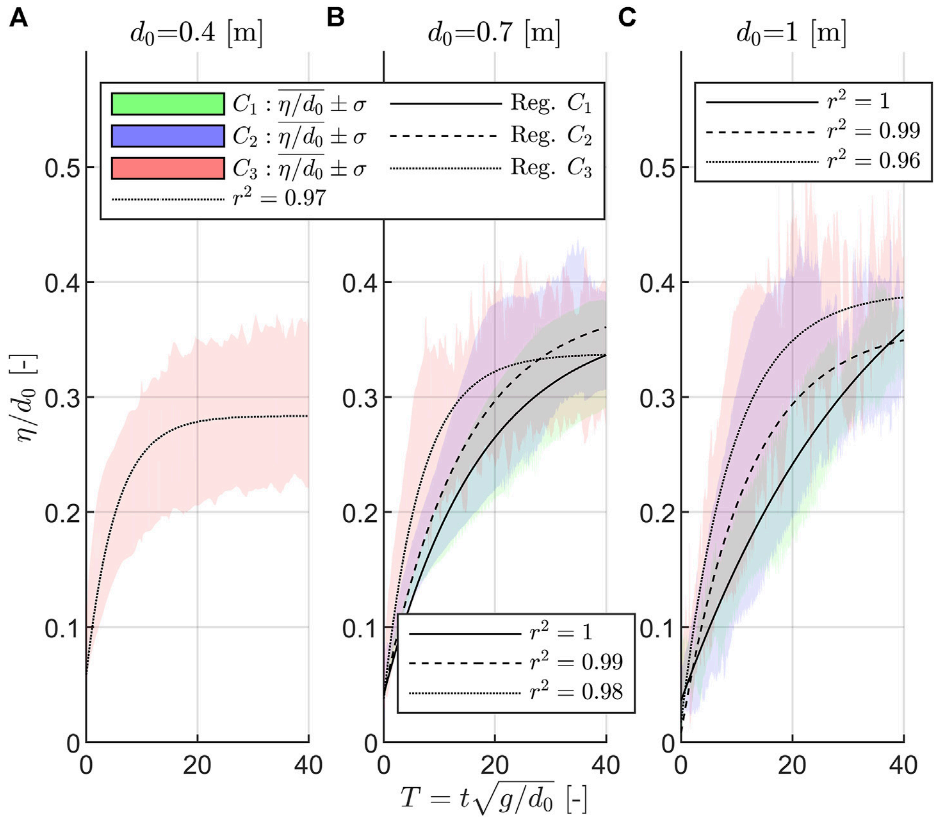

FIGURE 9 | Class-averaged normalized surface elevation time history (η/d_0, on the ordinate) separated by classes (C1–C3) at the transition point (x = 0 **m**) over dimensionless time ($T = t\sqrt{g/d_0}$) and separated by initial impoundment depth **(A–C)**. Colored areas represent class-averaged surface elevation time history plus-minus the standard deviation. Lines represent an approximation following **Eq. 3**. Coefficients of determination (r^2) between time histories and approximations are given.

TABLE 4 | Coefficients to **Eq. 3**.

	a	b	c	d	f	g
C_1	−0.490	0.016	−0.096	0.124	0.474	0.038
C_2	−0.044	−0.310	0.041	0.041	−0.064	0.427
C_3	−0.248	−0.126	−0.133	0.241	0.180	0.212

Figure 11 covers all front velocities for tests belonging to C1–C3, and C4 (almost the entire reflection) is excluded as almost no overland flow occurred in this class. The following can be extracted from the data analysis and **Figure 11**:

1) The higher the horizontal plane, the lower the front velocity. This observation is plausible since the larger the height of the horizontal plane, the more pronounced the reflections, and thus the energy dissipation increases considerably.
2) The median c/c_{ref} - values are always smaller than unity. The median wavefront velocity is slower than the corresponding reference. Due to energy dissipation on the composite bathymetry, which is not present in the reference class, this observation is plausible too.
3) In contrast to all other data points, the data for the smallest dimensionless height of the horizontal plane (w/d_0 = 0.1) shows a 75th percentile larger than one, indicating that the wavefront is moving faster than the reference class. This phenomenon can be explained by a fast-moving leading bore front (see **Figure 10B**) observed in many of these tests.
4) The decreasing trend, indicated by the black solid line, is almost linear up to $W = 0.43$. For larger values, the front velocity, however, rapidly decreases. The linear trend is due to the fact that the larger the normalized height of the horizontal plane, the more pronounced the reflections. The rapid decrease for values beyond $W = 0.43$ is caused by almost the entire energy being dissipated at the slope. In line with the qualitative observations (see **Figure 8**), total reflections and consequently front velocities of zero are expected for values larger than $W \sim 0.55$.

The approximation and its extrapolation, to be seen in **Figure 11**, read as follows:

$$\frac{c}{c_{ref}} = e^{-0.53(w/d_0)} - 10^{-8}e^{33(w/d_0)}[-], \qquad (4)$$

where c is the front velocity of the overland flow, c_{ref} is the front velocity of the reference class at the same longitudinal distance to the waves' origin, w is the height of the horizontal plane, and d_0 is the initial impoundment depth. The

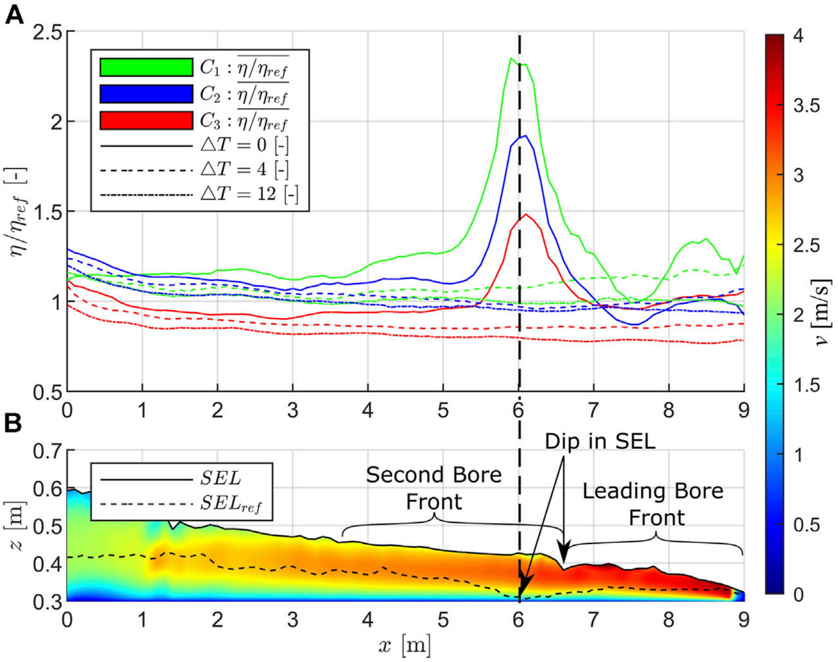

FIGURE 10 | Visualization of class-averaged surface elevation lines (SELs) over space **(A)**. Classes are indicated by color and instants in time by line type. Local flow velocities **(B)** are color coded according to the color bar, Reference SEL by a dashed line. Dimensionless time steps Δ***T*** describe the additional time after wavefront first reached the end of the horizontal plane at ***x*** = 9 **m**.

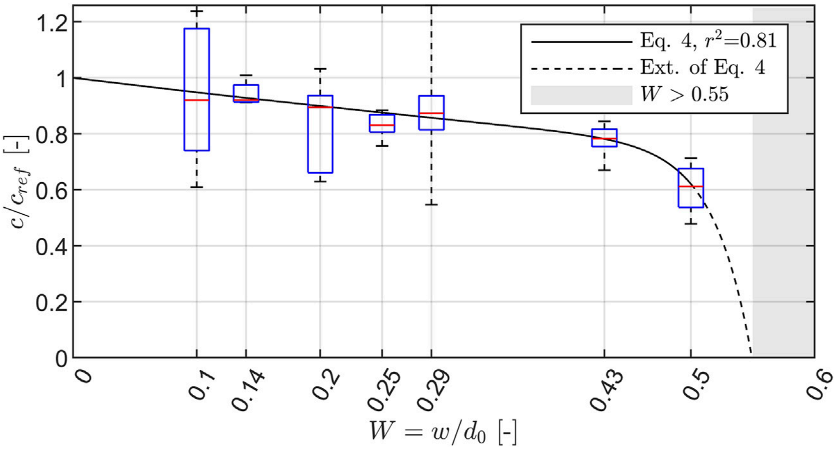

FIGURE 11 | Bore front velocities (***c***) normalized over the corresponding reference front velocities (***c_{ref}***, no compound beach present) and averaged over space using the median. Data are plotted over the height of the horizontal plane normalized over the initial impoundment depth (***W*** = ***w***/***d***$_0$). Boxplots are defined as follows: the median is indicated as a red bar, and the box indicates the 75th and 25th percentile, respectively. Whiskers extend to the most extreme data points. The black solid line represents the approximation given by **Eq. 4**. The dashed line indicates the extrapolation of **Eq. 4**. Gray-shaded area covers values of W larger than 0.55, where no overland flow is observed.

approximation correlates well with the median values (red bars in **Figure 11**, $r^2 = 0.81$).

3.2.3 Froude Number on Horizontal Plane

The dimensionless Froude number can be calculated based on the flow velocity and the corresponding water depth at a certain position over time and is frequently reported in studies about post-tsunami surveys (e.g., Fritz et al., 2006b). In **Figures 12G and H**, the depth-averaged Froude number at the transition point ($x = 0$ m) over dimensionless time is displayed beside the corresponding surface elevation time histories (**Figures 12A–C**) and depth-averaged flow velocities (**Figures 12D–F**) separated by initial impoundment depth

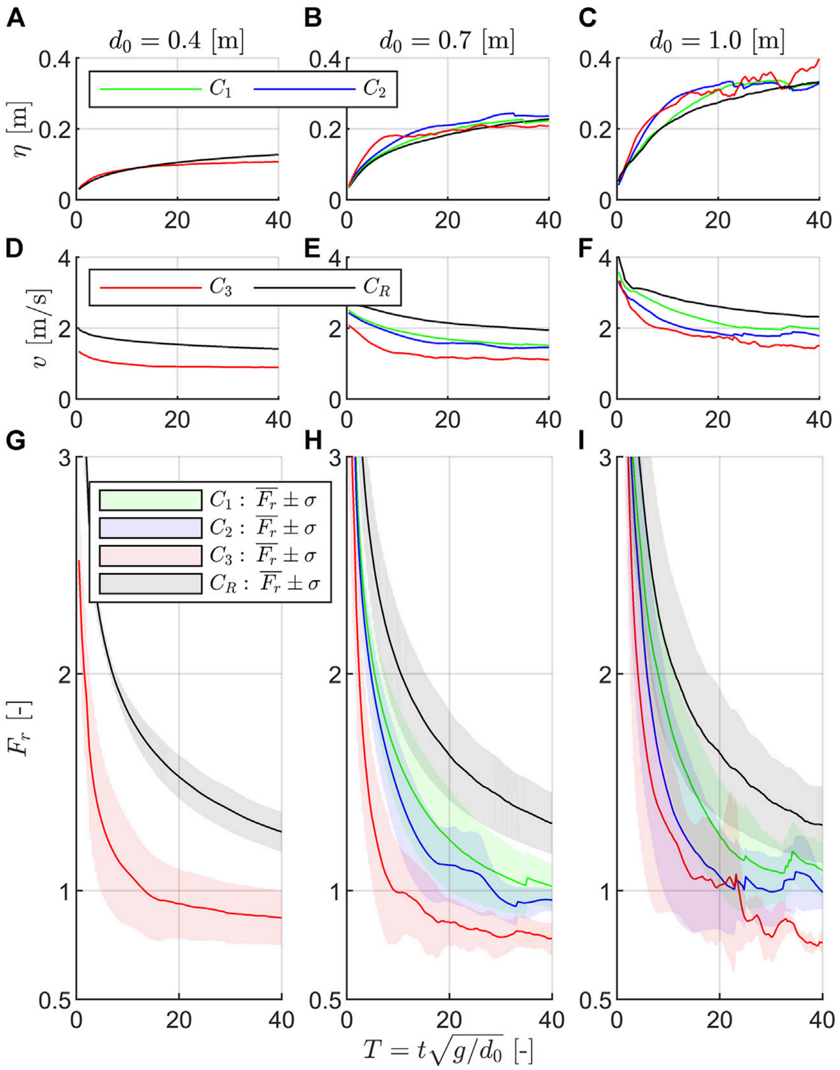

FIGURE 12 | Visualization of class-averaged surface elevation (η, **(A–C)**), depth- and class-averaged velocity (v, **(D–F)**), and class-averaged Froude number (Fr, **(F–I)**) at the transition point over dimensionless time and separated by initial impoundment depth (d_0). Standard deviation (2 σ) is displayed as a shaded area.

and class. Reference time histories are extracted from the reference tests for each considered test using the same distance between the idealized gate and transition point (since hydrodynamics change over space, as presented in **Section 3.1**). All time histories displayed in **Figure 12** are class averaged.

Figures 12A–C show that flow depths at the transition point are similar to the reference tests without a composite bathymetry present. **Figures 12D–F**, however, reveal flow velocities significantly smaller than the reference. The more pronounced the reflections (higher class number), the lower the depth-averaged flow velocities. In general, all velocity time histories show higher values at the beginning and decrease over time. The following can be extracted from **Figures 12G–I** displaying the Froude time histories:

1) In the first instant, very large Froude numbers are observed, rapidly decreasing over time. These high values are typical for dam-break waves and are due to the small flow depths combined with the large flow velocities in the wavefront.
2) The Froude numbers at the transition point of a composite bathymetry are generally smaller compared to those without such a bottom profile.
3) The more pronounced the reflections (thus, the higher the class number), the smaller the Froude numbers. This is caused by the flow velocities showing the same trend.
4) Class C3 shows, for later instants, Froude numbers smaller than one. Thus, the flow changes from super to subcritical.

To obtain spatial information about Froude numbers on the horizontal plane, three dimensionless instants in time ΔT after wavefront arrival at $x = 9$ m (end of the horizontal plane) are selected with $\Delta T = [4, 8, 12]$. **Figure 13** displays class-averaged Froude numbers over space (indicated as thin, colored lines) and

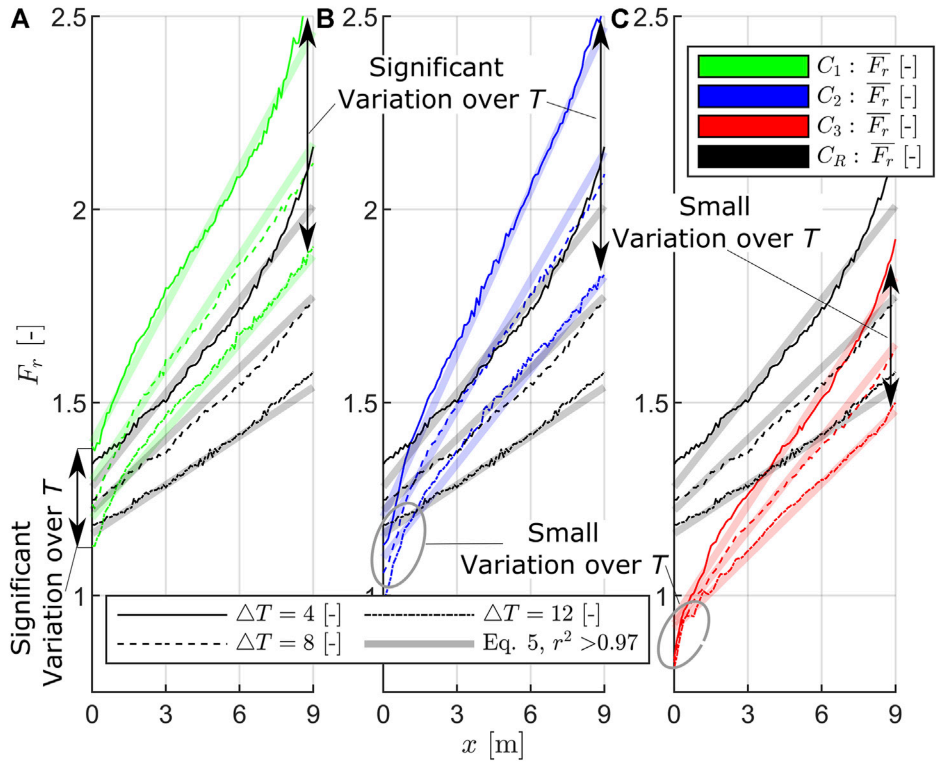

FIGURE 13 | Visualization of class-averaged Froude numbers (thin lines) over space (at the horizontal plane) at three dimensionless instants in time $\Delta \boldsymbol{T} = [4, 8, 12]$. Data are displayed separately per class **(A–C)**. The multilinear approximation is displayed as wide transparent lines.

the reference tests. A multilinear approximation as given by **Eq. 5** is indicated in wide, transparent lines.

The following findings can be extracted from **Figure 13**:

1) Froude numbers are independent of space, the smaller the Froude numbers are, the more pronounced the reflections (higher class numbers) are.
2) Class C3 (pronounced reflections) shows overall smaller Froude numbers than the reference, while for the classes with no and minor reflections (C1 and C2), Froude numbers are, except for the transition point at $x = 0$ m, always larger than the reference.
3) The Froude numbers rise over space; this is typical for dam-break waves showing the largest Froude numbers in the wavefront region, decreasing downstream, where water depth increases and flow velocities decrease.
4) The Froude numbers show an almost linear trend over space; the more pronounced the linear trend, the smaller the influences of the composite bathymetry. However, the reference class shows the weakest linear trend; especially for $\Delta T = 4$, the linear approximation underestimates the reference class at $x = 0$ m and $x = 9$ m. This can be explained as follows: for large x-values, the approximation underestimates all Froude numbers. For small x-values, the approximation underestimates the reference class significantly, while the composite bathymetry tests are slightly overestimated. This is due to the transition point lowering the Froude numbers here.
5) The differences between the Froude numbers at the transition point differ from class to class; while the reference and C1 (**Figure 13A**) show a significantly changing Froude number over time at $x = 0$ m (in the same order of magnitude of the reference class); tests with more pronounced (C2) and significant reflection (C3) show a small variation in Froude number at the transition point over time. This is probably due to the strong turbulence on the slope associated with classes C2 and C3, partially interrupting the original hydrodynamics of the dam-break wave. This is indicated by the flow velocity at the transition point being significantly reduced compared to the reference tests (see **Figures 12D–F**).
6) Over space, the differences in Froude numbers increase over time. Thus, the largest variations in Froude number over time are observed at $x = 9$ m.

The approximation displayed in **Figure 13** is a multilinear function over space and dimensionless time. It is determined individually per class, yields a high coefficient of determination of $r^2 > 0.97$, and reads as follows:

$$\boldsymbol{F_r}(\boldsymbol{x}, \boldsymbol{T}, \boldsymbol{C}) = \{\boldsymbol{a}\,\boldsymbol{T} + \boldsymbol{b}\}\boldsymbol{x} + \{\boldsymbol{c}\,\boldsymbol{T} + \boldsymbol{d}\}[-]. \qquad (5)$$

Coefficients in **Eq. 5** are given in **Table 5**.

TABLE 5 | Coefficients to **Eq. 5**.

	a	b	c	d
C_1	−0.005	0.139	−0.024	1.494
C_2	−0.008	0.171	−0.013	1.247
C_3	−0.004	0.116	−0.003	0.953

4 DISCUSSION

It was observed that the class occurrence (**Figure 8**) as well as the normalized flow depth at the transition point (**Figure 9**) change with changing initial impoundment depth d_0, even though the data are normalized over the initial impoundment depth, which is a common normalization. This phenomenon is unexpected since a dam-break wave is driven by gravity only and its energy/ momentum is correlated with the initial impoundment depth. Theoretically, the larger the impoundment depth, the larger the ability to overcome a certain elevation (height of the horizontal plane). However, this study, which evaluates a large data set and focuses on the flow features on the horizontal plane, does not cover the complex processes on the slope. It is expected that vortex patterns, interactions of the incoming and reflected wave energy as well as the associated energy dissipation over the slope highly depend on the slope geometry and the initial impoundment depth, and that dam-break waves of smaller impoundment depth are more strongly affected by these effects.

As shown in **Section 3.1**, the distance between the gate and the place under consideration x_{toe} (e.g., the position of test setup in a flume) must be considered since the hydrodynamics of a dam-break wave change over space. Therefore, a clear dependency between x_{toe} and the class number (**Figure 8**) was originally expected but was not found. It is assumed that the turbulence on the slope disturbs the hydrodynamics of the dam-break wave to such an extent that these effects override the influence of x_{toe}.

Instead of a single leading bore front, in some classes, sequences of bores riding on top or next to each other were observed (see **Figure 10**). This phenomenon appears for both, the reference tests and the tests with composite bathymetries, but only at a distance of approximately 20 m downstream of the idealized gate and only for tests with an initial impoundment depth of 1 m. The formation of the leading bore is either an effect of the collapsing water column (like observed by Lauber (1997)) once the dam-break is initiated or due to disintegration of the wave while propagating. However, this study focuses on the flow features on the horizontal plane of the composite bathymetry, and thus this phenomenon is beyond the study's scope. Further research is required to investigate the observed phenomenon.

Wall and bottom roughness are not varied within the study but set to a fixed equivalent sand roughness of $k_s = 0.001$, representing a smooth surface. This roughness value compares well to the smooth surface of the composite bathymetry used in the physical tests and is a conservative assumption for the numerical parameter study since it leads to little friction and thus to large Froude numbers. Systematically varying the roughness with also three values (as performed for d_0, x_{toe}, w, and l_{sl}) would have increased the number of tests in the parameter study from 81 to 243 combinations. This would have tripled the computational time for the entire data set (from 50 days to about half a year), which would not have been possible within the scope of this study. However, it is expected that the bottom roughness influences the features of the overland flow, and hence future research should deepen research on this topic.

Froude numbers are found to be always larger than unity in the experiments, except for class C3 close to the transition point ($x = 0$ m in **Figure 13C**). In general, the larger the class order, the lower the Froude numbers. However, Fritz et al. (2006b) have reported that Froude numbers were close to unity during the 2004 Indian Ocean tsunami. Thus, even though a composite bathymetry can reduce Froude numbers in the experiment, the bathymetry profile alone is not enough to reach fully matching Froude numbers. It is expected that roughness elements (like the build environment) and debris lead to the lower Froude number observed by Fritz et al. (2006b). Generally, for both numerical and physical tests, Froude numbers should always be measured and test results qualified in terms of their comparability to real tsunami events.

The dimensionless ratio of the height of the horizontal plane to the initial impoundment depth $W \sim 0.55$ is found to be a delimitation criterion. For W values larger than approximately 0.55, only class C4 was observed and thus almost total reflection of the wave and only a little water on the horizontal plane. The wavefront did not reach the end of the computational domain within the simulation time. Shen and Meyer (1963) investigated the run-up of dam-break waves on a sloping bathymetry and found the following relationship:

$$\boldsymbol{R} = \boldsymbol{U}^2 / (2\boldsymbol{g}). \tag{6}$$

Equation 6 is based on the nonlinear shallow water equation, where R is the run-up height and U is the velocity on the slope toe. This relationship yields a dimensionless run-up height of $R/d_0 \sim 0.3$ for $U\,(d_0 = 0.4\text{ m}) \sim 1.5$ m/s observed in this study, being much smaller than the delimitation criterion $W = w/d_0 \sim 0.55$. However, as mentioned by Lu and Liu (2017), **Eq. 6** underestimates the run-up due to simplifications made by the shallow water equation, which is not capable of representing the flow features as observed in **Section 2.2**. Even though more refined approximations exist, they are not applicable to the present dataset due to using different boundary conditions (like an initially wet flume and limited reservoir length in Barranco and Liu (2021)) or waves (breaking dam-break waves used by Lu et al. (2018)) or bores (resulting from solitary waves used by Jensen et al. (2003)). The delimitation criterion found here should be verified in future work as well.

5 CONCLUSION

This study utilizes large-scale physical flume tests to validate and calibrate a numerical, two-dimensional CFD model. The numerical model is then used to investigate the flow features of a dam-break wave swashing over a composite bathymetry. Therefore, a parameter study is conducted altering all parameters influencing the dam-break waves' hydrodynamics and the geometry of the composite bathymetry. The study focuses on the flow features observed on the horizontal plane in analogy to an urbanized site inundated by a tsunami propagating over a sloping bathymetry. The following findings are obtained and justified by data:

1) Classes are first proposed based on a qualitative rating system to distinguish between typical flow patterns based on visual inspection, which allows an assessment of the degree of reflection or energy dissipation due to the bathymetry profile.
2) These classes are correlated with the parameters systematically altered within the parameter study. This allows for predicting the class that will occur within the investigated parameter range. In addition, the typical flow features associated with a class are related to reference tests, where no composite bathymetry is present.
3) Flow features observed and associated with a class are described quantitatively (flow depth, velocity, and Froude number) over space and time, and the observations are linked to the underlying physical processes.
4) Empirical equations for the flow depth, velocity, and Froude number are presented based on the proposed classes and hence provide an approximate prediction for each test investigated. It is found that the flow features on the horizontal plane are governed by the (dimensionless) height of the horizontal plane and the initial impoundment depth. The slope angle and the distance between dam-break initiation and the toe of the slope are of minor importance.
5) Apart from the parameter study, simple and basic analytical considerations are made to display the changing hydromechanics of a dam-break wave over space and time. Therefore, the distance between dam-break initiation and test setup should always be given and, ideally, also justified.

The findings and approximations presented in this study first allow for predicting the flow regime on the horizontal plane of a composite bathymetry and, therefore, provide an approximate design tool for laboratory testing and significantly gain process understanding of real-world tsunami inundations.

DATA AVAILABILITY STATEMENT

The raw data supporting the conclusions of this article will be made available by the authors, without undue reservation.

AUTHOR CONTRIBUTIONS

HvH, HB, and NG contributed to the conceptualization. HvH, CK, HB, and NG developed the methodology. HvH carried out the numerical simulations, with the supervision of HB and NG. HvH wrote the first draft of the manuscript and prepared the visualizations. HB and NG provided supervision. NG is responsible for project administration and funding acquisition. All authors contributed to manuscript revision and read and approved the submitted version.

FUNDING

The support of the Volkswagen Foundation (project 'Beyond Rigidity-Collapsing Structures in Experimental Hydraulics', No. 93826) through a grant held by NG is greatly acknowledged. We acknowledge support by the Open Access Publication Funds of Technische Universität Braunschweig.

REFERENCES

Ablain, M., Dorandeu, J., le Traon, P.-Y., and Sladen, A. (2006). High Resolution Altimetry Reveals New Characteristics of the December 2004 Indian Ocean Tsunami. *Geophys. Res. Lett.* 33 (21), 1–6. doi:10.1029/2006GL027533

Al-Faesly, T., Palermo, D., Nistor, I., and Cornett, A. (2012). Experimental Modeling of Extreme Hydrodynamic Forces on Structural Models. *Int. J. Prot. Struct.* 3 (4), 477–505. doi:10.1260/2041-4196.3.4.477

Aránguiz, R., Esteban, M., Takagi, H., Mikami, T., Takabatake, T., Gómez, M., et al. (2020). The 2018 Sulawesi Tsunami in Palu City as a Result of Several Landslides and Coseismic Tsunamis. *Coast. Eng. J.* 62 (4), 445–459. doi:10.1080/21664250.2020.1780719

Arnason, H., Petroff, C., and Yeh, H. (2009). Tsunami Bore Impingement onto a Vertical Column. *J. Disaster Res.* 4, 391–403. doi:10.20965/jdr.2009.p0391

Aureli, F., Dazzi, S., Maranzoni, A., Mignosa, P., and Vacondio, R. (2015). Experimental and Numerical Evaluation of the Force Due to the Impact of a Dam-Break Wave on a Structure. *Adv. Water Resour.* 76, 29–42. doi:10.1016/j.advwatres.2014.11.009

Bihs, H., Kamath, A., Alagan Chella, M., Aggarwal, A., and Arntsen, Ø. A. (2016). A New Level Set Numerical Wave Tank with Improved Density Interpolation for Complex Wave Hydrodynamics. *Comput. Fluids* 140, 191–208. doi:10.1016/j.compfluid.2016.09.012

Barranco, I., and Liu, P. L.-F. (2021). Run-up and Inundation Generated by Non-Decaying Dam-Break Bores on a Planar Beach. *J. Fluid Mech.* 915, A81. doi:10.1017/jfm.2021.98

Bernard, E., and Titov, V. (2015). Evolution of Tsunami Warning Systems and Products. *Phil. Trans. R. Soc. A* 373 (2053), 20140371. doi:10.1098/rsta.2014.0371

Borrero, J. C., Synolakis, C. E., and Fritz, H. (2006). Northern Sumatra Field Survey after the December 2004 Great Sumatra Earthquake and Indian Ocean Tsunami. *Earthq. Spectra* 22, 93–104. doi:10.1193/1.2206793

Brufau, P., and Garcia-Navarro, P. (2000). Two-Dimensional Dam Break Flow Simulation. *Int. J. Numer. Meth. Fluids* 33 (1), 35–57. doi:10.1002/(sici)1097-0363(20000515)33:1<35::aid-fld999>3.0.co;2-d

Cannata, G., Petrelli, C., Barsi, L., Fratello, F., and Gallerano, F. (2018). A Dam-Break Flood Simulation Model in Curvilinear Coordinates. *WSEAS Trans. Fluid Mech.* 13, 60–70.

Chan, I.-C., and Liu, P. L.-F. (2012). On the runup of Long Waves on a Plane Beach. *J. Geophys. Res. Oceans* 117 (8), 8006. Available at: https://www.scopus.com/inward/record.uri?eid=2-s2.0-84864859069&doi=10.1029%2f2012JC007994&partnerID=40&md5=ccce87da3709e91f78a82acef4b9ca81. doi:10.1029/2012jc007994

Chanson, H. (2009). Application of the Method of Characteristics to the Dam Break Wave Problem. *J. Hydraulic Res.* 47 (1), 41–49. doi:10.3826/jhr.2009.2865

Chanson, H. (2006). Tsunami Surges on Dry Coastal Plains: Application of Dam Break Wave Equations. *Coast. Eng. J.* 48 (4), 355–370. doi:10.1142/S0578563406001477

Chock, G., Carden, L., Robertson, I., Olsen, M., and Yu, G. (2013). Tohoku Tsunami-Induced Building Failure Analysis with Implications for U.S. Tsunami and Seismic Design Codes. *Earthq. Spectra* 29, 99–126. doi:10.1193/1.4000113

Chorin, A. J. (1968). Numerical Solution of the Navier-Stokes Equations. *Math. Comp.* 22 (104), 745–762. doi:10.2307/200457510.1090/s0025-5718-1968-0242392-2

Cross, R. H. (1967). Tsunami Surge Forces. *J. Wtrwy. Harb. Div.* 93, 201–231. doi:10.1061/jwheau.0000528

Derschum, C., Nistor, I., Stolle, J., and Goseberg, N. (2018). Debris Impact under Extreme Hydrodynamic Conditions Part 1: Hydrodynamics and Impact Geometry. *Coast. Eng.* 141, 24–35. doi:10.1016/j.coastaleng.2018.08.016

Dressler, R. F. (1952). Hydraulic resistance Effect upon the Dam-Break Functions. *J. Res. Natl. Bur. Stan.* 49, 217. doi:10.6028/jres.049.021

Dressler, R. F., and Stoneley, R. (1958). Unsteady Non-Linear Waves in Sloping Channels. *Proc. R. Soc. Lond. A* 247 (1249), 186–198. doi:10.1098/rspa.1958.0177

Farahmandpour, O., Marsono, A. K., Forouzani, P., Md Tap, M., and Abu Bakar, S. (2020). Experimental Simulation of Tsunami Surge and its Interaction with Coastal Structure. *Int. J. Prot. Struct.* 11 (2), 258–280. doi:10.1177/2041419619874082

Fernandez-Feria, R. (2006). Dam-Break Flow for Arbitrary Slopes of the Bottom. *J. Eng. Math.* 54 (4), 319–331. doi:10.1007/s10665-006-9034-5

Fritz, H. M., Borrero, J. C., Synolakis, C. E., and Yoo, J. (2006b). 2004 Indian Ocean Tsunami Flow Velocity Measurements from Survivor Videos. *Geophys. Res. Lett.* 33 (24), 1–5. doi:10.1029/2006GL026784

Fritz, H. M., Petroff, C. M., Catalán, P. A., Cienfuegos, R., Winckler, P., Kalligeris, N., et al. (2011). Field Survey of the 27 February 2010 Chile Tsunami. *Pure Appl. Geophys.* 168 (11), 1989–2010. doi:10.1007/s00024-011-0283-5

Fritz, H. M., Phillips, D. A., Okayasu, A., Shimozono, T., Liu, H., Mohammed, F., et al. (2012). The 2011 Japan Tsunami Current Velocity Measurements from Survivor Videos at Kesennuma Bay Using LiDAR. *Geophys. Res. Lett.* 39 (7), 1–6. doi:10.1029/2011GL050686

Fritz, H. M., Synolakis, C. E., and McAdoo, B. G. (2006a). Maldives Field Survey after the December 2004 Indian Ocean Tsunami. *Earthq. Spectra* 22, 137–154. doi:10.1193/1.2201973

Ghobarah, A., Saatcioglu, M., and Nistor, I. (2006). The Impact of the 26 December 2004 Earthquake and Tsunami on Structures and Infrastructure. *Eng. Struct.* 28 (2), 312–326. doi:10.1016/j.engstruct.2005.09.028

Ghodoosipour, B., Stolle, J., Nistor, I., Mohammadian, A., and Goseberg, N. (2019). Experimental Study on Extreme Hydrodynamic Loading on Pipelines Part 2: Induced Force Analysis. *J. Mar. Sci. Eng.* 7 (8), 262. doi:10.3390/jmse7080262

Goff, J., Liu, P. L.-F., Higman, B., Morton, R., Jaffe, B. E., Fernando, H., et al. (2006). Sri Lanka Field Survey after the December 2004 Indian Ocean Tsunami. *Earthq. Spectra* 22, 155–172. doi:10.1193/1.2205897

Goseberg, N., and Schlurmann, T. (2014). "Non-Stationary Flow Around Buildings during run-Up of Tsunami Waves on a Plain Beach," in Proceedings of the Coastal Engineering Conference, Seoul, Republic of Korea, 2014-January. https://www.scopus.com/inward/record.uri?eid=2-s2.0-84957625748&partnerID=40&md5=4bfcf145c56fef3f5cf81766453d6f77. doi:10.9753/icce.v34.currents.21

Goseberg, N., Wurpts, A., and Schlurmann, T. (2013). Laboratory-Scale Generation of Tsunami and Long Waves. *Coast. Eng.* 79, 57–74. doi:10.1016/j.coastaleng.2013.04.006

Grue, J., Pelinovsky, E. N., Fructus, D., Talipova, T., and Kharif, C. (2008). Formation of Undular Bores and Solitary Waves in the Strait of Malacca Caused by the 26 December 2004 Indian Ocean Tsunami. *J. Geophys. Res.* 113 (C5), 1–14. doi:10.1029/2007JC004343

Hooshyaripor, F., Tahershamsi, A., and Razi, S. (2017). Dam Break Flood Wave under Different Reservoir's Capacities and Lengths. *Sādhanā* 42 (9), 1557–1569. doi:10.1007/s12046-017-0693-x

Hunt, B. (1983). Asymptotic Solution for Dam Break on Sloping Channel. *J. Hydraul. Eng.* 109 (12), 1698–1706. doi:10.1061/(asce)0733-9429(1983)109:12(1698)

Hunt, B. (1984). Perturbation Solution for Dam-Break Floods. *J. Hydraul. Eng.* 110 (8), 1058–1071. doi:10.1061/(asce)0733-9429(1984)110:8(1058)

Iaccarino, G., Ooi, A., Durbin, P. A., and Behnia, M. (2003). Reynolds Averaged Simulation of Unsteady Separated Flow. *Int. J. Heat Fluid Flow* 24 (2), 147–156. doi:10.1016/S0142-727X(02)00210-2

Jaffe, B. E., Borrero, J. C., Prasetya, G. S., Peters, R., McAdoo, B., Gelfenbaum, G., et al. (2006). Northwest Sumatra and Offshore Islands Field Survey after the December 2004 Indian Ocean Tsunami. *Earthq. Spectra* 22, 105–135. doi:10.1193/1.2207724

Jensen, A., Pedersen, G. K., and Wood, D. J. (2003). An Experimental Study of Wave run-Up at a Steep Beach. *J. Fluid Mech.* 486, 161–188. doi:10.1017/S0022112003004543

Jeschke, A., Pedersen, G. K., Vater, S., and Behrens, J. (2017). Depth-Averaged Non-Hydrostatic Extension for Shallow Water Equations with Quadratic Vertical Pressure Profile: Equivalence to Boussinesq-Type Equations. *Int. J. Numer. Meth. Fluids* 84 (10), 569–583. doi:10.1002/fld.4361

Jiang, G.-S., and Shu, C.-W. (1996). Efficient Implementation of Weighted ENO Schemes. *J. Comput. Phys.* 126, 202–228. doi:10.1006/jcph.1996.0130

Khan, A. A., Steffler, P. M., and Gerard, R. (2000). Dam-Break Surges with Floating Debris. *J. Hydraul. Eng.* 126 (5), 375–379. doi:10.1061/(asce)0733-9429(2000)126:5(375)

Krautwald, C., Stolle, J., Robertson, I., Achiari, H., Mikami, T., Nakamura, R., et al. (2021). Engineering Lessons from September 28, 2018 Indonesian Tsunami: Scouring Mechanisms and Effects on Infrastructure. *J. Waterw. Port Coast. Ocean Eng.* 147 (2). doi:10.1061/(ASCE)WW.1943-5460.0000620

Kuswandiand Triatmadja, R. (2019). The Use of Dam Break Model to Simulate Tsunami run-Up and Scouring Around a Vertical Cylinder. *J. Appl. Fluid Mech.* 12 (5), 1395–1406. doi:10.29252/JAFM.12.05.29216

Lauber, G. (1997). Experimente zur talsperrenbruchwelle im glatten geneigten rechteckkanal. *Mitteilungen Der Versuchsanstalt Fur Wasserbau Hydrologie Und Glaziologie Der Eidgenossischen Tech. Hochschule Zurich* 152, X–122. Available at: https://www.scopus.com/inward/record.uri?eid=2-s2.0-7044284910&partnerID=40&md5=438fbfb667430f61499e69ab48cc044a.

Lauber, G., and Hager, W. H. (1998). Experiments to Dambreak Wave: Horizontal Channel. *J. Hydraulic Res.* 36 (3), 291–307. doi:10.1080/00221689809498620

Li, X., Li, G., and Ge, Y. (2020). A New Fifth-Order Finite Difference WENO Scheme for Dam-Break Simulations. *Adv. Appl. Math. Mech.* 13 (1), 58–82. doi:10.4208/aamm.OA-2019-0155

Liang, D. (2010). Evaluating Shallow Water Assumptions in Dam-Break Flows. *Proc. Institution Civ. Eng. - Water Manag.* 163 (5), 227–237. doi:10.1680/wama.2010.163.5.227

Lu, S., and Liu, H. (2017). "An Experimental Study of the Maximum Run-Up Height under Dam-Break Flow on the Initial Dry-Bed," in The 9th International Conference on Asia and Pacific Coasts 2017 (APAC 2017), 19-21 October 2017, Pasay City, Philippines. doi:10.1142/9789813233812_0030

Lu, S., Liu, H., and Deng, X. (2018). An Experimental Study of the Run-Up Process of Breaking Bores Generated by Dam-Break under Dry- and Wet-Bed Conditions. *J. Earthq. Tsunami* 12 (02), 1840005. doi:10.1142/S1793431118400055

Madsen, P. A., Fuhrman, D. R., and Schäffer, H. A. (2008). On the Solitary Wave Paradigm for Tsunamis. *J. Geophys. Res.* 113 (12), 1–22. doi:10.1029/2008JC004932

Madsen, P. A., and Schäffer, H. A. (2010). Analytical Solutions for Tsunami runup on a Plane Beach: Single Waves, N-Waves and Transient Waves. *J. Fluid Mech.* 645, 27–57. Available at: https://www.scopus.com/inward/record.uri?eid=2-s2.0-77952357556&doi=10.1017%2fS0022112009992485&partnerID=40&md5=acf686fbaf1b29b60f6c120968191e69. doi:10.1017/s0022112009992485

Maqtan, R., Yusuf, B., and Hamzah, S. B. (2018). Physical Modeling of Landward Scour Due to Tsunami Bore Overtopping Seawall. *MATEC Web Conf.* 203, 01003. doi:10.1051/matecconf/201820301003

Matsutomi, H., Okamoto, K., and Harada, K. (2010). "Inundation Flow Velocity of Tsunami on Land and its Practical Use," in Proceedings of 32nd Conference on Coastal Engineering, 30 June-5 July 2010, Shanghai, China. Available at: https://www.scopus.com/inward/record.uri?eid=2-s2.0-84864456954&partnerID=40&md5=c7a636e6c0606091eca5f0bcf450a550.

Matsuyama, M., Ikeno, M., Sakakiyama, T., and Takeda, T. (2007). A Study of Tsunami Wave Fission in an Undistorted Experiment. *Pure Appl. Geophys.* 164 (2–3), 617–631. doi:10.1007/s00024-006-0177-0

Mikami, T., Shibayama, T., Esteban, M., and Matsumaru, R. (2012). Field Survey of the 2011 Tohoku Earthquake and Tsunami in Miyagi and Fukushima Prefectures. *Coast. Eng. J.* 54 (1), 1250011-1–1250011-26. doi:10.1142/S0578563412500118

Mikami, T., Shibayama, T., Esteban, M., Takabatake, T., Nakamura, R., Nishida, Y., et al. (2019). Field Survey of the 2018 Sulawesi Tsunami: Inundation and Run-

Up Heights and Damage to Coastal Communities. *Pure Appl. Geophys.* 176 (8), 3291–3304. doi:10.1007/s00024-019-02258-5

Moon, W. C., Law, C. L., Liew, K. K., Koon, F. S., and Lau, T. L. (2019). Tsunami Force Estimation for Beachfront Traditional Buildings with Elevated Floor Slab in Malaysia. *Coast. Eng. J.* 61 (4), 559–573. doi:10.1080/21664250.2019.1672125

Mori, N., Takahashi, T., Hamaura, S.-E., Miyakawa, K., Tanabe, K., Tanaka, K., et al. (2014). Nationwide Post Event Survey and Analysis of the 2011 Tohoku Earthquake Tsunami. *Coast. Eng. J.* 54 (1), 1250001-1–1250001-27. doi:10.1142/S0578563412500015

Naito, C., Cercone, C., Riggs, H. R., and Cox, D. (2014). Procedure for Site Assessment of the Potential for Tsunami Debris Impact. *J. Waterw. Port. Coast. Ocean. Eng.* 140 (2), 223–232. doi:10.1061/(ASCE)WW.1943-5460.0000222

Nistor, I., Goseberg, N., Stolle, J., Mikami, T., Shibayama, T., Nakamura, R., et al. (2017b). Experimental Investigations of Debris Dynamics over a Horizontal Plane. *J. Waterw. Port Coast. Ocean Eng.* 143 (3), 04016022. doi:10.1061/(ASCE)WW.1943-5460.0000371

Nistor, I., Goseberg, N., and Stolle, J. (2017a). Tsunami-Driven Debris Motion and Loads: A Critical Review. *Front. Built Environ.* 3, 2. doi:10.3389/fbuil.2017.00002

Nouri, Y., Nistor, I., Palermo, D., and Cornett, A. (2010). Experimental Investigation of Tsunami Impact on Free Standing Structures. *Coast. Eng. J.* 52 (1), 43–70. doi:10.1142/S0578563410002117

Nsom, B., Debiane, K., and Piau, J.-M. (2000). Bed Slope Effect on the Dam Break Problem. *J. Hydraulic Res.* 38 (6), 459–464. doi:10.1080/00221680009498299

Oertel, M., and Bung, D. B. (2012). Initial Stage of Two-Dimensional Dam-Break Waves: Laboratory Versus VOF. *J. Hydraulic Res.* 50 (1), 89–97. doi:10.1080/00221686.2011.639981

Osher, S., and Sethian, J. A. (1988). Fronts Propagating with Curvature-Dependent Speed: Algorithms Based on Hamilton-Jacobi Formulations. *J. Comput. Phys.* 79 (1), 12–49. Available at: http://www.sciencedirect.com/science/article/pii/0021999188900022. doi:10.1016/0021-9991(88)90002-2

Ostapenko, V. V. (2007). Modified Shallow Water Equations Which Admit the Propagation of Discontinuous Waves over a Dry Bed. *J. Appl. Mech. Tech. Phy* 48 (6), 795–812. doi:10.1007/s10808-007-0103-y

Oumeraci, H. (2010). More Than 20 Years of Experience Using the Large Wave Flume (GWK) - Selected research Projects. *Kuste* 77, 179–239. Available at: https://hdl.handle.net/20.500.11970/101652.

Ozmen-Cagatay, H., and Kocaman, S. (2010). Dam-Break Flows during Initial Stage Using SWE and RANS Approaches. *J. Hydraulic Res.* 48 (5), 603–611. doi:10.1080/00221686.2010.507342

Palermo, D., Nistor, I., Saatcioglu, M., and Ghobarah, A. (2013). Impact and Damage to Structures during the 27 February 2010 Chile Tsunami. *Can. J. Civ. Eng.* 40 (8), 750–758. doi:10.1139/cjce-2012-0553

Park, H., Cox, D. T., Lynett, P. J., Wiebe, D. M., and Shin, S. (2013). Tsunami Inundation Modeling in Constructed Environments: A Physical and Numerical Comparison of Free-Surface Elevation, Velocity, and Momentum Flux. *Coast. Eng.* 79, 9–21. doi:10.1016/j.coastaleng.2013.04.002

Paulik, R., Gusman, A., Williams, J. H., Pratama, G. M., Lin, S.-L., Prawirabhakti, A., et al. (2019). Tsunami Hazard and Built Environment Damage Observations from Palu City after the September 28 2018 Sulawesi Earthquake and Tsunami. *Pure Appl. Geophys.* 176 (8), 3305–3321. doi:10.1007/s00024-019-02254-9

Ramsden, J. D. (1996). Forces on a Vertical Wall Due to Long Waves, Bores, and Dry-Bed Surges. *J. Waterw. Port. Coast. Ocean. Eng.* 122 (3), 134–141. doi:10.1061/(asce)0733-950x(1996)122:3(134)

Ritter, A. (1897). Die Fortpflanzung der Wasserwellen. *Sonderabdr. Aus Der Z. Des. Vereines Dtsch. Ingenieure* 36, 947.

Rodriguez, H., Wachtendorf, T., Kendra, J., and Trainor, J. (2006). A Snapshot of the 2004 Indian Ocean Tsunami: Societal Impacts and Consequences. *Disaster Prev. Manag.* 15 (1), 163–177. doi:10.1108/09653560610654310

Shafiei, S., Melville, B. W., and Shamseldin, A. Y. (2016). Experimental Investigation of Tsunami Bore Impact Force and Pressure on a Square Prism. *Coast. Eng.* 110, 1–16. doi:10.1016/j.coastaleng.2015.12.006

Saatcioglu, M., Ghobarah, A., and Nistor, I. (2006). Performance of Structures in Indonesia during the December 2004 Great Sumatra Earthquake and Indian Ocean Tsunami. *Earthq. Spectra* 22, 295–319. doi:10.1193/1.2209171

Satake, K., Rabinovich, A. B., Dominey-Howes, D., and Borrero, J. C. (2013). Introduction to "Historical and Recent Catastrophic Tsunamis in the World: Volume I. The 2011 Tohoku Tsunami". *Pure Appl. Geophys.* 170 (6–8), 955–961. doi:10.1007/s00024-012-0615-0

Schimmels, S., Sriram, V., and Didenkulova, I. (2016). Tsunami Generation in a Large Scale Experimental Facility. *Coast. Eng.* 110, 32–41. doi:10.1016/j.coastaleng.2015.12.005

Shen, M. C., and Meyer, R. E. (1963). Climb of a Bore on a Beach Part 3. Run-Up. *J. Fluid Mech.* 16 (01), 113. doi:10.1017/S0022112063000628

Soares-Frazão, S., and Zech, Y. (2008). Dam-Break Flow through an Idealised City. *J. Hydraulic Res.* 46 (5), 648–658. doi:10.3826/jhr.2008.3164

Soares-Frazão, S., and Zech, Y. (2007). Experimental Study of Dam-Break Flow against an Isolated Obstacle. *J. Hydraulic Res.* 45, 27–36. Available at: https://www.scopus.com/inward/record.uri?eid=2-s2.0-34247257289&partnerID=40&md5=36161575712fc4ec2d741cc8bbf9534e. doi:10.1080/00221686.2007.9521830

Sriram, V., Didenkulova, I., Sergeeva, A., and Schimmels, S. (2016). Tsunami Evolution and run-Up in a Large Scale Experimental Facility. *Coast. Eng.* 111, 1–12. doi:10.1016/j.coastaleng.2015.11.006

Stolle, J., Derschum, C., Goseberg, N., Nistor, I., and Petriu, E. (2018). Debris Impact under Extreme Hydrodynamic Conditions Part 2: Impact Force responses for Non-Rigid Debris Collisions. *Coast. Eng.* 141, 107–118. doi:10.1016/j.coastaleng.2018.09.004

Stolle, J., Ghodoosipour, B., Derschum, C., Nistor, I., Petriu, E., and Goseberg, N. (2019). Swing Gate Generated Dam-Break Waves. *J. Hydraul. Res.* 57, 675–687.

Stolle, J., Ghodoosipour, B., Derschum, C., Nistor, I., Petriu, E., and Goseberg, N. (2019a). Swing Gate Generated Dam-Break Waves. *J. Hydraulic Res.* 57 (5), 675–687. Available at: https://www.scopus.com/inward/record.uri?eid=2-s2.0-85053464519&doi=10.1080%2f00221686.2018.1489901&partnerID=40&md5=a516fd4954fe89d7129df7a9bb064418. doi:10.1080/00221686.2018.1489901

Stolle, J., Goseberg, N., Nistor, I., and Petriu, E. (2019b). Debris Impact Forces on Flexible Structures in Extreme Hydrodynamic Conditions. *J. Fluids Struct.* 84, 391–407. doi:10.1016/j.jfluidstructs.2018.11.009

Stolle, J., Krautwald, C., Robertson, I., Achiari, H., Mikami, T., Nakamura, R., et al. (2020). Engineering Lessons from the 28 September 2018 Indonesian Tsunami: Debris Loading. *Can. J. Civ. Eng.* 47 (1), 1–12. doi:10.1139/cjce-2019-0049

Stolle, J., Nistor, I., and Goseberg, N. (2016). Optical Tracking of Floating Shipping Containers in a High-Velocity Flow. *Coast. Eng. J.* 58 (2), 1650005. doi:10.1142/S0578563416500054

Stolle, J., Nistor, I., Goseberg, N., and Petriu, E. (2020a). Development of a Probabilistic Framework for Debris Transport and Hazard Assessment in Tsunami-Like Flow Conditions. *J. Waterw. Port Coast. Ocean Eng.* 146 (5). doi:10.1061/(ASCE)WW.1943-5460.0000584

Stolle, J., Nistor, I., Goseberg, N., and Petriu, E. (2020b). Multiple Debris Impact Loads in Extreme Hydrodynamic Conditions. *J. Waterw. Port Coast. Ocean Eng.* 146 (2). doi:10.1061/(ASCE)WW.1943-5460.0000546

Sun, G. C., Wei, W. L., Liu, Y. L., Wang, X., and Liu, M. Q. (2012). Numerical Simulation of 2D Circular Dam-Break Flows with WENO Schemes. *Adv. Mater. Res.* 468-471, 2201–2205. Available at: https://www.scientific.net/AMR.468-471.2201. doi:10.4028/www.scientific.net/amr.468-471.2201

Taubenböck, H., Goseberg, N., Lämmel, G., Setiadi, N., Schlurmann, T., Nagel, K., et al. (2013). Risk Reduction at the "Last-Mile": an Attempt to Turn Science into Action by the Example of Padang, Indonesia. *Nat. Hazards* 65 (1), 915–945. doi:10.1007/s11069-012-0377-0

Taubenböck, H., Goseberg, N., Setiadi, N., Lämmel, G., Moder, F., Oczipka, M., et al. (2009). "Last-Mile" Preparation for a Potential Disaster - Interdisciplinary Approach towards Tsunami Early Warning and an Evacuation Information System for the Coastal City of Padang, Indonesia. *Nat. Hazards Earth Syst. Sci.* 9 (4), 1509–1528. Available at: https://www.scopus.com/inward/record.uri?eid=2-s2.0-76249103357&partnerID=40&md5=6568eb4e96e3ab261d3518111ed59eab. doi:10.5194/nhess-9-1509-2009

Tomiczek, T., Prasetyo, A., Mori, N., Yasuda, T., and Kennedy, A. (2016). Physical Modelling of Tsunami Onshore Propagation, Peak Pressures, and Shielding Effects in an Urban Building Array. *Coast. Eng.* 117, 97–112. doi:10.1016/j.coastaleng.2016.07.003

Tomita, T., Imamura, F., Arikawa, T., Yasuda, T., and Kawata, Y. (2006). Damage Caused by the 2004 Indian Ocean Tsunami on the Southwestern Coast of Sri Lanka. *Coast. Eng. J.* 48 (2), 99–116. doi:10.1142/S0578563406001362

Triatmadja, R., Hijah, S. N., and Nurhasanah, A. (2011). "Scouring Around Coastal Structures Due to Tsunami Surge," in 6th Annual International Workshop & Expo on Sumatra Tsunami Disaster & Recovery 2011 In Conjunction with 4th South China Sea Tsunami Workshop, 22 November 2011-24 November 2011, Banda Aceh, Indonesia.

von Häfen, H., Goseberg, N., Stolle, J., and Nistor, I. (2019). Gate-Opening Criteria for Generating Dam-Break Waves. *J. Hydraulic Eng.* 145 (3). doi:10.1061/(ASCE)HY.1943-7900.0001567

von Häfen, H., Stolle, J., Goseberg, N., and Nistor, I. (2018). "Lift and Swing Gate Modelling for Dam-Break Generation with a Particle-Based Method," in 7th IAHR International Symposium on Hydraulic Structures, ISHS 2018, May 15-18, 2018, Aachen, Germany, 464–473. doi:10.15142/T3R34Q

von Häfen, H., Stolle, J., Nistor, I., and Goseberg, N. (2021). Side-by-Side Entrainment and Displacement of Cuboids Due to a Tsunami-Like Wave. *Coast. Eng.* 164, 103819. doi:10.1016/j.coastaleng.2020.103819

von Hippel, F. N. (2011). The radiological and Psychological Consequences of the Fukushima Daiichi Accident. *Bull. Atomic Sci.* 67 (5), 27–36. doi:10.1177/0096340211421588

Wang, W., Martin, T., Kamath, A., and Bihs, H. (2020). An Improved Depth-Averaged Nonhydrostatic Shallow Water Model with Quadratic Pressure Approximation. *Int. J. Numer. Meth Fluids* 92, 803–824. doi:10.1002/fld.4807

Whitham, G. B., and Lighthill, M. J. (1955). The Effects of Hydraulic resistance in the Dam-Break Problem. *Proc. R. Soc. Lond. A* 227 (1170), 399–407. doi:10.1098/rspa.1955.0019

Wilcox, D. (2006). *Turbulence Modeling for CFD*. Third Edition. (Hardcover).La Canada, CA: DCW Industries, Inc..

Winter Andrew, O., Alam Mohammad, S., Krishnendu, S., Motley Michael, R., Eberhard Marc, O., Barbosa Andre, R., et al. (2021). Tsunami-Like Wave Forces on an Elevated Coastal Structure: Effects of Flow Shielding and Channeling. *J. Waterw. Port Coast. Ocean Eng.* 146 (4), 4020021. doi:10.1061/(asce)ww.1943-5460.0000581

Wüthrich, D., Pfister, M., Nistor, I., and Schleiss, A. J. (2018). Experimental Study of Tsunami-Like Waves Generated with a Vertical release Technique on Dry and Wet Beds. *J. Waterw. Port Coast. Ocean Eng.* 144 (4). doi:10.1061/(ASCE)WW.1943-5460.0000447

Wüthrich, D., Ylla Arbós, C., Pfister, M., and Schleiss, A. J. (2020). Effect of Debris Damming on Wave-Induced Hydrodynamic Loads against Free-Standing Buildings with Openings. *J. Waterw. Port Coast. Ocean Eng.* 146 (1). doi:10.1061/(ASCE)WW.1943-5460.0000541

Xu, Z., Melville, B. W., Wotherspoon, L., and Nandasena, N. A. K. (2020). Stability of Composite Breakwaters under Tsunami Attack. *J. Waterw. Port Coast. Ocean Eng.* 146 (4). doi:10.1061/(ASCE)WW.1943-5460.0000571

Yeh, H. H., Ghazali, A., and Marton, I. (1989). Experimental Study of Bore run-Up. *J. Fluid Mech.* 206, 563–578. doi:10.1017/S0022112089002417

Yeh, H. H. (1991). Tsunami Bore runup. *Nat. Hazards* 4 (2), 209–220. doi:10.1007/BF00162788

Conflict of Interest: The authors declare that the research was conducted in the absence of any commercial or financial relationships that could be construed as a potential conflict of interest.

6 APPENDIX

6.1 Convergence Study on Cell Size

The reference test with $d_0 = 1.0$ m is used to investigate numerical convergence on cell size. Therefore, the test is calculated five times on a regular grid with cell sizes altered from 0.005 m to 0.02 m. The time histories of all numerical wave gauges are compared in each calculated time step to the test with the finest resolution using the coefficient of determination r^2. **Figure 14** displays the coefficient as well as the computational time.

6.2 Settings of Reef3D

Settings made within the input file of Reef3D which are not on default and which are not specific to the computing server used (like the number of cores) or the output (like the time step of vtk. output files) are summarized in **Table 6**.

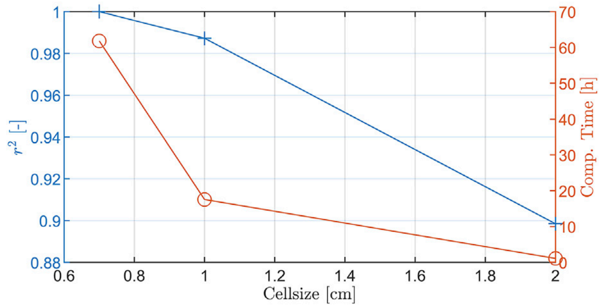

FIGURE 14 | Convergence on cell size.

TABLE 6 | Settings of Reef3D.

Parameter	Description	Input
D 10 7	Discretization of the convection terms in the momentum equation	WENO3 FLUX
D 20 2	Treatment of the diffusion term in the momentum equation	Implicit
F 30 3	Free surface level set time scheme	Third-order TVD Runge–Kutta
F 40 3	Free surface reinitialization time scheme	Third-order TVD Runge–Kutta
F 50 4	Fixed water level set for in and outflow	None fixed
N 40 2	Time scheme for the momentum equations	Second-order TVD Runge–Kutta
N 47 0.1	Relaxation factor for time step size	0.1
T 10 22	Turbulence model	URANS with k-ω
T 36 1	Free surface boundary condition for turbulent dissipation	On

frontiers | Frontiers in Built Environment

TYPE Original Research
PUBLISHED 29 August 2022
DOI 10.3389/fbuil.2022.884692

OPEN ACCESS

EDITED BY
Jane McKee Smith,
Engineer Research and Development Center (ERDC), United States

REVIEWED BY
Rodolfo Silva,
Institute of Engineering, National Autonomous University of Mexico, Mexico
Ping Wang,
University of South Florida, United States

*CORRESPONDENCE
Mohamed A. Dabees,
md@humistonandmoore.com

SPECIALTY SECTION
This article was submitted to Coastal and Offshore Engineering, a section of the journal Frontiers in Built Environment

RECEIVED 26 February 2022
ACCEPTED 05 July 2022
PUBLISHED 29 August 2022

CITATION
Dabees MA, Fleming M and Damon M (2022), Natural and nature based features for environmental enhancement and coastal storm risk management: a case study on Marco Island, Florida, United States.
Front. Built Environ. 8:884692.
doi: 10.3389/fbuil.2022.884692

Natural and nature based features for environmental enhancement and coastal storm risk management: a case study on Marco Island, Florida, United States

Mohamed A. Dabees*, Matthew Fleming and Marc Damon

Humiston & Moore Engineers, Naples, FL, United States

Natural and Nature-Based systems provide an opportunity for adaptive response to Coastal Storm Risk Management and Sea Level Rise. The Tigertail Lagoon/Sand Dollar Island Restoration on Marco Island, Florida, presents a case study designed to maintain and enhance an existing coastal barrier system consisting of a 3-km-long sand spit and tidal lagoon ecosystem that is otherwise evolving toward closure. The case study is part of a nature-based adaptive management plan to restore and stabilize the sandspit and tidal lagoon through cyclic use of sediment within the system. This approach seeks to preserve existing protective habitats and landforms that also serve as natural coastal barriers to protect upland development. Design of the restoration plan considers the functions of a wildlife nature preserve and evolution of complex tidal inlet morphologic features bordered by a heavily developed barrier Island. The design aims to restore and enhance a sandspit degraded by a sequence of storms since Major Hurricane Irma impacted Southwest Florida in 2017 and improve the existing deteriorated habitat by enhancing tidal exchange through restoration of the lagoon flow channel. Total wetland area will be increased by relocating the sand spit seaward of its present location to where it was located in approximately 2017. The reconstructed beach berm will provide enhanced resiliency to high frequency weather events. Sediment will be sourced from the existing sand spit and an innovative sand trap that will maintain the lagoon entrance open while providing beneficial re-use for excess sediment that continues to accumulate at the end of the spit. Components of the project were analyzed using existing engineering models and methods such as the Coastal Modeling System (CMS) and XBeach. Enhancing and preserving this barrier island feature and productive ecosystem provides an example of the enhanced coastal resiliency provided by natural and nature-based systems that are adaptable and responsive to sea level rise and ongoing coastal processes.

KEYWORDS

coastal storm risk management, resiliency (environmental), sea level rise adaptation, barrier islands, inlet processes, geomorphology

1 Background

This paper discusses the use of natural and nature-based systems at the Tigertail Lagoon/Sand Dollar Island Restoration on Marco Island, Florida. The restoration plan provides an example of habitat restoration that enhances coastal resiliency. It is designed to preserve and enhance a productive natural coastal ecosystem that has existed in some form for approximately 20 years. The alternative "do-nothing" approach would result in deterioration, closure, and isolation of productive coastal ecosystems. The "do-nothing" approach has been observed to lead to progressive armoring of the coast as upland infrastructure becomes vulnerable, as illustrated in the regional examples of sand spit evolution presented in this paper.

The coastline of Southwest Florida includes a series of barrier islands separated by tidal inlets and bound by large back-bay waterbodies which present added challenges to coastal resiliency planning in the form of back-bay flooding. Potential vulnerabilities and flooding risks are compounded by Sea Level Rise (SLR) and barrier island evolution. Barrier islands and tidal inlets are dynamic in nature and their evolution occurs at larger time scales than the planning and design horizons of typical coastal projects. The timing of early beachfront development relative to the transitory barrier island and inlet processes is a primary factor in the potential long-term stability of constructed beach resiliency projects and long term sustainability relative to new equilibrium conditions (Dabees 2020). Southwest Florida developed along the coastline primarily in the middle of the 20th century conforming with the equilibrium planform at that time. Natural evolution and anthropogenic changes over the past century created geomorphologic changes in the coastal equilibrium planform that deviate from the planform at the time of development. Developed coastal areas that were once sheltered from direct open coast by sand spits and tidal lagoons become more vulnerable as those features evolve naturally or migrate landward toward existing development. Over the past few decades, the inlet processes associated with the collapse of sand spits onto developed barrier islands and subsequent erosion has been observed to lead to shoreline hardening or erosion control structures. Such structural solutions may address short term beach erosion and provide upland protection but don't provide long term adaptation to natural inlet and barrier island evolution or potential SLR. Natural coastal systems provide opportunities in planning and adaptation for Coastal Storm Risk Management as was recently identified in the US Army Corps of Engineer's South Atlantic Coastal Study Main Report Final Draft (2021). Use of natural and nature based features may range from including minor ecological elements in otherwise engineered systems to ecological restoration of heavily altered systems. The wide range of natural features and the level of inclusion in infrastructure planning and design makes it difficult to define natural and nature based features. Literature review and a proposed system of classification is provided in Chavez et al. (2021).

Dabees (2017 and 2018) discussed the evolution of sand spits along the barrier islands of the Florida Gulf coast through various case studies. The analysis indicated the large time scale of natural sand spit evolution and responses to anthropogenic changes. In cases where development encroached on an active sand spit, future erosion of that feature often led to a chronic erosion condition and loss of habitat for beach and aquatic species, sometimes referred to as "Coastal Squeeze". Shoreline stabilization strategies typically result in beach restoration with or without coastal structures to protect vulnerable development or existing infrastructure. Figure 1 shows an example at Big Carlos Pass in Lee County, Southwest Florida where the onshore migration of the sand spit and tidal lagoon collapse have increased the vulnerability of existing coastal development. In prior decades, the shoal and sand spit served as coastal protection from high frequency and major storm events. Since the spit has attached and eroded ongoing erosion threatens existing infrastructure while sand from the eroded sand spit accumulated at the inlet bank. The present condition represents the end point of approximately 40 years of landward migration of the protective emergent shoals. As a result of this coastal squeeze, seawalls and beach restoration are being considered at vulnerable areas at the time of writing this paper. Figure 2 shows another example of erosion control structures implemented to manage shoreline retreat at a location where a sand spit and tidal lagoon once provided natural coastal protection to upland development at Longboat Pass in Manatee County, Florida. At this location a sand spit persisted over several decades and sheltered the north part of Longboat Key. Natural inlet evolution processes and cumulative dredging of the ebb shoal impacted the sandspit (Dabees and Kraus 2008). The sandspit collapse presented coastal management challenges related to vulnerabilities to existing upland development and excess sediment accumulation at the inlet bank and closure of the lagoon. At present, this area has been managed by placement of sediment, installation of erosion control structures, and an existing older seawall that becomes exposed between fill placement events. In both cases, the shoal and sandspit features provided transient protection which is lost or nearly lost as barrier island evolution progresses. While the sand spit growth and collapse in many cases can be caused by natural inlet evolution, anthropogenic influences can also factor in the evolution of sandspits and future management of upland areas in their shadows. The intersection between an evolving inlet/sandspit system bordered by a developed barrier island presents added coastal management challenges that can lead to coastal armoring. Such armoring creates a fixed coastal interface that often results in less effective coastal protection and does not allow for future adaptation to inlet processes and SLR.

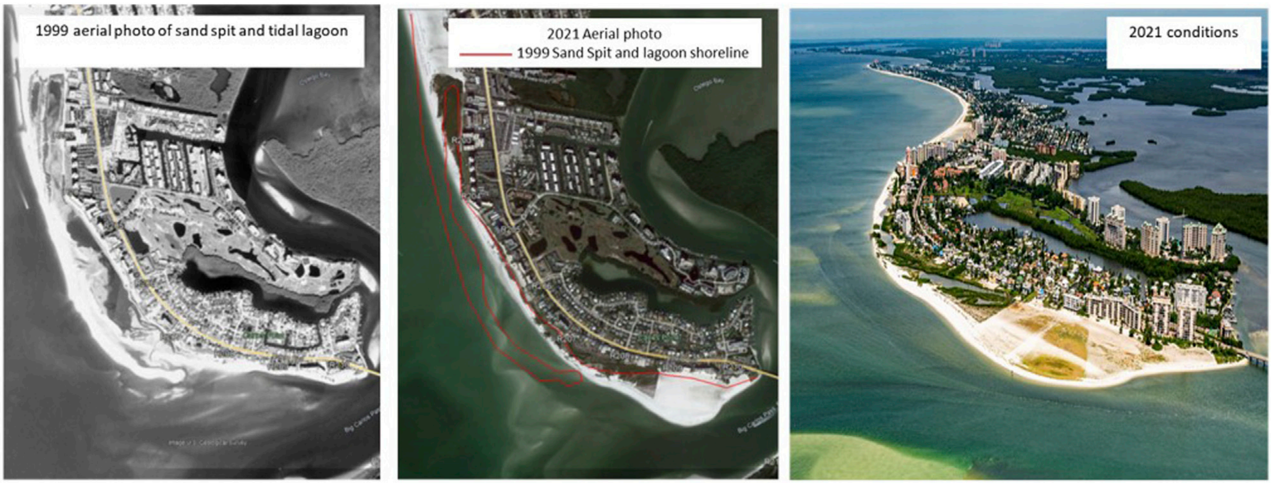

FIGURE 1
Evolution of sandspit at Big Carlos Pass, Southwest Florida.

FIGURE 2
Evolution of sandspit and coastal management at Longboat Pass, Florida.

In this paper a case study aims at restoration of a sand spit and tidal lagoon system as an example of natural and nature-based solutions that sustain and enhance the natural environment and also maintain the protection from coastal storm flooding and sea level rise afforded by natural coastal systems. The project implements regional sediment management principles in the beneficial re-use of excess sediment removed from areas of accumulation and applied to areas of need.

1.2 Marco island case study

This case study, located along the north part of the Gulf of Mexico coastline of Marco Island, Florida, discusses a coastal restoration project that will restore and enhance a deteriorating coastal lagoon and sandspit that provide critical habitat and upland storm protection. The tidal wetland and large island/sand spit have provided vital environmental habitat for wildlife,

TABLE 1 Coastal habitats at Tigertail Lagoon.

Habitat description	Acreage (ha)	Percent cover (%)
Beach Sand	25.9	16.7
Coastal Scrub and Brush	13.4	8.6
Coastal Scrub	0.49	0.3
Other Shrubs	0.20	0.1
Tropical Hardwoods	10.9	7.1
Bays and Estuaries	44.0	28.5
Mangrove	27.7	17.9
Saltwater Marsh	18.0	11.6
Seagrass	14.3	9.2
Total	154.9	100.0

TABLE 2 Seagrass coverage and lagoon width.

Survey	Acreage (ha)	Lagoon width (m)
2018	10.7	76.2
2020	14.3	36.0
2021	13.3	17.1

coastal protection, and recreational benefits for over 2 decades. This case study demonstrates an alternative to typical coastal management practice of shore protection in areas of protected natural preserves. Typical coastal management in Florida, and the United States generally, would not intervene in designated natural preserves areas until erosion met a critical threshold threatening upland infrastructure. By that time, storm protective functions and valuable habitat will have been lost. Restoration of storm protective functions at this point often results in shoreline hardening and would not restore aquatic habitat similar to what would have been lost. The paper focuses on the technical approach demonstrating the concept of maintaining natural morphological features as sustainable coastal protection measures for both environmental habitat and upland development. The technical approach and management efforts in this case study are guided by environmental protection statutes and rules mandated by state and federal agencies in the US. Coastal management in the US in general and Florida in particular is generally more heavily constrained by environmental protection ahead of other issues.

1.3 Habitat description

The lagoon provides significant habitat for flora and fauna such as terrestrial wildlife, and submerged benthic communities such as seagrasses that support endangered manatees, and Essential Fish Habitat (EFH). This area is also designated as federal critical habitat for threatened species including piping plover and red knot shorebirds, as well as nesting and foraging habitat for state threatened species. A summary description of the habitat is provided here. Detailed data, maps and analysis of the ecosystem for Tigertail Lagoon and Sand Dollar Island are discussed in (Turrell, Hall and Associates 2021B).

As of summer 2021, the most recent data available, the island and lagoon system consisted of dry beach, mangrove estuaries, salt marsh, open water and aquatic habitats as summarized in Table 1 according to the Florida Land Use, Cover, and Forms Classification System (FDOT, 1999). There were 31 species of upland flora and 26 species of birds identified during surveys in 2021. There were 13 species of marine flora and 43 species of marine fauna identified in surveys from 2017 through 2021 including seagrasses, manatee, conch, crab, sponge, and a variety of fish. Loggerhead Sea Turtles nest on the Gulf facing beach, although the habitat is marginal and nest success is rare.

Seagrasses represent a habitat type that is highly valued by US Federal and Florida regulations and policy. Seagrass habitats are generally valued for the diversity of species present and use throughout various life stages. Seagrasses also serve as a food source for the endangered West Indian Manatee, which commonly visit Tigertail Lagoon. Seagrass surveys were conducted in recent years and total acreage is provided in Table 2. The reach of seagrass within the lagoon has increased over time, extending into the narrow portion behind the Gulf fronting beaches. In this area, sand overwash regularly occurs, resulting in long term retreat on the order of 12–15 m per year along over 900 m of shoreline. This retreat continues to bury existing seagrass beds and eliminate potential recruitment areas. In the absence of intervention, the area will evolve to only landlocked marine seagrasses, representing a loss of available seagrass habitat and food sources available to marine fauna.

1.4 Sand spit evolution

The lagoon system presently consists of a 3-km-long sand spit (Sand Dollar Island) sheltering a large tidal wetland and lagoon (Tigertail Lagoon) with salt marsh and interior mangrove shoreline areas that provide natural protection to the upland areas landward on Marco Island. Sand Dollar Island represents a front line of protection and resiliency to Sea Level Rise (SLR) and flooding that is rapidly deteriorating.

The lagoon system provides multi-tiered protection against coastal storms by wave height reduction on the sandy beach and limiting run-up and coastal flooding through the lagoon and mangrove systems. Monitoring data indicates onshore migration and degradation of these features over the past decade, especially following Hurricane Irma, a major Hurricane that landed on Marco Island in 2017. Irma reduced the height and resiliency of the central section of Sand Dollar Island resulting in high frequency storm wave

FIGURE 3
Sandspit and tidal Lagoon case study in Marco Island, Florida.

and sand over wash into the lagoon. By the end of 2020 the degradation of the system became critical and the middle part of Sand Dollar Island was near attaching to the upland mangrove shoreline, which threatens to reduce the 3 km long tidal lagoon into smaller landlocked ponds and increase coastal vulnerability along the northwest part of Marco Island.

Figure 3 shows the location of the study area which extends from the central part of Marco Island's Gulf coast to the northwest part of the island. The evolution of Tigertail Lagoon and Sand Dollar Island is part of the ongoing large scale natural tidal inlet evolution at the north end of Marco Island. Prior to the 1960s, Big Marco Pass was the main inlet between Marco Island and Sea Oat Island. In 1967 Capri Pass developed when Sea Oat Island was breached by natural processes. The breach on the up-drift side of Big Marco Pass created a dual inlet system that persisted for a few decades until Capri Pass became the main inlet for this system in the early 2000s.

Figure 4 shows the inlet configuration in 1969, 2 years after Capri Pass was opened, and a comparison of more recent conditions represented by 2011 aerial photos with the 1965 shoreline before Capri Pass opened. The opening of Capri Pass created a dual inlet system of Capri Pass and Big Marco Pass separated by a small island (Coconut Island) and by a large and complex ebb shoal system (Dabees and Kraus, 2004).

The reduction of tidal prism of Big Marco Pass resulted in onshore migration of its large ebb shoal rendering the pass more restrictive to tidal flow. The newer inlet became more dominant as it gradually captured a larger share of the tidal prism. This dual inlet process continued until the south inlet closed in the 2000s. Onshore movement of the ebb shoal at the closed inlet provides a large volume of sand to the down-drift beach (Marco Island) and formation of the active ebb shoal continues to the north. Formation of the new ebb shoal caused significant erosion on the north side of Capri Pass, along the south end of Sea Oat Island. The up-drift beach erosion is represented on the right side of Figure 4.

Sand Dollar Island formed as the relict Big Marco Pass ebb shoal gradually migrated toward Marco Island, eventually becoming emergent and attaching to the middle of Marco Island. This bypassing process from North to South was previously discussed by Humiston (1988) and is presumed to have shaped the present northwest coastline of Marco Island. Figure 5 shows the varying stages of Sand Dollar Island in decadal stages. First, Sand Dollar Island was a detached emergent shoal in the 1980s along the south side of the Big Marco Pass. The island then became a sand spit when the south end of it attached to Marco Island in the 1990s. During the 2000s Sand Dollar Island continued to migrate onshore causing Big Marco Pass to close completely. In the mid 2000s, the small island that separated Big Marco Pass from Capri Pass collapsed onshore and eventually welded with the north end of the Sand Dollar Island sand spit during the 2010s. The collapsing sand shoal, spit and lagoon system is consistent with typical inlet processes. In this case, management of the spit and lagoon system is planned to maintain the system as an open, functioning feature. This feature provides benefits in terms of storm damage mitigation and high value environmental habitat that would otherwise be lost, as illustrated in the other regional examples provided in this paper.

1.5 Existing conditions and recent morphologic changes

Recent morphologic changes from 2010 to present (2021), indicate continued onshore migration of the sand spit at the northwest corner of Marco Island. Figure 6 illustrates the change in the sand spit shoreline from 2010 to 2018. The morphologic changes associated with the closure of Big Marco Pass include the shoaling and narrowing of Tigertail Lagoon, the water body between the Sand Dollar Island sand spit and Marco Island. In the absence of tidal currents from Big Marco Pass, waves dominating the coastal processes along the north end of Marco Island continue to transport sand from the westernmost point near the center of the sand spit towards the lateral ends of Sand Dollar Island (north and south). Along the south part of the island, sand is transported from north to south towards the attachment point south of the spit

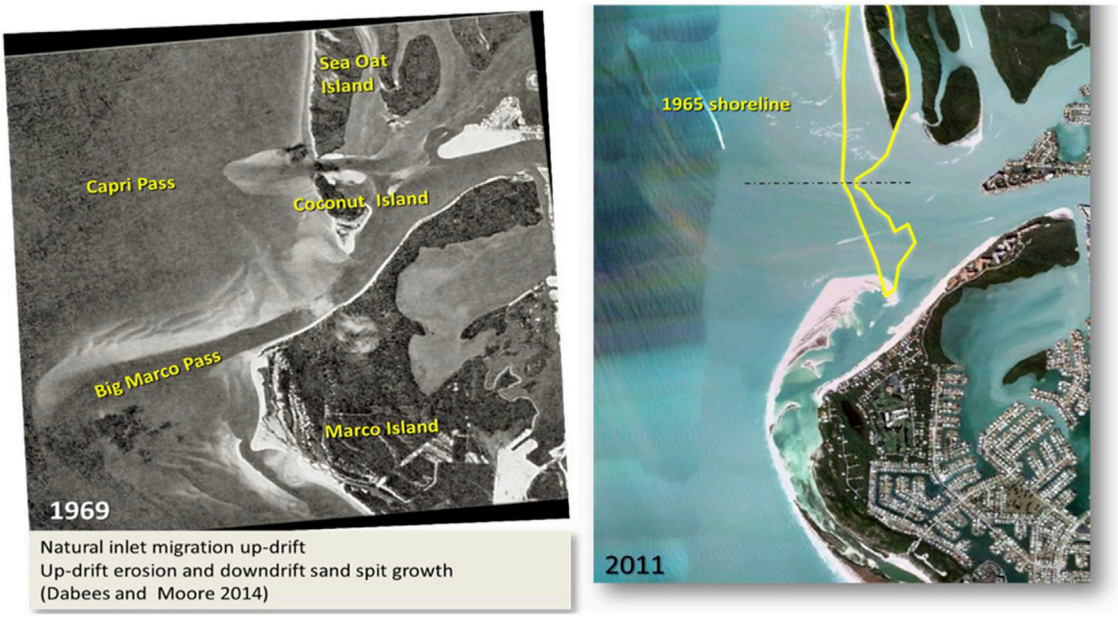

FIGURE 4
Comparison of the 1960s and existing conditions at the study area.

creating a very wide beach. On the north part of the sand spit sand is transported from south to north causing the growth and elongation of the sand spit. The sand spit growth and interaction with waves and currents push the north end of the sand spit towards Hideaway Beach. The sand spit attachment to Hideaway Beach, which would close off the opening of Tigertail Lagoon to the Gulf of Mexico, is managed by periodic dredging. This dredging keeps the lagoon open to tidal exchange when it would otherwise have become a closed system over a decade ago. Continued tidal exchange is essential to the water quality and ecology of the lagoon.

1.6 Storm effects on sand spit evolution

In addition to the day-to-day coastal processes contributing to the elongation and onshore migration of Sand Dollar Island, storm events have significant influence on the sand spit evolution. Dabees (2018) discussed the effects of Hurricane Irma on Sand Dollar Island and are summarized here to illustrate the magnitude of change due to storm events.

Hurricane Irma was a major Hurricane in the 2017 tropical season that reached Category five and caused catastrophic damage in parts of the northeastern Caribbean and the Florida Keys. Irma made its landfall on Florida’s mainland on Marco Island south of Naples as a major Hurricane then tracked north along southwest Florida. The storm track and wind circulation influenced water levels and waves with high intensity and varying conditions over a relatively short time. The waves accompanied by the onshore storm surge phase added to the forcings affecting beaches, inlets and estuaries that make up the coastal system of southwest Florida.

Post storm observations and survey data collected pre and post storm along the study area of Sand Dollar Island highlighted the morphological response of the spit to the storm surge and waves. General trends included beach and dune erosion with significant sand overwash landward. Figure 7 shows an example of the morphologic response to Hurricane Irma on the lagoon and sand spit. The survey data and aerial photos indicated a landward migration of the sand spit of over 20 m and sand overwash on the lagoon side of the spit of over 30 m. The beach profile comparisons shown in the figure quantify the scale of the morphologic change in this area.

Major storms impacting this area such as Hurricanes Wilma (2005) and Irma (2017) occur at approximately decadal frequency. When they occur, they cause significant morphologic response. In the case of Sand Dollar Island, the storms caused lowering of the beach elevations in the middle part of the sand spit leaving it more vulnerable to erosion and overwash during typical weather related storm events that may occur several times a year. For example, over the tropical season of 2020, two tropical storms passed offshore in the Gulf of Mexico, Cristóbal (June 2020) and Eta (November 2020). These two events generated mild storm surge and wave height but caused significant morphologic response at the middle section of Sand Dollar Island due to the low elevation of that section.

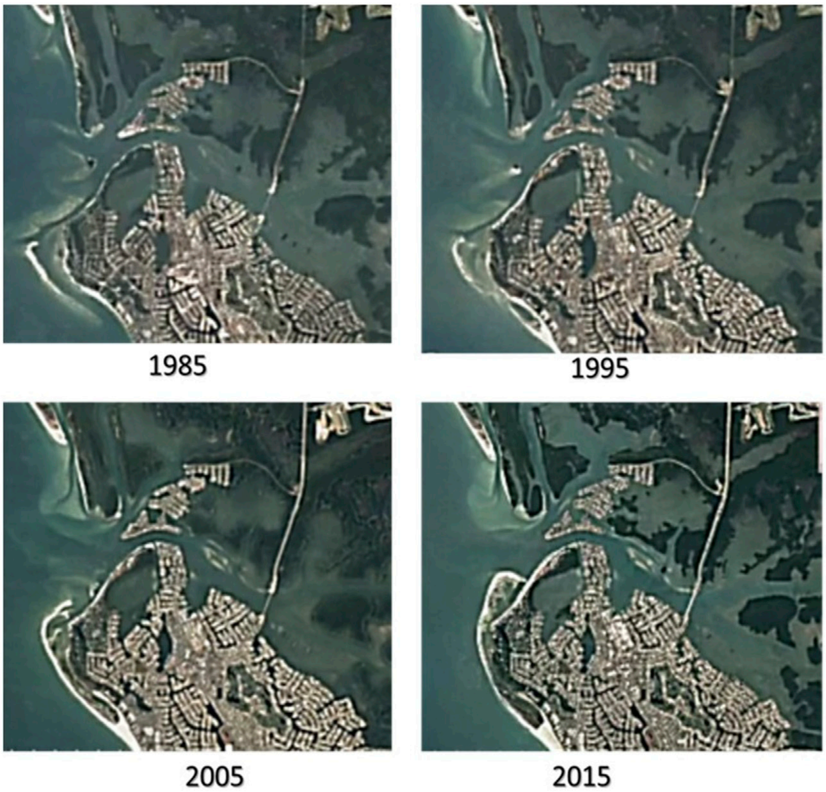

FIGURE 5
Decadal stages of Sand Dollar Island evolution.

In summary, the ecosystem and its storm protection functions are severely threatened due to overwash and storm impacts especially since Hurricane Irma's effects on Sand Dollar Island in 2017 (Dabees 2018). The Island has been migrating shoreward and its mid-section is low in elevation due to storm overwash, leaving a span of 1.5 km as an area of high vulnerability to storm damage. Environmental resources such as seagrasses within the lagoon have been systematically overwashed and covered with sand. In addition, littoral processes and inlet dynamics are eroding sand from this coastal frontline area towards the north end of the sandspit where shoaling is threatening to close off the lagoon entrance and only connection to Gulf tides. Figure 8 provides an illustration of the sediment transport processes including longshore sand transport and sand overwash which control the morphologic evolution of the sand spit. The figure also shows the morphologic response over the 2018 to 2021 period illustrating the collapse of the overwash area in the middle of the sand spit and the significant growth at the terminal north end of the sandspit.

2 Nature based restoration plan

The nature-based restoration plan consists of reconstructing an elevated sand spit at its 2017 shoreline location to provide increased lagoon aquatic habitat, enhanced multi-tier shore protection against flooding and nature-based adaptation to sea level rise, improved tidal exchange and regional sediment management. Figure 9 provides an illustration of the restoration plan. The proposed Tigertail Lagoon/Sand Dollar Island Restoration Plan proposes to restore the vulnerable segment of this sand barrier with a more resilient beach berm by dredging areas of overwash from the lagoon side of the island and place that material along the Gulf side of the island, essentially to reset the Gulf shoreline to conditions in 2017 and restore lagoon acreage and tidal exchange.

Elements of the restoration plan were assessed and optimized to avoid and minimize potential impacts to natural resources and also provide a sustainable design for future resiliency. The design elements were coordinated with local, state, and federal agencies that are stakeholders of this critical wildlife area and those in charge of permitting environmental and coastal projects.

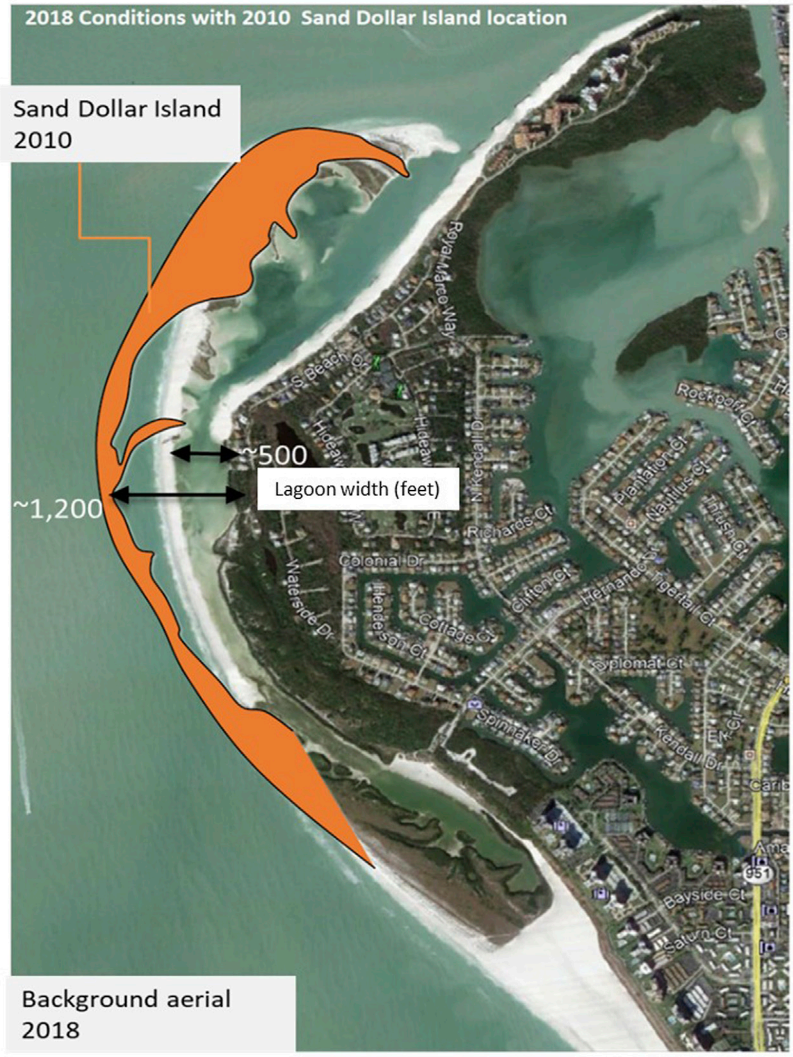

FIGURE 6
Recent shoreline changes of Sand Dollar Island.

2.1 Project design elements

The restoration plan is designed to establish adaptive management of the coastal system and nature-based adaptation to Sea Level Rise. Sand Dollar Island is located along the only segment of Marco Island that does not have a coastal management program in place. Retreat of the sandspit and loss of the tidal lagoon has reduced the coastal protection and resulted in deterioration of the critical environmental habitat within the lagoon system. Sand Dollar Island has been retreating at 12–15 m per year over the past decade, choking off the tidal exchange within the lagoon. The Florida Healthy Beaches program monitoring data has indicated increasingly frequent poor water quality events within the lagoon during the past 5 years. A summary of the design elements is described here, detailed engineering design and alternatives' analysis are provided in the project technical reports (Humiston & Moore Engineers 2021B; Humiston & Moore Engineers 2021A).

The plan is focused primarily on reconstructing lagoon conditions and a protective sand spit. This morphologic restoration will allow for natural recruitment of flora and fauna as occurred prior to overwash and deterioration. The project will conserve and rehabilitate what remains of marine habitat and also restore other portions that have been overwashed. The enhanced beach berm will reduce the rate of overwash, allowing longer and more sustained recruitment and habitat compared to what occurred naturally. The plan will restore the Gulf shoreline and is estimated to maintain improved tidal exchange for four to 5 years post construction.

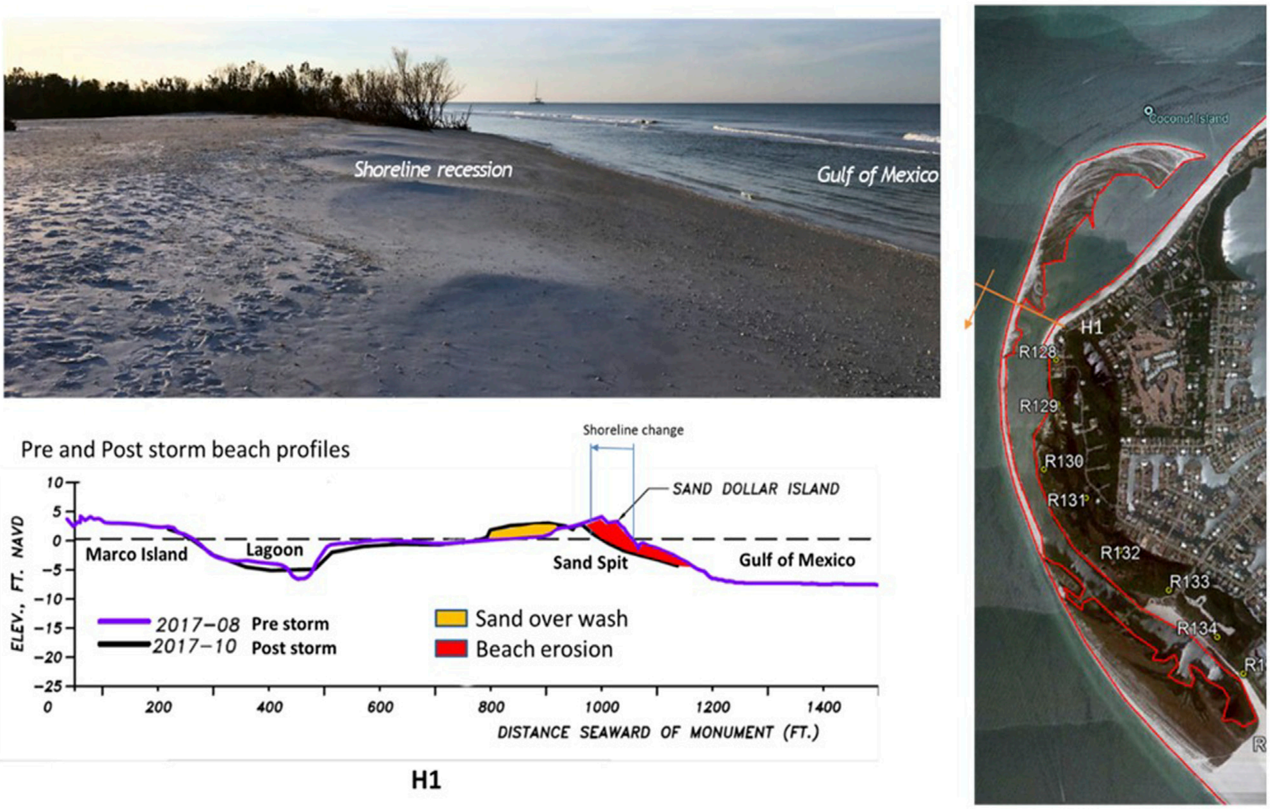

FIGURE 7
Morphologic response to hurricane Irma at a profile across the lagoon and sand spit.

The plan includes monitoring and management to support adaptive nature-based resiliency plans by recycling local sand sources from shoaling areas to the vulnerable areas within the system. The reconstructed beach will be situated at a higher elevation to reduce storm overwash and flooding by creating a broad sandy barrier on the gulf shoreline where minimal protection currently exists.

Numerical modeling and data analysis provided a basis to assess the function and resiliency of the proposed design. The restoration plan consists of three primary components that are necessary to the overall effectiveness of the plan but function essentially independent of one another. The three elements are:

1) Flow channel improvement,
2) Beach berm reconstruction, and
3) Renewable sediment source and sand trap.

Each element was analyzed independently to determine the preferred design for that element. The optimal design is the result of combining the preferred design elements.

2.1.1 Tidal Wetland Restoration: flow channel improvement

Sustainability of the system requires tidal flow supported by maintaining the lagoon entrance at the north end of the system. The entrance connects the lagoon to the Gulf tide, and a continuous channel is required to maintain adequate flow throughout the 3-km long lagoon. Design of an improved flow channel must balance the relative improvements from a given channel geometry with the presence of seagrasses in the vicinity. The improved flow channel should result in bathymetric conditions suitable for seagrass recruitment, but also be of sufficient size to be practical for construction and provide a reasonable design life between maintenance events. For example, a channel that is small and narrow will have the advantage of avoiding seagrasses and minimize potential impacts during construction but may not provide adequate dimensions to improve tidal circulation and be sustainable. A channel that is too small and narrow would have a limited capacity to accumulate sediment over time and maintain effectiveness, leading to poor performance and/or increased frequency of maintenance events. On the other hand, an overly large

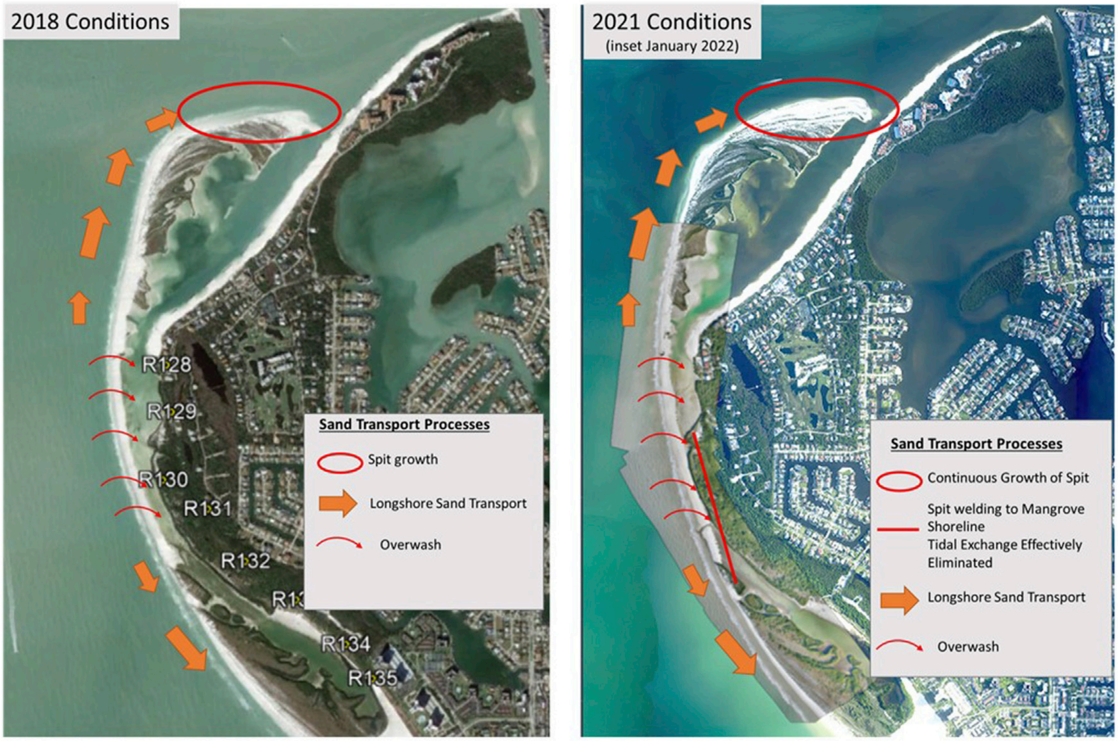

FIGURE 8
Schematic of coastal processes and morphologic responses (2018–2021).

channel might be economically unfavorable, deliver diminishing returns, and could potentially impact seagrass beds. The location of the improved channel is a primary consideration. The channel has been designed and will be constructed such that it will not directly impact existing seagrass beds. This is accomplished by locating the channel within overwashed areas as much as practical, while avoiding any mapped seagrasses when working in water. This will return the overwashed areas to wetlands and create an improved flow channel to improve flushing throughout the lagoon. Several channel alternatives were evaluated through hydrodynamic modeling and assessment of flow throughout the lagoon and the environmental constraints for this Critical Wildlife Area. Hydrodynamic modeling of 2017 and 2020 conditions using the Coastal Modeling System (CMS, 2006) was used to simulate past, present, and design alterative conditions. The model was calibrated with field measurement from gages installed within the system and Gulf measured conditions. The model quantified the tidal flow throughout the lagoon and the change in flow over time as the central part of the lagoon became more restrictive. Several scenarios were considered for design. The final project design is presented in this paper for brevity. Engineering design followed typical coastal design methods using industry standard modeling packages and software.

Figure 10 shows example model results for one timestep during low tide. The model results indicate that conditions have deteriorated between 2017 and 2020, and in 2020 the lagoon becomes completely disconnected from the Gulf of Mexico at spring low tide which is consistent with field measurements and observation. The water levels for several tidal cycles were extracted from the model at the lagoon location and presented as a time series for all simulations in Figure 11. The water level from the Gulf of Mexico was added as a black dashed line for comparison. Tidal range envelope for the Gulf of Mexico, 2017, and 2020 conditions are overlaid with different colors to highlight the differences in tidal ranges. The figure illustrates the deterioration of conditions from 2017 to 2020 as shown in the tidal range decrease between the two survey dates. The water levels with the channel design illustrate an increased water level range when compared to both the 2017 and 2020 conditions. The increased range will improve flushing of the lagoon. The average tidal range was computed for all simulations and compared to the tidal range from the Gulf of Mexico. These ratios are presented at the bottom of the figure. The model indicates that the average Lagoon to Gulf tidal range ratio was 0.41 in 2017 and declined to 0.23 in 2020. The channel design would bring this ratio up to 0.76, indicating a larger tidal prism and improved flushing of the lagoon.

FIGURE 9
Schematic of nature-based restoration elements.

2.1.2 Sandspit Resiliency: beach berm design

The tidal lagoon system and seagrass habitats have evolved in the calm waters between Sand Dollar Island and Marco Island. The sandspit provides natural protection from incoming Gulf waves that break on the dynamic beach face, providing protection to the environmental resources and upland development. In addition to tidal flow enhancement needed to restore the lagoon, the viability of the system also requires maintaining the integrity of the sandspit (Sand Dollar Island) as a coastal barrier sheltering the lagoon and maintaining the entrance open. This section addresses stabilizing the mid-section of Sand Dollar Island where frequent overwash, since Hurricane Irma in 2017, is progressing towards closing the lagoon system. As such, restoration and resiliency of Sand Dollar Island is necessary to preserve the lagoon system. In the absence of the proposed restoration plan, the natural evolution of this sandy barrier will cause it to attach to Marco Island closing the middle part of the lagoon and preventing tidal exchange in the southern portion. The sandy beach would then continue to erode and then expose the existing mangroves to the Gulf of Mexico. Loss of the sandy beach at the northwest corner of Marco Island could then lead to erosion of adjacent beaches as the sand supply diminishes. This area would again be exposed to the open Gulf of Mexico as it was in the 1970s, but this time without the vast submerged inlet shoals that formerly supported Big Marco Pass and the adjacent shoreline.

In order to restore the lagoon area to 2017 (pre Hurricane Irma conditions), the reconstructed section of Sand Dollar Island will need to be a more resilient sandy barrier located seaward of the current position, returning the Gulf Mean High Water line to its late 2016 position. Reconstructing the beach berm provides an opportunity to reduce overwash and landward migration by elevating the berm to reduce the frequency of storm overtopping. Initial designs consisted of a conventional berm and dune profile which was modified after consultation with staff from Rookery Bay Aquatic Preserve. In response to their input, the beach berm is designed as a broad and relatively flat profile to provide the open spaces preferred by some shore bird species. The proposed beach slope is 1 V:15 H consistent with sea turtle protection standards. A nearshore berm is also proposed at approximately the Mean Low Water elevation to provide an intertidal flat and minimize escarpment formation during beach profile initial adjustments. Figure 12 shows typical cross section of the design flow channel and reconstructed beach berm.

2.1.2.1 XBeach modeling for resiliency evaluation

The existing beach that is frequently overwashed has peak elevations less than 1 m above mean high-water level (MHW). Two alternatives were evaluated, one with berm elevations of +1.25 m and the other at +1.75 m above mean MHW. The engineered beaches at other segments of Marco Island Beach are constructed to elevation of approximately +1.5 m above MHW.

The XBeach morphology numerical model (Unesco-IHE et al., 2009) was used in the evaluation of beach berm resiliency design. The model was first set to simulate the morphologic change associated with Hurricane Irma to calibrate and test the model's ability to simulate overwash processes associated with storms. Then, the model was used to evaluate alternatives under two different storm conditions.

The XBeach simulations were based on 2020 bathymetric and topographic surveys representing existing conditions and various design alternatives. The purpose of the simulations was to compare the performance of Sand Dollar Island during a high frequency storm and major storms with and without the restoration project alternatives. The XBeach model was set up to simulate the waves and the rising and receding water from the storm surge of a high frequency storm (less than 10-year return storm) such as Tropical Storm Eta (2020, surge: approx. +1 m) and from a lower frequency major storm such as Hurricane Irma (2017 surge: approx. +1.5 m) which is comparable to a 10-year return storm. Modeled berm conditions post storm impact were evaluated to determine the level of resiliency provided by each alternative.

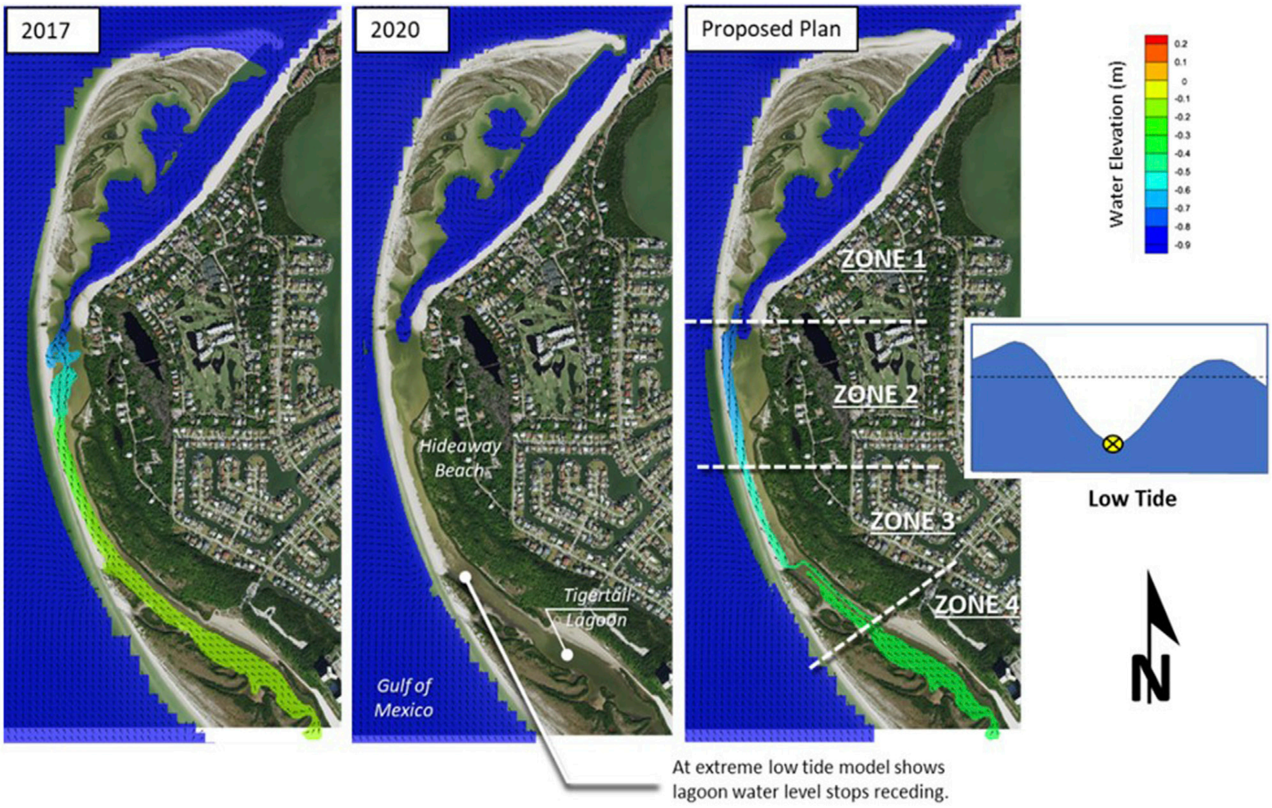

FIGURE 10
CMS model results at low tide for 2017, 2020 and design conditions.

Existing conditions

Figure 13 shows the simulation results for existing conditions (2020). Three-time steps were extracted from the model at T1 (initial condition), T2 (conditions at peak surge) and T3 (conditions at end of simulation). Each timestep is presented in the figure as a regional contour map. The maps are color coded as described in the figure for elevations ranging from 0 m to -2.5 m (-8.2 ft) NAVD88. The water surface is represented as a semitransparent blue overlay.

At peak surge (T2), the model shows the water level (including waves) overtopping Sand Dollar Island. At that stage the berm has already started to shift landward (towards the east). At the end of the simulation (T3), the model results show the shifted shoreline. The lagoon channel is narrower than the initial conditions. The model also shows breaches through the berm connecting the Gulf of Mexico to the lagoon. Such breaches were documented during tropical storm Eta. Their exact location can vary and will typically follow areas along the berm with the lowest elevations. Because of the high sediment transport in the region and low tidal prism from the lagoon, these breaches tend to fill in with sand carried along the shore through wave action. Figure 14 presents the same model results extracted at four profiles along Tigertail for the existing conditions at left. For each profile, the initial conditions are shown as a dashed line and the final profile is indicated in blue with areas of erosion and shoaling shaded in blue and orange respectively. Profiles one through three show a landward shift of the berm, shoreline recession, and narrowing of the channel. Profile four falls in one of the areas which experienced breaching during the simulated storm, therefore the eroded profile is flat because the berm completely eroded.

Proposed design—minor storms

The same simulation was generated for the 2020 conditions with the proposed enhanced berm design alternatives. The enhanced beach berm included a wide elevated berm and mild sloped beach face that includes a submerged nearshore berm that further assists in wave energy dissipation and provides a milder profile that supports ecological needs in the area. Figure 14 shows the model results for the enhanced berm for the same four profiles at right. The cross sections show typical profile adjustment on the shore face without overwash or shoaling in the lagoon. The model also indicated the berm function in separating the lagoon water from the open gulf

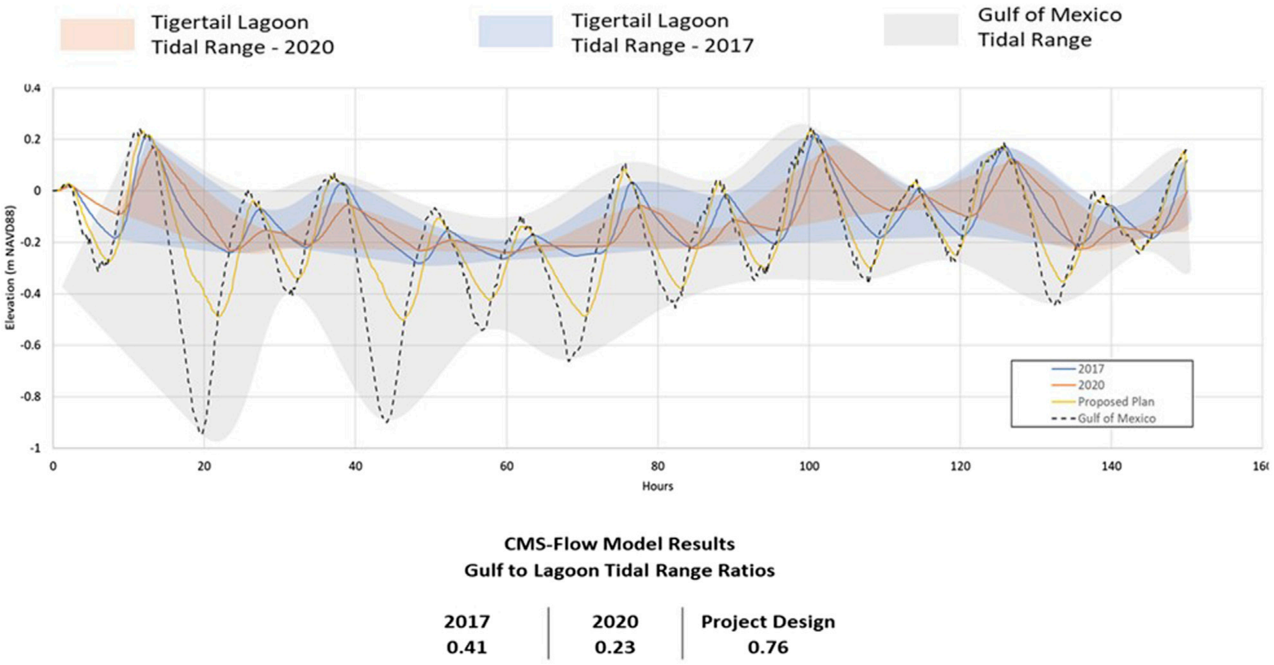

FIGURE 11
CMS model for 2017, 2020 and design conditions.

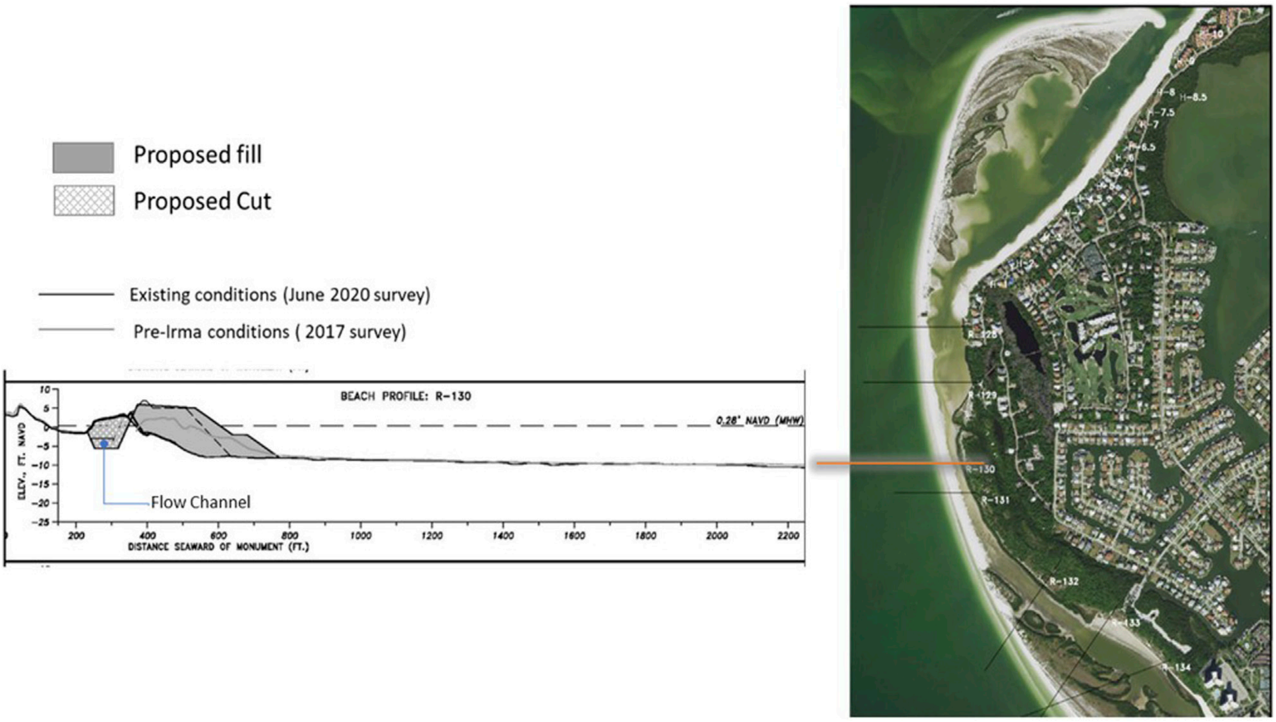

FIGURE 12
Flow channel and resilient beach berm design profile.

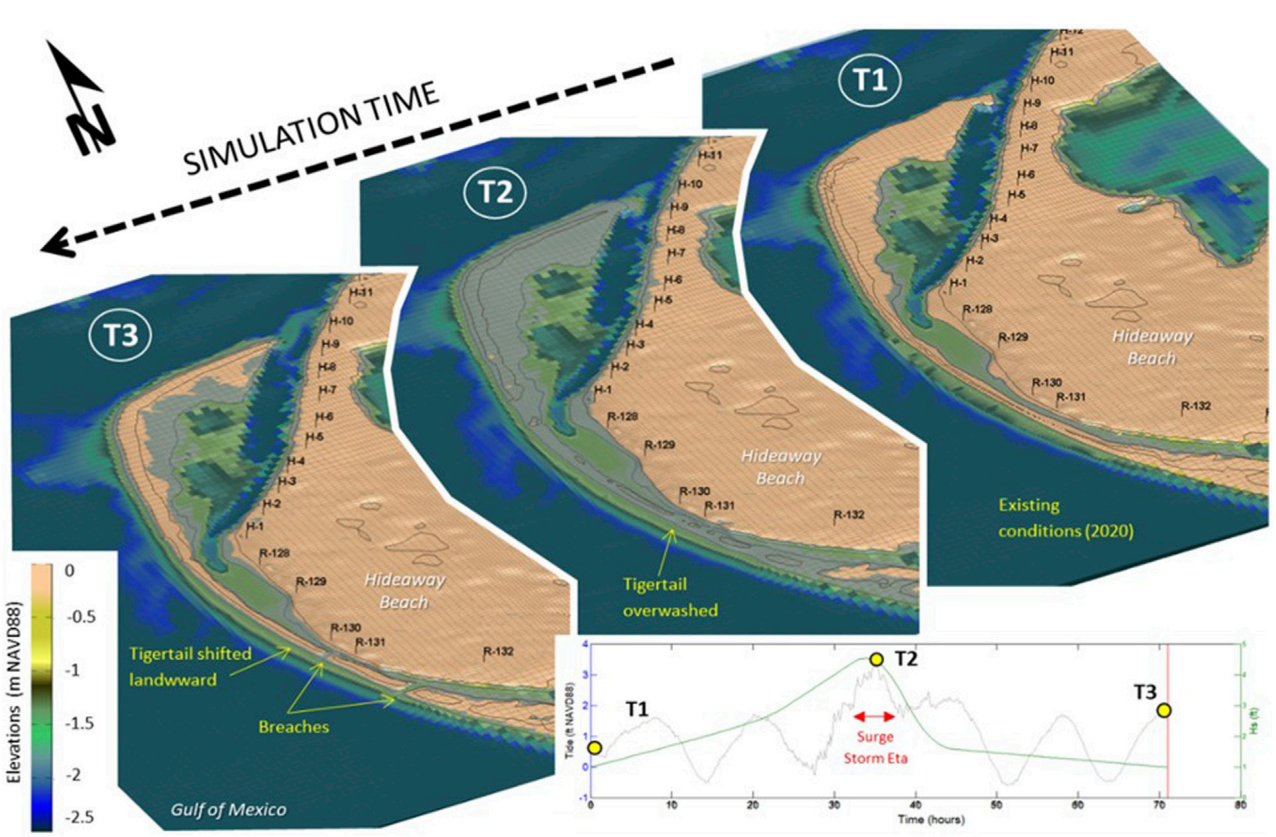

FIGURE 13
XBeach simulation of existing conditions under high frequency storm event.

for that level storm. This functioning of the beach berm and enhanced profile effectively reduces shoaling with the lagoon from overwash and minimizes potential for suspended sediment settling in the lagoon under high frequency storms.

Overall, the model results show that the proposed berm design would enhance the resiliency of Sand Dollar Island to high frequency storms similar to the 2020 tropical storm Eta. The improved resiliency of Sand Dollar Island will help maintain the lagoon channel, tidal flushing, and water quality.

Proposed design—major storms

The second model test scenario examined the existing conditions and design alternatives under major storm conditions or a 10-year return storm such as 2017 Hurricane Irma. The model results show that for existing conditions under major Hurricane the sandspit would migrate landward with significant overwash filling in the lagoon, resulting in the barrier beach welding onshore in the center 1.5 km of the sandspit. For the elevated design berm, under a major Hurricane, the enhanced berm would prevent overwashing of the berm into the lagoon along the protected mid-section of Sand Dollar Island. The areas outside of the project area would still experience some level of overtopping at peak surge.

The optimal elevation and width of the design berm was selected at +1.75 m based on the results of simulations that showed resiliency for a 10-year return storm. A 10-year return design threshold is considered appropriate for the design life of this project and represents a significant improvement over the existing conditions. This selection is supported by the consideration that the model results represent initial conditions after construction and do not consider the compound effects of multiple storms and progressive longshore erosion over time. Monitoring and adaptive management allowing for maintenance at a manageable frequency of 4–5 years to restore the resilient berm to its design conditions would assist in maintaining the level of resiliency against major storms.

2.1.2.2 Proposed design—long term evolution

Volumetric change for the beach face at the retreating Gulf-facing beaches was determined using multiple survey datasets since 2001. This analysis requires isolating longshore and overwash components, which was done by subtracting overwash accumulation from the total change measured on

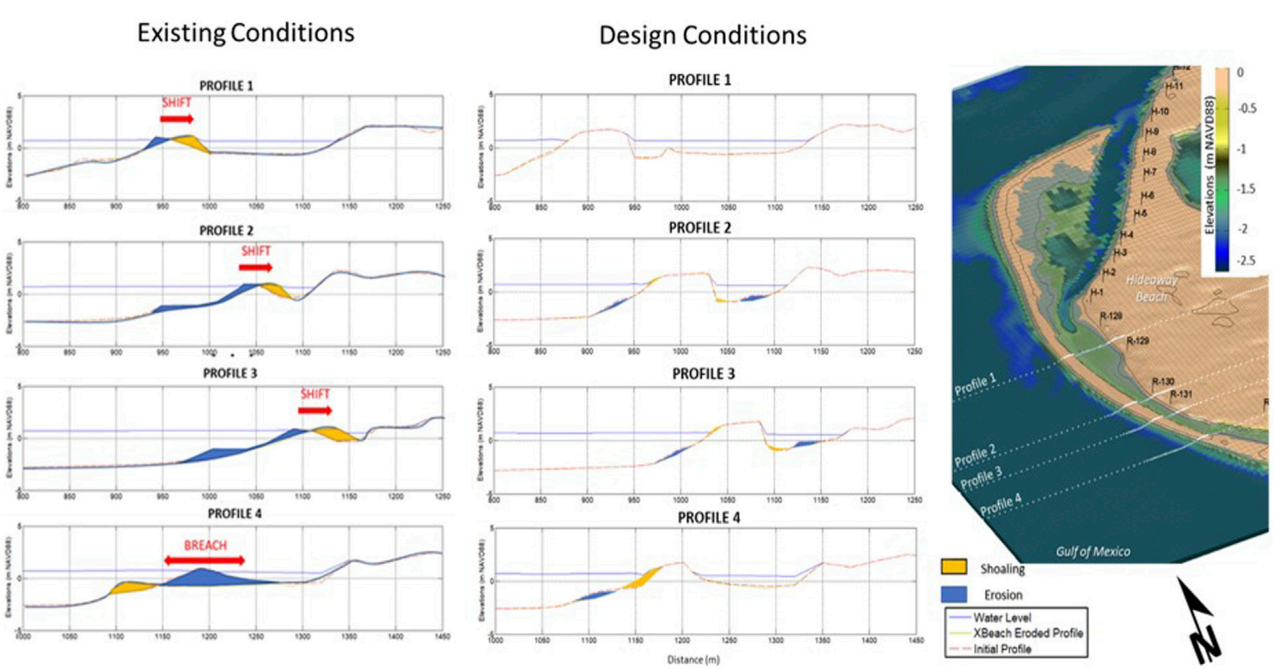

FIGURE 14
XBeach morphologic evolution under high frequency storm event.

TABLE 3 Annualized volumetric change at eroding gulf beach face.

From (year)	To (year)	Duration (years)	Overwash (m3/yr)	Longshore (m3/yr)	Total (m3/yr)
2001	2005	3.9	1900	10,600	12,500
2005	2009	3.8	2,500	14,800	17,300
2009	2014	4.9	2,600	6,500	9,100
2014	2017	3.2	5,700	9,300	15,000
2017	2020	2.7	6,900	12,700	19,700
Overall			3,600	10,500	14,100

the active beach face. These are provided in Table 3, along with annualized rates of change, and overall totals and rates. The data show an interesting trend of increasing rates of overwash, while longshore rates vary, likely in response to changes in curvature resulting from morphologic evolution. Longshore erosion rates have increased since 2009, which suggests that this is representative of the existing planform.

As shown by the X-Beach simulations, overwash will be eliminated for storms of less than 10% probability at the post-construction condition. However over time other factors such as rainfall, wind, storm conditions, etc are likely to reduce the overall berm height resulting in some degree of overwash. Likewise longshore transport may be anticipated to increase as wave energy that previously propagated over the berm will now break on the active beach face. Fill adjustment and re-establishing the curvature will also contribute to potentially higher longshore sediment transport than was previously observed. This suggests longshore erosion losses on the order of average (10,500 m^3/yr) to recent observations (12,700 m^3/yr), or higher should be anticipated. A reasonable engineering estimate of an average annual rate of 11,000 to 15,000 m^3/yr is considered appropriate for long term estimates. Fill placement is estimated to be on the order of 300,000 m^3. Project experience with coastal nourishment indicates that about half of the total fill will adjust cross-shore and laterally in the initial one to 2 years, suggesting 150,000 m^3 will remain to provide protection. After 5 years approximately half (75,000 m^3) of the protective volume can be expected to have eroded, which combined with reductions in berm height is likely to leave minimal protection and require maintenance. Storms of less than 10% probability may also decrease protective capability, indicating a 3–5 year nourishment cycle.

2.1.3 Lagoon Entrance Enhancement and Renewable Sand Source: Sand trap design

The integrity and viability of the lagoon is dependent on two main features, the sand barrier of Sand Dollar Island and tidal exchange with the Gulf through the maintained entrance at the north end of the system. The entrance at the north end has been maintained open through dredging in 2010, 2013, 2016, and 2019 to avoid closure and attachment of the north tip to Marco Island. However, each dredging event occurred at a different location to

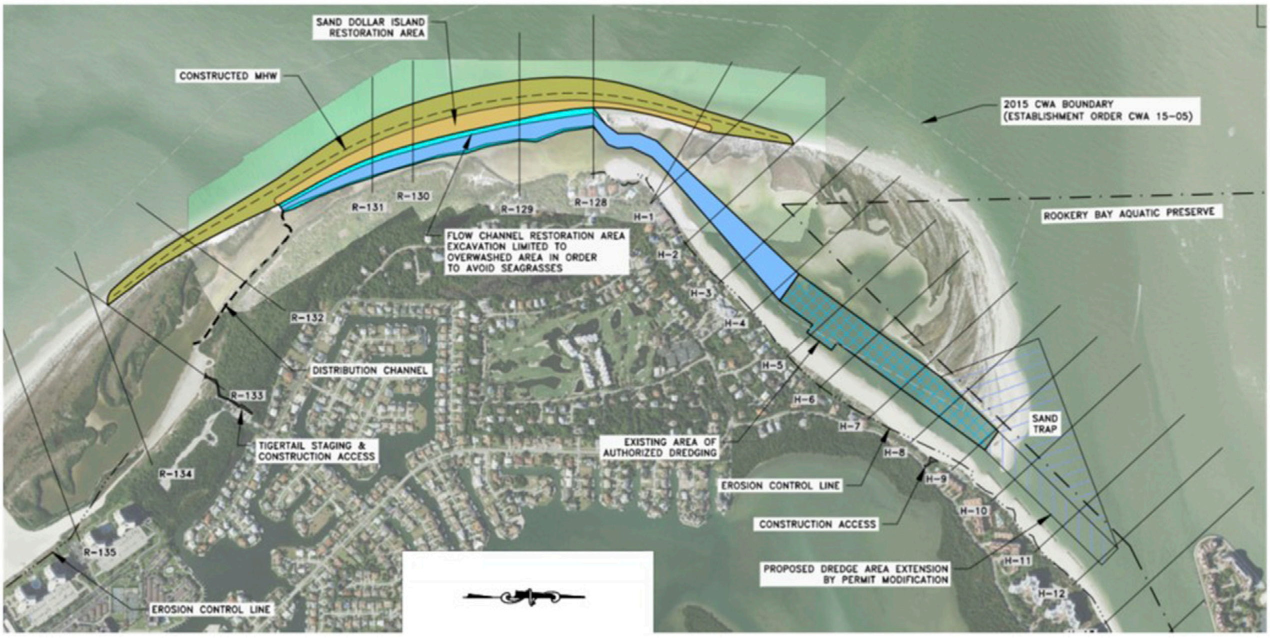

FIGURE 15
Final project design plan view.

keep up with the growth of the sand spit toward the northeast. At present time further extension of the entrance in the northeast direction to maintain the entrance open is becoming unsustainable. This is due to the physical and hydrodynamic restriction as the spit further encroaches on Big Marco River where flow confluence will force attachment and closure of the entrance. On the other hand, the lagoon area and tidal prism have been in decline over the past decade mainly due to shoaling and overwash of the middle section of Sand Dollar Island. The reduction of lagoon area and potential collapse of the middle part of the lagoon will further reduce the tidal flow at the entrance forcing closure at the northeast beyond the current dredging program.

To address both features necessary to restore the system, a resilient berm at the midsection of Sand Dollar Island is needed as well as stabilization of the entrance to earlier, more stable conditions. Reconstruction of the beach berm at Sand Dollar Island will require a source of sediment in addition to sediment from the proposed flow channel. This source must also be available for future reconstruction events.

Sand Dollar Island has grown significantly during the past 2 decades. Establishing a Sand Trap to remove sediment from this area will provide a renewable sand source that will also benefit the management of the entrance to the lagoon by intercepting the sediment before it accumulates at the entrance. A sediment source for the berm reconstruction in this area will also return the sediment to an up-drift position where it will erode back toward the end of the island, creating a renewable cycle of regional sediment management. The renewable cycle will maintain the existing sediment cycle, which would otherwise deteriorate beginning with onshore attachment of Sand Dollar Island and accelerate when the erosion reaches the mangrove shoreline resulting in lack of sediment supply to the adjacent beaches.

3 Design plan

The final design is shown on Figure 15 and would consist of establishing a flow channel within the overwash and shoaled areas of the Tigertail Lagoon and to improve the resiliency of the Gulf-fronting shoreline of the sandspit (Sand Dollar Island) using sediment dredged from the flow channel and a sand trap at the north end of the sandspit. The design restores and enhances the protective function of the sandspit, the total wetland area, and will maintain sediment bypassing to adjacent beaches. All of these functions would be lost in the absence of the project.

The sandspit/tidal lagoon system in this case is a natural but altered system which has been maintained artificially by dredging the entrance at the north end of the sand spit on 3-year intervals since 2010. This allowed tidal flushing of the 3-km long lagoon to maintain water quality suitable for various wildlife resources and habitats. Water quality data collection was limited over the past few years. As part of the implementation of this project, a fixed data logger will be installed to record water levels and water quality measures near the south end of the lagoon to collect continuous water quality data to support analysis of project influence on water quality and environmental resources. A detailed biological monitoring plan was also prepared and approved by the permitting agencies to provide benchmark information and future monitoring of resources, physical and biological data that will from the basis for future maintenance and adaption requirements (Turrell, Hall and Associates 2021A).

4 Discussion

This paper focuses on the technical approach to implement the concept of maintaining natural morphological features as sustainable coastal protection measures for both environmental habitat and upland development. The technical approach and management efforts in this case study are guided by environmental protection statutes and rules mandated by state and federal agencies in the United States. Coastal management in the US in general and Florida in particular is regulated primarily for environmental protection ahead of other issues.

Barrier islands are dynamic, and the time scale of their evolution is longer than engineering project time scales. In this case Marco Island is a heavily developed barrier island, surrounded by multiple undeveloped/natural islands. Chronic erosion occurs due to the temporal intersection of upland coastal development and morphological evolution as the natural evolution changes the equilibrium planform relative to that at time of early development. Anthropogenic influences, including shoreline hardening, coastal structures and navigation dredging can also alter the equilibrium planform of barrier islands and associated morphologic features.

Integrating the objectives of the environmental preservation of natural resources and upland development coastal management objectives is a challenge. An incremental nature-based approach can start with preserving morphologic features that existed and functioned at time scales of years to decades. This approach would also allow for an adaptive management that is able to adjust in response to barrier island dynamics, influences and climate change and would be more sustainable than conventional methods of typical flood wall, barriers and hardened shorelines. In this case sustainability is established by the circular use of sediment from the terminal end of the sand spit that also allows for the lagoon entrance to remain open.

One of the important aspects of this case study is the intersection between an evolving coastal system bordered by a heavily developed barrier island. While the sand spit growth and on-going collapse is mainly caused by natural inlet evolution, in this case the anthropogenic influence has also factored in the presence and existence of the Tigertail Lagoon over the past 2 decades. The entrance to the lagoon has been kept open by artificial dredging on a 3-year cycle since 2010, thus allowing the 3 km long tidal lagoon to maintain wetland habitat with seagrass beds and interior mangrove shoreline. For such a quasi-natural systems to exist, management and maintenance is needed to restore and support the vitality of such system otherwise the erosion and retreat of the sand spit will continue until it reaches the upland development. In many instances upland developments do not qualify for hard shore protection or structural solutions unless meeting eligibility and vulnerability requirements. As such, areas that are subject to chronic erosion without active beach management efforts would eventually qualify for conventional shore protection measures in the future via various types of shoreline hardening or coastal structures.

This case study focuses on development of an adaptive management plan that supports the presence of a natural barrier system to coexist and provide coastal protection to a heavily developed barrier island. Coastal management including beach restoration and coastal structures cover most of the Gulf-front shorelines except the northwest part of the island designated as a Critical Wildlife Area. As such, the sandspit and lagoon area is designated as a Critical Wildlife Area managed by state and local environment agencies aimed at preservation of existing ecosystems and environmental resources. Because most of the current wildlife areas are typically managed to evolve naturally, those areas are sometimes not included in regional coastal management efforts. Preservation of such areas becomes unsustainable when chronic erosion gradually degrades a temporal coastal defense. As erosion progresses, those critical wildlife areas will be allowed to erode and migrate onshore until they intersect with upland developments. At that point of time, restoration of such features will not be possible and hardened shorelines or typical beach restoration would be the only available measure. These do not provide the multiple layers of protection provided by a system of sand spits, lagoons, and mangrove shoreline. However, timely restoration and adaptive measures at a manageable frequency can be implemented to maintain such system and this example showcases one of those cases where active management can integrate environmental conservation and shore protection efforts.

Among the challenges to this approach is to develop a plan that stratify environmental protection objectives and those with upland development for coastal and flood risk reduction. Often the objectives of upland development and protected preserve areas are not coordinated, and as a result are managed independent of each other. Coastal flooding resiliency efforts typically focus on reducing risks for flooding of infrastructure and protecting habitable structures under future SLR scenarios and increased intensity of storms.

On the other hand, environmental protection and preservation of ecosystems can be focused on protecting existing natural setting (natural preserves). Some aspects of that preservation are managed by designation of undeveloped ecosystems as natural preserves. When not maintained, the sand-spits and erosion progress until hard shore protection is necessary.

As such the main objective for this case is to restore and maintain the existing natural 3 km long sand spit as a coastal barrier and avoid its ongoing collapse. This will be followed by active monitoring and maintenance to preserve the ecosystem and natural and nature based coastal defense features.

5 Conclusion

The Tigertail Lagoon/Sand Dollar Island Ecosystem Restoration Plan has been designed to incorporate improvements to aquatic and upland habitat while preserving and enhancing the resiliency of the natural system. This Plan demonstrates the advantages of working with the natural environment and coastal processes to preserve and enhance existing habitat in a naturally evolving system. The project also provides nature based coastal resiliency to the environmentally sensitive area fronting upland communities. Establishing resiliency through nature based solutions such asmulti-tiered sandy barriers, coastal lagoons, and mangrove shorelines sets an example for future consideration elsewhere. Such examples are valuable for future planning as coastal cities and developed coastal areas are assessing future vulnerabilities to sea level rise and developing adaptation plans for improved coastal storm resiliency.

The intersection of natural evolution and upland development provided the unique conditions where a critical wildlife area had been created initially by natural evolution of inlet features and altered by limited frequent dredging which kept the tidal lagoon viable as wildlife habitat area. This ecosystem and its components are dependent on tidal lagoon environment. The frequent entrance dredging maintains the tidal exchange to the lagoon allowing seagrass to grow and mangrove shoreline habitat to persist on interior shorelines. The collapse of the middle section of the sand spit/and lagoon shoaling as well as the sand accumulation at the north end represented a physical detriment to the system. Expanding the dredging at the north end and using the sand to reinforce the vulnerable section of the spit provides an opportunity to restore and maintain the integrity of the sand spit and tidal lagoon as a coastal front. Its current presence and restoration provide a multitier coastal barrier system that maintains valuable natural resources and provide coastal protection to the upland. The conventional option of allowing the sandspit to collapse onshore then erosion to progress towards upland development will eventually lead to unnatural or hardened coastal front that will not allow for adaption to future barrier island dynamics nor sustain the environmental habitat value of the system that existed over the last 2 decades.

The design is based on working with nature to support the integrity and function of a natural barrier system that can adapt with changing sea levels while providing resiliency to storms. Sustainability and adaption are planned through monitoring and management plans to implement maintenance projects to elevate the sandy barrier and achieve desired resiliency coupled with cyclic use of sand within the system to maintain hydraulic viability of the tidal lagoon and address shoaling areas. Key elements in this plan also include integrated efforts with the upland community, the City of Marco Island, state and federal agencies, Rookery Bay National Estuarine Research Reserve and Critical Wildlife Area administration to maintain the integrity of a natural barriers system as an element to protect and manage coastal flooding vulnerability, wildlife habitat, and the City of Marco Island.

Data availability statement

The raw data supporting the conclusion of this article will be made available by the authors, without undue reservation.

Author contributions

MoD provided overall concept, design leadership, and manuscript preparation. MF and MaD provided technical analysis and documentation.

Funding

The work at Tigertail Lagoon/Sand Dollar Island is conducted by Humiston and Moore Engineers for the City of Marco Island funded by the Hideaway Beach Tax District.

Acknowledgments

The authors would like to thank the Hideaway Beach Tax District for supporting this work. The authors would also like to thank all stakeholders, professionals and permitting agencies who provided feedback and collaboration on the development of this nature-based restoration plan.

Conflict of interest

Authors MoD, MF and MaD were employed by Humiston & Moore Engineers.

Publisher's note

References

Chávez, V., Lithgow, D., Losada, M., and Silva, R. (2021). Coastal green infrastructure to mitigate coastal squeeze. *J. Infrastruct. Preserv. Resil.* 2, 7. doi:10.1186/s43065-021-00026-1

CMS-Coastal Modeling System (2006). *Two-dimensional depth-averaged circulation model*, U. S. Army Engineer Research and Development Center, Coastal and Hydraulics Laboratory, 3909 Halls Ferry Road, Vicksburg, MS 39180-6199.

Dabees, M. A. (2017). "Evolution of barrier island sand spits and effects on beach management practices. Case studies in central Florida gulf coast, USA," in Proceedings of Coastal Dynamics 2017, Helsingor, Denmark, June 12–16, 2017.

Dabees, M. A. (2018). "Hurricane Irma's morphologic response on beaches and tidal inlets in southwest Florida, USA," in Proc. Of the 36th International Conference on Coastal Engineering, Baltimore, USA, July 30–August 3, 2018. http://www.eventscribe.com/2018/ASCE-36ICCE/assets/handouts/675702.pdf.

Dabees, M. A., and Kraus, N. C. (2004). Evaluation of ebb-tidal shoals as a sand source for beach nourishment: General methodology with reservoir model analysis. Proc. 17th National Conf. on Beach Preservation Technology, Tallahassee, FL, February, 2004, Tallahassee, FL: CD-ROM, FSBPA, 21 pp.

Dabees, M. A., and Kraus, N. (2008). "Cumulative effects of channel and ebb shoal dredging on inlet evolution in southwest Florida, USA," in Proceedings of the 31st International Conference on Coastal Engineering, Hamburg, Germany, August 31–September 5, 2008 (World Scientific), 2303–2315. http://cirp.usace.army.mil/Downloads/PDF/dabees-kraus-ICCE08.pdf.

Dabees, M. A., and Moore, B. D. (2014). "Evaluation of beach erosion up-drift of tidal inlets in southwest and central Florida, USA," in Proceedings of 34th Conference on Coastal Engineering, Seoul, Korea, 2014.

Dabees, M. (2020). Beach planform equilibrium, application and methodologies for climate change resiliency consideration. *Int. Conf. Coast. Eng.*, (36v), 43. https://youtu.be/gWsbmi6VIo0. doi:10.9753/icce.v36v.management.43

FDOT-Florida Department of Transportation (1999). Florida Land use, cover and forms classification system. *Handbook* 92. https://www.fdot.gov/docs/default-source/geospatial/documentsandpubs/fluccmanual1999.pdf.

Humiston & Moore Engineers (2021A). Tigertail lagoon/sand dollar island ecosystem restoration project, alternatives' analysis, technical report. Prepared for Hideaway Beach Tax District, City of Marco Island (43 p.) https://www.humistonandmoore.com/tigertaillagoon

Humiston & Moore Engineers (2021B). Tigertail lagoon/sand dollar island ecosystem restoration project, engineering management plan, technical report. Prepared for Hideaway Beach Tax District, City of Marco Island (132 p.) https://www.humistonandmoore.com/tigertaillagoon

Humiston, K. H. (1988). "The effects of the growth and migration of Big Marco pass ebb tidal shoal on Marco island beaches," in Proceedings 1st National Conference on Beach Preservation Technology, Tallahassee, FL, March 23–25, 1988 (Florida Shore & Beach Preservation Association).

South Atlantic Coastal Study Main Report Final Draft (2021). *South Atlantic coastal study main report final Draft*. US Army Corps of Engineers. Washington, D.C., United States

Turrell, Hall & Associates (2021A). Tigertail lagoon/sand dollar island ecosystem restoration project, biological monitoring plan, technical report. Prepared for Florida Department of Environmental Protection. Tallahassee Florida. (33 p.) https://www.humistonandmoore.com/tigertaillagoon

Turrell, Hall & Associates (2021B). Tigertail lagoon/sand dollar island ecosystem restoration project, environmental management plan, technical report. Prepared for Hideaway Beach Tax District, City of Marco Island (270 p.) https://www.humistonandmoore.com/tigertaillagoon

Unesco-IHE, Deltares, and Tu, D. (2009). "XBeach model description and manual,". Report Z4175. Available at: https://xbeach.readthedocs.io/en/latest/user_manual.html.

frontiers | Frontiers in Built Environment

TYPE Original Research
PUBLISHED 31 August 2022
DOI 10.3389/fbuil.2022.923965

OPEN ACCESS

EDITED BY
Spyros Hirdaris,
Aalto University, Finland

REVIEWED BY
Matthew V. Bilskie,
University of Georgia, United States
Sooyoul Kim,
Kumamoto University, Japan

*CORRESPONDENCE
Kayla Ostrow,
ostrowk@oregonstate.edu

SPECIALTY SECTION
This article was submitted to Coastal and Offshore Engineering, a section of the journal Frontiers in Built Environment

RECEIVED 20 April 2022
ACCEPTED 03 August 2022
PUBLISHED 31 August 2022

CITATION
Ostrow K, Guannel G, Biondi EL, Cox DT and Tomiczek T (2022), State of the practice and engineering framework for using emergent vegetation in coastal infrastructure.
Front. Built Environ. 8:923965.
doi: 10.3389/fbuil.2022.923965

State of the practice and engineering framework for using emergent vegetation in coastal infrastructure

Kayla Ostrow[1]*, Greg Guannel[2], Esteban L. Biondi[3], Daniel T. Cox[1] and Tori Tomiczek[4]

[1]School of Civil and Construction Engineering, Oregon State University, Corvallis, OR, United States, [2]Caribbean Green Technology Center, University of the Virgin Islands, St. Thomas, United States Virgin Islands, [3]Applied Technology and Management/Geosyntec Consultants, Inc, West Palm Beach, FL, United States, [4]Department of Naval Architecture and Ocean Engineering, United States Naval Academy, Annapolis, MD, United States

Natural and Nature-Based Features (NNBF) are promoted as alternatives to structural flood protection measures. Progress has been made in understanding the physics and engineering of these systems; however, engineering, ecological, and social barriers to implementation remain. This paper identifies these barriers using the results of a literature review and summary of expert opinion; contrasts the state of the practice of NNBF with traditional structures; and details the main engineering challenges to NNBF implementation, including the uncertainty in current calculation techniques and lack of engineering design guidelines. We suggest that emergent vegetation systems can be designed with the current body of information, and an example framework is proposed for assessing these systems for their wave attenuation performance. The framework is discussed in the context of risk, and future research priorities are presented.

KEYWORDS

engineering with nature, natural and nature-based features, working with nature, building with nature, emergent vegetation, wave attenuation, design guidelines, nature-based solutions

Introduction

Over the last few decades, ecosystems have been promoted as viable alternatives to conventional (structural or gray) coastal protection structures (Arkema et al., 2013; Silver et al., 2019). Several studies have demonstrated the protective and restorative values of wetlands, reefs, seagrass beds, and/or vegetated dunes (Scyphers et al., 2011; Anderson and Smith, 2014; Ozeren et al., 2014; Taylor et al., 2015; Guannel et al., 2016; Narayan et al., 2016; Chang et al., 2019; Lei and Nepf, 2019; Maza et al., 2019; Tomiczek et al., 2020a, 2020b, 2022; Elko et al., 2021; Kelty et al., 2022). These types of solutions for shoreline protection are termed "Natural and Nature-Based Features (NNBF)," and are landscape features that are used to provide engineering functions, while producing additional economic, environmental, and/or social benefits. There are many definitions, but the common element among all of these definitions is the focus on conserving, restoring, and engineering natural systems for the benefit of people and the ecosystems they inhabit (Bridges et al., 2021). NNBF for flood and erosion protection include natural features such as emergent vegetation, beaches and dunes, reefs, or islands, and nature-based features (*i.e.,* engineered ecosystems that mimic characteristics of natural features) such as constructed wetlands, nourished beaches, and artificial reefs (Bridges et al., 2015). These systems have also been referred to as "Nature-Based Solutions (NbS)," "Natural Infrastructure," or "Green Infrastructure," among other terms (Bridges et al., 2021). NNBF solutions are attractive because they have the potential to provide ecological, social, and economic benefits in addition to shoreline protection services (Barbier et al., 2011; Arkema et al., 2015; Ruckelshaus et al., 2016), and are often viewed as a "win-win" approach to coastal engineering (Hochard et al., 2019; Menéndez et al., 2020; Cunha et al., 2021; Feagin et al., 2021). As a result, several major initiatives by U.S. government agencies (Bridges et al., 2015, 2021; Webb et al., 2019), non-profit groups (Sarasota Bay Estuary Program, 2018; Narayan et al., 2019), and international organizations (PIANC, 2018; Browder et al., 2019; UNDRR, 2020; Castellari et al., 2021; Science for Environment Policy, 2021), have focused on leveraging NNBF as resilient adaptation alternatives for shoreline protection.

One type of natural habitat widely discussed by practitioners and in the literature is emergent vegetation, which includes mangroves (*e.g., Rhizophora* sp., *Avicennia* sp., *Laguncularia racemosa*) and marsh vegetation such as grasses, rushes, or reeds (*e.g., Spartina* sp., *Juncus* sp., *Phragmites* sp.). Among other benefits, these intertidal ecosystems have been noted for their wave and storm surge attenuation capabilities (Mazda et al., 1997; McIvor et al., 2012; Zhang et al., 2012; Montgomery et al., 2019; Chen et al., 2021), carbon sequestration (Alongi, 2008; Sanderman et al., 2018), habitat services for native fauna (Odum et al., 1982; USFWS, 1999), and cultural and recreational values (Uddin et al., 2013; Spalding and Parrett, 2019). However, the quantification and prediction of engineering performance (*e.g.,* wave height attenuation) of emergent vegetation to inform design lags behind the quantification of hydraulic responses for conventional engineering systems. Indeed, practicing engineers may be hesitant to design NNBF due to the lack of design standards and differences with the traditional design process for gray infrastructure. The coastal engineering practice, as well as civil engineering in general, is guided by established manuals of practice, design standards, and guidance documents (*e.g.,* USACE, 2002; FEMA, 2011; ASCE, 2014, 2022; Bridges et al., 2021). Although recent efforts have made strides in developing general guidelines for NNBF at international, national, state, and local levels (*e.g.,* Miller et al., 2015; World Bank, 2017; Webb et al., 2019; Bridges et al., 2021), current guidance documents do not provide the NNBF equivalent of the comprehensive calculation methodologies common in traditional engineering design manuals (Bridges et al., 2021). Moreover, compared with conventional systems, NNBF have unique concerns, because their performance may be affected by biological factors and physical events. For example, although scientists have found evidence of engineering benefits provided by emergent vegetation under specific circumstances (*e.g.,* McIvor et al., 2012), few conclusions are applicable for storm conditions (Pinsky et al., 2013), and only recently has research been focused on storm performance (*e.g.,* Vuik et al., 2016; Kelty et al., 2022). Therefore, it is important that guidance on coastal protection benefits be provided, clearly identifying the range of applicability of expected benefits.

Even with recent advancements in knowledge about utilizing emergent vegetation for coastal risk mitigation in hydraulics or engineering models, barriers to implementation remain (*e.g.,* Close et al., 2017; Cherry et al., 2018). These barriers exist throughout the implementation process as identified by Bridges et al. (2021), with challenges noted for technical design, socioeconomic considerations, financing, permitting, construction, and maintenance (Close et al., 2017; Cherry et al., 2018; Zuniga-Teran et al., 2020; King et al., 2021). A broad set of conditions needs to be addressed to facilitate and promote the appropriate use of NNBF for coastal protection, which requires not only coastal engineers, but also experts in other disciplines in engineering, ecology, and social science.

To improve our abilities to predict the engineering performance of NNBF, there is a need to 1) develop technical recommendations on how to incorporate NNBF as part of coastal hazard mitigation solutions; 2) quantify wave attenuation performance; and 3) establish prescriptive standards for design, construction, and monitoring of projects to create, restore, or enhance NNBF systems.

This paper addresses the various issues raised above by summarizing the state of the practice and providing practical guidance for the design of NNBF, based on recent advances in the quantification of wave attenuation by emergent vegetation. We also describe the engineering, ecological, and social conditions that influence the use of these systems for coastal protection. Based on these considerations, we propose a conceptual engineering framework for evaluating existing natural systems or designing new NNBF or hybrid systems, and make recommendations in the engineering, ecological, and social dimensions to facilitate and promote the appropriate use of these systems.

State of the practice

Expert opinion

To gain a deeper insight into the use of emergent vegetation in engineering design, implementation, and construction, we asked practitioners in different fields working with NNBF projects to comment on the state of the practice by answering the following questions:

1) In your experience, what is the current level of understanding regarding the performance of emergent vegetation in coastal protection applications? Is available information applied adequately for analysis of alternatives and for design?
2) What additional progress from a scientific, engineering, or design standpoint is needed to encourage adequate consideration and better implementation of these types of nature-based solutions?
3) What steps from a policy or regulatory standpoint could be taken to encourage adequate consideration and better implementation of these solutions?
4) Please share any other thoughts/comments/concerns about the present status and future needs regarding the use of nature-based solutions (especially emergent vegetation) for coastal hazards mitigation and climate adaptation.

A total of 32 professionals responded, representing academia (6), consulting (9), government (13), and nonprofit organizations (4), resulting in a variety of perspectives and experience on emergent vegetation projects. The responses primarily inform on the existing knowledge in the field and progress needed for NNBF strategies to be more widely adopted. Responses were organized according to two broad themes: 1) current knowledge and 2) future needs, and within these themes, responses were separated into engineering, ecology, and social categories.

While many respondents recognize that there is ample information supporting NNBF performance, designers are unable to apply it in a quantitative way needed for design (19/32). Two consultants and one government professional note that the information requires expertise to understand, making it difficult to access (3/32). Furthermore, experience from case studies is highly location-specific and unable to be extrapolated (5/32). Rather than designed solutions, many NNBF projects are structured as vulnerability studies (1/32). Physical space is also a concern, as there may not be enough space for emergent vegetation in urban environments or on steep and narrow banks (2/32). From a socioeconomic perspective, respondents identify the current regulatory framework as inadequate for NNBF, with many suggesting changes to policies and permitting (21/32). Stakeholders may advocate against or be reluctant to implement NNBF projects due to loss of space and view, attraction of mosquitos, and maintenance considerations (5/32). There are concerns about a perception among some stakeholders that vegetation can always be used as a solution, even though many situations call for another strategy or multi-tiered solution (2/32). Responses from academia, government, and consulting describe a disconnect between the engineering, architecture, and environmental disciplines, with some noting that engineers tend to ignore NNBF solutions, while architects and environmental professionals tend to overestimate the protection that vegetation can provide and do not understand the need for quantitative design guidelines for engineers (4/32).

Responses identify future engineering needs; a summary of broad categories is shown in Figure 1. The most frequently cited need is the further development of engineering design standards (19/32), an observation that agrees with previous studies (Cherry et al., 2018; Zuniga-Teran et al., 2020). Some responses describe specific criteria that would be needed in engineering design guidelines: 1) coastal geomorphology considerations, including sediment; 2) nearshore conditions, such as bathymetry, tidal range, and wave conditions; 3) vegetation considerations, such as species, age, number of plants, density, height, and width of patch, and under what environmental conditions and in what locations they would be able to thrive; 4) contrasting design considerations for gray, green, and hybrid systems; 5) maintenance requirements, including best management practices; 6) performance over the design life, including recovery time between storms and changes in protection as vegetation ages; and 7) survivability, especially in the face of climate and environmental changes such as water quality, salinity, diseases, and extreme weather events. These criteria should be predictive and could consider navigation.

Additional engineering challenges remain beyond the development of comprehensive engineering design guidelines. For example, a broader consensus is required on how to incorporate emergent vegetation into varied methodologies of calculating wave runup and total water level (1/32). Government respondents identify a need for monitoring criteria to show success, such as 1) metrics for reporting vegetation density, areal extent, and root structure of plants; and 2) guidelines for duration and spatial resolution of the monitoring program (4/32). There is also a need for additional pilot projects in all types of locations that measure efficacy and detail designs (9/32). Similarly, research should include field experiments especially in locations where NNBF projects may be implemented, such as tropical environments, and develop a greater understanding of the applicability of solutions from one location to another (5/32). This response echoes the need to understand transferability of NNBF results between locations (Close et al., 2017). Future research should also characterize the performance of emergent vegetation under extreme events, higher tidal ranges, and future relative sea level rise scenarios (7/32), and provide a better quantification of erosive processes (2/32). Finally, respondents found that experiments are needed to further quantify and prove efficacy, including the translation of results from flume experiments to field parameters (6/32).

Many responses mention the necessity of ecological research advances for successful implementation of NNBF (6/32), including studies that assess connectivity, comprise a wide range of habitat types and environmental conditions, monitor interaction with substrate and changes over the project's life

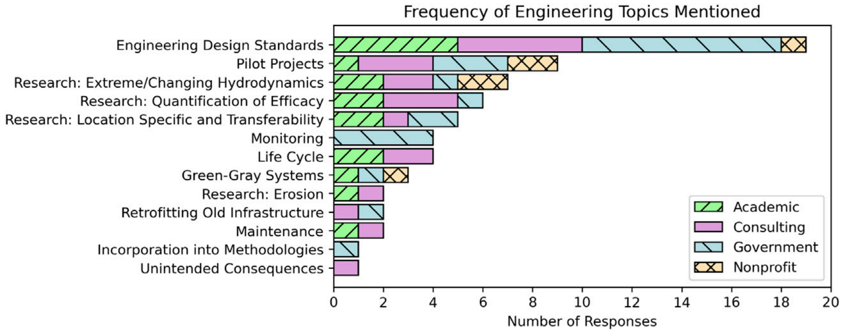

FIGURE 1
Frequency of categories of future engineering needs for emergent vegetation implementation cited by experts in survey responses (N=32).

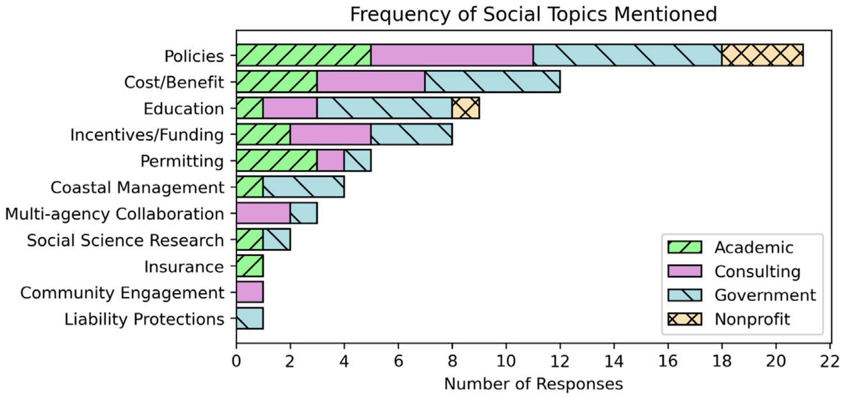

FIGURE 2
Frequency of categories of future socioeconomic and policy needs for emergent vegetation implementation cited by experts in survey responses (N=32).

cycle, and characterize the impacts of invasive species. In order to obtain the best performance of a restored or hybrid system, projects should imitate the ecology of nearby natural systems (4/32). This observation is consistent with the findings of Waryszak et al. (2021), who determined that the designers of most successful hybrid projects have a strong knowledge of site hydrological and ecological history. Furthermore, vegetation may be optimized based on the carbon cycle (3/32). Materials scientists and engineers can be brought into interdisciplinary teams for design (1/32). The engineering and ecology responses are highly related, with species considerations, performance over design life, maturation, and survivability requiring ecological expertise. One future research topic is converting existing ecological parameters, such as basal area, to engineering parameters, such as projected area (1/32). NNBF designs may also create unintended consequences (1/32).

We also asked subject matter experts about sociopolitical barriers to NNBF implementation (Figure 2). The most cited recommendations center on policies (21/32), including 1) prioritizing green solutions over traditional (structural) alternatives; 2) allowing NNBF projects to count for other environmental credits such as for stormwater; 3) requiring vegetation experts or plans to be included in projects; 4) encouraging redundancy in planning; 5) considering longer life cycles of up to 100 years; and 6) developing regulations specifically for hybrid systems. Of these policy responses, multiple suggest permitting modernization (5/32), which is also identified in the literature (Cherry et al., 2018). Suggestions include fast-tracking NNBF permits and modifying USACE Nationwide Permits to prioritize NNBF over gray infrastructure. Permitting modernization would focus on the removal of artificial barriers to NNBF project approval, allowing NNBF to be given equal consideration with traditional solutions. One potential area of conflict within policy arises from habitat regulations, as one government professional and two consultants note the need for flexibility with habitat conversion regulations (3/32), while an academic and nonprofit representative state the need for policies to protect existing emergent vegetation from degradation (2/32).

In addition to policies, responses describe other social considerations that would catalyze future progress in NNBF implementation. Incentives should be created to encourage NNBF projects, including additional dedicated sources of funding (8/32). Additionally, cost-benefit analyses are in need of improvement, and should consider the full lifecycle cost of the project (12/32). These observations agree with recent studies that have identified challenges in quantifying costs, benefits, and co-benefits of NNBF (Close et al., 2017; Cherry et al., 2018; Zuniga-Teran et al., 2020). Collaboration across multiple government agencies is needed for effective projects (3/32), a recommendation which supports findings from previous workshops (Cherry et al., 2018; Zuniga-Teran et al., 2020). Community engagement is cited as an important component to creating a successful project (1/32), a finding also highlighted in the literature (Zuniga-Teran et al., 2020; Waryszak et al., 2021). Responses note the need for broader coastal management, such as 1) considering regional planning and retreat, perhaps utilizing a different term than the politicized “retreat”; 2) having government agencies acquire vegetated lands; and 3) developing tools specifically for coastal management (4/32). Education and updated materials for the public, project applicants, regulators, maintenance workers, students, and engineers are needed (9/32).

NNBF in the context of traditional structures

To elucidate the challenges of incorporating emergent vegetation systems in coastal infrastructure design, it is helpful to compare requirements for NNBF with practices for conventional infrastructure. In traditional civil engineering design, a coastal protection structure is sized and justified by performance objectives, such as flood risk management, erosion control, and/or wave and current mitigation under both extreme design events and normal operational conditions (*e.g.,* USACE, 2002). In the design process, a clear understanding emerges on how the structure accomplishes its purpose, how success is measured, and the length of time the structure can maintain its desired performance. The structure’s performance is predictive, that is, based on a set of widely accepted, controllable assumptions and uncontrollable hazards. The structure’s performance and failure limits can also be determined, such as the storm surge height that can overwhelm the structure, wave types that can damage the structure, or storm conditions and durations that can generate significant erosion.

Established design methods exist for one form of NNBF: beach nourishment (*e.g.,* USACE, 2002; Elko et al., 2021). Engineers select a grain size to be compatible with the existing geomorphological processes of the native beach, and calculate the volume of sand that can provide an acceptable dynamic response under a set of design parameters. Additional design decisions may include adding vegetation and widening the beach in front of a dune. However, since the “structure” (*i.e.,* beach profile) dynamically adjusts through time to environmental conditions, performance factors are harder to control, predict, and improve, and nourished beaches are usually adaptively managed through monitoring, maintenance, or renourishment works.

The design considerations are more complicated for types of NNBF that consist of living systems, such as wetlands or reefs. From a large body of evidence based on field observations, physical modeling, and numerical modeling, engineers have been able to characterize key variables for specific ecosystems that control wave, water level, and erosion mitigation. After decades of observations, it emerges that different NNBF provide different types of coastal protection benefits. Table 1 builds off previous work (*e.g.,* Cunniff and Schwartz, 2015; Bridges et al., 2021) to summarize current knowledge on protection mechanisms, performance, and services of NNBF. In this paper, we focus on emergent vegetation systems (salt marshes and mangroves).

Emergent vegetation can provide protection to inland areas by affecting nearshore hydrodynamics and attenuating wave heights (*e.g.,* NAS, 1977; McIvor et al., 2012), nearshore currents (*e.g.,* Guannel et al., 2015), and storm surge heights (*e.g.,* Zhang et al., 2012). As a result, emergent vegetation may reduce the risk of erosion (Coops et al., 1996) and flooding (*e.g.,* Narayan et al., 2017, 2019; Dong et al., 2020), as well as wave forces and resulting damage to coastal structures (Kyprioti et al., 2021; Mitchell, 2021) and ecosystems, both in response to chronic (La et al., 2015; Thuy et al., 2017; Tomiczek et al., 2022) and acute hazards (Narayan et al., 2019; Tomiczek et al., 2020a; Menéndez et al., 2020). Additionally, emergent vegetation can dynamically respond to increases in sea level by trapping sediment and moving landward, unless it is squeezed by development or rapid rates of submergence (Borchert et al., 2018; Saintilan et al., 2020). It is important to note that all protection services are relative and may be significantly reduced depending on various factors.

Despite this large body of evidence, evaluating the performance of NNBF is more complicated than for conventional systems. The protection services delivered by vegetation arise due to the drag force they exert on nearshore waters, and are a function of the morphology of emergent vegetation and the hydrodynamic forcing offshore (*e.g.,* NAS, 1977; Dalrymple et al., 1984). Guannel et al. (2015) showed how the choice of a drag coefficient is sensitive to wave model formulation, and Kelty et al. (2022) were among the few to test such models under storm conditions. Additionally, contrary to conventional systems, the performance of NNBF is determined by ecological factors, which engineers cannot fully control, and can positively or negatively impact the performance

TABLE 1 Protection provided by common NNBF typologies.

Habitat	What makes it protect				How it protects			Protection service				Long-term viability	Non-engineering benefits
	Performance factor	*"Uncontrollable"* performance variable	*"Controllable"* performance variable	Failure variable during storm	Reduce nearshore wave energy	Reduce nearshore currents	Reduce surge height	Reduce inundation level	Reduce risk of erosion of private property		Storm water storage	Keeps up with SLR	
									Chronic	Acute			
Beaches[1]	Height, width	Sediment size, beach slope	Sediment supply, vegetation	Consecutive storms prevent replenishment	Strong[2]—forms sandbars	No	No	Moderate[3]—height of berm	Strong—width		No	Strong - landward migration	Recreation, habitat for critters, tourism, landscape
Sand Dunes	Height, width	Sediment size	Beach height and width, vegetation	Fails if erodes too much, consecutive storms prevent replenishment	No	No	No	Strong—barrier (until fails)	Strong—height and width		No	Strong - landward migration	Recreation, habitat for critters, landscape
Salt marshes	Physical characteristics, width	Climate, species	Sediment and water supply, water quality	Flattens, breaks	Strong—drag force	Strong*—drag force	Low[4]—drag force	Low-Moderate*	Strong		Strong	Moderate - build up or landward migration	Habitat, fisheries water filtration, carbon sequestration, recreation, landscape
Mangroves	Physical characteristics, width	Climate, species	Sediment and water supply, water quality	Branches break, trees uproot	Strong—drag force	Strong*—drag force	Moderate—drag force	Moderate	Strong		Strong	Moderate - build up or landward migration	
Seagrasses	Physical characteristics, water depth, distance to shore	Climate, species	Nearshore water quality	Flattens, uproots	Strong—drag force	Moderate*—drag force	No	No	Strong*	Low*	No	Moderate - moves in newly created bed	Habitat, fisheries, carbon sequestration
Oyster Reef	Height, width, percent cover, water depth, distance to shore	Ocean water quality	Nearshore water quality	Destroyed	Strong—relative depth and roughness	Moderate*	No*	No*	Strong*	No*	No	Low - build up	Habitat, fisheries, water filtration, carbon sequestration
Coral Reef	Water depth, distance to shore, percent cover (roughness)	Ocean water quality	Nearshore water quality	Coral destroyed	Strong—relative depth and roughness	Moderate*	Low*	Low*	Strong*	Moderate*	No	Low - build up	Habitat, fisheries, recreation, tourism

*More research is needed to fully prove the claim.

[1] Excludes the nourishment process

[2] Strong measurable impact

[3] Moderate measurable impact

[4] Low measurable impact

of the system. For example, the ability of natural systems and their constituent species to grow, increase in density, and survive can be influenced by local or global processes like local climate, sea level rise, ocean acidification and warming, water quality, sedimentation rates, or the spread of diseases (Ross and Adam, 2013; Salimi et al., 2021). These factors, which are often influenced by humans (IPCC, 2013), impact the physical characteristics of natural systems (*e.g.,* stem density and diameter) and hence their ability to moderate coastal hazards.

While traditional structural components may have controllable design parameters (*e.g.,* rock weight for a rubble mound breakwater), emergent vegetation systems have design parameters that change both spatially (*e.g.,* natural variability in trunk or prop root diameters, prop root distribution, and stem densities) and temporally (*e.g.,* vegetation may grow and forest density may increase or recede over a system's life cycle (*e.g.,* Maza et al., 2021)). Moreover, while traditional projects can be built, maintained, and repaired immediately according to set specifications, NNBF need time to grow into the morphology that provides the desired protection benefits. For NNBF projects, engineers have less control of the performance of the system and contend with a higher level of uncertainty than for traditional coastal protection structures; a range of design parameters must be evaluated for NNBF systems.

2.3 Characterizing the performance of NNBF

To compute traditional design metrics in the presence of NNBF–overtopping, runup, wave force on inland structures, or cross-shore erosion–engineers incorporate vegetation modules in wave or nearshore circulation models, and couple these outputs with other established performance metrics models. For example, forces on structures behind emergent vegetation can be calculated using formulas such as Goda (2010) by accurately accounting for wave height attenuation due to vegetation (Mitchell, 2021).

Table 2 provides an overview of existing wave and hydrodynamic models available for emergent vegetation (see also Suzuki et al., 2019; Piercy et al., 2021). This table shows the wealth of numerical models that are now available, including Reynolds Averaged Navier Stokes (RANS) models, which resolve the highest level of physics, phase-averaged models, which summarize the wave conditions as wave spectra, and 1-Dimensional (1D) models, which use representative values of wave height and period. Details of vegetation implementation in each model are described in the references listed in the respective row of Table 2. Other models exist beyond those listed in Table 2, such as the Boussinesq-type model FUNWAVE (Blackmar et al., 2014), and the 1D phase-averaged wave and nearshore current model CSHORE, which can incorporate stem flexibility (Ding et al., 2022). Progress in computer modeling has allowed for a better understanding and quantification of the effects of vegetation on nearshore hydrodynamics.

Most of the models in Table 2 incorporate the effects of vegetation using Morison-type equations, which require information on the system's morphological and hydrodynamic parameters. The accuracy of these parameters will determine the quality of the results (*i.e.,* relying on drag coefficients from reduced scale laboratory studies may result in inaccurate amounts of wave attenuation). By necessity, models make simplifications or idealizations to the system to allow the model to run; however, the more physics that a model simplifies, the more uncertain the outputs. For example, many models neglect flexibility, an important parameter for marshes (*e.g.,* van Veelen et al., 2020; Ding et al., 2022). Models also vary in their ability to layer different characteristics of vegetation elements in the water column, an important characteristic of mangroves such as *Rhisophora* sp. (*e.g.,* Suzuki et al., 2019; Kelty et al., 2022), and to represent other fluid mechanics properties such as porosity (important in denser forests (Suzuki et al., 2019)), turbulence, and wave nonlinearity (Maza et al., 2015). Many models also do not reproduce wave transformation and water level changes in intertidal zones (Guannel et al., 2015; van Rooijen et al., 2016).

Importantly, although recent studies have validated some numerical models under certain storm and field conditions (*e.g.,* Vuik et al., 2016; Baron-Hyppolite et al., 2019; Garzon et al., 2019), to the authors' knowledge, the models are only validated under limited conditions, that is, against reduced-scale laboratory studies that do not consider storm conditions (see "Validation and Verification" in Table 2 and associated references). In fact, only one full-scale laboratory study has been carried out for storm wave attenuation of mangroves (Kelty et al., 2022). This study shows that, for the tested conditions, to have wave height attenuation of order 25%, an 18-m-wide forest needs to have a high density and still water elevation lower than the root system. Conversely, low density, high still water elevations with respect to the root system, and narrow fringes provide wave height attenuation on the order of 5% or less. While more research is needed to generalize these results, the data support the assertion that mangroves can provide storm wave attenuation, but not under every incident condition.

Beyond modeling the hydrodynamics, the ecological performance of NNBF systems must be characterized. During storms, trees bend and break, reducing the capacity of the forest to attenuate waves compared with the ideal conditions modeled in the design phase. Storms may also create conditions such as ponding, leading to delayed mortality of vegetation (*e.g.,* Craighead and Gilbert, 1962; Lagomasino et al., 2021). Even if the emergent vegetation is successful at its purpose of protecting the built environment during a storm, the delayed mortality will cause the decomposing forest to break down and not provide the same level of service during the next storm. Likewise, damages to

TABLE 2 Commonly used computational and analytical models for determining wave height attenuation through emergent vegetation.

Computational effort/ Level of physics included		**High** →									**Medium**		**Low**
Type of model		**RANS**			**Other phase-resolving**				**Phase-averaging**			**Overland**	**Empirical**
Model name		**OpenFOAM**		**NHWAVE**	**SWASH**	**COULWAVE**	**XBeach**		**SWAN**		**STWAVE**	**WHAFIS**	**WATTE**
Model Reference		Jasak et al. (2007), Higuera et al. (2014)		Ma et al. (2012)	Zijlema et al. (2011)	Lynett et al. (2002)	Roelvink et al. (2009)		Booij et al. (1999)		Smith et al. (2001)	FEMA, (2021)	Foster-Martinez et al. (2020)
Processes Included		Wave, Nearshore Circulation		Wave, Nearshore Circulation	Wave, Nearshore Circulation	Wave, Nearshore Circulation	Wave, Nearshore Circulation		Wave		Wave	Wave	Wave
Approach	Vegetation Reference	Maza et al. (2015, 2016) "Microscopic"	Maza et al. (2015) "Macroscopic"	Ma et al. (2013)	Suzuki et al. (2019)	Yang et al. (2018)	van Rooijen et al. (2016) Non-hydrostatic	Surfbeat[1]	Jacobsen et al. (2019)	Suzuki et al. (2012)	Anderson and Smith, (2015)	FEMA, (2021)	Foster-Martinez et al. (2020)
	Underlying Equation for Vegetation	N/A	Morison-type	Morison-type	Morison-type	Morison-type	Morison-type	Mendez and Losada, (2004)	Morison-type	Mendez and Losada, (2004)	Mendez and Losada, (2004)	Modified NAS, (1977)	Kobayashi et al. (1993)
	Flexibility	Y	Y	Y	N	N	N	N	N	N	N	Y	N
	Inertial Force	Y	Y	Y	Y	N	N	N	N	N	N	N	N
	Layering	Y	Y	Y	Y	N	Y	Y	N	Y	N	N	N
	Horizontal Cylinders	Y	Y	N	Y	N	N	N	N	N	N	N	N
	Canopy and Porosity Hydrodynamics	Y	Porosity incorporated as modified k-ε and drag force	Canopy flow through turbulence	Porosity, Canopy flow converted to TKE	N	Porous in-canopy flow		Nonlinearity in canopy flow	N	N	N	N
	Maximum Dimensionality	3D		3D	3D	2D	2D		2D		2D	1D	1D

(Continued on following page)

the built

TABLE 2 (*Continued*) Commonly used computational and analytical models for determining wave height attenuation through emergent vegetation.

Computational effort/ Level of physics included		**High** →								**Medium**		**Low**
Type of model		**RANS**			**Other phase-resolving**			**Phase-averaging**			**Overland**	**Empirical**
Model name		**OpenFOAM**		**NHWAVE**	**SWASH**	**COULWAVE**	**XBeach**	**SWAN**		**STWAVE**	**WHAFIS**	**WATTE**
Inputs	Vegetation	Exact morphology		Section height, density, stem size, Young's modulus	Section height, stem size, density	Average height, stem size, density	Section height, stem size, density	Average height, stem size, density	Section height, stem size, density	Average height, stem size, density	Average height, stem size, density, fraction of coverage, frontal area ratio[2]	Classified raster of land type
	Calibrated Parameters	N/A	Drag coefficient	Drag coefficient, virtual mass coefficient	Added mass coefficient, drag coefficient, TKE and dissipation rate coefficients	Drag coefficient	Drag coefficient	Drag coefficient		Drag coefficient	Drag coefficients, seacoast region parameters[2]	Exponential decay constant
Validation and Verification	Vegetation Implementation	Reduced-scale lab		Reduced-scale lab	Analytical (Mendez and Losada, 2004), Reduced-scale lab, Numerical (SWAN)	Reduced-scale lab	Reduced-scale lab	Reduced-scale lab	Analytical (Mendez and Losada, 2004), Reduced-scale lab	Analytical (Mendez and Losada, 2004)		Field

[1] Short wave phase-averaged

[2] Inputs vary with vegetation type

environment may occur even without a failure of the emergent vegetation itself. It is therefore important to distinguish between "engineering" failure (*i.e.,* failure to provide the required hydraulic response) and "ecological" failure (*i.e.,* inability to withstand the environmental conditions during a storm or owing to longer-term changes) in the design of NNBF; current approaches do not incorporate the latter.

As shown above, advances in computational methods allow for the improved quantification of emergent vegetation's engineering performance. For example, based on information from results such as those by Kelty et al. (2022) and Maza et al. (2019), engineers may assess either 1) the cross-shore distance required to achieve a desired wave height reduction for a design condition, or 2) hybrid alternatives (*e.g.,* structural measures) that can provide a second line of defense to provide the remaining required wave height attenuation. Engineers may also be able to assess expected wave height reduction, lowering design requirements on inland structural measures or near-coast structures. However, these models have limitations (Table 2), and designers should consider the impact these limitations have on the ability to design systems to meet performance requirements. Professional practice dictates that engineers have a primary responsibility to "protect the health, safety, and welfare of the public" (ASCE, 2022b). In traditional design, engineers rely on engineering design standards to produce design parameters that have a low, commonly accepted probability of failure, allowing engineers to have a high level of confidence that their designs will protect the public. Such standards do not exist for emergent vegetation, and questions about the uncertainty of the results, such as those raised above, linger. Therefore, it is difficult for engineers to have a high level of confidence in NNBF designs, and engineering design standards for NNBF are needed (Figure 1).

As a step toward design standards, we propose a framework to evaluate NNBF in such a way that engineers can ensure that lives and properties are protected, while simultaneously accounting for the engineering performance of natural systems following engineering design principles.

Evaluation and design framework

Even though there are many uncertainties that remain in the quantification of the physical behavior of emergent vegetation under hydrodynamic loads and their long-term performance in the face of uncontrollable ecological variables, the existing body of knowledge can be used for practical purposes (Figure 3). Since wave impact forces can generate significant damage to near-coast infrastructure (Robertson et al., 2007; FEMA, 2011; Duncan et al., 2021), this framework focuses on providing a methodology to quantify wave attenuation performance. The proposed framework can be used for the assessment of existing wetlands and for the design of new features. It should be integrated in a comprehensive process that includes other engineering evaluations (*e.g.,* overtopping) as well as ecological (Piercy et al., 2021) and social dimensions (King et al., 2021), as suggested in Figure 4.

The proposed analytical approach for the design of new emergent vegetation systems considers five key points (Figure 3). Step 1 involves calculating a baseline performance of the system without the contribution of vegetation (*e.g.,* USACE, 2002). The quantification of this baseline is recommended because engineering design standards do not yet prescribe a method of calculating wave attenuation for emergent vegetation, and newly planted NNBF may perform as if no vegetation is present. The system including NNBF will therefore be overdesigned, as vegetation is expected to moderate forcing parameters over its lifetime.

The second step comprises of determining relevant physical parameters that will allow for the quantification of wave attenuation performance, for example, by measuring forest morphological parameters in the field (Figure 4). Stem density and height can be measured through traditional ecological methods (Cintrón and Schaeffer-Novelli, 1984). A variety of methods have been developed to characterize projected area (see Yoshikai et al., 2021 for an overview), including empirical models (*e.g.,* Ohira et al., 2013; Mori et al., 2022), 3D laser scanning (*e.g.,* Chang et al., 2019; Kelty et al., 2022), photogrammetry (*e.g.,* Zhang et al., 2015; Maza et al., 2019), and remote sensing (Figueroa-Alfaro et al., 2022). Eventually, field measurement of engineering morphological parameters could be integrated with ecological field work. For new plantings, the framework recommends measuring the physical parameters of a benchmark nearby forest. This is analogous to the standard ecological design of NNBF, which includes the thorough understanding of ecological variables (*e.g.,* terrain elevation, water elevation ranges, vegetation species composition) of a nearby wetland community (UNEP-Nairobi Convention/USAID/WIOMSA, 2020). The reference forest's capability of representing a future condition of the proposed wetland should be validated through an ecological evaluation. The field measurement collection process can be simplified by considering a set of scenarios that are relevant to the study goals. For example, to quantify the economic benefit of an existing, healthy mangrove forest, a scenario with a degraded forest may be used for comparison. The framework conservatively neglects the forest canopy when designing for storm conditions, assuming all leaves are gone and small branches have broken. For engineering purposes, the minimum attenuation performance is more important than average conditions, and should be the aim of measurements. For the drag coefficient, estimates vary widely (Pinsky et al., 2013) as relationships for coefficients based on the Reynolds number (*Re*) derived from small-scale flume studies do not match with recent full-scale studies (Kelty et al., 2022), owing to kinematic scaling differences between the Froude and Reynolds numbers under Froude similitude (Heller, 2011).

Recent prototype-scale physical models have suggested equations for the drag coefficient as a function of *Re*, with the coefficient approaching 0.6 for large values (Kelty et al., 2022).

Because the actual wetland vegetation morphology cannot be fully predicted and future storm conditions have increasing uncertainty (IPCC, 2013), the third step defines various scenarios of vegetation morphology, storm parameters (*e.g.,* storm surge, wave heights) and sea levels. Emergent vegetation consists of, by definition, living systems that grow and adapt to changing environmental conditions at various time scales; the physical structure of the wetland at the design storm's time of impact is likely to be different from the conditions at the time of design, and is uncertain and uncontrollable to a certain extent. In addition, storm conditions may cause emergent vegetation to fail during the event (*e.g.,* Doyle, 1995), meaning it no longer has its protective capabilities (Table 1). This uncertainty can be accounted for by quantifying the performance of alternative (but similar) ecosystems, assessing possible growth rates, stressors, and more. This understanding should inform the adoption of a set of representative conditions for calculation (scenarios), and analysis of performance results for a given design storm under each scenario. Additionally, this step should be used to assess the resilience of NNBF to climate change stressors and to explore potential adaptation scenarios. At a minimum, alternative design storm parameters (*e.g.,* different return periods) and the influence of sea level rise on storms should be evaluated (Biondi and Guannel, 2018). It may also be appropriate to qualitatively consider a broader range of other potential conditions, but a quantitative calculation may only be required for a limited number of selected scenarios, depending on the design goals.

Step 4 involves using validated tools to quantify wave attenuation based on the physical parameters and scenarios identified in Steps 2 and 3. Multiple tools exist for completing these calculations in Step 4 (Table 2), but it is recommended to use tools that have been validated for prototype-scale laboratory studies or field studies that cover a wide range of initial conditions, such as the Mendez and Losada (2004) equation for the conditions in Kelty et al. (2022). In models, the spatial scale should be sufficient to evaluate a forest between tens and hundreds of meters wide, and the vertical structure of the forest should be reproduced and sensitive to changing water elevations. Once wave attenuation by the emergent vegetation is calculated, other engineering performance parameters of the original design, such as overtopping, wave forces, and runup, can be assessed using appropriate engineering tools. Based on these analyses, a range of performance results under different conditions and assumptions can be identified. These quantitative data should be adequate for the engineer to make appropriate design decisions, weighing uncertainties, costs, performance, and risk. Engineering, ecological, and social benefits can also be evaluated across different types of solutions. With these results, engineering criteria can be used to justify a design of an emergent vegetation system (Step 5).

Due to the living nature of emergent vegetation, the morphological parameters of a system will change over time for both new designs and already existing marshes and forests. As the built wetland changes over time (*e.g.,* growth), or responds to acute disturbances (*e.g.,* storm events) or ecological changes (*e.g.,* disease), monitoring of physical morphology can be used to update expected wave attenuation performance. After the project has been implemented, Steps 2 and 4 should be repeated to obtain updated morphological parameters and calculation results, which should be evaluated by the engineer as part of a revisited Step 3. In a created wetland, the analysis should use measurements from the wetland itself, removing uncertainty derived from using parameters of a reference forest. In existing, restored, or created forests, calculation updates can be done in response to observed changes in the forest structure, either due to growth, ecological stress, or storm damage. Given the biological and engineering performance of NNBF, additional actions may be taken over the project lifetime to improve its performance of overall benefits. This can be part of an adaptive management approach, as described in NNBF design guidance (de Looff et al., 2021; Piercy et al., 2021).

Discussion

The framework presented in this paper provides ways for engineers, designers, and stakeholders to include emergent vegetation in coastal infrastructure design in a way that both demonstrates the value of the protection services delivered and creates a pathway for the creation of rigorous design standards in the future. To some extent, the present state of the practice of engineering with nature for emergent vegetation is reminiscent of the development of rubble mound structure methodologies, which began in the 1950s with limited data available and evolved over time to have well-established standards (Hudson, 1958, 1974; USACE, 1977, 1984, 2002). Alternative formulations and coefficients were used by engineers to inform a decision-making process, even with uncertainty of the structural performance.

The proposed framework allows for prudent, conservative approaches to incorporating NNBF in coastal engineering designs. This approach is also appropriate for engineers to be in compliance with ASCE guidance. Currently, to the authors' knowledge, the only mention of NNBF in existing engineering design standards in the United States is in ASCE 24 (ASCE, 2014). ASCE 24-14 4.3 states that projects "shall not remove or otherwise alter sand dunes and mangrove stands, unless an engineering report documents that the alterations will not increase potential flood damage by reducing the wave and flow dissipation characteristics of the sand dunes or mangrove stands" (ASCE, 2014). Notwithstanding environmental

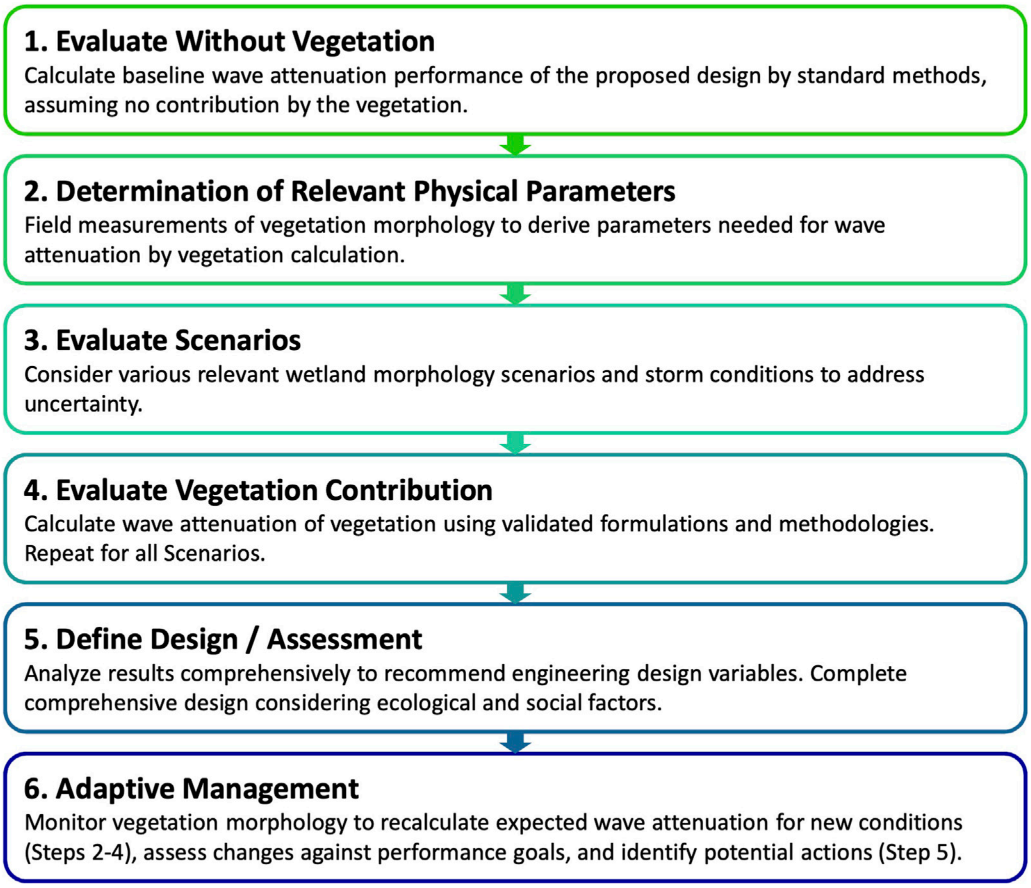

1. Evaluate Without Vegetation
Calculate baseline wave attenuation performance of the proposed design by standard methods, assuming no contribution by the vegetation.

2. Determination of Relevant Physical Parameters
Field measurements of vegetation morphology to derive parameters needed for wave attenuation by vegetation calculation.

3. Evaluate Scenarios
Consider various relevant wetland morphology scenarios and storm conditions to address uncertainty.

4. Evaluate Vegetation Contribution
Calculate wave attenuation of vegetation using validated formulations and methodologies. Repeat for all Scenarios.

5. Define Design / Assessment
Analyze results comprehensively to recommend engineering design variables. Complete comprehensive design considering ecological and social factors.

6. Adaptive Management
Monitor vegetation morphology to recalculate expected wave attenuation for new conditions (Steps 2-4), assess changes against performance goals, and identify potential actions (Step 5).

FIGURE 3
Framework for characterizing the wave attenuation performance of an emergent vegetation system.

regulations that would typically prevent the removal of mangroves, the burden of proof requires that the engineer prove that alterations would not exacerbate wave impacts. Therefore, from an engineering perspective (*i.e.,* ASCE compliance) no removal of natural features can be justified because research demonstrates that a mangrove stand always provides some level of wave attenuation, and therefore removal will cause some increase in the potential damage. Even under unfavorable circumstances, mangrove protection can increase over time (*e.g.,* growth in height, root density), so present conditions cannot be used to justify that the removal will not increase potential damage.

However, expanding upon the spirit of ASCE 24-14, it is also worth considering how wetlands provide protection under future climate change scenarios. Rising sea level and changes to the frequency, intensity, and speed of storms (Emanuel, 2005; Mendelsohn et al., 2012; Kossin, 2018; Sweet et al., 2022) will affect the performance of mangroves and wetlands as their footprint and composition are required to adapt to changing conditions (Hagen et al., 2013; Lovelock et al., 2015; Woodroffe et al., 2016). These changes will in turn impact the performance of coastal infrastructure (Biondi and Guannel, 2018). While these facts are not yet part of engineering design standards, they should be accounted for by practicing engineers and considered in the definition of scenarios (Figure 3). The wave protection afforded by emergent vegetation should be considered as a part of resilience and adaptation strategies where these systems are a viable alternative from a physical and ecological standpoint.

In addition to providing an opportunity to improve engineering guidance, the proposed framework creates opportunities for convergence among academic and professional disciplines. First, the plants themselves could have unintended consequences (Figure 4). For example, emergent vegetation can modify nearshore currents and sediment transport, which may be detrimental for a particular site (*e.g.,* Allen, 1998), become refuge for mosquitos (*e.g.,* Rey et al., 2012), contribute to trash and debris buildup (Cunniff and Schwartz, 2015), or become projectile debris during an extreme storm event. Edge effects should be characterized at locations where emergent vegetation integrates with other shoreline

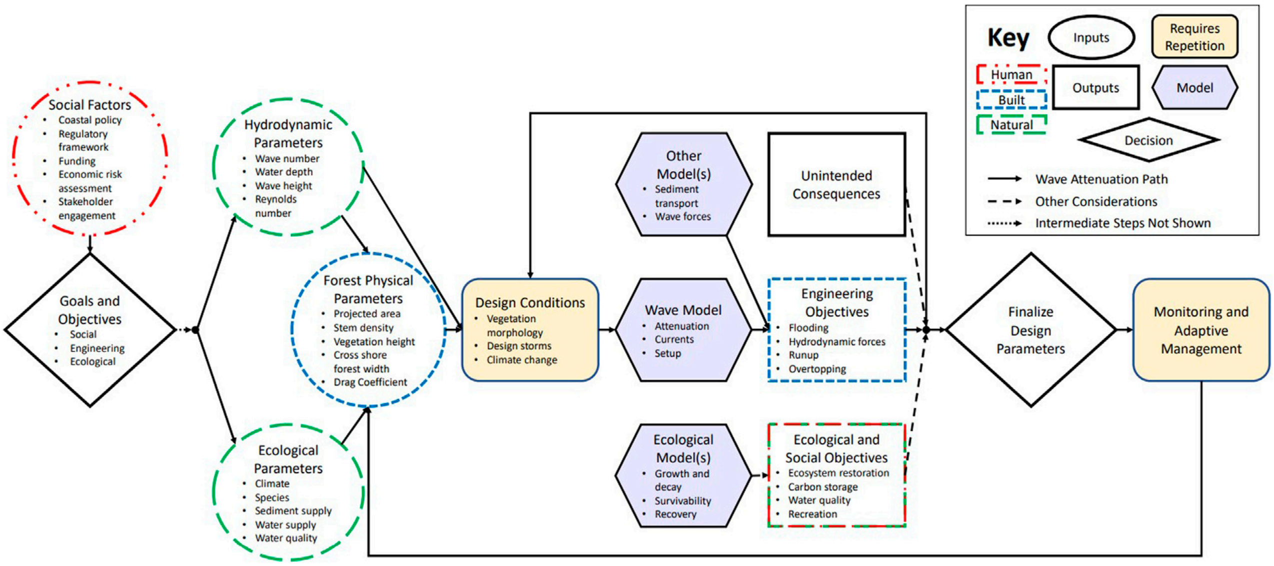

FIGURE 4
Expanded framework for NNBF describing objectives, variables affecting system performance, models for assessing performance, and engineering, ecological, social, and unintended outcomes.

typologies. These issues can be addressed if considered as part of the design, and the inclusion of researchers, practitioners, and stakeholders during monitoring efforts can help direct future guidance that includes both engineering and ecological dimensions.

Furthermore, implementation of NNBF must consider the sociopolitical context in the locations in which they are deployed, requiring skills beyond pure engineering and environmental sciences. Implementing NNBF projects requires navigating the factors that were cited as barriers to implementation (Figure 2; see also Cherry et al., 2018; Zuniga-Teran et al., 2020) such as convoluted permitting processes, limited funding streams, public perception, and enhanced coordination. Community engagement and appropriate socioeconomic analyses over a project's life cycle are also cited as critical for successful implementation of projects but are often insufficiently considered (Zuniga-Teran et al., 2020).

One way to garner public support is to properly account for the full value of NNBF. NNBF projects, which often include public access and amenity features (*e.g.,* boardwalks, kayak trails, kayak launches), can have significant economic, recreational, and aesthetic value (Prato and Hey, 2006; Pueyo-Ros et al., 2018), and provide habitat and improved water quality that can support fisheries and biodiversity (Odum et al., 1982; USFWS, 1999; Struve and Falconer, 2001; Wang et al., 2010). Consequently, the full evaluation of the benefits delivered by emergent vegetation used for coastal protection requires a solid understanding of the relationship between the engineering, ecological, and social dimensions at play at a particular site. While coastal protection may be a benefit driving a particular project, all potential benefits should be pursued. These multiple performance objectives must be evaluated during the planning and design process, and subsequently monitored along with engineering performance objectives to assess the system's overall performance (van Zanten et al., 2021).

Future research priorities

In this paper, we summarized a state of the practice through a review of the literature and elicitation of expert opinion, and proposed a framework that can increase the adoption of NNBF by various stakeholders. We identify three main areas of focus for more widespread implementation of emergent vegetation systems:

1) Validating existing models and characterizing uncertainty in ecological and engineering parameters;
2) Understanding lifecycle performance, including factors that affect survivability and relevant time scales; and
3) Anticipating unintended social, environmental, and engineering consequences.

Engineers require comprehensive validation of the methodology to quantify wave attenuation and develop design standards. This validation would involve blind model studies; presently, most validation studies tune model parameters to fit data. Furthermore, work is needed to determine conservative values for, and uncertainties associated with, input parameters in the wave height attenuation and/or other models for engineering performance output variables. This knowledge would help to characterize the reliability of NNBF systems. Further quantification needs to be determined for forests with a mixed composition of species, hybrid systems, and 3-Dimensional effects.

Future work should also quantify the lifecycle performance and survivability of emergent vegetation with respect to acute stressors and long-term changes. Recovery after a storm should be analyzed to determine what human interventions are needed and over what time scales recovery occurs. Currently, no model in Table 2 incorporates survivability; mangroves are assumed to survive no matter how severe the event and associated environmental conditions. However, damage assessments show that mangrove tree limbs break during extreme events due to wind or debris impact, and can be at risk of delayed mortality due to extreme ponding or other ecological stressors (Tomiczek et al., 2020a; Radabaugh et al., 2020). In the future, process-based ecological models (Charbonneau et al., 2022) could be adapted for emergent vegetation. These models could also be coupled with wave and nearshore hydrodynamic models for better predictions over time (Hagen et al., 2013).

Conclusion

This paper presents a review of the state of the art in leveraging emergent vegetation for coastal engineering design through a synthesis of expert opinion and recent literature. It further provides a design framework for emergent vegetation, identifying critical ecological and morphological parameters affecting system evolution and capability, required variables for wave height attenuation calculations, selection criteria for wave numerical models used for evaluating system performance, and scenarios to build up a set of performance outputs that can be evaluated based on project requirements to make design decisions. Following the methodology presented in Figures 3 and 4 is anticipated to yield estimates of wave attenuation to adequately inform the design and assessment of wave attenuation engineering performance of emergent vegetation NNBF.

Future research priorities are outlined to advance scientific knowledge and to reduce the uncertainty associated with the engineering performance of these systems, which can result in the development of design standards for emergent vegetation. While additional work is needed to provide the same level of detail as for conventional engineering systems, engineers must start broadening the implementation of emergent vegetation and other NNBF systems in the near-term future with the existing knowledge in systems engineering performance. Engineering coastal feasibility studies and design should also broaden the definition of performance objectives from solely engineering requirements to include ecological and social objectives. In the face of sea level rise and climate change, a paradigm shift is required in engineering design to embrace risk management methodologies and propose projects within a long-term adaptive management strategy.

Data availability statement

The raw data supporting the conclusions of this article will be made available by the authors, without undue reservation.

Author contributions

Conceptualization, EB, DC, GG, KO, and TT; Methodology, EB, DC, GG, KO, and TT; Formal Analysis, KO; Investigation, EB, DC, GG, KO, and TT; Writing–Original Draft Preparation, EB, DC, GG, KO, and TT; Writing–Review & Editing, EB, DC, GG, KO, and TT; Visualization, KO, GG; Supervision, EB, DC, GG, KO, and TT; Project Administration, EB, DC, GG, KO, and TT; Funding Acquisition, DC, GG, TT.

Funding

This project was supported by funding from the National Science Foundation CBET Grant #s 2110262 and 2110439, National Science Foundation OIA Grant #1946412, and from the US Army Corps of Engineers through Sponsor Award Number W912HZ2120045. Any opinions, findings, and conclusions or recommendations expressed in this material are those of the authors and do not necessarily reflect the views of the National Science Foundation, the US Army Corps of Engineers, or United States Naval Academy.

Acknowledgments

The authors are grateful to those individuals who provided expert opinion on the state of the art in emergent vegetation.

Conflict of interest

Author EB was employed by Applied Technology and Management/Geosyntec Consultants, Inc.

The remaining authors declare that the research was conducted in the absence of any commercial or financial relationships that could be construed as a potential conflict of interest.

Publisher's note

References

Allen, J. (1998). Mangroves as alien species: The case of Hawaii. *Glob. Ecol. Biogeogr. Lett.* 7, 61–71. doi:10.2307/2997698

Alongi, D. M. (2008). Mangrove forests: Resilience, protection from tsunamis, and responses to global climate change. *Estuar. Coast. Shelf Sci.* 76, 1–13. doi:10.1016/j.ecss.2007.08.024

Anderson, M. E., and Smith, J. M. (2015). *Implementation of wave dissipation by vegetation in STWAVE. Vicksburg, MS.* U.S: U.S. Army Engineer and Research Development Center.

Anderson, M. E., and Smith, J. M. (2014). Wave attenuation by flexible, idealized salt marsh vegetation. *Coast. Eng.* 83, 82–92. doi:10.1016/j.coastaleng.2013.10.004

Arkema, K. K., Guannel, G., Verutes, G., Wood, S. A., Guerry, A., Ruckelshaus, M., et al. (2013). Coastal habitats shield people and property from sea-level rise and storms. *Nat. Clim. Chang.* 3, 913–918. doi:10.1038/nclimate1944

Arkema, K. K., Verutes, G. M., Wood, S. A., Clarke-Samuels, C., Rosado, S., Canto, M., et al. (2015). Embedding ecosystem services in coastal planning leads to better outcomes for people and nature. *Proc. Natl. Acad. Sci. U. S. A.* 112, 7390–7395. doi:10.1073/pnas.1406483112

ASCE (2022b). Code of ethics. *Am. Soc. Civ. Eng.* Available at: https://www.asce.org/career-growth/ethics/code-of-ethics (Accessed April 18, 2022).

ASCE (2014). *Flood resistant design and construction*. Reston, VA: American Society of Civil Engineers. ASCE/SEI 24-14. doi:10.1061/9780784413791

ASCE (2022a). *Minimum design loads and associated criteria for buildings and other structures*. ASCE/SEI 7-22: ASCE 7 standard. doi:10.1061/9780784415788

Barbier, E. B., Hacker, S. D., Kennedy, C., Koch, E. W., Stier, A. C., and Silliman, B. R. (2011). The value of estuarine and coastal ecosystem services. *Ecol. Monogr.* 81, 169–193. doi:10.1890/10-1510.1

Baron-Hyppolite, C., Lashley, C. H., Garzon, J., Miesse, T., Ferreira, C., and Bricker, J. D. (2019). Comparison of implicit and explicit vegetation representations in SWAN hindcasting wave dissipation by coastal wetlands in chesapeake Bay. *Geosciences* 9, 8. doi:10.3390/geosciences9010008

Biondi, E. L., and Guannel, G. (2018). Practical tools for quantitative analysis of coastal vulnerability and sea level rise impacts—Application in a caribbean island and assessment of the 1.5 °C threshold. *Reg. Environ. Change* 18, 2227–2236. doi:10.1007/s10113-018-1397-4

Blackmar, P. J., Cox, D. T., and Wu, W.-C. (2014). Laboratory observations and numerical simulations of wave height attenuation in heterogeneous vegetation. *J. Waterw. Port. Coast. Ocean. Eng.* 140, 56–65. doi:10.1061/(ASCE)WW.1943-5460.0000215

Booij, N., Ris, R. C., and Holthuijsen, L. H. (1999). A third-generation wave model for coastal regions: 1. Model description and validation. *J. Geophys. Res.* 104, 7649–7666. doi:10.1029/98JC02622

Borchert, S. M., Osland, M. J., Enwright, N. M., and Griffith, K. T. (2018). Coastal wetland adaptation to sea level rise: Quantifying potential for landward migration and coastal squeeze. *J. Appl. Ecol.* 55, 2876–2887. doi:10.1111/1365-2664.13169

Bridges, T. S., King, J. K., Simm, J. D., Beck, M. W., Collins, G., Lodder, Q., et al. (2021). *International guidelines on natural and nature-based features for flood risk management*. (U.S.): Engineer Research and Development Center. Available at: https://hdl.handle.net/11681/41946.

Bridges, T. S., Wagner, P. W., Burks-Copes, K. A., Bates, M. E., Collier, Z. A., Fischenich, C. J., et al. (2015). *Use of natural and nature-based features (NNBF) for coastal resilience. Vicksburg, MS.* US: U.S. Army Engineer and Research Development Center. Available at: https://hdl.handle.net/11681/4769.

Browder, G., Ozment, S., Rehberger Bescos, I., Gartner, T., and Lange, G.-M. (2019). *Integrating green and gray: Creating next generation infrastructure.* Washington, DC: World Bank Group. doi:10.1596/978-1-56973-955-6

Castellari, S., Zandersen, M., Davis, M., Veerkamp, C., Förster, J., Marttunen, M., et al. The European Environment Agency (2021). *Nature-based solutions in Europe policy, knowledge and practice for climate change adaptation and disaster risk reduction*. Luxembourg: Publications Office. doi:10.2800/919315

Chang, C.-W., Mori, N., Tsuruta, N., and Suzuki, K. (2019). Estimation of wave force coefficients on mangrove models. *J. Jpn. Soc. Civ. Eng. Ser. B2* 75, I_1105–I_1110. doi:10.2208/kaigan.75.I_1105

Charbonneau, B. R., Duarte, A., Swannack, T. M., Johnson, B. D., and Piercy, C. D. (2022). Doonies: A process-based ecogeomorphological functional community model for coastal dune vegetation and landscape dynamics. *Geomorphology* 398, 108037. doi:10.1016/j.geomorph.2021.108037

Chen, Q., Li, Y., Kelly, D. M., Zhang, K., Zachry, B., and Rhome, J. (2021). Improved modeling of the role of mangroves in storm surge attenuation. *Estuar. Coast. Shelf Sci.* 260, 107515. doi:10.1016/j.ecss.2021.107515

Cherry, C., Dix, B., Asam, S., Webb, B., and Douglass, S. (2018). *Peer exchange summary report: Nature-based solutions for coastal highway resilience*. Washington, DC: Federal Highway Administration. Available at: https://trid.trb.org/view/1539901.

Cintrón, G., and Schaeffer-Novelli, Y. (1984). "Methods for studying mangrove structure," in The mangrove ecosystem: Research methods *monographs on oceanographic methodology*. Editors S. C. Snedaker and J. G. Snedaker (Paris: The United Nations Educational, Scientific and Cultural Organization), 251.

Close, S. L., Montalto, F., Orton, P., Antoine, A., Peters, D., Jones, H., et al. (2017). Achieving sustainability goals for urban coasts in the US northeast: Research needs and challenges. *Local Environ.* 22, 508–522. doi:10.1080/13549839.2016.1233526

Coops, H., Geilen, N., Verheij, H. J., Boeters, R., and van der Velde, G. (1996). Interactions between waves, bank erosion and emergent vegetation: An experimental study in a wave tank. *Aquat. Bot.* 53, 187–198. doi:10.1016/0304-3770(96)01027-3

Craighead, F. C., and Gilbert, V. C. (1962). The effects of hurricane donna on the vegetation of southern Florida. *Q. J. Fla. Acad. Sci.* 25, 1–28.

Cunha, J., Cardona, F. S., Bio, A., and Ramos, S. (2021). Importance of protection service against erosion and storm events provided by coastal ecosystems under climate change scenarios. *Front. Mar. Sci.* 8. doi:10.3389/fmars.2021.726145

Cunniff, S., and Schwartz, A. (2015). *Performance of natural infrastructure and nature-based measures as coastal risk reduction features*. New York: Environmental Defense Fund.

Dalrymple, R. A., Kirby, J. T., and Hwang, P. A. (1984). Wave diffraction due to areas of energy dissipation. *J. Waterw. Port. Coast. Ocean. Eng.* 110, 67–79. doi:10.1061/(asce)0733-950x

de Looff, H., Welp, T., Snider, N., and Wilmink, R. (2021). "Chapter 7: Adaptive management," in *International guidelines on natural and nature-based features for flood risk management*. T. S. Bridges, J. K. King, J. D. Simm, M. W. Beck, G. Collins, Q. Lodder, et al. (Vicksburg, MS: U.S. Army Engineer Research and Development Center).

Ding, Y., Chen, Q. J., Zhu, L., Rosati, J. D., and Johnson, B. D. (2022). Implementation of flexible vegetation into CSHORE for modeling wave attenuation. Vicksburg, MS: US Army Engineer Research and Development Center. doi:10.21079/11681/43220

Dong, S., Abolfathi, S., Salauddin, M., Tan, Z. H., and Pearson, J. M. (2020). Enhancing climate resilience of vertical seawall with retrofitting - a physical modelling study. *Appl. Ocean Res.* 103, 102331. doi:10.1016/j.apor.2020.102331

Doyle, T. W. (1995). Wind damage effects of hurricane andrew on mangrove communities along the southwest coast of Florida, USA. *J. Coast. Res.* 11, 159–168.

Duncan, S., Cox, D., Barbosa, A. R., Lomónaco, P., Park, H., Alam, M. S., et al. (2021). Physical modeling of progressive damage and failure of wood-frame coastal residential structures due to surge and wave forces. *Coast. Eng.* 169, 103959. doi:10.1016/j.coastaleng.2021.103959

Elko, N., Briggs, T. R., Benedet, L., Robertson, Q., Thomson, G., Webb, B. M., et al. (2021). A century of U.S. beach nourishment. *Ocean. Coast. Manag.* 199, 105406. doi:10.1016/j.ocecoaman.2020.105406

Emanuel, K. (2005). Increasing destructiveness of tropical cyclones over the past 30 years. *Nature* 436, 686–688. doi:10.1038/nature03906

IPCC (2013). in *Climate change 2013: The physical science basis. Contribution of working group I to the fifth assessment report of the intergovernmental panel on* *climate change*. T. F. Stocker, D. Qin, G.-K. Plattner, M. Tignor, S. K. Allen, J. Boschung, et al. (Cambridge, United Kingdom and New York, NY, USA: Cambridge University Press). doi:10.1017/CBO9781107415324

Feagin, R. A., Bridges, T. S., Bledsoe, B., Losos, E., Ferreira, S., Corwin, E., et al. (2021). Infrastructure investment must incorporate Nature's lessons in a rapidly changing world. *One Earth* 4, 1361–1364. doi:10.1016/j.oneear.2021.10.003

Fema (2021). *Guidance for flood risk analysis and mapping: Coastal overland wave propagation*. India: FEMA.

Fema (2011). *Principles and practices of planning, siting, designing, constructing, and maintaining residential buildings in coastal areas*. 4th Edition. India: FEMA.

Figueroa-Alfaro, R. W., van Rooijen, A., Garzon, J. L., Evans, M., and Harris, A. (2022). Modelling wave attenuation by saltmarsh using satellite-derived vegetation properties. *Ecol. Eng.* 176, 106528. doi:10.1016/j.ecoleng.2021.106528

Foster-Martinez, M. R., Alizad, K., and Hagen, S. C. (2020). Estimating wave attenuation at the coastal land margin with a GIS toolbox. *Environ. Model. Softw.* 132, 104788. doi:10.1016/j.envsoft.2020.104788

Garzon, J. L., Miesse, T., and Ferreira, C. M. (2019). Field-based numerical model investigation of wave propagation across marshes in the Chesapeake Bay under storm conditions. *Coast. Eng.* 146, 32–46. doi:10.1016/j.coastaleng.2018.11.001

Goda, Y. (2010). *Random seas and design of maritime structures*. 3rd ed. Singapore: World Scientific. doi:10.1142/7425

Guannel, G., Arkema, K., Ruggiero, P., and Verutes, G. (2016). The power of three: Coral reefs, seagrasses and mangroves protect coastal regions and increase their resilience. *PLOS ONE* 11, e0158094. doi:10.1371/journal.pone.0158094

Guannel, G., Ruggiero, P., Faries, J., Arkema, K., Pinsky, M., Gelfenbaum, G., et al. (2015). Integrated modeling framework to quantify the coastal protection services supplied by vegetation. *J. Geophys. Res. Oceans* 120, 324–345. doi:10.1002/2014JC009821

Hagen, S. C., Morris, J. T., Bacopoulos, P., and Weishampel, J. F. (2013). Sea-level rise impact on a salt marsh system of the lower st. Johns river. *J. Waterw. Port. Coast. Ocean. Eng.* 139, 118–125. doi:10.1061/(ASCE)WW.1943-5460.0000177

Heller, V. (2011). Scale effects in physical hydraulic engineering models. *J. Hydraulic Res.* 49, 293–306. doi:10.1080/00221686.2011.578914

Higuera, P., Lara, J. L., and Losada, I. J. (2014). Three-dimensional interaction of waves and porous coastal structures using OpenFOAM®. Part I: Formulation and validation. *Coast. Eng.* 83, 243–258. doi:10.1016/j.coastaleng.2013.08.010

Hochard, J. P., Hamilton, S., and Barbier, E. B. (2019). Mangroves shelter coastal economic activity from cyclones. *Proc. Natl. Acad. Sci. U. S. A.* 116, 12232–12237. doi:10.1073/pnas.1820067116

Hudson, R. Y. (1974). *Concrete armor units for protection against wave attack*. Vicksburg, MS: U.S. Army Engineer Waterways Experiment Station.

Hudson, R. Y. (1958). *Design of quarry-stone cover layers for rubble-mound breakwaters*. Vicksburg, MS: U.S. Army Engineer Waterways Experiment Station.

Jacobsen, N. G., McFall, B. C., and van der A, D. A. (2019). A frequency distributed dissipation model for canopies. *Coast. Eng.* 150, 135–146. doi:10.1016/j.coastaleng.2019.04.007

Jasak, H., Jemcov, A., and Tukovic, Z. (2007). "OpenFOAM: A C++ library for complex physics simulations," in *International workshop on coupled methods in numerical dynamics* (Dubrovnik, Croatia), 20.

Kelty, K., Tomiczek, T., Cox, D. T., Lomonaco, P., and Mitchell, W. (2022). Prototype-scale physical model of wave attenuation through a mangrove forest of moderate cross-shore thickness: LiDAR-based characterization and Reynolds scaling for engineering with nature. *Front. Mar. Sci.* 8. doi:10.3389/fmars.2021.780946

King, J. K., Simm, J. D., and Bridges, T. S. (2021). "Chapter 2: Principles, frameworks, and outcomes," in *International guidelines on natural and nature-based features for flood risk management*. T. S. Bridges, J. K. King, J. D. Simm, M. W. Beck, G. Collins, Q. Lodder, et al. (Vicksburg, MS: U.S. Army Engineer Research and Development Center).

Kobayashi, N., Raichle, A. W., and Asano, T. (1993). Wave attenuation by vegetation. *J. Waterw. Port. Coast. Ocean. Eng.* 119, 30–48. doi:10.1061/(asce)0733-950x

Kossin, J. P. (2018). A global slowdown of tropical-cyclone translation speed. *Nature* 558, 104–107. doi:10.1038/s41586-018-0158-3

Kyprioti, A. P., Taflanidis, A. A., and Kennedy, A. B. (2021). Dissipation effects of coastal vegetation on nearshore structures under wave runup loading. *J. Struct. Eng.* 147, 06020010. doi:10.1061/(asce)st.1943-541x.0002902

La, T. V., Yagisawa, J., and Tanaka, N. (2015). Efficacy of Rhizophora apiculata and Nypa fruticans on attenuation of boat-generated waves under steep slope condition. *Int. J. Ocean. Water Resour.* 19, 1103–1111.

Lagomasino, D., Fatoyinbo, T., Castañeda-Moya, E., Cook, B. D., Montesano, P. M., Neigh, C. S. R., et al. (2021). Storm surge and ponding explain mangrove dieback in southwest Florida following Hurricane Irma. *Nat. Commun.* 12, 4003. doi:10.1038/s41467-021-24253-y

Lei, J., and Nepf, H. (2019). Wave damping by flexible vegetation: Connecting individual blade dynamics to the meadow scale. *Coast. Eng.* 147, 138–148. doi:10.1016/j.coastaleng.2019.01.008

Lovelock, C. E., Cahoon, D. R., Friess, D. A., Guntenspergen, G. R., Krauss, K. W., Reef, R., et al. (2015). The vulnerability of Indo-Pacific mangrove forests to sea-level rise. *Nature* 526, 559–563. doi:10.1038/nature15538

Lynett, P. J., Wu, T.-R., and Liu, P. L.-F. (2002). Modeling wave runup with depth-integrated equations. *Coast. Eng.* 46, 89–107. doi:10.1016/S0378-3839(02)00043-1

Ma, G., Kirby, J. T., Su, S.-F., Figlus, J., and Shi, F. (2013). Numerical study of turbulence and wave damping induced by vegetation canopies. *Coast. Eng.* 80, 68–78. doi:10.1016/j.coastaleng.2013.05.007

Ma, G., Shi, F., and Kirby, J. T. (2012). Shock-capturing non-hydrostatic model for fully dispersive surface wave processes. *Ocean. Model. (Oxf).* 43, 22–35. doi:10.1016/j.ocemod.2011.12.002

Maza, M., Lara, J. L., and Losada, I. J. (2019). Experimental analysis of wave attenuation and drag forces in a realistic fringe Rhizophora mangrove forest. *Adv. Water Resour.* 131, 103376. doi:10.1016/j.advwatres.2019.07.006

Maza, M., Lara, J. L., and Losada, I. J. (2021). Predicting the evolution of coastal protection service with mangrove forest age. *Coast. Eng.* 168, 103922. doi:10.1016/j.coastaleng.2021.103922

Maza, M., Lara, J. L., and Losada, I. J. (2016). Solitary wave attenuation by vegetation patches. *Adv. Water Resour.* 98, 159–172. doi:10.1016/j.advwatres.2016.10.021

Maza, M., Lara, J. L., and Losada, I. J. (2015). Tsunami wave interaction with mangrove forests: A 3-D numerical approach. *Coast. Eng.* 98, 33–54. doi:10.1016/j.coastaleng.2015.01.002

Mazda, Y., Magi, M., Kogo, M., and Hong, P. N. (1997). Mangroves as a coastal protection from waves in the Tong King delta, Vietnam. *Mangroves Salt Marshes* 1, 127–135. doi:10.1023/A:1009928003700

McIvor, A. L., Möller, I., Spencer, T., and Spalding, M. (2012). *Reduction of wind and swell waves by mangroves. Natural Coastal Protection Series: Report 1. Cambridge Coastal Research Unit Working Paper 40.* The Nature Conservancy and Wetlands International, 27. Available at: https://www.conservationgateway.org/ConservationPractices/Marine/crr/library/Documents/wind-and-swell-wave-reduction-by-mangroves.pdf.

Mendelsohn, R., Emanuel, K., Chonabayashi, S., and Bakkensen, L. (2012). The impact of climate change on global tropical cyclone damage. *Nat. Clim. Chang.* 2, 205–209. doi:10.1038/nclimate1357

Mendez, F. J., and Losada, I. J. (2004). An empirical model to estimate the propagation of random breaking and nonbreaking waves over vegetation fields. *Coast. Eng.* 51, 103–118. doi:10.1016/j.coastaleng.2003.11.003

Menéndez, P., Losada, I. J., Torres-Ortega, S., Narayan, S., and Beck, M. W. (2020). The global flood protection benefits of mangroves. *Sci. Rep.* 10, 4404. doi:10.1038/s41598-020-61136-6

Miller, J. K., Rella, A., Williams, A., and Sproule, E. (2015). *Living shorelines engineering guidelines*. New Jersey: New Jersey Department of Environmental Protection.

Mitchell, W. T. (2021). *Effect of an idealized mangrove forest of moderate cross-shore width on loads measured on a sheltered structure and comparison with predicted forces*. Corvallis, OR.

Montgomery, J. M., Bryan, K. R., Mullarney, J. C., and Horstman, E. M. (2019). Attenuation of storm surges by coastal mangroves. *Geophys. Res. Lett.* 46, 2680–2689. doi:10.1029/2018GL081636

Mori, N., Chang, C.-W., Inoue, T., Akaji, Y., Hinokidani, K., Baba, S., et al. (2022). Parameterization of mangrove root structure of Rhizophora stylosa in coastal hydrodynamic model. *Front. Built Environ.* 7, 782219. doi:10.3389/fbuil.2021.782219

Narayan, S., Beck, M. W., Reguero, B. G., Losada, I. J., Wesenbeeck, B. V., Pontee, N., et al. (2016). The effectiveness, costs and coastal protection benefits of natural and nature-based defences. *PLOS ONE* 11, e0154735. doi:10.1371/journal.pone.0154735

Narayan, S., Beck, M. W., Wilson, P., Thomas, C. J., Guerrero, A., Shepard, C. C., et al. (2017). The value of coastal wetlands for flood damage reduction in the northeastern USA. *Sci. Rep.* 7, 9463. doi:10.1038/s41598-017-09269-z

Narayan, S., Thomas, C., Matthewman, J., Shepard, C. C., Geselbracht, L., Nzerem, K., et al. (2019). *Valuing the flood risk reduction benefits of Florida's mangroves*. Arlington, VA: The Nature Conservancy.

NAS (1977). *Methodology for calculating wave action effects associated with storm surges*. Washington, DC: National Academy of Sciences.

Odum, W. E., McIvor, C. C., and Smith, T. J. (1982). *The ecology of the mangroves of south Florida: A community profile*. US: U.S. Fish and Wildlife Service.

Ohira, W., Honda, K., Nagai, M., and Ratanasuwan, A. (2013). Mangrove stilt root morphology modeling for estimating hydraulic drag in tsunami inundation simulation. *Trees* 27, 141–148. doi:10.1007/s00468-012-0782-8

Ozeren, Y., Wren, D. G., and Wu, W. (2014). Experimental investigation of wave attenuation through model and live vegetation. *J. Waterw. Port. Coast. Ocean. Eng.* 140, 04014019. doi:10.1061/(ASCE)WW.1943-5460.0000251

PIANC (2018). *Environmental commission guide for applying working with nature to navigation infrastructure projects*. Brussels: PIANC.

Piercy, C. D., Pontee, N., Narayan, S., Davis, J., and Meckley, T. (2021). "Chapter 10: Coastal wetlands and tidal flats," in *International guidelines on natural and nature-based features for flood risk management*. T. S. Bridges, J. K. King, J. D. Simm, M. W. Beck, G. Collins, Q. Lodder, et al. (Vicksburg, MS: U.S. Army Engineer Research and Development Center).

Pinsky, M. L., Guannel, G., and Arkema, K. K. (2013). Quantifying wave attenuation to inform coastal habitat conservation. *Ecosphere* 4, art95. doi:10.1890/ES13-00080.1

Prato, T., and Hey, D. (2006). Economic analysis of wetland restoration along the Illinois river. *J. Am. Water Resour. Assoc.* 42, 125–131. doi:10.1111/j.1752-1688.2006.tb03828.x

Pueyo-Ros, J., Garcia, X., Ribas, A., and Fraguell, R. M. (2018). Ecological restoration of a coastal wetland at a mass tourism destination. Will the recreational value increase or decrease? *Ecol. Econ.* 148, 1–14. doi:10.1016/j.ecolecon.2018.02.002

Radabaugh, K. R., Moyer, R. P., Chappel, A. R., Dontis, E. E., Russo, C. E., Joyse, K. M., et al. (2020). Mangrove damage, delayed mortality, and early recovery following hurricane irma at two landfall sites in southwest Florida, USA. *Estuaries Coast.* 43, 1104–1118. doi:10.1007/s12237-019-00564-8

Rey, J. R., Walton, W. E., Wolfe, R. J., Connelly, C. R., O'Connell, S. M., Berg, J., et al. (2012). North American wetlands and mosquito control. *Int. J. Environ. Res. Public Health* 9, 4537–4605. doi:10.3390/ijerph9124537

Robertson, I. N., Riggs, H. R., Yim, S. C., and Young, Y. L. (2007). Lessons from hurricane katrina storm surge on Bridges and buildings. *J. Waterw. Port. Coast. Ocean. Eng* 133, 463–483. doi:10.1061/(asce)0733-950x

Roelvink, D., Reniers, A., van Dongeren, A., van Thiel de Vries, J., McCall, R., and Lescinski, J. (2009). Modelling storm impacts on beaches, dunes and barrier islands. *Coast. Eng.* 56, 1133–1152. doi:10.1016/j.coastaleng.2009.08.006

Ross, P. M., and Adam, P. (2013). Climate change and intertidal wetlands. *Biology* 2, 445–480. doi:10.3390/biology2010445

Ruckelshaus, M. H., Guannel, G., Arkema, K., Verutes, G., Griffin, R., Guerry, A., et al. (2016). Evaluating the benefits of green infrastructure for coastal areas: Location, location, location. *Coast. Manage.* 44, 504–516. doi:10.1080/08920753.2016.1208882

Saintilan, N., Khan, N. S., Ashe, E., Kelleway, J. J., Rogers, K., Woodroffe, C. D., et al. (2020). Thresholds of mangrove survival under rapid sea level rise. *Science* 368, 1118–1121. doi:10.1126/science.aba2656

Salimi, S., Almuktar, S. A. A. A. N., and Scholz, M. (2021). Impact of climate change on wetland ecosystems: A critical review of experimental wetlands. *J. Environ. Manage.* 286, 112160. doi:10.1016/j.jenvman.2021.112160

Sanderman, J., Hengl, T., Fiske, G., Solvik, K., Adame, M. F., Benson, L., et al. (2018). A global map of mangrove forest soil carbon at 30 m spatial resolution. *Environ. Res. Lett.* 13, 055002. doi:10.1088/1748-9326/aabe1c

Sarasota Bay Estuary Program (2018). *Living shorelines: Guidance for sarasota Bay watershed*. FL: Sarasota.

Science for Environment Policy (2021). *The solution is in nature*. Bristol: Science Communication Unit.

Scyphers, S. B., Powers, S. P., Jr, K. L. H., and Byron, D. (2011). Oyster reefs as natural breakwaters mitigate shoreline loss and facilitate fisheries. *PLOS ONE* 6, e22396. doi:10.1371/journal.pone.0022396

Silver, J. M., Arkema, K. K., Griffin, R. M., Lashley, B., Lemay, M., Maldonado, S., et al. (2019). Advancing coastal risk reduction science and implementation by accounting for climate, ecosystems, and people. *Front. Mar. Sci.* 6. doi:10.3389/fmars.2019.00556

Smith, J. M., Sherlock, A. R., and Resio, D. T. (2001). *Stwave: Steady-state spectral wave model user's manual for STWAVE, version 3.0*. Vicksburg, MS: U.S. Army Engineer and Research Development Center.

Spalding, M., and Parrett, C. L. (2019). Global patterns in mangrove recreation and tourism. *Mar. Policy* 110, 103540. doi:10.1016/j.marpol.2019.103540

Struve, J., and Falconer, R. A. (2001). Hydrodynamic and water quality processes in mangrove regions. *J. Coast. Res.*, 65–75.

Suzuki, T., Hu, Z., Kumada, K., Phan, L. K., and Zijlema, M. (2019). Non-hydrostatic modeling of drag, inertia and porous effects in wave propagation over dense vegetation fields. *Coast. Eng.* 149, 49–64. doi:10.1016/j.coastaleng.2019.03.011

Suzuki, T., Zijlema, M., Burger, B., Meijer, M. C., and Narayan, S. (2012). Wave dissipation by vegetation with layer schematization in SWAN. *Coast. Eng.* 59, 64–71. doi:10.1016/j.coastaleng.2011.07.006

Sweet, W. V., Hamlington, B. D., Kopp, R. E., Weaver, C. P., Barnard, P. L., Bekaert, D., et al. (2022). *Global and regional sea level rise scenarios for the United States: Updated mean projections and extreme water level probabilities along U.S. Coastlines. Silver spring, MD*. Spring, MD: National Oceanic and Atmospheric Administration. National Ocean Service Available at: https://oceanservice.noaa.gov/hazards/sealevelrise/noaa-nostechrpt01-global-regional-SLR-scenarios-US.pdf.

Taylor, E. B., Gibeaut, J. C., Yoskowitz, D. W., and Starek, M. J. (2015). Assessment and monetary valuation of the storm protection function of beaches and foredunes on the Texas coast. *J. Coast. Res.* 31, 1205–1216. doi:10.2112/JCOASTRES-D-14-00133.1

Thuy, N. B., Nandasena, N. A. K., Dang, V. H., Kim, S., Hien, N. X., Hole, L. R., et al. (2017). Effect of river vegetation with timber piling on ship wave attenuation: Investigation by field survey and numerical modeling. *Ocean. Eng.* 129, 37–45. doi:10.1016/j.oceaneng.2016.11.004

Tomiczek, T., O'Donnell, K., Furman, K., Webbmartin, B., and Scyphers, S. (2020a). Rapid damage assessments of shorelines and structures in the Florida keys after hurricane irma. *Nat. Hazards Rev.* 21, 05019006. doi:10.1061/(ASCE)NH.1527-6996.0000349

Tomiczek, T., Wargula, A., Lomónaco, P., Goodwin, S., Cox, D., Kennedy, A., et al. (2020b). Physical model investigation of mid-scale mangrove effects on flow hydrodynamics and pressures and loads in the built environment. *Coast. Eng.* 162, 103791. doi:10.1016/j.coastaleng.2020.103791

Tomiczek, T., Wargula, A., O'Donnell, K., LaVeck, V., Castagno, K. A., and Scyphers, S. (2022). Vessel-generated wake attenuation by *Rhizophora mangle* in key west, Florida. *J. Waterw. Port. Coast. Ocean. Eng.* 148, 04022002. doi:10.1061/(ASCE)WW.1943-5460.0000704

Uddin, Md. S., de Ruyter van Steveninck, E., Stuip, M., and Shah, M. A. R. (2013). Economic valuation of provisioning and cultural services of a protected mangrove ecosystem: A case study on sundarbans reserve forest, Bangladesh. *Ecosyst. Serv.* 5, 88–93. doi:10.1016/j.ecoser.2013.07.002

UNDRR (2020). *Ecosystem-based disaster risk reduction: Implementing nature-based solutions for resilience*. Bangkok, Thailand: United Nations Office for Disaster Risk Reduction – Regional Office for Asia and the Pacific.

UNEP-Nairobi Convention/USAID/WIOMSA (2020). *Guidelines on mangrove ecosystem restoration for the western Indian ocean region*. Nairobi: UNEP. Available at: https://www.nairobiconvention.org/CHM%20Documents/WIOSAP/guidelines/GuidelinesonMangroveRestorationForTheWIO.pdf.

USACE (2002). *Coastal engineering manual*. Washington, DC: USACE.

USACE (1977). *Shore protection manual*. Vicksburg, MS: U.S. Army Coastal Engineering Research Center.

USACE (1984). *Shore protection manual*. Vicksburg, MS: U.S. Army Engineer Waterways Experiment Station.

USFWS (1999). *South Florida multi-species recovery plan*. Atlanta, GA: U.S. Fish and Wildlife Service.

van Rooijen, A. A., McCall, R. T., van Thiel de Vries, J. S. M., van Dongeren, A. R., Reniers, A. J. H. M., and Roelvink, J. A. (2016). Modeling the effect of wave-vegetation interaction on wave setup: Wave Setup Damping by Vegetation. *J. Geophys. Res. Oceans* 121, 4341–4359. doi:10.1002/2015JC011392

van Veelen, T. J., Fairchild, T. P., Reeve, D. E., and Karunarathna, H. (2020). Experimental study on vegetation flexibility as control parameter for wave damping and velocity structure. *Coast. Eng.* 157, 103648. doi:10.1016/j.coastaleng.2020.103648

van Zanten, B., Arkema, K., Swannack, T., Griffin, R., Narayan, S., Penn, K., et al. (2021). "Chapter 6: Benefits and costs of NNBF," in *International guidelines on natural and nature-based features for flood risk management*. T. S. Bridges, J. K. King, J. D. Simm, M. W. Beck, G. Collins, Q. Lodder, et al. (Vicksburg, MS: U.S. Army Engineer Research and Development Center).

Vuik, V., Jonkman, S. N., Borsje, B. W., and Suzuki, T. (2016). Nature-based flood protection: The efficiency of vegetated foreshores for reducing wave loads on coastal dikes. *Coast. Eng.* 116, 42–56. doi:10.1016/j.coastaleng.2016.06.001

Wang, M., Zhang, J., Tu, Z., Gao, X., and Wang, W. (2010). Maintenance of estuarine water quality by mangroves occurs during flood periods: A case study of a subtropical mangrove wetland. *Mar. Pollut. Bull.* 60, 2154–2160. doi:10.1016/j.marpolbul.2010.07.025

Waryszak, P., Gavoille, A., Whitt, A. A., Kelvin, J., and Macreadie, P. I. (2021). Combining gray and green infrastructure to improve coastal resilience: Lessons learnt from hybrid flood defenses. *Coast. Eng. J.* 63, 335–350. doi:10.1080/21664250.2021.1920278

Webb, B. M., Dix, B., Douglass, S. L., Asam, S., Cherry, C., Buhring, B., et al. (2019). *Nature-based solutions for coastal highway resilience: An implementation guide*. Washington, DC.

Woodroffe, C. D., Rogers, K., McKee, K. L., Lovelock, C. E., Mendelssohn, I. A., and Saintilan, N. (2016). Mangrove sedimentation and response to relative sea-level rise. *Annu. Rev. Mar. Sci.* 8, 243–266. doi:10.1146/annurev-marine-122414-034025

World Bank (2017). *Implementing nature-based flood protection: Principles and implementation guidance*. Washington, DC: World Bank.

Yang, Z., Tang, J., and Shen, Y. (2018). Numerical study for vegetation effects on coastal wave propagation by using nonlinear Boussinesq model. *Appl. Ocean Res.* 70, 32–40. doi:10.1016/j.apor.2017.09.001

Yoshikai, M., Nakamura, T., Suwa, R., Rollon, R., and Nadaoka, K. (2021). “Measurement and modeling of above-ground root systems as attributes of flow and wave attenuation function of mangroves,” in *Mangroves: Ecology, biodiversity and management*. Editors R. P. Rastogi, M. Phulwaria, and D. K. Gupta (Singapore: Springer), 279–303. doi:10.1007/978-981-16-2494-0_12

Zhang, K., Liu, H., Li, Y., Xu, H., Shen, J., Rhome, J., et al. (2012). The role of mangroves in attenuating storm surges. *Estuar. Coast. Shelf Sci.* 102–103, 11–23. doi:10.1016/j.ecss.2012.02.021

Zhang, X., Chua, V. P., and Cheong, H.-F. (2015). Hydrodynamics in mangrove prop roots and their physical properties. *J. Hydro-environment Res.* 9, 281–294. doi:10.1016/j.jher.2014.07.010

Zijlema, M., Stelling, G., and Smit, P. (2011). Swash: An operational public domain code for simulating wave fields and rapidly varied flows in coastal waters. *Coast. Eng.* 58, 992–1012. doi:10.1016/j.coastaleng.2011.05.015

Zuniga-Teran, A. A., Staddon, C., de Vito, L., Gerlak, A. K., Ward, S., Schoeman, Y., et al. (2020). Challenges of mainstreaming green infrastructure in built environment professions. *J. Environ. Plan. Manag.* 63, 710–732. doi:10.1080/09640568.2019.1605890

frontiers | Frontiers in Built Environment

TYPE Original Research
PUBLISHED 26 October 2022
DOI 10.3389/fbuil.2022.907608

EDITED BY
Jens Figlus,
Texas A&M University, United States

REVIEWED BY
Christine Angelini,
University of Florida, United States
Takayuki Suzuki,
Yokohama National University, Japan

*CORRESPONDENCE
Leigh A. Provost,
leigh.a.provost@usace.army.mil

SPECIALTY SECTION
This article was submitted to Coastal and Offshore Engineering, a section of the journal Frontiers in Built Environment

RECEIVED 29 March 2022
ACCEPTED 28 September 2022
PUBLISHED 26 October 2022

CITATION
Provost LA, Eisemann ER, Anderson CP and Waldron MCB (2022), Wrack placement to augment constructed dunes: A field investigation.
Front. Built Environ. 8:907608.
doi: 10.3389/fbuil.2022.907608

Wrack placement to augment constructed dunes: A field investigation

Leigh A. Provost[1]*, Eve R. Eisemann[1,2], Carlton P. Anderson[3] and Margaret C. B. Waldron[3,4]

[1]Coastal and Hydraulics Laboratory, US Army Engineer Research and Development Center, Vicksburg, MS, United States, [2]Institute of Marine Sciences, University of North Carolina, Chapel Hill, NC, United States, [3]Gulf Coast Geospatial Center, The University of Southern Mississippi, Long Beach, MS, United States, [4]School of Ocean Science and Engineering, The University of Southern Mississippi, Ocean Springs, MS, United States

Natural and nature-based features have become increasingly popular in recent years for several reasons including reduced costs and maintenance, sustainability, and ecological benefits. One such nature-based feature which contributes to coastal resiliency is dune systems. Extensive research shows that dune systems provide great value for coastal protection, with vegetation and belowground biomass emerging as crucial factors for dune stability. Alternative dune construction and dune maintenance methods are needed to improve the resilience and stability of these dune systems. Wrack, vegetation and macroalgae that naturally washes up along the coast, is often removed during routine beach maintenance, but could serve to increase dune biomass, sand trapping, and overall dune resiliency. This manuscript documents preliminary results following the placement of wrack along constructed dunes on the Mississippi mainland coast. Terrestrial lidar surveys were used to evaluate morphological responses of a 550 m stretch of the beach, with varying raking and wrack management practices implemented in designated sections. Elevation and volumetric change calculated from these data were compared across storm erosion and fair-weather recovery periods to quantify the potential benefits of utilizing natural wrack material in the dunes and reducing beach raking.

KEYWORDS

wrack, terrestrial LIDAR, dunes, biomass, field study, beach management

Highlights

- A net volume increase over the entire study period was only observed in the ramp morphologic region of the ungroomed zone and the ungroomed and wrack-treated zone. Although volume was lost from the dunes in all zones, the greatest net volume loss was observed in the dune of the control zone.
- Major events that brought the highest water levels, Hurricane Zeta and Hurricane Ida, contributed to large volume loss across all zones, but the ungroomed and wrack-treated dune remained intact, and the dune toe remained stable throughout

the entire study period. In contrast, both the control and ungroomed dune were flattened after Hurricane Ida.

- Through the unprecedented 2020 hurricane season, all storms caused notable volume changes, but not all storms caused net erosion. The response is complicated, suggesting that some events even lead to significant net deposition, particularly on the berm. The relatively minor events even contributed volume to the dunes in some cases. This variability is largely attributed to differences in wind and wave dynamics, but given limited data availability within the region, such direct comparisons could not be made.

Introduction

Increased emphasis is being placed on utilizing natural and nature-based features (NNBF) as a means for improving flood-risk protection both in coastal and inland environments. Beach dunes are a primary example of one such feature that can provide protection from coastal flooding (Borsje et al., 2011). Coastal dunes have a storied history in their importance to the coast both ecologically, and from a flood-risk perspective. By acting as a physical barrier, dunes provide protection from inundation and wave action (Hanley et al., 2014). As the frequency and intensity of tropical storm events continue to increase, utilizing these natural features advantageously is critical.

One such area of specific need for coastal resiliency is the United States Gulf Coast. The Gulf Coast has a history of being subject to severe storm events. From 2010 to 2020, the Gulf Coast from the southernmost point of Texas through the Florida Keys, experienced roughly 30 tropical events, a third of which occurred in 2020 (NOAA, 2022). Of these storms, 2 made direct landfall on the Mississippi coastline, while others, though not direct hits, caused storm surge and large waves in the area. Tropical Storm Cristobal, which made landfall in Louisiana June 7th of 2020, contributed as much as 1.88 m of storm surge to some Louisiana locations. In Mississippi, a peak water level of 1.74 m MHHW was recorded at Bay Waveland Yacht Club (Berg, 2021).

Harrison County, Mississippi, is located along the Mississippi coast, with undeveloped barrier islands (Gulf Islands National Seashore) > 10 km offshore of the populated mainland coast. The focus of this study is the populated mainland coast, stretching along the Mississippi Sound. The Mississippi Sound is a protected, shallow (1–3 m deep) estuary between the mainland and the barrier islands (Blumberg et al., 2001; Byrnes et al., 2013). The wave climate on the outer barrier islands is low-energy, with modeled wave transformations indicating breaking wave heights less than 0.6 m, leaving the Mississippi Sound behind these islands exposed to very minimal wave energy (Cipriani & Stone, 2001). Under these conditions, Harrison County mainland coastline, along with the rest of the mainland Mississippi coast, is naturally a muddy, shallow-sloped coastline, fringed by marsh. This is evidenced by the few remaining unaltered sections of coast (e.g., the Hancock County Marsh Coastal Preserve, and the Grand Bay National Estuarine Research Reserve, Figure 1).

In the 1920s, a seawall was constructed along the Hancock and Harrison County mainland shoreline (Schmid, 2002) and beach sand was placed sound-ward of the seawall beginning in 1967 (Hancock County Historical Society, 2022). As the wave energy is too low to naturally produce sandy beaches along the mainland MS coast, the only sand source is nourishment, and sand loss occurs via hydrodynamic processes during erosive events and via aeolian transport as material is blown further landward. Samples taken from the berm in November 2020 showed a D50 of 0.61–0.67 mm (coarse sand), with the finer fraction likely being blown on to the dunes or lost on to the road that lies landward of the seawall. Thus, the area must be periodically re-nourished to maintain beach width.

Tropical cyclones frequently impact the Mississippi Coast, with an average return period of 11 years for all hurricanes and 26 years for major hurricanes within 50 nautical miles of the Mississippi coast (NOAA, 2020). In the past five hurricane seasons (2016–2021), five named storms have impacted within this radius, far exceeding the average return period (NOAA, 2022). Several major Hurricanes have heavily damaged the beaches and seawall of Hancock and Harrison Counties in recorded history, including Hurricane Camille in 1969 and most recently Hurricane Katrina in 2005. Following Katrina, the beach was re-nourished along Hancock and Harrison Counties and dune features were created and planted with dune grasses as part of the Mississippi Coastal Improvements Program (MsCIP), with the goal of providing enhanced protection from storm events as well as additional habitat for shore and migratory birds.

Bryant D. B. et al., 2019 demonstrated in a laboratory experiment the role of vegetation in dune response to wave attack. It was reported that vegetation, including both below and aboveground biomass contributes significantly to reducing sediment loss under extreme events. Within the same works, it is also noted that innovating dune construction methods by incorporating biomass material within the construction phase may improve dune stability under extreme events. This has further been evaluated by follow-on laboratory studies which demonstrated that increased below-ground biomass can contribute greatly to sediment retention of a dune under wave attack (Bryant D. et al., 2019). The results of these works suggest that periodic incorporation of natural biomass material into dune systems may increase their sediment retention ability.

Like many coastal regions, the Harrison County coastline experiences frequent accumulation of vegetative detritus, composed typically of sea or marsh grasses, commonly referred to as "wrack" (Figure 2A). Wrack is any organic material that is deposited on the beach along the swash line. It is typically composed of macroscopic algae, seagrass, driftwood, and marsh grasses (Hemminga and Nieuwenhuize,

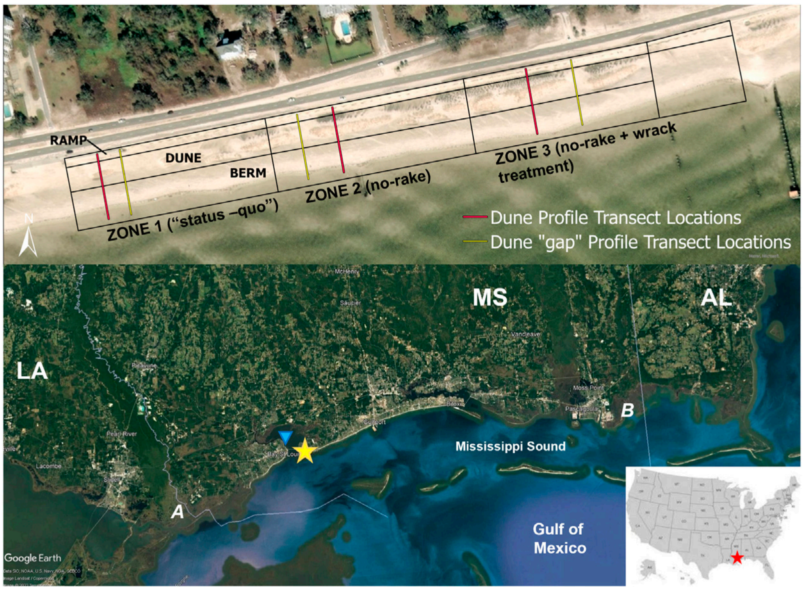

FIGURE 1
(Top): Study area polygon, broken down by geomorphologic region (ramp, dune, berm) and zone, with transect locations shown in yellow. (Bottom): Satellite image showing the location of study area as a yellow star. The NOAA water level station is indicated by the blue triangle. A indicates Hancock County Marsh Coastal Preserve and B indicates Grand Bay National Estuarine Research Reserve. The small inset map shows the location of this region relative to the United States.

1990; Dugan and Hubbard, 2010; Sigren et al., 2015). This material can trap windblown sand on its own, but often also contains the seeds and live rhizomes of dune vegetation species, enabling the growth and initiation of the bio-geomorphic interaction that forms dunes (Godfrey, 1977). In regions which experience excessive of wrack accumulation, beach raking or grooming is often used to remove the material (Provost et al., 2022). The purpose, most commonly, being to maintain clean, safe beaches for recreation. However, the availability of this material locally offers a unique source of biomass material that can be used to encourage natural dune growth. Dugan & Hubbard, 2010 as well as Hemminga and Nieuwenhuize, 1990 emphasize the importance of wrack to both sediment trapping as well as dune formation. Experimental studies performed by the University of Florida, demonstrated the use of surrogate wrack to improve both sediment accumulation and plant growth (Hooton et al., 2020). Ecological benefits of wrack material have been well documented as well, with several studies citing its importance to water quality, the coastal food chain, and species richness and abundance to organisms such as shorebirds and macrofauna (Harrison and Mann, 1975; Duggins et al., 1989; Dugan, 1999; Elias et al., 2000; Dugan et al., 2003; Orr et al., 2005; Heerhartz et al., 2016). Further summarization of both ecological and geomorphological impacts of wrack is reviewed in Provost et al., 2022.

Harrison County, MS receives frequent wrack deposition along the beach. This stretch of coast provides an ideal site to test alternative wrack management strategies and the usefulness of wrack for dune improvements along the constructed and managed dune system that stretches the length of the county. This study investigates the response of periodic wrack placements on a test segment of the constructed dunes and evaluated the change in response relative to extreme storm events and recovery periods. Local biomass material, consisting primarily of aquatic and marsh vegetation was collected from the wrack line (high-water line) of the beach, and placed at the dune toe to promote aeolian deposition and encourage natural dune growth. Terrestrial lidar surveys conducted quarterly were used to evaluate dune stability following tropical events, as well as dune recovery during periods of fair weather. At the time of this publication, the area was monitored for a total of 19 months, with the initial survey beginning in June of 2020.

Materials and methods

To evaluate the effectiveness of utilizing beach wrack to enhance dune stability, a field study was implemented in Pass Christian, Mississippi (Figure 1). A 550 m section of beach, near Henderson Point Beach, was selected as the study location through collaboration with the county Sand Authority. This project site encompassed the beach starting at coordinates 89.27853W, 30.30473N and ending at coordinates 89.27303W, 30.30579 N. The study site

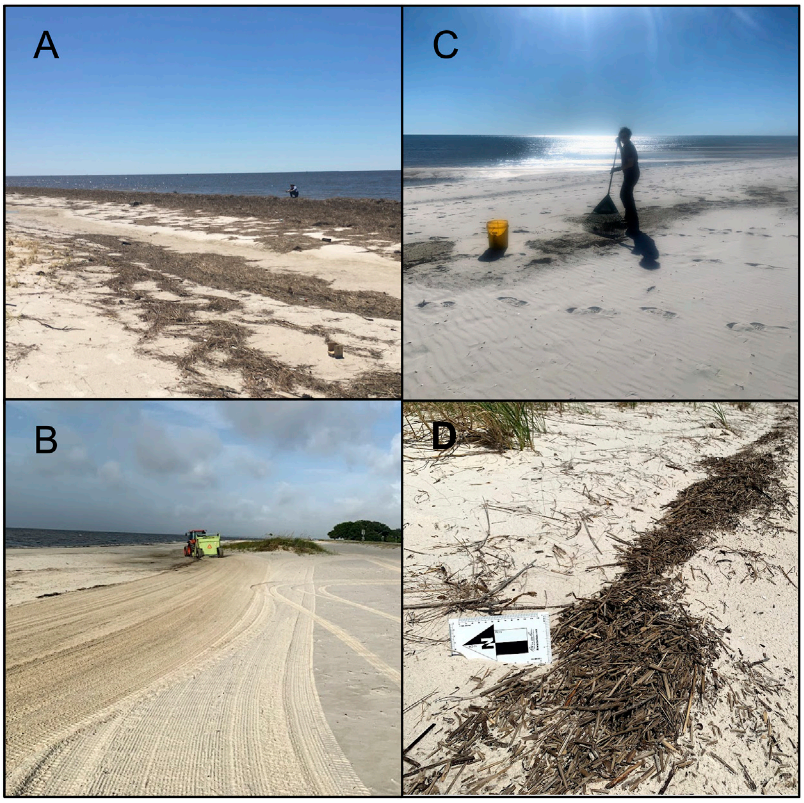

FIGURE 2
(A) Wrack observed at the field site on 12 June 2020. This large amount of marsh grass and other organic material was deposited during Tropical Storm Cristobal. **(B)** Beach grooming in progress at the field site, with visible rake lines and equipment. Photo taken September 1, 2020. **(C)** Gathering wrack from the berm for placement. **(D)** Wrack on the dune toe post-placement with sand gathering visibly on the seaward side.

was divided into three zones, each 183 m, with Zone 1 as the control, Zone 2 being left un-groomed, and Zone 3 both un-groomed and treated with wrack material (Figure 1). In addition to the study zones, each zone was further broken down into key geomorphological areas to allow changes to be observed separately in each sub-zone. These areas include the berm, the dune, and the ramp (the area between the dune and the seawall). The ramp area is often the site of aeolian ramp built up against the seawall (Figure 1), whose height is roughly 3 meters along this section of beach. Monitoring of the study location began in June of 2020 and is ongoing as of the publication of this paper. Monitoring of the study location began in June of 2020 and the final survey was conducted in 2022.

Field methods

Grooming practices

Beach grooming (or raking) is the processes of using mechanical equipment to remove debris from the beach. Grooming practices regularly performed by the county Sand Authority include using tractors to rake the beach between the water line and the dune toes. The beach is also raked between dune segments and behind the dunes up to the seawall. Beach grooming in the area occurs in order to keep the beach safe and accessible for beach-goers by clearing any trash that is deposited or debris that may wash ashore in addition to wrack (Figure 2). The frequency of grooming is typically associated with the frequency of wrack or debris deposition, which is variable by storm and most regularly seen during hurricane season (Figure 2A).

Zone 1, which begins at coordinates 89.27853W, 30.30473N and ends at coordinates 89.27663 W, 30.30509 N, was designated as the “Status-Quo” (i.e., existing state) control zone. In this section of beach, the standard beach grooming practices were allowed to continue. As such, the tractors are used to rake between the water line and the dune toe, between dune segments, and behind the dune (Figure 2B).

In Zones 2 and 3, grooming is limited to the berm only, and the rakes are not allowed to come into contact with the dune toe. Grooming is continued on the berm in these zones, as the county

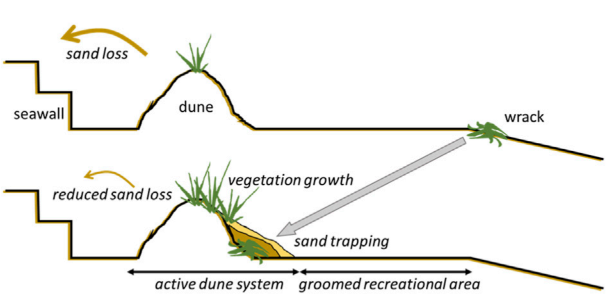

FIGURE 3
Diagram displaying typical wrack deposition location, and the placement location on a dune and expected behavior.

wishes to keep that portion clear of debris for beach-goers. Zone 2, beginning at the end of Zone 1 and ending at coordinates 89.27476 W, 30.30545 N, is considered the "No-Rake" zone. The area directly in front of, in-between, and behind the dunes will be left undisturbed. Zone 3 begins at the end of Zone 2 and ends at coordinates 89.27303, 30.30579 N. This zone was designated as the no-rake and treatment zone. In this zone, the dunes will again be left undisturbed and wrack material that is deposited will be placed at the dune toe. Signage was posted at the start and ends of each zone to indicate to raking crews the areas to avoid.

Wrack placement

In Zone 3, wrack material was collected and placed along the dune toe (Figures 2C). Wrack typically deposits on the seaward edge of the beach berm, and the goal was to move this material directly to the dune toe to enhance sand trapping and reduce problematic sand loss from the beach (Figures 2D, 3). Prior to beach grooming, conducted by the local sand beach authority, wrack material available at the wrack line on the berm was collected and cleared of non-organic debris and trash. The material was raked and gathered in 5-gallon buckets by hand, then transferred directly to the dune toe. Alongshore concentration of wrack placed on the toe was kept approximately the same as that originally deposited (i.e., wrack was moved from the wrack line directly to the toe without adding additional material per length of shoreline). The volume of wrack placed was tracked utilizing the 5-gallon buckets (0.023 m^3 each) (Figure 2C). Placement dates and volumes are recorded for comparison with storm events and survey times (Figure 4). In addition to wrack placements, the timeline also presents the dates of terrestrial lidar surveys, as well as storms which occurred during the study periods. Wrack placements were performed pending local site conditions and material availability.

Data collection

The data collection for this effort was supported by the US Army Corps of Engineers Coastal and Hydraulics Lab Field Data Collection and Analysis Branch (FDCAB) and the University of Southern Mississippi's Gulf Coast Geospatial Center (GCGC).

Survey methods

Beach and dune monitoring surveys using terrestrial Light Detection and Ranging (LiDAR) were conducted quarterly by the GCGC from October 2020 to January 2022 (Table 1), with the preliminary survey performed in June of 2020 by the FDCAB. A total of eight surveys were completed during this time, each collecting high-resolution LiDAR elevations across the entire study area. To ensure maximum precision and accuracy as well as

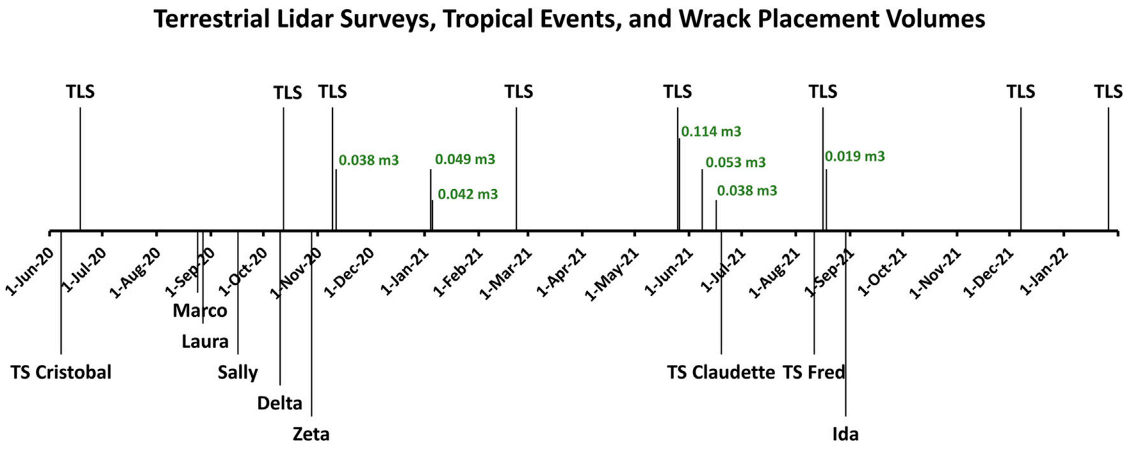

FIGURE 4
Project timeline depicting terrestrial lidar survey (TLS) dates, named storm events, and wrack treatments with the placed volumed.

TABLE 1 Survey dates, including beginning and end date for each full survey, and associated precisions/accuracies.

Dates	Resection horizontal precision (m)	Resection vertical precision (m)	Vertical distance of return from nearest measured benchmark height (m)			
			μ	σ	ΔMax	ΔMin
06/18/20[a]	-	-	-	-	-	-
10/06/20–10/07/20	0.005	0.008	-0.028	0.009	0.041	0.01
10/12/20–10/14/20	0.005	0.008	-0.012	0.016	-0.056	0
11/09/20–11/11/20	0.005	0.008	-0.021	0.011	-0.045	-0.004
02/22/21–02/24/21	0.005	0.012	0.003	0.019	0.053	0
05/24/21–05/26/21	0.007	0.012	-0.004	0.008	0.02	0.001
08/16/21–08/17/21	0.005	0.011	-0.0019	0.003	0.023	0.01
12/06/21–12/07/21	0.015	0.008	0.001	0.008	0.019	0.001
01/26/22–01/27/22	0.005	0.008	0.002	0.007	0.019	0

[a] Taken by FDCAB.

TABLE 2 Total Volume Change (m^3) in each geomorphological division and zone by survey date comparison. For each set of dates, the values are calculated by subtracting the temporally first date from the second so that positive values represent accretion, and negative represent erosion. The last row shows total volume change from first to last survey.

	Berm			Dune			Ramp		
	Zone 1	Zone 2	Zone 3	Zone 1	Zone 2	Zone 3	Zone 1	Zone 2	Zone 3
Jun ‘20 to Oct ‘20	-895.09	-908.86	-668.29	-263.48	-122.46	46.42	-87.33	-65.33	-76.92
Marco, Laura, Sally, Delta									
Oct ‘20 to Nov ‘20	233.55	358.2	418.55	-122.79	-260.69	-521.43	-19.67	-5.88	-1.83
Zeta									
Nov ‘20 to Feb ‘21	46.85	39.29	-72.15	77.40	111.58	73.28	19.80	22.50	20.12
Feb ‘21 to May ‘21	-282.61	-450.93	-324.09	-205.49	-147.26	0.68	-16.96	-65.95	-41.65
Thunderstorms									
May ‘21 to Aug ‘21	128.63	179.75	254.85	11.4	106.73	171.63	4.7	14.63	27.07
TS Claudette, TS Fred									
Aug ‘21 to Dec ‘21	330.07	162.73	272.15	-456.65	-584.5	-704.5	90.69	254.14	238.3
Ida									
Dec ‘21 to Jan ‘22	53.95	104.42	108.58	1.47	23.07	41.62	5.46	1.24	9.97
Jun ‘20 to Jan ‘22	-372.99	-348.59	-56.97	-958.53	-873.43	-892.5	-67.17	30.13	61.68
Total Change									

consistency among surveys, a control mark was established using a semi-permanently installed marker centrally located within the study site along the seawall (seawall face). An integrated approach of Global Navigation Satellite System (GNSS)/Total station surveying was used to establish LiDAR scan stations approximately 50 m apart along the seawall face and between the shoreline and dunes. A Trimble SX10 Scanning Total Station and 360 Prism were used for Electronic Distance Measurements (EDM), and a Trimble R10 was used for GNSS measurements (Trimble Inc., 2016). A single resection total station setup was performed using two GNSS measurements to establish the initial point of beginning

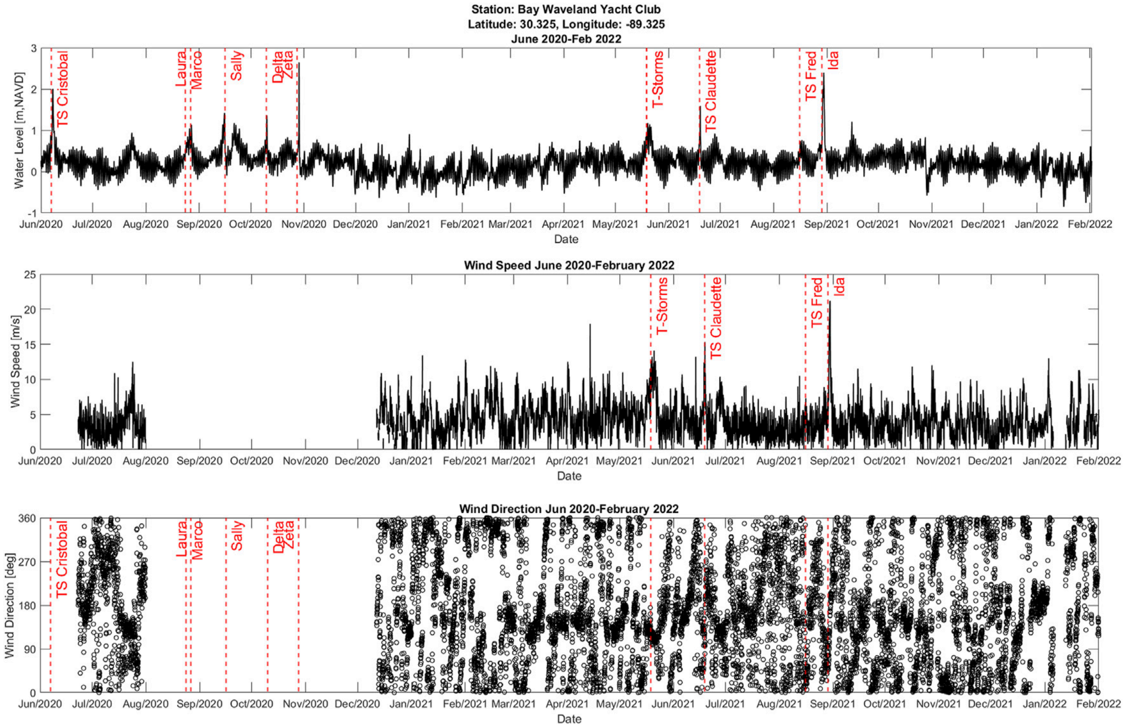

FIGURE 5
Water Level, wind speed, and wind direction time series from June 2020 to February 2022. Red dotted lines indicate storm events within recorded timeframe. NOAA Station 8747437 at the Bay Waveland Yacht Club, Bay St. Louis, MS, 30.325N, 89.325 W.

(POB) located at the site's established control mark for each monitoring survey. GNSS positions for the two resection measurements were corrected real time to ±2 cm horizontal and vertical precision using the University of Southern Mississippi Gulf Coast Geospatial Center Real Time Network (University of Southern Mississippi Gulf Coast Geospatial Center, 2022). All positions referenced the North American Datum 1983 (2011) and NAVD83. LiDAR scan stations were subsequently established along each survey face using EDM total station leveling. LiDAR scans were then collected to create a seamless point cloud of the study site for each complete survey.

Post processing

Post-processing of the scan data was completed in Trimble Business Center. All scan station setup positions were quality checked and accuracy assessments were performed on LiDAR point clouds. The vertical distance of twenty individual returns along the top of the seawall from two permanently encased benchmarks were measured to assess vertical error, with the ten closest returns to each benchmark assessed. The surface of the seawall was assumed to be of constant height surrounding each benchmark. Point clouds were colorized using panoramic photos obtained by the SX10 at time of each scan. Noise was removed and the point clouds were classified using Trimble Business Center's automated classification algorithm, with classes coded in accordance with American Society for Photogrammetry and Remote Sensing (ASPRS) Standard LiDAR Point Classes (Point Data Record Format 6–10) specified by LAS Format Version 1.4 (ASPRS - American Society for Photogrammetry & Remote Sensing, 2019). The classified point cloud was quality checked and adjusted using field panoramas. Classes included Ground, Low Vegetation, User Defined: Signage, Benches, Fencing, and Garbage Cans, and Debris. Positional accuracy of the final point cloud was validated based on two topographic control points measured at the permanent benchmarks along the seawall (Table 2). Finalized point clouds were exported in LAS v1.4 and projected to UTM Zone 16N in ArcGIS Pro.

Digital Elevation Models (DEMs) were created in ArcGIS Pro from the ground class of the post-processed point cloud at 0.2-m resolution using the mean of the ground values in each cell. Data voids were filled using a natural neighbor method. All finalized DEMs are referenced to NAVD88.

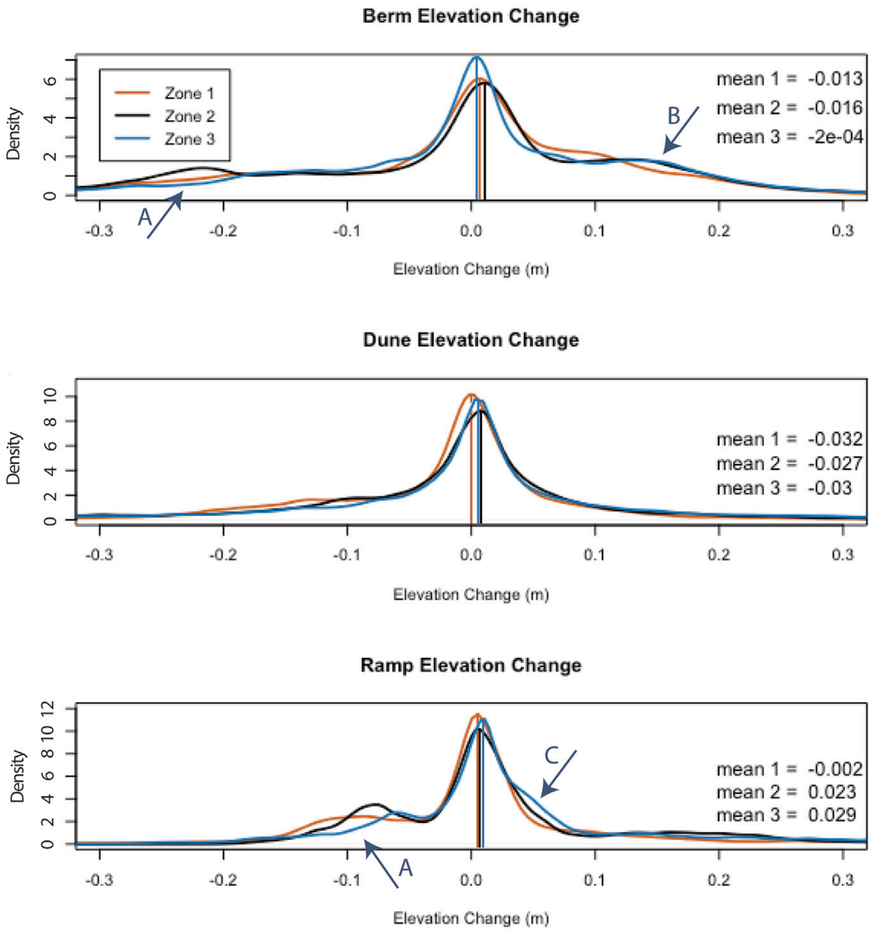

FIGURE 6
Probability density functions displaying the cumulative elevation change density over the entire study period in meters within the berm, dune, and ramp regions for each zone. The probability density functions show the shape of the frequency histogram for each dataset. Mode values are indicated by the vertical lines, and mean values are included on each plot. Arrows A: highlight a secondary mode in erosion. Arrow B: highlights a secondary mode in deposition. Arrow C: highlights skewness into deposition from the main mode.

Analysis methods

Each main zone (1–3) is divided into three polygons representing the major morphological sections in the cross shore, as previously mentioned (Figure 1). Elevation change is calculated by subtracting one DEM from another to produce an elevation change raster with the same cell size as the original DEMs. Positive changes are associated with accretion, whilst negative change is associated with erosion. Elevation changes within each polygon are summed to find the net volume change between the two survey dates. Two cross-shore profile transects from each zone are used to observe profile changes over the course of the study (Figure 1). In each zone, a profile crosses the center of a dune segment (Figure 1, red transect line), and the center of a gap between dune segments (Figure 1, yellow transect line). All elevation and elevation change values are represented in meters, and volumes are in meters cubed. Volumetric and profile analyses and their visualizations were conducted in ESRI ArcGIS Pro and Python in ArcGIS Pro.

Results

The influence of the wrack treatment and changes in beach grooming practices were evaluated by calculating volume changes in the berm, dune, and ramp of each zone as well as comparing profile shape and elevation changes between surveys. These results were considered relative to storm events and fair-weather periods between June 2020 and January 2022 (first and last survey dates).

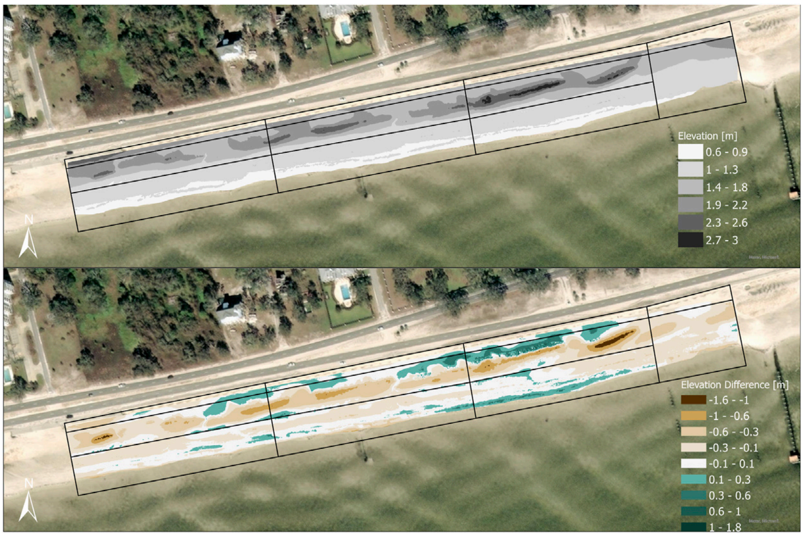

FIGURE 7
A (top): Elevation raster from the survey taken at the beginning of the study period. The survey was performed by the US Army Corps of Engineers Engineer Research and Development Center Field Data Collection and Analysis Branch, 18 June 2020. B (bottom): Elevation change between the initial survey on 18 June 2020 and final survey 26 Jan 2022. Positive values indicate accretion. All units in meters, NAVD88.

Water levels and winds

Nine named tropical cyclones and one notable thunderstorm system passed close enough to impact the site during the study period (Figure 4). The project site is located in a region protected by barrier islands. As such, hydrodynamics in this region varies from those in the open Gulf. To better understand local storm impacts, NOAA wind and water level data from a nearby station located slightly inside the mouth of the St. Louis Bay estuary (Figure 1, triangle) was used to observe changes during storm events impacting the survey area. Given the limited availability of station locations within the region protected by the barrier island, this station was selected for comparison though it is further inland than desirable. From this station, water level, wind speed and wind direction time series were developed for the length of the study (Figure 5). The NOAA station did not report wind data between August and mid-December of 2020, which excludes most of the 2020 hurricane season when some of the strongest storms impacted. Water level data was available for the entire study period, however, and provides some comparison between relative severity of all the events that impacted the area during this time (Figure 5, top).

Water level spikes appear during the passage of the tropical cyclones and the severe thunderstorms, with a peak water level of 2.64 m occurring during Hurricane Zeta's impact. The National Weather Service of New Orleans reported maximum wind gust speeds in the nearby city of Gulfport at 45 m/s. As demonstrated by the time-series, winds in the region are highly variable with no clear dominant direction, though densities of the scatter show that wind directions from between 90 and 180° (i.e., from the southeast, on-shore) may occur more frequently. Sustained wind speeds generally ranged between 0 and 10 m per second throughout the study period, but were occasionally exceeded, typically during weather-events such as the thunderstorm event, Tropical Storm Claudette, Tropical Storm Fred, and Hurricane Ida, with a maximum sustained wind speed during Hurricane Ida over 20 m/s. To further understand the variability of the wind data, the wind directions were sorted relative to the Beaufort Wind Scale (World Meteorological Organization and Commission for Maritime Meteorology, 1970) The Beaufort Wind Scale empirically classifies wind intensity based on condition observations. Using the range of wind speeds identified by the Beaufort Wind Scale, the time series data wind data was sorted into bins for each wind speed category to determine if dominate wind directions were associated with wind speed. From this, it was noted that in “calm” to “light breeze” conditions, i.e. wind speeds less than 3.1 m/s, wind direction varied greatly. However, in stronger wind conditions, with speeds greater than 3.1 m/s, a dominant direction from the southeast was evident, which is indicative of tropical events from the Gulf of Mexico being the most frequent source of elevated wind speeds.

Total LiDAR-Derived elevation change

All elevation change observations, including change values for each cell between each pair of surveys, are examined as distributions for each zone and geomorphological division

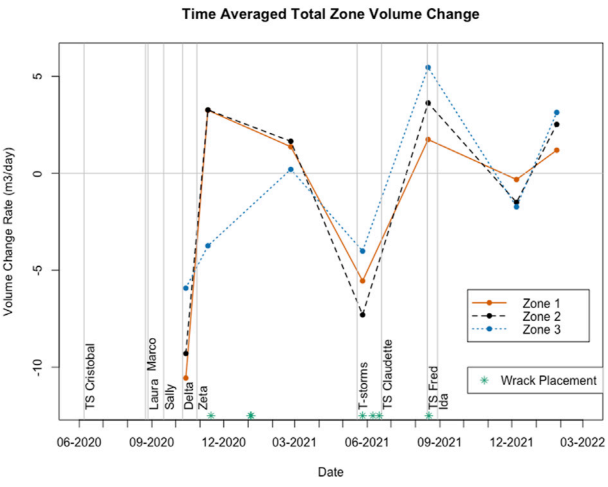

FIGURE 8
Total time-averaged volume change in each zone (Berm, dune, and ramp combined). The data point is plotted at the time of the second survey.

(Figure 6). A Mann-Whitney test compared all elevation change observations from Zones 2 and 3 (n = 1.82 million and n = 1.73 million respectively) individually with Zone 1 (n = 1.79 million). The null hypothesis that the elevation change distribution observed in Zones 2 and 3 is statistically the same as that of Zone 1 was rejected with 95% confidence in both cases, meaning that there is no evidence that the elevation changes observed in Zones 2 and 3 are statistically the same as those in Zone 1.

When broken into individual geomorphic zones, the elevation change mode values are consistently above zero in zones 2 and 3, with both slightly higher than that of zone 1 in the dune and the ramp. In the dune, the distributions are dominated by a single mode, with lower occurrence of erosion or deposition above 0.1 m compared with the berm and ramp. Within the dune, zones 2 and 3 show slightly positive modes, whereas zone 1 showed ~ 0 elevation change over the study period. Berm and ramp elevation change frequencies are also dominated by a single mode,but show small secondary modes in erosion and deposition. Zone 3 shows the smallest erosion signal in the berm and ramp (Figure 6, arrows A). Zone 3 also shows a higher frequency of deposition in the ramp at ~0.5 m (Figure 6, arrow C). Within the berm, zone 2 shows a peak in erosion and zones 2 and 3 both peak in deposition (Figure 6, arrow B).

Overall, the elevation change density distributions are dominated by peaks near zero elevation change or slightly above zero, indicating that the most cells experienced a net-zero or slightly net positive change over the entire study period. In the berm and dune, the mean values are slightly negative, indicating a negative skew. Only the ramp of zones 2 and 3 show slight positive means. The approximately zero dominant mode on all of these datasets does not reflect on the overall volume change, as lower frequencies in the larger deposition or erosion values can outweigh the mode value.

LiDAR-derived volume change

From the terrestrial lidar data, volumetric calculations between zones and their individual geomorphological areas (berm, dune, and ramp), Figure 1 were performed to quantify how sediment accretion and erosion varied between zones throughout the study period (Table 2). Elevation change rasters were created, and volume change was calculated from these between each survey, as well as between the first and last survey of the study period to find the total change (Figure 7; Table 2). Total volumetric change over the study period shows net erosion in the dune in all three zones, with the most occurring in Zone 1 (~960 m^3) and the least erosion occurring in Zone 2 (~870 m^3), the un-groomed and untreated zone (Figure 7, bottom). In the berm region, again net erosion occurred in all zones, with the greatest volume loss observed in Zone 1 (~370 m^3), and the smallest volume loss in Zone 3 (~60 m^3). In the ramp region, erosion occurred in Zone 1 (~70 m^3), however accretion occurred on the ramp in Zones 2 and 3, with a maximum volume gain of ~60 m^3 in Zone 3 (Figure 8).

A number of the survey comparisons captured storm events and offer unique insight into the grooming reduction and wrack treatments' potential ability to improve resiliency of the dune (Table 2). To account for variable periods of time between surveys, data is examined as net volume change but also volume change rate (Figure 8). The first survey comparison, between 18 June 2020 and 12 October 2020 captured the impacts of Hurricanes Marco, Laura, Sally, and Delta. Within these dates, all zones saw net erosion, and regions, with the exception of the Zone 3 dune, eroded (Figure 8, Table 2). During this period, in the berm, the smallest volume loss was observed in Zone 3 (~668 m^3). In the dune region, accretion occurred in Zone 3 (~46 m^3), and erosion occurred in Zones 1 and 2 however less erosion occurred in the ungroomed zone, Zone 2 (~263 m^3 and ~122 m^3). In the ramp region, erosion was seen in all zones, with the least erosion occurring in Zone 2 (~65 m^3).

Hurricane Zeta impacted the coast between the following two surveys, October 12th and November 9th of 2020. Hurricane Zeta brought the largest increase in water level (2.64 m) observed during the study period (Figure 5). During this time, accretion was seen in all zones in the berm region, with the greatest volume increase in Zone 3 (~420 m^3). This berm accretion was significant enough to lead to net volume increase during this period in Zones 1 and 2 (Figure 8, Table 2). Sediment loss, however, occurred in all zones of the dune region, with the most loss occurring in Zone 3 (loss of ~520 m^3), leading to a net loss in this zone overall. In the ramp region, erosion occurred in all zones as well, but sediment loss was minimal, ranging from ~20 m^3 to ~2 m^3.

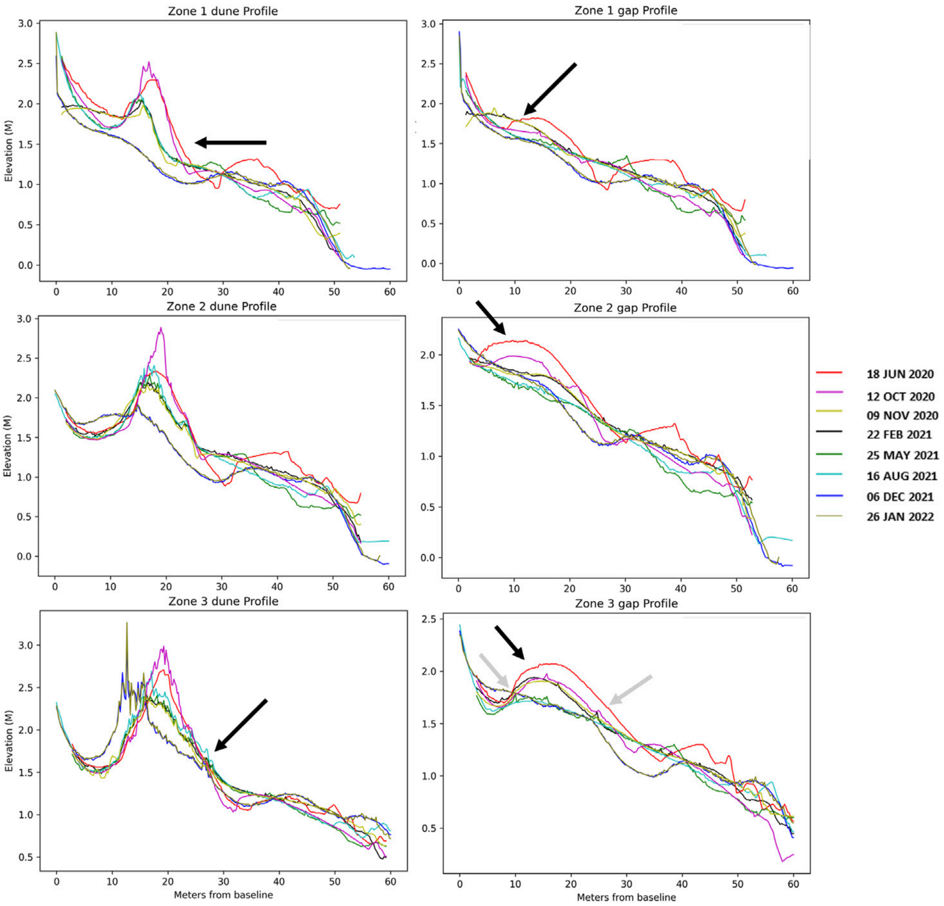

FIGURE 9

Elevation profiles at select transect locations (see Figure 2) showing changes in a dune and gap location in each zone. Seaward is to the right in all figures. Notable changes are highlighted in the figure with arrows.

Severe thunderstorms impacted the study area between the February and May surveys of 2021. These caused erosion in nearly all sections of all zones, with the maximum erosion occurring in the Zone 2 Berm (~450 m^3). Despite large volume loss in the dunes of Zone 1 and 2 (~200 m^3 and 150 m^3 respectively), the Zone 3 dune neither gained or lost significant volume (slight gain of 0.7 m^3).

Between the May and August surveys of 2021, Tropical Storms Claudette and Fred impacted, but no zones were eroded during this time. All zones experienced volume increases, with Zone 3 seeing the largest net volume increase observed during the study (Figure 8, Table 2). Volume gain was observed across all geomorphic areas, with a maximum gain in the berm, with Zone 3 gaining 250 m^3. The smallest volume gain for each geomorphological area was consistently observed in Zone 1, and the largest volume gain observed in Zone 3. In the dune, for example, Zone 3 gained fifteen times more sediment than Zone 1.

Hurricane Ida brought the second largest surge and second highest wind speeds to the area during the study period. This impact was captured between the August and December surveys of 2021, with all zones losing volume (Figure 8, Table 2). The greatest volume loss observed was in the dune of Zone 3 with >700 m^3 eroded, and the greatest dune volume loss observed throughout all individual survey differences. In contrast to this dune erosion, the berm and ramp both saw accretion in all zones.

Two periods between surveys did not receive a notable event; November 2020 to February 2021, and December 2021 to January 2022. These fair weather periods should allow time for the beach and dunes to naturally accrete sediment, *via* wave delivery to the beach and aeolian transport into the dunes. During the first period, between 9 November 2020 and 22 February 2021, minor deposition occurred across most areas, with a maximum gain of ~100 m^3 in the Zone 2 dune. This is the largest dune volume gain observed in the study. ~70 m^3 of sediment was lost from the Zone 3 berm, while minimal gains were observed in the other berm zones.

During the second recovery period, between 6 December 2021 and 26 January 2022, all regions within all zones saw accretion. Within both the dune and ramp region, Zone 3 saw the largest accretion. The largest volume gains within each zone was observed in the berm, with the largest in Zone 3 with a ~100 m^3 increase. Moderate volume increases in the dune and ramp were observed, with most below 10 m^3, but Zones 2 and 3 gained ~20 and ~40 m^3 respectively in the dune.

LiDAR-derived cross-shore profiles

Elevation profiles are plotted for select dune and dune "gap" (spaces between dune segments) transects (Figure 9). These comparisons provide context for the volume change results, with morphological changes resulting from dune erosion or accretion appearing clearly in the profile change.

Over the study period, the Zone 1 dune profile lost significant elevation in the dune itself, and the dune toe retreated significantly (Figure 9, Zone 1 dune profile arrow). There is slight erosion at the toe of the dune between June 2020 and October 2020, followed by significant erosion of the dune face during Hurricane Zeta as evident by the November 2020 survey. There is little change between November 2020 at the dune face during the passage of Tropical Storms Claudette and Fred in the summer of 2021. The dune along this transect is then nearly completely flattened by December 2021, during the time slice encompassing the Hurricane Ida impact. Though a number of months passed between Ida's impact and the following survey, no other significant erosional events occurred during this window. Site visits to the area confirmed that the significant erosion observed during this time was caused by Hurricane Ida. As such, the majority of change which occurred during that time is attributed to that event.

The dune profile in Zone 3 shows a different response from that of Zone 1. Zone 3 received wrack placements to the toe, and raking was limited. The dune maintains elevation over the course of the study, and the dune toe remains relatively stationary in contrast with the significant retreat observed in Zone 1. Some seaward dune expansion is observed, which does not occur during any periods in the Zone 2 or Zone 1 dune profiles (Figure 9, Zone 3 dune profile, black arrow). There is elevation loss in the dune crest during the October to November 2020 period, encompassing Hurricane Zeta's impact, as well as the August to December 2021 period, including Hurricane Ida. The dune crest (the highest point on the dune) and the dune heel (the landward edge of the dune) move landward with each of these events.

In the Zone 2 where wrack was not placed, but raking was limited, the dune did not retain as much elevation as Zone 3, however, it retained more than its raked counterpart. Clear elevation changes in the dune face are still limited to October to November 2020 and August to December 2021; Hurricane Zeta and Hurricane Ida. Similar to Zone 3, the dune toe remains stable through Hurricane Zeta's passage, however, the toe does retreat significantly, and the dune appears to be completely flattened by December 2021, after Hurricane Ida.

Alternatively, transects taken between the dune segments, or "gaps" were compared. In all zones there are noticeable changes in elevation over time near the landward limit of the profiles. The initial profiles in all zones (June 2020) show a similar feature, highlighted by black arrows. By the end of the study, the gap profiles all approach a flat slope. This flattening occurred most rapidly in Zone 1, whereas in Zone 2 elevation was maintained until November of 2020. In Zone 3 however, much more of the elevation remained until May of 2020. Within Zone 3 as well, as indicated by the left-most gray arrow, the profile regained some volume, shown by the slight change between the pink line representing the October 2020 survey, *versus* the yellow and black lines, from the November 2020 and February 2021 surveys. The right-most gray arrow indicates a slight elevation increase on the seaward side of the gap. Overall, from the transect profiles provided, the starkest difference in elevation change was seen in Zone 1.

Discussion

Results presented in this manuscript demonstrate morphological changes to the beach over a duration of approximately 19 months. Notable results can be summarized by the following:

- A net volume increase over the entire study period was only observed in the ramp of Zones 2 and 3. Although volume was lost from the dunes in all zones, the greatest net volume loss was observed in the dune of Zone 1.
- Major events that brought the highest surges, Hurricane Zeta and Hurricane Ida, contributed to large volume loss across all zones, but the Zone 3 dune remained intact, and the dune toe remained stable throughout the entire study period. In contrast, both the Zone 1 and Zone 2 dune was completely flattened after Hurricane Ida (Figure 9).
- Through the unprecedented 2020 hurricane season, all storms caused notable volume changes, but not all storms caused net erosion. The response is complicated, suggesting that some events even lead to significant net deposition, particularly on the berm. The relatively minor events even contributed volume to the dunes in some cases (Table 2).

Dune resiliency is imperative for coastal infrastructure protection as well as the preservation of ecological benefits of a healthy beach and dune system (Hemminga & Nieuwenhuize, 1990; Dugan, 1999; Dugan & Hubbard, 2010). This manuscript provides an overview of preliminary monitoring results from the trial of alternative management strategies on a constructed beach and dune system. Results suggest that a reduction in beach grooming, and the incorporation of natural wrack material into the dune system can encourage natural resilience even in the face of major hurricane impacts and may reduce sand volume loss in the long term.

Although the net change over the full study period is erosive in most areas, and modal elevation change observations always hover around 0 (Table 2; Figure 6), Zones 2 and 3 separate themselves from Zone 1 on the deposition side of the distribution, especially in the Berm and the Ramp. Volume change and profile data from individual storm and fair-weather periods throughout the study also come together to clearly illustrate the impact of the reduced grooming practices in Zones 2 and 3, and possible impacts of wrack placement. Considering volume changes alone, Zones 2 and 3 consistently fared better than Zone 1 during the relatively minor tropical events, including Hurricanes Marco, Laura, Sally, and Delta as well as Tropical Storms Claudette and Fred.

The larger impacts, from Hurricanes Zeta and Ida, brought a much larger surge. Hurricane Zeta was the first event of the season, and likely the first event in many years, that completely overtopped all the dune crests. The highest dunes in the study area before Zeta were in Zone 3 at ~3 m NAVD 88, the seawall height in the area is ~3 m NAVD88 and the surge during Zeta reached 2.6 m. This surge with additional waves on top easily eroded the dune crests across the study site, whereas previous events were only able to scarp these highest dunes (e.g., Tropical Storm Cristobal). Dunes in Zones 2 and 3 were eroded down to a similar elevation with those in Zone 1 during Zeta (Figure 9). Zone 3 dunes were able to maintain dune crest elevation even through hurricane Ida, which mostly flattened the dunes of Zone 1 and 2 (Figure 9). Although these large events led to more dune volume loss in the zones with reduced raking, these dunes were initially much higher so had more volume to lose and maintained some dune-crest elevation and a relatively stationary dune toe, while the continually raked dunes were flattened and de-stabilized.

Overall, Zone 3 dunes were also able to maintain and transfer some of their volume landward, while raking in Zone 1 likely re-distributed this material after one grooming. This pattern of distributing volume landward is also evident in the elevation differences provided by Figure 7. Like the cross-shore profiles, the LiDAR image representing elevation change demonstrates a reduction in elevation at the dunes, with an elevation gain immediately behind the dune segments, suggesting an overall migration of the material inland.

The stability of the Zone 3 dune during both Zeta and Ida suggests that not only the reduction in raking, but the addition of wrack material had an impact. Both un-raked zones maintained a stationary dune toe during Hurricane Zeta, but only Zone 3 (un-raked and with added wrack) maintained a stationary dune toe during Ida as well. The added wrack material on the toe even led to slight dune toe progradation/accretion in Zone 3 during the fair-weather period following Zeta (Figure 9). The wrack material was observed to begin trapping sand shortly after placement both on the dune toe, and in the gaps between dunes. The gaps between dune segments focus the wave and surge energy during high water events, leading to lobate wash over fan deposition. These fans show up as the broad rounded features visible in the profiles. Accretion on the placed wrack-line is visible in the gap transect for Zone 3, and this added material likely led to the greater stability of the fan feature in Zone 3 (Figure 9, Zone 3 gap Profile, gray arrow). However, though the wrack placements are evident in the transect profiles, it is critical to note that overall accretional changes within Zone 3 could also be due to the dunes in Zone 3 having been more established dune systems at the inception of the study, thus existing vegetation and biomass within the system may play a larger role it its ability to trap sediment.

With increased dune toe stability, and greater maintenance of dune crest elevation in the un-raked zones as well as visible deposition on the placed wrack line of Zone 3, the benefits of these practices are clear. If these practices were put in place long term, especially during years with fewer major hurricane impacts, the benefits would likely compound, leading to larger and more stable dunes in areas with reduced raking and added wrack biomass.

Wind and hydrodynamics

The nearshore environment is incredibly complex with regard to both hydrodynamic and geomorphologic behavior. Wind dynamics are critical in evaluating aeolian transport, however, due to lack of data, several storm events, including hurricanes Laura, Marco, Sally, Delta and Zeta, could not be explicitly compared with survey results, and as such comparisons with those storms were investigated from a hydrodynamic standpoint. As mentioned previously, the hydrodynamic data referenced, was recorded at an inland bay, and as such still does not offer full insight to the site hydrodynamics such as wave height and direction, at the project site and only water level alone could be evaluated. Though greater wind speeds were associated with directions from the southeast, day to day winds varied greatly, which may have contributed to the variability in accretive trends associated with the recovery periods. Improved wind and hydrodynamic data availability on this coastline, would be of great benefit to improving interpretation of both this and similar monitoring studies, especially considering the complexities provided by the barrier islands protecting the region.

Limitations of the zone approach

By dividing the site into zones and geomorphologic segments, a broader picture of the physical processes occurring throughout the study duration can be lost. For example, some survey results demonstrated erosion at the dune region, even in the treated zone. However, as water inundated the region, it is anticipated that though erosion is occurring at the dune, there is a net transport of sediment onshore. This is evident in the results displayed comparing profiles before and after Hurricane Ida, between August 16th of 2021 and December 6th of 2021. As noted in Table 2, volumetrically, Zone 3 in the dune region saw a loss of ~705 m^3 of material, whilst the ramp region is Zone 3, saw accretion of ~240 m^3. Observational data taken during a site visit following the passage of Ida noted volumes of sand further along the sea wall and into the roadway area, suggesting additional material potentially was transported well beyond the cross-shore measured in the study region. This pattern of inland transport may contribute to larger accretive changes occurring directly behind the dune segments, while the dunes showed erosion across each zone (Figure 7, bottom).

It is also probable wind and wave direction played a large role in lateral transport. As previously mentioned, wind and wave data were limited, however this trend can again be seen in the comparison of surveys taken before and after Hurricane Ida between August and December of 2021. In this case, Zone 3 saw greater volumes of sediment erosion compared to Zones 1 and 2. This potentially suggests a transport of material along shore from Zone 3, into Zones 1 and 2. However, as noted previously larger erosion of Zone 3 may also be attributed to a larger starting elevation of the dunes in that zone.

Following analysis of the terrestrial lidar data, evidence in the survey collected in January of 2022 suggests that prior to this survey, raking may have occurred in the no-raking zone of the study area. This largely may have been due to beach signage being washed away following Hurricane Ida, thus the study zones were not as clearly indicated to grooming crews. No evidence of raking in the no-rake zones were found in the previous survey results, given the authors were not present during grooming there is the potential it may have occasionally occurred, especially if it was a matter of maintaining beach safety in the region.

Wrack placement and field site limitations

Being a field study, a variety of environmental, as well as social factors can occur throughout the experiment, impacting its implementation. As noted in Figure 4, seven wrack placements occurred throughout the study period, one in November of 2020, two in early January of 2021, and the remainder in the summer of 2021. Though the volumes of wrack placed throughout the study were low relative to volumes accumulated on the beach, the material that was placed is notable regarding the alternative methods of biomass development including dune plantings. In placing wrack material, though most is dead vegetation, biomass is incorporated into the dune system instantaneously, whereas the same level of biomass could take years to establish through root growth on its own. As noted, total volume change varied greatly across the study area, however, the treated zone saw a greater positive volume change in the zone entirety by the final survey.

Wrack placement was impacted by several factors, including availability of material as well as beach accessibility following severe events. As an example, Hurricane Ida not only brought a significant surge to the area, resulting in road closures, but damages in surrounding areas resulted in an influx of people to the area in search of gasoline and food, ultimately resulting in severe traffic. Furthermore, though copious amounts of wrack material often accumulated during severe weather events, not all material could be placed at the dune. In many cases, hazardous debris (i.e. scrap material such as wood with nails) was incorporated in the material and required removal to maintain safe beach conditions, or the wrack material was washed inland beyond the seawall and road. As such, though large amounts of wrack accumulated during storms, not all material could be placed at the dune toe.

Summary

Sandy coastal environments invoke complex hydrodynamic and geomorphological processes. This study serves to document a new nature-based management practice of placing wrack on existing constructed dunes. Additionally, reduction in beach grooming around the dunes is considered. Deposition and erosion patterns varied in a complex way through storm events and across the study area. Clear differences emerged in the response of dunes in the zones with reduced grooming and with added wrack material, both to storm impacts and the fair-weather periods between them.

To further understand the response of wrack to dune resiliency, it is suggested that monitoring data of treatments be expanded both spatially and temporally. Incorporating a longer test section of coast, as well as varying coastal locations, could contribute to understanding of how wrack placements and reduced grooming affect the dunes and the beach profile. In addition, longer temporal datasets may provide additional insight into wrack-placement-specific benefits, as well as offer more insight into whether sediment processes are altered primarily by wrack placements or by the alteration in grooming patterns.

Data availability statement

The raw data supporting the conclusions of this article will be made available by the authors, without undue reservation.

Author contributions

All authors listed have made a substantial, direct, and intellectual contribution to the work and approved it for publication.

Funding

This work was funded through the US Army Corps of Engineers Regional Sediment Management Program, research task “Field Implementation of Belowground Biomass (BGB) for Increased Dune Stability and Resiliency”.

Acknowledgments

The authors would like to acknowledge and thank the USACE Mobile District and the Harrison County Sand Beach authority for both their permission in executing this effort, as well as their involvement and assistance in its successful execution.

Conflict of interest

The authors declare that the research was conducted in the absence of any commercial or financial relationships that could be construed as a potential conflict of interest.

Publisher’s note

References

ASPRS - American Society for Photogrammetry & Remote Sensing. (2019). LAS specification 1.4-R14 release information. November 2011, 1–50. Available at: http://www.asprs.org/wp-content/uploads/2019/03/LAS_1_4_r14.pdf.

Berg, R. (2021). National hurricane center tropical cyclone report: Tropical storm cristobal (AL032020). National hurricane center. Available at: https://www.nhc.noaa.gov/data/tcr/AL032020_Cristobal.pdf.

Blumberg, A. F., Ahsan, Q., Li, H., Kaluarachchi, I. D., and Lewis, J. K. (2001). “Circulation, sediment and water quality modeling in the northern Gulf of Mexico,” in World Water and Environmental Resources Congress, ASCE, Orlando, Florida, May 20–24 2001. doi:10.1061/40569(2001)257

Borsje, B. W., van Wesenbeeck, B. K., Dekker, F., Paalvast, P., Bouma, T. J., van Katwijk, M. M., et al. (2011). How ecological engineering can serve in coastal protection. *Ecol. Eng.* 37, 113–122. doi:10.1016/j.ecoleng.2010.11.027

Bryant, D. B., Bryant, M. A., and Grzegorzewski, A. S. (2017). *Erosion of coastal foredunes: A review on the effect of dune vegetation*. (Vicksburg, MS: U.S. Army Engineer Research and Development Center). ERDC/CHL CHETN-I-94. doi:10.21079/11681/21464

Bryant, D. B., Bryant, M. A., Sharp, J. A., Bell, G. L., and Moore, C. (2019). The response of vegetated dunes to wave attack. *Coast. Eng.* 152, 103506. doi:10.1016/j.coastaleng.2019.103506

Bryant, D., Hoch, C., Provost, L., Bell, G., and Bryant, M. (2019). The role of belowground biomass on short term dune evolution. *Coast. Sediments* 2019, 1188–1202.

Byrnes, M. R., Rosati, J. D., Griffee, S. F., and Berlinghoff, J. L. (2013). “Historical sediment transport pathways and quantities for determining an operational sediment budget: Mississippi sound barrier islands,” in *Understanding and predicting change in the coastal ecosystems of the northern Gulf of Mexico*. Editors J. C. Brock, J. A. Barras, and S. J. Williams (Charlotte, NC: Coastal Education & Research Foundation), 63, 166–183. Coconut Creek (Florida), ISSN 0749-0208.

Cipriani, L. E., and Stone, G. W. (2001). Net Longshore Sediment Transport and Textural Ch iments along the Southwest Alabama and Mississippi Barrier Islands, U.S.A. *J. Coast* 17, 458. West Palm Beach (Florida), ISSN 0749–0208.

Dugan, J. (1999). *Utilization of sandy beaches by shorebirds: Relationships to population characteristics of macrofauna prey species and beach morphodynamics*. Santa Barbara, California: Coastal Research Center, Marine Science Institute, University of California. MMS OCS Study 99–0069.

Dugan, J. E., and Hubbard, D. M. (2010). Loss of coastal strand habitat in Southern California: The role of beach grooming. *Estuaries Coasts* 33, 67–77. doi:10.1007/s12237-009-9239-8

Dugan, J. E., Hubbard, D. M., McCrary, M. D., and Pierson, M. O. (2003). The response of macrofauna communities and shorebirds to macrophyte wrack subsidies on exposed sandy beaches of Southern California. *Estuar. Coast. Shelf Sci.* 58, 25–40. doi:10.1016/s0272-7714(03)00045-3

Duggins, D. O., Simenstad, C. A., and Estes, J. A. (1989). Magnification of secondary production by kelp detritus in coastal marine ecosystems. *Science* 245 (4914), 170–173. PMID: 17787876. doi:10.1126/science.245.4914.170

Elias, S. P., Fraser, J. D., and Buckley, P. A. (2000). Piping Plover Brood Foraging Ecology on New York Barrier Islands. *J. Wildl. Manag.* 64 (2), 346–354. doi:10.2307/3803232

Godfrey, P. (1977). J.: Climate, plant response and development of dunes on barrier beaches along the US East Coast. *Int. J. Biometeorol.* 21, 203–216. doi:10.1007/bf01552874

Hancock County Historical Society. (2022). Vertical Files - Beach History. Available at: http://www.hancockcountyhistoricalsociety.com/reference/vf.php?t=subjects&vf=Beach%20History. [Accessed October 28, 2019].

Hanley, M. E., Hoggart, S. P. G., Simmonds, D. J., Bichot, A., Colangelo, M. A., Bozzeda, F., et al. (2014). Shifting sands? Coastal protection by sand banks, beaches, and dunes. *Coast. Eng.* 87, 136–146. doi:10.1016/j.coastaleng.2013.10.020

Harrison, P. G., and Mann, K. H. (1975). Detritus formation from eel-grass (Zostera marina L.): the relative effects of fragmentation, leaching and decay. *Limnol. Oceanogr.* 20, 924–934. doi:10.4319/lo.1975.20.6.0924

Heerhartz, S. M., Toft, J. D., Cordell, J. R., Dethier, M. N., and Ogston, A. S. (2016). Shoreline Armoring in an Estuary Constrains Wrack-Associated Invertebrate Communities. *Estuaries Coasts* 39, 171–188. doi:10.1007/s12237-015-9983-x

Hemminga, M. A., and Nieuwenhuize, J. (1990). Seagrass wrack-induced dune formation on a tropical coast (Banc d'Arguin, Mauritania). *Estuar. Coast. Shelf Sci.* 31, 499–502. doi:10.1016/0272-7714(90)90040-x

Hooton, N., Miller, D. L., Thetford, M., and Claypool, S. (2020). Building Coastal Dunes with Sea Oats and Surrogate Wrack: WEC364/UW409, 2/2016. *EDIS* 2016 (7), 4. Available at: https://journals.flvc.org/edis/article/view/128002.

Martínez, M. L., Psuty, N. P., and Lubke, R. A. (2004). "A perspective on coastal dunes," in *Coastal dunes: Ecology and conservation,*. Editors M. L. Martínez, N. P. Psuty, and R. A. Lubke (Berlin: Springer), 3–10.

NOAA. (2022). Historical Hurricane Tracks. Available at: https://coast.noaa.gov/hurricanes/#map=4/32/-80 (Accessed June 2022).

NOAA. (2020). Tropical Cyclone Climatology. Available at: https://www.nhc.noaa.gov/climo/ (Accessed June 2022).

Orr, M., Zimmer, M., Jelinski, D. M., and Mews, M. (2005). Wrack deposition on different beach types: spatial and temporal variation in the pattern of subsidy. *Ecology* 86 (6), 1496–1507. doi:10.1890/04-1486

Provost, L. A., Bryant, M. A., Eisemann, E. R., and Bryant, D. B. (2022). *Coastal resilience: Benefits of wrack and dune systems and current management practices.* ERDC/TN RSM-22-6. (Vicksburg, MS: U.S. Army Engineer Research and Development Center). doi:10.21079/11681/45282

Schmid, K. (2002). *Biennial report of sand beaches; Harrison county. 2001*. (United States: Mississippi Office of Geology), 33. Open-File Report 111B.

Sigren, J. M., Figlus, J., and Armitage, A. R. (2015). Coastal sand dunes and dune vegetation: Restoration, erosion, and storm protection. *Shore Beach* 82 (4), 5–12.

Trimble Inc. (2016). Datasheet - Trimble SX10 Scanning Total Station. Available at: https://geospatial.trimble.com/sites/geospatial.trimble.com/files/2019-10/Datasheet-SX10ScanningTotalStation-EnglishUSL-Screen.pdf.

University of Southern Mississippi Gulf Coast Geospatial Center (USM GCGC). (2022). GCGC Real Time Network. Available at: www.rtn.usm.edu.

World Meteorological OrganizationCommission for Maritime Meteorology (1970). *The Beaufort scale of wind force : (technical and operational aspects).* Geneva: WMO.

Frontiers in
Built Environment

Innovations in the engineering of sustainable buildings, cities, and urban spaces

An innovative journal that advances our knowledge of civil engineering. It focuses on the development of sustainable methodologies for the design and management of resilient buildings and infrastructure.

Discover the latest Research Topics

See more →

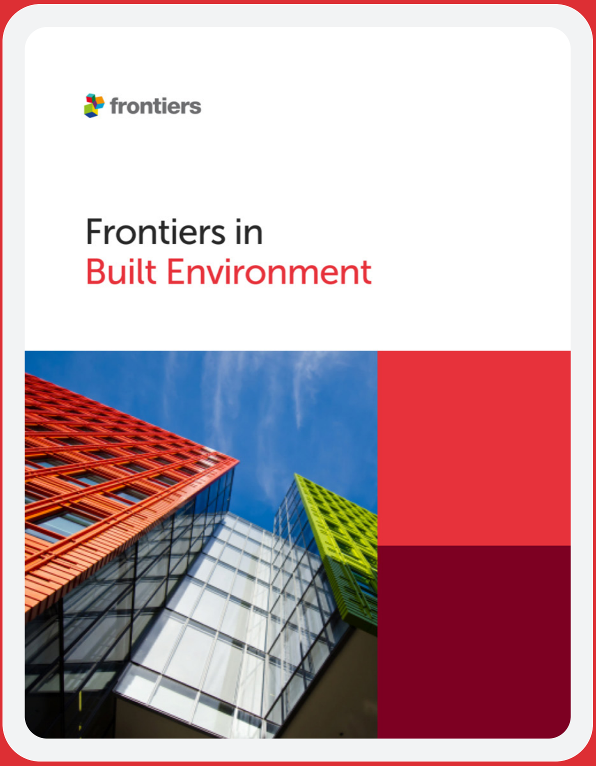
frontiers

Frontiers in
Built Environment

Frontiers

Avenue du Tribunal-Fédéral 34
1005 Lausanne, Switzerland
frontiersin.org

Contact us

+41 (0)21 510 17 00
frontiersin.org/about/contact